Thermomechanical Behavior of Advanced Manufactured Parts, Subcomponents, and Their Weldments for Gen3 CSP

Chad Augustine,[1] Julian D. Osorio,[1] Judith Vidal,[1] Youyang Zhao,[1] Zhenzhen Yu,[2] Timothy Pickle,[2] Abdelrahman Abdelmotagaly,[2] Wei Zhang,[3] Xuesong Gao,[3] Edgar Vidal,[4] Jeremy Iten,[5] and Ben Rafferty[5]

1 National Renewable Energy Laboratory
2 Colorado School of Mines
3 Ohio State University
4 NobelClad
5 Elementum 3D

Thermomechanical Behavior of Advanced Manufactured Parts, Subcomponents, and Their Weldments for Gen3 CSP

Chad Augustine,[1] Julian D. Osorio,[1] Judith Vidal,[1] Youyang Zhao,[1] Zhenzhen Yu,[2] Timothy Pickle,[2] Abdelrahman Abdelmotagaly,[2] Wei Zhang,[3] Xuesong Gao,[3] Edgar Vidal,[4] Jeremy Iten,[5] and Ben Rafferty[5]

1 National Renewable Energy Laboratory
2 Colorado School of Mines
3 Ohio State University
4 NobelClad
5 Elementum 3D

Preface

Agency/Office/Program	DOE/EERE/Solar Energy Technologies Office	
Award Number	DE-EE00036334	
Project Title	Thermomechanical Behavior of Advanced Manufactured Parts, Subcomponents, and Their Weldments for Gen3 CSP	
Principal Investigator	Dr. Chad Augustine Senior Analyst	
Technical Contact	Dr. Julian D. Osorio Julian.Osorio@nrel.gov	
Business Contact	Dr. Craig Turchi Thermal Energy Systems Group Manager Craig.Turchi@nrel.gov	
Submission Date	6/30/2024	
DUNS Number	8059480510000	
Recipient Organization	National Renewable Energy Laboratory	
Project Period	**Start:** 02/01/2020	**End:** 6/30/2024
Project Budget	Total $2,536,665 (DOE: $2,029,332; C/S: $507,333)	
Submitting Official Signature		

Acknowledgments

Acronyms

ASME	American Society of Mechanical Engineering
AWS	American Welding Society
BCC	body-centered cubic
CSM	Colorado School of Mines
CSP	concentrating solar power
CWJCR	Center for Welding, Joining, and Coatings Research
DED	directed energy deposition
DOE	U.S. Department of Energy
DSW	dissimilar welding
EBAM	electron beam additive manufacturing
EBSD	electron backscatter diffraction
EDS	electron dispersive spectroscopy
EXW	explosion welding
FCAW	flux core arc welding
FEA	finite element analysis
FEM	finite element model
FZ	fusion zone
GB	grain boundary
GMAW	gas metal arc welding
HAZ	heat affected zone
HEA	high entropy alloys
h	hour
IPF	inverse pole figure
in	inch
LD	longitudinal direction
LMP	Larson Miller Parameter
LOM	light optical microscope
L-PBF	laser-powder bed fusion
max	maximum
min	minute
MPEA	multi-principal element alloys

ND	normal direction
NDE	non-destructive evaluation
NREL	National Renewable Energy Laboratory
ORNL	Oak Ridge National Energy Laboratory
PA-UT	phased array-ultrasonic testing
PMZ	partially melted zone
PWHT	post weld heat treatment
RT	room temperature
SAC	strain age cracking
SEI	secondary electron image
SEM	scanning electron microscope
SRC	stress relaxation cracking
SS	stainless steel
TD	transverse direction
TEA	techno-economic analysis
TES	thermal energy storage
UTS	ultimate tensile strength
YS	yield strength
WM	weld metal

Executive Summary

Generation 3 (Gen3) concentrating solar power (CSP) plants may require the use of molten chloride salt storage systems, solar receivers, and supercritical-CO_2 primary heat exchangers (PHXs). The temperatures that would be expected in these parts and subcomponents could approach 760°C for the hot side and as low as 500°C for the cold side at peak operating conditions. With the design limitations, highly corrosion- and creep-resistant alloys are needed to maximize component lives. In this project, creep enhanced ferritic alloy Grade 91, austenitic stainless-steel (SS) 304H, Ni claddings Ni201 and C22, and nickel-based superalloys Inconel 740H and Haynes 282 and 230 were evaluated for potential applications in Gen3 CSP systems. We investigated advanced manufacturing of these parts, subcomponents, and their welds and conducted a full techno-economic analysis in comparison to conventional manufacturing techniques. The manufacturing techniques explored are explosion clad welding and combustion synthesis/combustion reaction for transfer pipes; additive manufacturing (AM), including laser-powder bed fusion (L-PBF) and electron beam AM (EBAM) with wire feedstock for PHX and solar receivers; and conventional fusion welding for similar and dissimilar joining of these various parts and subcomponents. The key takeaways from each advanced technology, including thermomechanical behavior and techno-economic analysis (TEA) of the corresponding fabricated parts and components, are summarized below.

Explosion Welding (EXW) for Hot and Cold Clad Pipes

1. With respect to thermomechanical behavior, both SS 304H and Gr 91 as mechanical backers meet the property requirements (>80% of backer strength). SS 304H cladded with C22 has the best mechanical properties at room and service temperatures compared to the other candidates.

2. Ni201 is not recommended as a cladder alloy for this application, because it deteriorates the mechanical properties of its cladded plates compared to the C22 alloy.

3. The nominal chemical composition of the clad layer is preserved after explosion cladding and arc welding with a matching filler to the clad, which is important to maintain the corrosion resistance of the explosion cladded pipes at the same level as the clad alloy.

4. Depending on market prices, the option of using a nickel-alloy cladder in the hot loop (720°C) is a viable alternative. At time of publication, the price of nickel in the market is depressed, which does not make cladding favorable, but this could change with an increase in demand of this metal (e.g., battery demand).

Additive Manufacturing (AM) Technologies for PHX and Solar Receivers

1. The process parameters used in this study for wire-feed EBAM with Haynes 282 and 230 need further optimization to reduce keyhole defects and cracking, respectively, and potentially enhance the mechanical strength.

2. L-PBF of Haynes 282 is demonstrated to be effective and beneficial for complex PHX design based on thermomechanical, weldability, corrosion, and isothermal fatigue testing.

Similar and Dissimilar Welding

1. Gas tungsten arc welding (GTAW) of L-PBF components to wrought ones requires modification of weld procedures from what is recommended for wrought materials due to the molten fluid flow behavior changes associated with absorption of surface-active elements during L-PBF. Weld discontinuities may be expected at the similar L-PBF-to-wrought welds, which could be mitigated with a higher weld current (e.g., 180 vs.150 amperes) within the supplier-recommended weld current range for Haynes 282.

2. Regarding dissimilar welding (DSW) of Haynes 282 and Inconel 740H to 304H SS, respectively, the failure location occurs consistently on the weaker 304H SS side of the weld joint—namely, in the heat affected zone (HAZ) and weld fusion zone (FZ) boundary.

Table of Contents

1 Introduction

The Department of Energy (DOE) Solar Energy Technologies Office (SETO) Generation 3 Concentrating Solar Power Systems (Gen3 CSP) program supports the development and de-risking of high-temperature concentrating solar-thermal power (CSP) technologies.[1] A key objective of Gen3 CSP is to achieve operating temperatures greater than 700ºC using a supercritical carbon dioxide power cycle, compared to an operating temperature of 565ºC with steam Rankine cycles for commercial Gen2 CSP plants. The higher temperatures and new power train have the potential to increase plant efficiency while also reducing the size of the power generation equipment.

The temperature conditions for Gen3 CSP plants and associated challenges with fabricating and connecting subcomponents are illustrated in Figure 1. Conventional fabrication of novel designs for next-generation (Gen3) CSP subcomponents—such as the primary heat exchanger (PHX) to the supercritical CO_2 power cycle and the solar receiver (SR)—is expensive because the higher temperatures require more stainless steel or expensive special alloys to meet material strength requirements. Further, large-scale machining, forging, casting, and welding of these subcomponents can take many months. Ni superalloys are the most promising alloys because of the thermal stresses generated at the high operating temperatures (540ºC–720ºC), particularly when resistance to creep and/or fatigue is needed. Advanced manufacturing techniques that reduce material requirements or allow the use of less expensive materials for structural integrity could also reduce the costs of these subcomponents.
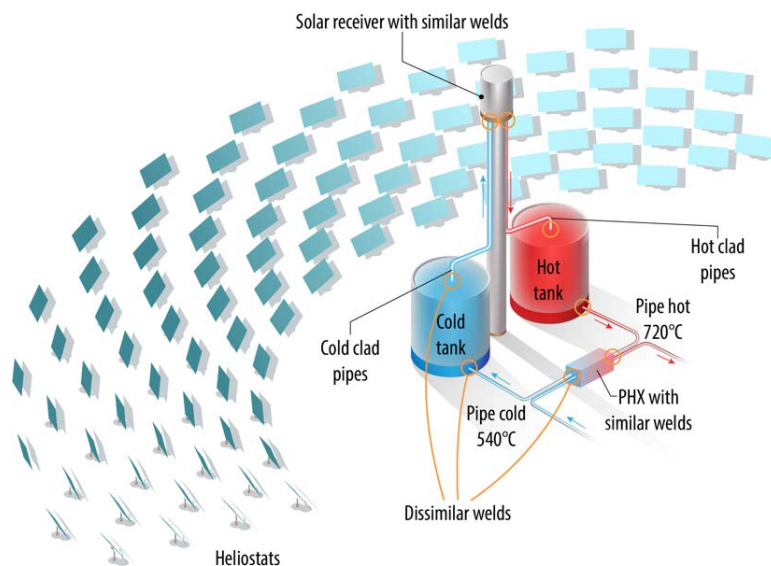
Figure 1. Conceptual Gen3 CSP sections and subcomponents using proposed advanced manufacturing: clad pipes, additive manufacturing for PHX and solar receiver, and similar/dissimilar welding

---

[1] https://www.energy.gov/eere/solar/generation-3-concentrating-solar-power-systems-gen3-csp

1

Gen3 CSP is a new market because of the new temperature range and because few fabricators and Gen2 CSP operating plants exist. Limited information exists on the performance of welded bulk similar/dissimilar alloys for Gen3 CSP operating conditions regarding low-cycle thermal fatigue and failure-mode analysis. This situation makes it difficult for companies to invest significant resources on research and development (R&D) toward demonstrating technical feasibility of advanced manufacturing approaches.

Because each subcomponent will operate at different temperature, pressure, and thermal cycling conditions, Gen3 CSP plants will likely be fabricated using dissimilar alloys. Because welding of selected alloys will be required to integrate the plant, those weldments—welded zone plus modified surrounding bulk microstructure—can become the weakest area. The CSP community is aware of reliability concerns in weldments at the tanks and heat exchanger on today's CSP generation—tower and trough [1, 2]. Gen3 requires a dramatic step up in temperature and pressure and it faces sizeable temperature swings during thermal cycling. Therefore, to eliminate reliability risks, the industry needs to address and mitigate these issues through a fundamental understanding of mechanical failure mechanisms of manufactured parts and subcomponents and weldments.

1.1 Project Overview and Team

To address these concerns, the National Renewable Energy Laboratory (NREL) led the development and execution of a project under DE-FOA-0002064 to study the thermomechanical behavior of advanced manufactured parts, subcomponents, and their weldments for Gen3 CSP. The proposal pulled together multiple industry and academic partners and proposed exploring two advanced manufacturing areas: additive manufacturing (AM) and cladded-metal manufacturing. For each area, two different manufacturing techniques were considered. For each advanced manufacturing area, the proposal team planned to evaluate the thermomechanical properties of samples from the advanced manufacturing techniques and of welds of the advanced manufacturing samples to similar and dissimilar metals compared to base metals. The team also planned to model some of the welding processes using finite element modeling. Finally, the team planned to select promising advanced manufacturing technologies and perform techno-economic analysis on Gen3 CSP subcomponents fabricated using advanced manufacturing techniques compared to conventional options. For example, AM can be used in the fabrication of heat exchangers and receivers. Clad metal can be used to fabricate pipe that has a thin cladding of Ni-superalloy on the inside to prevent corrosion while the bulk of the pipe is made of a cheaper steel to provide structural strength. The overall proposal strategy is illustrated in Figure 2.
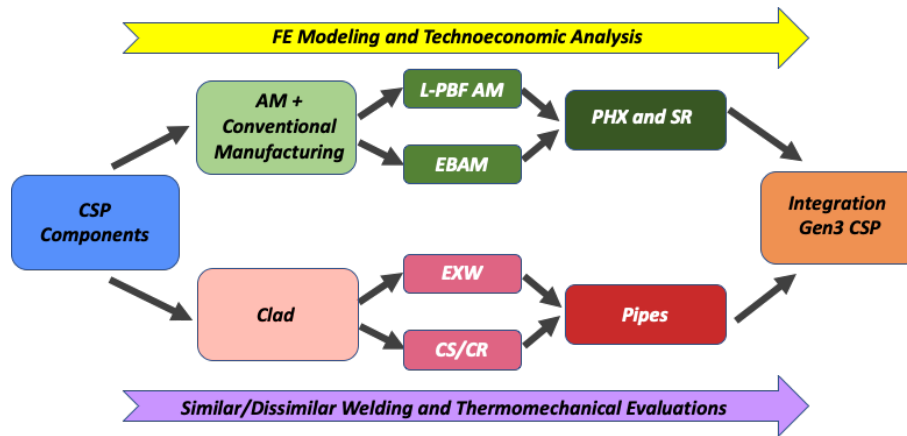
Figure 2. Flow diagram for proposed research (PHX = primary heat exchanger, SR = solar receiver)

The project team included four industry partners that each provided samples for one of the advanced manufacturing techniques shown in Figure 2. The partners and their manufacturing techniques are:

- Elementum 3D (E3D): laser powder bed fusion additive manufacturing (L-PBF AM)
- Sciaky Inc.: electron-beam additive manufacturing (EBAM)
- NobelClad, a DMC Global Inc. company: explosion welding (EXW) of dissimilar metals to fabricate clad sheets
- Advanced Material Solutions (AMS): combustion synthesis with centrifugal rotation (CS/CR) to fabricate clad pipes.

Additionally, the team included Haynes International Inc., which provided some metal alloys for the project, as an industrial partner.

The project team also included two academic partners that were responsible for most of the experimental and modeling work of the project:

- Colorado School of Mines (CSM) and its Center for Welding, Joining, and Coatings Research (CWJCR) led and performed metallurgical characterization, welding, and thermomechanical testing of samples, as well as analysis of results.
- Ohio State University (OSU) developed models and simulations of the welding process.

NREL, as the lead institution, managed the project. NREL also provided corrosion testing of samples and techno-economic analysis of advanced manufacturing techniques.

1.2 Advanced Manufacturing Techniques

1.2.1 Laser-Powder Bed Fusion Additive Manufacturing

The L-PBF process uses a computer-controlled laser to selectively melt powder feedstock layer by layer to form a three-dimensional part. Figure 3 illustrates this AM technique. The process is material- and energy-efficient because the feedstock powder that is not fused can be reused.

3
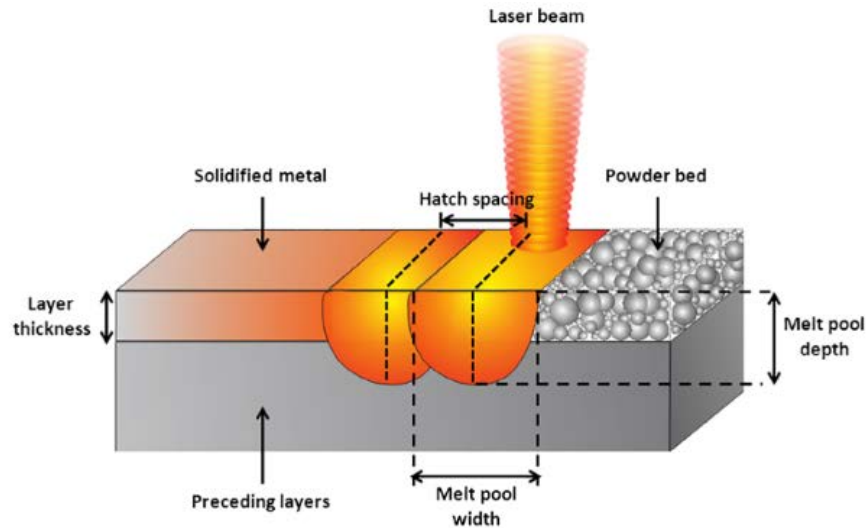
Figure 3. Laser-powder bed fusion (L-PBF) technique schematic [3]

Some process limitations are associated with the need for weldable material as feedstock material, making those materials that suffer from solidification cracking, hot cracking, or quench cracking unsuitable. In addition, unique processing conditions must be developed for each new material, including complex laser-scan strategies, to enable production of complex components from nearly full relative density parts with intricate features while maintaining high geometric accuracy with suitable microstructures and properties. Insufficient energy input could result in defects such as lack of fusion, whereas excessive energy input could result in keyholing defects and can produce excessively large grain sizes and intergranular cracking.

1.2.2 Electron-Beam Additive Manufacturing With Wire

The EBAM process, a direct energy deposition (DED) process, utilizes an electron beam gun along with wire fed deposition, as seen in Figure 4. Unlike the L-PBF process, EBAM with wire feedstock deposition allows for higher deposition rates (faster time per volume of build) suitable for thicker components. EBAM exists for the purpose of producing near-net shape components with improved techno-economic benefit in comparison to conventional manufacturing techniques that require casting and machining. The challenge associated with EBAM is the anisotropic thermomechanical properties, dependent on orientation with respect to the build direction, which may be beneficial or detrimental. Such characteristics must be considered when designing the building strategy and assembly of EBAM components using fusion welding technologies.

4
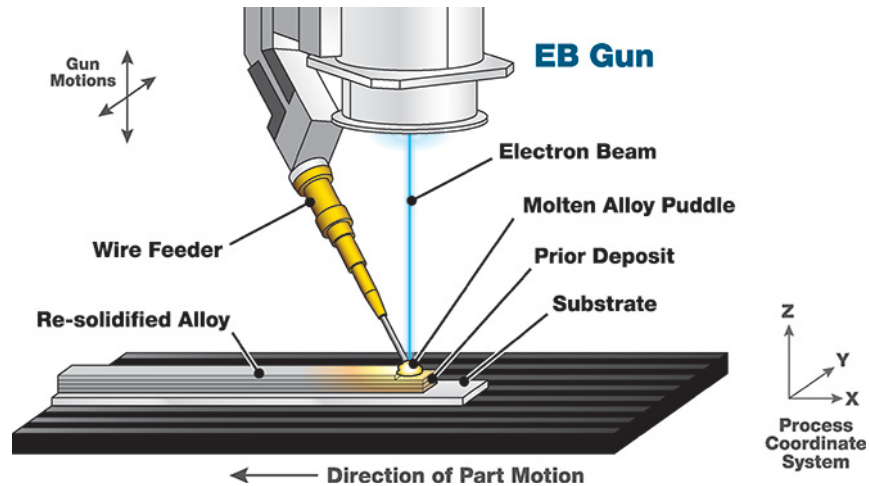
Figure 4. Electron beam additive manufacturing (EBAM) with wire feedstock. Image from Sciaky Inc.

1.2.3 Explosion Welding Cladding

As shown in Figure 5, the EXW cladding process has multiple steps, but the mechanism can be summarized as a solid-state welding event where two dissimilar metals are joined by an incredible amount of energy, generating a truly metallurgical bond with a characteristic "wavy" interface. This interface exhibits very limited interdiffusion (~100–300 nm), with a resulting metallurgical bond so strong that tensile stress failure typically occurs in the bulk of the weakest alloy and not at the bond itself. The structural integrity of the pipe is provided by the thicker, low-cost backer alloy that has the required mechanical strength and malleability to bend the pipe to final shape with minimum residual stress. The cladder is the material responsible for mitigating the corrosion from molten chlorides, controlling the chemical degradation and carburization from sCO_2, or reducing the erosion problems caused by flowing particles. Once the clad is formed, the plate will be rolled and seam-welded together to produce the pipe using similar conventional manufacturing of seam pipes.
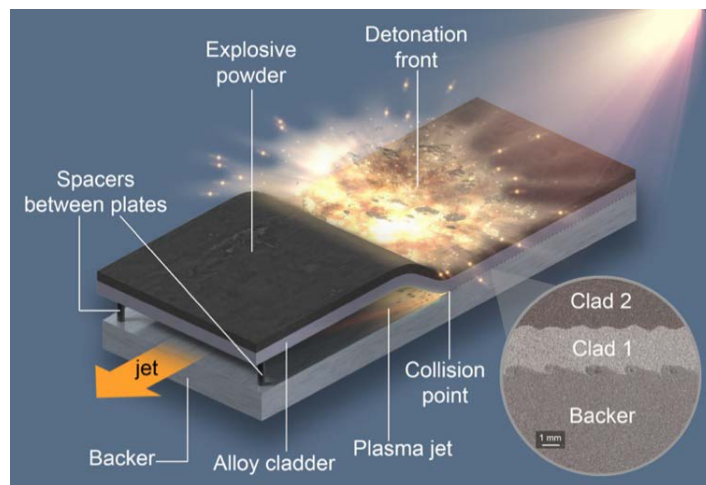
Figure 5. Mechanism of the explosion welding (EXW) cladding. Bond interface microstructure. Image from NobelClad

5

1.2.4 Combustion Synthesis with Centrifugal Rotation Cladding

The CS/CR cladding approach synthesizes a "coating" that acts as the cladder (see Figure 6). CS uses highly exothermic particulate mixtures that, once ignited, can generate high heat and rapidly produce the targeted materials. It is efficient and economical because it can be performed in situ inside a host pipe, and it requires only a small energy input to ignite the precursor exothermic mixture. High purity can be obtained because volatile impurities are vaporized. CR is a well-established method to coat internal pipes that are continuously rotating about their axes at high speeds while a molten metal is poured. The molten metal is centrifugally thrown toward the inside mold wall, where it solidifies after cooling.

10 mm

Figure 6. A ~4-mm-thick SS316 cladder on a carbon steel backing pipe (27 mm OD, 12 mm thick, 500 mm long) using CS/CR. Courtesy of AMS

1.2.5 Summary of Advanced Manufacturing Techniques and Their Applications

To summarize the advanced manufacturing R&D opportunities for CSP, we developed a matrix listing candidate advanced manufacturing techniques for major Gen3 CSP plant components in each technology pathway (Table 1). We considered the current Gen2 CSP technology and the three Gen3 pathways (gas, liquid, and particle). The major components are divided into five groups: receiver, valves/pumps, pipes, heat exchangers (HX), and tanks.

Table 1. Summary of Current and Advanced Manufacturing R&D Opportunities for CSP Component Materials and Construction Methods

Application	Receiver	Valves/Pump	Pipes	HX	Tanks
Gas Pathway					
sCO$_2$			EXW, CS/CR	L-PBF, EBAM, EXW	
Liquid Pathway					
Molten Chlorides	L-PBF, EBAM		EXW, CS/CR	L-PBF, EBAM, EXW	EXW
Molten Nitrates	L-PBF, EBAM		EXW, CS/CR	L-PBF, EBAM, EXW	EXW
Particle Pathway					
Particles*					EXW

L-PBF: laser powder bed fusion, EBAM: electron-beam additive manufacturing, EXW: explosion welding
CS/CR: combustion synthesis/centrifugal rotation
* More information about component design is needed to better address the opportunities

2 Project Objectives

This project had several objectives. The first objective was to validate the use of additive manufacturing (AM) techniques for intricate subsections in primary heat exchangers (PHXs) and solar receivers (SRs), with mitigated crack susceptibility demonstrated by thermomechanical performance. Two manufacturing techniques—EBAM and L-PBF—were evaluated to determine whether they can survive the thermal stresses generated during harsh operating conditions, including high temperatures and pressures, and thermal cycling. Physical metallurgy and thermomechanical resistance evaluations were performed to determine failure mechanisms. The second objective was to develop feasible approaches for cladding large pipes (clad pipe) in the cold and hot sections of Gen3 CSP that are thermomechanically reliable to yield a pipe system lifetime of at least 30 years. Two manufacturing technologies—EXW and CS/CR—were evaluated. The third objective was to thermomechanically validate the welding parameters and heat treatment of dissimilar alloys that will likely need to be joined in Gen3 facilities.

To achieve these objectives, we developed the tasks and milestones detailed in the tables below. We divided the tasks into three budget periods:

- Budget Period 1: Design and characterization of manufacturing and welding procedures. Material selection and down-selection.
- Budget Period 2: Rigorous testing and validation of manufactured materials and weldments. Component fabrication.
- Budget Period 3: Detailed testing of cracking and fatigue of fabricated component samples. Techno-economic analysis of components manufactured at scale.

At the conclusion of each budget period, the project team reviewed the work with SETO to select materials and techniques for further analysis in the next budget period and to determine whether changes to the project plan were needed. The tables reflect the tasks and milestones that were performed over the course of the project. Changes and material down-selection are discussed in detail within the report.

2.1 Project Tasks

The list of tasks, including high-level description, for the duration of the project are outlined in Table 2.

This report is available at no cost from the National Renewable Energy Laboratory at www.nrel.gov/publications.

Table 2. Project Tasks and Descriptions

#	Task	Description
1	Management and design of experiments	Project management, including placement and approval of subcontracts and agreements, and gathering of detailed information for experimental conditions determination.
2	Explosion welding clad pipes with dissimilar alloys for Gen3 CSP	Cladding of dissimilar metals via explosion welding (EXW). Pipes will be evaluated and optimized to meet thermomechanical strength required to avoid mechanical failures during expected lifetime.
3	Combustion synthesis with centrifugal rotation clad pipes for Gen3 CSP	Cladding of dissimilar metals via combustion synthesis (CS) with centrifugal rotation (CR) for pipes will be evaluated and optimized to meet thermomechanical strength required to avoid mechanical failures during expected lifetime.
4	Additive manufacturing (AM) and welding of intrinsic joint nozzles and connection parts	AM will target connection points for heat exchangers (complex/intricate sections), including elbows and T-joints. They should survive thermal stresses generated during harsh operating conditions, including high temperatures and pressures, and thermal cycling for Gen3 CSP applications.
5	Joining of dissimilar alloys and advanced manufactured connector to wrought alloys	Eliminate concerns associated with weldment performance. Design and optimize similar/dissimilar welding processes and understand the influence of thermal profiles and mechanical loads on the creep and fatigue life of subcomponents' weldments to improve cracking resistance.
6	Finite element (FE) modeling of dissimilar alloy welding	Develop and validate FE models for joining/welding of similar/dissimilar alloys to help advanced manufacturing production/fabrication routes that will enhance required metallurgical microstructures and mechanical properties of weldments to increase lifetime.
7	Techno-economic analysis (TEA)	Baseline, preliminary, and optimized analyses will be used to demonstrate that selected advanced manufacturing (clad, AM, and their welding/joining) can increase the reliability and availability of the Gen3 CSP plant while being cost-effective.

2.2 Project Milestones by Budget Period

In this project, there are three main budget periods. Budget Period 1 (BP1) covers the design and characterization of manufacturing and welding procedures. In BP1, we selected the materials and down-selected materials for more rigorous testing to be completed in Budget Period 2 (BP2). In BP2, detailed metallurgical analysis, thermomechanical testing, and modeling were conducted. Validation of manufactured materials and weldments, including component fabrication (e.g., pipe fabrication using EXW technique) was completed in BP2. Budget Period 3 contained more detailed testing of fabricated component samples, such as isothermal fatigue and crack susceptibility. Additionally, a final techno-economic analysis (TEA) of components manufactured at Gen 3 CSP plant scale was completed.

The milestones for BP1, BP2, and BP3 are described in Table 3, Table 4, and Table 5, respectively. Each milestone is categorized in the left-hand column by budget period (1, 2, or 3),

task/subtask (1–7) based on Table 2, and milestone (starting at 1) within each task/subtask category. The performer for each item (e.g., NREL) is also included.

Table 3. Budget Period 1 (BP1) Milestones

NREL = National Renewable Energy Laboratory; NC = NobelClad; AMS = Advanced Material Solutions Inc.; E3D = Elementum 3D; S = Sciaky; CSM = Colorado School of Mines; OSU = The Ohio State University

TWP Item Number (Tasks, Subtasks, and Milestones)	Item Description	Item Performer
M (1.1.1)	Project management	NREL
M (1.1.2)	Design of experiments for dissimilar alloy systems to be evaluated	All
M (1.2.1)	Down-selection of explosion welding (EXW) clad dissimilar alloys systems	NC
M (1.3.1)	Combustion synthesis (CS) and centrifugal rotation (CR) cladding process parameters	AMS
M (1.3.2)	CS/CR clad of pipes	AMS
M (1.4.1)	Additive manufacturing (AM) processes developed for selected high temperature alloys	E3D; S
M (1.4.2)	AM heat treatment development and property testing	E3D; S
M (1.4.3)	AM fabricated welding characterization specimens	ED3; S; CSM
M (1.5.1)	Design of dissimilar alloys joining	CSM; OSU
M (1.5.2)	Bonding strength evaluations and metallurgical characterizations of butt-welded EXW clad coupons	NC; CSM
M (1.6.1)	Finite element (FE) simulation of butt-welded EXW clad coupon	OSU; CSM
M (1.7.1)	Techno-economic baseline for solid Ni superalloys	All

10

Table 4. Budget Period 2 (BP2) Milestones

NREL = National Renewable Energy Laboratory; NC = NobelClad; AMS = Advanced Material Solutions Inc.; E3D = Elementum 3D; S = Sciaky; CSM = Colorado School of Mines; OSU = The Ohio State University

TWP Item Number (Tasks, Subtasks, and Milestones)	Item Description	Item Performer
M (2.2.1)	Thermomechanical testing of welded EXW clad coupons	NC; CSM
M (2.3.1)	CS/CR clad pipe characterization	AMS; CSM
M (2.4.1)	Welding of AM samples to similar wrought alloys	CSM; E3D; S
M (2.5.1)	Joining of dissimilar alloys	CSM; OSU
M (2.5.2)	Thermomechanical evaluation of longitudinally welded EXW and CS/CR clad pipe sections	NC; CSM
M (2.5.3)	Corrosion in molten chlorides	NREL
M (2.6.1)	FE model optimization of welding process of AM samples to wrought metal	OSU; CSM; E3D; S
M (2.7.1)	Preliminary techno-economic analysis for advanced manufacturing	All

Table 5. Budget Period 3 (BP3) Milestones

TWP Item Number (Tasks, Subtasks, and Milestones)	Item Description	Item Performer
M (3.5.1)	Weldment crack susceptibility and cracking mechanisms	All
M (3.5.2)	Low-cycle thermal fatigue and failure mode analysis of weldments	All
M (3.7.1)	Techno-economic analysis	All

3 Design Requirements for Gen 3 CSP Application (Task 1)

3.1 Operating Conditions and Performance Criteria

The main outcome of this milestone was to assemble comprehensive tables for the design of experiments. We gathered information about potential candidate alloys for Gen3 applications. The list of potential candidates includes information about high-temperature and corrosion-resistant alloys analyzed by NREL and other national laboratories, including Sandia National Laboratories, Idaho National Laboratory, and Oak Ridge National Laboratory, as a part of Gen3 molten salt consortia and Topics 1 and 2. This information was used to select suitable sets of materials to be evaluated in the project that satisfy mechanical requirements, present good corrosion resistance (for those in contact with molten salt), and offer opportunities for cost reduction.

From the initial discussion, several sections of the solar receiver (SR), primary heat exchanger (PHX), storage tanks, and piping seem to offer opportunities for improvement and cost reduction using dissimilar alloys and cladding (Figure 1). Additional information about design characteristics for these components is required to quantify the advantage with respect to current operating CSP systems. A summary of general design and operating parameters for Gen3 systems is presented in Table 6. This table was reviewed by experts at NREL working on other projects related to the Gen3 program. For Gen3 CSP, the low (cold side) temperature is expected to be 500°C and the high (hot side) temperature is expected to be 720°C for pipes and some joints and 800°C (max) for connections and joints within the solar receiver.

3.2 Candidate Alloys

The list of candidate alloys for consideration of use in Gen3 CSP components is shown in Table 7. The table also contains a summary of the alloy composition, requirements for use in project experiments, filler options, and potential applications. Complete chemical compositions of the candidate alloys are listed in the appendix. The initial list of potential candidate alloys has been carefully built by leveraging the knowledge of previous and current projects for Gen3 Topics 1 and 2, manufacturer recommendations, and a literature review of advanced alloys for high-temperature and corrosion-resistant applications.

3.2.1 Mechanical Properties

A comparison of properties for all the alloys as a function of temperature is presented in Figure 7. Cold and hot operational temperatures for Gen3 CSP plants are displayed in this figure. H233, In740H, and H282 have the highest yield strength (YS) and ultimate tensile strength (UTS) among considered alloys. Conversely, they present the lowest ductility. Both the YS and UTS of all alloys decrease with temperature. For most Ni-based alloys, YS and UTS drop after 800°C. In terms of ductility, H233, C-22, and H230 report the highest ductility in the studied temperature range Figure 7(c). No major changes occur in YS, UTS, and ductility at temperatures lower than 500°C (the cold side operating temperature limit).

12

Table 6. Assessment of High-Temperature Structural Materials for Gen3 Systems

Sizes are provided for a general range and will be continually evaluated as design aspects mature

Component	Condition	Pathway					
		Liquid		Gas		Solid Particle	
		Pilot (2 MWt)	Commercial	Pilot	Commercial	Pilot	Commercial
Receiver	Temperature/ Pressure	~780°C / <1 MPa		Up to 780°C / 25 MPa		N/A	
	Description: Product Form(s)	Tubular configurations: tubes or diamond/rectangular tubes		Internally supported shell: sheet and foil or tubular configuration			
	Sizes	"Thin wall"	1–2-in. OD, receiver tubes walls 0.04–0.06 in.	Plate/Fin: 0.004–0.012-in. thickness Tubular: ¼-in. OD, 0.028-in. wall			
Receiver Collection	Temperature	720°C–740°C / <1 MPa		up to 750°C / 25 MPa		N/A	
	Description: Product Form(s)	Vessels, headers		Vessels, headers			
	Sizes	Similar to piping		Similar to piping			
Piping	Temperature	500–720°C / <1 MPa		730–740°C / 25 MPa		N/A	
	Description: Product Form(s)	Pipes		Pipe	Pipe		
	Sizes	2.0–2.5-in. ID, 0.187–0.218-in. wall	TBD	-6-in. OD	10-in. OD, 1.125-in. wall		
Primary Heat Exchanger	Temperature	720°C / <1 MPa (salt), ~30 MPa (sCO$_2$)		715°C–740°C (could be higher?)		700°C–775°C (could be higher) n/a / ~30 MPa (sCO$_2$)	
	Description: Product Form(s)	Various designs under consideration; thin sheet tubes possible		Shell and plate		Multiple designs under consideration: plates and others	
	Sizes	~0.010–0.020-in. thickness		Plate/fin: 0.004–0.012-in. thickness		~0.010–0.020-in. thickness	
Balance of Plant	Temperature	500°C–720°C / <1 MPa		730–740°C		None identified to date	
	Description: Product Form(s)	Pump and valve casing: block forgings		Fittings, forgings			
	Sizes	TBD	TBD	TBD	TBD	TBD	TBD

Table 7. Candidate Alloys for Gen3 CSP

Material				Manufacturing			Notes
Name	Type	Composition	Product Form	Required Dimensions	Similar or Dissimilar Welding	Application	
Hastelloy X	Ni-Base	49Ni-22Cr-18Fe-9Mo-1.5Co		~1.5 ft long CS/CR pipe, diameter TBD	S- E/ERNiCrMo-2 [4]	Hot piping, valves, and fittings	
Haynes 230	Ni-Base	57Ni-22Cr-14W-2Mo-3Fe-5Co	Automized powder 15-45 μm	250 mm x 250 mm platform, height depends on amount of powder for L-PBF	S- ERNiCrWMo-1 [5]	Hot piping, valves, fittings, solar receiver components, and molten salt tanks	
C-276	Ni-Base	57Ni-16Cr-16Mo-2.5Co-5Fe-4W	Automized powder 15-45 μm		S- E/ERNiCrMo-4 [4] D with Monel 400- ERNiCrMo-3 [6] D with ASS 321- ERCrNiMo-4 [7]	Cold piping, valves, and fittings	Not commonly used for hot corrosion applications
Inconel 740H	Ni-Base	Ni-25Cr-20Co-1.4Al-1.4Ti-1.5Nb			S- Inconel 740H [8]	Hot piping, valves, fittings, and solar receiver components	
SS304H	Austenitic SS	Fe-18Cr-8Ni			S-308L [9] S- SS304 (or overalloyed grade) [10] D with Monel400- ENiCu-7 [11] [12]	Cold piping, valves, and fittings; hot and cold tanks (with liner)	
Incoloy 800H	Mix of FeNiCr	40Fe-30Ni-19Cr			S- ERNiCr- 3 [4]		
Inconel 617	Ni-Base	44.5Ni-20Cr-10Co-8Mo-3Fe-0.8Al			S- E/ERNiCrCoMo-1 [4]	Under consideration for valves and fittings	
SS709/ TP310MoCbN	Austenitic SS	Fe-25Ni-20Cr-1.5 Mo-Cb					
Haynes 282	Ni-Base	57Ni-20Cr-10Co-8.5Mo-2.1Ti-1.5Al-1.5Fe			S- Haynes 282 [13]	Under consideration for valves and fittings, solar receiver components	
SS316H (CF8M)	Austenitic SS	Fe-16Cr-10Ni-2Mo			S- 316L [9]	Under consideration for valves and fittings, nuclear reactors	
SS347H	Austenitic SS	Fe-17Cr-9Ni-(0.04-0.1) C-Nb (10 X C)			S- 347 [9]	Cold piping, valves, and fittings; hot and cold tanks	Considered standard SS alloy for CSP with molten salt
Haynes 244	Ni-Base	Ni-22.5Mo-8Cr-6W-2Fe(max)		250 mm x 250 mm platform, height depends on amount of powder for L-PBF	S- Haynes 244 [14]		
Haynes 233	Ni-base	Ni-19Cr-19Co-7.5Mo-3.25Al-1.5Fe(max)					Alumina forming alloy
Inconel 625	Ni-Base	Ni-21.5Cr-9Mo-Fe (5 max)-Nb(+Ta)4.5			S- E/ERNiCrMo-3 [4]	Solar receiver components	
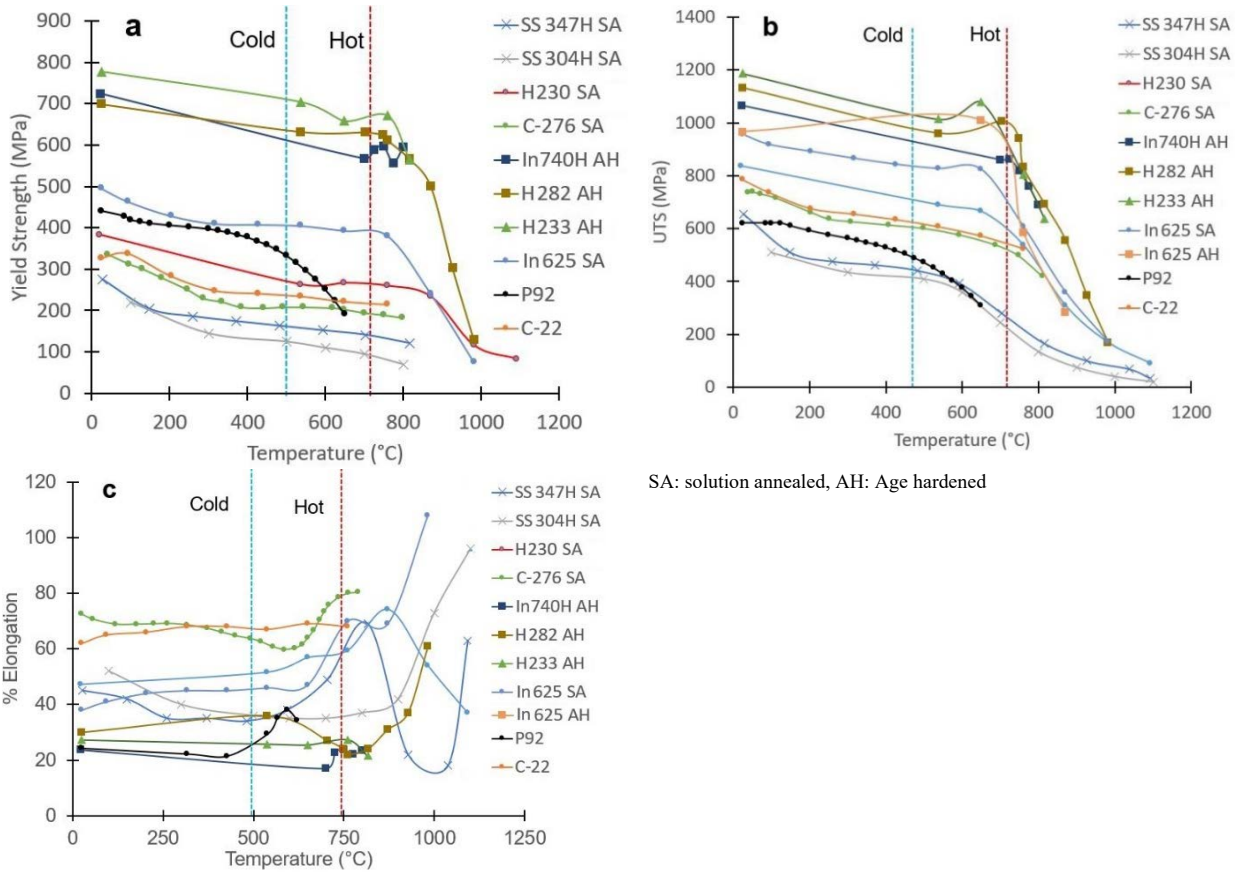
Figure 7. Comparison of mechanical properties as a function of temperature for alloy candidates: (a) yield strength, (b) ultimate tensile strength, and (c) ductility [5, 8, 13–21]

A ranking of alloys based on their mechanical properties for the cold and the hot side of the Gen3 CSP plant is presented in Table 8. In this table, In740H (highlighted in yellow) has been selected as a baseline to compare properties. The properties were evaluated at 500°C for the cold side and 720°C for the hot side; then, based on these values, alloys were compared and ranked from high to low value. Alloys in green and orange background have better and inferior properties than In740, respectively.

Table 8. Ranking of Alloys Based on Mechanical Properties for Cold and Hot Side of the Gen3 CSP Plant

Rank	Yield Strength		Ultimate Tensile Strength		Ductility	
	Cold side	Hot side	Cold side	Hot side	Cold side	Hot side
1	H233 AH	H233 AH	In625 AH	H282 AH	C-22 SA	C-276 SA
2	H282 AH	H282 AH	H233 AH	H233 AH	C-276 SA	C-22 SA
3	In740H AH	In740 AH	H282 AH	In740H AH	H230 SA	In625 SA
4	In625 SA	In625 SA	In740H AH	In625 SA	In625 SA	H230 SA
5	P92	H230 SA	H230 SA	H230 SA	H282 AH	SS347H SA
6	H230 SA	C-22 SA	C-22 SA	C-22 SA	SS304H SA	SS304H SA
7	C-22 SA	C-276 SA	C-276 SA	C-276 SA	SS347H SA	H233 AH
8	C-276 SA	SS347H SA	SS347H SA	SS347H SA	H233 AH	H282 AH
9	SS347H SA	SS304H SA	P92	SS304H SA	P92	In740H AH
10	SS304H SA		SS304H SA		In740H AH	

3.2.2 Coefficient of Thermal Expansion

The thermal expansion behavior of potential alloys for the hot and cold sides is presented in Figure 8. Thermal expansion for most of the Ni-base alloys is similar (Figure 8(a)). Thermal expansion is also similar among stainless steels but larger than that of Ni-based alloys (Figure 8(b)). The expansion/contraction induces strain with thermal cycles during plant operation. Because the CTE directly depends on temperature, this effect is expected to be less pronounced in component cycling under lower temperature differences. For dissimilar alloy welding, it is desirable to have similar CTE for both materials. It is important to note that the P92 alloy presents a similar CTE to Ni-based alloys, making it a good backer candidate for cold sections.
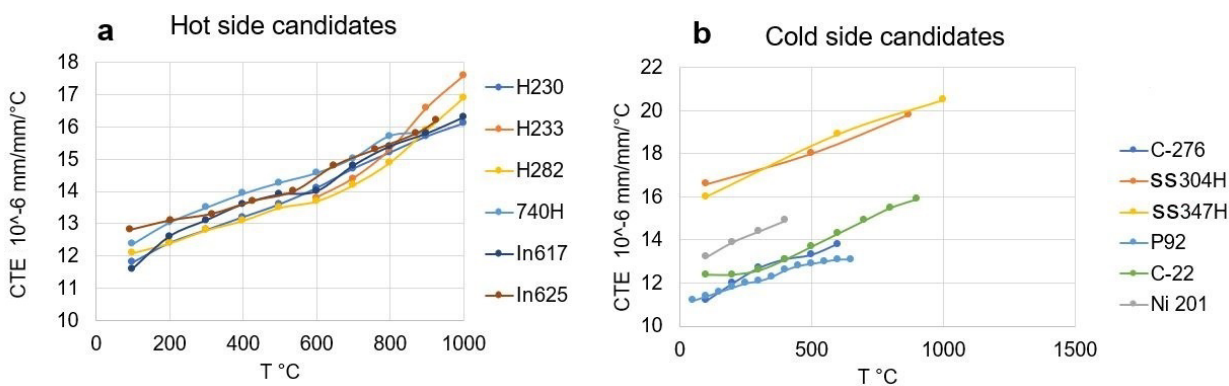
Figure 8. Coefficient of thermal expansion of potential alloys for the hot and cold sides of the Gen3 CSP plant [5, 8, 13–21]

16

This report is available at no cost from the National Renewable Energy Laboratory at www.nrel.gov/publications.

3.2.3 Service Performance (Corrosion, Creep)

Creep resistance

Creep rupture information for 100,000 hours and different average temperatures for several of the candidate alloys is presented in Figure 9. Three main groups can be identified: Ni-based alloys that exhibit the highest creep resistance (H282 is the most creep-resistant alloy), ferritic steels with lower creep resistance, and austenitic steels (including stainless steels) for which creep resistance lies between the other two groups of alloys.
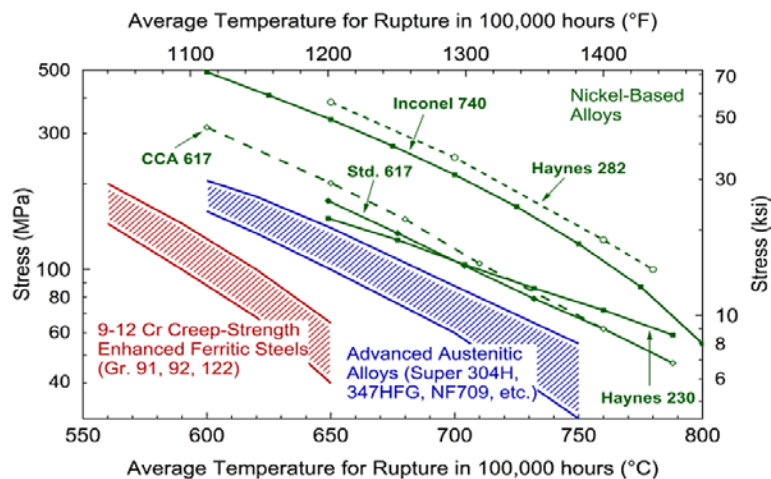
Figure 9. Creep rupture data for Ni-based, austenitic, and ferritic alloys [22, 23]
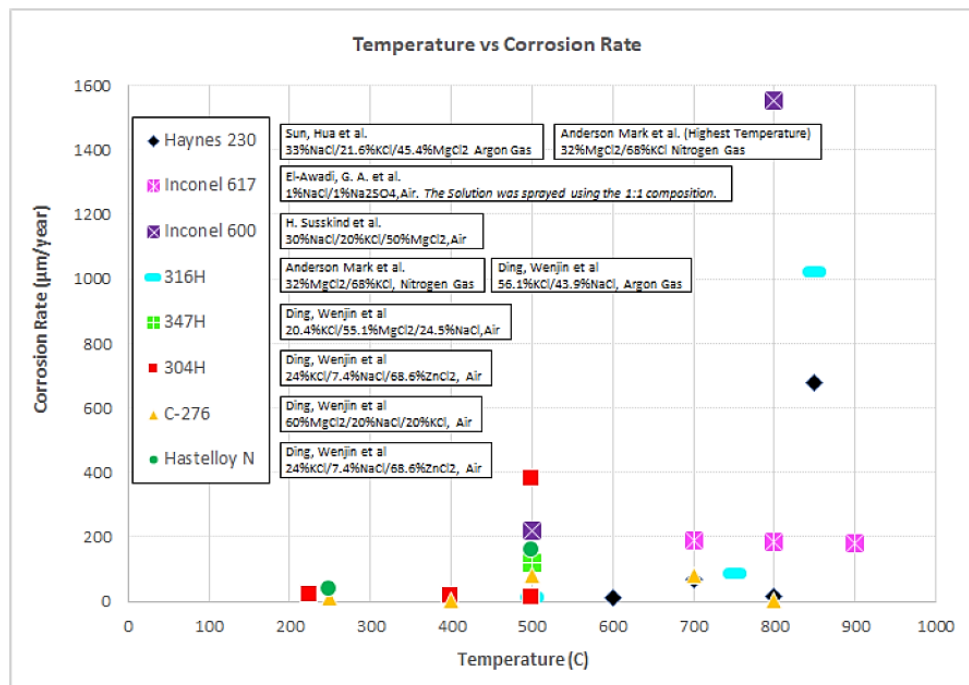
Figure 10. Corrosion data for candidate alloys at different temperatures and corrosion media [24]

Corrosion information for several candidate alloys is listed in the appendix, and a summary is shown in Figure 10. The Hastelloy C-276 alloy was found to exhibit high corrosion resistance in

17

molten NaCl–KCl–ZnCl$_2$ salt at 500°C compared to Hastelloy N and C-22 [25]. The good corrosion resistance exhibited by C-276 with 22 wt.% Cr agrees with the findings reported by Michel et al. [24], where Ni alloys with Cr content around 20 wt.% were found to possess high corrosion resistance in molten salts. In comparison, Si content was reported to deteriorate the corrosion resistance in Si-containing alloys [26], and Hastelloy N contains almost 10 times as much Si as C-276. Other alloys such as H230 also present a good corrosion resistance for temperatures lower than 800°C. For several alloys, information about corrosion resistance in molten salts is not available. In particular, the Haynes 282 (H282) alloy merits additional evaluation of corrosion in molten salts, as it is an excellent candidate from a mechanical point of view, with a cost comparable to H230.

3.2.4 Weldability-SAC/SRC, Hot Cracking, and SCC

Weldability is a fundamental feature for successful fusion-based manufacturing. The weldability and printability of the material includes the ability to fuse and bond with the previous layer, and importantly, the ability to solidify and cool without introducing cracks. Cracking during solidification or from stresses introduced by the process and thermal cracking is a common problem that prevents fusion-based printing for many alloys. Solidification behavior is influenced by many factors, including the size of the mushy (solid-liquid) zone, solute concentrations, phases formed, nucleation sites, and preferred crystal growth directions. Compositions and processes that favor solidification to a finer-grained microstructure are generally less susceptible to solidification cracking. Alloys with a low coefficient of thermal expansion are favorable for reducing internal stresses from shrinkage during cooling, which can build up with each layer. Alloys with high ductility and without brittle phases at the grain boundaries are also less likely to exhibit cracking problems [4].

Many nickel alloys tend to have good weldability due to the FCC crystallographic nature of the material and ability to create a solid solution with elements such as iron, copper chromium, tungsten, and molybdenum. The ASM handbook Vol. 6 highlights that molybdenum-alloyed nickel alloys are explicitly designed to address corrosion in a non-oxidizing environment [28]. The ASM Handbook lists H230, C-276, and IN625 as good options for an alloy that has resistance to stress, corrosion, and hot cracking at high temperatures and can also withstand the corrosive environment. Newer alloys such as Haynes 233 and 244 also seem to be good options. More details about the weldability and weld crack susceptibility are discussed in Section 4.4.4.

3.2.5 Previous Studies and Recommendations

Down-selected alloys for the liquid, solid particle, and gas pathways are presented in Table 9. For pilot-scale CSP plants, the liquid phase pathway to SunShot project [27] recommended H230 alloy for the hot piping side with a target fluid state of 750°C at 73 psi (0.5 MPa) and C-276 alloy for the cold piping side with a target fluid state of 500°C at 160 psi (1.1 MPa). These recommendations were based on the combination of high-temperature strength (see Figure 246), manufacturability, and corrosion resistance (see Figure 10) of the two alloys. In addition, Inconel (IN) 740H (for the hot side) and 304H (for the cold side) are being suggested by Topic 1 Liquid pathway as more cost-effective candidates for a commercial-scale plant. However, more robust strength and corrosion testing will be required to qualify 304H and IN740H alloys for the Gen3 CSP service conditions [27].

Table 9. Summary of Down-Selected Alloys for Gen3 Liquid, Solid Particles, and Gas Pathways

Pathway	Alloy	Notes
Liquid	H230 C-276 In740H SS304H	H230 and C-276 are recommended for the hot and cold piping applications to be in direct contact with molten chlorides, respectively. Inconel 740H (for the hot side) and SS304H (for the cold side) are suggested as more economic replacements to H230 and C-276, respectively, when only mechanical resistance is considered for a commercial-scale plant.[a]
Solid particles	H230, In740H In625, In617 IN800H	Alloys selected for a Gen3 CSP particle pilot plant and associated with the heat exchanger and sCO$_2$ loop.[b]
Gas	H230 In740H SS347H	H230 and In740H alloys are considered for high-temperature sections of equipment, while SS347H was suggested for the piping material for the lower-temperature parts.[c]

[a] NREL Milestone Report for "Liquid-Phase Pathway to Sunshot."
[b] Information provided by Sandia National Laboratories.
[c] Information provided by Brayton Energy.

3.3 Summary of Material Selection

3.3.1 Hot Side Alloy Candidates for Operation at >720°C

The following Gen3 CSP hot side alloys are selected from the list of potential candidates (see Table 7), based on the analyses of mechanical properties, compatibility for welding, and corrosion behavior when in contact with molten chlorides.

- **H230** has high strength. It is a good candidate for a single-material component. It has excellent thermal stability (no ductility dip during extreme temperature conditions).
- **H282** presents higher strength and creep resistance than H230 with similar cost. It can be a good option for backer material.
- **In740H** also has strength and creep resistance comparable to H282. Both H282 and In740H are age-hardened alloys and require post weld heat treatment (PWHT). Thus, fabrication cost could be higher than when using H230. H282 and In740H are more susceptible to reheat cracking than H230 [29].
- **H244 and H233** present excellent mechanical properties; however, they were excluded due to their high cost.
- **In617 and In625** are both solid solution strengthened alloys, which means they do not necessarily require PWHT. However, if PWHT is required for residual stress relief or maintaining corrosion resistance, the temperature range from 750°C to 950°C should be avoided in the Nb bearing In625 alloy to avoid losses in ductility and toughness due to formation of δ (Ni$_3$Nb) intermetallic brittle phase [4]. On the other hand, Co is the main solid solution strengthening element in In617 instead of Nb. In617 has a narrower solidification range (higher resistance to solidification cracking) than In625 [4], which makes it a better choice. The allowable stress at service temperature (similar for both alloys) is relatively low (50 MPa) [30], which requires the applied stress to be low enough that the required pipe design thickness remains reasonable.

19

- **Hastelloy X and HR-120** both give slightly less strength than In617 and In625 at service temperature. Thus, they may not be promising candidates.

3.3.2 Cold Side Alloy Candidates for Operation at 500°C

The following Gen3 CSP cold side alloys are selected from the list of potential candidates (see Table 7), based on the analyses of mechanical properties, compatibility for welding, and corrosion behavior when in contact with molten chlorides.

- **H230** has a high thermal stability that can withstand fabrication conditions as a cladder for any backer choice without necessarily requiring PWHT due to the high thermal stability and solid solution strengthening instead of age hardening.
- **C-22** is well known as a high-resistance alloy and is less prone to sensitization than C-276, and thus can withstand the complex welding-related heat treatments required by the low-cost P92 or P91 backer. It is a good option to reduce material cost.
- **C-276** presents excellent corrosion resistance; however, as it is prone to sensitization (as shown in Figure 11), it should not be exposed to heat treatments above 583°C. It can be used with SS304H backer as no PWHT is required for SS304H, unlike P92 steel. However, the effect of heat input associated with welding on its corrosion resistance needs to be evaluated.
- **P91** has the lowest material cost, but it requires PWHT at temperatures around 760°C. Fabrication cost increases need to be considered vs. material cost savings.
- **SS304H**—because sensitization is not a concern for this alloy as a backer, high carbon content (H) can be used to increase strength. Compared to P91, SS304H has higher creep resistance, and because sensitization or corrosion resistance is not a concern for the backer, SS304H may not require PWHT. It can be used with C-276 cladding to reduce fabrication cost.
- **Ni-201** presents good corrosion resistance; however, severe grain growth could occur at elevated temperatures, impacting mechanical resistance. Because it is considered as a cladder, no mechanical property restrictions are considered, because only a few millimeters are needed.
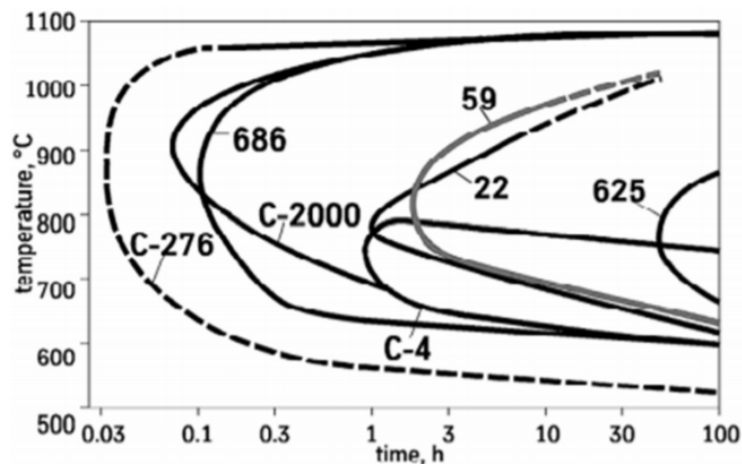
Figure 11. Time-temperature sensitization curves for various Ni-based alloys [31]

20

4 Project Results and Discussion

The results are categorized by the main tasks and technologies as listed in the technical work plan (TWP) document. Therefore, the subsections are broken down by technology with experiments, modeling, and techno-economic analysis:

5. Task 2: Explosion Clad Welding (EXW)
6. Task 3: Combustion Synthesis/Centrifugal Rotation (CS/CR)
7. Task 4: Additive Manufacturing (AM) and Welding of AM
8. Task 5: Joining of Dissimilar and Advanced Manufacturing Alloys
9. Task 6: Finite Element Analysis (FEA)
10. Task 7: Techno-Economic Analysis (TEA)

Some discrepancies in the specific subtasks and milestones led to further organization of subsection to improve readability. For example, the EXW milestone (1.5.2 and 2.5.2) associated with Task 5 is moved to Task 2 subsection. Task 5 includes mainly dissimilar joining experiments of Haynes 282 and Inconel 740H to 304H SS and weldability and fatigue testing of L-PBF welds.

Table 10. BP1 Summary Work Completed Separated by Task and Technology

Task/Milestone	Additive Manufacturing		Cladding		Dissimilar Weldments
	L-PBF	EBAM	CS/CR	EXW	
Down-selection of candidate alloys	x	x	x	x	x
Fabrication and characterization of samples	H282 IN740H H230	H282 H230	SS304H - C276	SS304H - C22 SS304H-Ni201 Gr91-C22 Gr91-Ni201	
Characterization tests	Density		Dilution	Bonding strength	
Welding and heat treatment	H282 HT study			Plate butt welds	
Modeling	FEA			FEA	Thermocalc
TEA baseline materials costs	x	x	x	x	x

The results completed for each task and milestone can be further categorized by each advanced manufacturing technique. Table 10, Table 11, and Table 12 contain this information separated by BP1, BP2, and BP3, respectively. These tables serve as a visual representation of the down-selection procedure for material and manufacturing techniques throughout the project from BP1 to BP3. For example, after completion of BP2, the remaining experimental work and TEA in BP3 was focused primarily on subcomponents manufactured with L-PBF or EXW, respectively. The text in red represents a "no-go" on continuation of work of those materials for subsequent

budget periods, while the text in green represents materials that meet the metrics (e.g., thermomechanical properties, dilution, etc.) defined for each milestone. Each section to be presented contains the more detailed milestone descriptions and metrics.

Table 11. BP2 Summary Work Completed Separated by Task and Technology

Tasks/Milestones	Additive Manufacturing		Cladding		Dissimilar Weldments
	L-PBF	EBAM	CS/CR	EXW	
Corrosion of samples in Gen3 molten chloride salt	H282 IN740H	H282	SS304H - C276		
CS/CR pipe microstructure characterization			SS304H - C276		
Welding and heat treatment	1) H282 & IN740H AM-to-wrought 2) Fluid flow study of H282	H282 AM-to-Wrought		Cladded pipe section fabrication	H282 - to - SS304H IN740H - to - SS304H
Thermomechanical testing of weldments	H282 IN740H AM-to-wrought	H282 AM-to-Wrought		**Pipes** SS304H - C22 Gr91-C22	
Finite element (FE) modeling	x			x	
Preliminary TEA	x			x	

Table 12. BP3 Summary Work Completed Separated by Task and Technology

Tasks/Milestone	Additive Manufacturing	Cladding
Weldment crack susceptibility and cracking mechanisms (Gleeble)	1) L-PBF H282 simulated HAZ 2) L-PBF IN740H simulated HAZ 3) L-PBF to L-PBF H282 as-welded 4) Wrought-to-wrought H282 as-welded	
Low cycle thermal fatigue and failure mode analysis of weldments	1) L-PBF H282 aged 2) Wrought H282 aged 3) L-PBF to L-PBF H282 aged welds 4) Wrought to wrought H282 aged welds	
Detailed TEA		Pipe SS304H - C22 Gr91-C22

22

4.1 Task 2: Explosion Clad Welding

This section will serve as an overview of the work done regarding the explosion clad plates produced by NobelClad and the corresponding welding experiments. Four cladded plates were down-selected: 304H/Ni201, 304H/C22, P91/Ni201, and P91/C22. The 304H plates were tested for the hot as well as cold side temperatures, while the P91 steel plates were only considered for the cold side due to their lower limit for service temperature. All plates were cut and beveled for butt welding at Enerfab. After butt welding of all four plates, tensile and metallurgical samples were extracted for mechanical testing and metallurgical characterization, respectively.

4.1.1 Down-Selection of EXW Clad Dissimilar Alloy Systems (Milestone 1.2.1)

This milestone summarizes the quality control evaluations conducted by NobelClad on the down-selected four clad couples. Produced clads of dissimilar alloy systems are considered successful if they have a minimum bond strength and do not have a substantial number of physical discontinuities to ensure that the two metals do not detach from each other during operation at the stress levels and temperatures expected.

Table 13. Milestone 1.2.1 Details

Milestone	Description	Metric	Success Value	Assessment Tools
1.2.1: Down-selection of explosion welding (EXW) clad dissimilar alloy systems	Produced clads of dissimilar alloy systems (taken from M1.1.2) will be successful if they have a minimum bond strength and do not have substantial number of physical discontinuities to ensure that the two metals do not detach from each other during operation at the stress levels and temperatures expected.	1. EXW clad interface discontinuity between the two dissimilar metals	1. <1 inch in thickness	ASTM A265 Class A Clad and NobelClad DMC100 specification using ultrasound to determine if the bond between the two dissimilar metals is sound. All tested samples (at least three) should meet target with 10% errors based on standard deviation.
		2. EXW clad shear strength at the interface at room temperature	2. Minimum specified in ASTM standard and DMC100 specification	ASTM A265 Class A Clad and NobelClad DMC100 specification using shear stress mechanical testing. All tested samples (at least three) should meet target with 10% errors based on standard deviation.

The selected clad metal systems are:

a) Ni201(>1 mm) // P91-class 2 (>3/4 in.)   c) Ni201(>1 mm) // SS304H (>3/8 in.)
b) C-22(>1 mm) // P91-class 2 (>3/4 in.)   d) C-22(>1 mm) // SS304H (>3/8 in.)

NobelClad has produced and delivered four clad plate systems (Figure 12 and Table 14). These combinations were down-selected after a careful review of the requirements set forth by NREL, Colorado School of Mines (CSM), and NobelClad.
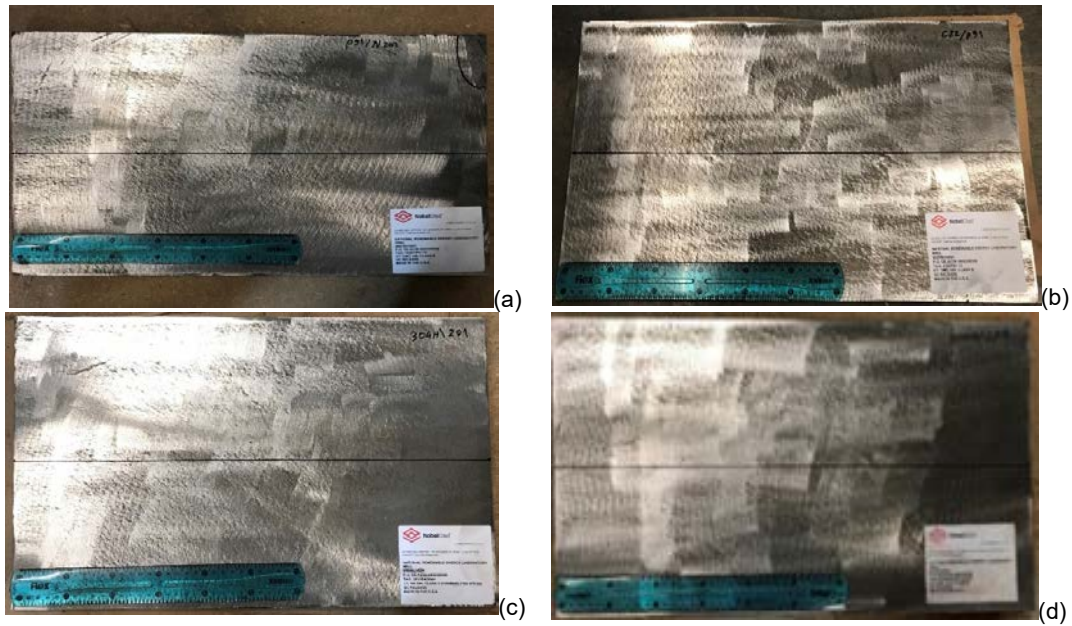
Figure 12. As-received explosion-welded clad plates showing the cladded surface: (a) Ni201// P91-class 2, (b) C-22 // P91-class 2, (c) Ni201 // SS304H, (d) C-22 // SS304H

The down-selection process was chosen based on operational conditions expected in the molten chloride CSP plant. It was assumed that the hot side operation temperature was 750°C, while the cold section would operate at 500°C with a maximum pressure of 1,150 psi. Under those conditions, C22 cladders would corrode at <20 µm/year. For ease of fabricability, a minimum of 3 mm thickness was selected and would be based on commercially available plates. SS304H plates were considered for both the hot and cold side, while P91 steel plates were only considered for the cold side due to its limited maximum service temperature.

Table 14. Explosion-Welded Clad Systems for Molten Chloride CSP Components

Cladder [b]	Backer	Backer thickness (in.)	Length (in.)	Width (in.)
Nickel SB-162-201	P91-type 2 SA-387-91-2	0.750 nominal	20	12
		0.687 minimum		
	SS304H SA-240-304H	0.375 nominal		
		0.312 minimum		
Hastelloy C22 SB-575	P91-type 2 SA-387-91-2	0.750 nominal		
		0.687 minimum		
[a] Clad plates certified to DMC100 Rev.3 / UT: Class B.				
[b] Cladder is 0.125 inch nominal, 0.105 inch minimum				

The quality control evaluations based on ASTM A265 Class A and NobelClad DMC100 specification were conducted by NobelClad, and they are presented in Table 15. Mechanical shear stress and ultrasound evaluations allowed for determination of the bond strength between the dissimilar alloys.

24

Table 15. Quality Control Based on ASTM A265 Class A and NobelClad DMC100 Specification

Cladder	Backer	Ultrasonic	Dimensions	Flatness	Surface Finish	Shear >20 ksi	Specification
Nickel SB-162-201	P91-class 2 (SA-387-91-2)	Accept	Accept	Accept	Accept	39.4 ksi	DCM 100
	SS304H (SA-240-304H)	Accept	Accept	Accept	Accept	46.4 ksi	SA-265 & DCM 100
C22 SB-575	P91-class 2 (SA-387-91-2)	Accept	Accept	Accept	Accept	74.8 ksi	DCM 100
	SS304H (SA-240-304H)	Accept	Accept	Accept	Accept	101.8 ksi	SA-265 & DCM 100

4.1.2 Bond Strength Evaluations and Metallurgical Characterization of Butt-Welded EXW Coupons (Milestone 1.5.2)

This subtask deals with ambient temperature mechanical properties of the transverse weld samples extracted from the butt-joints performed along each of the four cladded plates.

Table 16. Milestone 1.5.2 Details

Milestone	Description	Metric	Success Value	Assessment Tools
1.5.2: Bond strength evaluations and metallurgical characterizations of butt-welded explosion welding (EXW) clad coupons	EXW clad coupons that have been butt-welded should not have formation of harmful secondary phases and shall pass bonding strength. Weldments must have a minimum strength to avoid premature failure in the heat affected zone (HAZ) or weld metal. Weldments should meet low dilution levels to maintain the corrosion resistance.	Dilution level	<25%	Three compositional line scans will be performed to calculate the dilution level at different depths in the weld region. The maximum dilution level in the majority region of the weldment should be below 25%. (Note that the dilution value will be equal to 1 once transiting into the base metal (BM). All tested samples (at least three) should meet target with 10% errors based on standard deviation.)
		Transverse joint strength at room temperature in comparison to the expected strength of the backer (structural metal)	>80%	Modified tensile and/or bend tests from ASTM E8/E8M and ASTM D6272.17, respectively, for bonding strength evaluation. Maintaining 80% of the tensile strength of the base metal is considered as a common target in fusion welding practices. All tested samples (at least three) should meet target with 10% errors based on standard deviation.

4.1.2.1 304H/Ni201 and 304H/C22 Clad Plate Welding Parameters

The 304H/Ni201 and 304H/C22 clad plates both underwent flux core arc welding (FCAW) on the 304H backer, and pulse gas metal arc welding (GMAW) on the respective clad passes. The two 304H cladded welds shared the same welding geometries, according to the welding parameters received from Enerfab. They were both welded on the face side (i.e., backer side) first with a single-v groove with an angle of 60° for the butt-weld. This can be seen in Figure 13.
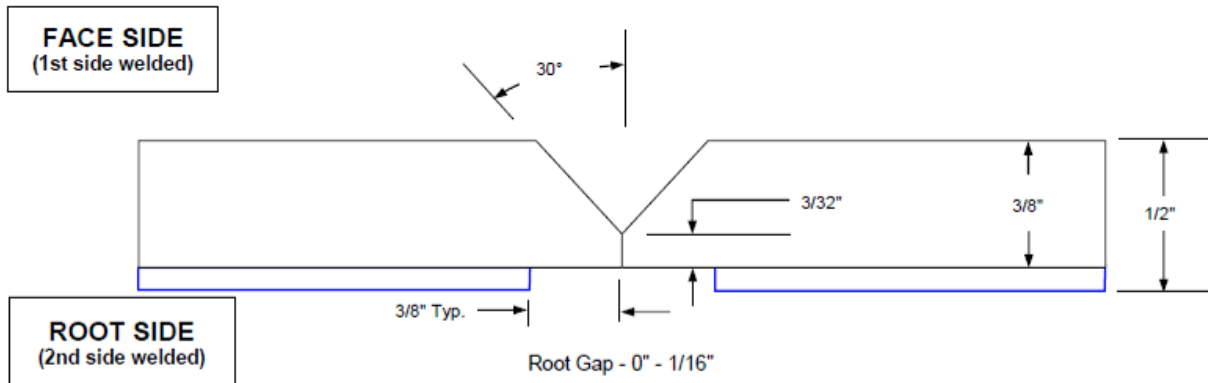
Figure 13. Welding geometry of the 304H/Ni201 and 304H/C22 explosion clad plates

There are notable differences in the number of passes performed on the two plates (i.e., the two 304H plates cladded with Ni201 and C22, respectively). Figure 14 displays a schematic for the order and number of passes on the two clad layers and the face and root sides for both plates. It displays the face side and root side FCAW beads using E308HT0/1-4 in blue and the two clad layer pulsed GMAW beads using ERNi-1 or ERNICRMo-10 in green, respectively. Both plates exhibit four face side FCAW passes and demonstrate that the plates were flipped over to add a fifth FCAW pass at the weld root prior to welding the clad layers. Furthermore, the key difference is that the Ni201 plate has eight total clad layer passes, whereas the C22 plate has ten.
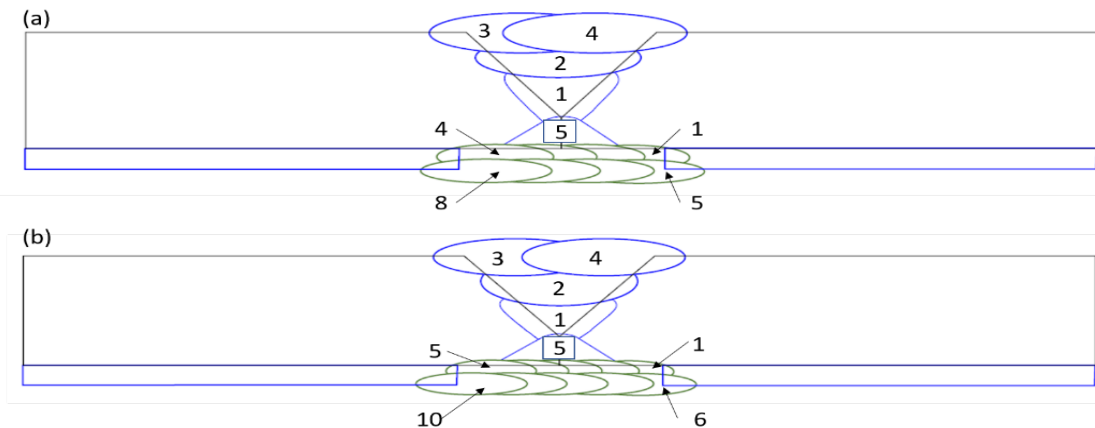
Figure 14. Bead placement and pass order overlay for (a) 304H/Ni201 and (b) 304H/C22 plate butt welds

4.1.2.2 304H/Ni201 and 304H/C22 Clad Plate Weld Sample Extraction

Figure 15 and Figure 16 show the photographs of the top and bottom surfaces of the 304H/Ni201 and 304H/C22 plates. It should be noted that the welding directions for both plates on the root side are in the same direction, and they are in opposite directions on the face side.
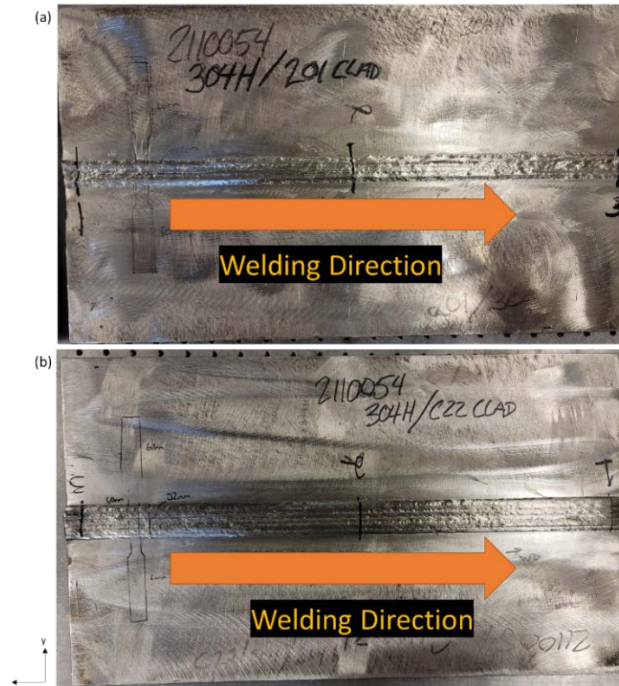
Figure 15. (a) 304H/Ni201 and (b) 304H/C22 explosion clad plates root side with the welding direction and XY axes marked out
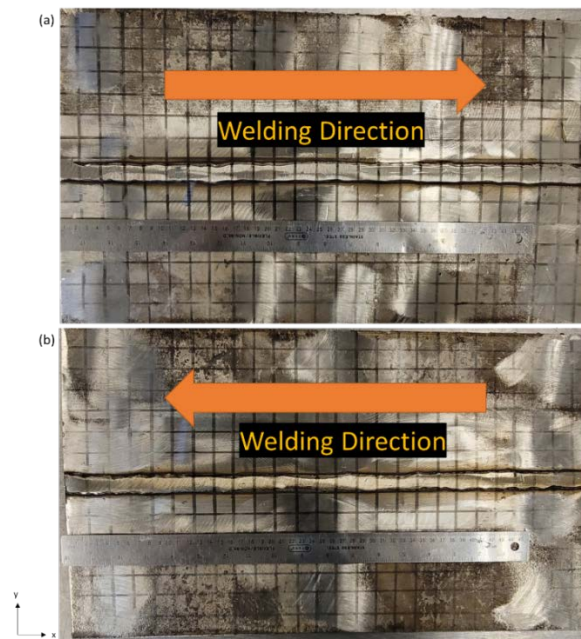
Figure 16. (a) 304H/Ni201 and (b) 304H/C22 explosion clad plates face side with the welding direction and XY axes marked out

27

Figure 17 illustrates the tensile coupon extraction locations in the welded plates. A total of seven tensile samples were extracted in each plate.
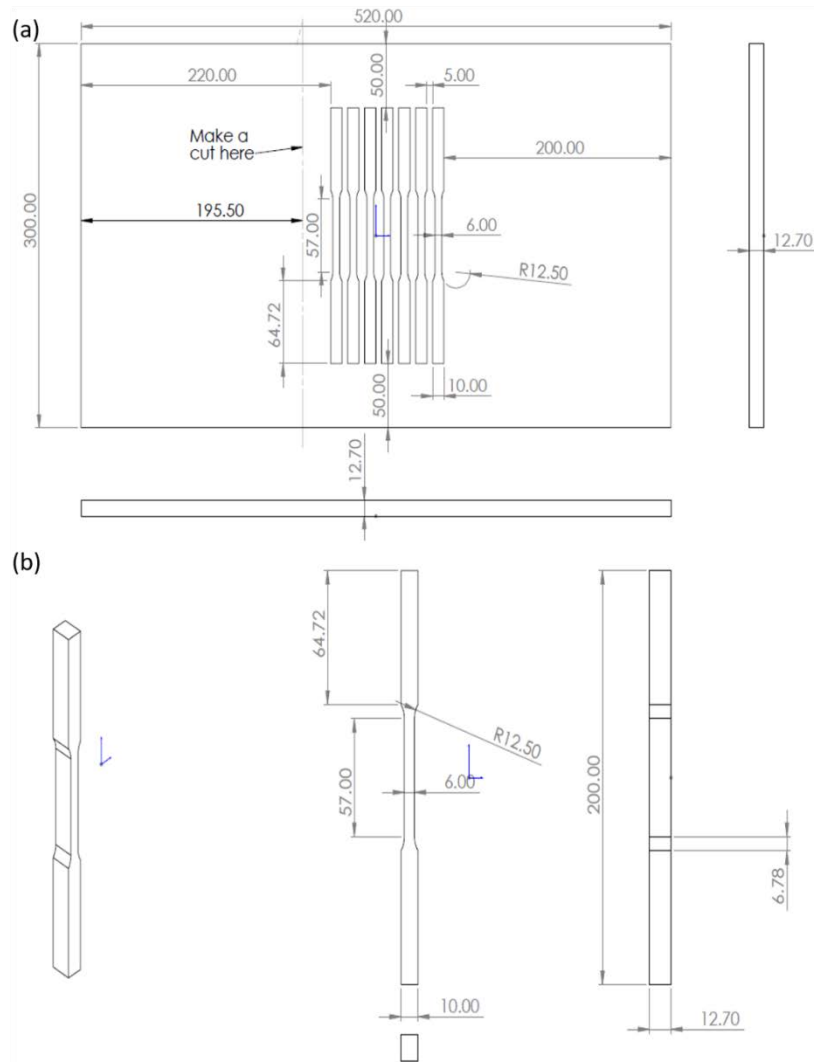
Figure 17. (a) Tensile sample extraction locations on welded plates (unit: mm) and (b) drawing of extracted tensile samples (unit: mm) from isometric, side, and front view (left to right)

The gage length of the tensile samples is long enough to include both the weld metal and heat affected zones (HAZs) on both sides of the weld centerline. The additional cut described in Figure 17(a) denotes the location where one rectangular sample was extracted for metallurgical characterization of the weldment. The same extraction plans were also used for the P91 plates.

4.1.2.3 304H/201 and 304H/C22 Clad Plate Weld Deflection Analysis

Plate deflection measurements were performed, which provide validation information for the modeling of welding process. Because the deformation of the 304H explosion clad plates was asymmetric across the horizontal weld line, it was necessary to use a dial indicator to take these measurements. To minimize the movement of the plates while collecting measurements, it was determined that it would be best to measure the deflection relative to the top surface. Additionally, a grid consisting of 20 mm by 20 mm squares across the whole top surface was

28

labeled on each plate. Dial indicator measurements were collected at each intersection point on the grid, which allowed for the creation of an XYZ plot that would display the plate deflection height (Z-direction) relative to each XY position on the plates.

It should be noted that the reference points for the measurements are on opposite corners, because the lowest point (set to Z = 0) was different on each plate. For the 304H/Ni201 plate, the reference point was at (520,300), and the 304H/C22 plate reference point was at the origin. This was done to minimize the number of negative values to correct for. Moreover, the dial indicator setup was unable to reach all the way to the center of the two clad plates. The arm of the dial indicator was only able to reach 80 mm, so a sizeable amount of data could not be collected. Contour maps of the deflection measurements on both 304H plates are shown below in Figure 18. These contour maps indicate that the plates are relatively symmetrical across the diagonal, rather than across the horizontal weld line. Thus, the corners of lowest deflection are at XY coordinates (0,0) and (520,300), while the corners of highest deflection are at (0,300) and (520,0,) on both plates. The maximum deflection value on the corners of the 304H/Ni201 and 304H/C22 plates were 9.00 mm and 8.39 mm, respectively.
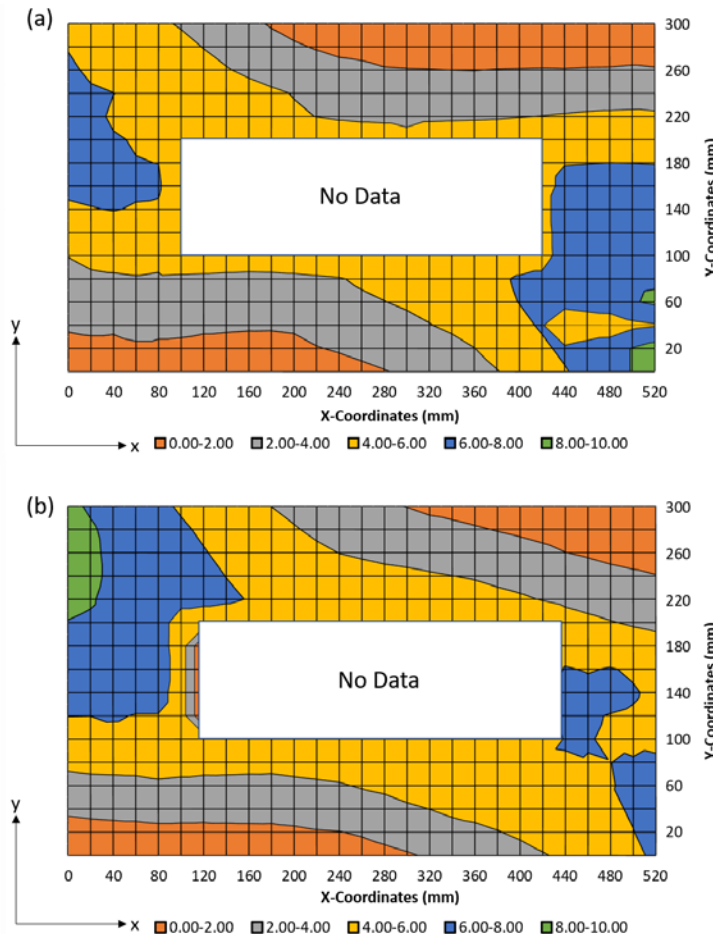
Figure 18. Deflection contour maps for (a) 304H/Ni201 and (b) 304H/C22 explosion clad plates. The maps are in the same orientation as the root side pictures in Figure 16

29

4.1.2.4 P91/201 and P91/C22 Clad Plate Welding Parameters

Figure 19 illustrates a schematic of the welding geometries of both plates, provided by Enerfab. The welding geometries are identical for both P91 clad welds. In contrast to the 304H clad weld geometry, the P91 clad welds were done using a double-v groove at an angle of 60°, with the clad layer on the top surface instead of the bottom surface.
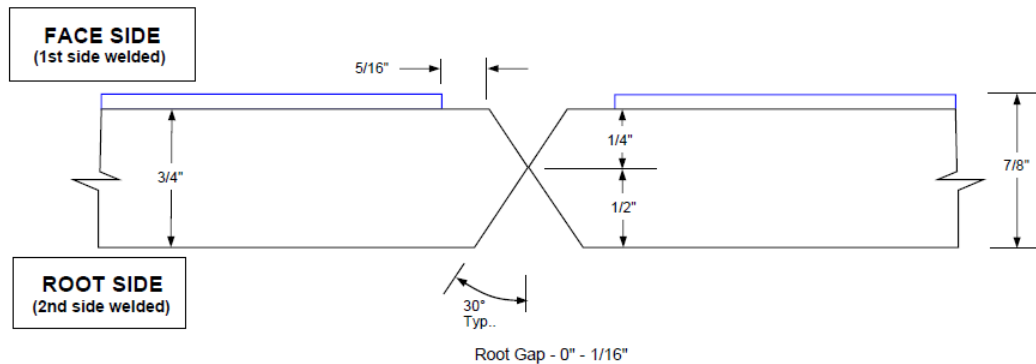
Figure 19. Welding geometry of the P91/Ni201 and P91/C22 butt welds. Face side is the top surface and root side is the bottom surface.

Additionally, the weld pass sequence for each weld is shown in Figure 20. The blue circles represent the FCAW beads for the face and root sides, and the green circles represent the pulse GMAW beads for all three clad layers, respectively.

The bead placement and pass order are different than the 304H clad welds. As with the 304H clad welds, the FCAW E91T1 backer passes were completed first, prior to the clad layers. Furthermore, the face side FCAW passes were welded before the root side passes on the P91 clads. The pulsed GMAW clad layers were completed last on the face side, after completion of all FCAW backer passes. For the P91/Ni201 clad weld, there are 13 total FCAW beads for the face and root sides with one pass (pass 9) being removed by arc gouging and griding due to porosity. The P91/C22 clad only has nine FCAW passes for the face and root sides. For the three clad layers, the Ni201 clad has 15 in total, while the C22 clad has 14 in total.
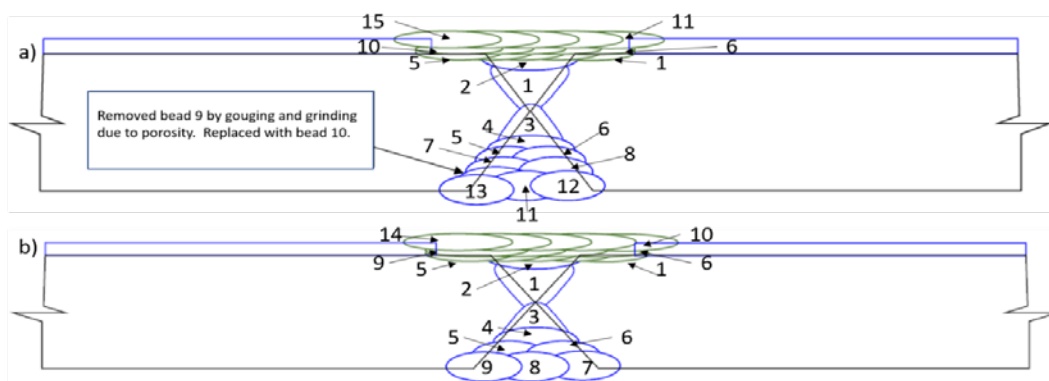
Figure 20. Bead placement and pass order overlay for (a) P91/Ni201 and (b) P91/C22 plate butt welds

After completion of pass 2 and the last FCAW passes but before the pulsed GMAW clad passes, bake outs of 600°F (315°C) for 1 hour were completed. The welds also underwent post weld heat treatments (PWHTs) after the completion of all welding. The plates experienced an unrestricted rise of temperature to 800°F (427°C) with a heating rate of 400°F/hr (204°C/hr). Furthermore, the soak temperature and time were 1350°F (732°C) and 2 hours, respectively. Finally, the maximum restricted cooling rate was 500°F/hr (260°C/hr), with unrestricted cooling from 800°F (427°C) to conclude the welding procedure.

4.1.2.5 Ambient Temperature Tensile Testing

Figure 21 summarizes the engineering stress-strain plots for eight tensile samples, i.e., two samples from each of the four plates. Figure 22 summarizes the average values for each plate (cladded couple) compared to the properties of the corresponding substrate base metal (from supplier's data). From these two figures, we can see that 304H/C22 samples gave the highest combination of ultimate tensile strength (UTS) and elongation compared to the other three plates. Moreover, cladding with Ni201 appears to reduce the UTS by 13% and 6% for 304H and 91 steel substrates, respectively, compared to the samples cladded with C22 on the same two substrates. Despite the slight reductions in UTS, this observation indicates that the clad layer material is interfering with the joint strength—especially for 304H/Ni201 samples that showed double steps in the stress/strain curves before fracture, which will be explained later.
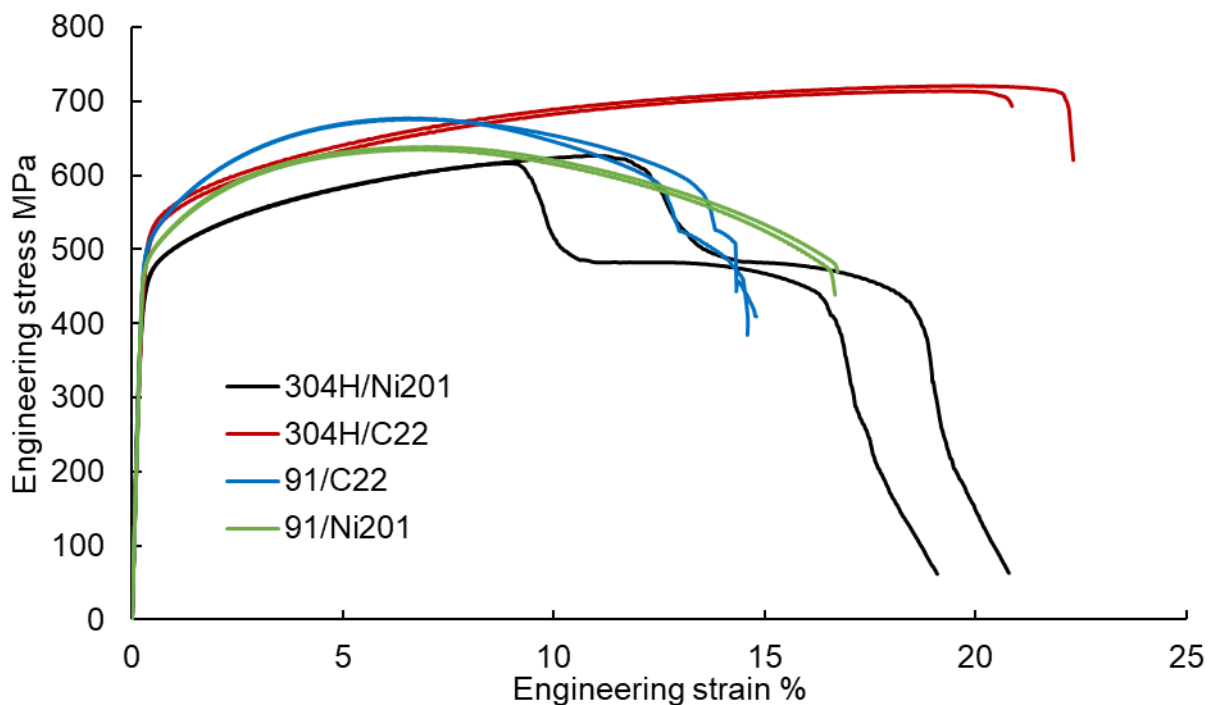
Figure 21. Engineering stress-strain curves for the butt-welded joints
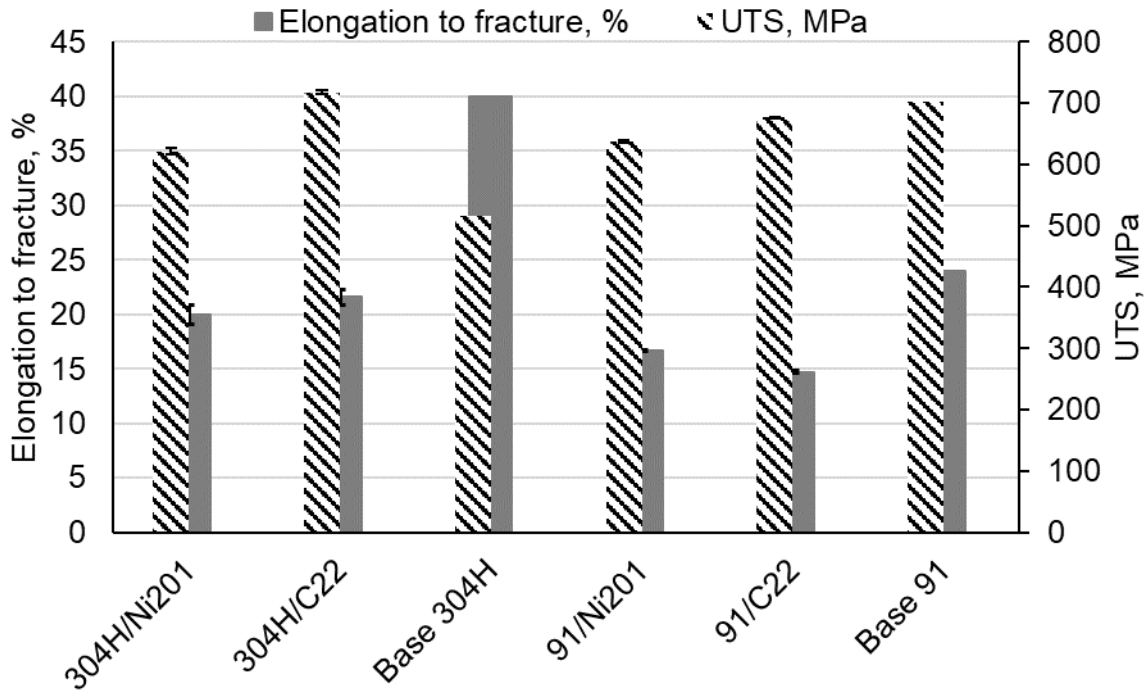
Figure 22. Average values of UTS and elongation for each plate compared to the substrate base metals

Table 17 shows that the strength of all tested samples passed the criteria of higher than 80% of the base metal's UTS. However, there is a considerable reduction in elongation.

Table 17. Comparing the Mechanical Properties of the Welded Joints to the Base Metal

Material	Butt weld joint (tested at CSM)		Substrate base metal (from suppliers' data)		Comparison	
	Total Elong., %	UTS, MPa	Total Elong. %	UTS, MPa	Total Elong. weld/base %	UTS weld/base %
304H/Ni201	19.9	621.5	40	51	49.9	120.2
304H/C22	21.6	717.4			54.0	138.8
91/Ni201	16.7	636.6	24	703	69.6	90.6
91/C22	14.7	676.4			61.3	96.2

4.1.2.6 Strain Partition and Microstructural Characterizations

Figure 21 summarizes the first set of uniaxial tensile tests of each weld using linear extensometers. Figure 23 shows an additional set of tests from each weld using 3D DIC methods for strain partition measurement.
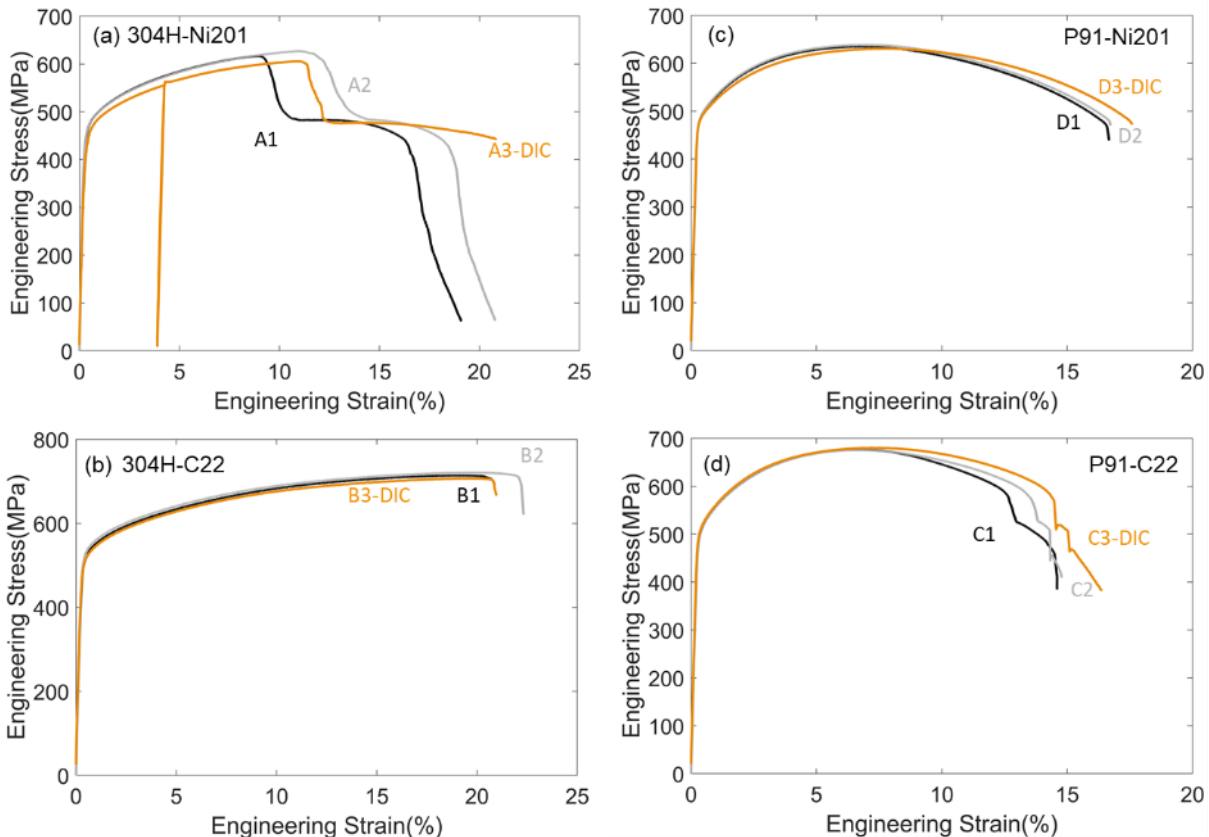
Figure 23. Engineering stress-strain curves from transverse butt welds of EXW cladded plates: (a) 304H-Ni201, (b) 304H-C22, (c) P91-Ni201, and (d) P91-C22. Digital image correlation (DIC) test using virtual extensometer from DIC method to calculate engineering strain in gauge section.

In summary, the 304H-C22 couple maintains the best UTS and elongation compared to the other three welds. In terms of failure locations, all P91 samples failed in the base metal via a relatively ductile fashion, while 304H samples either failed in the fusion zone or the HAZ. All the repeating tensile tests failed in the same locations with similar failure characteristics. Detailed characterizations for each weld case are described in the subsections.

4.1.2.6.1 304H With Ni201 EXW Clad

The two-step deformation behavior observed in 304H/Ni201 stress-strain curves in Figure 23(a) and Figure 24(a) corresponds to the three red arrows marked in the optical macrograph of the side surface of the weld specimen in Figure 24(a). Arrow 1 shows fracture initiation on the Ni201 layer surface and within HAZ, which then propagates close to the fusion line of ERNi-1 WM within the Ni201 clad layer. The DIC measurement results as strain increases are summarized in Figure 24(b). The sudden drop in the load corresponds to the initial crack forming in the Ni201 HAZ, as seen when transiting from the blue (11% strain) to the orange (15% strain) framed DIC images. The cracking propagates along arrow 2 within the 11%–15% average strain range along the ERNi-1/304H fusion boundaries inside the clad layer, directing the crack propagating parallel to the axial loading direction. Then, localized necking in the remaining 304H backer material starts at 15% total strain until failure in region 3. The presence of secondary phases and microcracks in the Ni201 HAZ (as seen later in Figure 29 and Figure 30) may be responsible for the lower UTS and % elongation to failure compared to the other cladded

33

welds. The progression of strains within the gauge section shows relatively symmetric behavior in Ni201 HAZ until 11% of total strain.
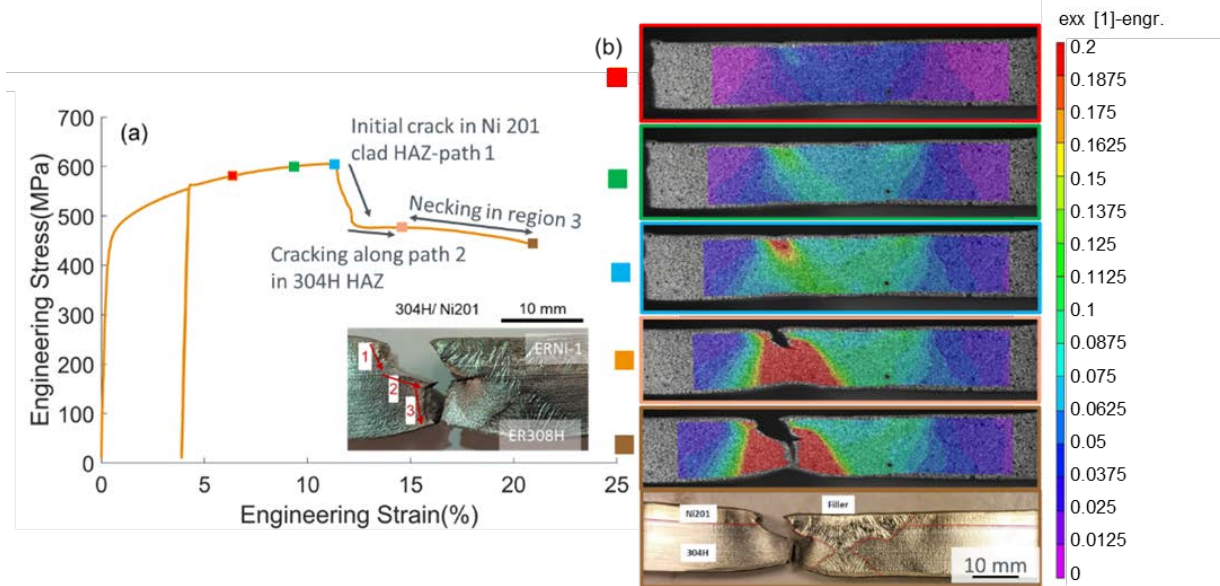
Figure 24. 304H-Ni201 DIC tensile test result: (a) engineering stress-strain curve calculated using a virtual extensometer along with the macrograph of fractured sample, and (b) DIC measured strain partition behavior during tensile loading corresponding to the highlighted stages by solid squares with various colors in (a), which are at overall loading strains of 6.5%, 9%, 11%, 15%, and after fracture, respectively

Vicker's microhardness mapping was performed on all four weld sets with vertical spacing (parallel to thickness direction) of 950 µm vertical for 304H welds and 1150 µm in P91 welds, and 500-µm spacing horizontally, using a 500 gram-force load. Assuming symmetry across the centerline of the weld, the microhardness maps were located only on one side of each weld. Figure 25(a) shows low hardness in the coarse-grained heat affected zone in the Ni201 (<120 HV). 304H side of the explosion clad bond away from the weld region exhibits the highest hardness of 440 HV. The pulsed GMAW process during the first and second clad deposition passes likely contributed to the grain coarsening as seen in the Ni201 HAZ in Figure 25(c) and is the explanation for the lowest microhardness and initiation of localized necking and cracking in Figure 25(b). Ni201 is hypothesized to have more severe grain coarsening in HAZ due to presence of less barriers (e.g., solutes, precipitates) for grain boundary mobility compared to other alloys, including C-22, 304, and 91 grades.

It should be noted that high hardness is observed along the explosion clad bond layer between the Ni201 clad and 304H SS substrate, as seen in Figure 26(a). A closer examination at the EXW bond interface and weld interfaces in Figure 26(c) shows the presence of dark etch bands within the deformed equiaxed grains, which is likely α' martensite due to the transformation induced plasticity (TRIP) mechanism that may occur during high strain rate working associated with explosion welding in austenitic stainless steel. The explosion welding process, being a high-pressure solid-state welding process, would provide sufficient mechanical energy to activate TRIP mechanism in the 304H backer. There are no obvious interface defects or other secondary phases observed at the EXW bonding interface. The presence of α' martensite, high dislocation

34

density, and recrystallized fine grains (as seen in Figure 26) are expected to be the main reasons for the high hardness near the interface in the 304H backer.
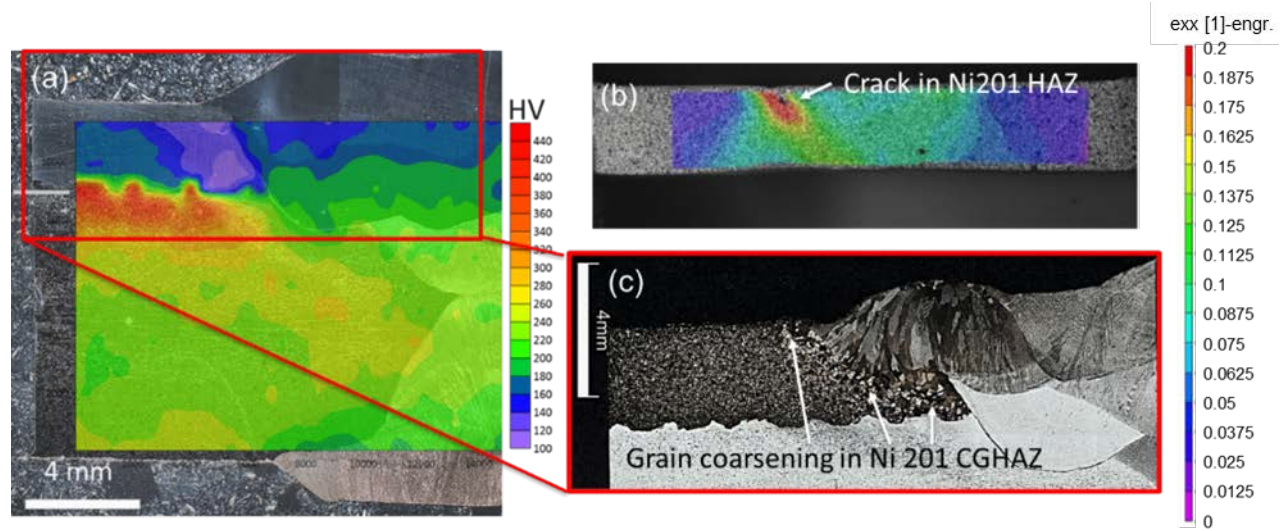
Figure 25. (a) Microhardness map of 304H-Ni201 explosion clad weld showing region of hardness below 120 HV in Ni201 HAZ, (b) initial cracking observed in Ni201HAZ, with (c) presence of significant grain growth due to the pulsed GMAW welding process
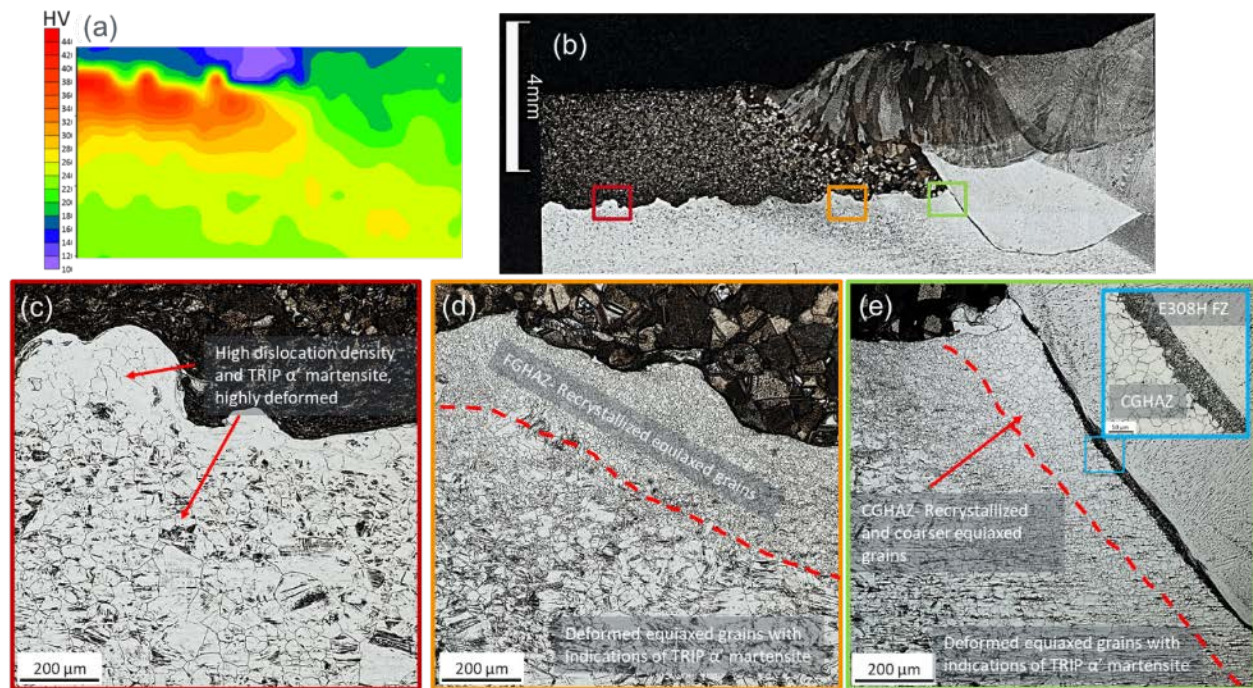
Figure 26. Metallurgical characterizations on 304SS backer with Ni201 clad: (a) microhardness map, and (b) light optical micrograph along with the magnified micrographs of (c) as-received explosion weld Ni201 on304H SS clad interface, (d) fine-grained HAZ (FGHAZ) from pulsed GMAW passes, and (e) CGHAZ in 304H SS backer

Additionally, microhardness decreases in both the Ni 201 HAZ and 304H SS HAZ, where noticeable grain coarsening occurs. As shown in Figure 26(e), significant grain coarsening occurred in the coarse-grained HAZ of 304 backer near the EXW bond interface, which is

attributed to a combination of high temperature thermal cycles during the weld process and high plastic strain introduced by EXW process. Note that EDS analysis for this sample was discussed in detail in the previous quarterly report (Q6). The top layer deposited showed a dilution level lower than 25%.

The composition of the backer, clad, and fillers for each base material from the suppliers are tabulated in Table 18.

Table 18. Compositions of 304H Backer, Ni 201 Cladder, E308H FCAW Wire, and ERNi-1 GMAW Wire from Material Test Reports

Element	Ni 201 Cladder	ERNi-1	304H Backer	E308H
Nickel	99.66	95.81	8.1	9.62
Molybdenum	-	-	0.3	0.02
Chromium	-	-	18.3	18.74
Iron	0.14	0.071	Balance	Balance
Manganese	0.04	0.35	1.8	1.3
Titanium	-	3.5	-	-
Carbon	0.02	0.029	0.05	0.06
Nitrogen	-	-	0.08	0.028
Phosphorus	-	<0.005	0.033	0.025
Sulfur	0.002	0.001	-	0.005
Silicon	0.06	0.08	-	0.49

A total of six areas of interest were investigated using EDS on the 304H SS/Ni201 welded clad. Figure 27 illustrates the locations of six EDS scan lines, and the results are summarized below:

- Line 1: 304H backer and Ni201 cladder explosion clad interface (see Figure 28)

The interface has a sharp transition in composition profiles, indicating very limited interdiffusion between the clad and the backer introduced by the solid-state explosion cladding process occurring within an extremely short time.

- Line 2: 304H backer and Ni201 cladder explosion clad interface closer to the weld fusion boundary (see Figure 29)

This region lies closer to the weld metal regions, and potentially within Ni201 HAZ induced by the pulsed GMAW process with ERNi-1 filler. There is an intermixing zone forming in the HAZ with a width of ~50 μm. Microcracks were observed at the fusion boundary of the clad fusion zone, which can adversely impact the local mechanical properties, and failure was observed to initiate from this region.

- Line 3: Ni201 cladder and ERNi-1 cladder filler (see Figure 30)

Weld metal using ERNi-1 filler contains 73 wt% of Ni and up to ~15 wt% of Fe, which deviates significantly from the nominal composition of ERNi-1 filler, as summarized in Table 18. This is likely due to dilution of the ErNi-1 filler because of mixing with the 304H backer and E308H filler while the weld pool is molten. The dilution is estimated to be approximately 25% based on the Ni content. In addition, more microcracks were observed at this location.

- Line 4: 304H backer and ERNi-1 cladder filler (see Figure 31)

36

Because the Ni content is less in the WM region compared to Line 3, there seems to be higher dilution % of the ERNi-1 cladder filler in this region (avg. 66 wt% of Ni). This region is the same cladder pass as Line 3, but the line scan is closer to the 304H backer.

- Line 5: E308H backer filler and ERNi-1 cladder filler (see Figure 32)

The chemical composition across this interface is similar to Line 4. Also, a transition zone could be observed along this interface.

- Line 6: 304H backer and E308H backer filler (see Figure 33)

There is no obvious compositional change across the interface from the 304H backer into the weld made with its matching filler.
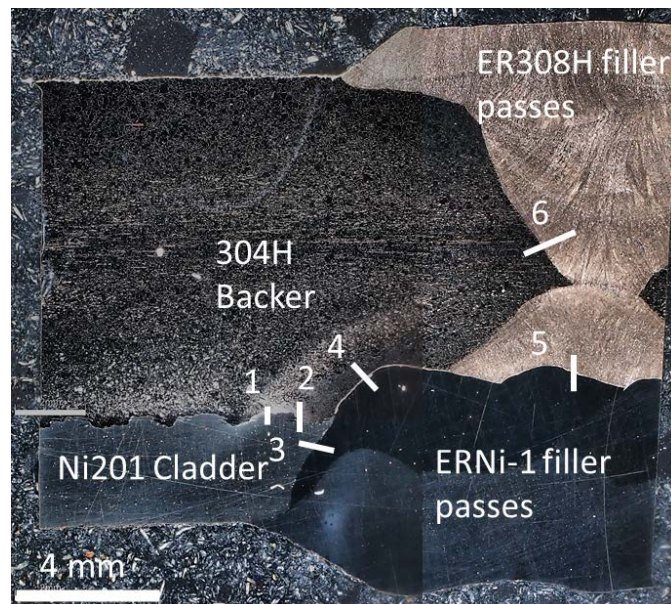
Figure 27. EDS line scan locations of 304H/Ni201 sample
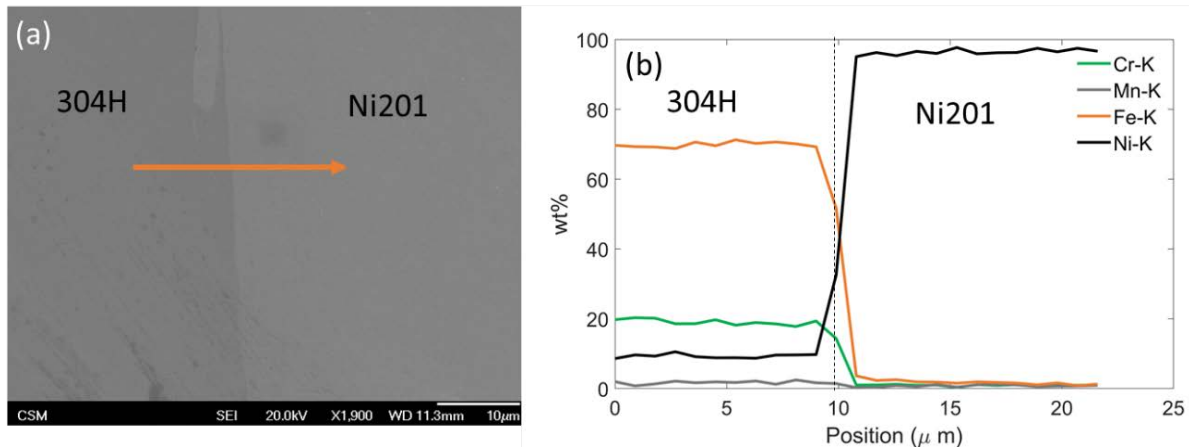
Figure 28. Line scan 1 304H-Ni201
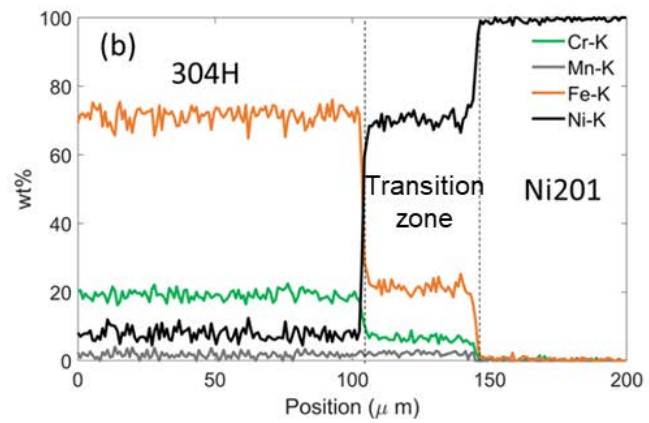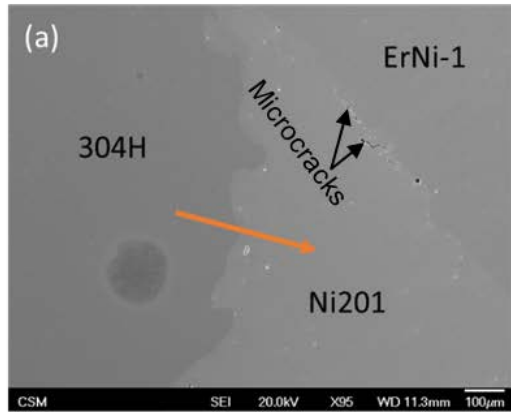
Figure 29. Line scan 2 304H-Ni201 closer to fusion boundary
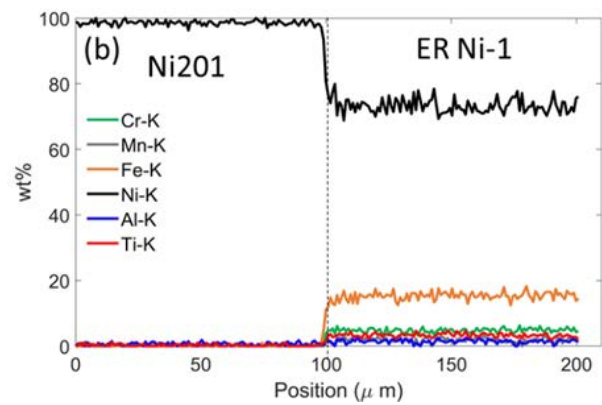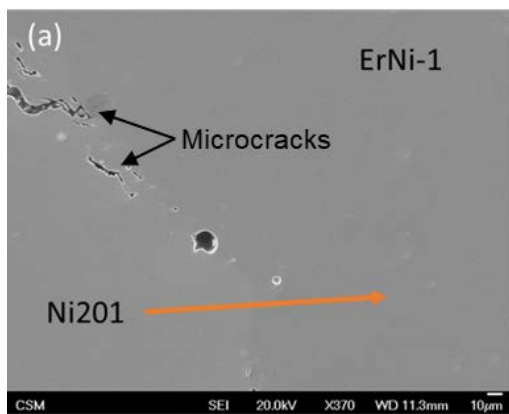
Figure 30. Line scan 3 Ni201-Er201
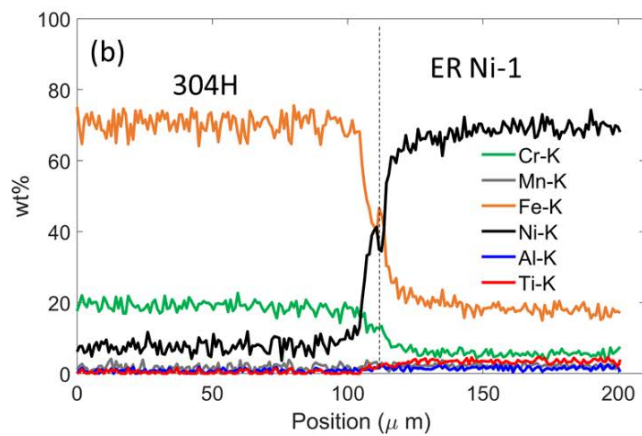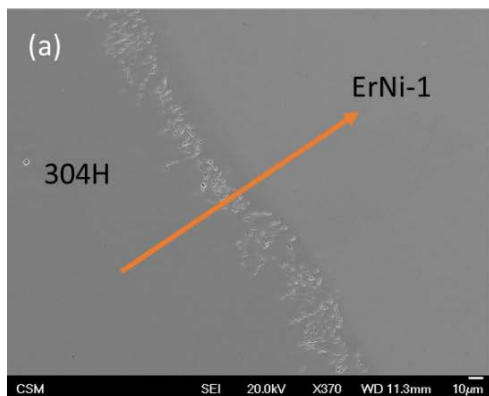
Figure 31. Line scan 4 304H-ErNi-1

38
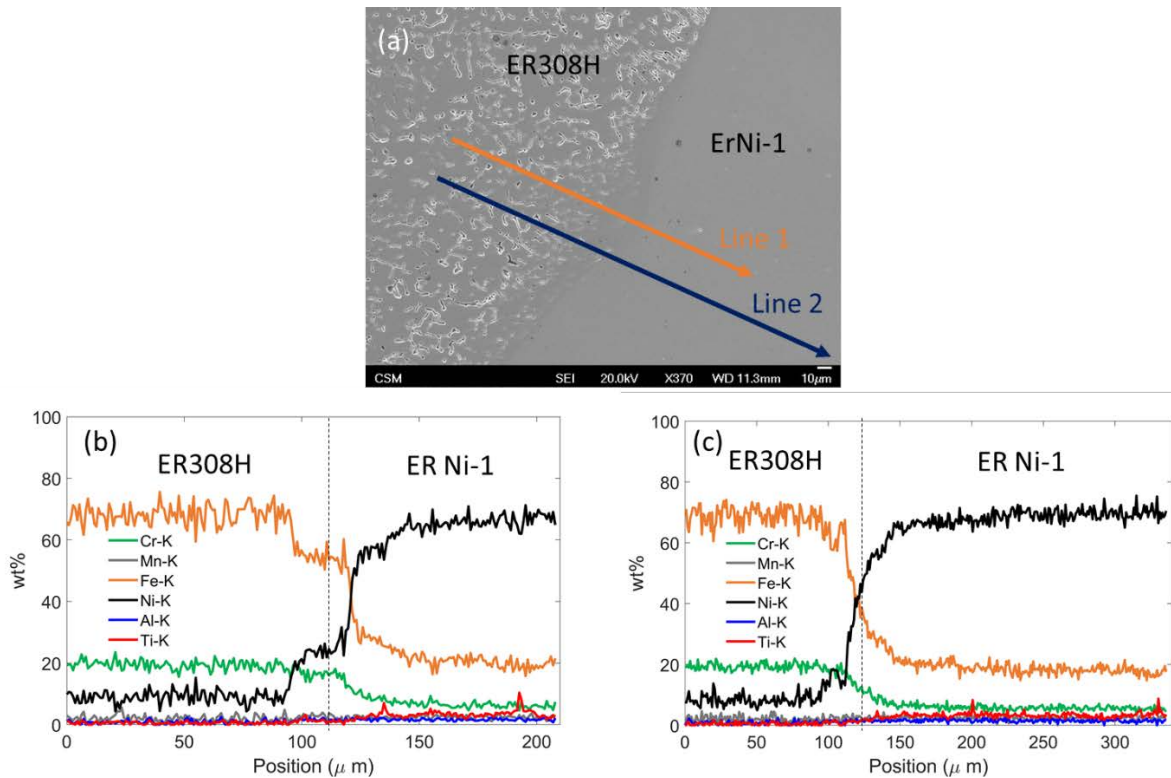
Figure 32. Line scan 5 ER308H-ERNi201
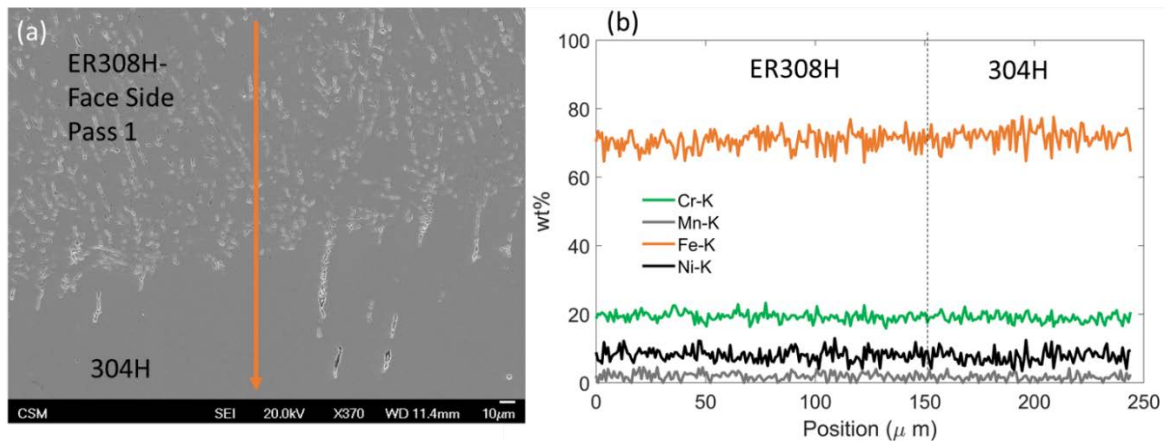
Figure 33. Line scan 6 ER308H-304H

4.1.2.6.2 304H With C22 EXW Clad

Figure 34 compares the DIC calculated strain partition, the microhardness map of the 304H-C22 EXW butt weld, and the tensile stress-strain curves. All the tensile samples failed along the weld centerline of the E308H and ERNiCrMo-10 FZ, as seen in Figure 34(a–b). This observation corresponds well to the lowest hardness observed within the E308H FZ, which is located at the low right corner of the hardness map contour in Figure 34(b). The 304H-C22 weld outperforms all other cases in terms of UTS and % elongation. Right before fracture at 20% elongation, the DIC image (last frame in brown) shows high localized strain above 60%. The microhardness in

39

the EXW clad interface region of the 304/C-22 couple was observed to be higher than that of the 304H-C22 couple. This could be caused by the higher strength of C22 than Ni 201 clad.
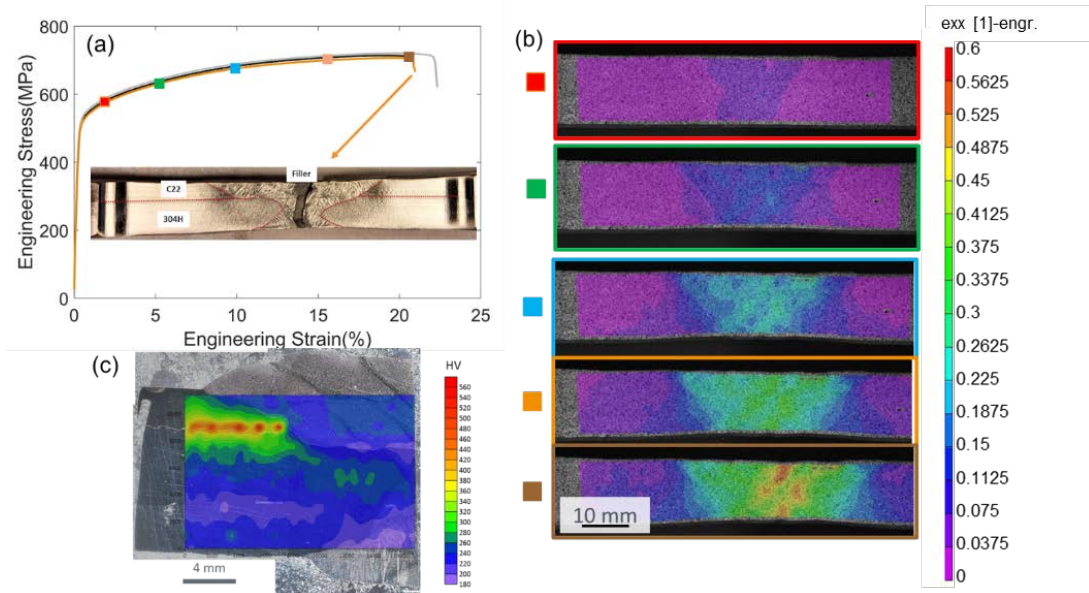
Figure 34. 304H-C22 DIC tensile test result: (a) engineering stress-strain curve calculated using a virtual extensometer along with the macrograph of fractured sample, and (b) DIC measured strain partition behavior during tensile loading corresponding to the highlighted stages by solid squares with various colors in (a), which are at overall loading strains of 2%, 5%, 10%, and 20%; and (c) cross-sectional microhardness map of the weld overlayed on the macrograph

Figure 27 shows the EDS line scanning locations on the weld cross-section. No interdiffusion was observed between the clad layer and backer at the explosion cladding interface, as shown by the sharp transition of the chemical composition profile across the interface in Figure 28. This finding was consistent for all other tested plates (clad couples), as the EXW technique is a rapid solid-state process that does not provide enough time for interdiffusion. In addition, the EDS mapping at the C22 clad layer and its filler ERNiCrMo-10 interface in Figure 30 show no change in the composition across the fusion boundary. Figure 32 shows a narrow, 20-µm-wide interdiffusion region between the C22 filler and the 304H base metal. The chemical composition of both sides beyond the interdiffusion region goes back to the original compositions.

The chemical compositions of 304H base metal and its filler E308H match sufficiently well and therefore no change in composition profile was observed across their interface, as shown in Figure 39. Finally, the chemical composition of the deposited C22 filler layers was constant across three layers, as shown in Figure 40, indicating negligible dilution from the weld region of 304H substrate.

40
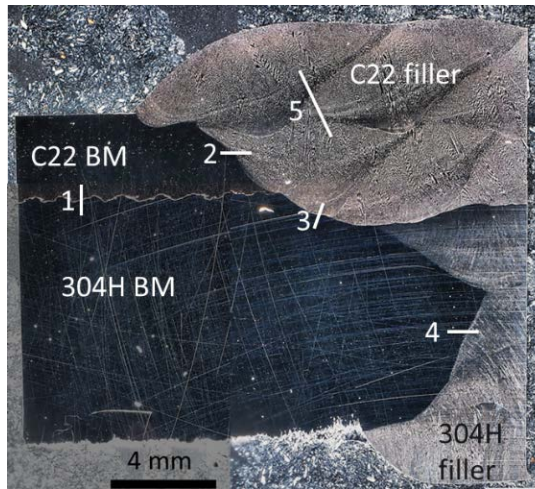
Figure 35. EDS line scan locations of C22/304H sample
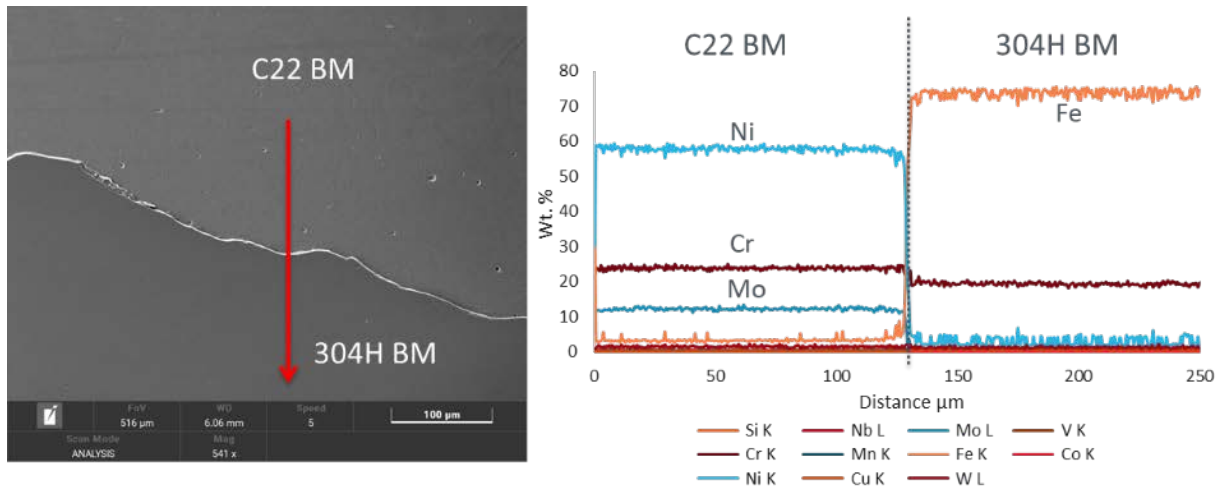
Figure 36. EDS scan (line 1 in Figure 27) from C22 clad to 304H substrate
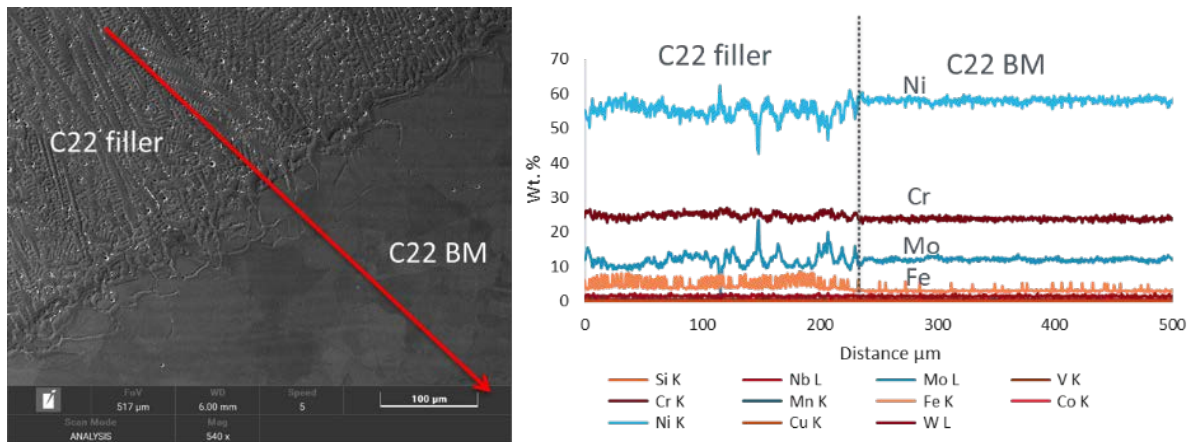
Figure 37. EDS scan (line 2 in Figure 27) from the filler ERNiCrMo-10 to C22 clad layer
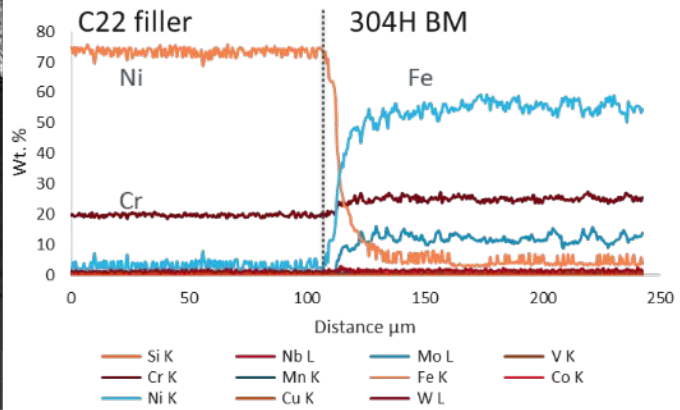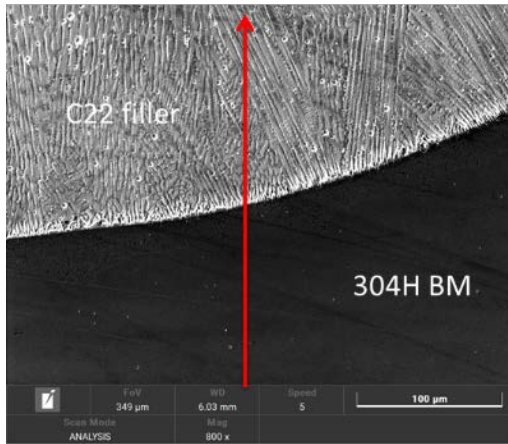
Figure 38. EDS scan (line 3 in Figure 27) from the filler ERNiCrMo-10 to 304H substrate
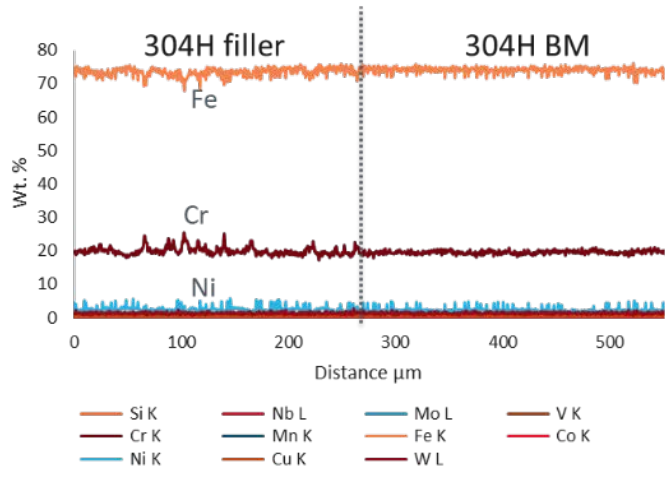
Figure 39. EDS scan (line 4 in Figure 27) from 304H filler to 304H substrate
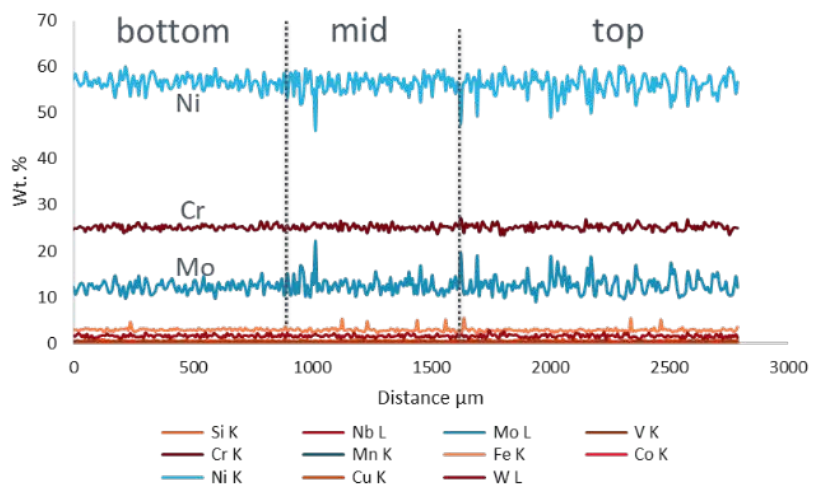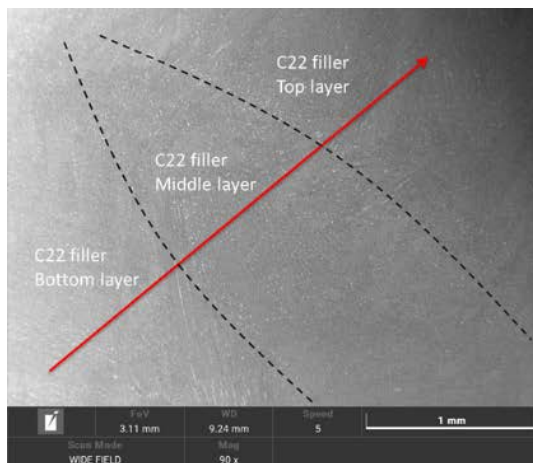
Figure 40. EDS scan (line 5 in Figure 27) in the multi-pass weld of C22 clad side

4.1.2.6.3 Gr. 91 Steel with Ni201 EXW Clad

Figure 41 summarizes the DIC and tensile results of Gr.91 backer and Ni201 cladder welds. Failure occurs in the BM for all three tests, with "round-house" yielding observed in high strength steels in Figure 41(a). The microhardness results show the weakest region to be the Ni201 region. The DIC strain maps show necking developing in the P91 and Ni201 BM regions. The ER91T FZ exhibited the highest microhardness and the lowest strain evolution, as seen in Figure 41(b).

Figure 42 shows the microstructural features present in the P91-Ni201 weld. Grain coarsening is observed in the Ni201 HAZ (Figure 42(c–d)). There seems to be a homogenous coarsening in the Ni201 clad layer, likely due to the PWHT of 760°C/2 hours performed after welding. There is potentially a complex combination of microstructural features in the ER91T-FZ in Figure 42(b), such as martensite that formed during welding, tempering of martensite, and nucleation of higher-temperature VC carbides during PWHT. As observed in Figure 42(e), a clear coarse-grained HAZ (CGHAZ) is present in the Gr.91 side and adjacent to the clad filler ERNiCr-3, which attributes to the low microhardness ≤180HV in Figure 41(c).
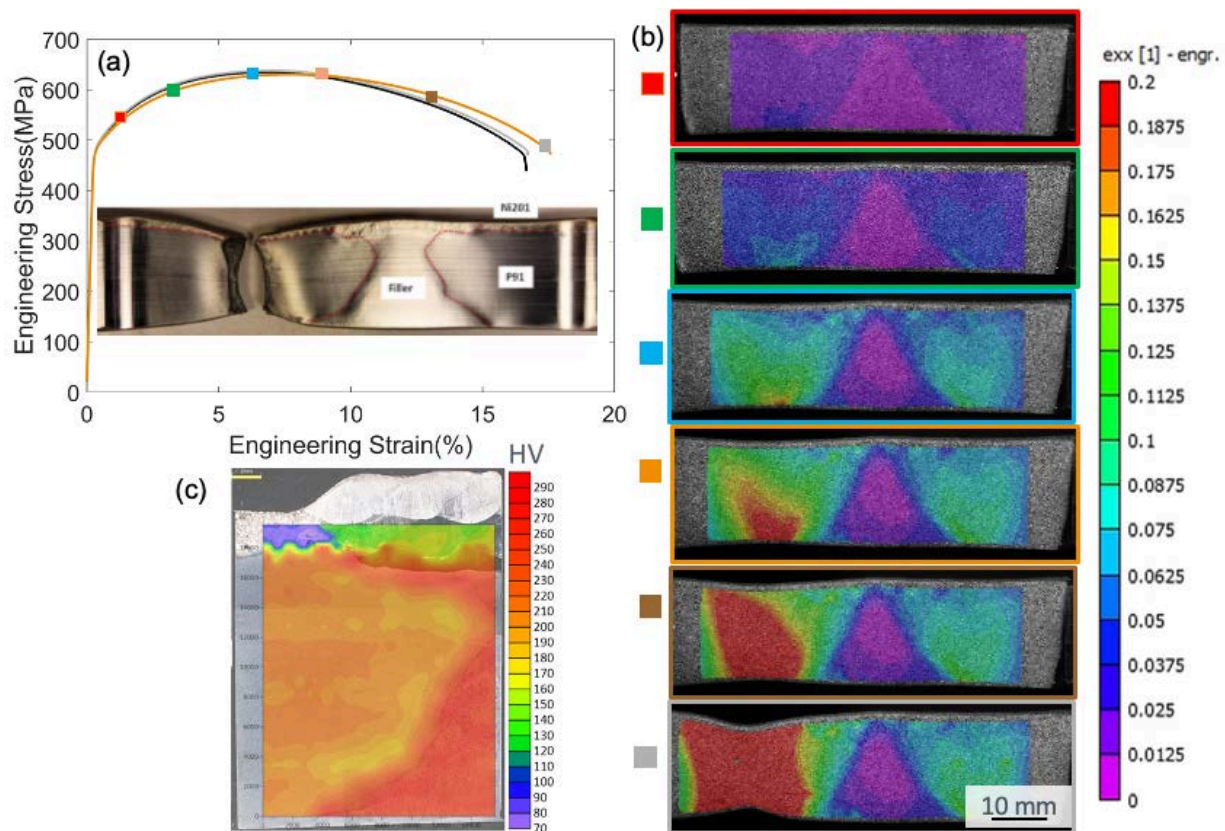
Figure 41. P91-Ni201 DIC tensile test result: (a) engineering stress-strain curve calculated using a virtual extensometer along with the macrograph of fractured sample, and (b) DIC measured strain partition behavior during tensile loading corresponding to the highlighted stages by solid squares with various colors in (a), which are at overall loading strains of 1.5%, 3.2%, 6.4%, 8.4%, 10.6%, and 17.2%; respectively; and (c) cross-sectional microhardness map of the weld overlaid on the macrograph

43
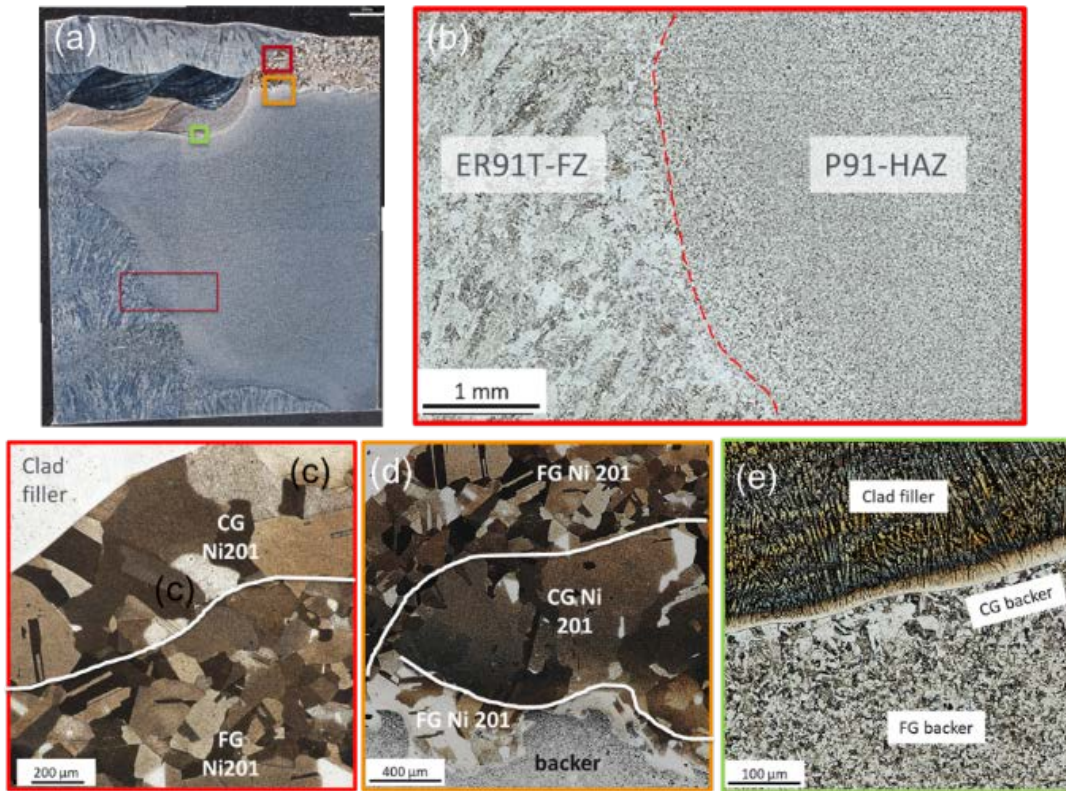
Figure 42. (a) Cross-sectional macrograph of P91-Ni201 weld, and the magnified micrographs in (b) ER91T-FZ and Gr. 91 HAZ, (c) interface between ERNi-1 FZ top layer (i.e., third layer) and Ni201 clad layer, (d) interface between Ni201 HAZ and P91 backer, and (e) fusion boundary between ERNiCr-3 first layer and P91 substrate

Figure 43. EDS line scan locations in the cross section of butt-welded 91 steel backer with Ni201 clad

Only a narrow 20-µm-wide interdiffusion region was found between the Ni201 clad filler of the first layer (ERNiCr-3) and the 91-steel base, as depicted in Figure 45. It is worth mentioning that there is about 10 wt.% Fe in the bottom layer of the clad filler, which is significantly higher than the nominal value of 0.7 wt.%. Such an increase in Fe content is attributed to dilution from the steel base metal during welding. Figure 46 shows that the second (middle) clad filler layer (ERNi-1) was enriched with 6.2% wt.% Cr and 2.3 wt.% Fe in comparison to 0% and 0.07%, respectively, in the nominal filler composition. Figure 47 shows minimal Cr and Fe enrichment in the top layer of the clad filler, indicating minimum dilution and maintaining of the corrosion resistance in the clad top layer.
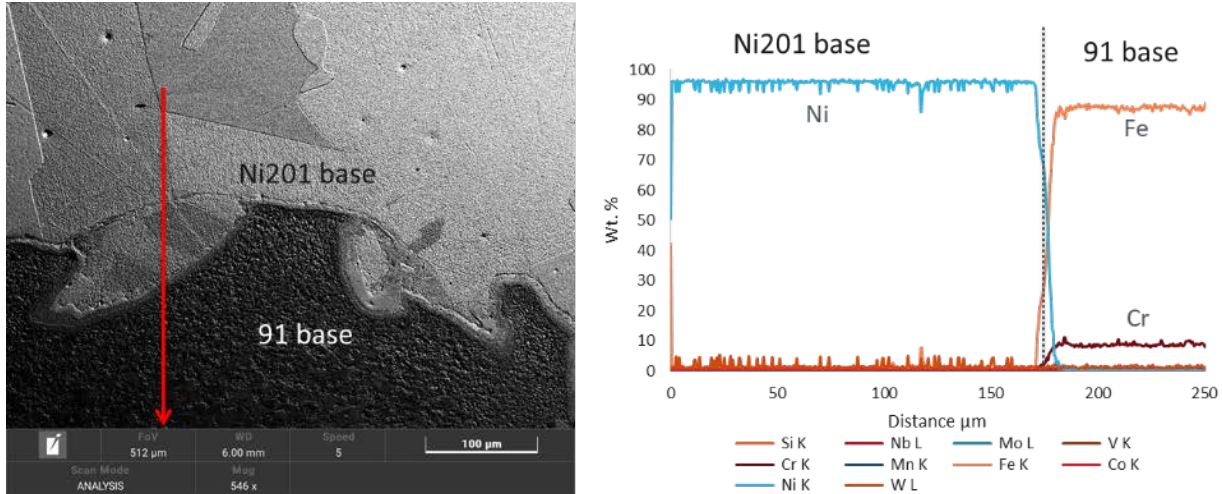
Figure 44. EDS scan (line 1 in Figure 43) from Ni201 clad to 91 substrate
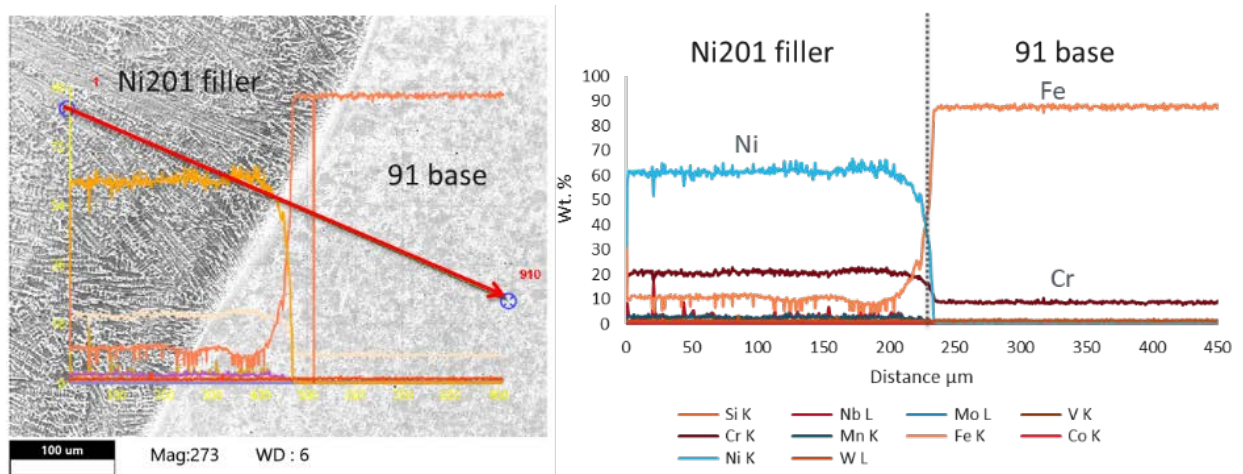
Figure 45. EDS scan (line 2 in Figure 43) from Ni201 first weld layer to 91 substrate

45
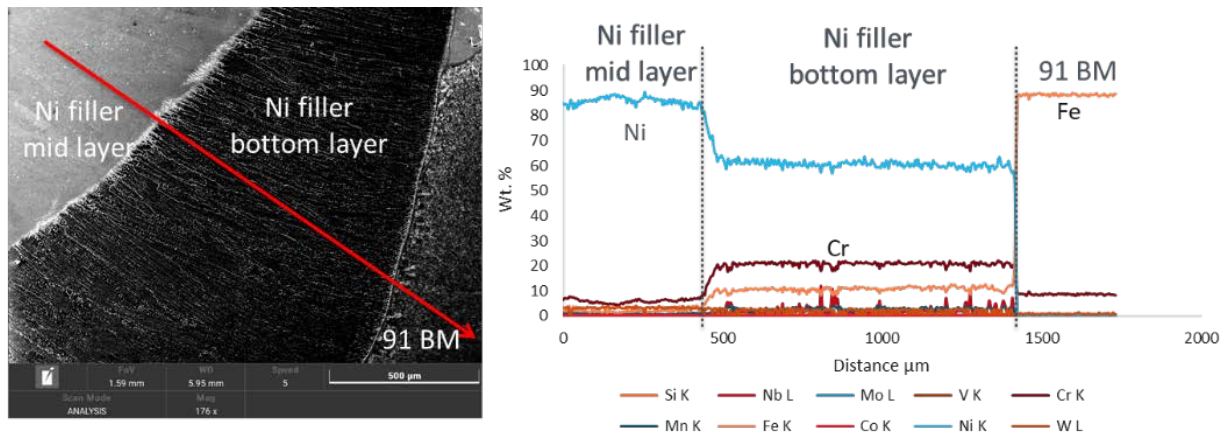
Figure 46. EDS scan (line 3 in Figure 43) from Ni201 middle weld layer, the bottom layer, to the 91 substrate
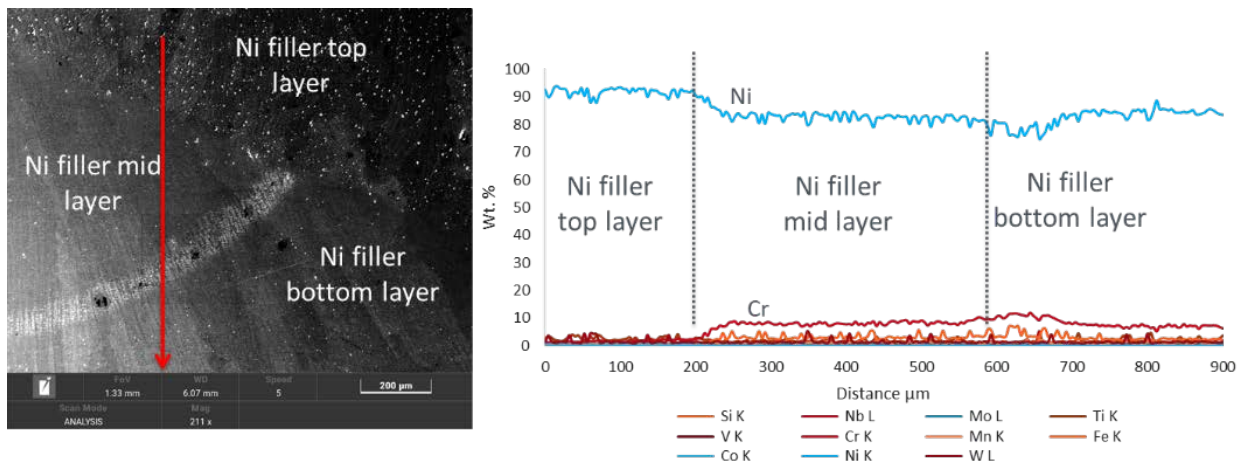
Figure 47. EDS scan (line 4 in Figure 43) from Ni201 weld top, middle to bottom layer

4.1.2.6.4 Gr. 91 Steel with C22 EXW Clad

Figure 48 summarizes the stress-strain curves; fracture location (in BM); DIC images for strains at 1.5%, 3.2%, 6.4%, 8.4%, 10.6%, and 17.2%; and microhardness of a half cross section of the as-received weld. Similar to the 91-Ni201 weld, this weld had been PWHT at 760°C after welding. The samples seem to show progression of initial strain deformation, first in the HAZ, then progressing until necking is observed (starting with 8.4% average strain), and eventually failing in the HAZ. The ER91T FZ filler metal strongly resists deformation over the Gr. 91 substrate. All three samples failed outside of the weld metal, which is in good agreement with the microhardness map where the lowest hardness is present outside of the Gr. 91 weld region, as seen in Figure 48(c).

This report is available at no cost from the National Renewable Energy Laboratory at www.nrel.gov/publications.
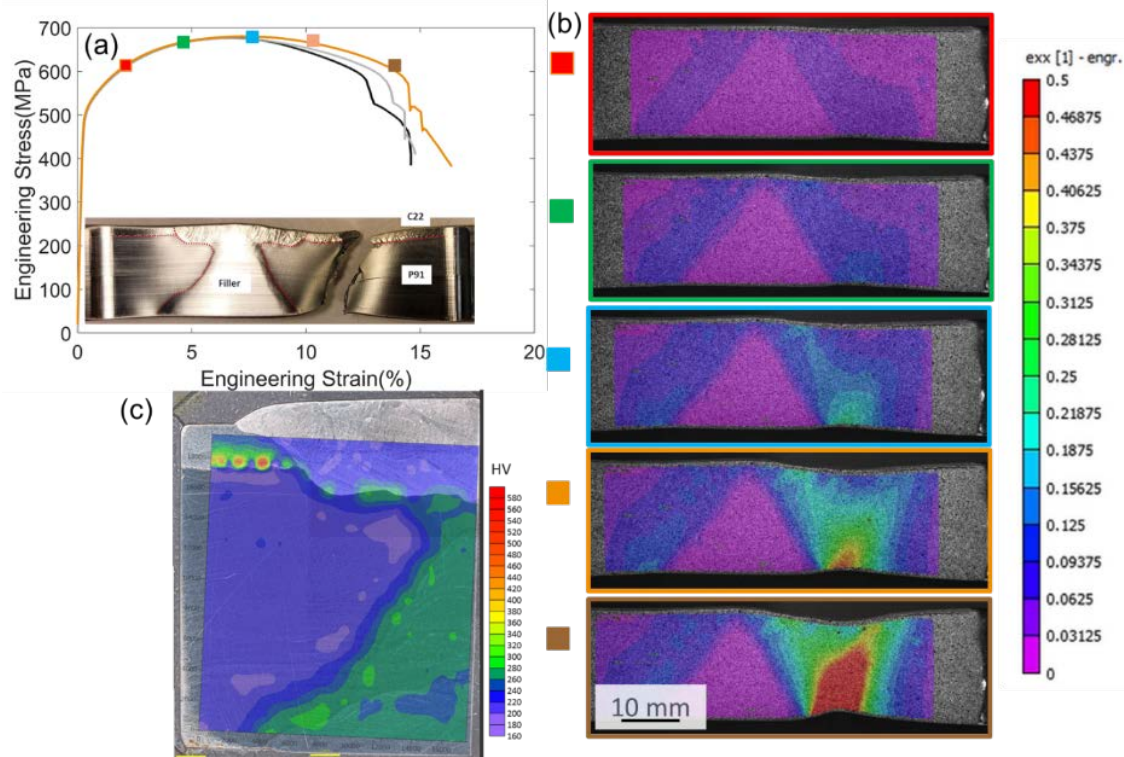
Figure 48. P91-C22 DIC tensile test result: (a) engineering stress-strain curve calculated using a virtual extensometer along with the macrograph of fractured sample, and (b) DIC measured strain partition behavior during tensile loading corresponding to the highlighted stages by solid squares with various colors in (a), which are at overall loading strains of 1.5%, 3.2%, 6.4%, 8.4%, and 15%, respectively; and (c) cross-sectional microhardness map of the weld overlayed on the macrograph
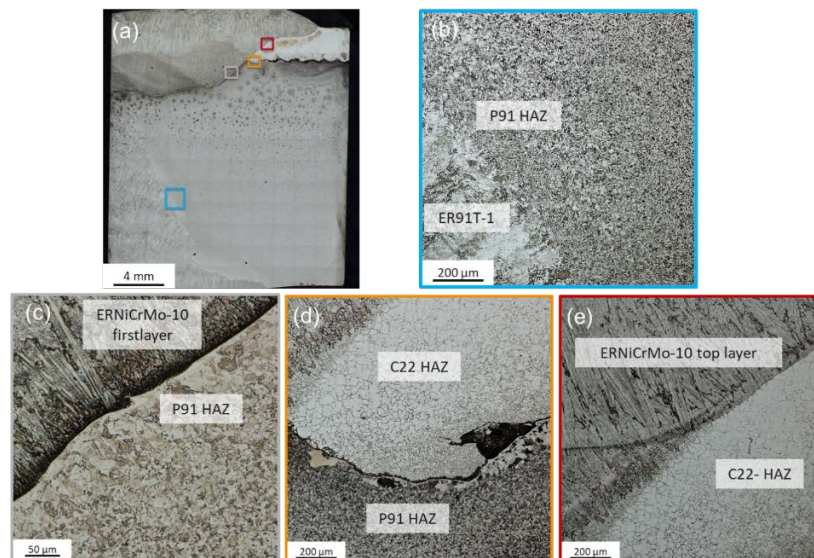
Figure 49. (a) Cross-sectional macrograph of Gr.91-C22 weld, and the magnified micrographs in (b) interface between ER91 FZ and Gr.91 HAZ; (c) interface between ERNiCrMo-10 first clad weld layer and Gr.91 HAZ; (d) intersection of ERNiCrMo-10 pass, C22 HAZ, Gr.91 HAZ, and EXW bond; (d) interface between Gr.91 HAZ and C22 EXW bond; and (e) interface between the top two layers of ERNiCrMo-10 and C22 HAZ

47

Figure 49 shows some microstructural features of the Gr.91-C22 weld. The Gr.91 backer weld filler and base metal shows similar characteristics in the 91-Ni201 weld. However, the weld region within the 91-C22 interface has much finer grains in the C22 HAZ than the Ni201 HAZ, by comparing Figure 49 to Figure 37, which likely determines the higher microhardness along the EXW interface in this weld than that of a Ni201 cladder. Further metallurgical examination is needed to confirm the exact location of failure, such as the specific HAZ region. In all, the P91 welds seem to show promising results in addition to the 304H-C22 mechanical results, but elevated temperature tests are needed to understand microstructural and mechanical property changes over time during service.

There is a very narrow interdiffusion distance present at the EXW bond interface between C22 clad and Gr.91 substrate, and between C22 bottom weld layer ERNiCrMo-10 and Gr. 91 substrate, as shown in Figure 51 and Figure 52. Very consistent chemical composition profile was observed between the 91-steel base metal and filler (E91T1) in Figure 53. On the other hand, the first two layers of the clad filler showed enrichment in Fe content in Figure 54, while the third (top) layer of the C22 filler matched the nominal composition of the alloy, indicating a good corrosion resistance is maintained.
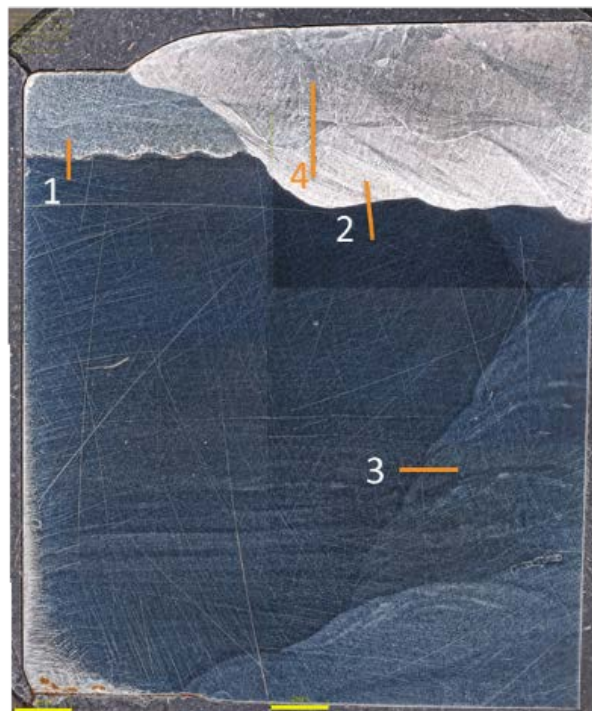
Figure 50. EDS line scan locations in the butt-welded Gr.91 substrate with C22 clad
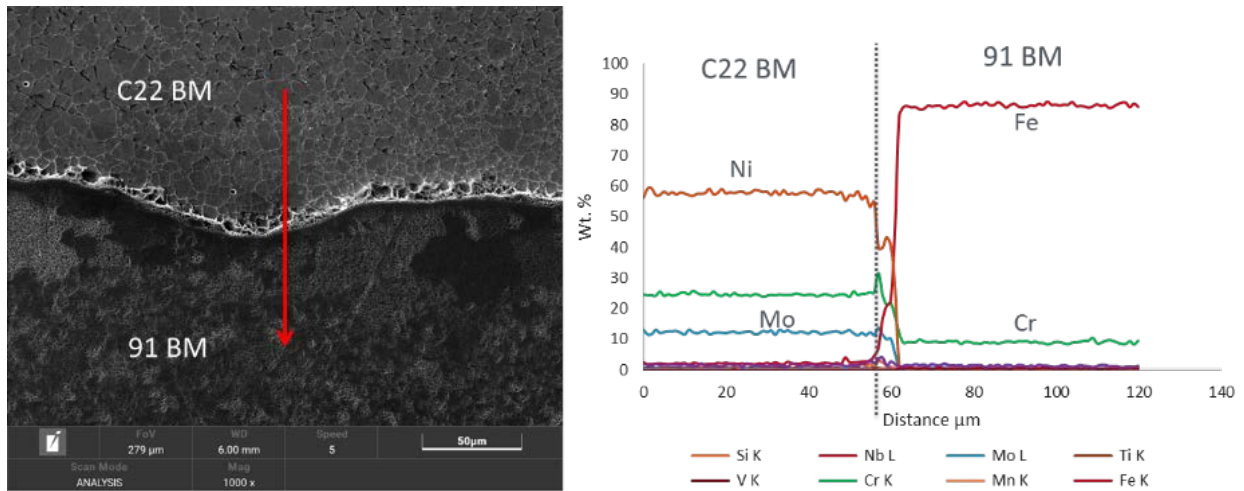
Figure 51. EDS scan (line 1 in Figure 50) from C22 clad to Gr. 91 substrate
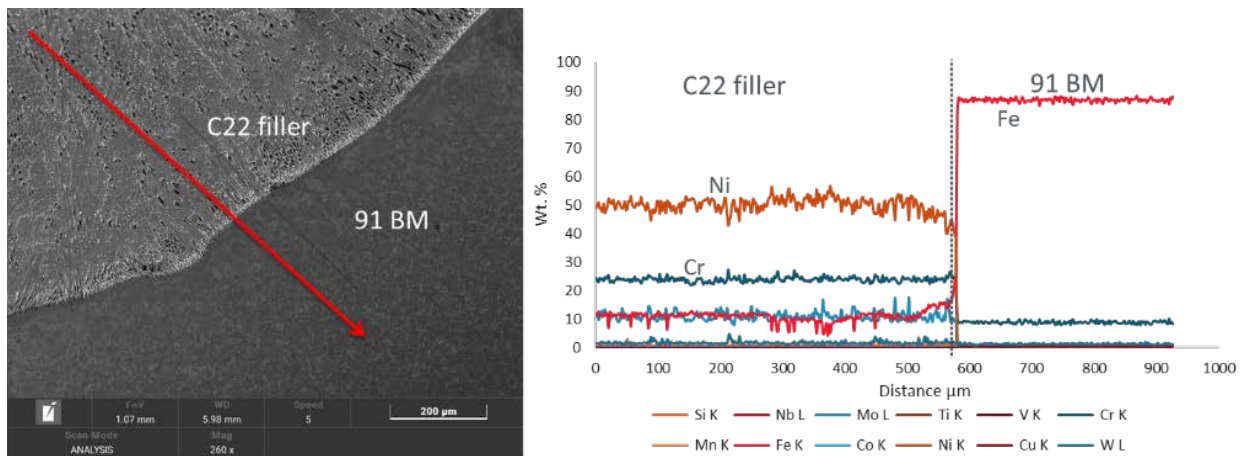
Figure 52. EDS scan (line 2 in Figure 50) from C22 bottom weld layer to Gr. 91 substrate
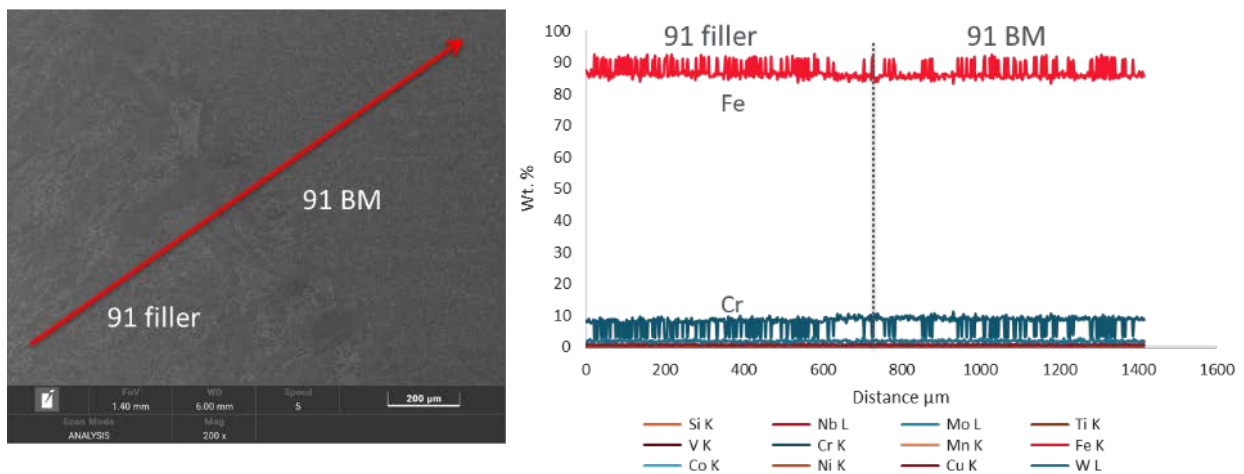
Figure 53. EDS scan (line 3 in Figure 50) from 91 filler to 91 substrate
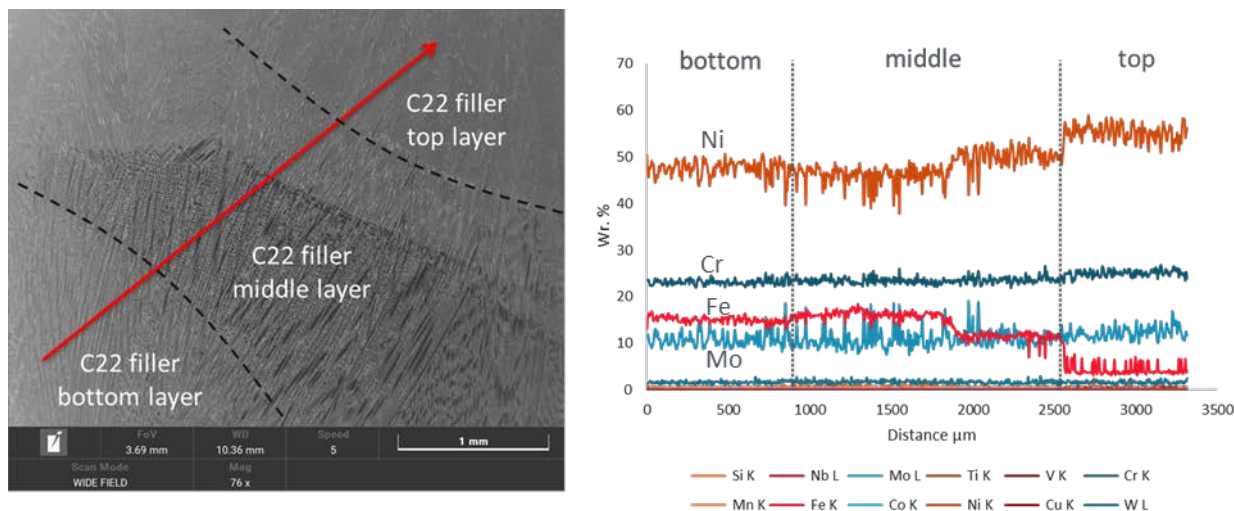
Figure 54. EDS scan (line 4 in Figure 50) from C22 filler bottom, middle to the top layer

4.1.2.7 Conclusions for Ambient Temperature Strength Evaluations and Metallurgical Characterizations of Butt-Welded EXW Coupons

- The clad couples are ranked based on UTS and elongation, and the order is 304H-C22 > P91-C22 > P91-Ni201 > 304H-Ni201. 304H-C22 clad couple outperforms the others in tensile tests at room temperature, although failures occurred along the weld centerline in all 304H-C22 specimens. The C22 clad leads to a higher UTS in general than Ni201 clad. The Ni201 is not recommended as a clad layer due to the weaker mechanical strength, more severe grain coarsening in CGHAZ, and formation of microcracks and secondary phases in HAZ/PMZ of 304H-Ni201 weld.
- The microhardness map correlates well with the strain partition behavior observed from DIC measurements. Strain accumulations and failures preferentially occurred in the softest regions. A high hardness was observed near the bond interface at the 304H backer side due to the presence of high dislocation densities, grain refinement, and formation of α' martensite associated with the EXW process. This was not observed in the P91 welds, as PWHT likely normalized the microstructures.
- The rapid solid-state process of EXW cladding resulted in minimum to no interdiffusion between the cladder and backer at the bond interface. No delamination was observed at the EXW clad interface during the uniaxial tensile tests parallel to the bond, indicating a good bonding strength.
- Through EDS analysis, all the fusion welds showed acceptable dilution levels on the top layer, as demonstrated by the matching concentration of corrosion resistant elements to the nominal compositions of the clad materials.

4.1.3 Thermomechanical Testing of Welded EXW Clad Coupons (Milestone 2.2.1)

After completion of the room temperature tests, it was deemed necessary to run high-temperature tensile tests to determine the effect of service temperatures (500°C for cold side and 720°C for hot side) on flow behavior in all four cladded couples. Because P91 is restricted to the cold side service temperature, the P91 welds are tensile tested at 500°C, while the 304H SS welds are tested at both 500°C and 720°C. A total of three duplicates were completed for each P91 EXW

50

(six total tests), while two duplicates were completed for each 304H SS EXW and temperature (eight total tests).

Table 19. Milestone 2.2.1 Details

Milestone	Description	Metric	Success Value	Assessment Tools
2.2.1: Thermomechanical testing of welded EXW clad coupons	Welded EXW clad coupons should pass the thermomechanical testing at the service temperature (based on M1.1.2) by exceeding the strength limit of the clad alloy	Thermomechanical resistance of the weld at the service temperature compared to wrought metals	>80% for welds	Gleeble test simulator and fractography analysis using optical and electron microscopies with energy dispersive X-ray spectroscopy (EDS) and hardness mapping. All test samples (at least three) should meet target with 10% error based on standard deviation.

4.1.3.1 High-Temperature Tensile Test Method and Setup

A 2-in. long induction coil with a 1 in. diameter was used to introduce the high temperature for tensile testing, as seen in Figure 55. The gauge section of the sample was aligned and centered to the center of the induction coil. One set of thermocouples was placed in the center of the gauge section on the opposing surface of the DIC painted surface to allow for feedback control of the induction unit to control temperature. The samples were roughly heated up to temperature with an approximate heating rate of ~100°C/minute. Once reaching temperature, the sample was soaked at temperature for one minute to minimize unstable temperature gradients, which could lead to serrations in the stress-strain curve.
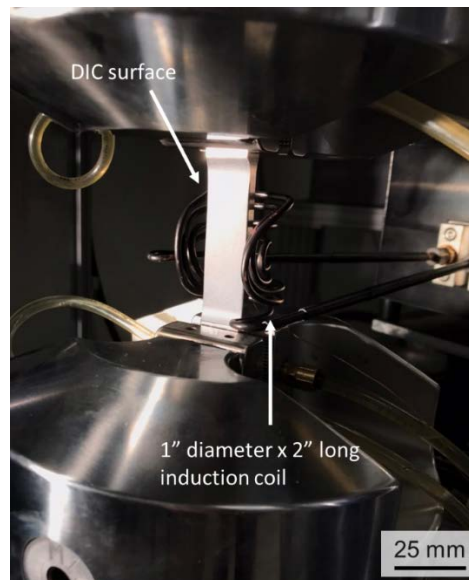
Figure 55. High-temperature DIC setup for uniaxial tensile testing using a 1-in. diameter x 2-in.-long induction coil with front surface open for DIC measurements

51

4.1.3.2 High-Temperature Tensile Results

The load-displacement curves for all high temperature tests are displayed in Figure 56, and the calculated engineering stress-strain curves are plotted in Figure 57. Based on strength comparisons and more certainty in elongation to failure, 304H-C22 and P91-C22 are the two best combinations. Because the thicknesses of the P91 plates are almost twice that of the 304H SS backer EXWs, the load bearing capacity of the P91 welds are higher. After normalizing to stress-strain, it seems the yield strength is higher in P91 welds vs. 304H welds at 500°C. However, strain hardening and uniform plasticity in the P91 welds at 500°C is significantly less than the 304H EXWs. There is significantly less true uniform strain in the P91 transverse weld component compared to the 304H EXWs based on the strain to necking in Figure 57. In all, the backers with C22 as the cladder performed best with both strength and elongation to failure.
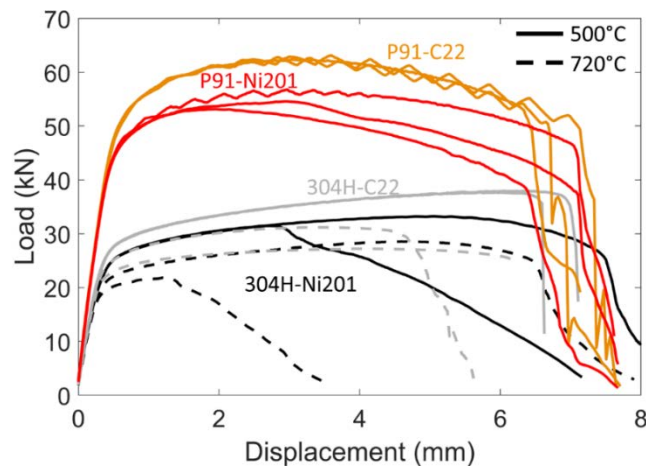
Figure 56. Elevated temperature tensile test (500°C, 720°C) load-displacement curves for all four EXW couples. Dotted line = 720°C, solid line = 500°C. The P91 EXWs were tested only at 500°C, representing the cold side service temperature, whereas 304H EXWs were tested at both 500°C and 720°C.
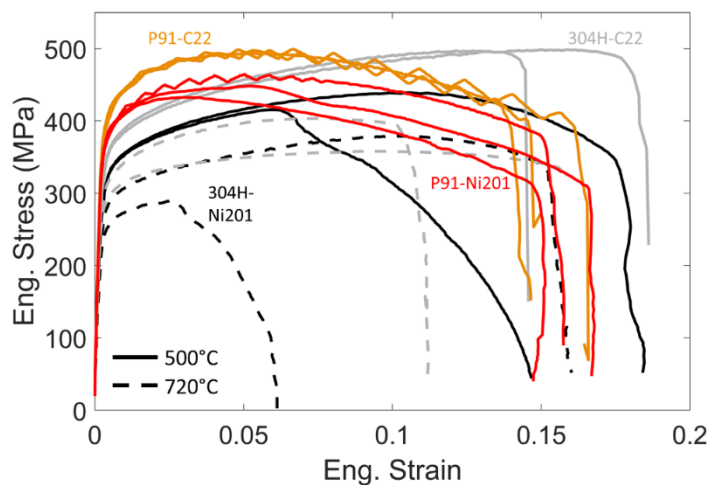
Figure 57. Elevated temperature tensile test (500°C, 720°C) engineering stress-strain curves for all four EXW couples using digital image correlation virtual extensometer. Dotted line = 720°C, solid line = 500°C. The P91 EXWs were tested only at 500°C, representing the cold size service temperature, whereas 304H EXWs were tested at both 500°C and 720°C.

52

Inconsistencies in the ductility to failure in the 304H-Ni201 welds are due to the location of initial necking. From analysis in previous reports, the location of initial necking at room temperature in the 304H-Ni201 welds correspond to the location for microcracking due to welding and prior to testing. There were two high-temperature tensile tests for 304H-Ni201 EXWs, each at both 500°C and 720°C (dotted lines), where the same location of microcracking at room temperature was the same reason for an abrupt decrease in stress with increasing strain, as seen in Figure 57.

The yield strengths of wrought material for 304H SS are 125 MPa and 90 MPa, for 500°C and 720°C, respectively, and the UTS and elongation for 304H SS are 410 MPa and 36% elongation at 500°C and 220 MPa and 36% elongation at 720°C [4,12]. Based on the analysis of the transverse weld joints, the yield strength for 304H SS weld metal (E308) exceeds the requirement of both YS and UTS for both temperature conditions. However, the bulk ductility to failure in the welds are generally less than the ductility in substrate material (<0.2 (20%)). The YS and UTS of P91 substrate material at 565°C are 353 and 390 MPa, respectively, with a ductility of 31% elongation based on studies of grade 91 in the normalized temperature condition. Based on the P91 YS and UTS, which are very close in value due to low uniform strain, it is expected at least 400 MPa in YS and 448 MPa UTS in Ni201 welds and a UTS of 497 MPa in P91-C22 welds. While the elongations for the transverse welds (15%–18%) are lower than wrought P91 material (34%) in the normalized and tempered condition, the strength of the P91 weld joint slightly exceeds the expected bulk strength of wrought plate. Therefore, the results indicate that the joint strength for all four welds exceed the substrate UTS at 500°C and 720°C. However, C22 cladder provides better EXW clad weld strength for both 304H and P91 backers and less inconsistent failure strain compared to 304H-Ni201 joint strength.

4.1.3.3 Digital Image Correlation Results

The strain localization maps for each test at elevated temperature are seen at necking for 304H-N201 in Figure 58, 304H-C22 in Figure 59, P91-Ni201 in Figure 60, and P91-C22 in Figure 61. The 500°C tests for 304H/Ni201 EXW are seen in Figure 58(a–d), where the initial necking location is similar to what has been seen in room temperature tests (the heat affected zone of Ni201 cladder). In contrast to other tests, the 720°C tensile test (see Figure 58(c)) led to failure along the weld centerline, where initiation develops in the initial cladder weld layer. Another duplicate at 720°C, with a gauge section not aligned with the weld filler, led to failure in the base metal area (see Figure 58(d)).

The 304H-C22 welds at 500°C and 720°C are displayed in Figure 59(a–b) and Figure 59(c–d), respectively. All samples failed along the weld centerline but initiated in different locations depending on the temperature. At 500°C, localized necking occurred initially in the cladder weld metal, while at 720°C, localized necking occurred initially in the 304H SS weld metal filler. The 304H-C22 weld behaved the best compared to the other three EXWs for both temperatures in terms of mechanical strength and ductility.

53
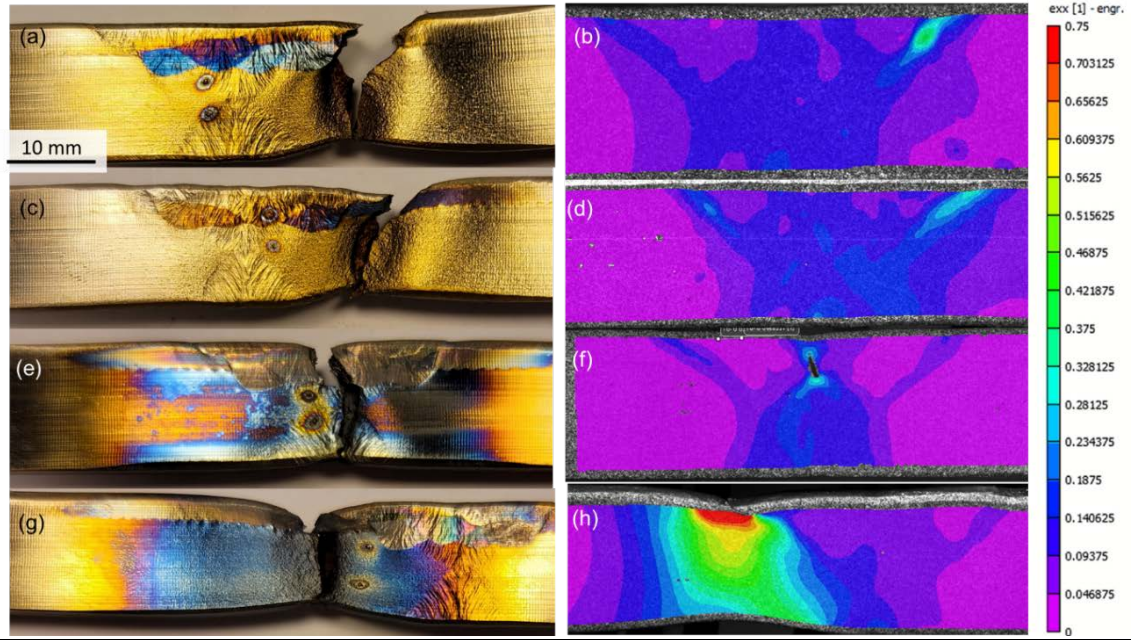
Figure 58. Necking location and DIC strain contour map of 304H-Ni201 at necking strain for first duplicate (a–b) and second duplicate (c–d) at 500°C, and first (e–f) and second (g–h) tests at 720°C, showing strain localization in the same location in the heat affected zone for 500°C and weld metal and base metal for 720°C. Notice second duplicate (g–h) had an off-center weld in the gauge section, which led to uncertainties in the stress-strain data. Further duplication is planned to ensure consistencies in deformation behavior.
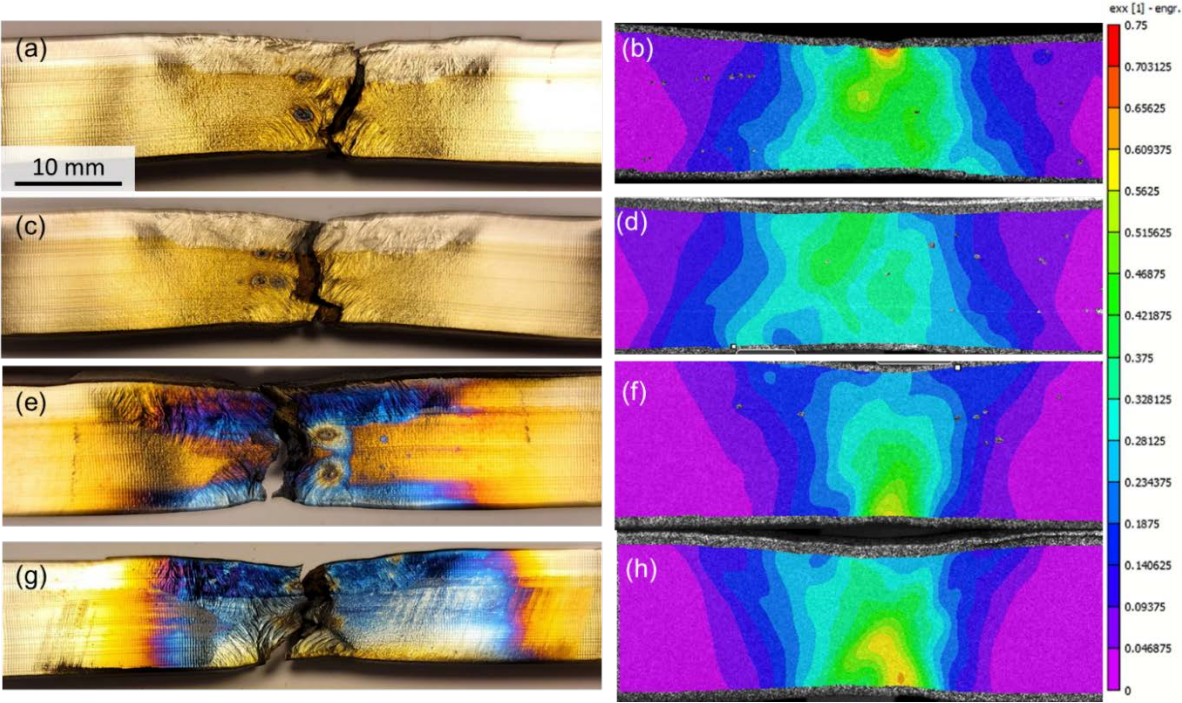
Figure 59. Necking location and DIC strain contour map of 304H-C22 at necking strain for first duplicate (a–b) and second duplicate (c–d) at 500°C, and first (e–f) and second (g–h) tests at 720°C, showing strain localization in the same location in the weld metal

54
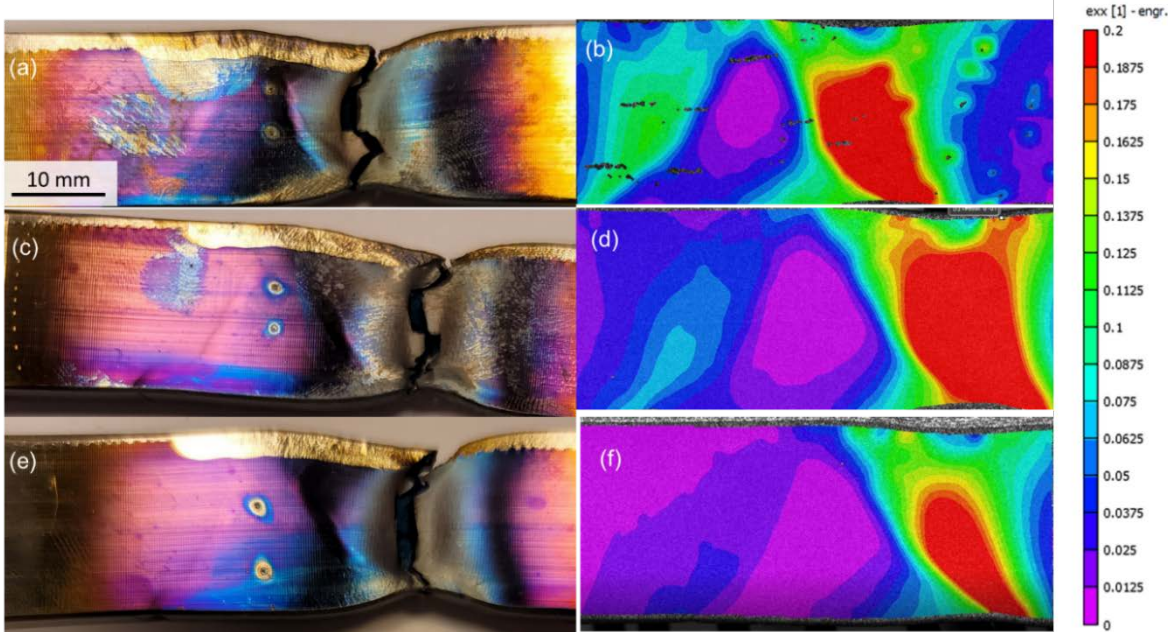
Figure 60. Necking location and DIC strain contour map of P91-Ni201 past necking strain (~7.5%) for first duplicate (a–b), second duplicate (c–d), and third duplicate (e–f), showing strain localization in the same location in the base metal
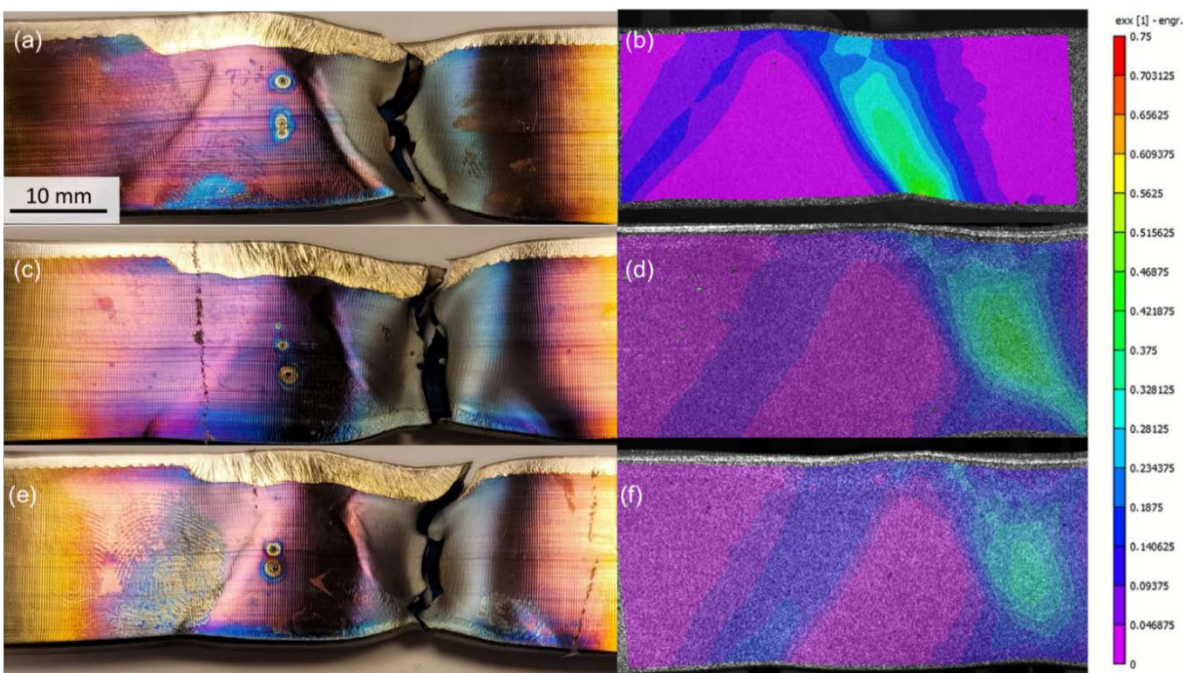
Figure 61. Necking location and DIC strain contour map of P91-C22 at necking strain (~5%) for first duplicate (a–b), second duplicate (c–d), and third duplicate (e–f), showing strain localization in the same location in the base metal

At service temperature conditions for Gr. 91 (500°C), the P91-C22 EXW maintained the best mechanical strength. The main contributor to depreciation in strength with the Ni201 EXWs was grain coarsening in the Ni201 HAZ compared to the C22 HAZ for room temperature tests. However, both P91 EXW clad welds performed well during elevated temperature testing at

500°C, where the failure location occurred in the base metal for all duplicates (see Figure 60 and Figure 61). While the strain to failure was the same regardless of the cladder material, the C22 outperformed the Ni201 in terms of mechanical strength (as seen in Figure 57).

4.1.3.4 Conclusions for Elevated Temperature Strength Evaluations of Butt-Welded EXW Clad Plates

- Elevated temperature tensile tests revealed similar relative ranking of mechanical testing at room temperature tests, where 304H-C22 outperformed 304H-Ni201 at both 500°C and 720°C in terms of mechanical strength and less inconsistencies in ductility dips. The location to failure in the 304H-C22 primarily occurs down the weld centerline, indicating ductility dips in the deposited weld metal centerline. However, the strength and ductility of the 304H-C22 EXW clad joint is overall better than the 304H-Ni201 EXW clad joint.
- P91-C22 and P91-Ni201 EXW clad welds had better yield strength than the 304H EXW clad welds but had very little uniform elongation at elevated temperature tensile tests (i.e., low true strains to necking). While the P91 EXW clad welds experienced higher yield strength, the 304H EXW clad welds had better work hardening behavior and therefore better ductility than the P91 welds at 500°C, even with lower yield strengths.
- Overall, C22 was demonstrated to outperform Ni201 as a clad material based on the thermomechanical test results for both P91 and 304H SS.

4.1.4 Thermomechanical Evaluation of Longitudinally Welded EXW pipe (Milestone 2.5.2)

In this task, Milestone 2.5.2 was completed based on details in Table 20. The results reported here include only the down-selected EXW pipe welds (304H and P91 backers with C22 cladder). Prior to commencement of this task, it was determined that the CS/CR process did not allow for a crack-free C-276 cladder, and even with machining off cracks, the chloride molten corrosion rates of C-276 cladder exceeded the minimum rate required for application. Therefore, only EXW work is reported here.

Table 20. Milestone 2.5.2 Details

Milestone	Description	Metric	Success Value	Assessment Tools
2.5.2: Thermomechanical evaluation of longitudinally welded EXW and CS/CR clad pipe sections	The EXW clad pipe section produced by longitudinal welding and CS/CR pipe section should pass the thermomechanical evaluation at the service temperature (based on M1.1.2) by having the cladded structure and its weld (for EXW) exceeding the strength limit when compared to expected strength of the backer.	Thermomechanical resistance at the service temperature (based on M1.1.2) of the weld compared to wrought metals.	> 80% for welds	Gleeble testing, fractographic analysis and optical and electron microscopies with energy dispersive X-ray spectroscopy (EDS) and hardness mappings. All tested samples (at least three) should meet target with 10% errors based on standard deviation.

56

In Subtask 2.2.1, SS 304H/C22 was down-selected as the top performing clad combination and P91/C22 as a secondary candidate for the production of large clad plates for further evaluation. In the subtask, two clad plates, one for each material couple, were fabricated and then rolled and welded along the longitudinal seam to produce a one-foot-long pipe section. Each pipe was cut in halves transversely at the center, and then a butt-joint was made to reattach the two halves to mimic the butt-welds between two pipes in a pipeline. The pipe manufacturing process physically simulates the production of the actual pipeline. Tensile samples were extracted from the pipe sections for thermomechanical evaluations at room and service (500°C and 720°C) temperatures. The objective of the pipe section thermomechanical testing is to compare the mechanical properties of the pipe section samples to those of the clad plate samples, as well as to wrought base metal baseline properties.

4.1.4.1 Weld Methodology and Sample Extraction

The explosion clad and arc welded one-foot-long pipes were received this quarter, including both P91 and 304H SS backers with C22 clad layer. After completion of the explosion clad welding (EXW) procedure in plate form, the plates were rolled to a 12.6-in.-diameter, 0.5-in.-thick pipe and longitudinally seam welded with gas tungsten arc welding (GTAW) technique. The pipes were then cut in half to 6-in.-long pipes and circumferentially welded using the same procedure and weld geometry. Figure 62 shows weld geometry and circumferential weld pass sequence, which consists of a single-V geometry and an open root weld on the inner diameter (ID) clad. The filler used for all passes was ERNiCrMo-10 filler (alloy 622).
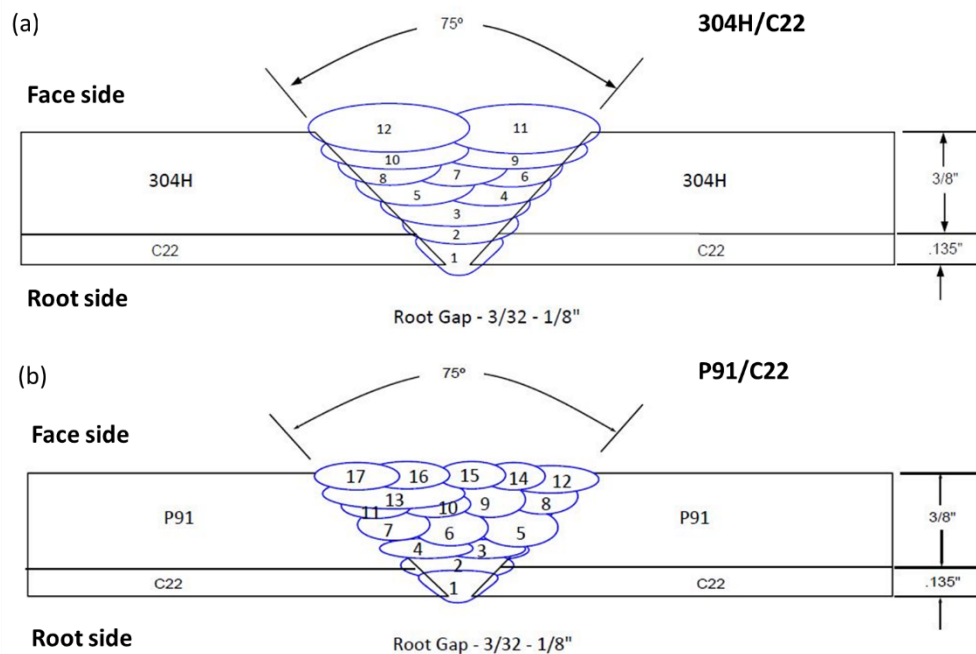
Figure 62. Circumferential butt GTAW of steel pipe cladded by C-22 on the ID with a single-V geometry using (a) 304H SS and (b) P91 backer on the face side

Tensile samples were extracted transverse to the butt circumferential weld as schematically illustrated in Figure 63, which is parallel to the longitudinal direction (LD) of the pipe but the transverse direction (TD) of the butt weld. In addition, samples were taken at a 90° arc angle from each seam weld, which were placed 180° from each other. The gauge section includes the

arc welded fusion zone (FZ), the heat affected zones (HAZs), and base metal clad substrates on each side of the weld centerline, as seen in Figure 63(c–d). The circumferential butt joints were evaluated using tensile tests at room temperature (RT) and elevated service temperatures of 500°C for both backers and only 720°C for the 304H SS backer. An induction coil was used to generate elevated temperatures of 500°C and 720°C. The digital image correlation (DIC) method was used to provide a virtual extensometer and a method to observe localized strain partition in the cross-weld samples.
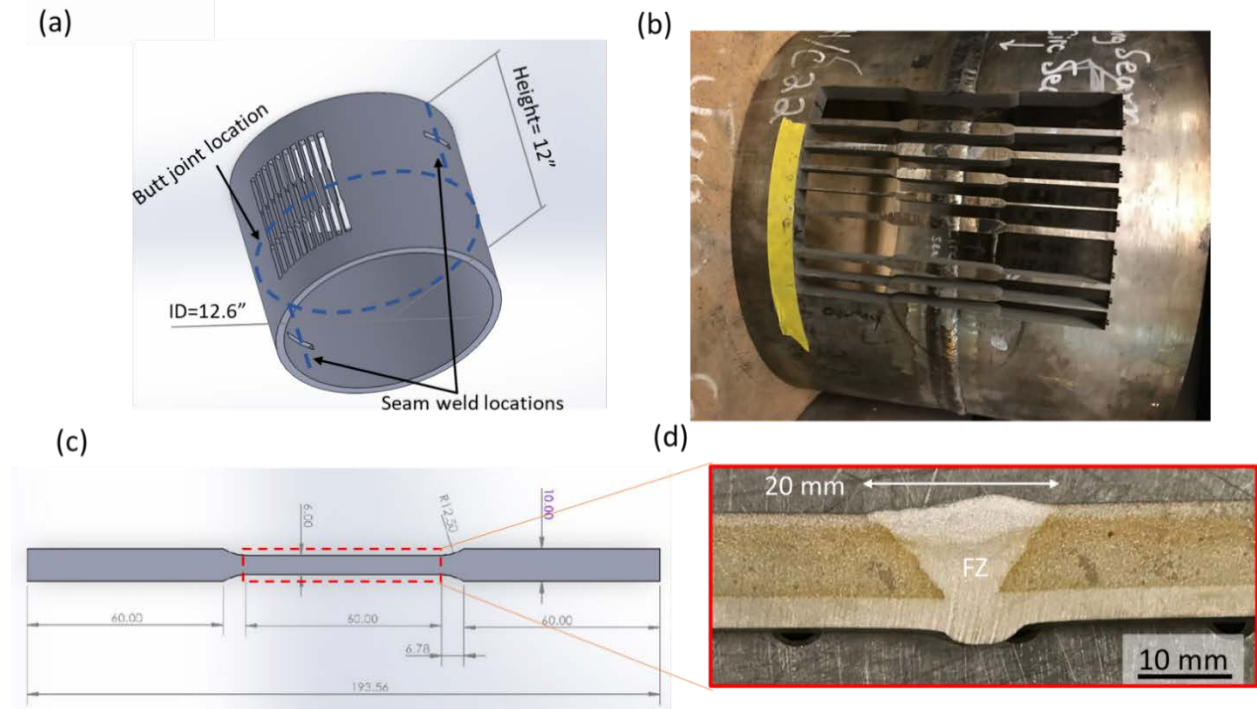
Figure 63. (a) Schematic showing tensile sample extraction locations within the pipe section relative to the locations of butt and seam joint, and the extracted metallurgical characterization samples across the seam weld, (b) picture of sample extraction, (c) sample geometry, and (d) close-up view of gauge section showing centering of FZ within gauge center

4.1.4.2 *Summary of Thermomechanical Properties*

Tensile test results of the pipe butt welds are summarized as load-displacement and engineering stress-strain curves in Figure 64(a) and (b), respectively. Thermomechanical properties of the 304H and P91 pipe circumferential welds are also tabulated in Table 21 and Table 22, respectively. Yield strength (0.2% strain offset), ultimate tensile strength (UTS), and strain to fracture are collected along with fracture location of each test. The strain to fracture corresponds to when fracture is initiated, which occurs after necking or during brittle fracture that is associated with defects. The reported strain to fracture in the samples with brittle fracture is taken at strain values when load drops abruptly instead of final fracture.

58
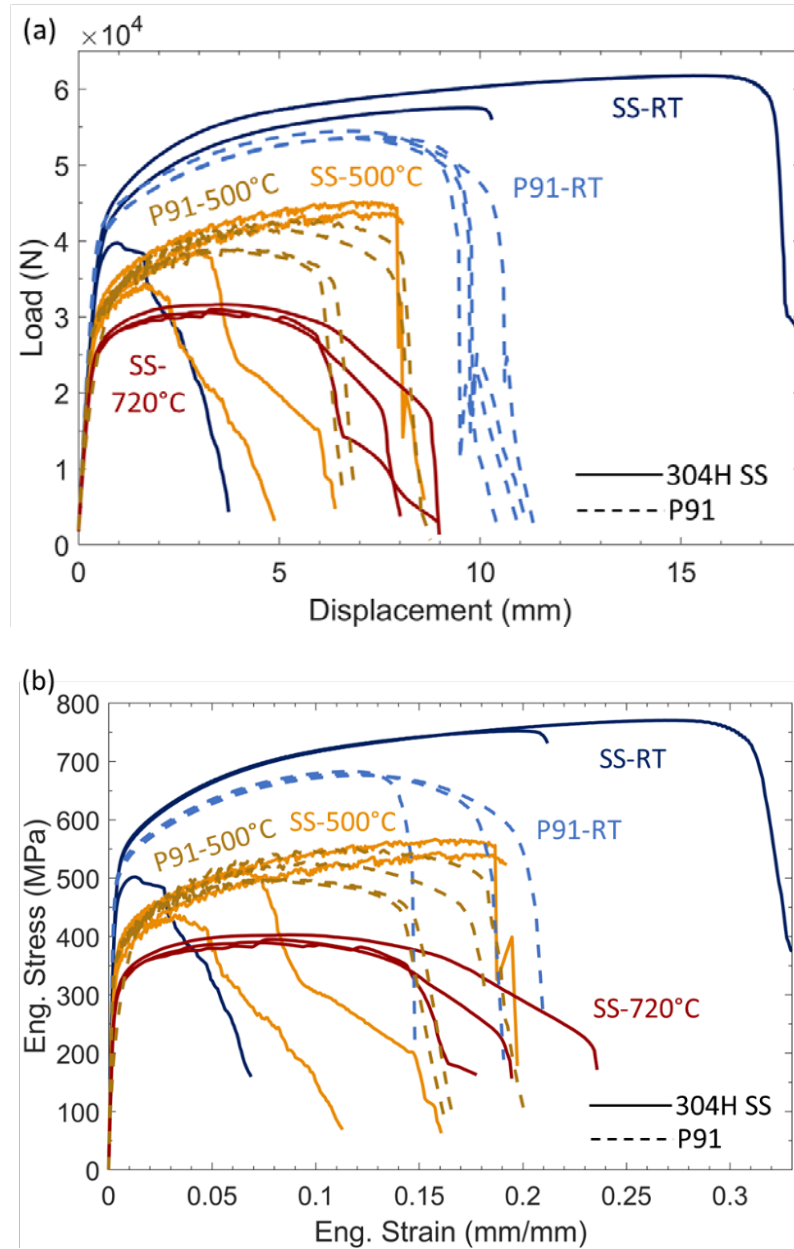
Figure 64. 304H/C22 (solid line) and P91/C22 (dashed line) explosion clad arc welded pipe thermomechanical test results at room temperature (RT), 500°C, and 720°C: (a) load-displacement and (b) engineering stress-strain curves

Yield strength is consistent in duplicate tests, except for one case where there was brittle fracture in SSPRT2 that stemmed from lack of fusion (LOF) in the ID clad root pass. As expected, the yield strength and UTS decrease with increasing temperature for both 304H SS and P91. Lower UTS are associated with low ductility samples with LOF defect as well. It should be noted that problems arose during deformation of some samples, for instance P915003 and P915004, where after initial yielding, the temperature dropped from 500°C to 450°C throughout the duration of the test. This can explain the fluctuation in P91/C22 weld UTS results at 500°C, where higher UTS might be correlated to the temperature fluctuation errors. The P91/C22 weld had more

59

consistent fracture location in contrast to the 304H/C22 SS welds with LOF defects in some of the extraction locations.

Table 21. Thermomechanical Properties of as-Welded EXW Arc Welded 304H/C22 Pipe Butt Weld

(HAZ = Heat Affected Zone; FZ = Fusion Zone; FB = Fusion Boundary; BM = Base Metal)

ID	Temp. (°C)	0.2% offset Y.S. (MPa)	UTS (MPa)	$\varepsilon_{fracture}$	Failure location
SSPRT1		512	752	0.21	304H FZ/C22 FB
SSPRT2	20	467	502	0.03	304H FZ/C22 FB
SSPRT3		513	770	0.32	HAZ/BM
SSP5001		359	544	0.19	304H FB
SSP5002	500	378	567	0.185	304H FB
SSP5003		370	513	0.09	304H FZ/C22 FB
SSP5004		348	437	0.06	304H FZ/C22 FB
SSP7201		303	395	0.19	HAZ/BM
SSP7202	720	306	389	0.16	HAZ/BM
SSP7203		312	403	0.23	HAZ/BM

Table 22. Thermomechanical Properties of post weld heat treated EXW P91/C22 Pipe Arc Weld

(HAZ = Heat Affected Zone; FZ = Fusion Zone; FB = Fusion Boundary; BM = Base Metal)

ID	Temp. (°C)	0.2% offset Y.S. (MPa)	UTS (MPa)	$\varepsilon_{fracture}$	Failure location
P91RT1*		516	679	-	BM
P91RT2	20	505	683	0.145	BM
P91RT3		502	676	0.21	BM
P91RT4		498	679	0.19	BM
P915001		363	497	0.16	HAZ/BM
P915002	500	368	498	0.165	HAZ/BM
P915003**		-	551	0.2	HAZ/BM
P915004		362	527	0.18	HAZ/BM

* P91RT1-DIC data acquisition stopped for about a third of the test, which influences strain to fracture

**P915003-sample buckled during pre-loading and led to inaccurate 0.2% Y.S. calculation

The success metric for this milestone, as well as other similar milestones previously, is to achieve weld strength larger than 80% minimum of the wrought material strength. The average yield strength and UTS are compared to the various experimental results from substrates, after EXW, and the ERNiCrMo-10 filler for room temperature properties and literature for elevated temperature strength data, as seen in Table 23. The UTS in both 304H and P91 explosion clad arc pipe welds meets the 80% weld efficiency criteria for all three temperatures, meeting design factors for the backer material. The properties compared here with 304H substrate is the solution annealed conditioned and P91 is normalized and tempered condition. After arc welding, P91 is again post weld heat treated (PWHT'd) to a normalized and tempered condition to facilitate precipitation and temper martensite, while the 304H weld remains in the as-welded condition. Additionally, the cross-weld UTS meets the 80% strength criteria compared to the EXW test results and the typical results of all weld metal provided by the supplier in material test report

60

(MTS). The weld filler would be typical of an overmatching Ni filler to provide additional thermal stability to the weld FZ and to have excellent weld efficiencies, such that the wrought material or substrate would be the weak point of failure. However, two observations seem to point to concern with the 304H/C22 weld in the as-welded condition: (1) failure along the fusion boundary of the overmatching ERNiCrMo-10 weld metal FZ and 304H SS, which indicates potential weldability concerns and (2) LOF defect between the matching ERNiCrMo-10 filler and C22 clad layer in the root pass. The next section discusses the DIC strain distribution map along with failure locations.

Table 23. Comparison of Explosion Clad Arc Welded Pipe Weld Strength with Supplier Base Metal, EXW, and Weld Metal Properties (From All Experimental Certificates) and Elevated Temperature Base Metal Properties from Literature

Material	Temp.	Circumferential Cross-Weld Results		304H/P91 Base Metal (from supplier's info)		C22 Base Metal (from supplier's info)		NobelClad Post EXW Test Certificate of Conformance		ERNiCrMo-10 Filler (alloy 622)	
		Y.S., MPa	UTS, MPa	Y.S., MPa	UTS, MPa	Y.S., MPa	UTS, MPa	Y.S., MPa	UTS, MPa	Y.S., MPa	UTS, MPa
304H/C22	25°C	497±26	675±150	277	611	372	786	507	721	570	790
	500°C	364±13	515±57	125	410	234	607	-	-	-	-
	720°C	307±5	396±7	90	220	214	524	-	-	-	-
91/C22	25°C	505±8	679±3	627	758	372	786	575	708	570	790
	500°C	364±3	507±17	333	472	234	607	-	-	-	-

4.1.4.3 DIC and Fracture Location

The cross weld DIC strain maps and failure location for 304H/C22 EXW arc pipe welds at RT, 500°C, and 720°C are shown in Figure 65, Figure 66, and Figure 68, respectively. The RT results are inconsistent in failure location, but the differences are primarily driven by LOF in the clad root pass, particularly in SSPRT2. In the cases without weld defects, such as SSPRT3, the failure location occurs in the HAZ where strain accumulation is the highest.

With respect to the 500°C condition, the fusion boundary (FB) between the ERCrNiMo-10 filler and 304H SS passes seem to be the region for preferential deformation and fracture. An example of another LOF on C-22 root pass was observed in SSP5004 sample. The fracture surfaces showing LOF on root weld and fracture along 304H fusion boundary are displayed in Figure 67. While the LOF is a weld quality issue, the failure along the 304H fusion boundary seems to implicate possible metallurgical effects on failure location, possibly stemming from diffusion induced phases from the over alloyed ERNiCrMo-10 filler.
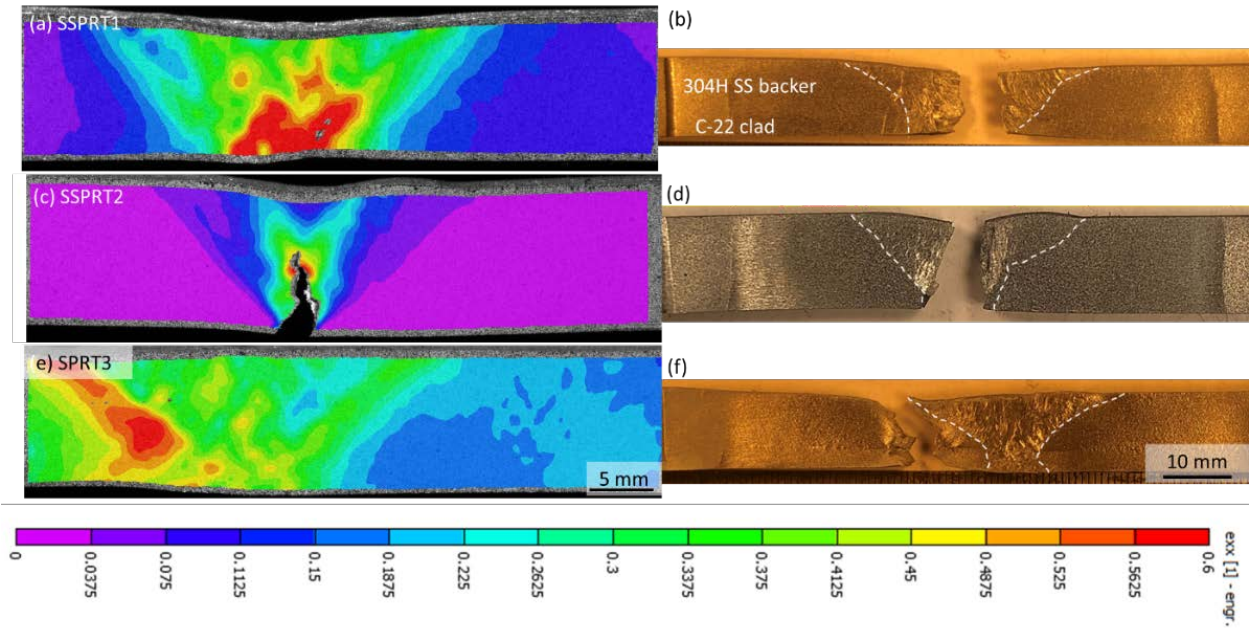
Figure 65. 304H/C22 room temperature DIC exx-engr. strain map and sample fracture location for specimens (a–b) SSPRT1, (c–d) SSPRT2, and (e–f) SSPRT3
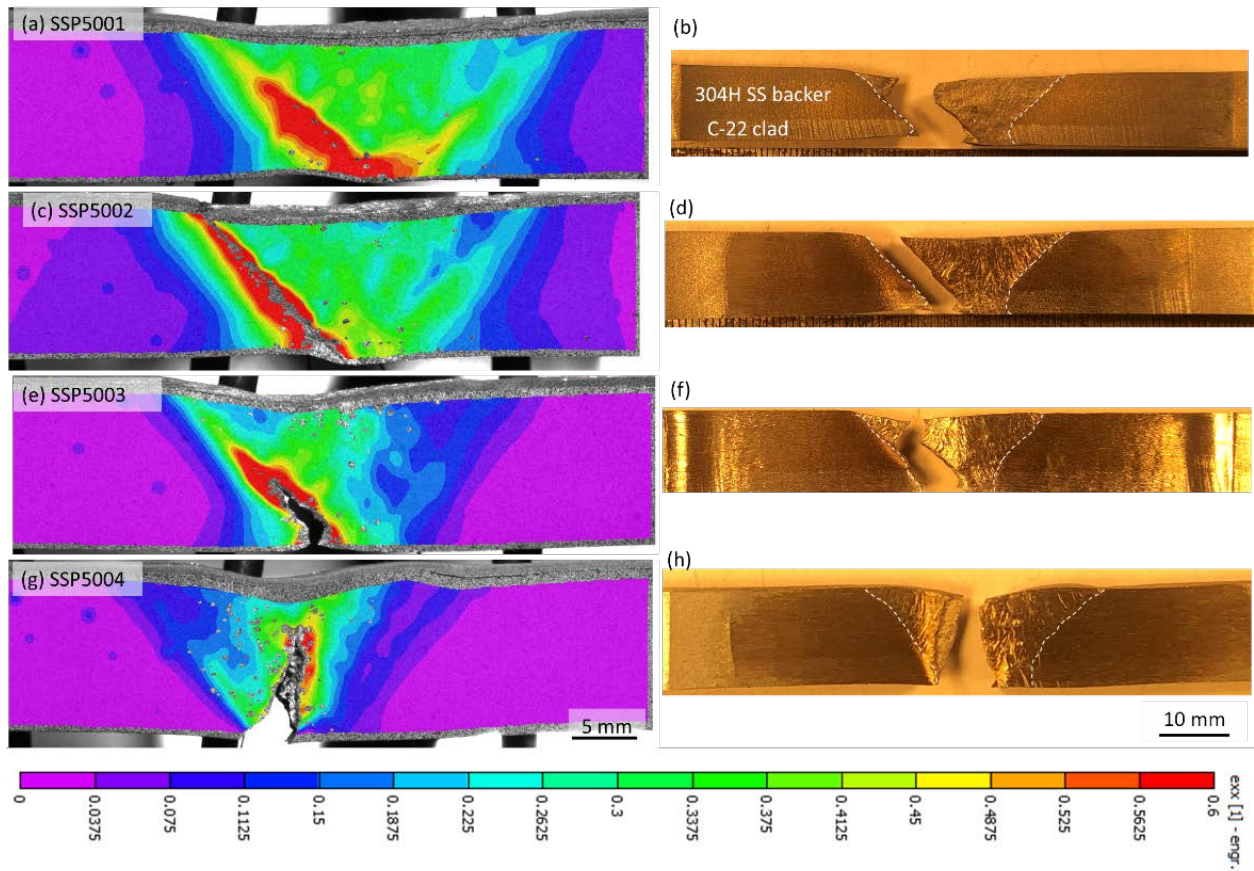
Figure 66. 304H/C22 500°C DIC exx-engr. strain map and sample fracture location for (a–b) SSP5001, (c–d) SS5002, (e–f) SSP5003, and (g–h) SSP5004 samples

62
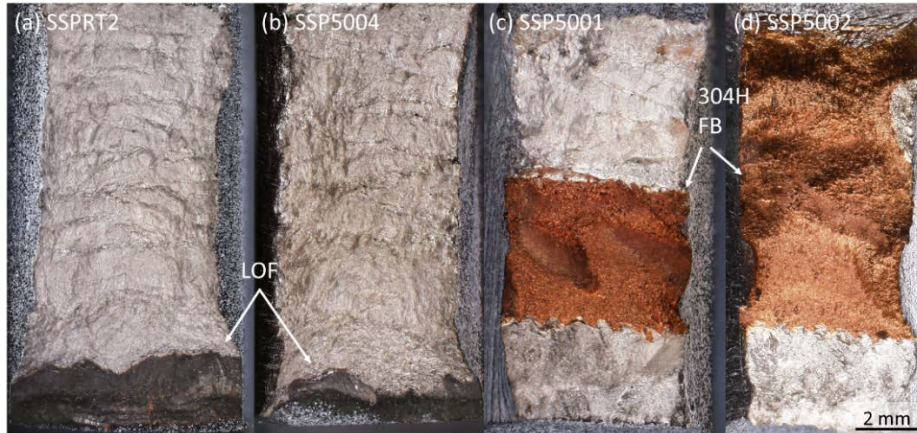
Figure 67. Fracture surfaces of (a) SSPRT2 and (b) SSP5004 showing LOF at C22 clad layer and (c) SSP5001 and (d) SSP5002 showing the fusion boundary (FB) fracture surface with orange oxide.

In contrast to RT and 500°C, the 720°C tests show more consistent failure location and deformation behavior as seen in Figure 68. The FZ resists deformation at 720°C and failure preferentially initiates in the HAZ near the OD of the pipe and progresses along the HAZ of the arc weld. It should also be noted that the FZ in the cladder weld passes accumulates more deformation than the backer weld passes. The 304H HAZ seems to be the weakest region in these higher temperature tests, and the fracture surfaces indicate a significant amount of area reduction in the 304H HAZ compared to the C-22 clad region of fracture surface as seen in Figure 69. The SSP7202 showed delamination between the explosion weld clad as seen in Figure 69(c–d), possibly due to the complex stress state and ductility differences between 304H and C22 at 720°C.
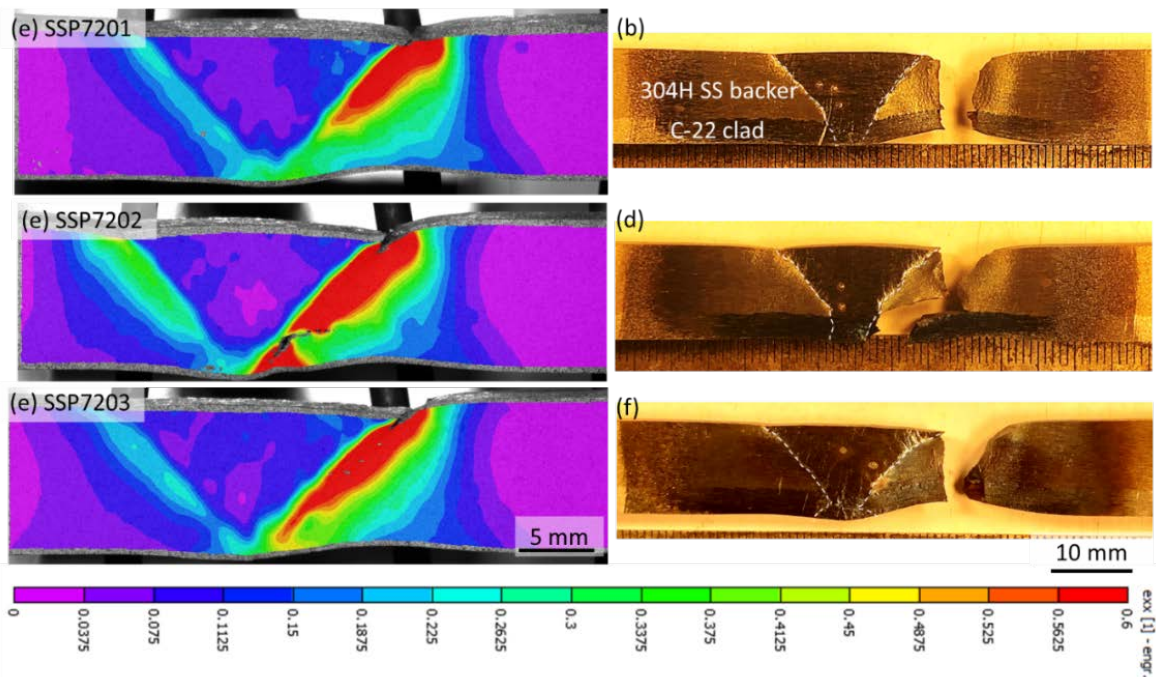
Figure 68. 304H/C22 720°C DIC exx-engr. strain map and sample fracture location for: (a–b) SSP7201, (c–d) SS7202, (e–f) and SSP7203 samples

63
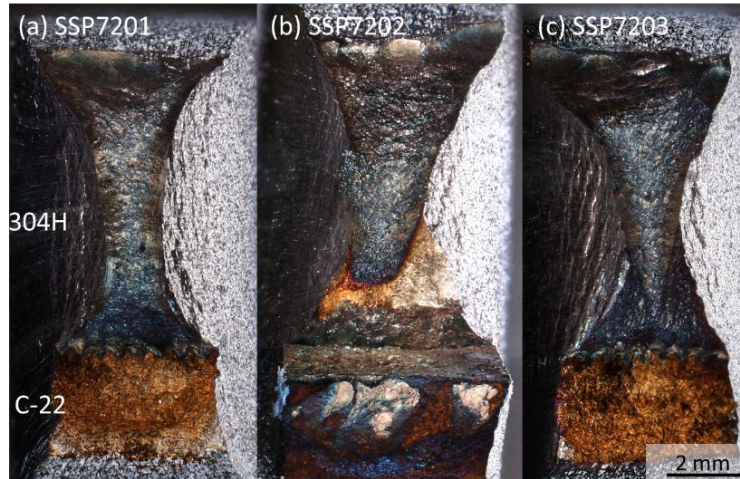
Figure 69. Fracture surfaces of 304H/C22 EXW arc pipe weld samples at 720°C: (a) SSP7201, (b) SSP7202, and (c) SSP7203
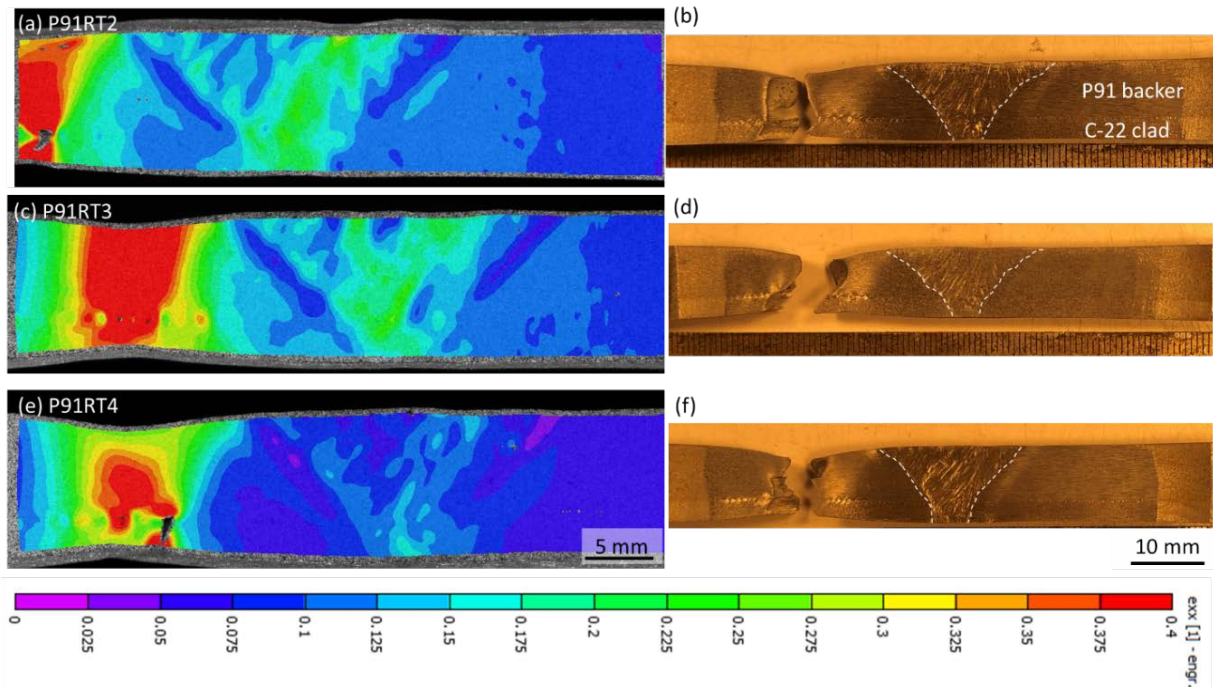
Figure 70. P91/C22 RT DIC exx-engr. strain map and fracture location for specimens: (a–b) P91RT2, (c–d) P91RT3, (e–f) and P91RT4

The DIC strain maps and fracture locations for the P91/C22 pipe welds are shown in Figure 70 and Figure 71 for RT and 500°C conditions, respectively. In contrast to the 304H/C22 welds, there were no observable weld defects that influenced the mechanical properties of these samples. All fractures initiated from necking within the BM/HAZ of the weld, particularly near the EXW bond interface, and there was no fracture within the FZ or along FZ boundaries. Some delamination was observed on the EXW bond line within the necking region. Initial yielding and deformation were observed in the weld FZ, but with a likely higher UTS, necking and fracture would eventually occur in the HAZ or BM. The microstructural variation in P91 weld region seems to influence behaviors observed in the DIC map. For instance, a region more resistant to

64

deformation is observed throughout the test, i.e., the lightly purpled region on each side of the FZ in Figure 70(e). Fresh martensite may form upon cooling during the welding procedure in the fine- and coarse- grained HAZs. While a PWHT was completed to temper martensite, it's likely this subregion still exhibits a higher strength than the other subregions of HAZ.
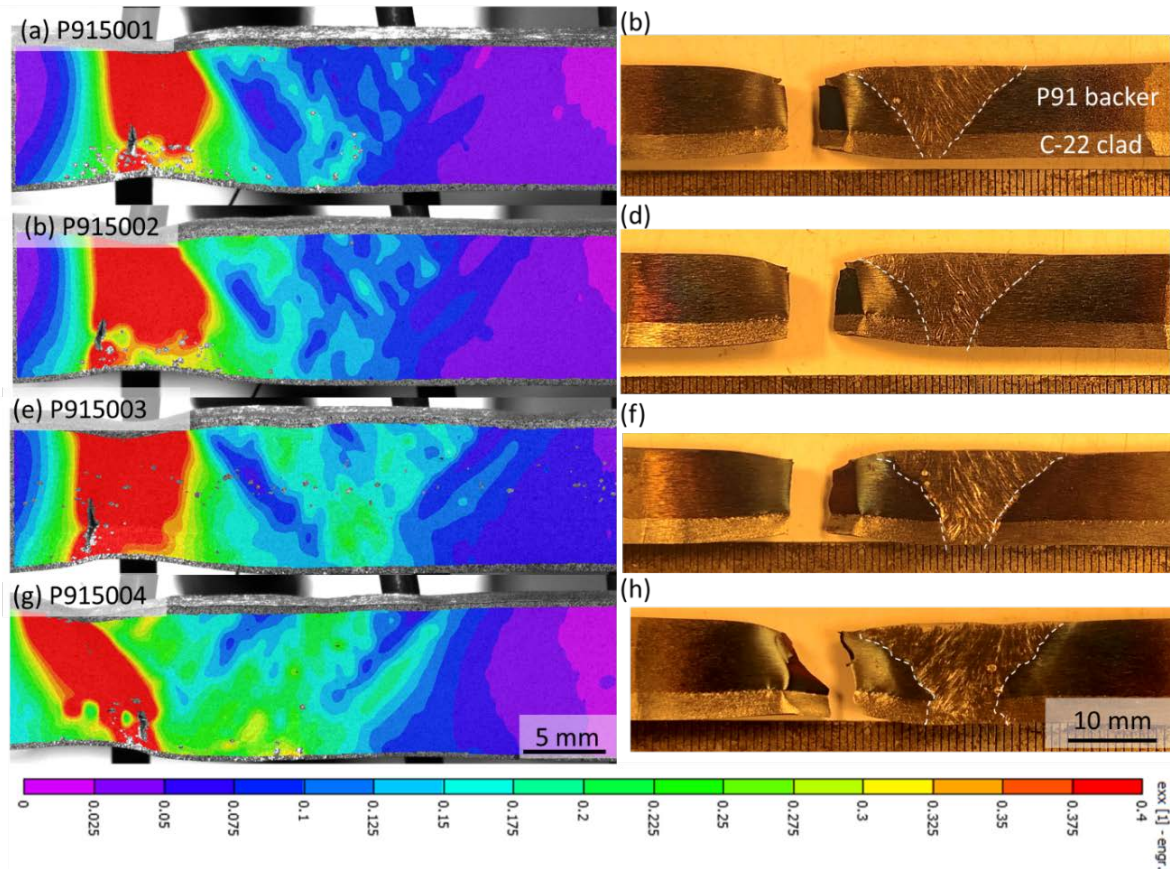
Figure 71. P91/C22 500°C DIC exx-engr. strain map and fracture location for specimens: (a–b) P915001, (c–d) P915002, (e–f) P915003, and (g–h) P915004

4.1.4.4 *Comparison Between Pipe and Plate Weld Thermomechanical Results*

Both explosion clad arc welded plate and pipe section welds are evaluated to provide a thermomechanical property comparison. The introduction of stresses or forming strains associated with the production of a 2-ft-diameter cylindrical component in manufactured clad pipes may influence the properties of the weld. It should be noted that the plate and pipe were welded differently based on the best practice available. The pipe weld has a 75° single-V groove with an open root gap of approximately 3/32–1/8 in., and the welding procedure utilized GTAW for both the clad and backer weld passes. The plates, on the other hand, are welded using a double-V geometry with flux-core arc welding (FCAW) for backer and pulsed gas-metal arc welding (GMAW) or clad passes. Another difference is that the pipe welds, both clad and backer were completed using ERNiCrMo-10 matching filler for the C-22 clad (alloy 622). This filler matches the clad layer but overmatches both 304H and P91 backer. The plate weld backer passes were filled with corresponding matching fillers E308H and E91T1. With these differences, the comparison may be convoluted.

The properties and failure locations are compared between the pipe and plate cross-weld thermomechanical tests. Figure 72 schematically illustrates the average UTS comparison between plate and pipe explosion clad arc welds. The P91/C22 UTS plate values were 678±2 MPa at RT and 497±2 MPa at 500°C. The pipe P91/C22 UTS contains a similar UTS as the plate UTS (679±3 and 507±17 MPa) for both temperature conditions. The 304H/C22 UTS plate values were 714±7 MPa at RT, 498±1 MPa at 500°C, and 381±32 MPa at 720°C. The pipe UTS in 304H/C22 weld are 675±150 at RT, 515±57 at 500°C and 396±7 at 720°C. The higher amount of error in the RT and 500°C in the304H/C22 pipe EXW arc weld UTS average correlate with variations in fracture location between duplicate tests. When not accounting for samples with LOF in the UTS average, the pipe UTS average at RT and 500°C are higher (761 MPa at RT and 541 MPa at 500°C), as seen in Figure 72(b), while the 720°C tests have similar UTS average values between the plate and pipe although with slightly higher error in the plate weld. Strain to fracture is similar as well between pipe and plate welds, but there is little uniform deformation (<5% before necking) in the P91 plate welds.
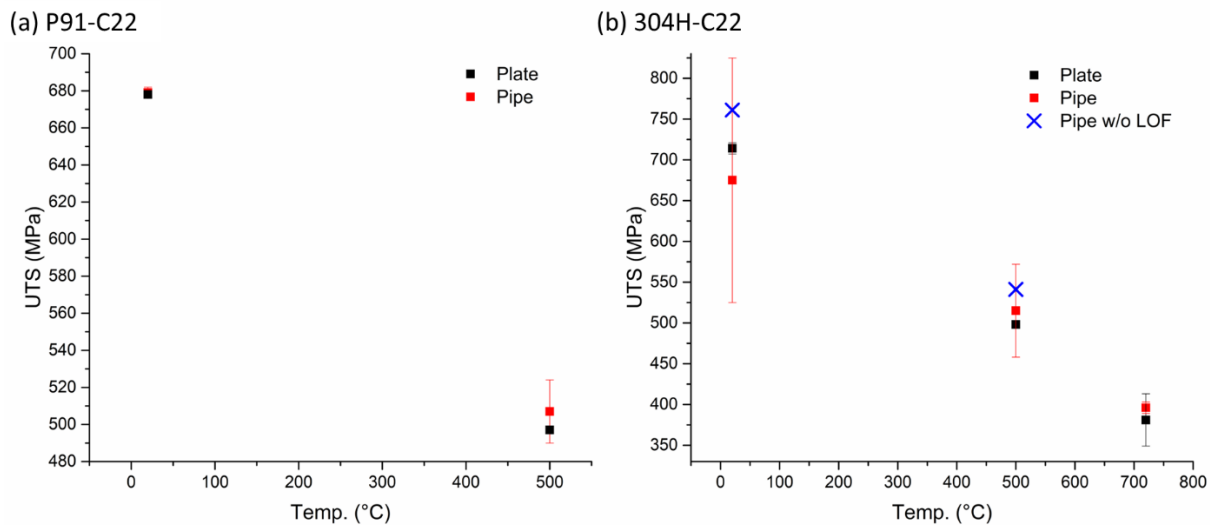
Figure 72. UTS comparison between plate and pipe for (a) P91-C22 and (b) 304H-C22 EXW arc welds

Plate and pipe welds using P91 as the backer all failed similarly at HAZ/BM for both RT and 500°C. In contrast, the 304H welds in plate form all failed down the weld centerline, while for pipe welds there is a mix of failure locations along the FZ boundary in the backer, lack of fusion in the clad root pass, and failure in the HAZ/BM (particularly at 720°C). Aside from weld defects, the backer FZ region seems more resistant to failure in the pipe vs. the plate condition, which could be due to the overmatching ERNiCrMo-10 filler used in the pipe weld while E308H was used for the plate weld. E308H would likely have a lower weld efficiency (ratio of strength in weld vs. substrate) compared to using ERNiCrMo-10 filler with a higher UTS and higher weld efficiency. The result would ideally be reduced failure in the weld FZ and strain localization in the HAZ. The observed differences in failure locations between the plate and pipe welds could be a combined effect of filler composition, microstructural features, and residual stress.

4.1.4.5 Metallurgical Characterization of Explosion Cladded SS 304H/ C22 Pipe Section Butt-Joint Weld

The weld macrograph in Figure 73 shows a 1.5-mm-long lack of fusion (LOF) crack located inside the weld root pass. This is a critical weld defect, as it considerably reduced the ductility and UTS of many tested tensile samples compared to defect free samples. In addition, because this defect is located on the inner diameter of the cladded pipe, it may serve as stress concentration point as well as molten salt trap, leading to a high probability of localized corrosion attack.
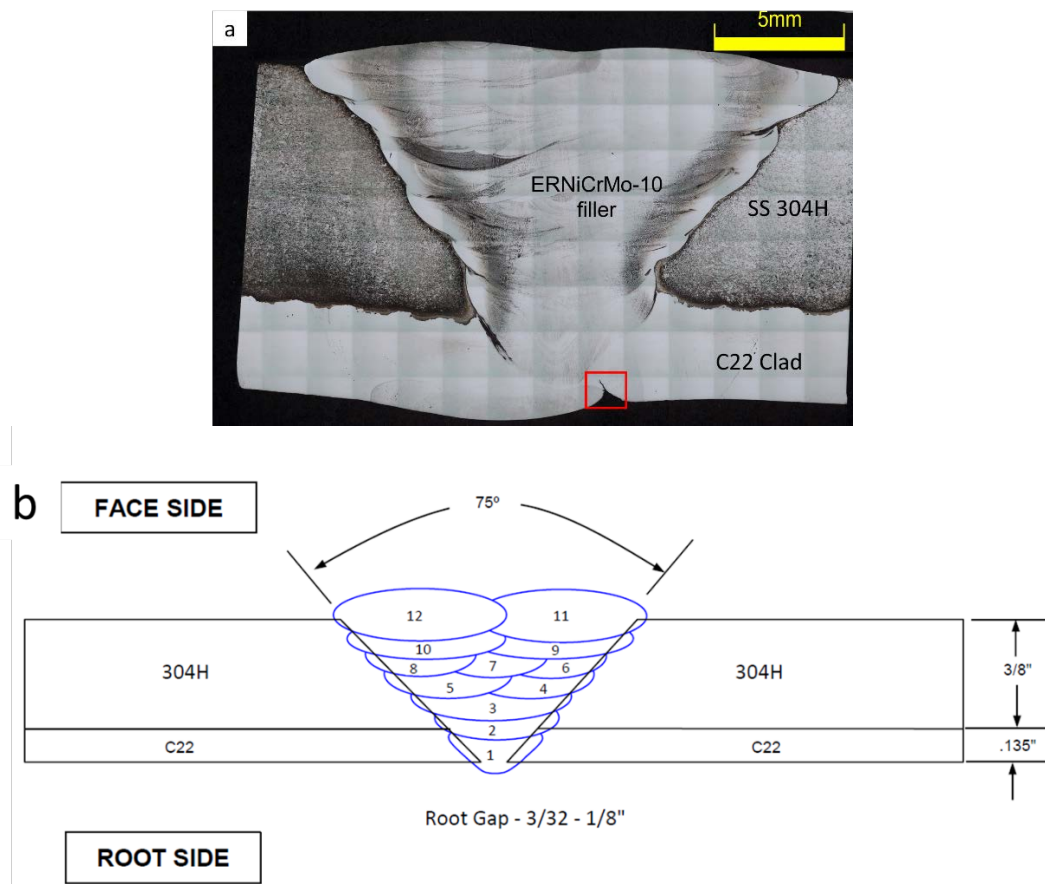
Figure 73. (a) Weld transverse cross sectional macrograph of the butt-joint (girth weld) of SS304H/C22 pipe section (sample was extracted from the center of the weld circumference). (b) Weld design schematic by Enerfab

Based on crack location in the weld root of C22 clad side, this LOF crack was likely caused by improper weld joint fit up and/or electrode alignment, as evidenced by the nonsymmetrical weld reinforcement shape. It seems the nonsymmetrical weld pass on the weld root may be a result of a second root pass on the root side to fix the underfill (also called suck back) from the first root pass on the top side. A contributing factor to underfill (suck back) is arc misalignment and improper backfill gas flow on initial open root weld. To fix the underfill, it appears that a second weld pass (not reported or planned in the schematic in Figure 73(b)) from the root side was completed with the intention to tie to the first root pass. However, this second pass from the root side was misaligned and did not tie into the initial root pass, leaving a weld defect seeming to be LOF. To note, Enerfab's radiographic testing (nondestructive technique) report did not show lack

of fusion or crack defects. Furthermore, SEM-EDS elemental maps in Figure 74 did not show any indication of secondary phases or any kind of segregation around the LOF crack. Thus, inherent metallurgical issues are not probable causes for this defect.
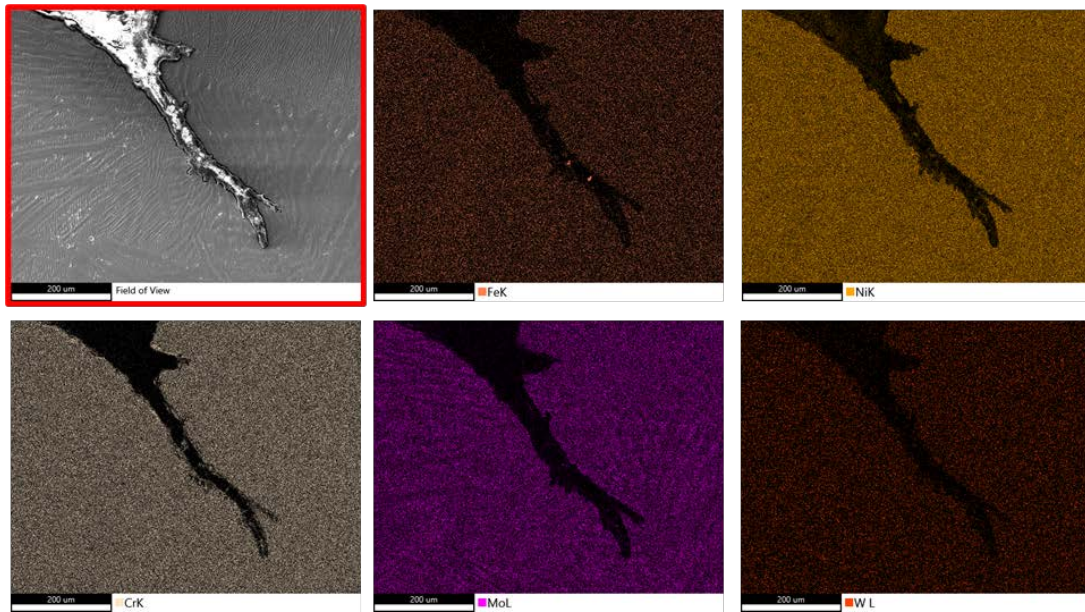
Figure 74. EDS elemental maps for weld root crack indicated by the red square in Figure 1

SS304H base metal microstructure is shown in Figure 75(a), which consists of austenitic matrix, delta ferrite bands, low fraction of martensite laths (likely induced from rolling strain), and annealing twins. More complex microstructure was formed in the severely deformed region caused by explosion cladding in SS304H at the cladding interface as shown in Figure 75(b). This region appears to have a high fraction of strain-induced martensite, which leads to high hardness regions around the cladding interface, as observed in the cladded plate samples previously. It should be noted that no post forming heat treatment or no post weld heat treatment (PWHT) was reported after rolling to pipe shape or after welding, which could revert the α' martensite back to γ-austenite.
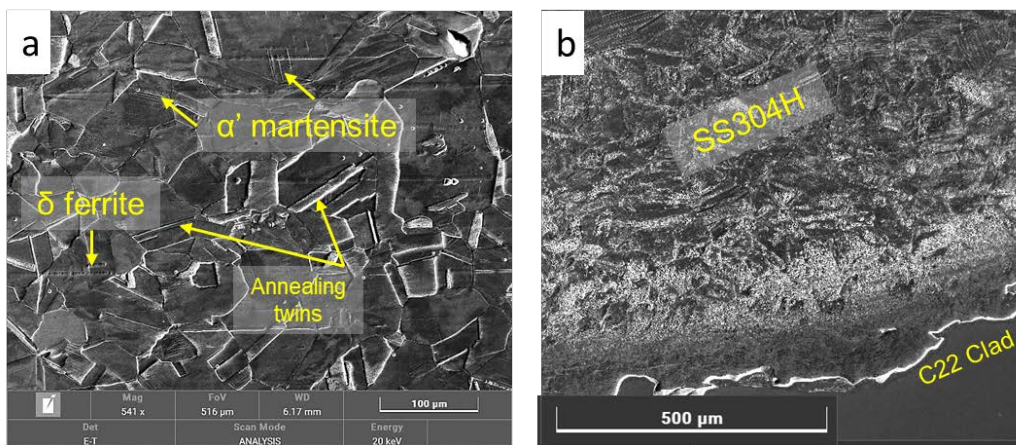
Figure 75. SEM images showing (a) typical microstructure of SS 304H base metal, and (b) highly deformed SS304H at the explosion cladding interface.

68
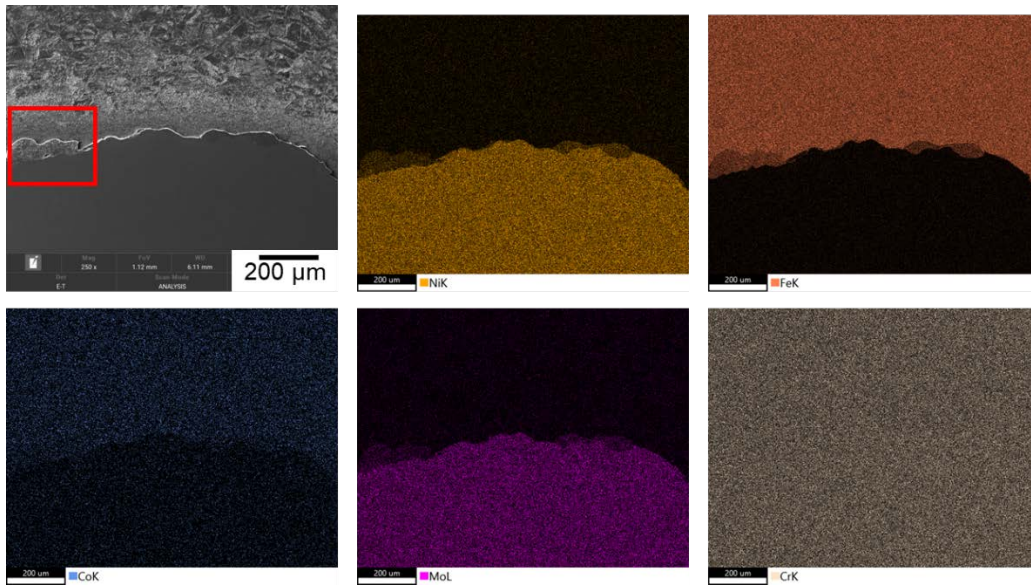
Figure 76. EDS elemental maps for SS304H/C22 explosion cladding interface
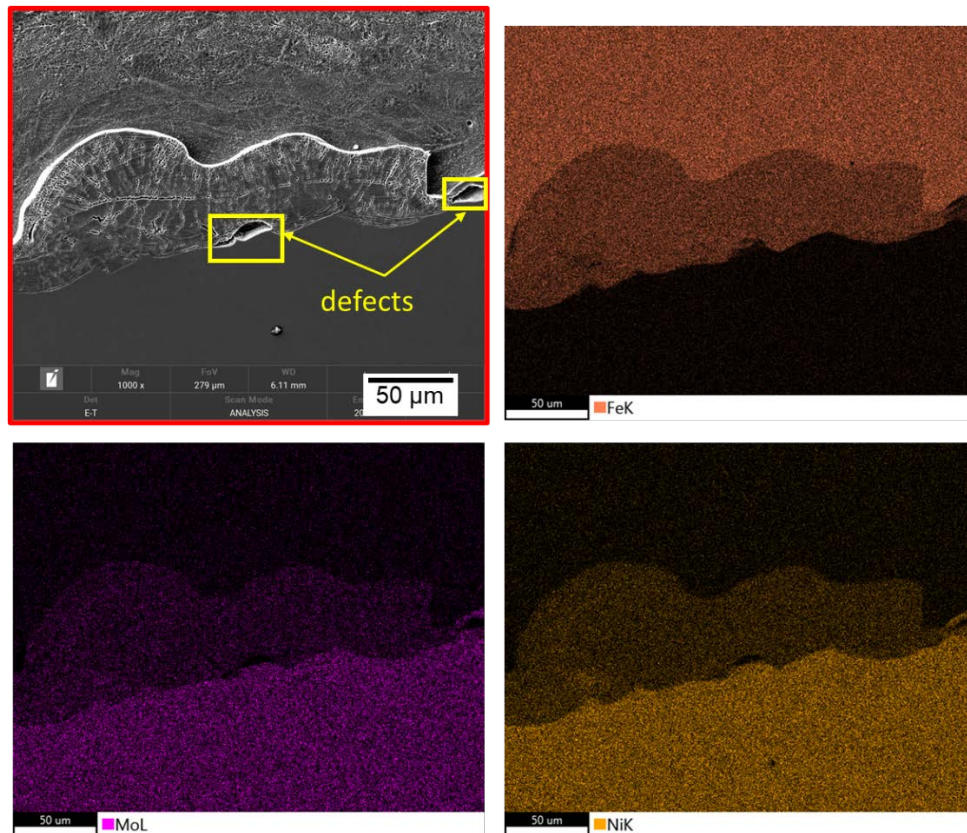
Figure 77. High-magnification EDS elemental maps showing local intermixing region at the cladding interface

Small intermixing islands are observed at the clad interface, as highlighted by the red box in Figure 76. Higher-magnification EDS maps for this region are shown in Figure 77. The images indicate the potential formation of partially mixed zones (PMZs) enriched with Fe, Ni, and Mo as the main elements being present. Furthermore, small defects were observed at the interface

69

adjacent PMZs. They appear as microcracks or elongated voids (30–50 µm) depleted from all the elements examined. No significant delamination was observed in the majority of tested tensile samples. Only one sample tested at 720°C, SSP7202, exhibited delamination of EXW bond-line from tensile tests.
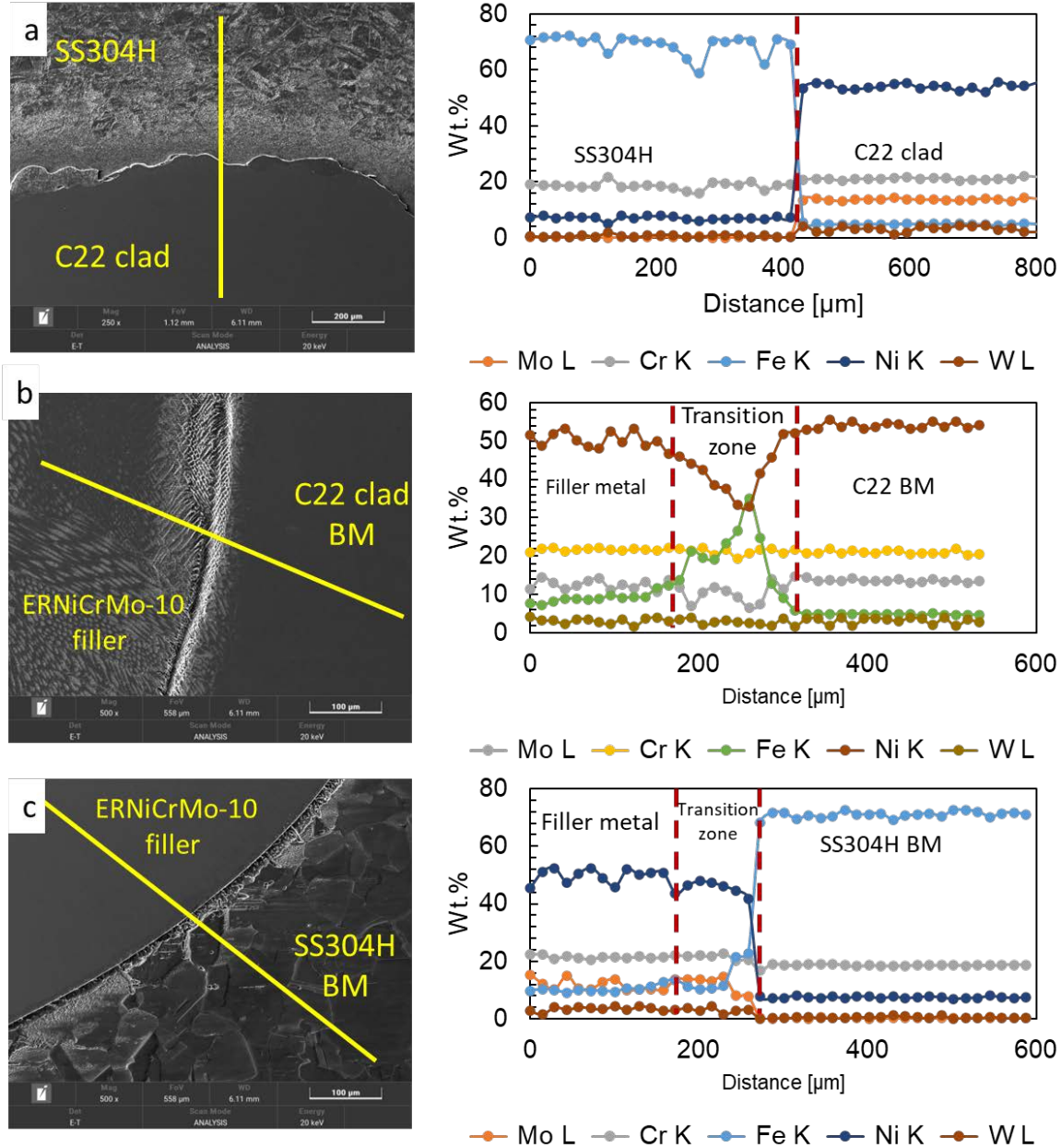
Figure 78. EDS line analysis for (a) SS034H/C22 cladding interface, (b) C22 clad/filler metal weld interface, and (c) SS304H/filler metal weld interface

The EDS line scan from the SS304H substrate to C22 in Figure 78(a) demonstrates a sharp transition in chemical composition, indicating minimum to no interdiffusion at the examined explosion clad interface location. In comparison, an interdiffusion transition zone can be observed between the ERNiCrMo-10 filler metal (matching filler for joining C22) and C22 clad

70

in (b) and SS304H in (c). The ERNiCrMo-10 filler region was found to be close to its nominal chemical composition with a slight 1–4 wt.% increase in Fe, caused by dilution from the SS304H substrate.

4.1.4.6 Conclusions for Thermomechanical Evaluations of EXW Clad Pipe Welds

- Overall, the thermomechanical properties are similar between the circumferential pipe and plate welds for both 304H/C22 and P91/C22, aside from weld defects observed in the 304H/C22 weld. The filler choice was different between the plate and pipe welds, due to the best practice available to different welding geometries, which introduced an additional variation factor to the strength comparison.
- The average weld efficiencies meet the 80% minimum strength criteria based on UTS values of base metals and expected properties from given certificates of conformance and literature.
- LOF defects in the 304H/C-22 root weld impacted mechanical properties and were not detected during radiographic non-destructive testing (NDT). Proper joint alignment is required to mitigate that defect.
- The P91/C22 welds fail in the HAZ/BM, while the 304H/C22 welds fail more randomly within the FZ, along fusion zone boundary (only at 500°C), and HAZ/BM (mostly at 720°C).
- Cladding interface had minimum to no interdiffusion, except for small intermixing islands, mainly composed of Fe, Ni, and Mo.
- Except for a slight Fe enrichment, the EDS analyzed chemical composition for ErNiCrMo-10 welding filler was similar to nominal composition.

4.2 Task 3: Combustion Synthesis/Centrifugal Rotation (CS/CR)

4.2.1 CS and CR Cladding Process Parameters (Milestone 1.3.1)

The details for Milestone 1.3.1 are included in Table 24.

Table 24. Milestone 1.3.1 Details

Milestone	Description	Metric	Success Value	Assessment Tools
1.3.1: Combustion synthesis (CS) and centrifugal rotation (CR) cladding process parameters	CS technique should form the required corrosion resistant alloy (CRA) compositions, from in M1.1.2, at normal gravity condition. Modification of CS/CR machine should meet specific production targets.	Characterization of CS process: 1. CS reaction temperatures; 2. Reaction Rate; 3. CRA compositions; 4. Slag separation from the molten CRA at 1G condition	1. 2000-2500°C 2. >5 mm/s 3. Compositions in the range defined in M1.1.2 4. > 90%	All tested samples (at least three) should meet target compositions within 10% of specification • Temperature measurements using thermocouples; • Ignition occurs successfully when triggered • Video recording to observe lateral reaction propagation rate; • Mass measurements of both CRA and the slag formed to determine the percentage of slag separated out. • Composition analysis using the Optical Emission Spectroscopy (OES) • Microstructure of the reacted CRA using the optical microscopes to examine slag entrapment at 1G. In this stage, microstructure analysis will be focused on the slag entrapment only. Other analysis will be carried out in M1.3.2, and M2.3.3
		CS/CR machine modification: a) High temperature cladding b) High centrifugal force c) Water cooling	a) 2000-2500°C b) Up to 200G. c) Allowing for easy water cooling. Are there cooling rate requirements, temperatures, temperature evenness? d) Allowing for cladding of backer pipe dimensions selected in M1.1.2	All tested samples (at least three) should meet the target with 10% errors based on standard deviation. • RPM measurements by an Tachometer to determine the G level; • Must be able to operate continuously for at least 30 minutes.

4.2.1.1 Material Selection and Procedure

A clad pipe includes a CRA layer to be metallurgically bonded to the inner diameter of a backer pipe. The CRA layer provides corrosion resistance, and the backer pipe provides structural support, while being potentially less costly than a pipe made of wrought CRA alloy. From the

combined consideration of mechanical property, corrosion resistance, and cost, it has been decided that AMS will conduct clad pipe production trials and deliver one clad pipe using SS304H as the backer with C-276 bonded as the CRA. The CS/CR procedure is illustrated in Figure 79.
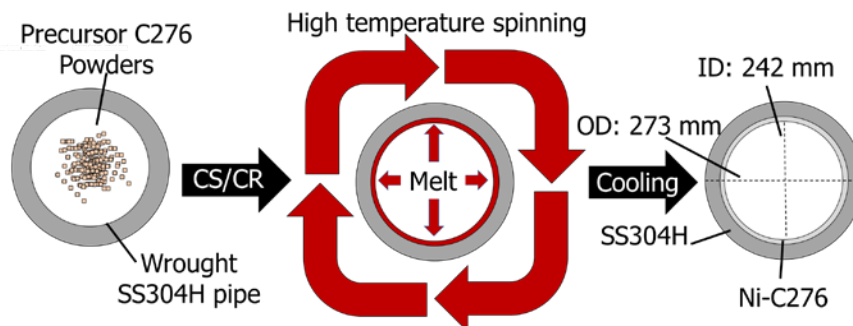
Figure 79. Combustion synthesis and centrifugal rotation (CS/CR) process

Because the AMS technology is a high-temperature fusion process similar to welding, there will be dilution of the CRA composition by that of the backer pipe. Therefore, the final CRA composition (C-276) could be off from commercial C-276 composition. It is expected that this composition deviation would have an insignificant effect on the performance of the CRA. The SS304H backer pipe with a 10.75-inch outside diameter and 0.5-inch wall thickness was purchased.

4.2.1.2 Combustion Synthesis Reaction and Reactant Powders

Various combinations of reactant materials have been analyzed and formulated to generate the C-276 composition and a slag of oxides by-product by the CS process. The adiabatic reaction temperatures have been calculated to allow slag separation from the molten CRAs during the reaction process. The CS reaction design was further refined based on the experimental results. Selected raw reactant powder candidates to produce the clad pipe are presented in Table 25.

4.2.1.3 Experimental CS Reaction and Characterization

Figure 80 presents the reaction rate as a function of the adiabatic temperature. Four exothermic CS reactions (A, B, C, and D shown in the figure) that can generate C276 have been analyzed. From this figure, the relationship between temperature and reaction rate is established.

Table 25. Candidate Reactant Materials for CS/CR Manufacture of Clad Pipes

Material	Particle Size (µm)	Purity
Nickel Oxide (NiO)	<45	99%
Molybdenum Trioxides (MoO$_3$)	<45	99%
Chromium Oxide (Cr$_2$O$_3$)	<45	99%
Chromium (Cr)	<60	99%
Fuels (proprietary, manufactured by AMS)	<250	99%
Molybdenum (Mo)	<45	99%
Tungsten (W)	1–5	99.9%
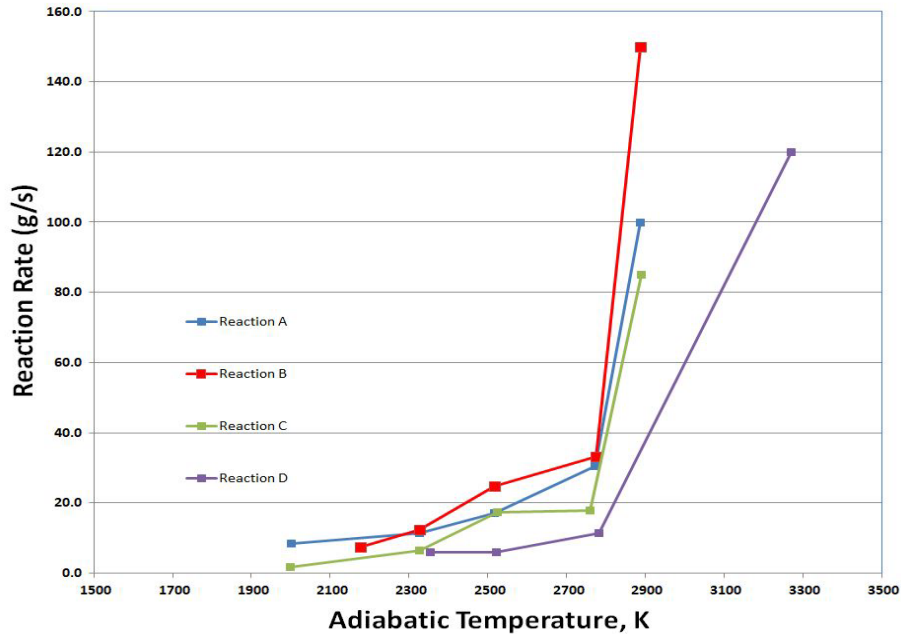
Figure 80. Reaction rate vs. adiabatic temperature for four CS reactions

CS reaction temperature has been measured using an infrared camera. The products of the CS reaction, i.e., the CRA and slag separation, have been characterized and meet the design requirements. The slag flows to the top of the molten C276 due to the large density difference. Figure 81(a) shows a sample after the CS reaction; the molten CRA is mostly protected from oxidation by the molten slag. Figure 81(b) presents the temperature variation of the sample after the CS reaction.

(a)

(b)
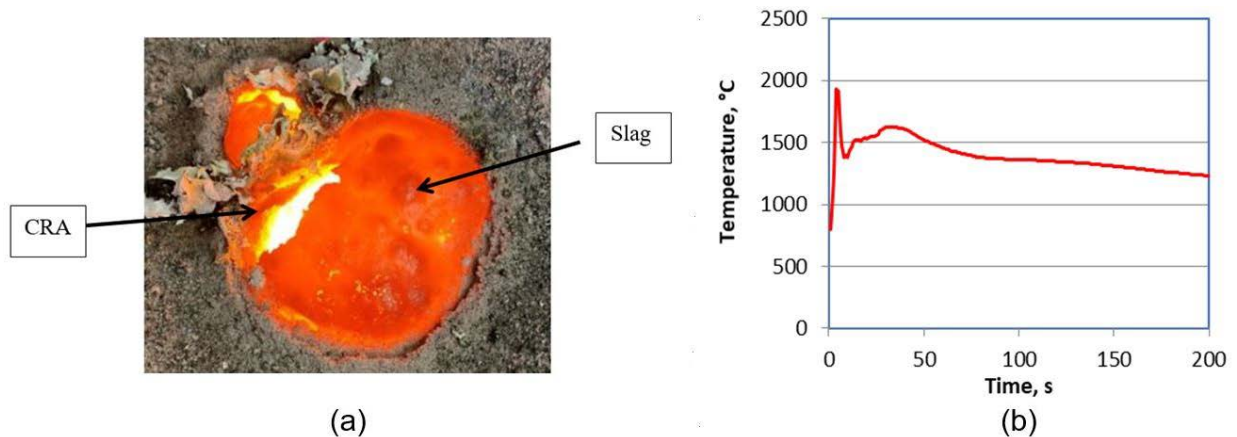
Figure 81. *(a)* Image of the CS sample and *(b)* temperature variation of the sample after the CS reaction in a normal gravity condition

4.2.2 CS/CR Clad of Pipes (Milestone 1.3.2)

The details for Milestone 1.3.2 are included in Table 26.

Table 26. Milestone 1.3.2 Details

Milestone	Description	Metric	Success Value	Assessment Tools
1.3.2: CS/CR clad of pipes	Pipes cladded using CS/CR process should be successfully produced and they must meet initial evaluation to be further analyzed in M2.3.3	1. Clad Production	1. Successful completion of the clad process.	Ignition and reaction, at specified rate, occur to completion across entire clad surface;
		2. Clad Initial Evaluation a) Metallurgical bonding between the CRA and backer pipe; b) Clad layer thickness; c) Metallurgical characterization of CRA; d) Surface finish; e) CRA Composition.	a) Achieve metallurgical bonding as verified by microscopic examination b) Uniform clad layer thickness specified in M1.1.2 c) Defects in CRA layer is <1%; (inclusions, voids, microcracks); d) Surface roughness size < 0.25 mm; Determine if surface machining is required in order to meet the flowing requirements of the molten salts; e) Composition within the range of the specification from M1.1.2.	• API specification 5LD and ASTM E165 • Dye Penetrant Inspection (DPI) • Optical Emission Spectroscopy (OES)

The received pipe from AMS was cross sectioned at three different spots, approximately 120° from each other. Figure 82 illustrates the extraction plan. The 304H SS backer is approximately 25.5 mm in thickness, and the synthesized cladder of C-276 is approximately 5.5 mm in thickness.
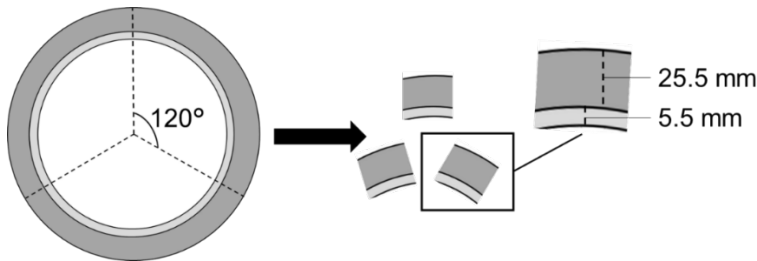
Figure 82. Schematic of CS/CR sample extraction for experimental characterizations

Initial scanning electron microscopy-electron dispersive spectroscopy (SEM-EDS) and imaging analysis was conducted primarily on the metallurgical bond between the synthesized C-276 cladder and 304H SS backer, as seen in Figure 83. First, no defects were observed on the bond line for all three samples. Second, two elements appear to be out of specification respect to both sides of the bond line, including Fe and W. Fe content is high in the C-276 cladder, while W is high in the 304H SS side compared to their initial compositions (304H SS does not have any W, while C-276 should have lower Fe content). W appears to have back diffused into the 304H SS side during the CS/CR process, but determining the source for high amount of Fe in the cladder is more complex. Three mechanisms could explain the higher Fe content in C-276 cladder,

including (1) interdiffusion of Fe and W between both sides, (2) melt back of backer and subsequent dilution of cladder, or (3) a higher amount of Fe in the cladder because of the imbalance of Fe content from the initial powder compositions and synthesis process. It should be noted that the Fe content on 304H SS side, shown in Figure 83, matches its own specification. Therefore, the last two mechanisms seem more likely or dominant.
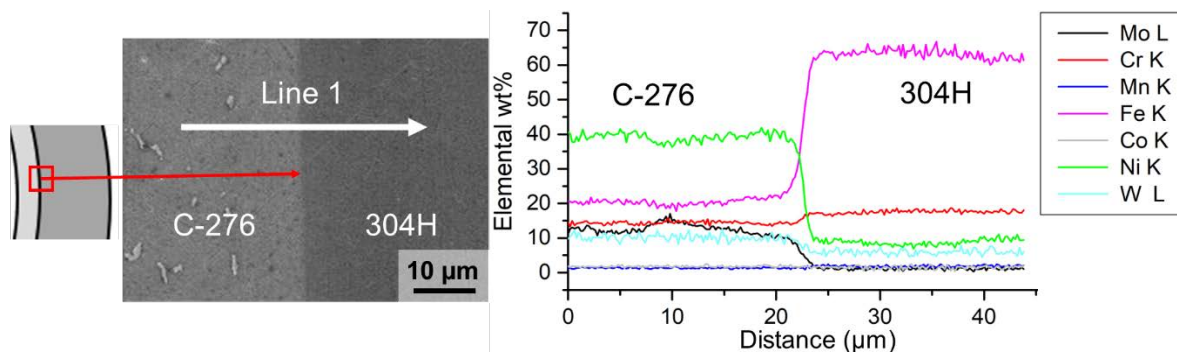
Figure 83. Initial scanning electron microscopy-electron dispersive spectroscopy (SEM-EDS) analysis of the metallurgical bond between C-276 cladder and 304H SS backer

The composition of the cladder on the ID was also observed. Additionally, the compositions of the cladder have been analyzed using spark optical emission spectrometry (OES) technique and EDS. Table 27 shows these results. While multiple iterations have been attempted to optimize the powder mixture and final synthesized composition, an Fe content three times the allowed amount was determined both with EDS and spark OES. Because the composition close to the ID matches the composition of the C-276 cladder near the bond line, there is very little bulk composition gradients across the cladder and a sharp transition region between the cladder and backer. Very likely, there was melt back of the 304H SS backer from the high heat of the combustion synthesis procedure and with the slow heating rate, homogeneity of the cladder would be possible. However, this mechanism has not been observed. Regardless, modifying the powders and procedures to produce a reaction with overall lower Fe content seems like the most practical approach because the bulk 304H SS composition would not deviate from nominal composition, but with four separate exothermic reaction events, as seen in Figure 80, controlling Fe composition may be challenging.

Table 27. C-276 Cladder Composition Analysis Using Electron Dispersive Spectroscopy (EDS) and Spark Optic Emission Spectrometry (OES) Techniques

Element (wt.%)	Nominal	EDS	Spark OES
Ni	Balance	39.11 ± 5.53	Balance
Mo	15 – 17	12.73 ± 4.28	15.2
Cr	14.5 –16.5	14.39 ± 0.76	16.83
Fe	4 – 7	20.3 ± 3.83	20.79
W	3 – 4.5	10.32 ± 0.47	4.26
Co	2.5	1.80 ± 0.02	.08
Mn	1	1.38	0.16
C	0.01	No Data	0.01
V	0.35	No Data	0.06
Cu	No data	No Data	0.12
P	0.04	No Data	No Data
S	0.03	No Data	No Data
Si	0.08	No Data	No Data

4.2.3 CS/CR Pipes' Characterization (Milestone 2.3.1)

The details for Milestone 2.3.1 are in included in Table 28. Because the first metric was not met with the CS/CR technology and 304H SS/C-276 pipe based on the results from previous milestone and results shown below, the mechanical properties outlined in the second metric were not analyzed.

Table 28. Milestone 2.3.1 Details

Milestone	Description	Metric	Success Value	Assessment Tools
2.3.1: CS/CR clad pipes' characterization	Characterization of CS/CR clad pipes shall prove that microstructure, and mechanical properties meet the specified targets	1. Microstructural characterization: a) Microstructure evolution at the heat affected zone (HAZ); b) Precipitation of harmful phases and nature of defects at the bonding interface, if any; c) Dilution of the clad layer;	a) Complete fusion of clad layer to the backer pipe (metallurgical bond) and no harmful secondary phases formed in the HAZ; b) No visible cracks/disbondment at the interface; c) < 30%	Optical and electron microscopies with energy dispersive X-ray spectroscopy (EDS), and hardness mapping will demonstrate complete fusion and no harmful secondary phases. All tested samples (at least three) meet target compositions with 10% errors based on standard deviation.
		2. Mechanical Properties (at room temperature): a) Vicker's hardness profile across the backer steel; b) Bond strength	a) Within the accepted range based on properties from M1.1.2; b) > 137.8MPa (2,000 psi as defined by API 5LD and ASTM A265);	All tested samples (at least three) should meet target with 10% errors based on standard deviation. • Vicker's Hardness; • Instron Tensile Machine; API 5L requirements • Charpy V.Notch;

4.2.3.1 Metallurgical Characterization of SS304H Backer and C-276 Cladder

EDS analysis of the cladder, adjacent to the metallurgical bond, shows extensive Mo segregation into a secondary phase within the microstructure in Figure 84. The Mo segregation could be detrimental for corrosion resistance, such as pitting corrosion, due to the lower Mo content in the bulk phase. An analysis of the whole cladder from the interface to the ID surface was conducted using SEM, as seen in Figure 85. From visual observation, there seemed to be an increase in the volume fraction of secondary phase closer to the ID, which may be a result of non-equilibrium solidification conditions where the segregation of secondary elements in the interdendritic regions increase throughout solidification (beginning from the interface toward final solidification on the ID).
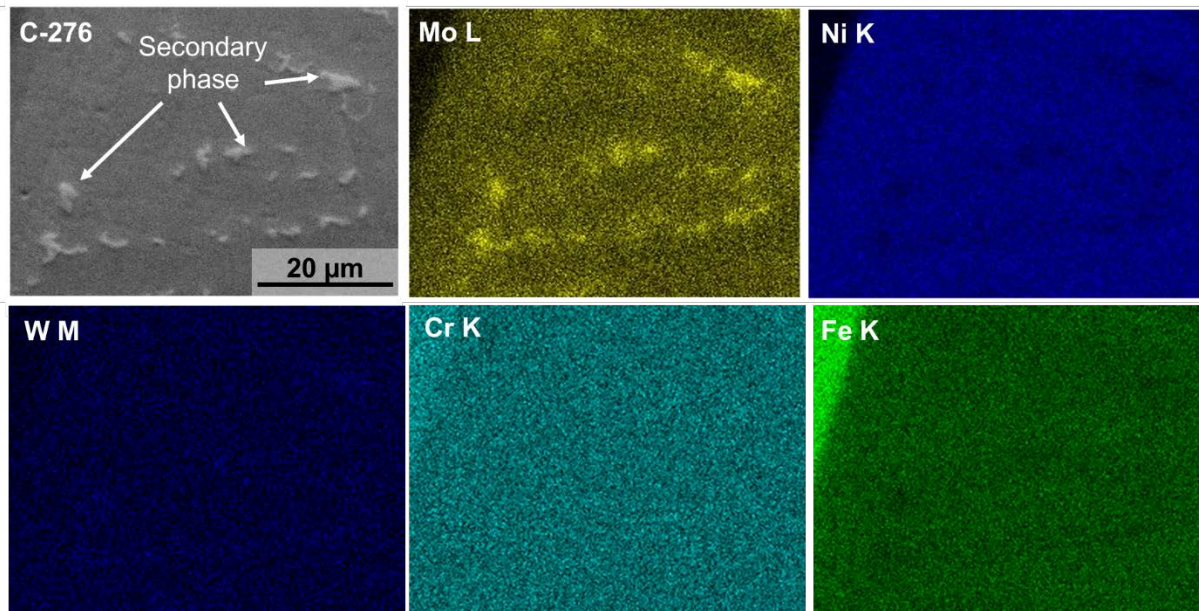
Figure 84. Qualitative EDS maps scans of synthesized C-276 cladder. Mo segregation into sigma phase can deteriorate the pitting/corrosion resistance.
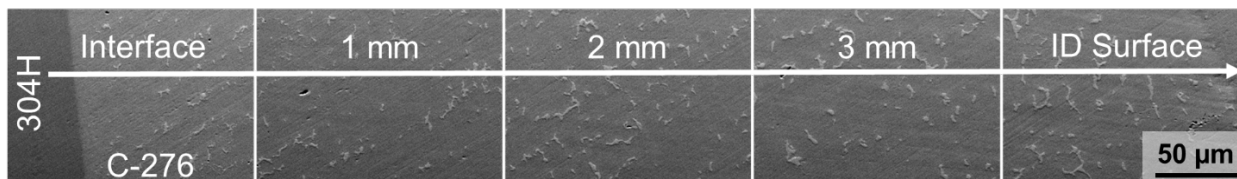
Figure 85. SEM images of the whole C-276 clad layer moving from the 304H/C-276 backer/cladder interface to inner diameter (ID) surface, showing increasing secondary phase. Likely due to a slower cooling rate, there would be more sigma phase on ID than backer/cladder interface.

Light optical microscopy (LOM) was conducted throughout the cladder thickness and bond interface. The most notable observation was 500-µm-long cracks extending from the ID surface into the cladder, as seen in Figure 86. The mechanism responsible for cracking would likely be solidification cracking during CS/CR procedure. This typically occurs within interdendritic regions in final solidification regions, which would be the ID. Higher-magnification images in Figure 86 show the same secondary rich Mo phase present behind the cracks as observed with SEM-EDS analysis. The secondary phase is likely the sigma phase, based on CALPHAD predictions shown in the next section.
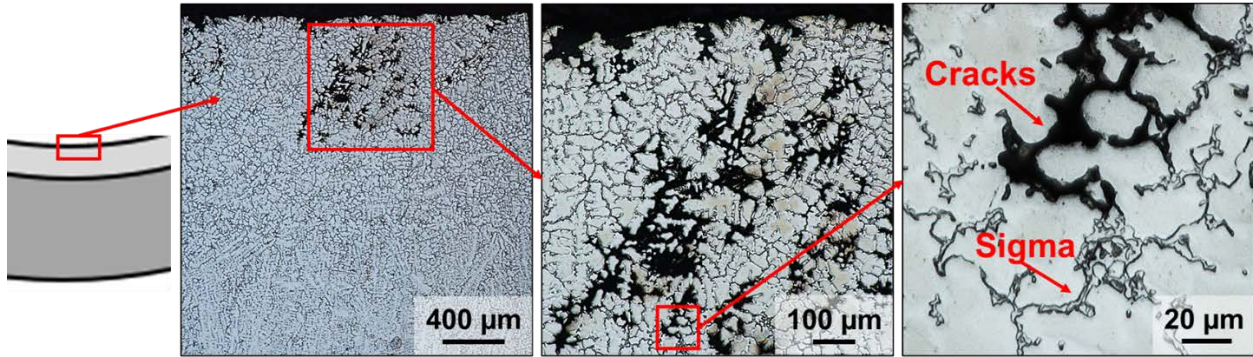
Figure 86. LOM images showing solidification cracking on the cladder ID, which are likely associated with secondary phases during solidification

4.2.3.2 CALPHAD Simulations

ThermoCalc software was used to predict the thermodynamic equilibrium microstructure and effect of solidification on microstructure using Scheil diagrams. Additionally, the PRISMA calculator was used for kinetic calculations, such as secondary phase nucleation and growth predictions.

Figure 87 shows the equilibrium single-axis phase diagrams for both the accepted nominal C-276 composition and synthesized C-276 cladder. The main observation gleaned from the synthesized cladder is the higher formation temperature of the sigma phase compared to the nominal composition (1050°C→1250°C). Additionally, a higher volume fraction and forming temperature of M_6C and Mu (intermetallic) phase is predicted with synthesized cladder composition.
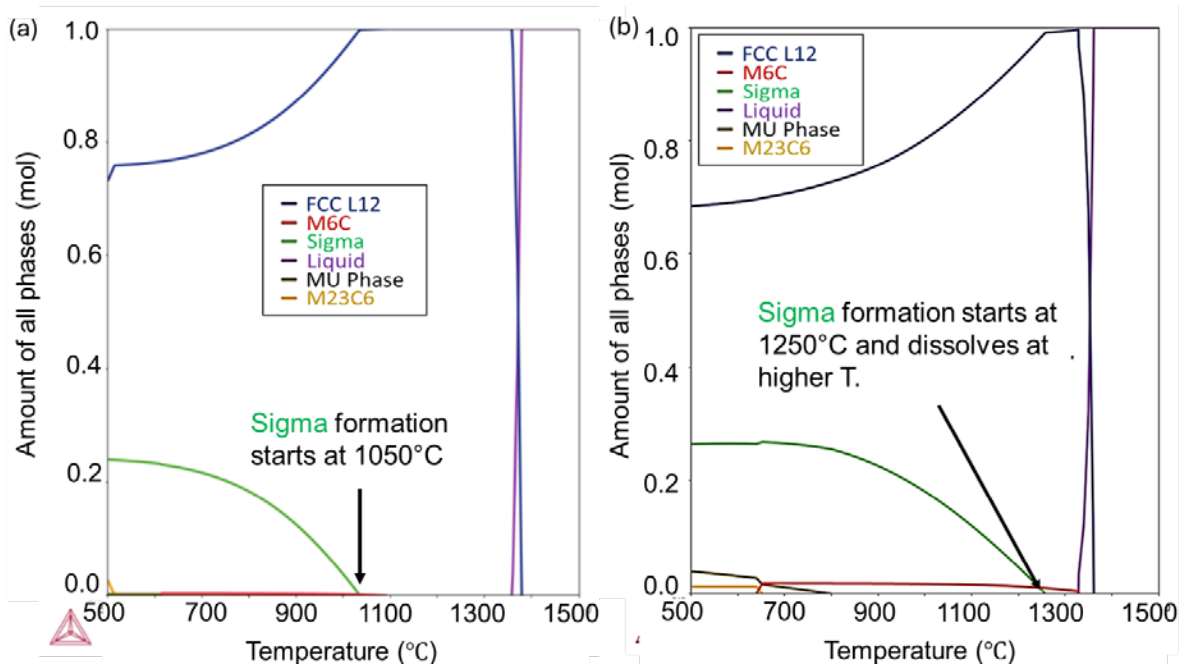
Figure 87. Equilibrium single-axis phase fraction as a function of temperature for (a) nominal C-276 composition and (b) synthesized C-276 cladder composition (using OES composition)

80
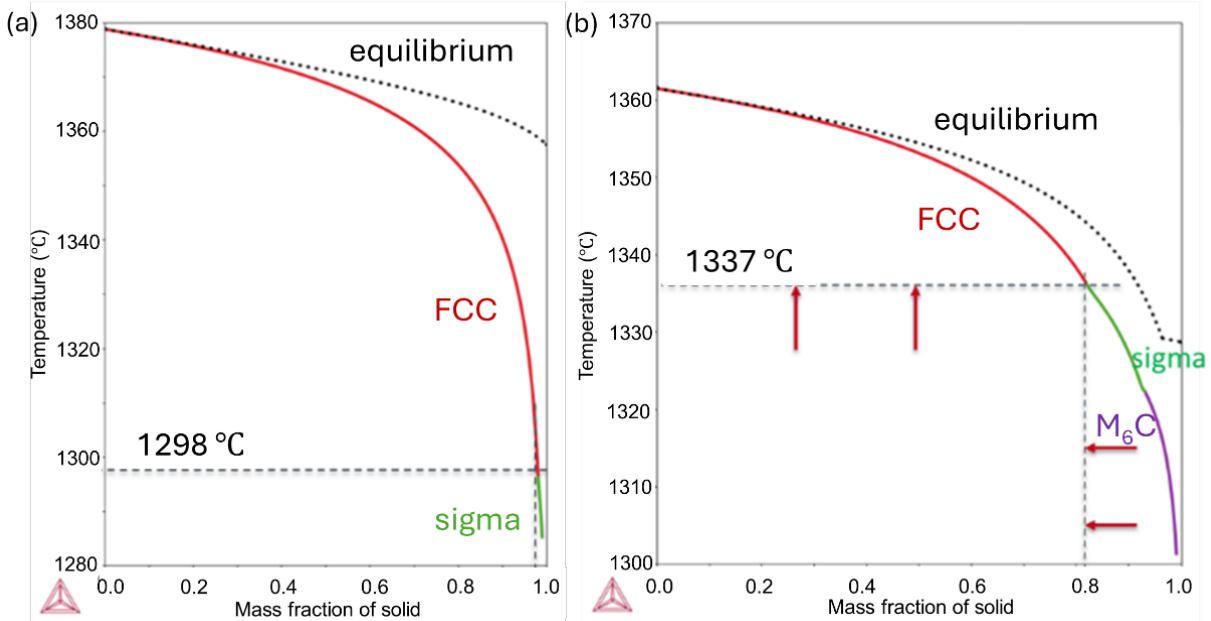
Figure 88. Scheil diagrams (solidification path) between equilibrium (very slow cooling) and non-equilibrium condition (assuming diffusion in liquid and no diffusion in solid) for (a) nominal C-276 composition and (b) synthesized composition of C-276 cladder

A brief analysis of the solidification conditions, both equilibrium and non-equilibrium conditions, were considered in CALPHAD analysis using Scheil diagrams. Figure 88 shows the Scheil diagrams for both nominal and synthesized cladder compositions. The first observation is that the slope of the equilibrium curve is sharper in the synthesized cladder, which ties into higher solidification cracking susceptibility based on the Kou susceptibility index [32]. Second, the non-equilibrium curves, assuming diffusion in liquid and no diffusion in solid), which is closer to the real-world case, show an earlier formation of sigma phase in the melt at approximately a 0.8 mass fraction of solid. The formation of sigma phase during solidification at 0.8 mass fraction of solid could explain embrittlement of the solidification grain boundaries and with sufficient cooling shrinkage, cracking would facilitate.

Figure 89 shows the time-temperature-transformation (TTT) diagram of sigma formation in a FCC-austenite matrix, which assumes isothermal assumption. A cooling path is shown, qualitatively, to illustrate a very fast cooling rate to avoid sigma phase with water quenching. However, with the high amount of Fe content and possible volume fraction of sigma phase, avoiding sigma phase may not be practically possible unless composition is first optimized to fit within the nominal composition limits of C-276.
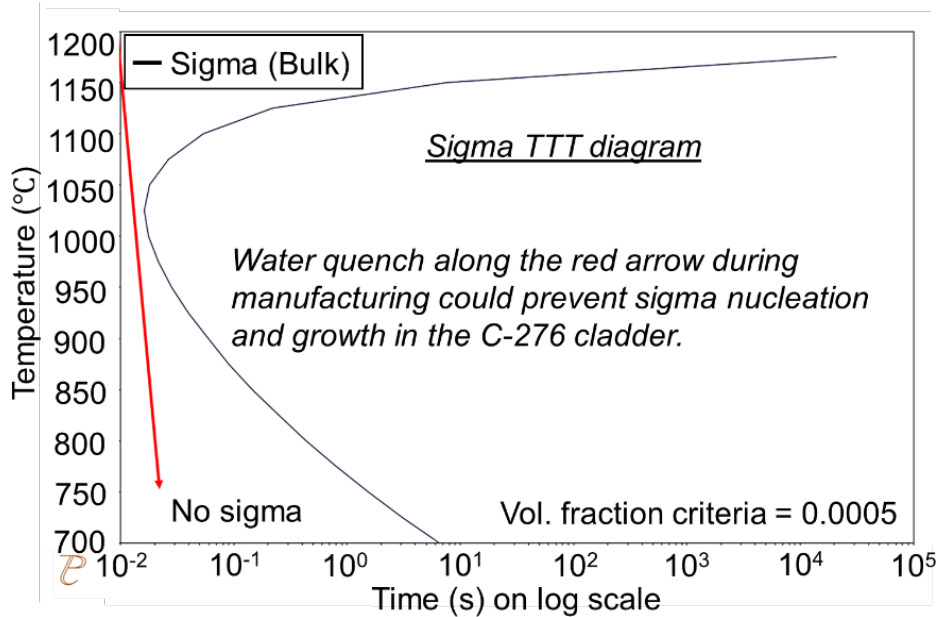
Figure 89. Time-temperature-transformation (TTT) diagram of sigma (bulk) phase in austenite matrix using a vol. fraction criterion of 0.0005. A cooling path to avoid sigma phase with water quenching during manufacturing/HT is shown.

4.2.3.3 Heat Treatment Effect

A heat treatment schedule to remove secondary phases has been determined using CALPHAD simulations. A temperature soak at 1260°C for 30 minutes followed by a water quench was followed using a box furnace. A comparison of the microstructure before and after heat treatment (HT) is shown in Figure 90, which demonstrates that the designed HT successfully dissolved the secondary phases as manifested by the clean grain boundaries adjacent to the cracks. In addition to the heat treatment, machining off approximately 0.5 mm of the ID after HT would be optimal to remove cracks.
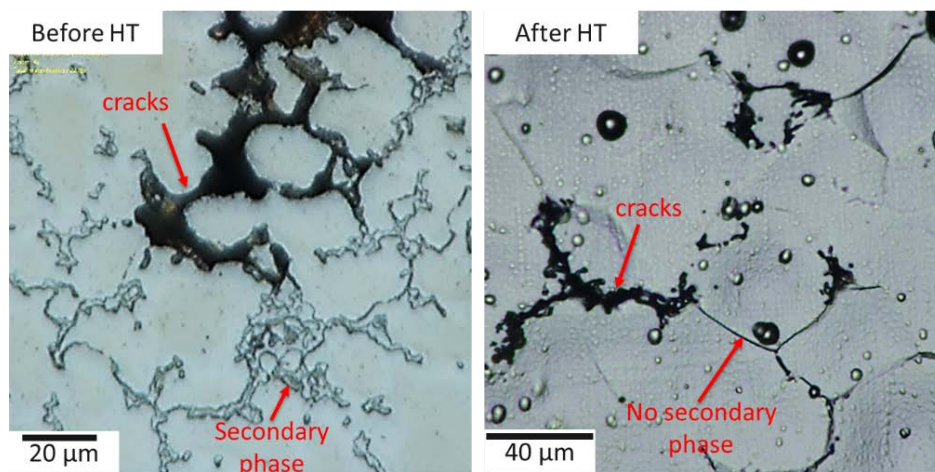
Figure 90. LOM of inner diameter C-276 cladded before and after high-temperature heat treatment (HT) at 1260°C for 30 minutes that shows dissolution of intergranular secondary phase, likely sigma phase

82

4.2.3.4 CS/CR C276/SS304H Corrosion Testing in Molten Chloride Salts

This piece of work is taken from milestone 2.5.3. corrosion in molten chlorides and added here to complete the work done on the CS/CR sample pipe section. Corrosion tests were performed at NREL on the synthesized C276 cladder before and after heat treatment to investigate the impact of the high iron content and the secondary phases on the corrosion resistance and to determine whether further study of CS/CR synthesized C276 was warranted. A set of CS/CR cladded pipe coupons were heat-treated (1260°C for 30 minutes followed by water quench) and then sent to NREL. The samples were machined using EDM to remove the SS304H backer so that only corrosion from the synthesized C276 cladder was present in the tests. The samples were immersed in a purified chloride salt mixture at 750°C for 100 hours and weighed before and after the test to measure the material loss. The corrosion tests resulted in a corrosion rate of 173 µm/year for heat-treated synthesized C276. This is well above the acceptable corrosion rate of 20 µm/year identified earlier. Based on these results, synthesized C276 from the CS/CR cladding process (which significantly differs in composition from wrought C276 in the nominal values) does not meet corrosion specifications, and further study of SS304H clad with current synthesized C276 using the air-cooled CS/CR manufacturing technique is not recommended.

4.2.4 CS/CR Conclusions

- Composition analysis showed that synthesized C-276 clad contains three times the Fe (~20 wt.%) content allowed by nominal composition limits, which is due to the limitation of the CS/CR process overall, including powders selected and parameters.
- Thermodynamic calculations (CALPHAD) suggest that the higher Fe content raises the equilibrium temperature for formation of sigma phase from 1050°C to 1250°C. Therefore, a slow cooling through higher-temperature regimes, which occurs during the process, enables a higher than desired volume fraction of sigma phase. Experimental results confirm the formation of secondary phase, likely sigma, which is enriched in Mo.
- The Mo-rich secondary phase formed in the interdendritic regions and potentially contributed to solidification cracks (~500-µm long) on the ID of the C-276 clad.
- Some remedies were suggested to (1) remove cracks, and (2) reduce and/or eliminate secondary phase in cladder, which would incorporate machining off the cracks and heat treatment, respectively. Based on CALPHAD predictions, a 1260°C soak temperature for 30 minutes followed by water quench was selected. The custom-designed heat treatment succeeded in dissolving Mo-rich secondary phase.
- However, corrosion tests in a purified chloride salt mixture at 750°C for 100 hours resulted in a 173 µm/year corrosion rate, which is almost nine times the allowed corrosion rate target of 20 µm/year.
- Overall, the higher than allowed Fe content and weak corrosion resistance of the C-276 cladder, largely driven by process, contributed to a decision to not forgo welding studies of CS/CR pipes. Instead, the EXW process was down-selected for further welding and techno-economic studies.

4.3 Task 4: Additive Manufacturing (AM) and Welding of AM

4.3.1 AM Process Developed for Selected High Temperature Alloys (Milestone 1.4.1)

The details for Milestone 1.4.1 are included in Table 29.

Table 29. Milestone 1.4.1 Details

Milestone	Description	Metric	Success Value	Assessment Tools
1.4.1: Additive Manufacturing (AM) processes developed for selected high temperature alloys	Printing processes must be developed to produce high relative density components that are free of significant microcracking. Surface conditions should be met for AM thermomechanical performance, flow performance, and to reduce the need for post AM processing to reduce part cost. Printing of CSP relevant geometries must be tested including a range of feature sizes to ensure the developed process conditions can fabricate relevant parts with challenging geometries.	1. Relative Density 2. Microcracking	1. > 99% relative density 2. No microcracking > 15 µm	Archimedes method (ASTM B962) and microscopy. All tested samples (at least three) should meet target with 10% errors based on standard deviation.
		3. Surface roughness 4. Subsurface porosity	3. Ra value < 10 µm 4. Subsurface porosity < 1.5%	Stylist profilometer or digital microscopy surface roughness and microscopy. All tested samples (at least three) should meet target with 10% errors based on standard deviation. Ra value (described by ASME B46.1) is the average of the absolute value of the surface height deviation from the mean.
		5. Feature dimensional tolerance. 6. Pressure tight thin walls.	5. Within 150 µm 6. <1-mm wall thickness.	All tested samples (at least three) should meet target with 10% errors based on standard deviation. 5. Dimensional measurements including microscopy. 6. Fit tubular thin-walled component to pressurized gas source and look for bubbles in submerged or soapy AM component.

4.3.1.1 L-PBF

Elementum 3D (E3D) is additively manufacturing alloy 230, a Haynes 230 equivalent atomized by Praxair, Haynes 282 (H282), and Inconel 740H (IN740H) using laser powder bed fusion (L-PBF) printing processes. The work completed toward the AM development of Haynes 282, IN740H, and Alloy 230—a Haynes 230 equivalent material—is summarized in Table 30. Whereas Alloy 230 required extra development in mitigating the microcracking in the microstructure, Haynes 282 and IN740H parameter development progressed much smoother. Laser parameters were developed for each alloy, fulfilling the design criteria outlined in Table 30.

Table 30. Elementum 3D Progress Made Toward 1-4-4.1 for Alloy 230 and Haynes 282

Milestone	Metric	Alloy 230	Haynes 282	IN740H
1.4.1	1. Relative Density	Complete	Complete	Complete
	2. Microcracking	Not complete	Complete	Complete
	3. Surface roughness	Complete	Complete	Complete
	4. Subsurface porosity	Complete	Complete	Complete
	5. Feature dimensional tolerance	Complete	Complete	Complete
	6. Pressure tight thin walls	Complete	Complete	Complete

4.3.1.1.1 Relative Density and Microcracking

4.3.1.1.1.1 Density of Alloy 230

E3D has created parameters for printing alloy 230 and H282. Figure 91and Figure 92 display the parameter development build of alloy 230 (five builds), and H282 (one build) needed to meet Milestone 1.4.1. Alloy 230 with a theoretical density of 8.97 g/cm^3, produced densities—calculated using Archimedes method (ASTM B926)—over 99%. Table 31 outlines the densities with an average relative density of 99.5% with standard deviation of 0.39%.

4.3.1.1.1.2 Density of Haynes 282

Process development for H282 has included investigation of a matrix of parameter combinations to produce a core process capable of delivering relative part densities of 99.5% or greater. H282 development was delayed due to a longer-than-anticipated procurement time for the atomized powder from Haynes International. The H282 is AM cut powder 15–45 μm and has produced good, printed results during the initial process development work. Table 32 presents an overview of the development of H282, with a theoretical density of 8.27g/cm^3. The 54 cubes produced (each with different processing conditions) have yielded an average relative density of 99.67% with a standard deviation of 0.39%.
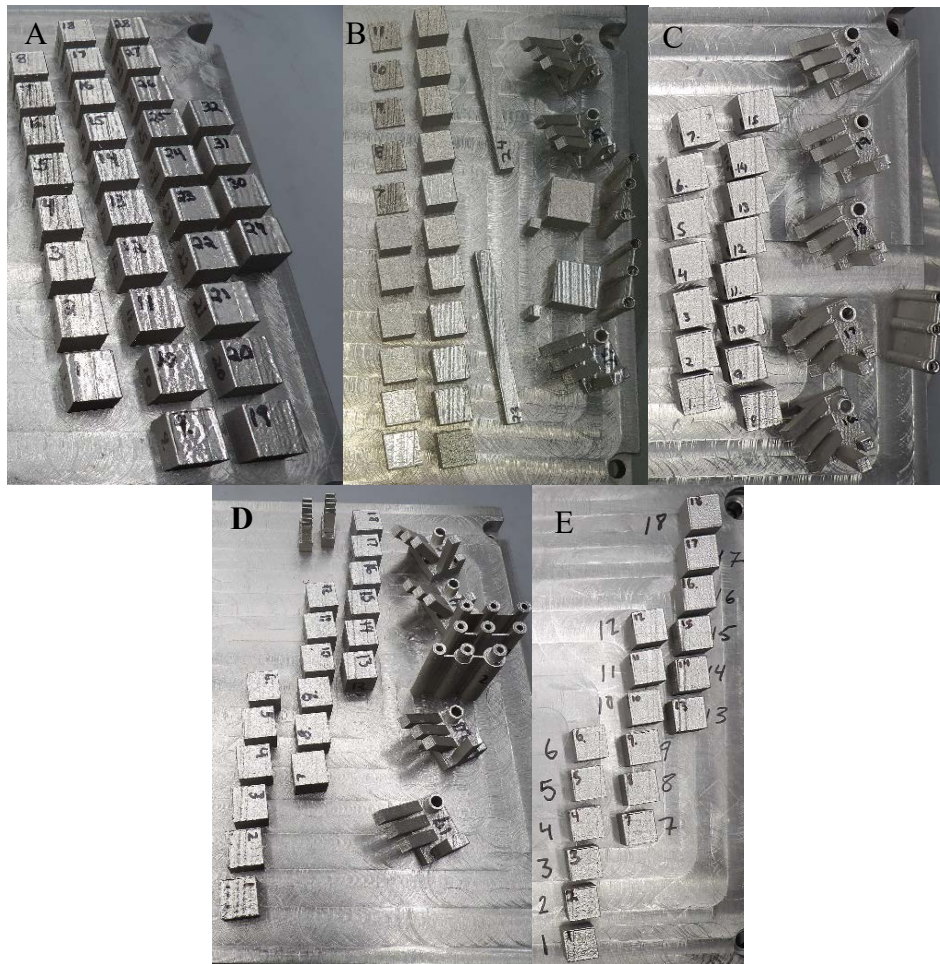
Figure 91. Alloy 230 development builds A, B, C, D, and E. Printing order from left to right.

Figure 92. Development build A for H282

Table 31. Densities for Development Build (from build E) Produced With the Most Updated Parameters Printed at Room Temperature

Alloy 230 Part	Energy (J/mm³)	Relative density	Open porosity
1	109.89	99.62%	0.23%
2	102.04	99.68%	0.16%
3	95.24	99.72%	0.13%
4	89.29	99.61%	0.17%
5	84.03	99.70%	0.12%
6	79.37	99.52%	0.22%
7	100.00	99.60%	0.11%
8	90.91	99.40%	0.16%
9	83.33	99.22%	0.20%
10	76.92	99.27%	0.13%
11	71.43	99.23%	0.11%
12	66.67	99.23%	0.06%
13	116.67	99.9	0.07%
14	97.22	99.9%	0.12%
15	83.33	99.88%	0.15%
16	72.92	98.92%	0.29%
17	64.81	99.07%	0.13%
18	58.33	98.90%	0.23%
Average		**99.50%**	**0.16%**
Standard Deviation		**0.39%**	**0.06%**

Table 32. H282 Metal Printing Development Parameter Overview for Development Build A

H282	Cubes	Power (W)	Energy (J/mm³)	Average relative density	Average relative density standard deviation
Dev. Build A	54	200-300	40-99	99.67%	0.39%

4.3.1.1.1.3 *Microstructure of Alloy 230*

Preventing microcracking in alloy 230 has taken the majority of engineering development for Milestone 1.4.1. The development has shown that 0.07–0.1-mm hatch spacing using 300 W with a 25°C substrate temperature is effective in reducing microcracking. Figure 93 displays the most recent microstructure in-skin parameters using an energy density of 67 J/mm³. During the alloy 230 development we have seen changes in microstructure from cracking to very little cracking and the presence of a second phase in the material. All images pasted in this report can be expanded to show the changes in microstructure development. Figure 94 shows the start of the alloy 230 development creating a relatively crack-free microstructure but with an energy density of 119 J/mm³. Figure 95 was built for confirmation that microcracking was not present in alloy 230 but proved not to be repeatable. Microcracks forming along columnar grain boundaries appeared. Figure 95 shows that a change in the build substrate temperature from 80°C to 25°C would improve microstructure considerably and allow for a large reduction in energy density believed to produce crack-free H230.
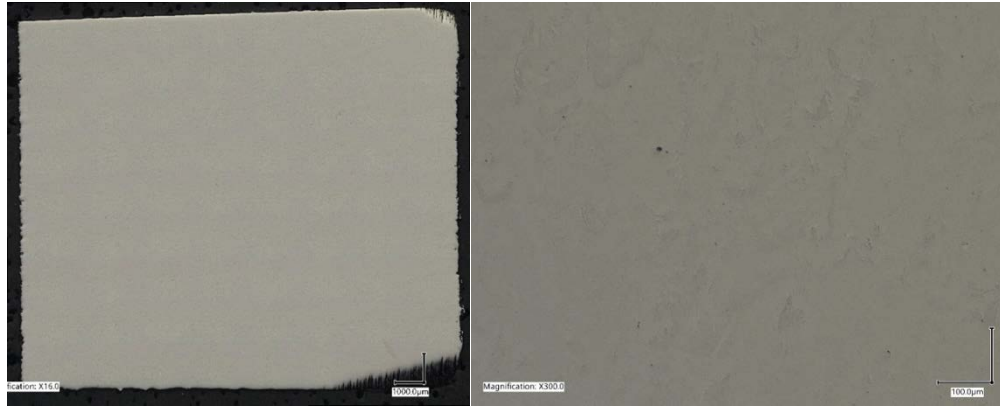
Figure 93. Development build D, alloy 230, cube 12 showing the side of the cube looking for columnar grain growth. 100X image stitch of the whole cube (left) and 300X closeup (right)

Figure 94. Development build A, alloy 230, cube 17. The cube used an energy density of 119 J/mm³ 100X image stitch of the whole cube (left) and 300X closeup (right)

Figure 95. Development build B, alloy 230, cube 10 (microcracking present.) Columnar grain growth was observed with cracking around the grain boundaries. The energy density used was 119 J/mm³. 100X image stitch of the whole cube (left) and 300X closeup (right)

4.3.1.1.1.4 Microstructure of H282

H282 in-skin parameter development has proven to be more responsive than alloy 230 with a comfortable process window of in-skin parameters producing crack-free microstructure. Figure

96 displays a favorable microstructure for H282 from development build A. The parameters used an energy density of 68 J/mm^3.

Figure 96. Development build A for H282 cube 15. 100X image stitch of the whole cube (left) and 300X closeup (right)

4.3.1.1.1.5 Inconel 740H Microstructure and Density

IN740H was successfully adapted to L-PBF with the development of a full laser parameter theme. Milestone 1.4.1-E3D was successfully fulfilled in two development builds for IN740H compared to the six required for Alloy 230. IN740H development builds consisted of: Build 1—density and in-skin development; and Build 2—subsurface porosity, surface roughness, feature dimensional tolerance, and thin hermetic walls. Figure 97 displays an image of each completed build plate. Build 1 consisted of 54 cubes, whereas Build 2 included cubes, angled bars, and leak-test tubes.

Figure 97. The In740h development builds showing the coupon designs utilized to fulfill the required criteria for Build 1 (left) and Build 2 (right)

IN740H in-skin parameter development has produced a wide process window of in-skin parameters with crack-free microstructures. Figure 98 displays a favorable microstructure for IN740H from development Build 2. The laser energy density used to produce was 94.7 J/mm^3. The resulting average Archimedes densities using the theoretical density of 8.17g/cm^3 along with the range of energy densities used to produce Build 2 are shown in Table 33.

Table 33. The In740h Metal Printing Development Parameter Overview for Dev Build 2

Haynes 282	Cubes	Energy (J/mm³)	Average relative density	Average relative density Standard Deviation
Dev. Build 2	32	52.5 – 104.1	99.71%	0.16%
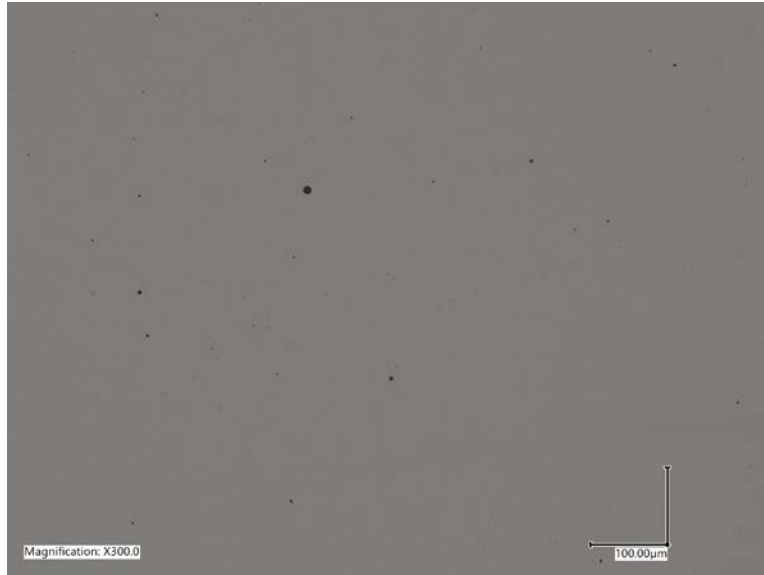
Figure 98. IN740H microstructure from the developed L-PBF parameters. This image, from IN740H development Build 2 cube number 13, was taken at 300X.

4.3.1.1.2 Surface Roughness and Subsurface Porosity

4.3.1.1.2.1 Surface Finish of Alloy 230

E3D has created the following surface roughness specimens to find the Roughness average (Ra) values for alloy 230. Figure 99 displays a non-contour specimen and a contour specimen with desired Ra values below 10 μm for up-skin. The down-skin for the contour angle finger is averaging 14.2 μm with the current contour parameter set. Table 34 outlines the current results for alloy 230 surface finish. The development for better down-skin surface is ongoing for alloy 230.

90
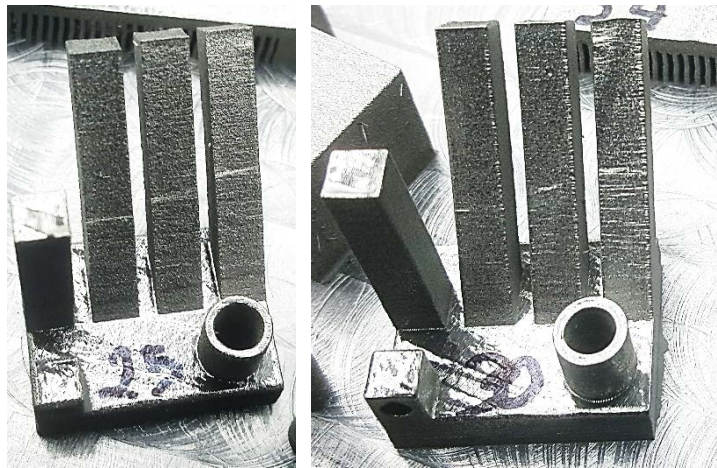
Figure 99. Image of alloy 230 development build B angled bars for surface roughness non-contour angled bars 25 (left) and contoured bars 30 (right)

4.3.1.1.2.2 Subsurface Porosity of Alloy 230

Alloy 230 contour development has proven effective in not creating subsurface porosity. Subsurface porosity is the porosity created from the contour laser parameter enclosing porosity in between the part and the contour. Figure 100 highlights the contours developed and resulting subsurface porosity for alloy 230. These samples were printed in development build D and show that alloy 230 has little susceptibility to subsurface porosity.

Table 34. Profilometry Results for Angled Bar Set 25 and 30 from Alloy 230 Development Build B

Parameter Set	Angle Degrees	Ra Avg. (µm)	Ra Up-Skin Overall Avg. (µm)	Ra Down-Skin Overall Avg. (µm)
Core settings only No contours (Part 25)	45	9.57	10.05 (Std. Dev. 1.34)	16.28 (Std. Dev. 3.22)
	45	20.80		
	50	8.71		
	50	15.69		
	55	10.02		
	55	15.43		
	90	11.88		
	90	13.19		
With Contours (Part 30)	45	5.66	6.05 (Std. Dev. 0.51)	14.19 (Std. Dev. 5.44)
	45	18.99		
	50	5.91		
	50	17.21		
	55	5.84		
	55	13.88		
	90	6.81		
	90	6.67		
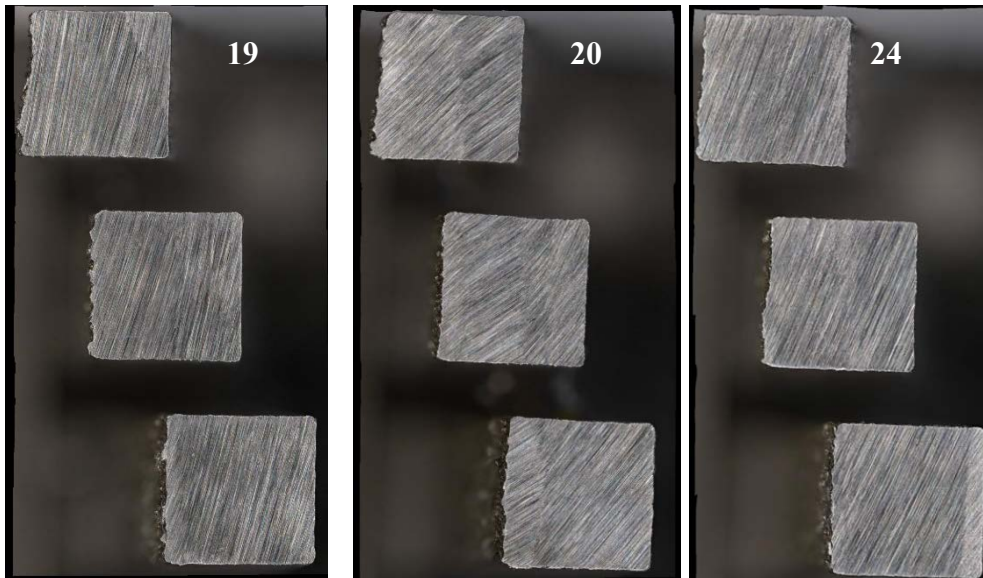
Figure 100. The top of fingers 19, 20, and 24 from alloy 230 development build D. No apparent subsurface porosity was created from the evaluation contour settings.

4.3.1.1.2.3 *Surface Roughness of IN 740H*

E3D has produced IN740H with acceptable surface roughness with the developed contour laser parameters. These developed contour parameters produce an average Ra of 6.85 µm for up-skins and 5.44 µm for down-skin. Table 35 outlines IN740H profilometry results for parameters with and without contours for the test range of angles. The down-skin parameters will be improved over next quarter to minimize the subsurface porosity and reduce the down-skins' Ra.

Table 35. Profilometry Results for Angled Bar Set 35 and 37 From IN740H Development Build 2

Angle Degrees	Core Settings Only, No Contours (Part 37)		Core Settings with Contours (Part 35)	
	Up-Skins Ra Avg. (µm)	Down-Skin Ra Avg. (µm)	Up-Skins Ra Avg. (µm)	Down-Skin Ra Avg. (µm)
45	9.12	22.85	7.98	7.17
50	7.57	27.23	6.23	5.29
55	9.57	23.46	6.36	3.86
90	7.68	X	3.04	X
Overall Avg. (µm)	8.75	24.51	5.90	5.44
Std. Dev	4.46	2.37	2.07	1.66

4.3.1.1.3 Feature Dimensional Analysis

4.3.1.1.3.1 *Feature Dimensional Tolerance of Alloy 230*

The developed alloy 230 process has proven to be suitable for producing dimensionally tolerant parts. To evaluate for part accuracy, the angled bars produced in development build D have a small tube printed on them to be measured for the feature dimensional tolerance. These were measured using National Institute of Standards and Technology (NIST)-traceable calibrated calipers. Figure 101 shows the critical features measured for this section of the milestone. Table 36 measurements show that X, Y, and outer diameter measure within 24 µm on average. The tube's inner diameter (ID) proves to be less precise in the parts tolerance ranging from 100–220

92

μm. Note repeatable measurement of ID with calipers is difficult; more investigation is needed for IDs.
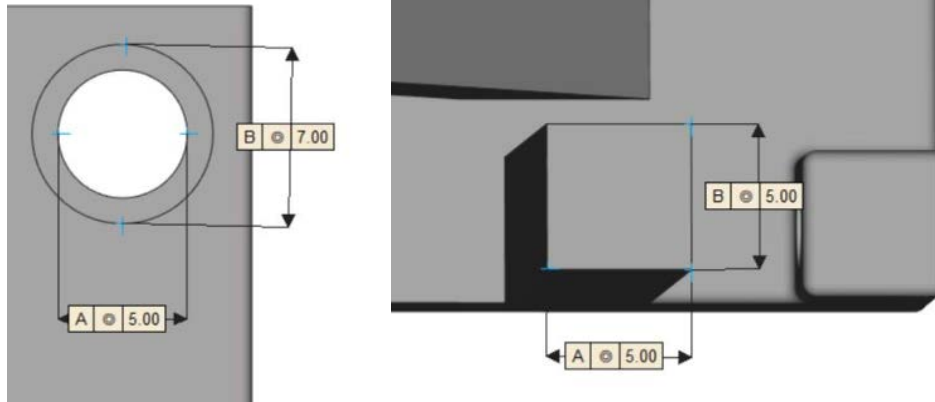
Figure 101. Dimensions measured for the feature dimensional tolerance evaluations for alloy 230 are displayed above. These dimensions were printed with the angle fingers on Dev build D

Table 36. Measurements Taken From Development Build D Parts 19, 20, 24, and 25 for Feature Dimensional Tolerance

	Dimension	Measure 1	Measure 2	Measure 3	Measure 4	Average (mm)	Difference (µm)	Actual (mm)
19	OD	7.00	6.98	6.99	6.95	6.98	20.00	7.00
	ID	4.88	4.92	4.91	4.89	4.90	100.00	5.00
	X	5.01	5.01	5	5.02	5.01	10.00	5.00
	Y	5.02	5.01	5.01	5.00	5.01	10.00	5.00
20	OD	7.02	6.95	6.95	7.00	6.98	20.00	7.00
	ID	4.89	4.9	4.85	4.9	4.89	115.00	5.00
	X	5.01	5.01	5.01	5.03	5.02	15.00	5.00
	Y	5.03	5.04	5.03	5.02	5.03	30.00	5.00
24	OD	6.95	6.94	7.00	7.04	6.98	17.50	7.00
	ID	4.64	4.77	4.86	4.85	4.78	220.00	5.00
	X	5.04	5.05	5.05	5.05	5.05	47.50	5.00
	Y	5.05	5.04	5.05	5.04	5.05	45.00	5.00
25	OD	6.99	7.02	7.01	7.00	7.01	5.00	7.00
	ID	4.89	4.9	4.9	4.85	4.89	115.00	5.00
	X	5.01	5.01	5.01	5.03	5.02	15.00	5.00
	Y	5.03	5.04	5.03	5.02	5.03	30.00	5.00

OD: Outer diameter, ID: Inner diameter, X: length, Y: width

4.3.1.1.3.2 *Feature Dimensional Tolerance of IN740H*

The developed IN740H laser parameters have proven to be suitable for producing dimensionally tolerant parts. To test for part accuracy, the angled bar feature plate produced in development Build 2 has a small tube and vertical bar printed on it for the feature dimensional tolerance analysis. These were measured using NIST-traceable calibrated calipers. shows the critical features measured in CAD for this section of the milestone. Figure 102 and Table 37 overview the measurements from a test feature plate without contours and with laser contours. The parts without contours had measured differences from the CAD model of 10 and 20 µm in the X and Y directions, respectively, for the vertical bar. The outer diameter (OD) has a measured difference of 100 µm and the inner diameter (ID) had a difference of 350 µm. With contours

added, the X and Y dimensions both had a difference of 40 and 70 μm, respectively. The OD difference was 15 μm, and the ID difference was 195 μm. Note: repeatable measurement of ID with calipers is difficult; more investigation is needed for IDs.
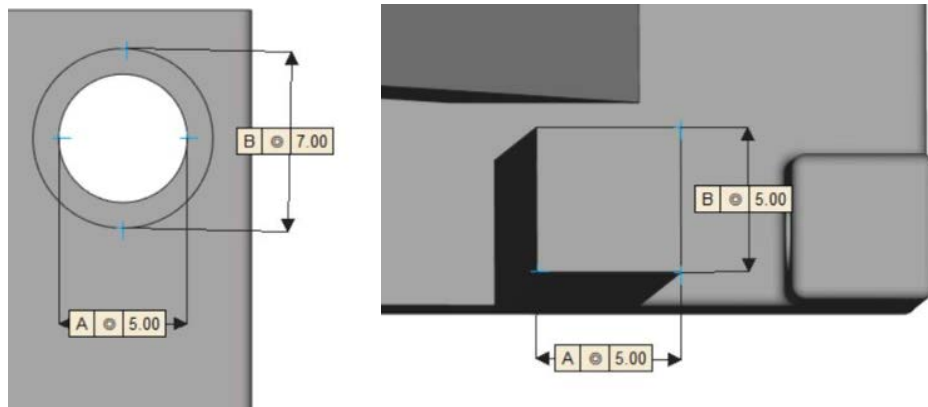
Figure 102. The dimensions measured for the feature dimensional tolerance tests are displayed above. These dimensions were printed with the angle fingers on Dev. Build 2.

Table 37. Measurements Taken from Dev. Build 2 Fingers 37 Non Contours and Fingers 35 Contours

	Dimension	Nominal (mm)	Average (mm)	Difference (μm)
No Contours (part 37)	OD-X	7.00	7.02	20
	OD-Y	7.00	7.01	10
	ID-X	5.00	4.81	190
	ID-Y	5.00	4.8	200
	X	5.00	5.06	60
	Y	5.00	5.03	30
Contours (part 35)	OD-X	7.00	7.04	40
	OD-Y	7.00	7.07	70
	ID-X	5.00	4.67	330
	ID-Y	5.00	4.63	370
	X	5.00	5.1	100
	Y	5.00	5.12	120

4.3.1.1.4 Thin Wall Pressure Evaluation

4.3.1.1.4.1 Thin Wall Pressure Evaluation of Alloy 230

Alloy 230 has been evaluated for thin wall pressure stability. The activities conducted for pressure stability at E3D serve as a pass-fail evaluation. The thin wall pressure evaluation is conducted up to 4 bar or 58 psi using compressed air and held for 30 seconds. Then, soapy water is applied to the surface to check for leaks. If bubbles appear, leaks are present, and the part fails. Figure 103 shows the tubes produced for the alloy 230 pressure evaluation. The 1-mm wall has proven leakproof at 4 bars for contours and no contours. Table 38 outlines the nine-test carried out for the pressure evaluation. E3D will conduct more pressure evaluations with thinner-walled samples less than 1 mm.

Table 38. The Thin Tube Pressure Results for Alloy 230 from Development Build D. All Test Samples Passed the Pressure Evaluation without Leaking at a Pressure of 4 Bar

Material	Parts	Parameter	Wall thickness	Air pressure 4 bar
H230	21	No Contour	1 mm	pass
		No Contour	2 mm	pass
		No Contour	3 mm	pass
	22	Contour 1	1 mm	pass
		Contour 1	1 mm	pass
		Contour 1	1 mm	pass
	23	Contour 2	1 mm	pass
		Contour 2	1 mm	pass
		Contour 2	1 mm	pass
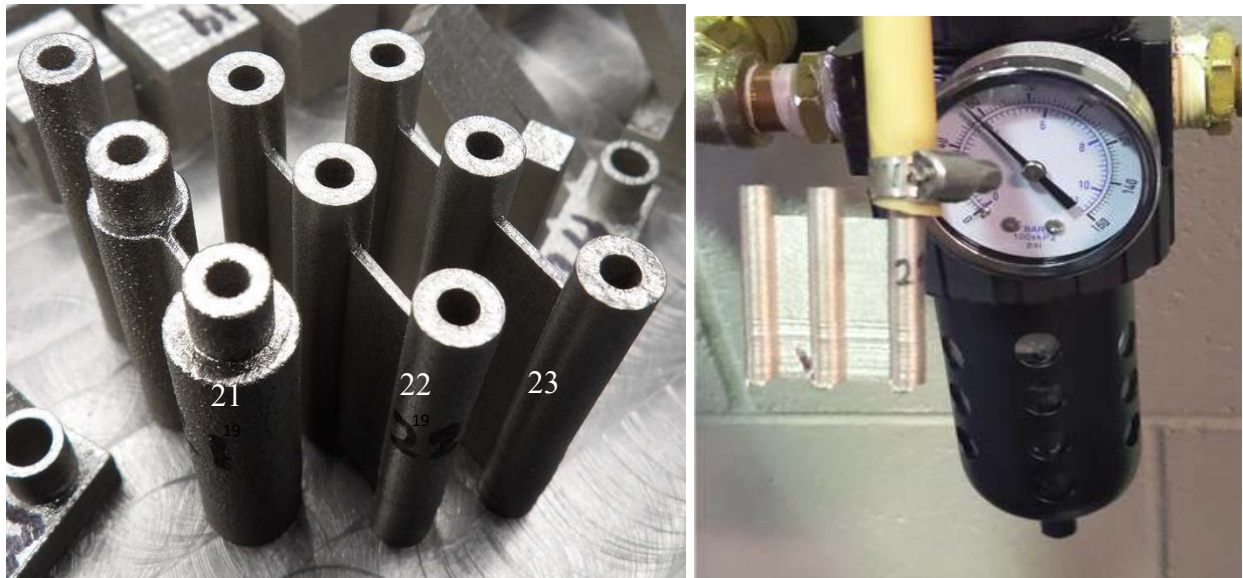
Figure 103. (Left) Pressure tubes for 1-mm thin wall evaluation. 21 is no-contour with 1 mm to 3 mm wall thickness. 22 and 23 are contour parameters with three tubes each targeting 1-mm wall thickness for repeatability. (Right) shows the setup for a pressure evaluation at Elementum 3D

4.3.1.1.4.2 Thin Wall Pressure Evaluation of IN740H

The IN740H was pressure tested to 4 bar using air. The test tubes' wall thicknesses are 0.75 mm, 0.50 mm, and 0.25 mm. Table 39 shows the results for each wall thickness and printer parameters. The pressure test is a pass-fail test to understand the materials. After testing IN740H tubes, it was found that it is possible to print tubes with hermetic 0.25 mm thick walls, which are shown in Figure 104.

95

Table 39. Pressure Test Results for Haynes In740H from Dev. Build 2

Parameter	Wall Thickness (mm)	Air Pressure: 4 Bar
No Contour	0.75	Pass
No Contour	0.5	Pass
No Contour	0.25	Pass
Contour 1	0.75	Pass
Contour 1	0.5	Pass
Contour 1	0.25	Pass
Contour 2	0.75	Pass
Contour 2	0.5	Pass
Contour 2	0.25	Pass
Contour 3	0.75	Pass
Contour 3	0.5	Pass
Contour 3	0.25	Pass
Contour 4	0.75	Pass
Contour 4	0.5	Pass
Contour 4	0.25	Pass

Figure 104. In740h pressure tubes with contours. No set of tubes leaked after being subjected to 4 bars of air pressure.

4.3.1.2 EBAM

The condition of the racetrack sample was received after heat treatment (solution anneal +age). To characterize the microstructure evolution as the build progresses, build samples were taken from the fully aged EBAM racetrack just above the baseplate, the middle of the build volume, and at the build surface. Figure 105 shows the microstructure parallel to the z-y plane. A distinct progression toward epitaxial growth in the build direction can clearly be seen as the build height progresses. The etchant seemed to show a higher presence of secondary phases disbursed

96

throughout the columnar morphology in the bottom location (Figure 105(b)). Passes in the middle and top location of the build have thinner deposited passes, indicating there might be more remelting taking place as seen with the remelted zones in Figure 105(d).
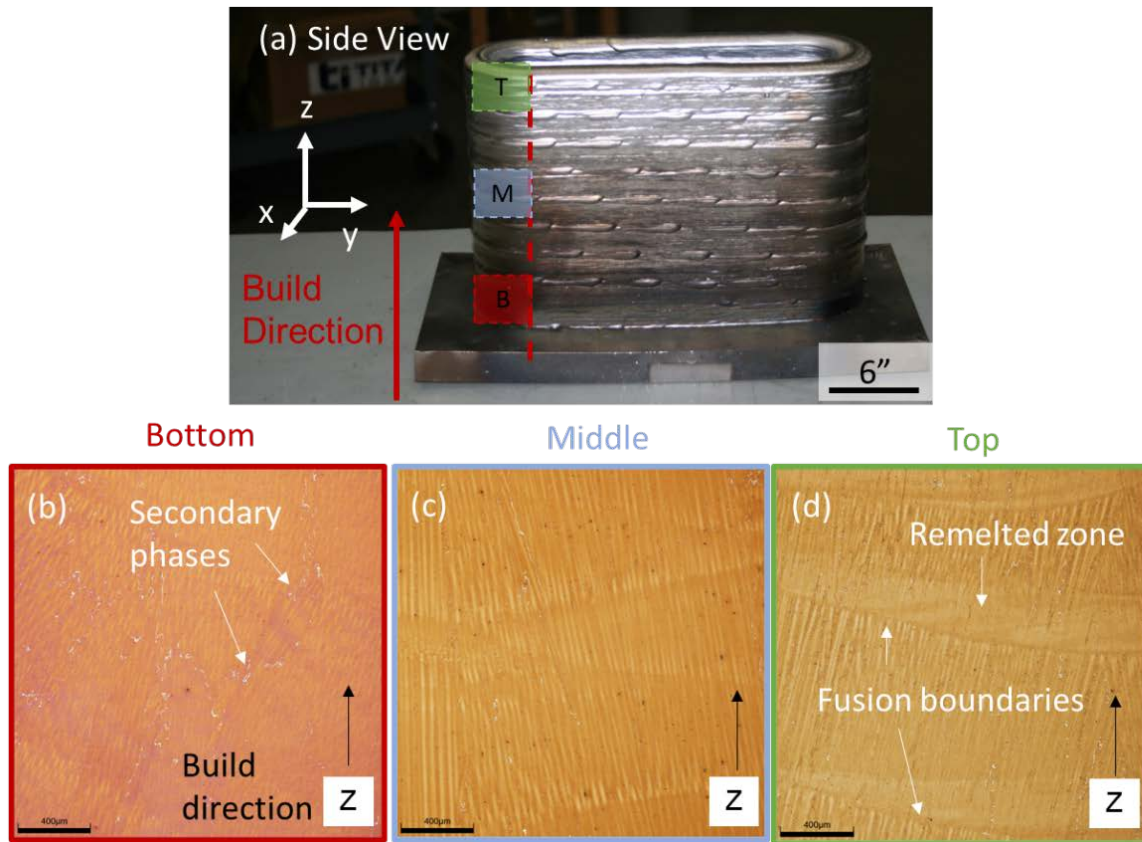
Figure 105. (a) Vertical (Z) sample extractions from aged EBAM racetrack for metallurgical analysis of the Z-Y plane of (b) bottom, (c) middle, and (d) top locations of the racetrack

Figure 106 shows characterizations at the same build locations but viewed at the x-y plane from top down along Z axis. The boundaries between deposition passes at each layer can be clearly seen and are annotated in Figure 106(b–d) by dashed red lines. Also note that a distinct crack or a line of porosity at fusion boundaries is present at the top locations. The mechanism for its formation requires further investigation, but speculatively, because the build has been heat-treated, it could be due to ductility dip cracking, stress relaxation, or strain age cracking, to name a few possibilities. Liquation cracking may be another possibility, as the crack aligns with the fusion boundary of the center and edge passes. More obviously, the microstructure seems to have a lot of remnant solidification morphology still present, indicating the solution anneal step in the heat treatment (1140°C, 30 min) was insufficient to mobilize the subgrain boundaries prior to aging steps. Remnant solidification subgrain boundaries were not easily observed within the L-PBF samples after HT.

This report is available at no cost from the National Renewable Energy Laboratory at www.nrel.gov/publications.
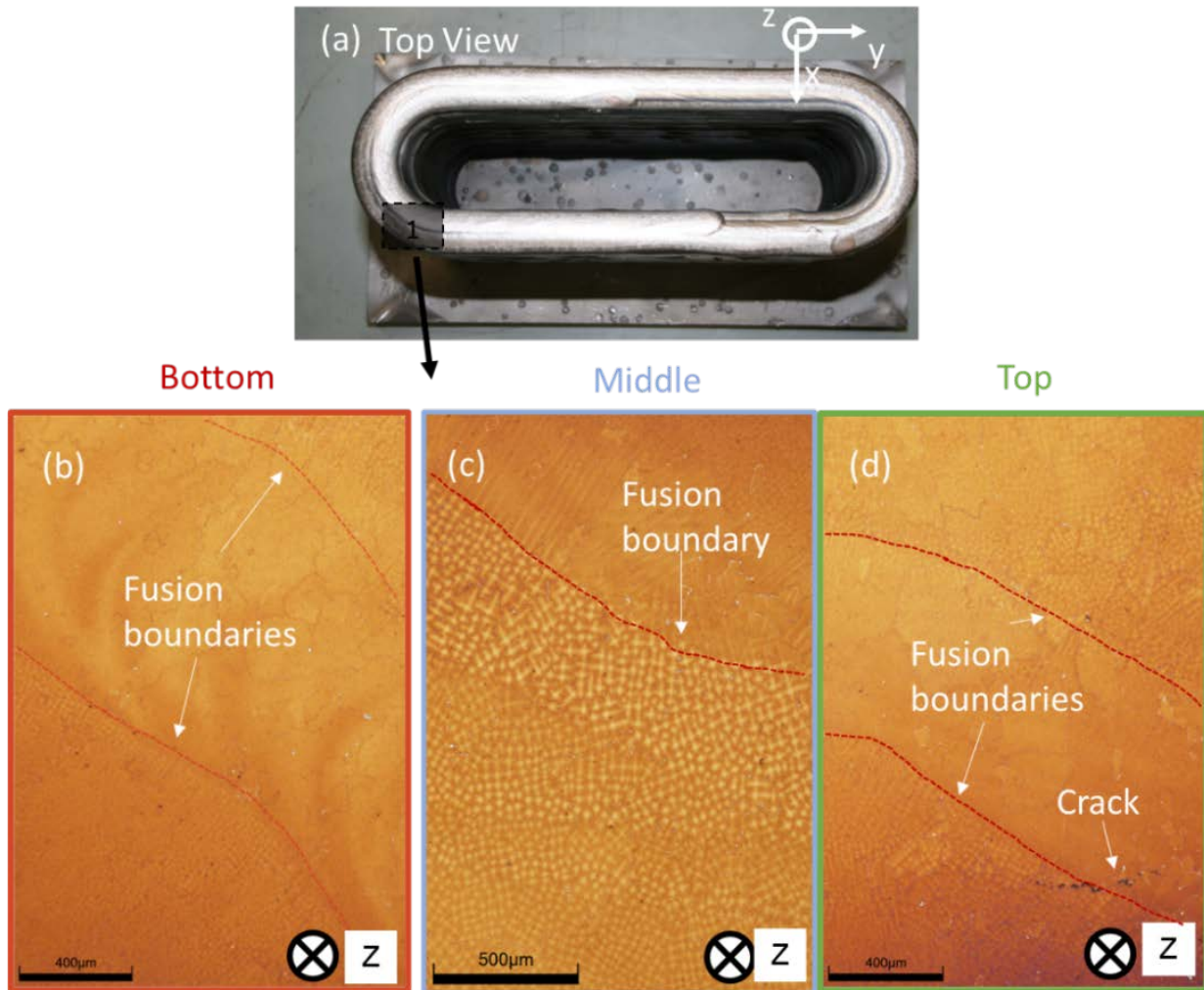
Figure 106. (a) Horizontal (x, y) sample extractions from aged EBAM racetrack for metallurgical analysis of (b) bottom, (c) middle, and (d) top locations of the racetrack

Figure 107 shows the summary of SEM microstructure observed of Haynes 282 build after heat treatment (using HT2 aging conditions, as shown in next section). With respect to defects, there was very little cracking, but keyhole porosity was observed more commonly. Because this was the first attempt Sciaky had made to create a build with Haynes 282, further process optimization could possibly help prevent keyhole porosity (e.g., lower beam energy density). Cr- and Mo-rich precipitates were observed along remnant columnar interdendritic regions along with a fine distribution of γ' phase. Further thermomechanical testing of these samples was conducted while trying to avoid specific regions with prominent porosity.
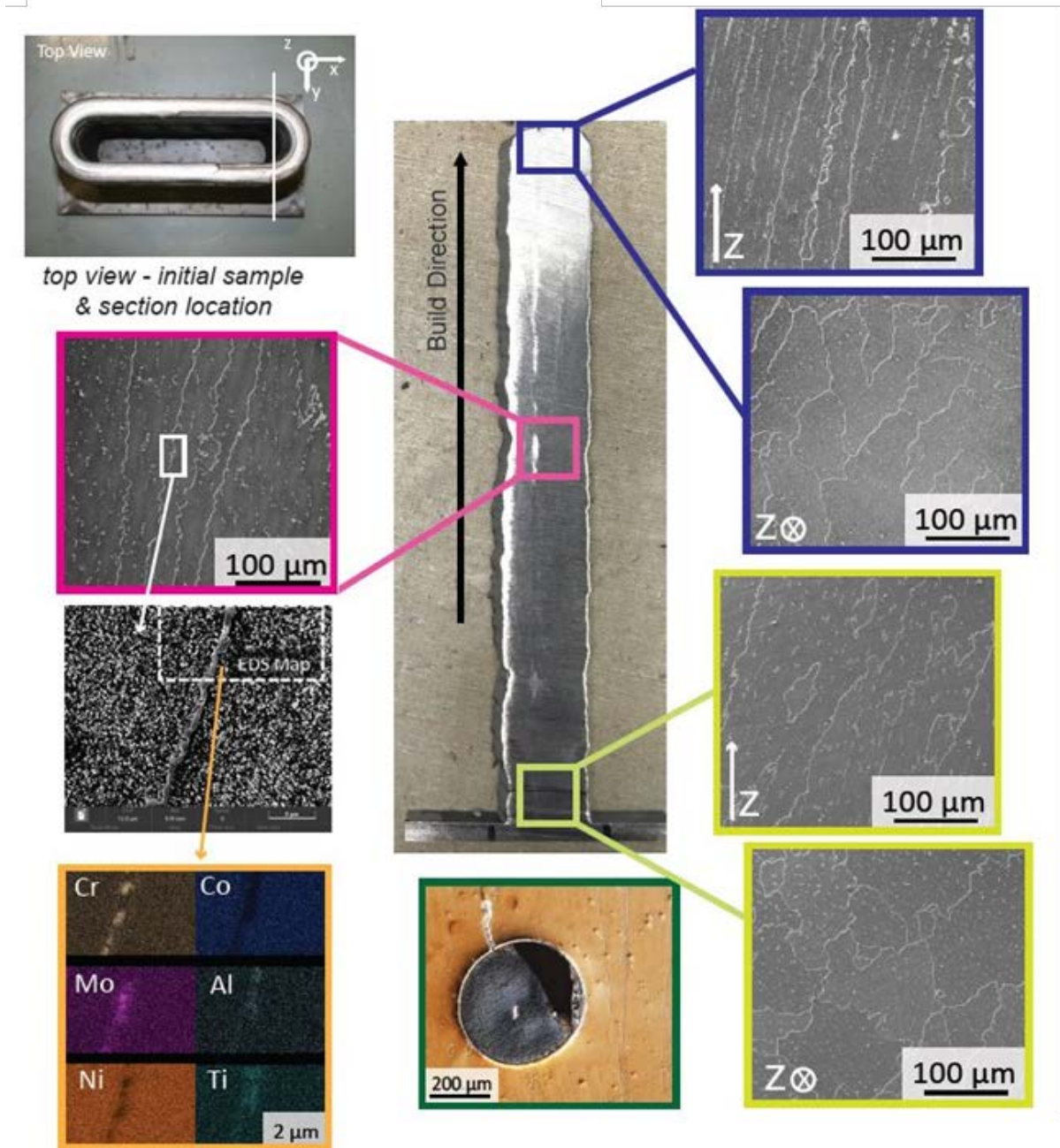
Figure 107. EBAM Haynes 282 microstructure (as built + HT condition) and defects (key-hole porosity)

In contrast to Haynes 282 build, Haynes 230 exhibited an unacceptable amount of cracking throughout the build height, as seen in Figure 108. It was observed there was secondary phase present along grain boundaries ahead of crack tips. Figure 109 shows an EDS line scan across the secondary phase ahead of cracks, which indicate W and Si enrichment. The cracking mechanism likely is solidification cracking, but there is possibility of reheating cracking during PBHT of 1230°C. Haynes 282 was further chosen as the better candidate for arc welding experiments of EBAM to wrought plate.

99
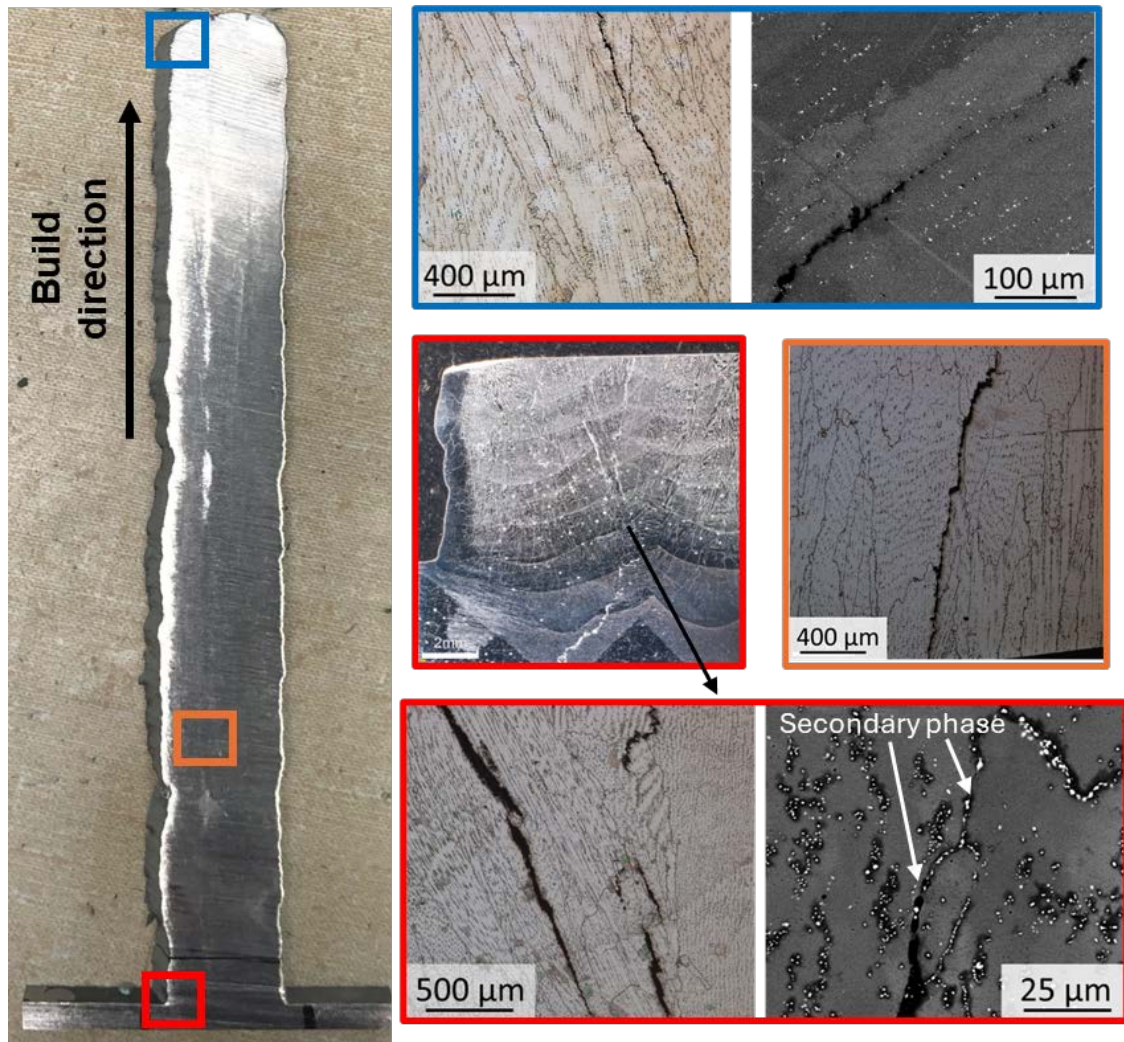
Figure 108. EBAM Haynes 230 as-built + HT. Very noticeable cracking issues throughout the build height
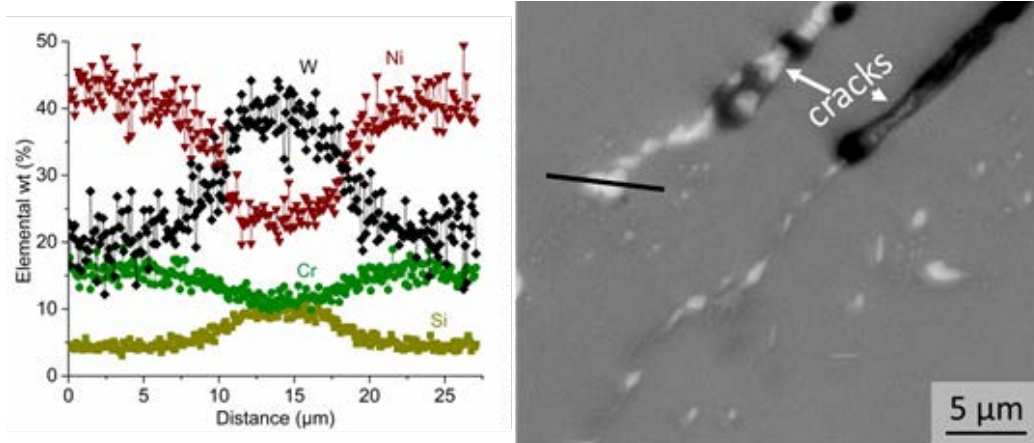
Figure 109. EDS line scan of secondary phase showing W enrichment ahead of secondary cracks in Haynes 230 build

100

4.3.2 AM Heat Treatment Development and Property Testing (Milestone 1.4.2)

Table 40. Milestone 1.4.2 Details

Milestone	Description	Metric	Success Value	Assessment Tools
1.4.2: AM heat treatment development and property testing	Prior to welding studies heat treatment development, property testing, and microstructure evaluation need to provide required tensile properties at room and service temperatures (based on M1.1.2).	Tensile properties at room and service temperatures (based on M1.1.2) compared to conventionally manufactured properties for each alloy.	> 80% yield and ultimate strengths. > 50% elongation.	Gleeble experimental simulator and/or high temperature tensile frame. All tested samples (at least three) should meet target with 10% errors based on standard deviation.

4.3.2.1 L-PBF

Table 41 shows the post build heat treatment schedules considered for L-PBF samples for Haynes 282, Inconel 740H, and Haynes 230.

Table 41. Post Build Heat Treatment (PBHT) Schedules Considered for L-PBF Samples

Material	Haynes 282 (Heat Treatment #1)	Haynes 282 (Heat Treatment #2)	IN740h	Haynes 230
Step 1	Solution-anneal 2 step	Solution-anneal 2 step	Solution Anneal	Solution-Anneal 1 step
Atmosphere	Argon	Argon	Argon	Argon
Heating rate	5°C/min	5°C/min	5°C/min	5°C/min
Hold temperature °C	1130	1140	1120	1230
Hold time (hr)	1	1	1	1
Cooling	Air Cool	Air Cool	water quench	water quench
Step 2	Age 1	Age 1	Age 1	
Atmosphere	Argon	Argon	Argon	
Heating rate	5°C/min	5°C/min	5°C/min	
Hold temperature °C	1010	899	800	
Hold time (hr)	2	4	5	
Cooling	Air Cool	Air Cool	Air Cool	
Step 3	Age 2	Age 2		
Atmosphere	Argon	Argon		
Heating rate	5°/min	5°/min		
Hold temperature °C	788	788		
Hold time (hr)	8	8		
Cooling	Air Cool	Air Cool		

Figure 110 shows the schematic of samples printed in the vertical and horizontal direction with respect to the XY plane.
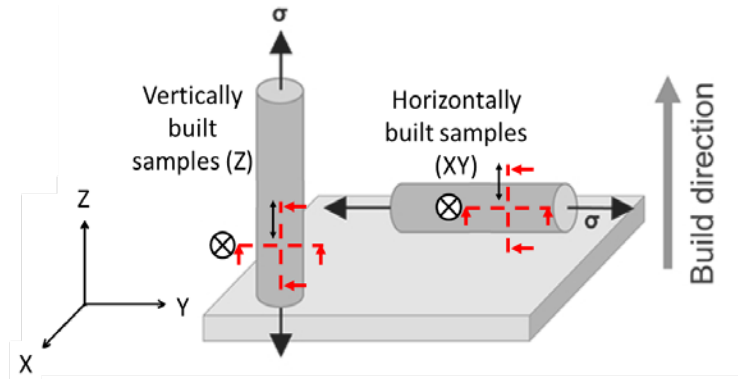
Figure 110. Schematic of L-PBF printed round bars used for property testing, crack susceptibility, and fatigue samples

4.3.2.1.1 Haynes 282

Table 42 shows the thermomechanical properties of L-PBF Haynes 282 samples categorized by HT. Figure 111 shows a summary of Haynes 282 results in the form of a spider chart. The main result discovered was the benefit of using HT2 to improve the ductility of the XY build orientation. For the remainder of HTs, HT2 was downselected as the preferable condition to improve elevated temperature ductility.

Table 42. Thermomechanical Properties of L-PBF Haynes 282 Round Bars

Build	Orientation	Temp °C	YS (KSI)	UTS (KSI)	El%	HT
A-2055	X,Y	RT	140.9 +/- 1.0	181.6 +/- 1.2	26.2 +/- 1.0	HT1
A-2200	X,Y	RT	124.3 +/- 0.3	178.1 +/- 0.3	23.6 +/- 0.7	HT2
A-2055	X,Y	520	124.3 +/- 1.0	158.5 +/- 1.4	23.8 +/- 1.4	HT1
A-2200	X,Y	520	110.5 +/- 0.2	157.7 +/- 0.7	19.2 +/- 1.3	HT2
A-2091	X,Y	760	114.8 +/- 0.2	115.9 +/- 0.2	5.5 +/- 0.5	HT1
A-2091	X,Y	760	91.3 +/- 1.1	114.9 +/- 0.9	23.4 +/- 3.5	HT2
A-2055	X,Y	780	110.8 +/- 0.1	117.1 +/- 5.0	6.1 +/- 1.2	HT1
A-2096	Z	RT	132.7 +/- 0.3	172.3 +/- 0.7	31.9 +/- 0.3	HT1
A-2200	Z	RT	115.8 +/- 0.4	166.0 +/- 0.1	30.6 +/- 0.8	HT2
A-2096	Z	520	117.1 +/- 3.1	149.2 +/- 3.6	24.8 +/- 2.7	HT1
A-2200	Z	520	101.3 +/- 0.3	146.2 +/- 0.8	20.5 +/- 1.	HT2
A-2108	Z	760	85.9 +/- 0.2	110.4 +/- 0.2	42.4 +/- 2.6	HT2
A-2096	Z	780	102.0 +/- 1.7	109.0 +/- 1.8	37.7 +/- 4.0	HT1
Haynes	Wrought	RT	103.7	166.4	30	
Haynes		538	94.1	143.8	34	
Haynes		760	91.1	124.2	22	HT1
Haynes		816	83.4	102.8	28	
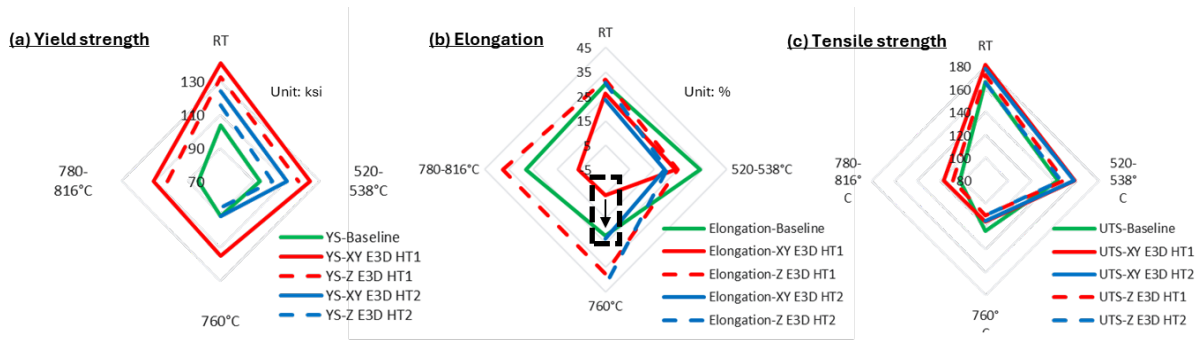
Figure 111. Spider chart representation of (a) yield strength, (b) elongation, and (C) ultimate tensile strength (UTS) of Haynes 282 components with HT1 and HT2 conditions

4.3.2.1.2 Comparison of Haynes 282 L-PBF and EBAM Microstructures with HT2

SEM and EDS chemical analysis was completed on EBAM samples for both the vertical and horizontal orientations but only in the middle location along z-direction of the build.
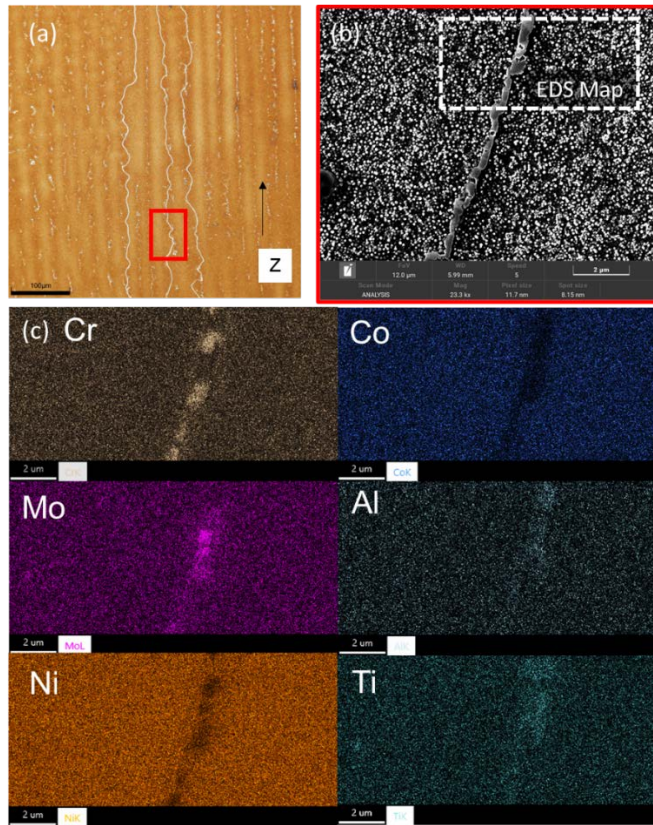
Figure 112. EBAM vertical orientation (Z) microstructure in middle of 150 mm tall build (a) LOM within a single weld pass, (b) SEI-SEM of secondary precipitates along columnar dendrites with intragranular γ' precipitates, and (d) EDS map (Cr, Mo, Ni, Co, Al, and Ti)

Figure 112 and Figure 113 represent the cross section on the z-y plane showing the effective vertical orientation. Figure 112 shows the microstructure and EDS of apparent interdendritic segregation and secondary phases precipitating during aging treatment, of the vertical orientation halfway through the vertical build. The microstructure shows a distribution of γ' particles on

103

either side of the solidification grain boundary (Figure 112(b)) enriched in Cr, Mo, Al, and Ti, which was also observed in L-PBF-HT2 microstructure. Figure 113 is a lower magnification SEM and EDS scan of more Cr and Mo rich grain boundaries, with the additional presence of coarse, blocky intragranular Mo (and Ti) carbides of MC type, as well as Cr (and Mo) rich $M_{23}C_6$ type carbides.
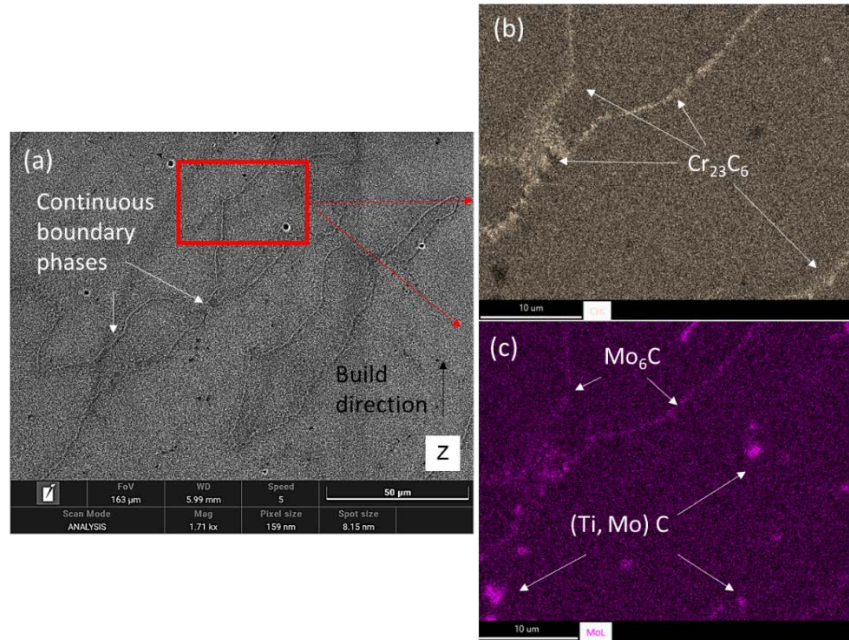
Figure 113. (a) Low magnification SEI-SEM of vertical (Z) sample having directionality of continuous boundary phases that are parallel to the columnar solidification grain orientation, and (b) EDAX map showing the presence of continuous $Cr_{23}C_6$, and (c) EDAX map of continuous precipitates containing Mo_6C and blocky type (Ti, Mo) C
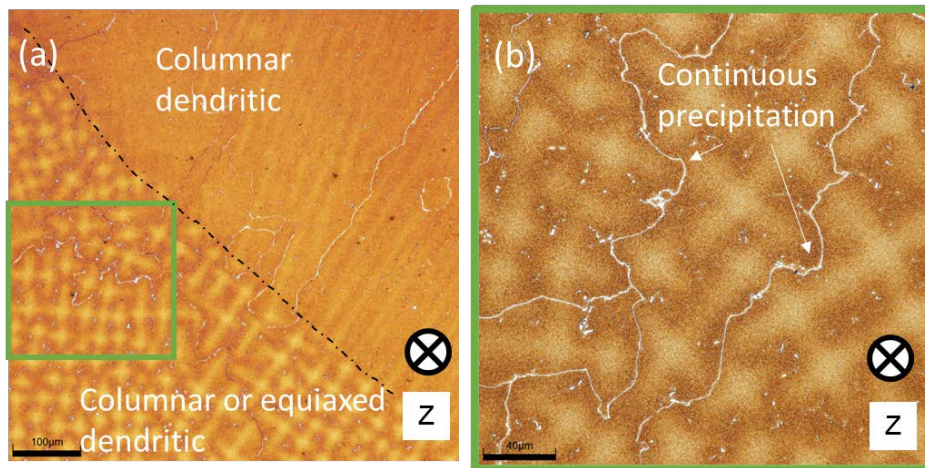
Figure 114. Horizontal (X,Y) microstructure in the middle section showing boundary between two columnar dendritic solidification grains of different orientations or a boundary between a columnar dendritic solidification grain and an equiaxed dendritic solidification grain, and (b) close up of etched dendrites with presence of continuous grain boundary precipitates

Figure 114, Figure 115, and Figure 116 represent the horizontal microstructure along the x-y plane. As shown in Figure 106, the presence of remnant solidification substructure after HT

(solution annealing + aging) is self-evident at higher magnification LOM in Figure 114. Interdendritic precipitation and indications of continuous precipitation are present, similarly seen in L-PBF samples. EBAM, being a DED process, has much higher beam energy and heat input than L-PBF, leading to slower solidification and cooling rates, leading to coarser substructure and wider dendritic spacing. Perhaps the solutionizing heat treatment did not properly "homogenize" the microstructure as seen in L-PBF samples, which may be due to either the presence of a coarser substructure that required higher solutionizing temperature or time.

Figure 115 and Figure 116 are SEM-EDS examples of horizontal orientation, where it becomes obvious those secondary precipitates along interdendritic regions are primarily Cr-rich $M_{23}C_6$ laced with Ti and Mo rich MC or M_6C. The aging heat treatment further validates the effect of HT2 on the EBAM microstructure just like the L-PBF microstructure, which is the formation of continuous interdendritic or solidification boundary carbides, particularly $M_{23}C_6$ or M_6C type, such as that seen in HT2 L-PBF microstructure in Figure 117(c–d). HT1 show more discrete precipitates (Figure 117(a–b)), which was hypothesized to allow for more void nucleation sites leading to reduced ductility. This led to the use of HT2 for EBAM samples as well.
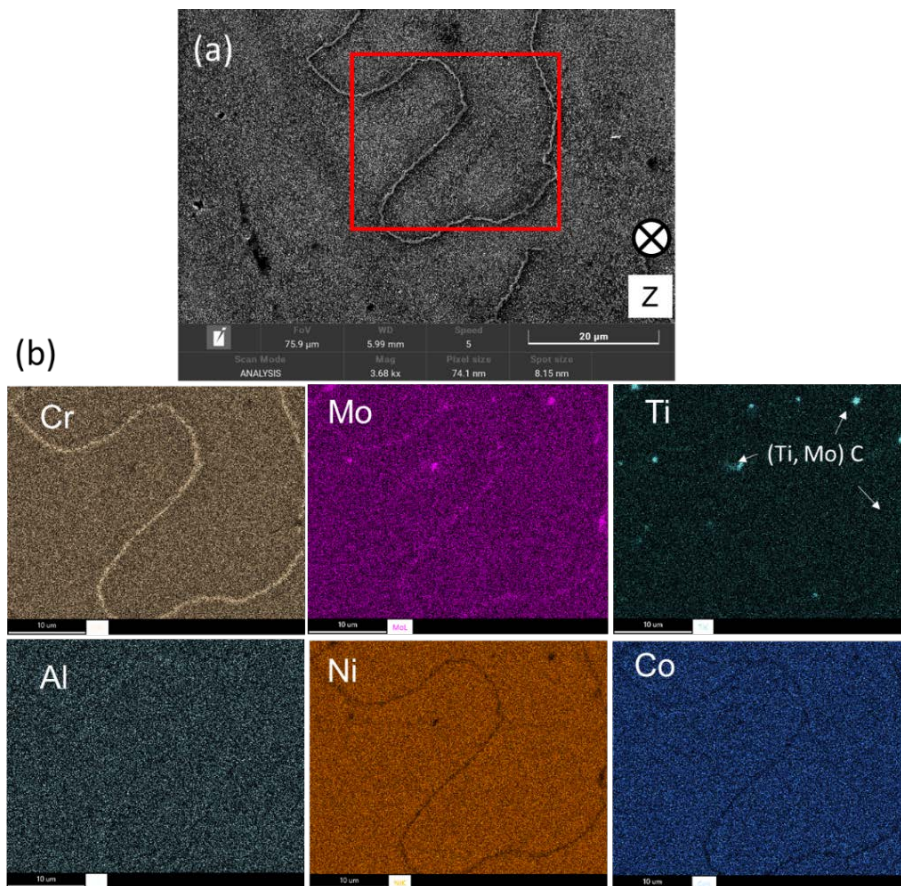
Figure 115. (a) Low-mag SEI-SEM image of top view (horizontal orientation) in location with continuous precipitates, and (b) EDS maps indicating the presence of grain boundary Cr-carbides and γ', with some blocky Ti, Mo C (high temperature carbides) present within the grains that likely have been in the matrix from EBAM process

105
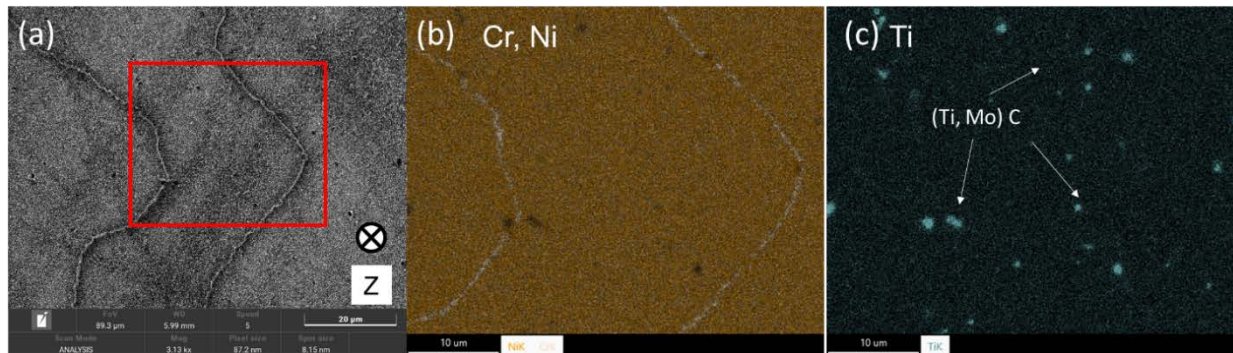
Figure 116. (a) Low-mag SEI-SEM image of top view (horizontal orientation) in second location with continuous precipitates, and (b) EDS maps indicating the presence of grain boundary Cr-carbides and depleted GB Ni, and (c) coarse, blocky Ti, Mo C (high temperature carbides) present within the grains that likely have been in the matrix from EBAM process
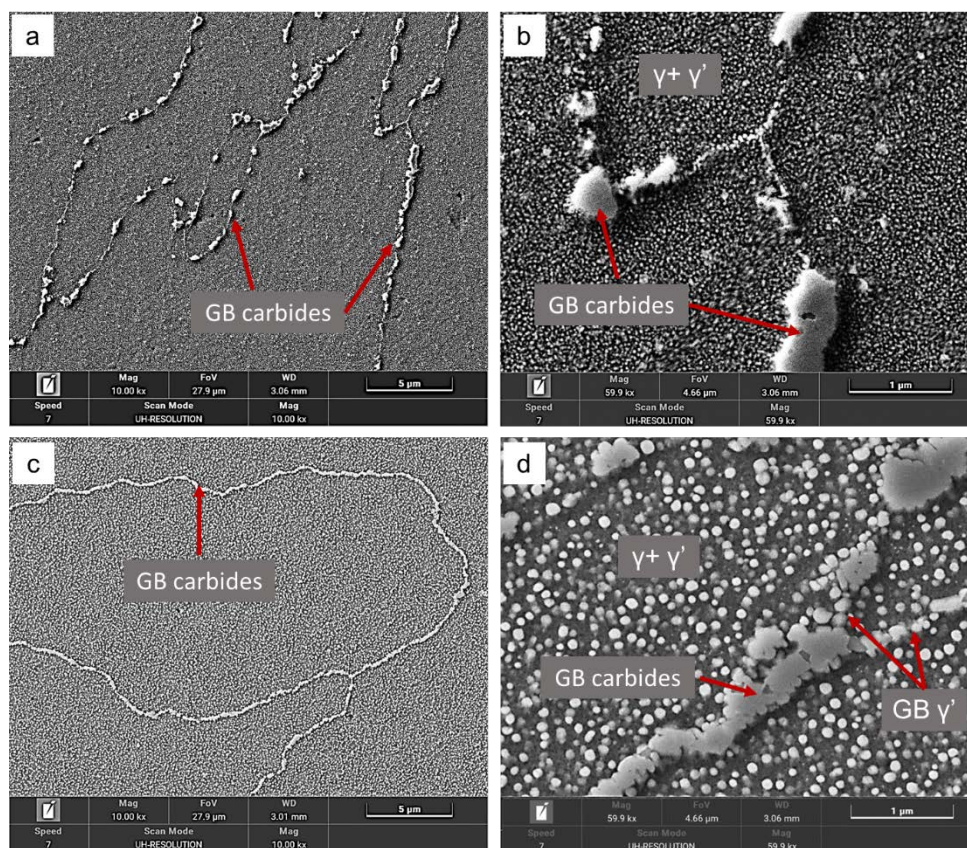
Figure 117. SEM images showing the microstructure of L-PBF H282, where (a, b) are for HT1, and (c, d) for HT2

Further EDS analysis on the L-PBF-HT2 samples in Figure 118 displays evidence of continuous grain boundary carbides, including both Cr-rich $M_{23}C_6$ and Mo-rich M_6C along with Ni depleted grain boundaries. A higher-magnification EDS scan in Figure 119 shows the presence of grain boundary Mo-rich M_6C, Cr-rich $M_{23}C_6$, and slight enrichment in GB Ti and Al, which is likely GB γ'. Additionally, the GB are depleted in Ni and Co, and intragranular Ti and Mo carbides were not observed. Another reason for continuous precipitates is the presence of the rich interdendritic cores, i.e., segregation of Cr and Mo, that lead to the formation of GB carbides

106

during heat treatment. The main differences seen in EBAM microstructure in contrast to L-PBF microstructures are the presence of intragranular Ti, Mo C (MC type), and a coarser solidification substructure (slower solidification and cooling rates in EBAM v. L-PBF). These reasons, along with evidence of cracks and voids in the EBAM material, explain the lower strength and ductility of EBAM compared to L-PBF in both orientations.
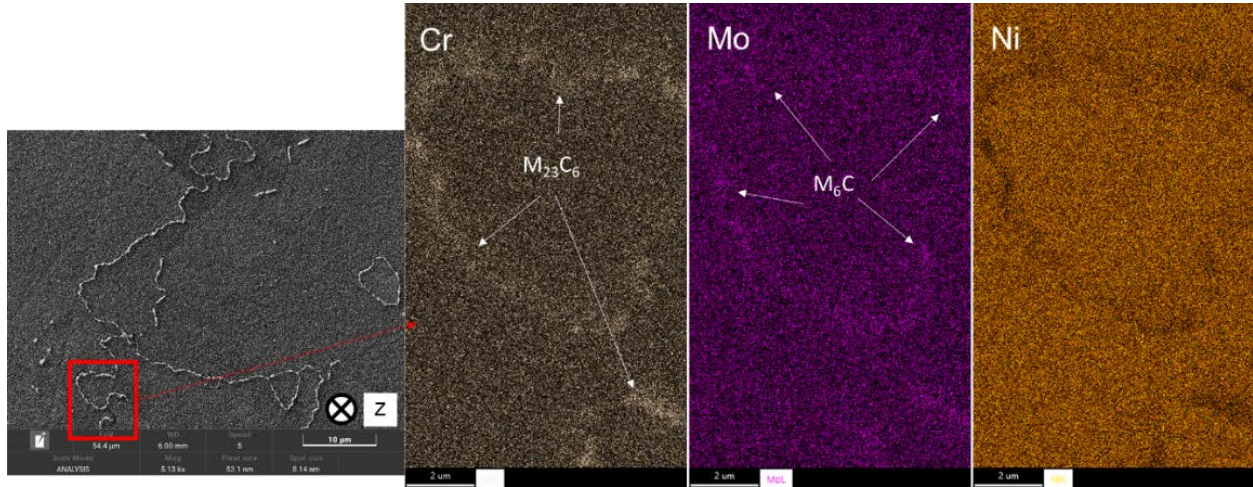
Figure 118. SEM-EDS of lower mag location showing Cr and Mo enrichment associated with the GB carbides, which are likely Cr$_{23}$C$_6$ and Mo$_6$C. No Ti particles
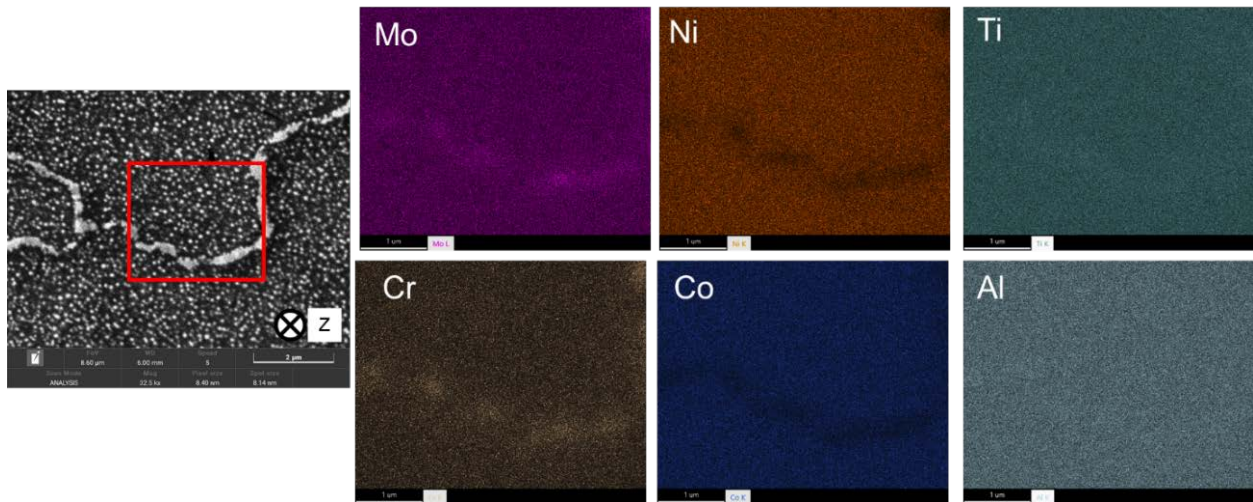
Figure 119. Higher magnification SEM-EDS map of L-BPF horizontal orientation (X,Y) in HT2 condition. Strong intensity appearance of continuous grain boundary Cr-rich M$_{23}$C$_6$ type and Mo-rich M$_6$C type carbides along with grain boundary depletion of Ni and Co. Slight enrichment of Al and Ti in grain boundaries indicates some grain boundary γ' (Ni$_3${Al, Ti})

4.3.2.1.3   Inconel 740H

Table 43 shows the thermomechanical properties of L-PBF Inconel 740H round bars after solutionizing plus aging.

107

Table 43. Thermomechanical Properties of L-PBF Inconel 740H Round Bars

Build	Orientation	Temp °C	YS (KSI)	UTS	El%
A-2203	X,Y	RT	129.8 +/- 3.2	177.7 +/- 6.9	25.9 +/- 1.7
A-2203	X,Y	520	116.9 +/- 0.9	154.3 +/- 1.0	21.9 +/- 0.5
A-2203	X,Y	760	100.1 +/- 1.1	101.9 +/- 0.7	2.3 +/- 0.2
A-2203	X,Y	780	92.3 +/- 0.7	93.2 +/- 0.9	2.0 +/- 0.2
A-2217	Z	RT	127.2 +/- 1.9	167.9 +/- 1.1	28.6 +/- 0.3
A-2217	Z	520	110.2 +/- 1.1	143.4 +/- 0.5	26.6 +/- 0.7
A-2217	Z	760	87.3 +/- 7.2	90.4 +/- 9.0	5.6 +/- 1.8
A-2217	Z	780	88.9 +/- 1.3	91.7 +/- 1.1	5.7 +/- 0.4
Special Metals	Plate	RT	105	154.6	23.7
Special Metals	Plate	750	86.4	118.6	23.9
Special Metals	Plate	800	86.2	100.2	23.5

4.3.2.2 Electron Beam Additive Manufacturing

Sciaky's EBAM Haynes 282 was thermomechanically tested to (1) ensure EBAM Haynes 282 meets baseline properties (strength and ductility) of wrought material and (2) provide a comparison between EBAM and L-PBF. Heat treatment option two (HT2-solution anneal and aged) was performed on EBAM samples in the racetrack printed condition and before machining, since HT2 championed ductility in the L-PBF Haynes 282 horizontally oriented samples. Three temperatures at room temperature (RT), 520, and 760°C, along with integrated DIC, was used with an induction coil (similar to previous and current thermomechanical tests of welded plate). Similar to L-PBF samples, samples were machined parallel to the vertical and horizontal print directions and at two different heights (A and B).
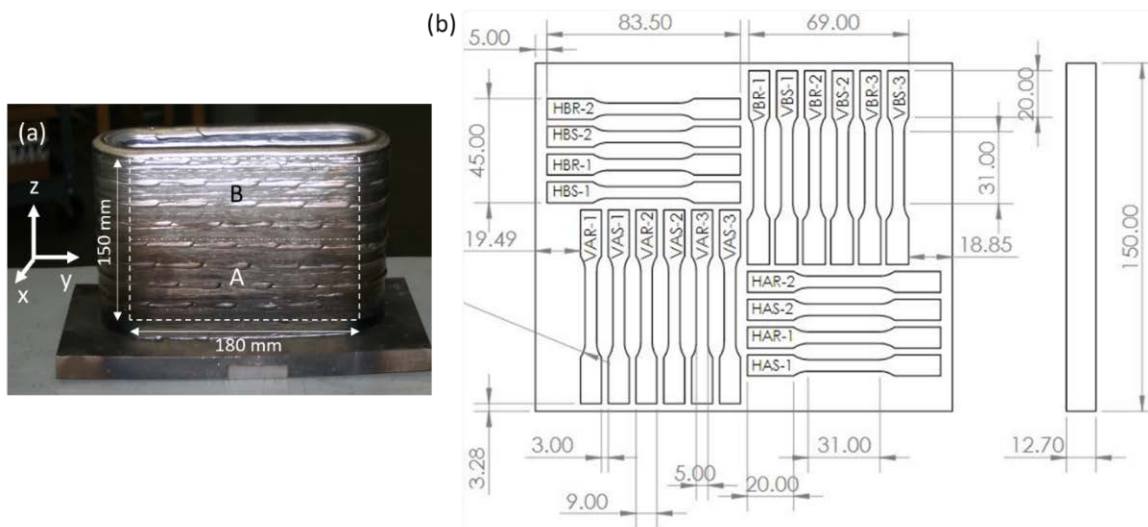
Figure 120. (a) Sciaky's H282 EBAM racetrack build (150-mm height x 180-mm length) (b) sample extraction schematic from one side of racetrack. VAR= vertical, bottom part, and tested at RT, HAR= horizontal, bottom part, and tested at RT, HBS = horizontal, top part, and tested at 760°C, VBR = vertical, top part, and tested at RT

108

Figure 120 shows the EBAM racetrack sample and sample extraction plan, including build orientation. Samples were labelled based on orientation relative to build direction (H = horizontal, V = vertical), location relative to the AM plate height (B = top part, A = bottom part), and tensile test temperature (R = room temperature, F = 520°C, and S = 760°C). The samples are machined from mid-thickness (12.7-mm-wide) within the three-pass wall thickness (20 mm). Samples contain the middle pass in the wall, and some overlap with the inner and outer passes. Prior to waterjet procedure to extract samples, EDM was performed to thin the walls from 20 mm down to 12.7 mm thick.

Load-displacement and stress-strain curves of Sciaky's Haynes 282 EBAM build are displayed in Figure 121 and Figure 122, respectively. The individual test results and averaged values are tabulated in Table 44. The average yield strength is slightly higher in horizontal orientation than the vertical orientation. Within the horizontal orientation, samples closer to the base of the build in location A have slightly higher yield strength values. However, this behavior was not as noticeable in vertical orientation samples.
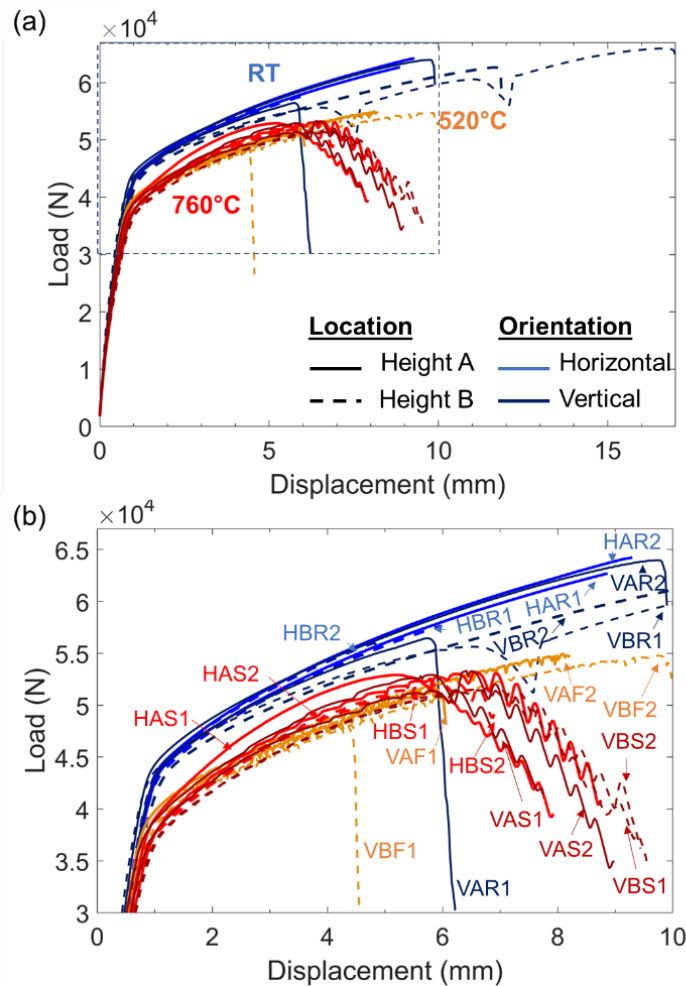
Figure 121. EBAM thermomechanical load-displacement data (a) full scale and (b) reduced section. Solid lines-height A. Dotted lines-height B. Horizontal orientation-lighter color. Vertical orientation-darker color.

109
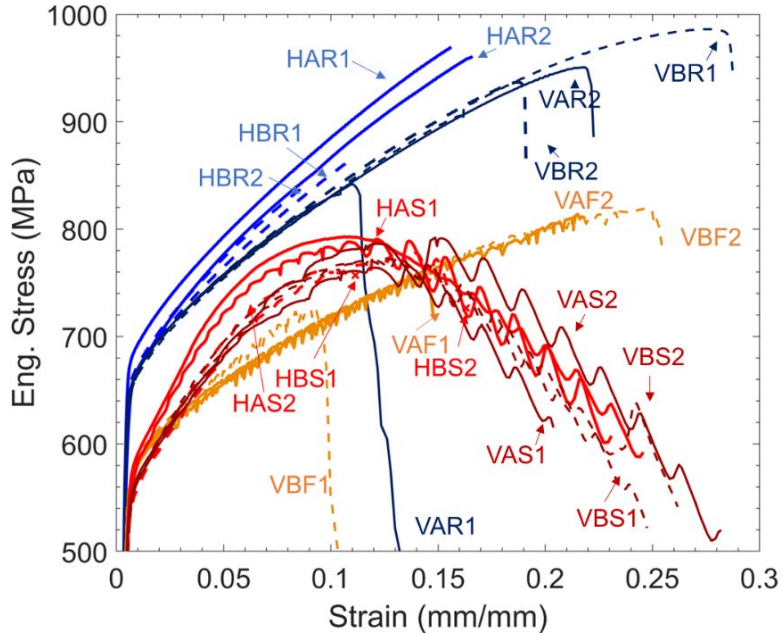
Figure 122. Engineering stress-strain curves for EBAM Haynes 282 at RT, 520, and 760°C. (H = horizontal, V = vertical; A = height location A, B = height location B; R = room temp, F = 520°C, S = 760°C)

Table 44. Yield Strength, UTS, and Total Elongation of EBAM Haynes 282

ID	Temp. (°C)	0.2% offset Y.S. (MPa)	Avg. Y.S.	UTS (MPa)	Avg. UTS	Total $\varepsilon_{fracture}$	Avg. $\varepsilon_{fracture}$
VAR1	25	653	651 ± 3	841	929 ± 62	0.138	0.21 ± 0.063
VAR2		654		951		0.223	
VBR1		649		986		0.288	
VBR2		649		937		0.191	
HAR1		680	662 ± 12	969	909 ± 65	0.156	0.13 ± 0.035
HAR2		655		961		0.163	
HBR1		653		866		0.112	
HBR2		660		841		0.089	
VAF1	520	560	564 ± 5	759	779 ± 45	0.148	0.18 ± 0.067
VAF2		565		813		0.219	
VBF1		571		725		0.105	
VBF2		560		819		0.254	
VAS1	760	548	551 ± 2	765	776 ± 11	0.203	0.25 ± 0.034
VAS2		552		792		0.282	
VBS1		553		773		0.247	
VBS2		552		773		0.262	
HAS1		580	561 ± 17	793	781 ± 15	0.245	0.18 ± 0.067
HAS2		570		791		0.23	
HBS1		549		760		0.101	
HBS2		545		778		0.159	

110

The UTS and ductility increase proportionally for the samples that failed in a near brittle mode, which includes all samples except VAS, VBS, and HAS samples that exhibit post-uniform elongation. The samples with post-uniform elongation show high fluctuations in stress after necking, which is an indicator of temperature instability from the coil. Duplicate tests with a high variance in ductility indicate that some tests had fracture induced from voids present within the samples prior to testing (likely during production of the racetrack). Aside from the ductility variability stemming from the voids, the horizontal orientation on average has lower ductility compared to the vertical orientation. Ductility is sensitive to the orientation of the product, which is expected to be lower in horizontal orientations from AM literature, as there are more solidification boundaries perpendicular to the tensile axis compared to the vertical orientation.
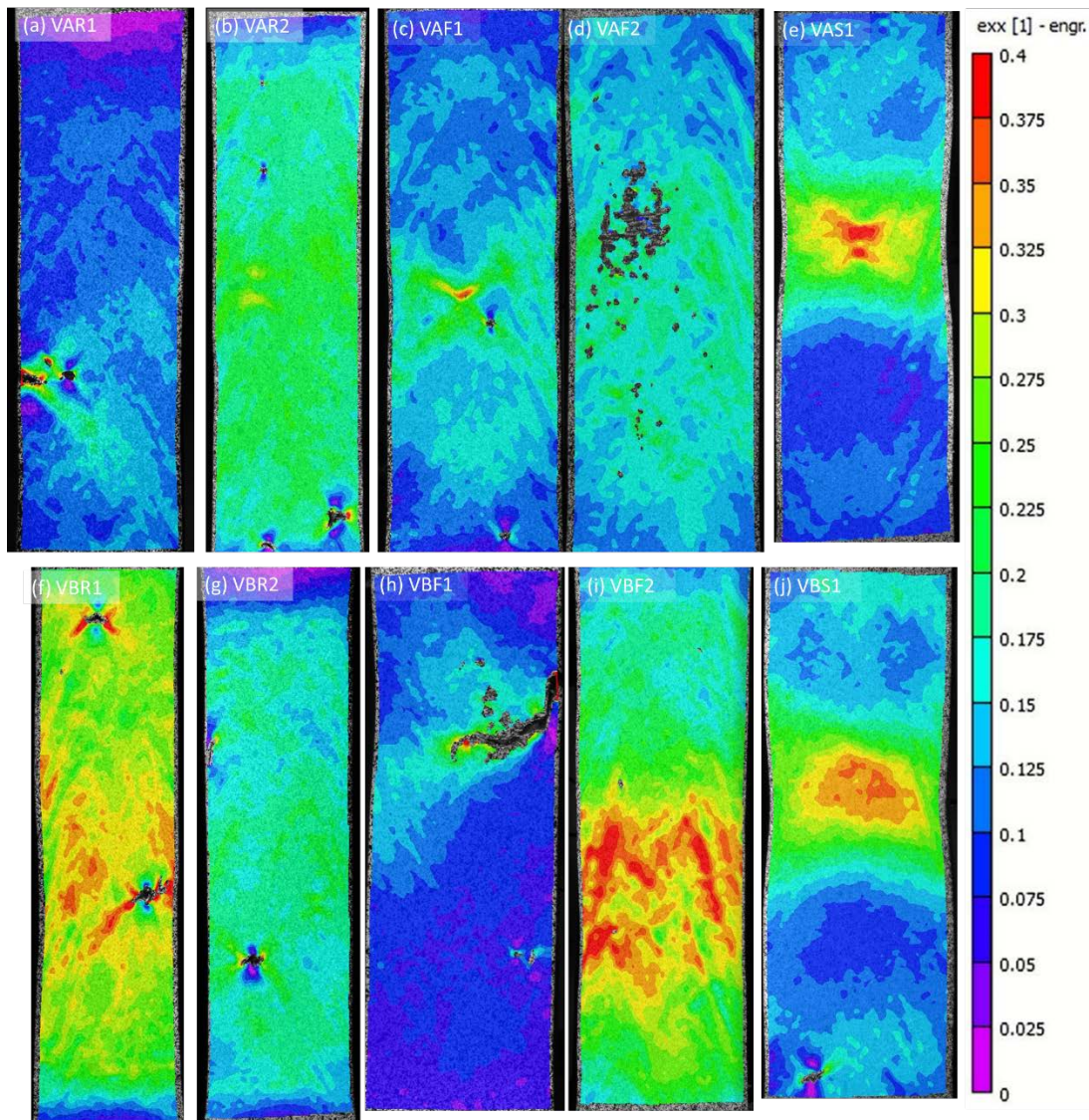
Figure 123. 2D DIC maps prior to failure for V-vertical orientation samples (a) VAR1, (b) VAR2, (c) VAF1, (d) VAF2, (e) VAS1, (f) VBR1, (g) VBR2, (h) VBF1, (i) VBF2, and (j) VBS1. (NOTE: VAF2 has paint chipping from surface leading to no measurements. Other samples show cracks opening or initial voids within EBAM microstructure. VAS2 and VBS2 are not shown but have similar behavior as VAS1 and VBS1, respectively.)

Overall, an increase in temperature reduces the yield strength, but the change in yield strength is negligible between the 520°C and 760°C conditions. Interestingly, the 760°C samples have a higher strain hardening rate (mostly HAS tests) compared to RT and 520°C conditions, but this came at the expense of reduced uniform elongation. The high strain hardening rate at 760°C may be attributed to more thermally activated dislocations impeded from motion by dislocation- γ' particle or solute interaction.

DIC plots for vertical orientation and horizontal orientation are displayed in Figure 123 and Figure 124, respectively. The strain plots are uniaxial strain and are shown in the frame prior to fracture. Most samples initiated from voids or lack of fusion, in which the DIC map picked up some of the details. The vertical samples' DIC plots show some samples to exhibit higher ductility than horizontal samples' DIC plots, and these samples indicate shapes resembling stretched columnar dendritic shapes in VAF2 (showing paint chipping, not crack/voids), VBR1 and VBF2.
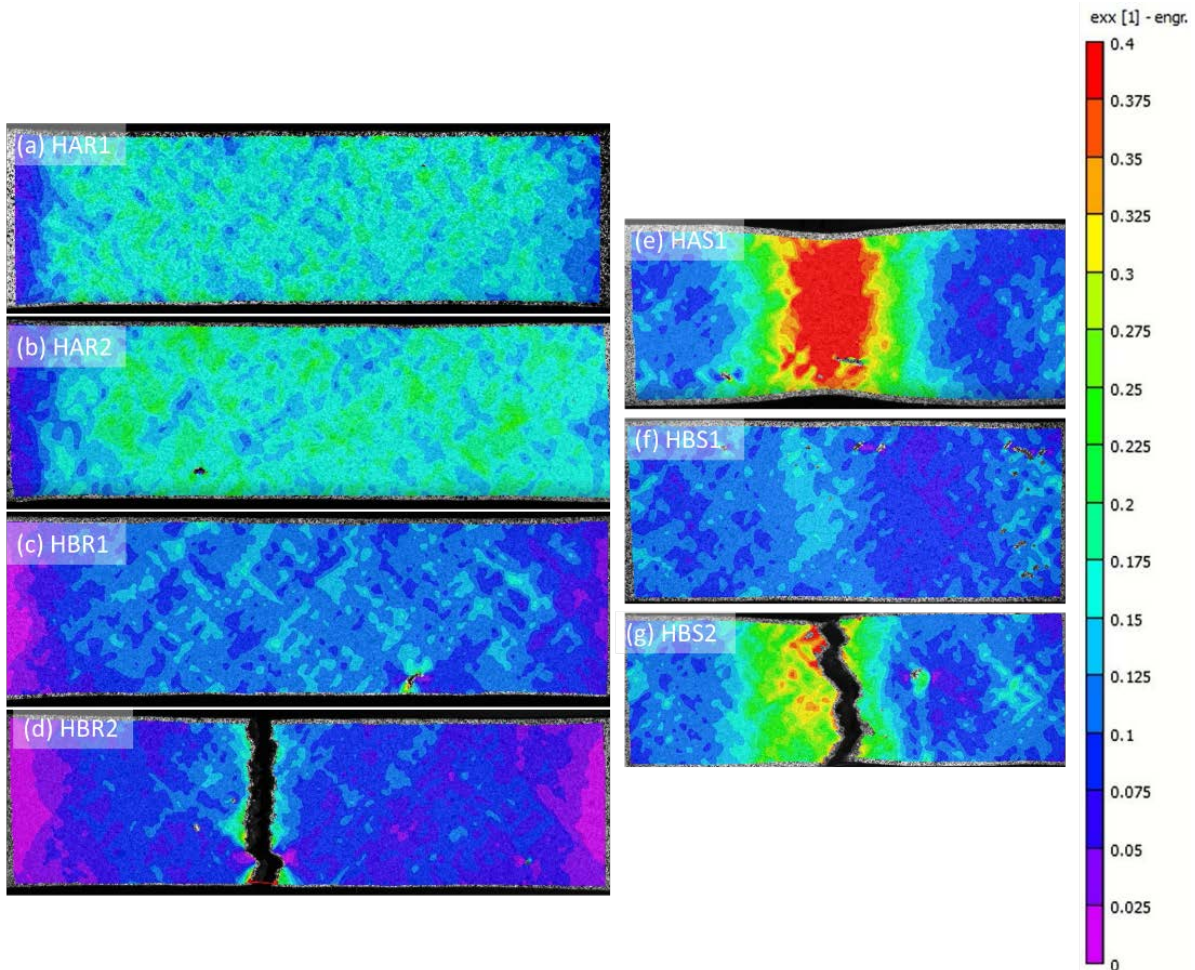
Figure 124. 2D DIC maps prior to failure for H-horizontal orientation samples (a) HAR1, (b) HAR2, (c) HBR1, (d) HBR2, (e) HAS1, (f) HBS1, and (i) HBS2. (NOTE: HAS2 not included, but results are same as HAS1.)

The fracture surfaces for the vertical and horizontal samples are shown in Figure 125 and Figure 126, respectively. The samples with low ductility stemming from voids and lack of fusion can be

112

seen, including VAR1, VAF1, VBR2, VBF1, and HBR1. Most voids only appear in the vertically oriented samples and can explain why some duplicate samples have low ductility. Some DIC images don't show voids or defects on the surface analyzed during deformation but are present within the thickness of the sample, including HBS1 and HBS2, which was shown to have large lack of fusion (LOF) indicated by the discolored elongated regions on the fracture surfaces (see Figure 126(g–h)). The horizontal orientation samples have a more brittle, shinier appearance, than the vertical orientation samples, that give indication of brittle fracture within the interdendritic regions. On the other hand, vertical orientation samples perform better in ductility generally, except those with defect sized big enough to affect ductility.
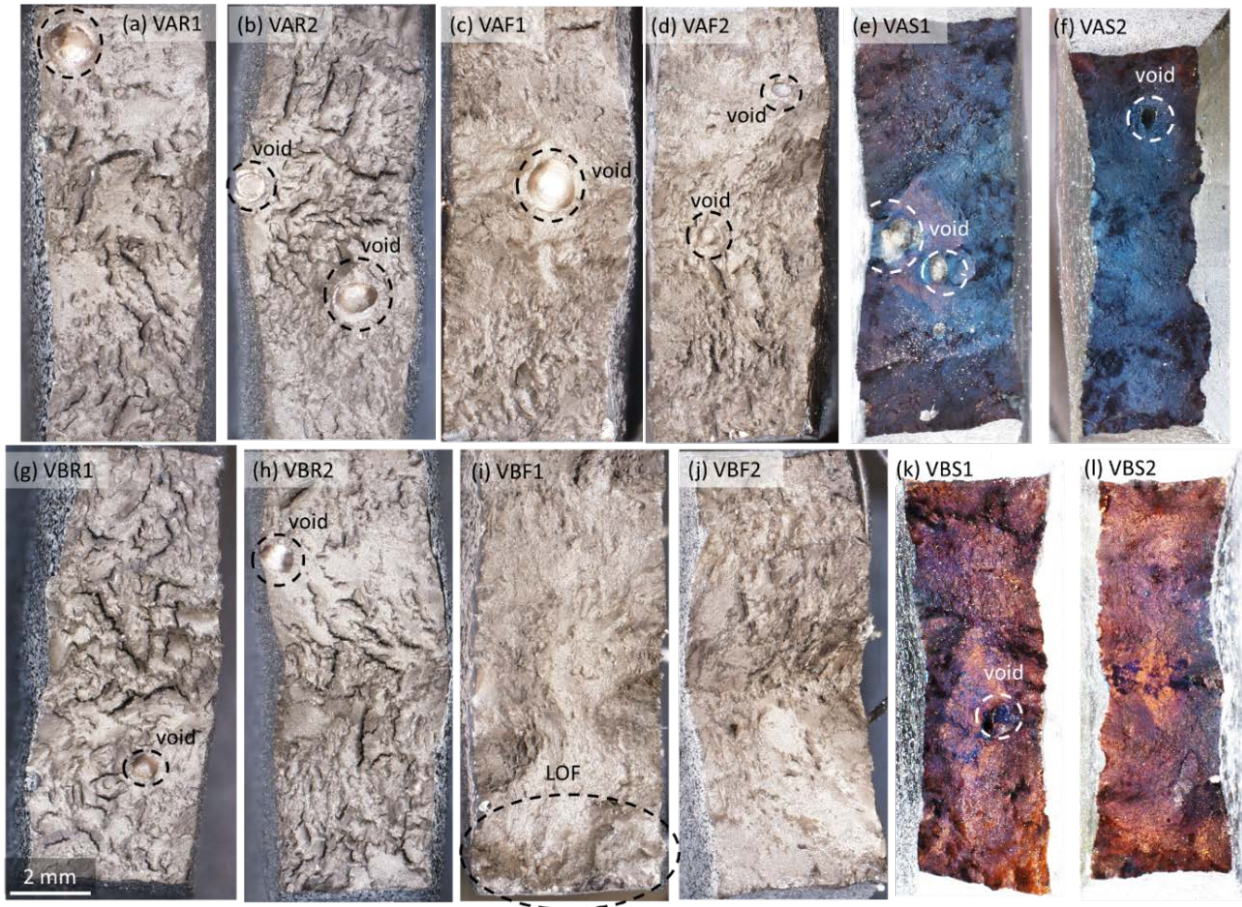
Figure 125. Fracture surfaces of V-vertical orientation samples (a) VAR1, (b) VAR2, (c) VAF1, (d) VAF2, (e) VAS1, (f) VAS2, (g) VBR1, (h) VBR2, (i) VBF1, (j) VBF2, (k) VBS1, and (l) VBS2. LOF denotes lack of fusion
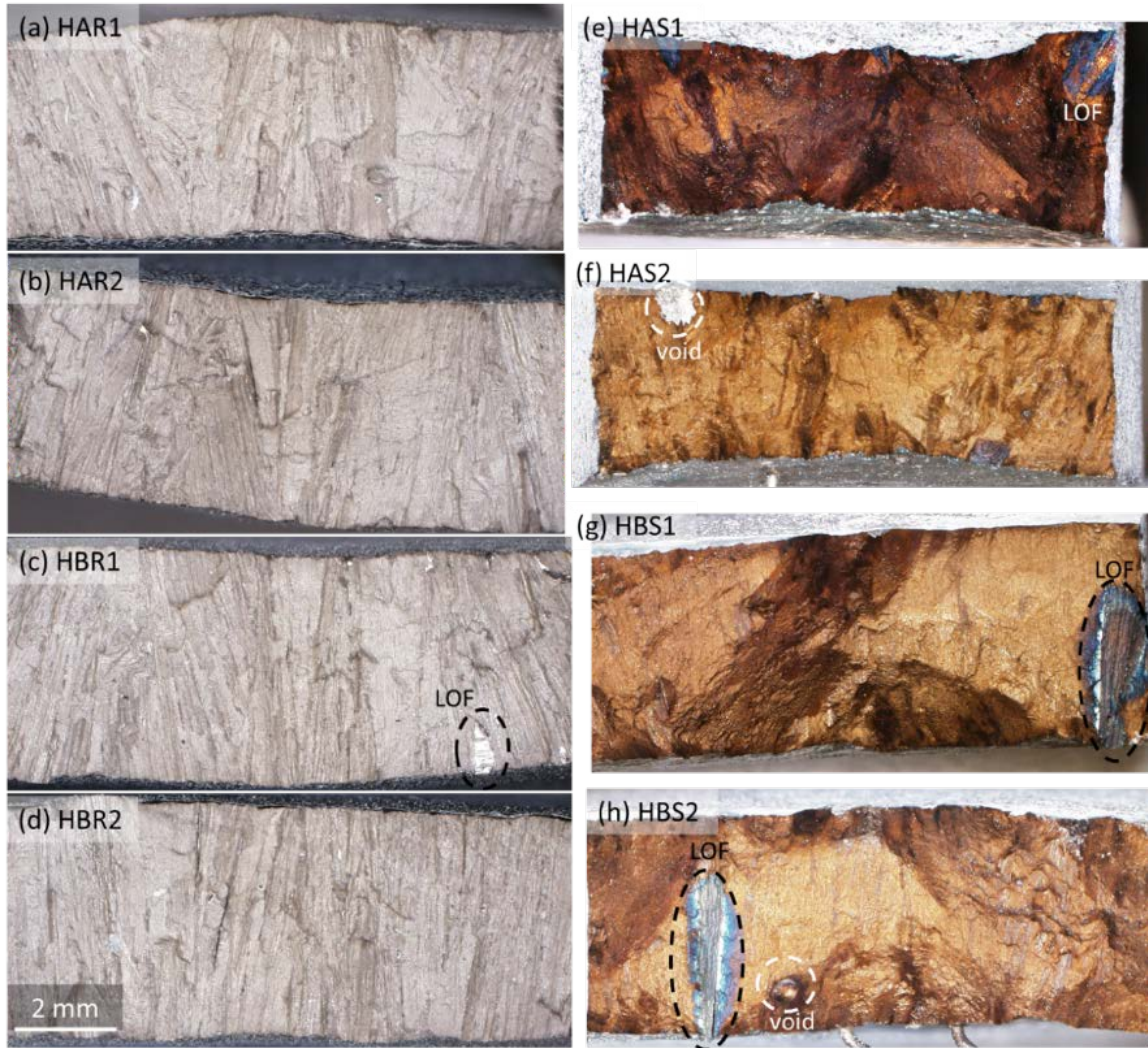
Figure 126. H-Horizontal sample fracture surfaces (a) HAR1, (b) HAR2, (c) HBR1, (d) HBR2, (e) HAS1, (f) HAS2, (g) HBS1, and (h) HBS2

4.3.2.3 Comparison of Thermomechanical Properties Between L-PBF and EBAM H282 Prints

The yield strength, UTS, and elongation as a function of temperature are compared between Haynes 282 L-PBF and EBAM samples, as seen in Figure 127. Only best performing HT2 L-PBF samples are plotted for comparison. L-PBF samples have exceptionally higher yield strength values at room temperature and 520°C compared to EBAM samples. The 760°C condition shows similar yield strength values between L-PBF and EBAM (within 100 MPa difference), even though L-PBF still outperforms the EBAM samples. The horizontal build orientation for both sets of data has higher yield strength, but at the expense of lower ductility. Vertical orientation ductility generally is higher than horizontal orientation ductility, which is in agreement with AM characteristics even with a solutionizing heat treatment. The main reason for high variability in ductility and UTS in the EBAM samples is the presence of void defects; however, it depended on if the final fracture location propagated from void defects. Some samples show indications of void defects in DIC map that did not correlate to location of final fracture, such as VBR1 in Figure 123(f).

114
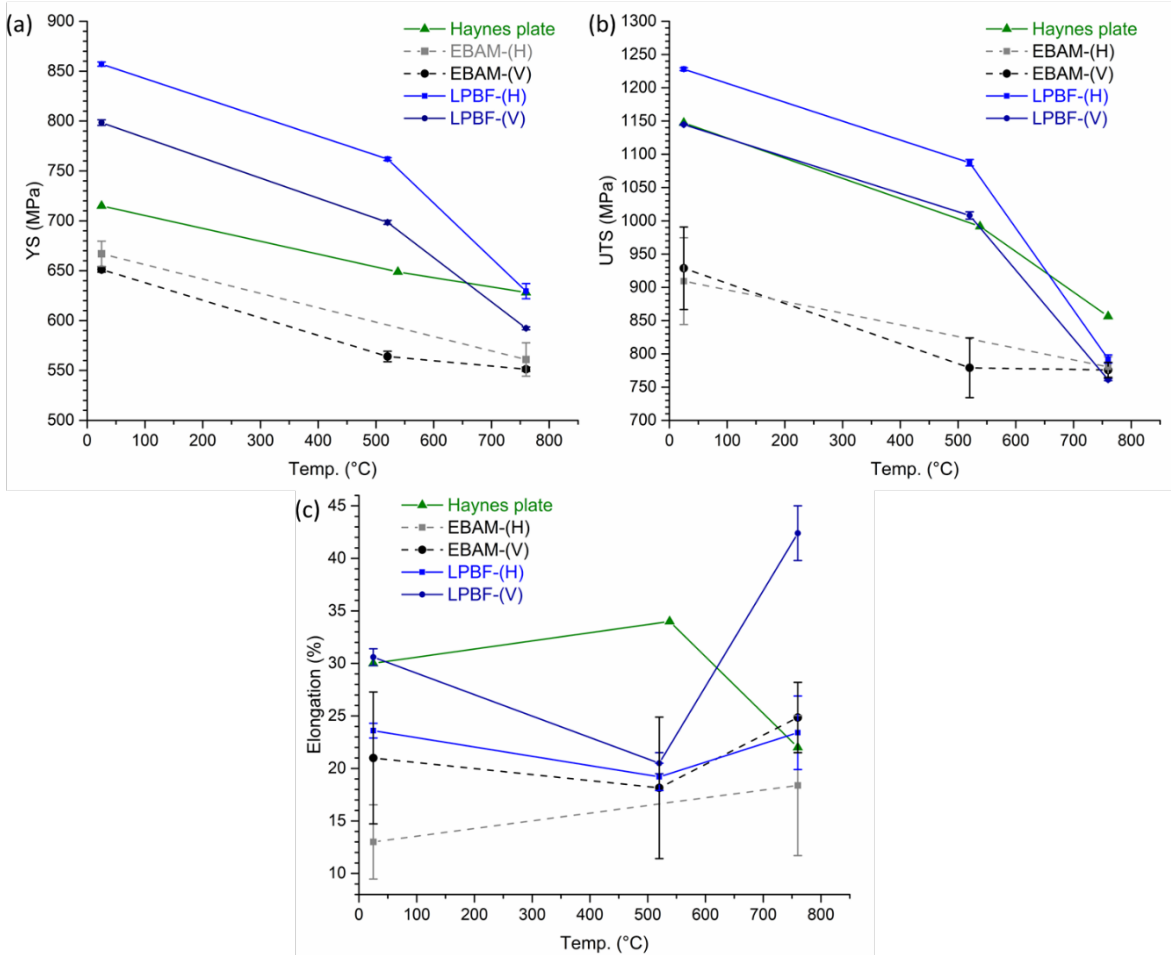
Figure 127. Thermomechanical property comparison between Haynes 282 EBAM and L-PBF samples, separated by build orientation (H or V) (a) 0.2% offset yield strength, (b) UTS, (c) % elongation. Haynes wrought properties are included for comparative purposes

4.3.3   Characterization of AM Fabricated Specimens (Milestone 1.4.3)

Table 45 shows the details of Milestone 1.4.3. E3D met the relative density target for flat plates to be arc welded in BP2 and BP3 tasks. The L-PBF plates delivered to CSM can be seen in Figure 118. The Haynes 282 EBAM plates used for BP2 welding tasks came from the remaining side of racetrack build shown in above sections (other side of racetrack was used for property testing).

Table 45. Milestone 1.4.3 Details

Milestone	Description	Metric	Success Value	Assessment Tools
1.4.3: AM fabricated welding characterization specimens	AM flat specimens printed for welding studies should meet relative density for their used in further joining processes in Budget Period 2.	Relative density	> 99%	Archimedes method (ASTM B962). All tested samples (at least three) should meet target with 10% errors based on standard deviation.
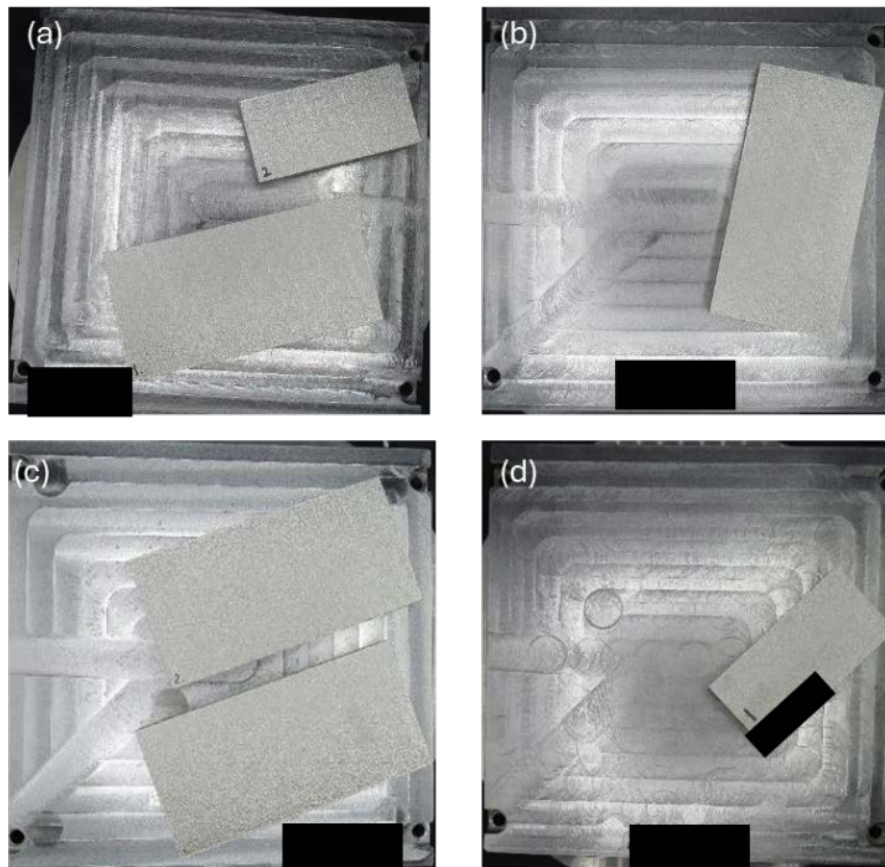
Figure 128. Images of four builds to produce the deliverables for milestone 2.4.4.4. (a) Haynes 282 weld plate 1 and weld test plate. (b) Haynes 282 weld plate 2. (c) IN740H weld plate 1 and 2. (d) IN740H weld test plate.

4.3.4 Similar Welding of AM to Wrought Alloys (Milestone 2.4.1)

Table 46. Milestone 2.4.1 Details

Milestone	Description	Metric	Success Value	Assessment Tools
2.4.1: Welding of additive manufacturing (AM) samples to similar wrought alloys	Weldments of AM samples to similar wrought alloys should have a symmetric weld morphology. Thermomechanical performance at the service temperature (based on M1.1.2) should demonstrate that the strength and resistance are retained at a minimum level compared with of the wrought metals.	1. Weld morphology. 2. Strength compared with the wrought metals.	1. <10% difference in width/depth ratio in fusion zone morphology between the AM and wrought side 2. > 80%	Varestraint, TransVarestraint, and/or Sigmajig tests, microstructural characterization, chemical composition changes. Tensile test with DIC method at room and elevated temperatures, and fractography analysis using optical and electron microscopies with EDS mapping. All tested samples (at least three) should meet target with 10% errors based on standard deviation.
		Thermomechanical resistance at the service temperature (based on M1.1.2) of weldment compared to wrought metals	> 80% for welds	Gleeble tests. All tested samples (at least three) should meet target with 10% errors based on standard deviation.

4.3.4.1 AM-to-Wrought Multi-Pass Welds

4.3.4.1.1 Experimental Procedures

The welding procedure for all AM to wrought welds is gas tungsten arc welding (GTAW). The weld geometry is a double-V groove as illustrated in Figure 129(a). The weld pass sequence is optimized to reduce distortion overall to get flat samples for thermomechanical testing. For all welds, transverse cross-weld samples are machined in a flat dog-bone as seen in the extraction plan drawing in Figure 129(b). The weld current chosen for BP2 AM-to-wrought welds is 150–160 amperes with a travel speed ranging from ~1.5–3 inches per minute. The voltage range is 11–14 V. The average arc energy per unit length is calculated to be 30–40 kJ/in., while the first three passes were closer to ~50–60 kJ/in. due to slower travel speeds.
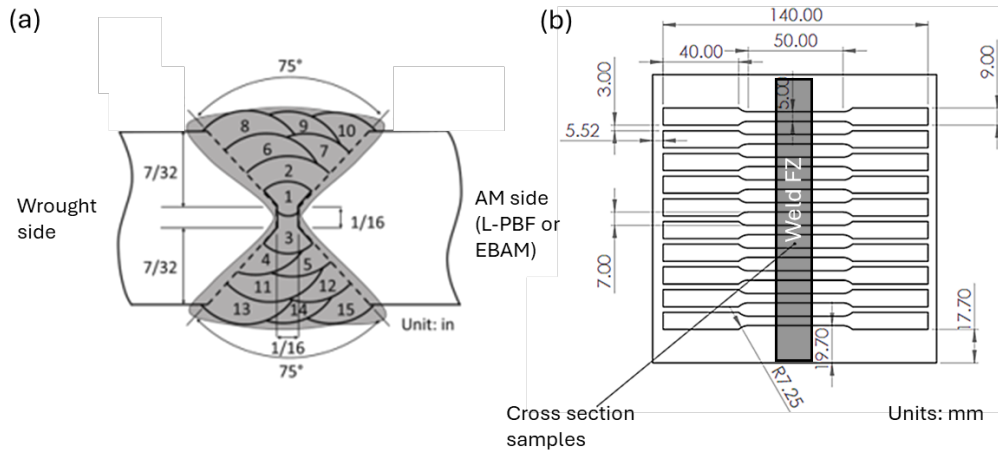
Figure 129. (a) Double V weld geometry with labeled pass sequence and (b) extraction plan of cross-weld tensile and metallurgical samples from top view

4.3.4.1.2 Haynes 282 L-PBF to Wrought GTA Welds

4.3.4.1.2.1 *Thermomechanical Testing and Digital Image Correlation (DIC)*

After welding of AM-to-wrought Haynes 282, samples were heat-treated using HT2 procedure developed from results from initial tensile testing of L-PBF printed parts that showed an improvement in ductility by changing the first aging step from 1010°C to 899°C. Samples were then tensile tested at room temperature (RT), 500°C, and 720°C. Figure 130 displays the load-displacement curves and stress-strain curves, with corresponding dots representing failure. All samples failed with a relatively low ductility in a brittle fracture mode (<12%). While the yield strength and UTS criteria for RT and 720°C pass, the yield strength only passes with the 500°C since the UTS was 77% of the baseline UTS strength (763/991) [13]. The yield strength surpassed the baseline strength values >97% (e.g., average of 701 MPa over an expected 715 MPa) [13]. Low ductility contributed to a drop in the true UTS value, as there was no appearance of necking prior to brittle fracture. Thus, the UTS values are lower than necessary for passing at 500°C. The experimental results are compared to HT1 test results. While the heat treatment may be good for AM material using a HT2 procedure, the HT2 effect on the weld and wrought metal may need to be investigated for determining correlation with HT2 and a ductility dip as a function of the first aging temperature/time. Table 47 contains mechanical property data for each test.

118
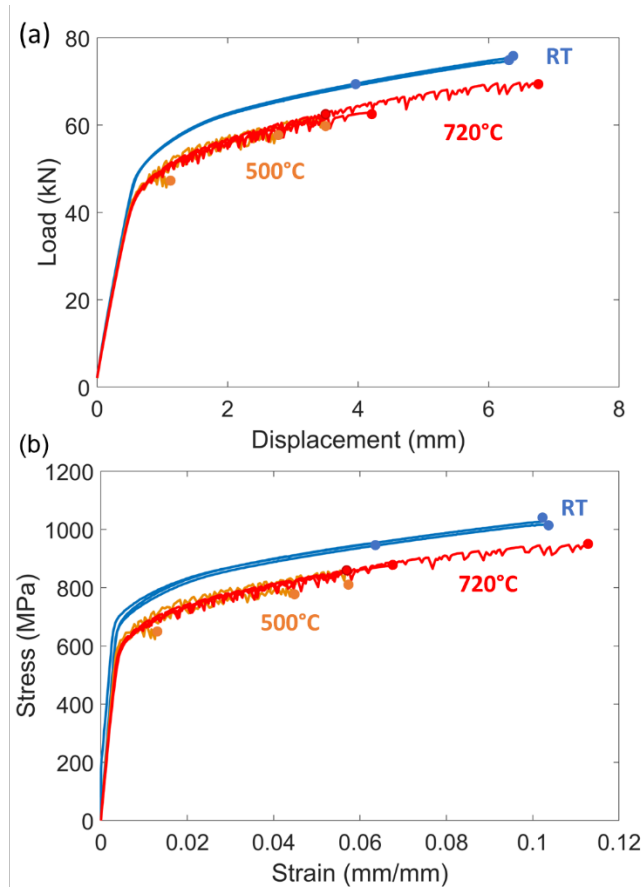
Figure 130. Room temperature (RT) and elevated temperature tensile tests (500°C, 720°C) (a) load-displacement and (b) engineering stress-strain curves. Dots represent strain when brittle failure occurs

Table 47. Tensile Test Properties of all 282-304H DSW Transverse Tensile Samples. All Samples Experienced HT2 After Machining and Before Tensile Testing

ID	Temp. (°C)	0.2% offset Y.S. (MPa)	UTS (MPa)	$\varepsilon_{fracture}$
R1		706	1026	0.1
R2	25	695	1019	0.1
R3		702	951	0.06
F1		626	652	0.013
F2	500	626	796	0.044
F3		637	841	0.057
S1		632	875	0.068
S2	720	630	947	0.11
S3		620	854	0.056

DIC measurements were made on the similar weld cross sections. Figure 131, Figure 132, and Figure 133 include DIC strain results and fracture surfaces for RT, 500°C, and 720°C tests, respectively. The RT tests showed brittle failure on the wrought Haynes 282 HAZ in R1, while R2 and R3 had fracture along the weld centerline. The location of failure does not always correlate with the regions of highest localized strain (wrought side) as the fracture occurs rapidly down the center, with very little indication of strain accumulation as observed in Figure 131. All the DIC images are shown right before fracture (within 500 ms). The appearance of voids within

119

the fracture surfaces possibly implicates weldability issues, including potential weld-induced microcracks or discontinuities such as inclusions, lack of penetration, porosity, etc.

The elevated temperature tensile tests showed similar deformation behavior with higher amounts of plastic strain, initial yielding, in the wrought side. However, most cracks initiated within the half-thickness and propagated straight through-thickness in the welds. During testing, large sounds were coming from the sample during deformation, likely the sound from the opening of the defects observed on the fracture surfaces. Characterization of the large voids, particularly within the FZ, require further investigation to determine potential solutions for improving ductility, including but not limited to welding process optimization, heat treatment modifications, or weld filler modifications. In summary, the fully aged Haynes 282 wrought to AM welds using H282 TIG filler showed strength greater than 80% of the wrought H282 (the passing criteria) in yield strength and UTS values when tested at RT or 720°C. However, samples tested at 500°C exhibited low ductility leading to a drop in the true UTS values to be around 77% of the wrought strength at that temperature. The failure was related to presence of weld defects (e.g., inclusions or porosity). Moreover, while HT2 was proven beneficial to maintaining the ductility of AM produced H282 at high temperature ranges in previous reports, that might be happening at the expense of the wrought and filler metal ductility leading to losing the ductility and strength of the welds as a whole.
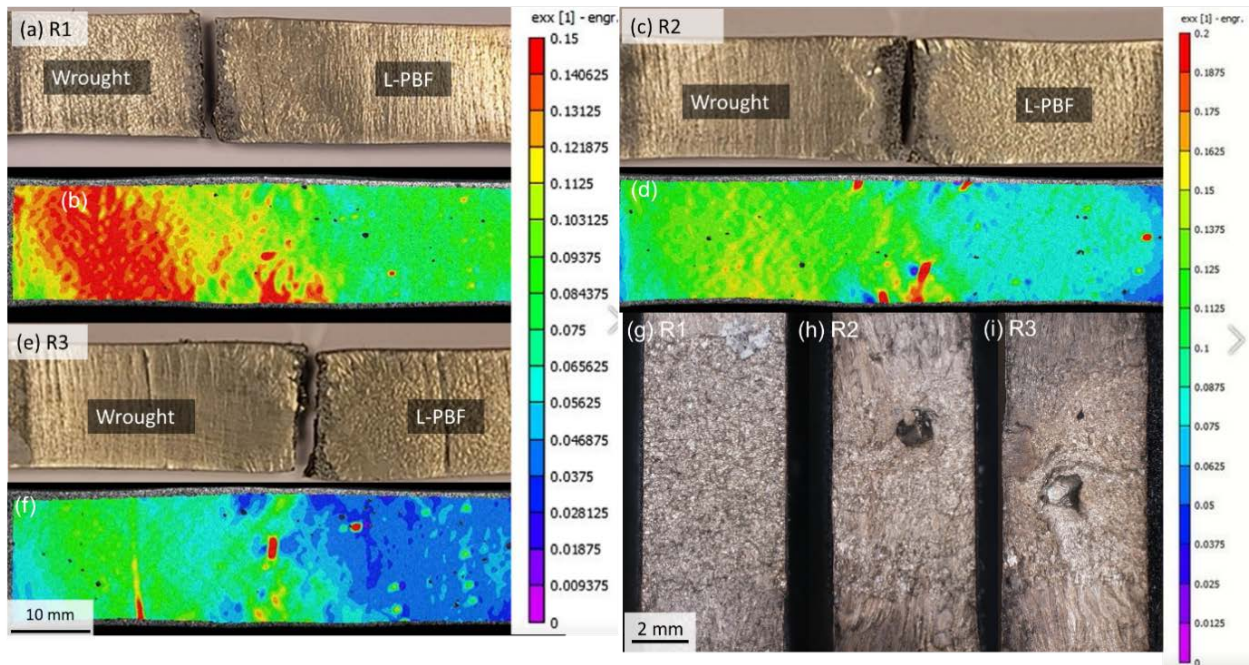
Figure 131. RT tensile test DIC results (a–b) R1 fracture location DIC engineering strain map, (c–d) R2 fracture location DIC engineering strain map, (e–f) R3 fracture location DIC engineering strain map, and (g–i) respective fracture surfaces
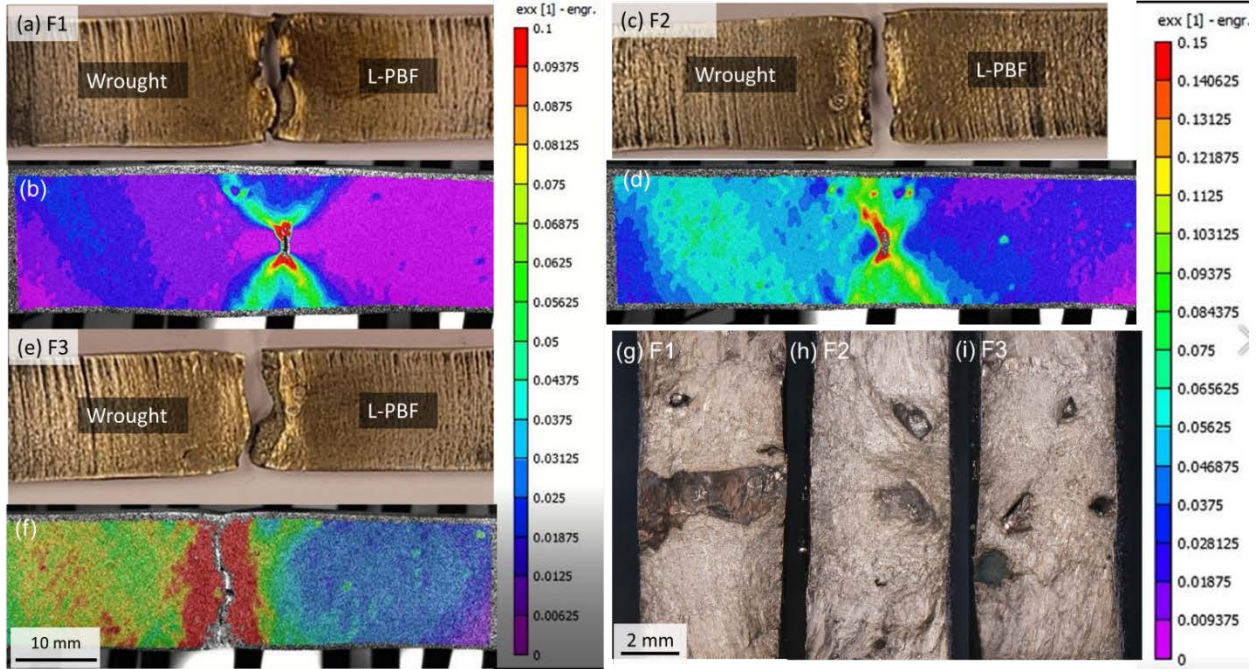
Figure 132. 500°C tensile test DIC results (a–b) F1 fracture location DIC engineering strain map, (c–d) F2 fracture location DIC engineering strain map, (e–f) F3 fracture location DIC engineering strain map, and (g–i) respective fracture surfaces
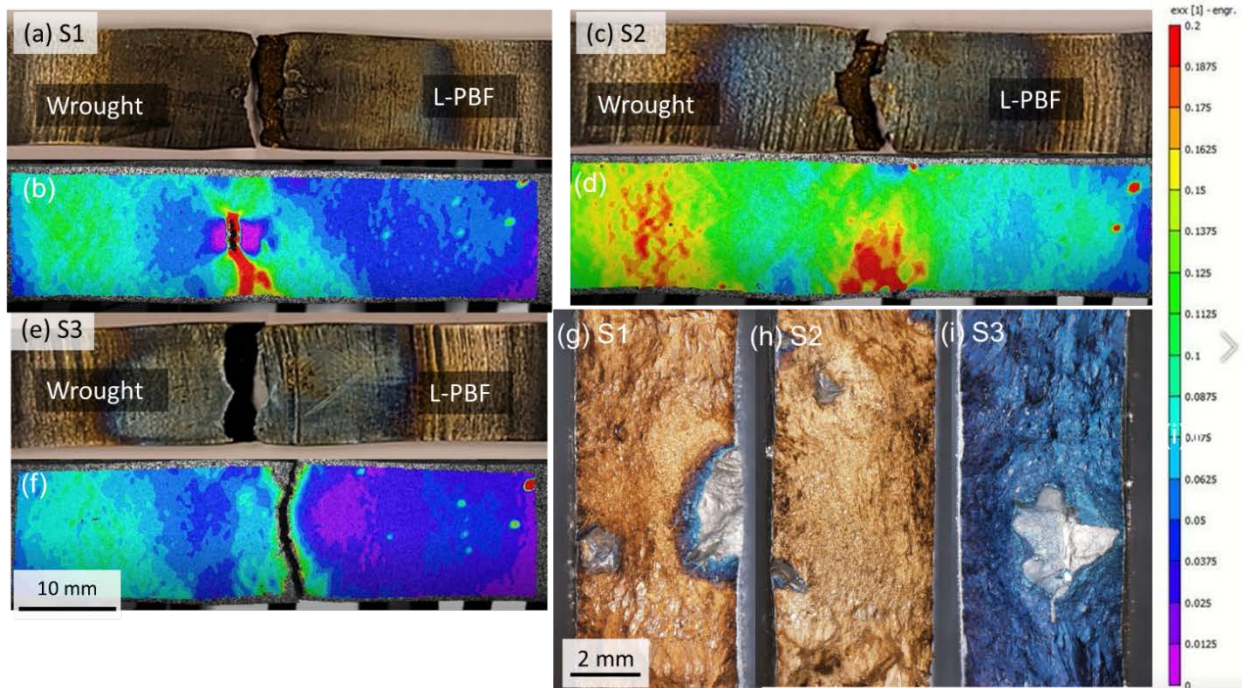
Figure 133. 720°C tensile test DIC results (a–b) F1 fracture location DIC engineering strain map, (c–d) F2 fracture location DIC engineering strain map, (e–f) F3 fracture location DIC engineering strain map, and (g–i) respective fracture surfaces

121

4.3.4.1.2.2 Metallurgical Characterization

All samples were polished up to 0.25-µm diamond suspension finish, and then etched using electrolytic etching in 10% oxalic acid aqueous solution at 3 V for 20 seconds. As expected, the EDS line scans in Figure 134 show perfect matching in the chemical composition between the H282 filler and both of AM and wrought H282. The visual and preliminary optical microscopy inspection of the cross sections of these samples showed some discontinuities inside the weld zone. The nature and reasons for these defects are still under investigation.
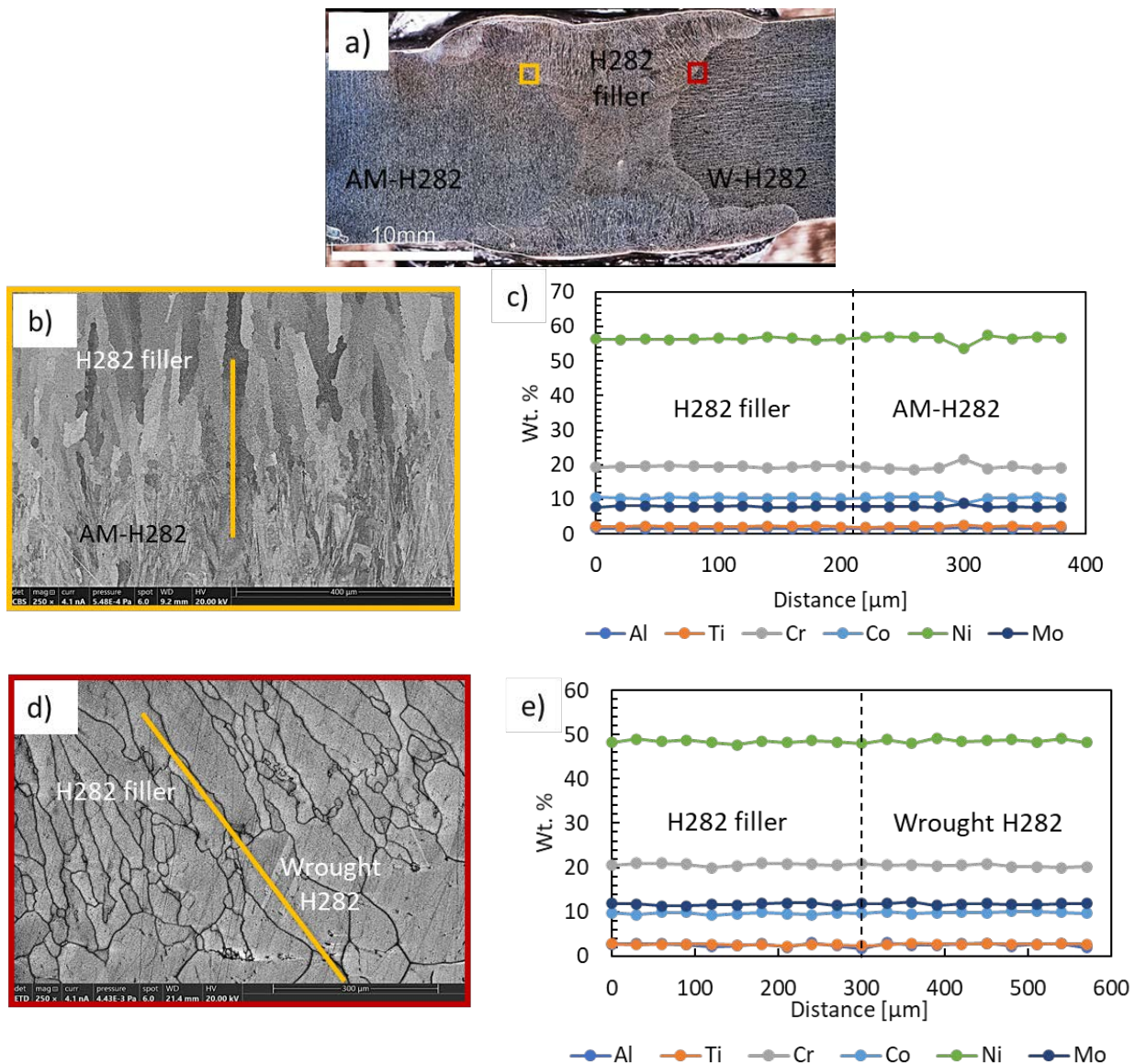
Figure 134. (a) Macrograph of fully aged similar AM to wrought H282 weld. (b, d) SEM images of the filler/AM side and filler/wrought side interfaces, respectively. EDS line scan showing the matching chemical composition between the filler and AM side (c), and the filler and wrought H282 side (e)

Although the two base metals and welding filler matched in chemical composition, the grains morphology differed (due to the difference in processing technique) in each region as shown in Figure 135. The AM side showed fine columnar grains, while coarser columnar grains were

122

observed in the welding filler. The wrought H282 exhibited equiaxed grain morphology. The higher magnification images showed relatively similar typical microstructure of fully aged H282 constituting from a gamma matrix, gamma prime secondary phase precipitates, Cr, Ti, and Mo rich carbides (inter and intra granular). However, the filler and wrought H282 showed more agglomeration of GB carbides. This observation can be attributed to the larger grain size seen in the latter two regions. The EDS maps in Figure 136 show inter and intragranular Ti and Mo-rich carbides as well as intergranular Cr-rich carbides in the H282 filler microstructure.
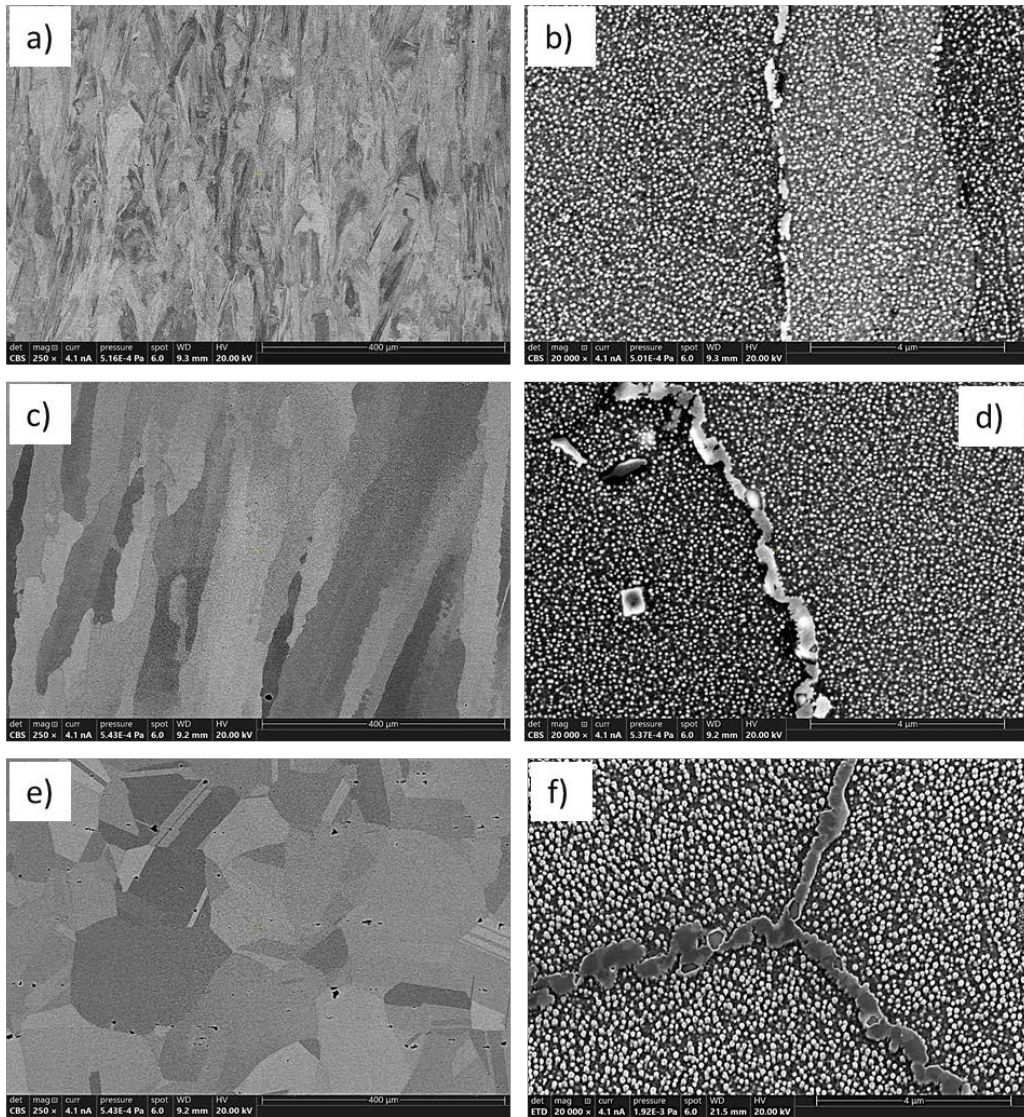
Figure 135. SEM images of the microstructure of fully aged AM to wrought weld taken in the base metal AM side (a, b), welding filler (c, d), and base metal wrought side (e, f)

123
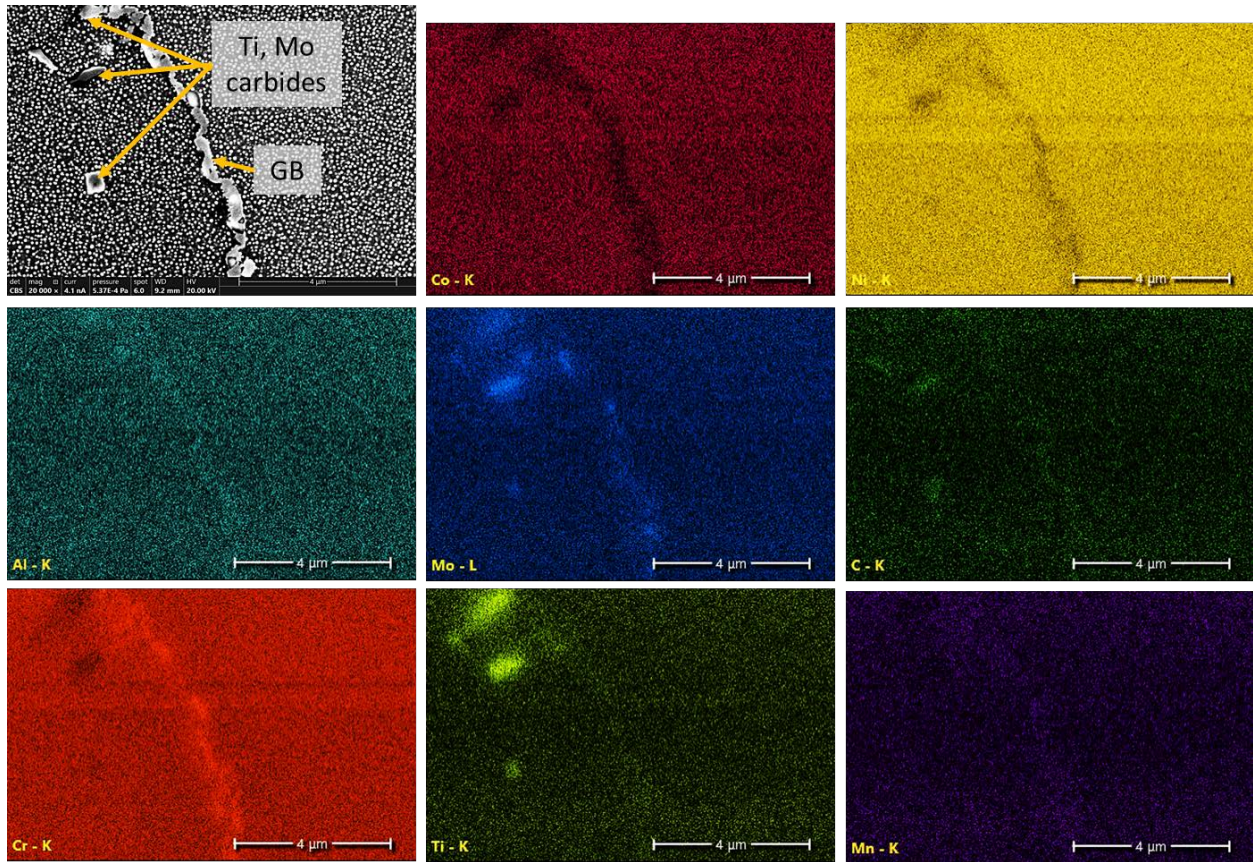
Figure 136. EDS elemental maps for the fully aged welding filler (from Figure 135(d))

Additional analysis of the weld microstructure near the cracks in the weld root on the L-PBF side was conducted, as seen in Figure 137. There is a significant presence of Al and O concentration (likely Al oxide) within the crack inside the FZ before and after aging. Additionally, a precipitate free zone can be seen corresponding to Ti-rich precipitates, which are present near the crack after aging heat treatment to the welds.
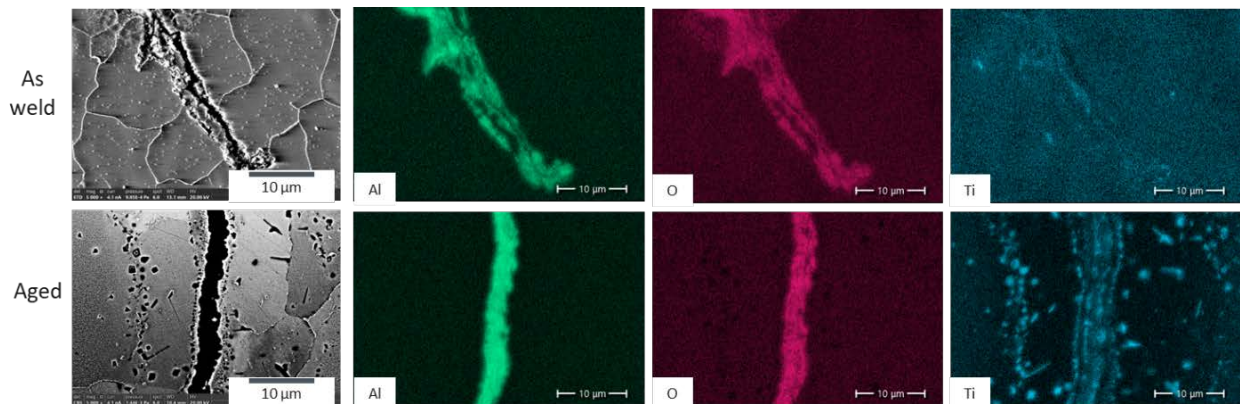
Figure 137. Haynes 282 weld microstructure (SEM-EDS) before and after HT2 (fully agreed condition) near weld root cracks

It is worth mentioning that all the tested tensile samples from the L-PBF to wrought weld were fully aged. Figure 138(a) and (b) show the failure location in one of those samples labeled R1.

124

Figure 138(c) shows that the hardness line profile results in the as-welded and heat-treated conditions. The heat treatment increased the overall hardness values across all regions, which is typical for an age-hardenable alloys. Also, the AM side showed higher hardness than the wrought side due to the finer microstructure inherited from the L-PBF process. In addition, a high hardness region was noticed in the HAZ in the as welded sample (marked with red arrows). This region was more pronounced in the AM side than the wrought side. It is likely that this region experienced a thermal history upon weld cooling that caused an effect like a partial localized age hardening. This observation can be further explained by welding simulations at OSU. The hardness line profile for the AM to wrought weld correlates well to the observed failure location in the fully aged condition. Strain localization occurred in the wrought side relatively soft HAZ as seen in Figure 138.
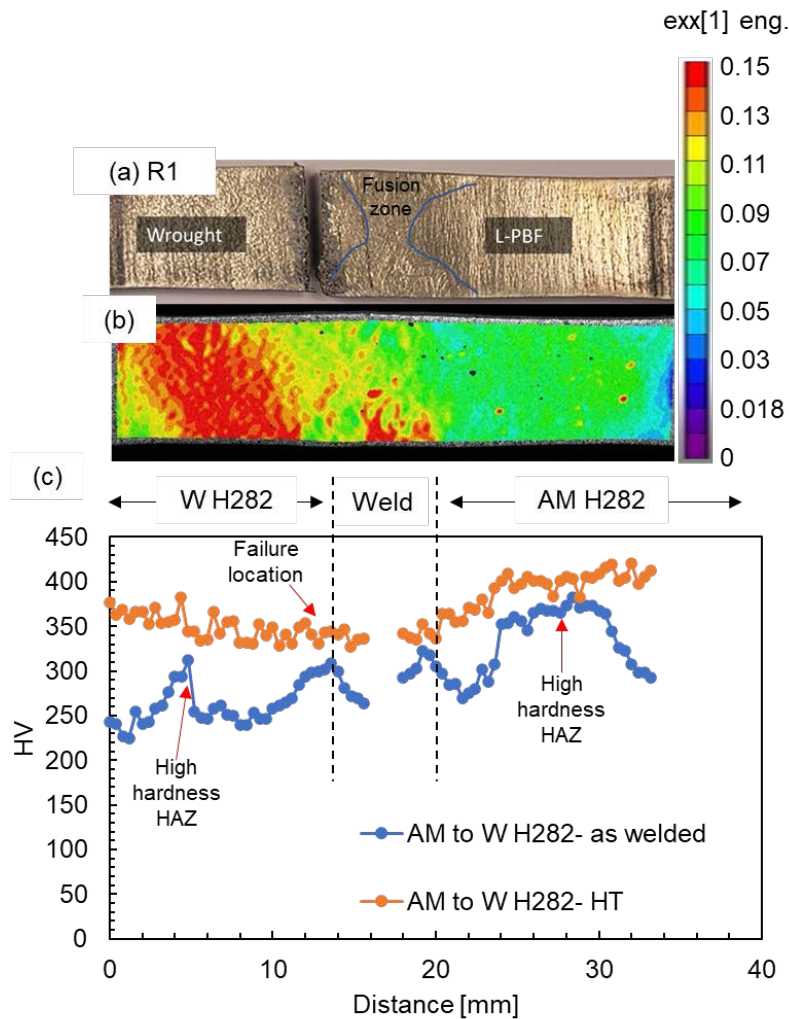
Figure 138. (a) macrograph for one AM to wrought weld sample labeled R1 (fully aged), (b) DIC map for engineering strain just before fracture in RT tensile testing for R1 sample, (c) hardness line profile for the as-welded and fully aged (HT) samples

4.3.4.1.3 Inconel 740H L-PBF to Wrought GTA Welds

4.3.4.1.3.1 *Thermomechanical Test Results and DIC*

The DIC results for first batch is in Figure 139, it appears that the primary location for yielding is within the HAZ on the wrought side of the weld, while there is little to no deformation on the AM side of the weld. The duplicated test results are shown in Figure 140, where the duplicates verify (1) strain partition into the wrought side HAZ and (2) brittle failure in the FZ at higher temperatures (720°C). Table 48 shows the summarized mechanical properties with updated failure location. Essentially, similar deformation behavior can be seen between Haynes 282 and In740H AM-to-wrought welds, in which the HAZ of wrought side accumulates more deformation than any other weld regions. INAM5004 seems to be the biggest outlier in terms of lowest ductility (5.8%), which seemed to be caused by a lack of fusion (LOF)/crack defect on the FZ boundary of the wrought side in mid-thickness (see Figure 139(d)). The updated load-displacement and stress-strain curves are summarized in Figure 141.
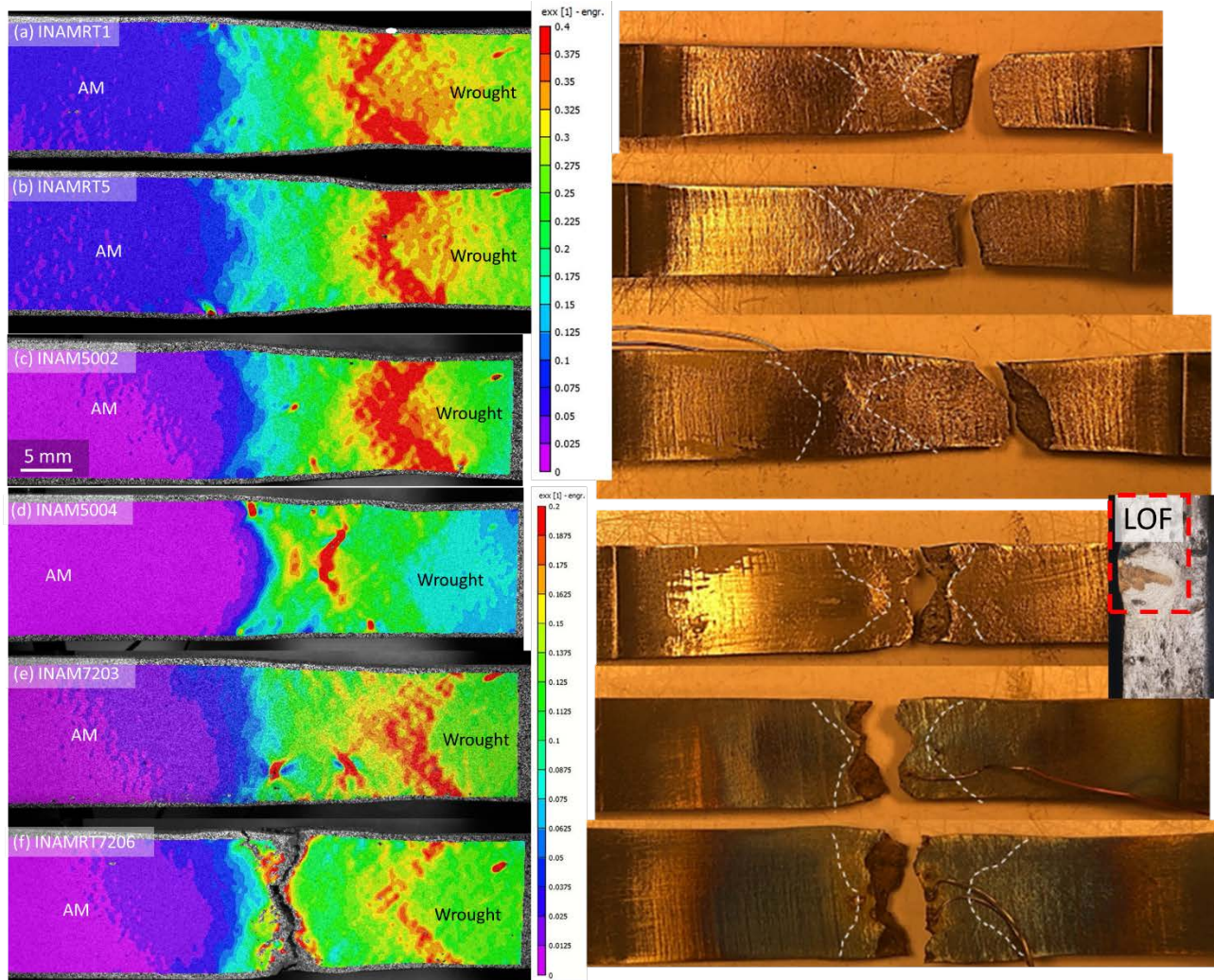
Figure 139. DIC strain and failure location results of In740H wrought to L-PBF weld (a) INAMRT1, (b) INAMRT5, (c) INAM5002, (d) INAM7203, and (f) INAMRT7206. The white dotted lines outline the fusion zone boundaries. RT = room temp; 500 = 500°C; 720 = 720°C
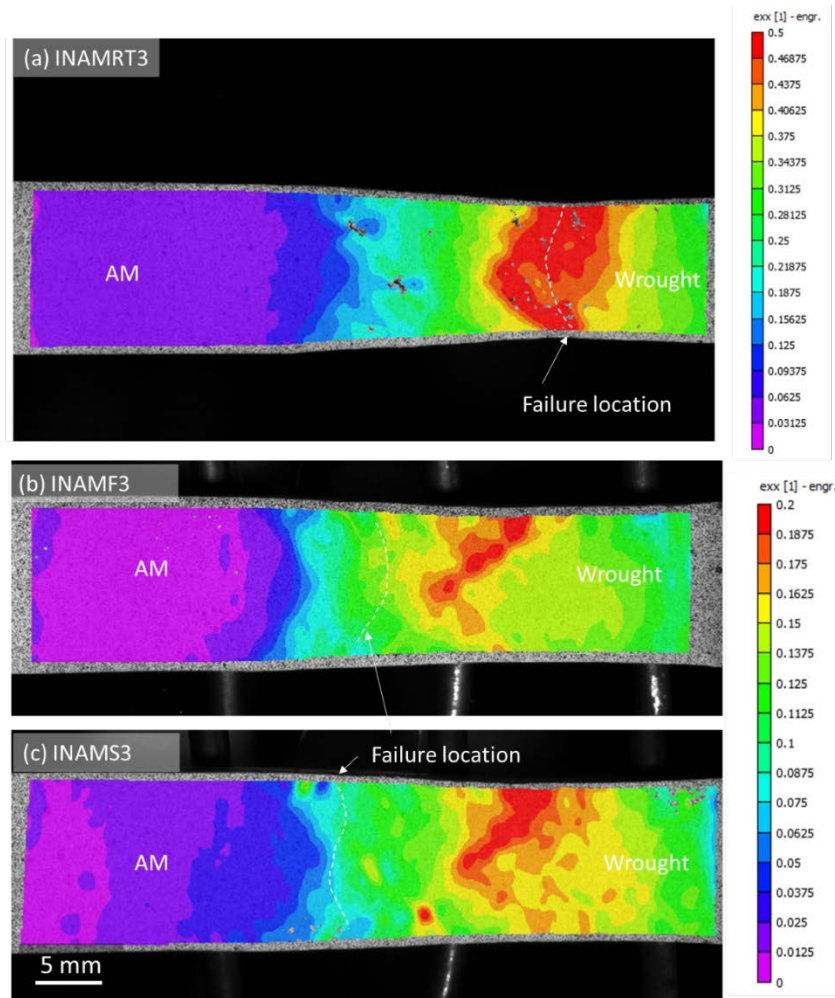
Figure 140. Additional duplicate DIC results for RT, 500°C, and 720°C. Failure location is similar to the other duplicates, where at RT max deformation and failure occurs in wrought side HAZ. However, at 500°C the fracture occurs closer to the wrought side FZ boundary and at 720°C the fracture occurs in the center of the FZ

Table 48. Yield Strength, UTS and Total Elongation of IN740H GTAW L-PBF-to-Wrought Weld in HT2 Condition

ID	Temp. (°C)	0.2% offset Y.S. (MPa)	UTS (MPa)	Total $\varepsilon_{fracture}$	Fracture location
INAMRT1		700	1061	0.186	Wrought-HAZ
INAMRT5	25	697	1051	0.190	Wrought-HAZ
INAMRT3		689	1055	0.23	Wrought-HAZ
INAM5002		563	881	0.164	Wrought-HAZ
INAM5004	500	568	757	0.058	FZ/wrought-HAZ
INAMF3		556	833	0.12	FZ/wrought-HAZ
INAM7203		552	810	0.077	FZ/wrought-HAZ
INAM7206	720	550	798	0.079	FZ center
INAMS3		532	765	0.086	FZ center

127
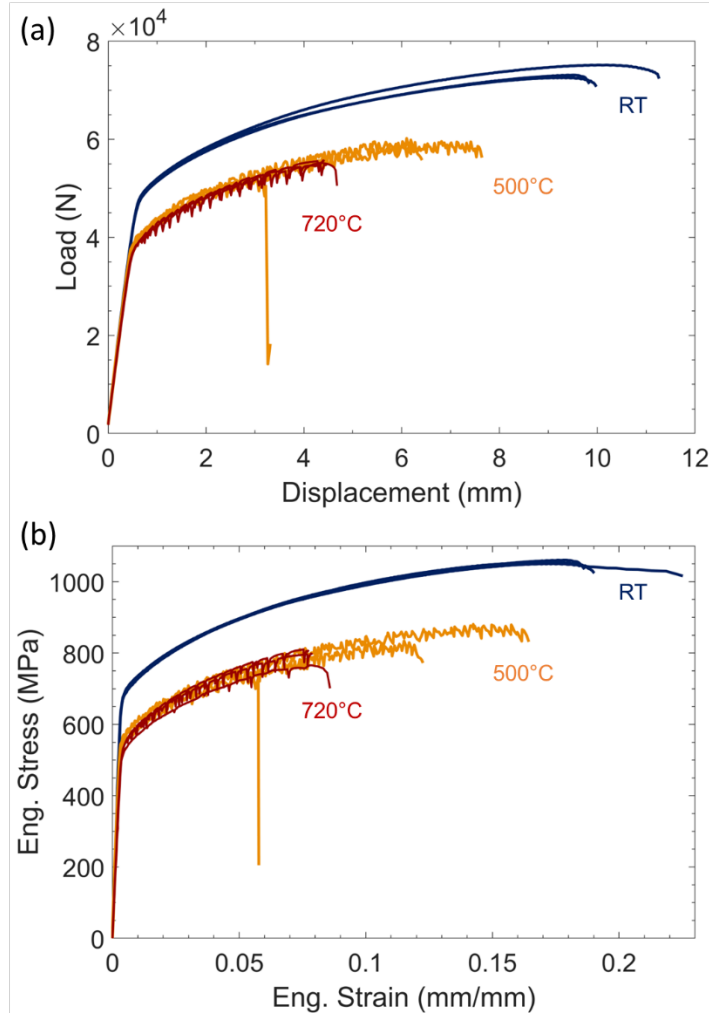
Figure 141. Updated (a) load-displacement curves and (b) stress-strain curves for IN740H AM-to-wrought welds at RT, 500°C, and 720°C

4.3.4.1.3.2 *Metallurgical Characterization and Microhardness*

Figure 142 shows the microstructure of different regions in the AM-to-wrought IN740H aged weld. It is worth mentioning that the low magnification images (a, c, and e) show the microstructure of samples etched with mixed acids etchant (15 ml HCl, 10 ml acetic acid, and 10 ml HNO₃) to reveal the grains structure. On the other hand, the high magnification images (b, d, and f) are taken after etching with electrolytic oxalic etchant to reveal the gamma prime particles. Columnar structure was observed in the AM side (c) by L-PBF compared to the equiaxed grains in the wrought side (a). The high magnification images showed discrete grain boundary (GB) precipitates in the AM side (d), and continuous GB precipitate chains in the wrought side (b).
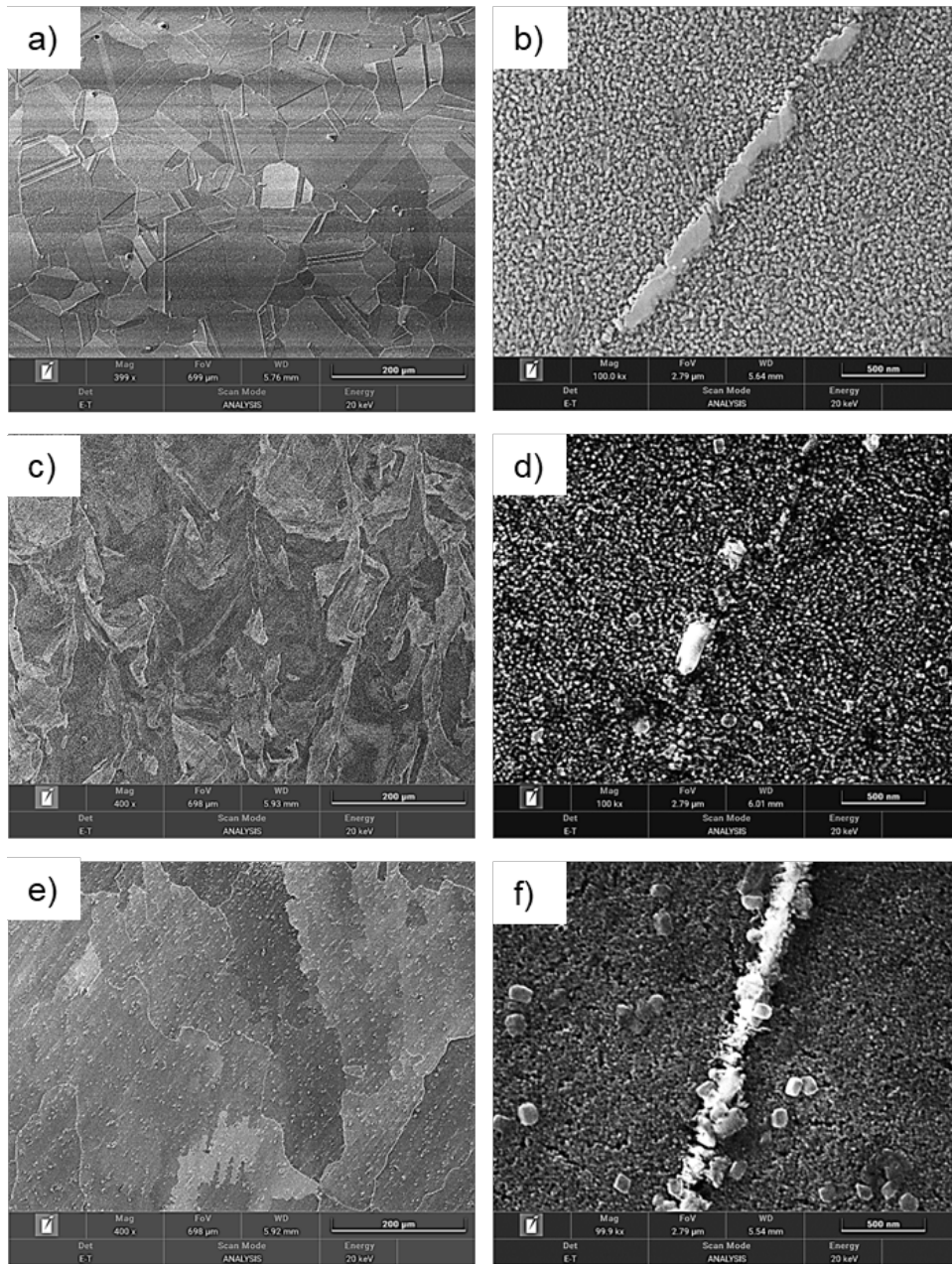
Figure 142. SEM images for microstructure of aged (a, b) wrought In740H, (c, d) L-PBF In740H, and (e, f) fusion zone

The EDS line scans in Figure 143 show nearly matching chemical composition across the two weld sides, L-PBF and wrought In740H. Note that the welds were made using a matching composition In740H GTAW filler. There was only a very slight enrichment in Co and Cr observed in the filler metal compared to the wrought or AM base metals. The chemical composition matching eliminates concerns of any dilution and corrosion resistance difference in these welds.
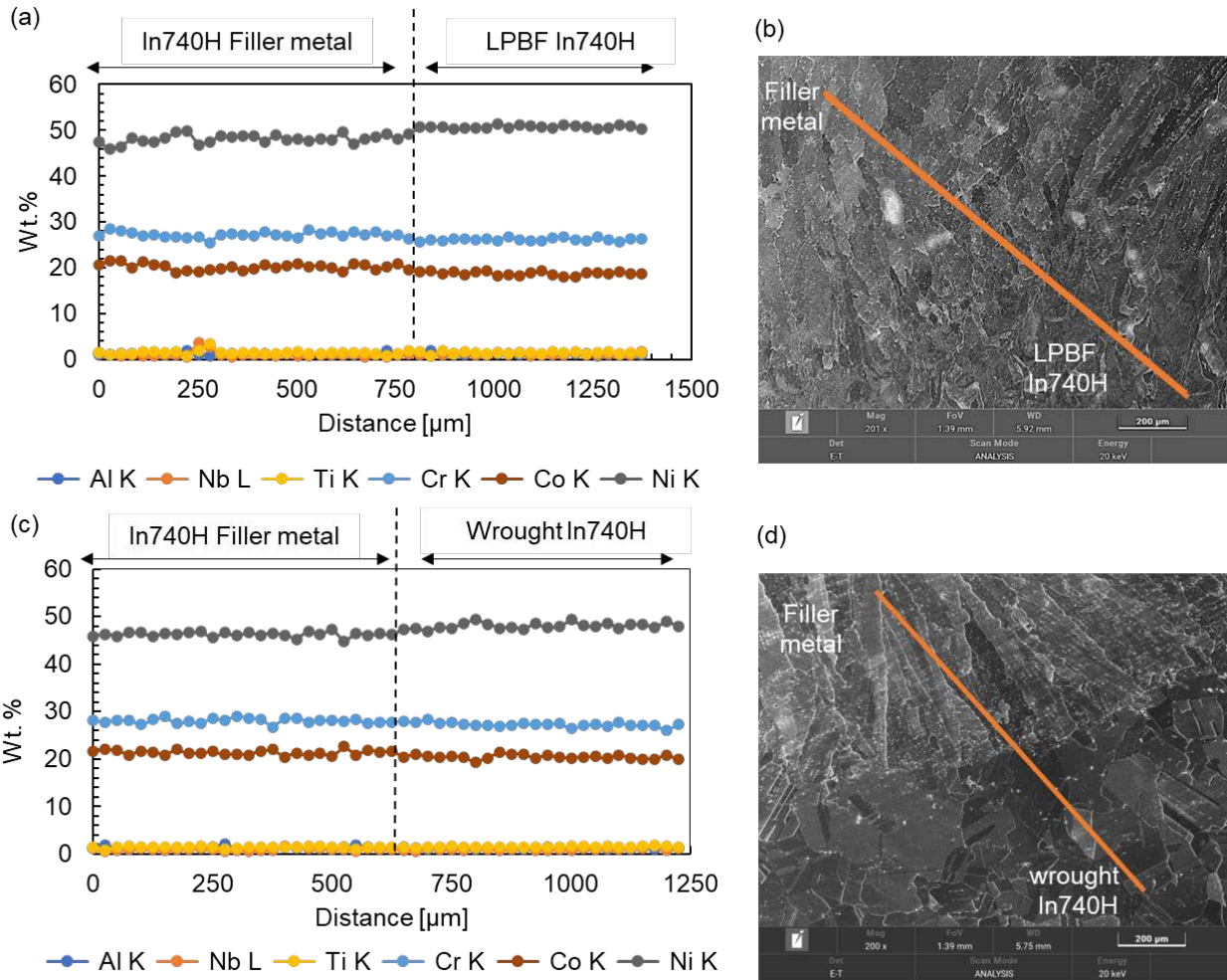
Figure 143. Chemical composition profile from EDS line scans and SEM images for In740H (a, b) L-PBF/filler metal interface, and (c, d) wrought/filler metal interface

A cross-section macrograph in Figure 144 shows a weld defect inside the fusion zone and near the L-PBF side. EDS elemental maps show significant presence of Al and Ti nitrides around the defect which were likely formed during ageing. From the shape and location of this defect, it is likely a lack of fusion (LOF). This type of defect is caused by low heat input, which can be solved by further increasing the welding current or decreasing the welding travel speed. Because the recommended welding current range is narrow (180 Ai ±5) [8], it is more practical to reduce the welding travel speed for the AM side to avoid this problem.

130
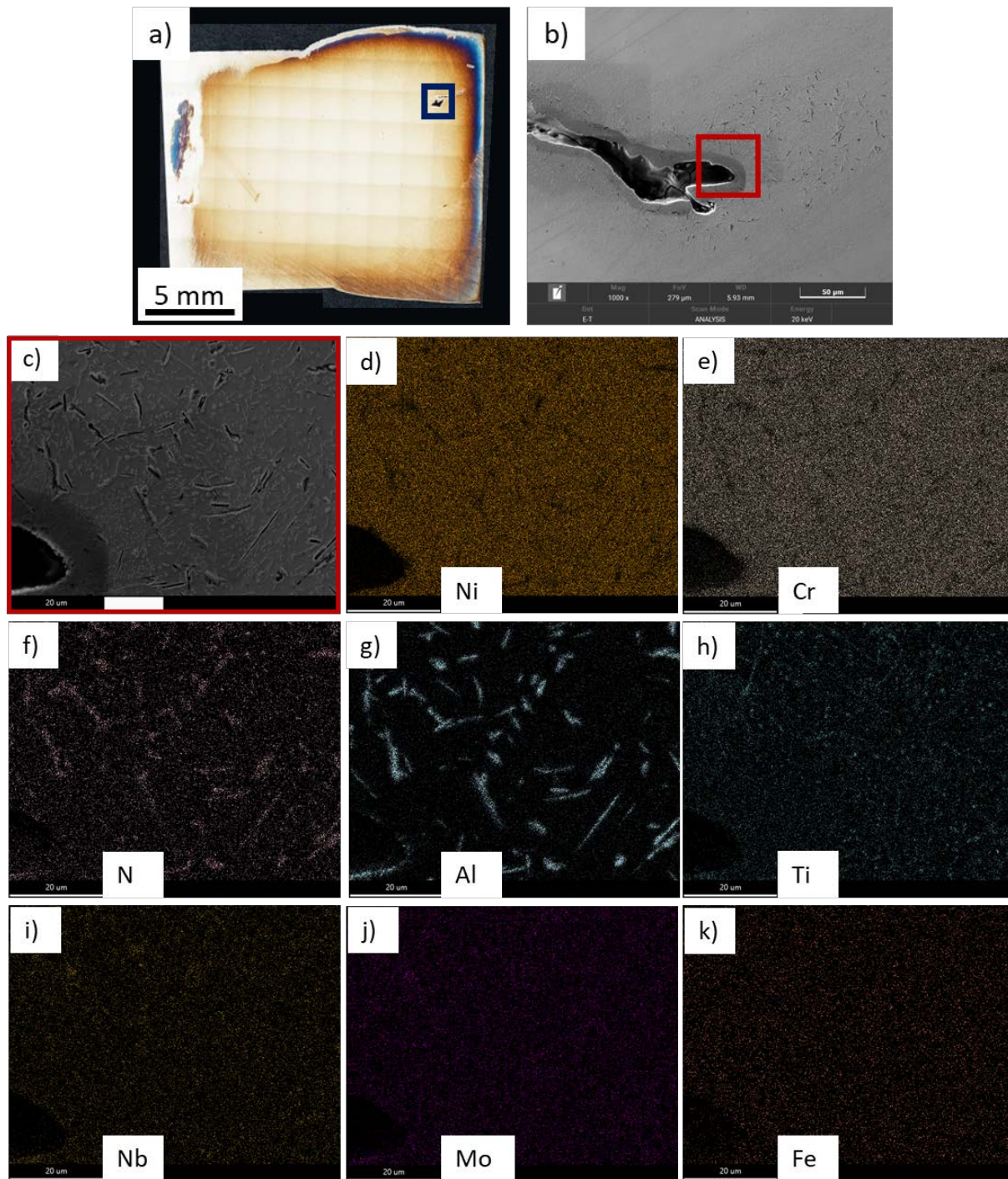
Figure 144. (a) Weld cross section macrograph of aged L-PBF IN740H side showing a defect in the fusion zone. (b, c) SEM images of the defect. (d–k) EDS elemental maps for the defect edge

Figure 145 shows that the average hardness of the wrought In740H side is lower than that of the AM side by approximately 50 HV. In addition, the weld region hardness matched the softer wrought side. The DIC strain partition map shown in Figure 145(b) agrees with the measured hardness profile, as most of the strain is localized in the softer region in the wrought side. The higher hardness in the AM side corresponds to the complex columnar microstructure with

131

relatively coarser gamma prime particles generated from the L-PBF process, while the lower hardness corresponds to the equiaxed wrought microstructure.
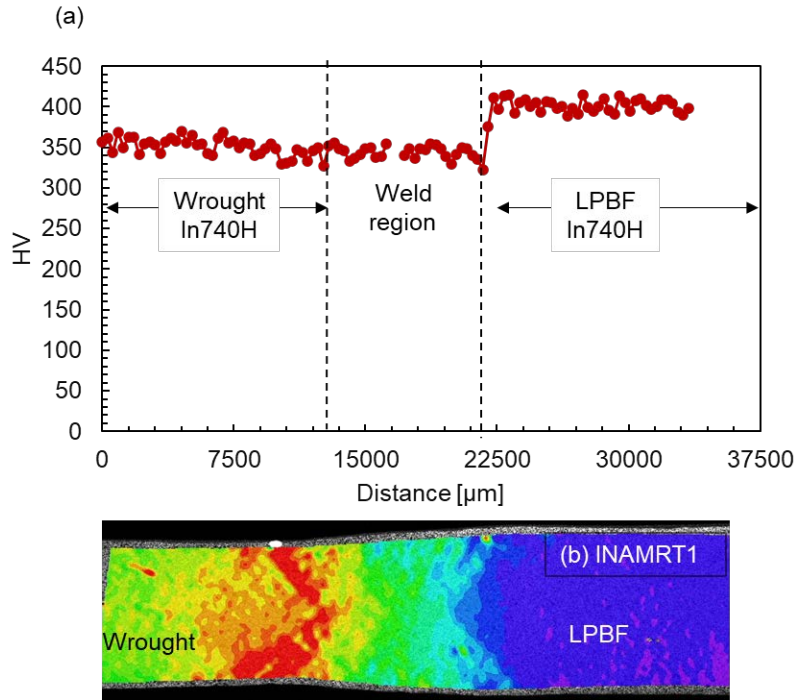
Figure 145. Correlation between (a) the hardness profile of In740H L-PBF-to wrought aged weld and (b) the strain localization shown by DIC result for an aged tensile sample tested at room temperature

4.3.4.1.4 Comparison of Thermomechanical Properties Between Haynes 282 and Inconel 740H L-PBF to Wrought GTA Welds

Figure 146 includes a summary of yield strength (0.2% offset) and ultimate tensile strength (UTS) comparison between Haynes 282 and Inconel 740H L-PBF to wrought welds for 25°C, 500°C, and 720°C.
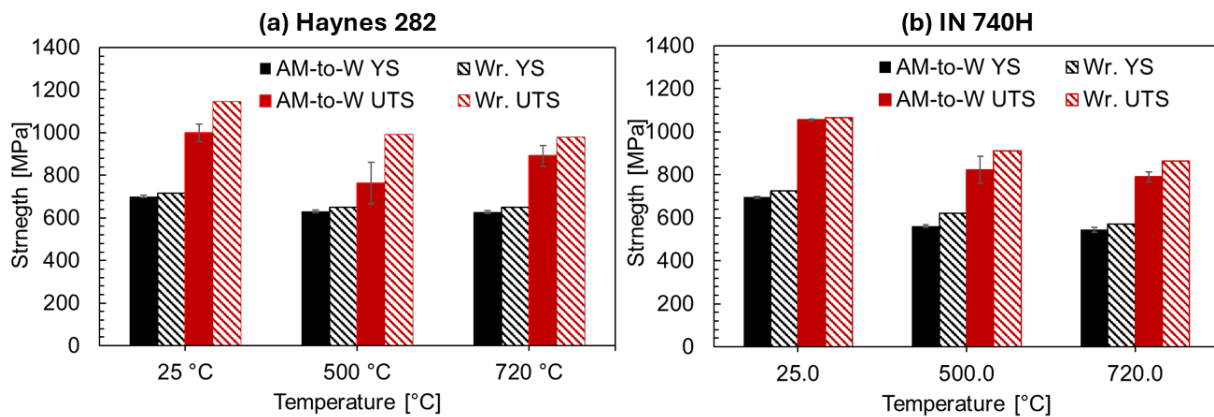
Figure 146. Yield strength (YS) and ultimate tensile strength (UTS) comparison between (a) Haynes 282 (HT2-solutionized + aged) and (b) Inconel 740H L-PBF (solutionized + aged) to wrought welds

132

A direct comparison between wrought products is included, too. Overall, all conditions except Haynes 282 weld at 500°C temperature met the 80% strength criterion requirement compared to wrought. It was determined that weld defects contributed to reduced ductility, which contributed to lower peak stress (denoted UTS). Aside from the weld defects, the yield strength of the Haynes 282 welds exceeds 600 MPa at 500°C and 720°C conditions, while the Inconel 740H yield strength at the same temperature conditions dropped to ~550-560 MPa.

4.3.4.1.5 Haynes 282 EBAM to Wrought GTA Welds

4.3.4.1.5.1 Thermomechanical Properties and Digital Image Correlation

After completion of the GTAW similar weld between EBAM and wrought Haynes 282, DIC integrated thermomechanical testing was completed at RT, 500°C, and 720°C with three duplicates each.
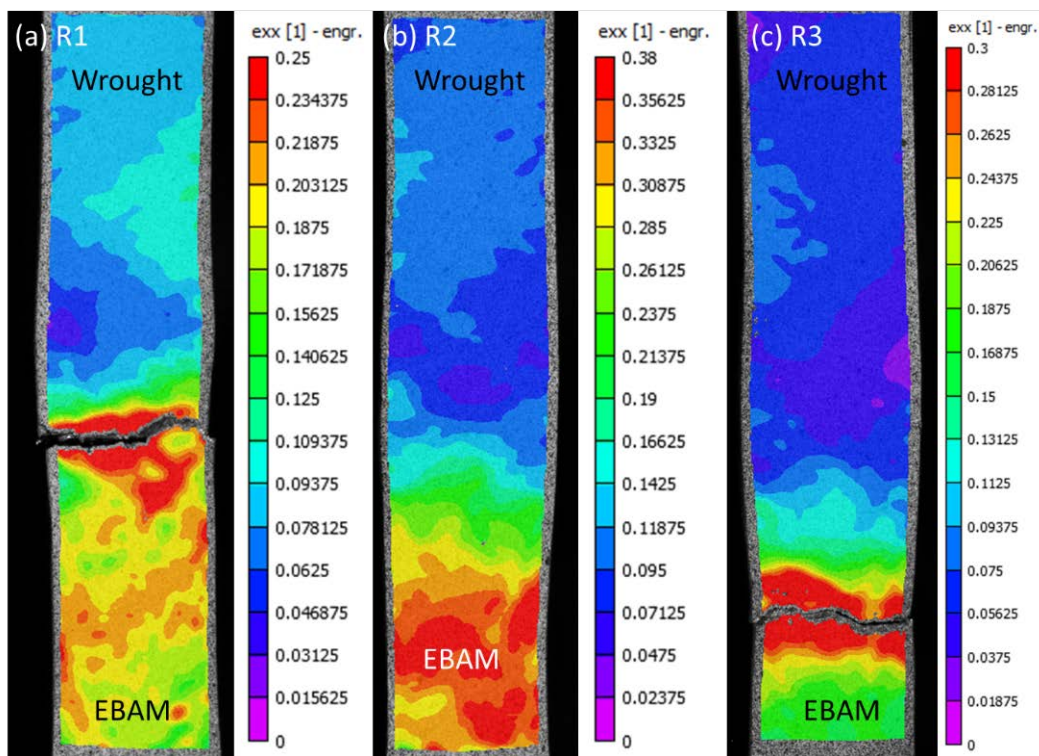
Figure 147. Three duplicates of EBAM-to-wrought GTAW room temperature DIC results on the transverse cross-sectional view of the similar weld. Print orientation of EBAM is vertical with respect to tensile orientation

The DIC measured engineering strain contour plots are shown for RT, 500°C, and 720°C in Figure 147, Figure 148, and Figure 149, respectively. The three figures demonstrate that the deformation occurred primarily on the EBAM side either in HAZ or base metal. To be more specific, RT and 500°C tests indicate more deformation in the EBAM HAZ, while for the 720°C case, deformation and subsequent failure is localized far away from the weld into the EBAM base metal. This observed trend is consistent with what was observed from the tensile tests on Haynes 282 L-PBF, wrought, and EBAM products, where the EBAM product generally exhibited the lowest yield strength and ultimate tensile strength (UTS) in comparison to the wrought and L-PBF ones. Note that at 760°C, the UTS of wrought and EBAM samples are

similar (~800 MPa). With decreasing temperature from 760°C, the differences in yield and UTS become more significant between wrought and EBAM with the EBAM base metal being weaker. Additionally, there is a temperature gradient of ~35-50°C at 500-720°C testing temperatures (measured with an IR camera and calibrated with thermocouples) within the gauge length of the tensile specimen.
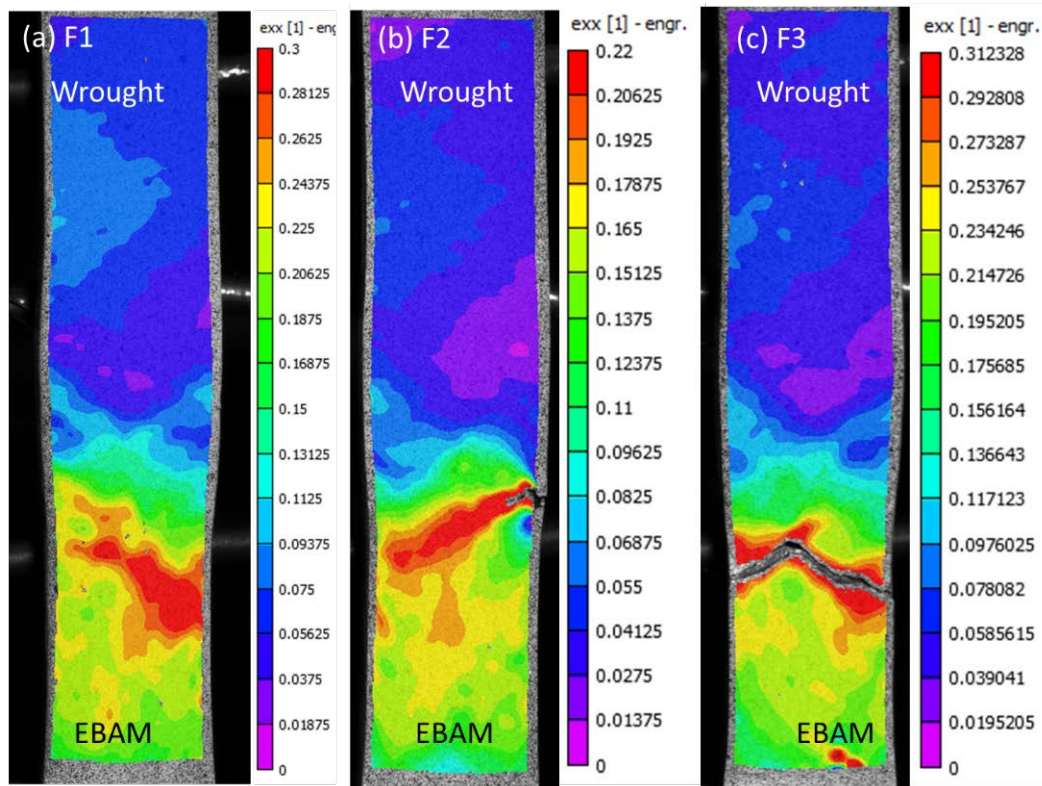
Figure 148. Three duplicates of EBAM-to-wrought GTAW 500°C DIC results on the transverse cross-sectional view of the similar weld. Print orientation of EBAM is vertical with respect to tensile orientation.

The thermomechanical properties and fracture location are summarized in Table 49. Overall, the yield strength of EBAM-to-wrought welds is comparable to the EBAM properties (reported last quarter). The 80% strength requirement is met with respect to wrought properties (715 MPa at RT; 650 MPa at 550°C; 625 MPa at 760°C). The max localized strains on the EBAM side of the similar welds are comparable to the max localized strains in the base EBAM properties (~0.2–0.3). Because the EBAM side contains highest localized strain, the ductility of the EBAM-to-wrought similar weld, in comparison to the EBAM base properties, appears to be lower, because whole gauge length includes wrought HAZ, FZ, EBAM HAZ and BM on each side where the deformation of the wrought side is more resistant. Essentially, the virtual extensometer produces an average strain across the multiple regions, and the overall ductility will be lower across this gauge length compared to a sample with just the EBAM base metal. Also, the presence of voids within the EBAM material may have an influence on variability in ductility, such as EBAMF3 and EBAMS2. The load-displacement and engineering stress-strain curves are plotted in Figure 150.
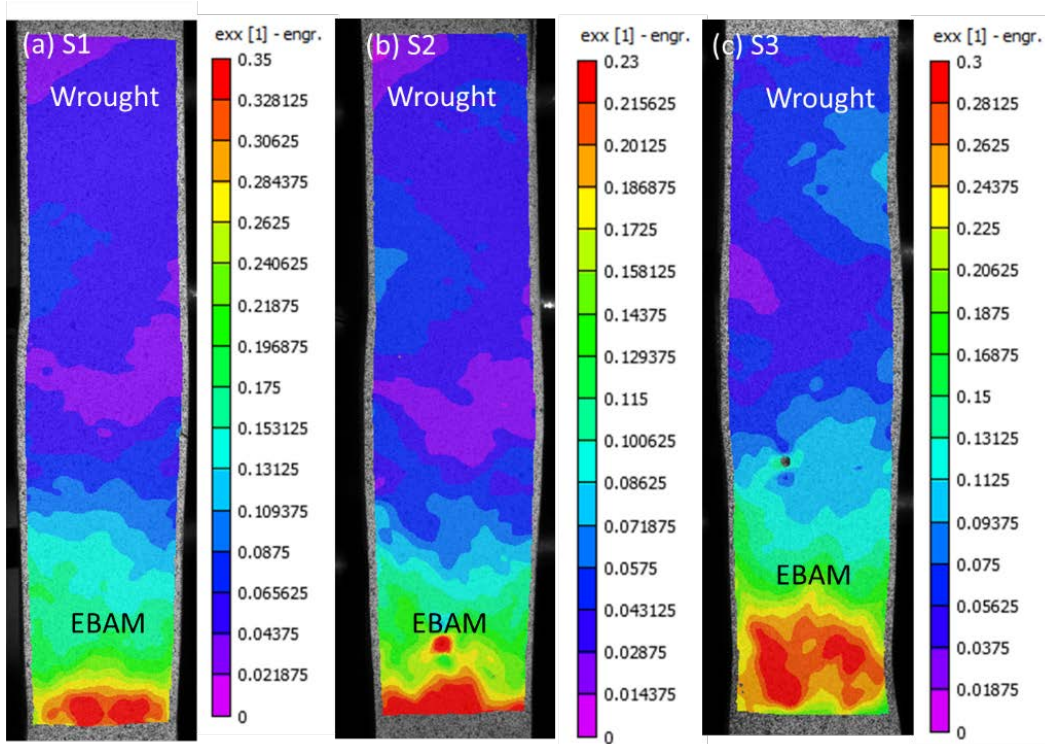
Figure 149. Three duplicates of EBAM-to-wrought GTAW 720°C DIC results on the transverse cross-sectional view of the similar weld. Print orientation of EBAM is vertical with respect to tensile orientation
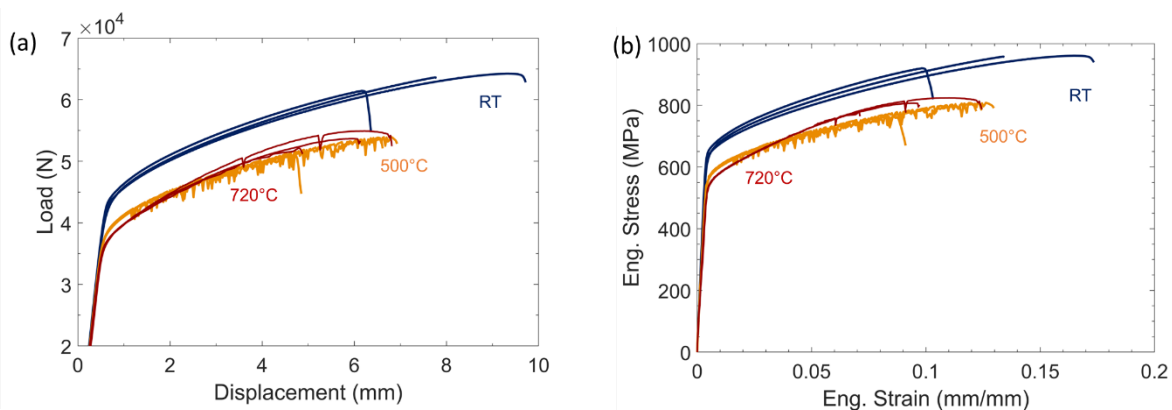
Figure 150. (a) load-displacement curves and (b) stress-strain curves for Haynes 282 EBAM-to-wrought welds at room temperature (RT), 500°C, and 720°C

4.3.4.1.5.2 *Metallurgical Characterization and Hardness Profile*

Figure 151 shows the microstructure of three different regions across the H282 EBAM-to-wrought weld. Although grain structure was hard to reveal using SEM imaging in the relatively lower magnification images (a, c, and e), it can still be seen that EBAM base metal (a) had columnar grains that were likely inherited from EBAM solidification structure. On the other hand, equiaxed grains were observed in the wrought base metal (e). The high magnification images (b, d, and f) show homogenous γ' precipitation over the three regions due to the post weld aging heat treatment.

Table 49. Summary of EBAM to Wrought Haynes 282 Thermomechanical Properties

ID	Temp. (°C)	0.2% offset Y.S. (MPa)	UTS (MPa)	Total $\varepsilon_{fracture}$	Fracture location
EBAMRT1	25	650	958	0.134	EBAM-HAZ
EBAMRT2		651	961	0.174	EBAM-HAZ/BM
EBAMRT3		661	920	0.103	EBAM-HAZ/BM
EBAMF1	500	581	808	0.13	EBAM-HAZ/BM
EBAMF2		576	807	0.122	EBAM-HAZ/BM
EBAMF3		572	763	0.091	EBAM-HAZ/BM
EBAMS1	720	555	807	0.097	EBAM BM
EBAMS2		554	778	0.071	EBAM BM
EBAMS3		551	824	0.125*	EBAM BM

*Issue with camera calibration that might influence DIC data, including strain values
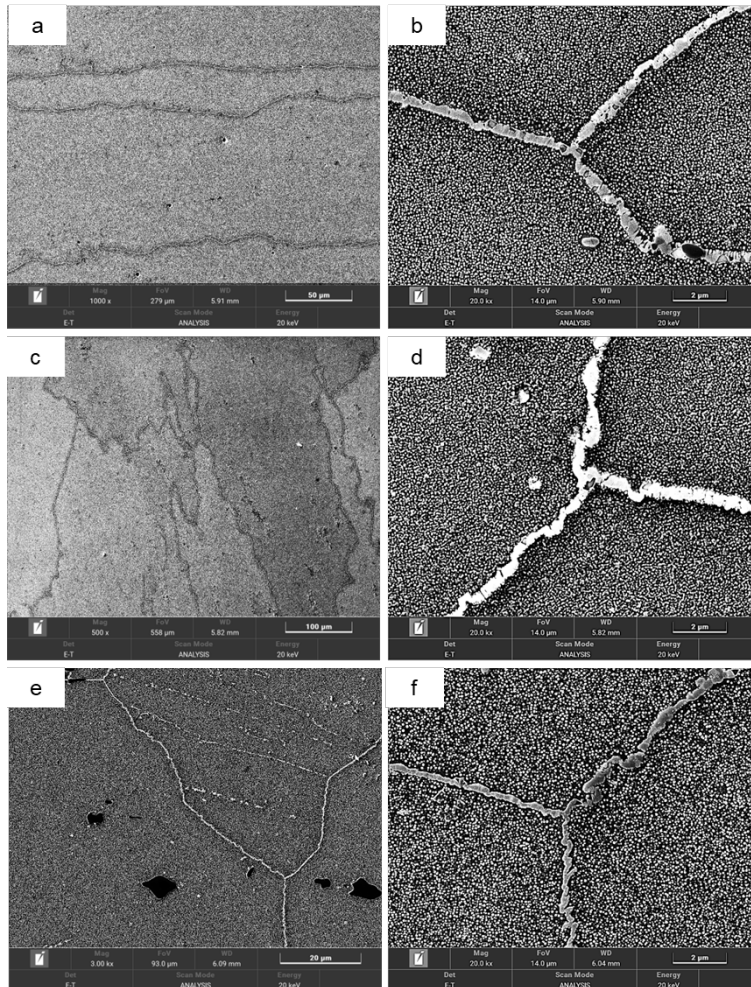
Figure 151. SEM images for microstructure of aged (a, b) EBAM H282 base metal, (c, d) H282 filler fusion zone, and (e, f) wrought H282 base metal

Figure 152 shows complete chemical composition homogeneity between the H282 filler metal and the EBAM base metal. Note that the welds were made using a matching H282 GTAW filler.

This observation eliminates concerns of any dilution and corrosion resistance mismatch in these welds.
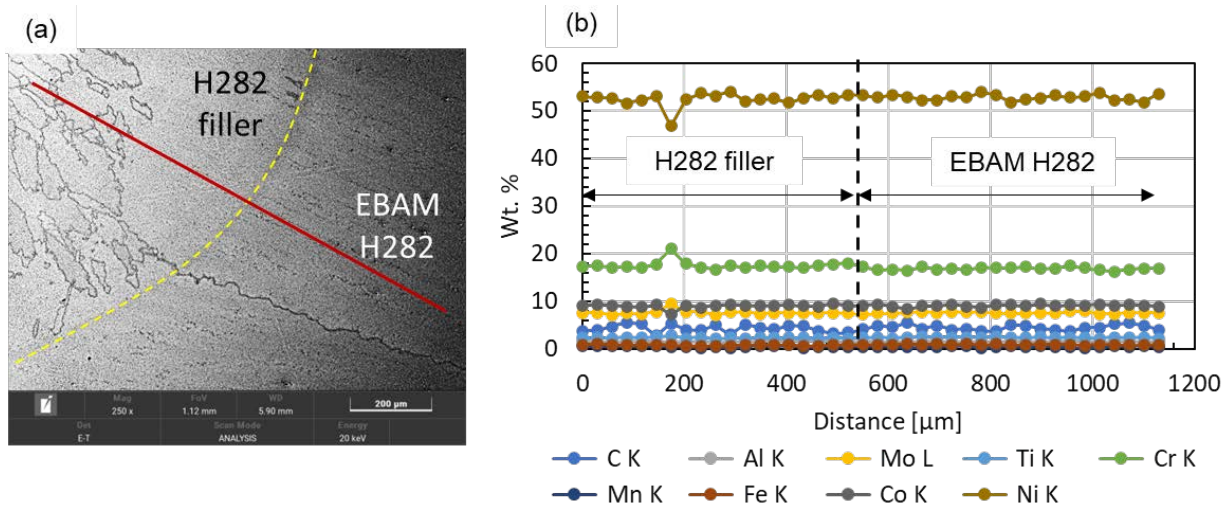
Figure 152. EDS chemical composition profile across H282 EBAM/ filler metal interface

A homogenous hardness profile can be observed across the weld in Figure 153. The similar hardness values can be attributed to the homogenous γ' precipitation in the three regions observed in Figure 151 after heat treatment.
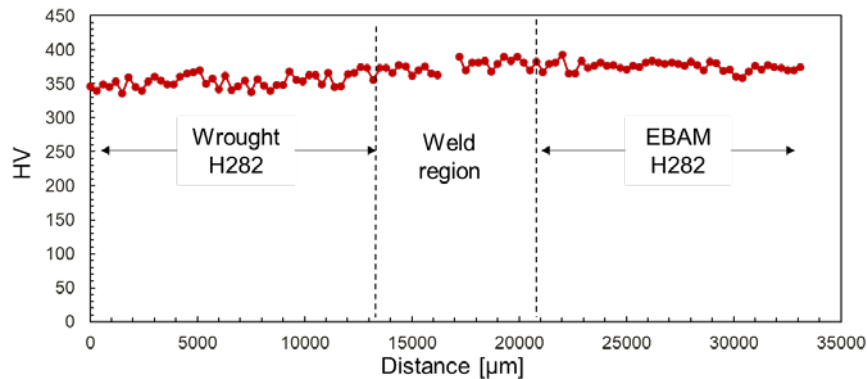
Figure 153. Hardness line profile across H282 EBAM-to-wrought weld

4.3.4.2 *Fusion Zone Morphology of L-PBF to Wrought Welds for Haynes 282*

The absorption of gas elements and loss of alloying elements due to evaporation during L-PBF process may lead to sufficient difference in the surface tension from the wrought material, which in turn significantly change the molten fluid flow behavior and the resulting morphology in fusion zone of L-PBF component. Because surface tension depends on both material composition and temperature, in this study, the impact of weld heat input is evaluated as well, which directly influences the peak temperature in fusion zone. The study is separated in two groups: (1) autogenous welds on L-PBF and wrought plate, respectively, with various heat inputs to reveal the impacts of composition and temperature on fluid flow behavior, and 2) autogenous butt welds of L-PBF to wrought plates to evaluate the symmetry of AM-to-wrought similar weld morphology for both ¼-in.-thick and ½"-in-thick plates.

137

In the first set of autogenous weld experiments, three weld experiments were performed on Haynes 282 AM and wrought plates, respectively, using 150, 200, and 230 A at 2.5 inch per minute (IPM) travel speed on 4 inches long, 1.5 inches wide and 0.5 inches thick plates. Voltage varied from 12-15 V and is on the higher end with higher weld current. A total of six welds were generated and their light optical macrographs are summarized in Figure 154. The etchant used to reveal the microstructures is a mixture of 15 mL hydrochloric acid, 10 mL nitric acid and 10mL distilled water. As the current increases from 150A to 230A, the fusion zone width in autogenous weld wrought plate steadily increases, while in L-PBF plates there is a more noticeable increase in weld depth. Additionally, the L-PBF weld morphology shows a trend in forming a convex shape on top surface while all the wrought welds exhibit a relatively flat surface. The observed phenomena indicate formation of an asymmetric fusion zone when welding of AM to wrought materials with high currents, i.e., high heat inputs, which could lead to weld defects such as lack of fusion.

Figure 155 displays the weld depth weld width, and depth-to-width (D/W) ratios of weld macros in autogenous welds of L-PBF and wrought material separately. Overall, the D/W ratio of the wrought weld decreases slightly with increasing current, mostly due to the higher rate increase in weld width as a function of weld current. On the other hand, the D/W ratio of L-PBF weld increases mostly from 150 to 200 Amperes and then saturates mostly between 200 and 230 Amperes. The rate of increase in the L-PBF weld penetration depth is greater than the rate of increase in the weld width with increasing current.
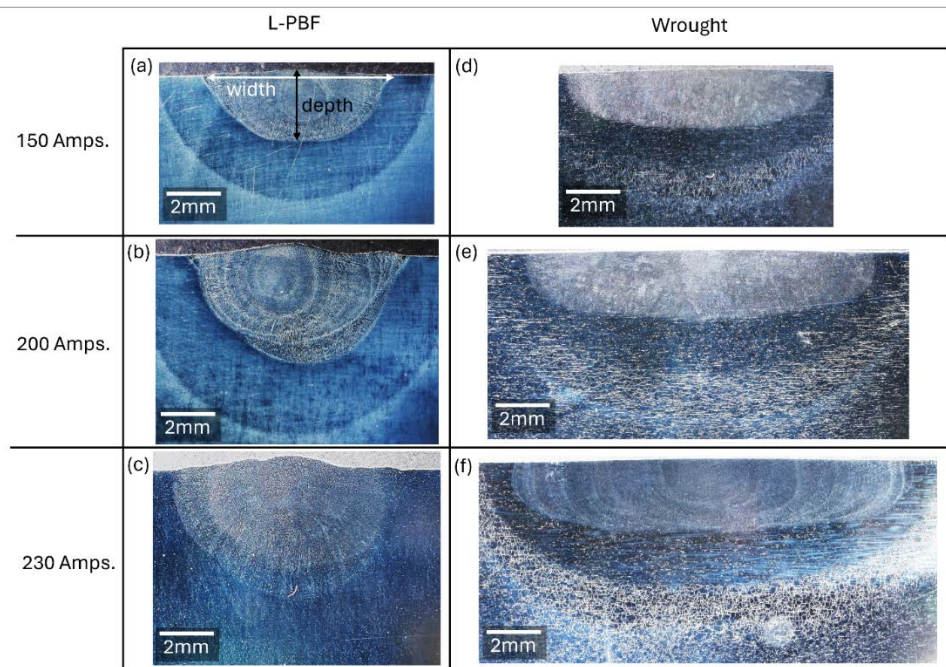
Figure 154. Haynes 282 autogenous welds on L-PBF (a–c) and wrought (d–f) plate samples (1/2-in. thick) using 150, 200, and 230 amperages
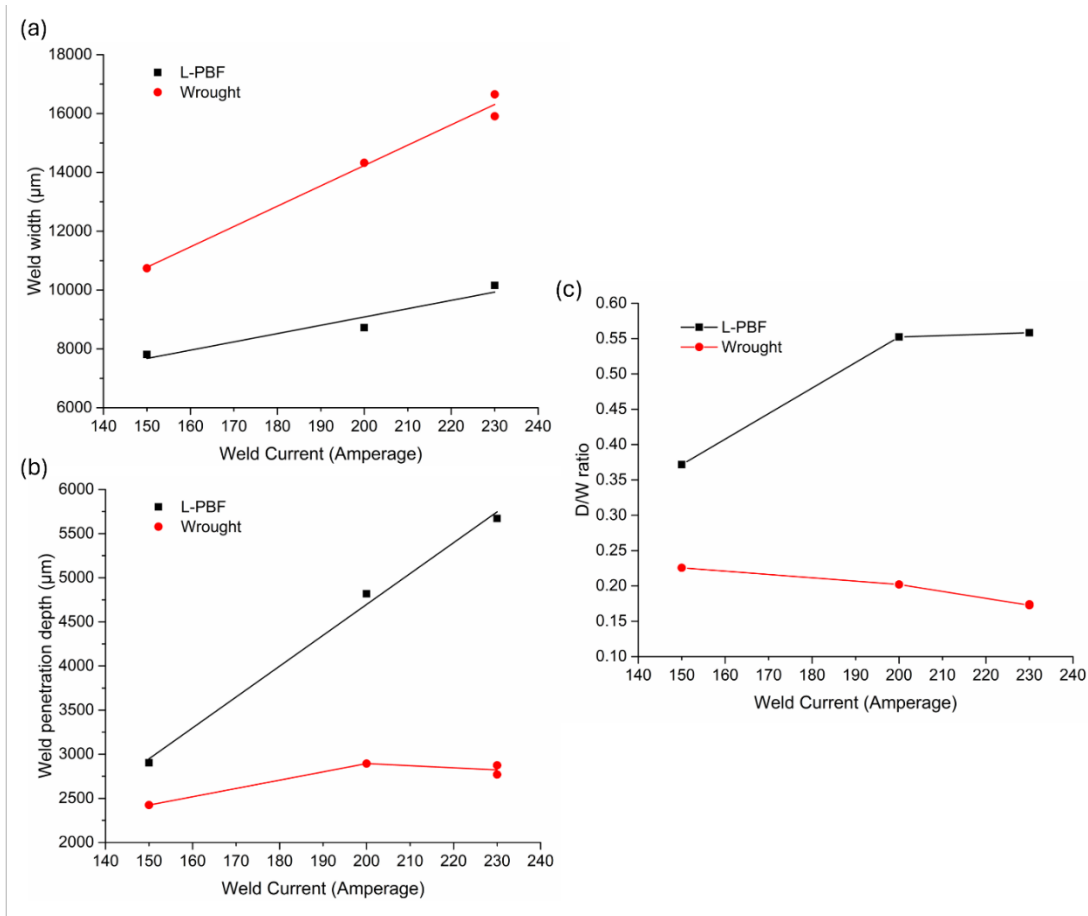
Figure 155. Haynes 282 wrought and L-PBF autogenous weld dimensions: (a) weld width, (b) weld penetration depth, and (c) depth-to-width (D/W) ratio

Initial welding experiments on ~1/4-in.-thick Haynes 282 wrought and L-PBF plate were performed to reveal the impact of surface-active element (O and N) on the fluid flow behavior and resulting weld fusion zone morphology. four autogenous welds with welding currents of 150, 200 and 230 amperages, using a simple butt joint configuration at a 2.3–2.5 inches per minute (IPM) travel speed with 14–15 volts for lower current welds and 17 volts for 230-amperes weld on 1.5-inch-long by 1-inch-wide samples. The outcome of this study would greatly assist in parameter optimization for mitigating weld defects in multi-pass welding of L-PBF to wrought welds.

Figure 156 displays the cross sections from the middle of the weld length of (a) 150, (b) 200, and (c) 230-amperage conditions. The weld with lower weld current (Figure 156(a)) displays a wide and shallow molten pool, where a similar depth of penetration exists for the whole weld FZ. The fusion zone centerline was observed to be slightly offset to the wrought side by about ~1 mm (AM side-4.5 mm; wrought side-6.5 mm). The offset could be possibly caused by an unintentional offset of heat source during welding, or a high outward Marangoni stress in the wrought side with a low O content in comparison to a possibly weak either inward or outward Marangoni stress in the AM side with a high O content. At this low heat input case, it is possible that heat transfer mode is mainly conductive, indicating that the fluid flow direction will not be

139

critical in determining the fusion zone morphology. Therefore, the wrought and AM sides exhibited similar fusion zone boundary in (a). Figure 156(a).

The higher current cross sections (Figure 156(b–c)) display a general higher depth-to-width ratio depth than 150-amperage conditions, while the AM displays slightly more depth of penetration compared to the wrought side. The AM side with 230 current melted through while the wrought side did not show this behavior, as seen in Figure 156(c). Figure 156(b–c) suggests that with increasing temperature and the presence of surface-active element O, a positive surface tension temperature coefficient could be generated, leading to an inward fluid flow driven by the Marangoni stress, as shown by the green arrow in Figure 156(b–c). A negative surface tension temperature coefficient at lower temperature regions, such as near the heat-affected zone on top surface, could be possibly present, leading to an outward fluid flow in this region as represented by the red arrow on the AM side. Hence, a fusion zone with a less smooth boundary is observed at the AM side due to the two competing forces in comparison to a smooth bowl-shaped fusion zone at the wrought side with an outward Marangoni stress only [4]. Another observation was the significant grain coarsening in the CGHAZ in the 200 and 230-amperage conditions, which could progressively result in weaker mechanical properties on AM side as a function of increasing current. In summary, welding procedures may need to be carefully designed for AM-to-wrought welds, e.g., torch angle, current, avoid lack of fusion and/or introduction of stress-risers due to a non-smooth fusion boundary. The wrought side may require more heat input, e.g., heat source offsetting toward the wrought side, to generate a weld as deep as the AM side. Our collaborators at OSU would be able to perform finite element simulation to assist in the welding process optimization for desired fusion zone morphology.
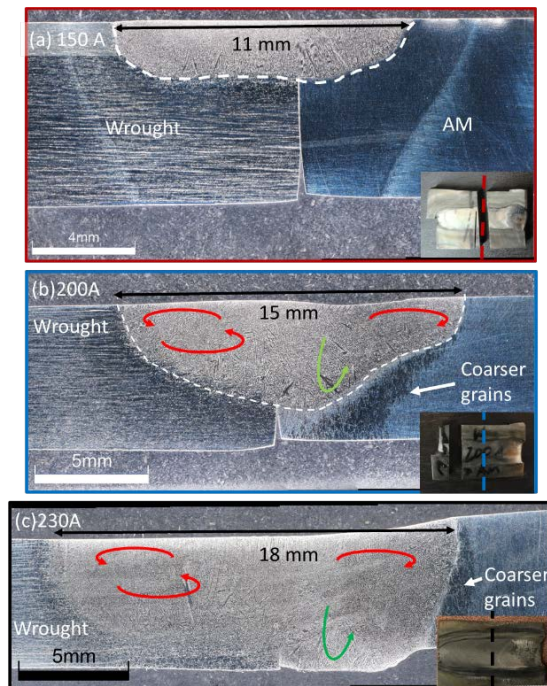
Figure 156. Autogenous single-pass GTAW butt welds on ¼-in.-thick H282 wrought and AM L-PBF samples using (a) 150 amperes, (b) 200 amperes, and (c) 230 amperes (positive and negative surface tension temperature coefficients regions are represented by green and red arrows, respectively)

140

The second set of autogenous butt weld samples were conducted using the same weld parameters as the separate autogenous weld samples. Additionally, the sample dimensions in the as-welded condition are the same. The main difference between these experiments and the initial experiments are that these were semi-mechanized using a bug-O track to ensure consistency in arc length, arc angles, etc., and that the thickness of these were increased to ½ in., similar to the multi-pass welding experiments. Two sets of welds were completed with flipping the weld direction to intentionally rule out other weld error effects, e.g., slight changes in weld angle that may favor melting one side more than the other.

Figure 157 displays the macrographs of Haynes 282 autogenous butt weld samples as a function of weld current. Some observations, similar to the initial experiments, are the concave cap on L-PBF side and asymmetric weld penetration and width on either side of the bond centerline. With increasing current, there appears to be an increase in weld width on both sides of the bond centerline whereas the maximum penetration depth is not typically aligned with the bond centerline.

Figure 158 shows the weld shape morphology dimensions of the autogenous L-PBF-to-wrought butt-welded Haynes 282 samples, particularly width and penetration depth. Because the weld morphology is mostly asymmetric for all amperage conditions, such that the wrought side width is greater than the L-PBF side width, except for one weld condition at 230 amperes (which had more arc instability during welding), as seen in Figure 158(b). The weld penetration depth generally increases with increasing weld current, but the location of max depth (either on L-PBF or wrought side) is not as straightforward as the weld centerline shift being primarily located in the wrought side. For low currents, the wrought side has higher penetration, but with higher currents, the max weld penetration shifts to the L-PBF side of the weld.
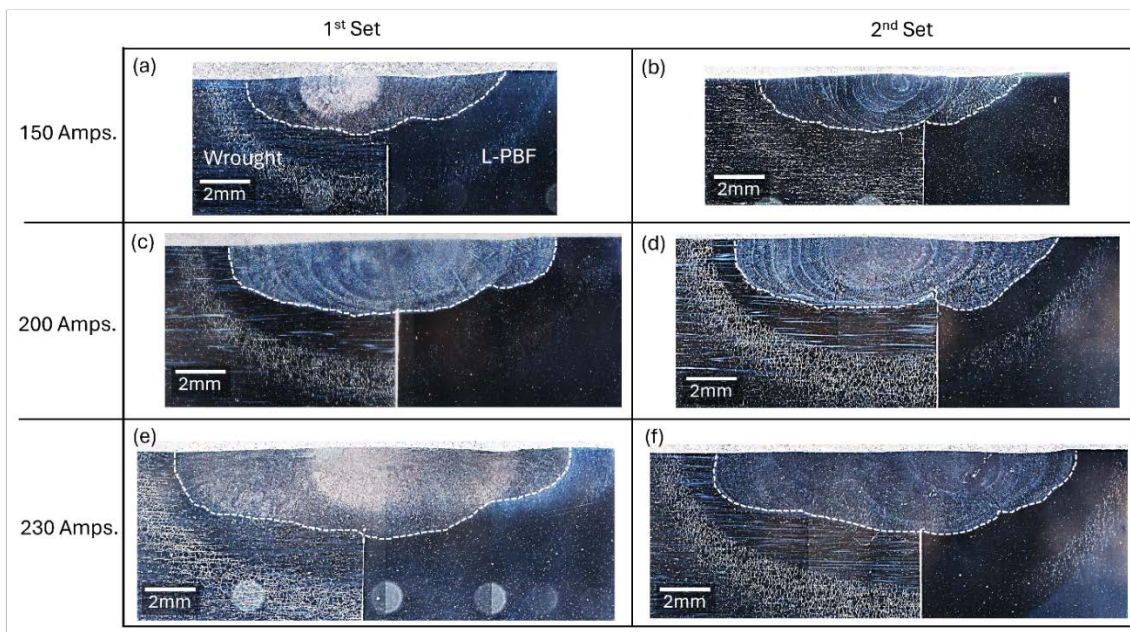
Figure 157. Haynes 282 autogenous butt weld macrographs of first set (a–c) and second set (d–f) categorized as a function of current. Note: wrought plate is on left side and L-PBF plate is on right side of bond centerline

141
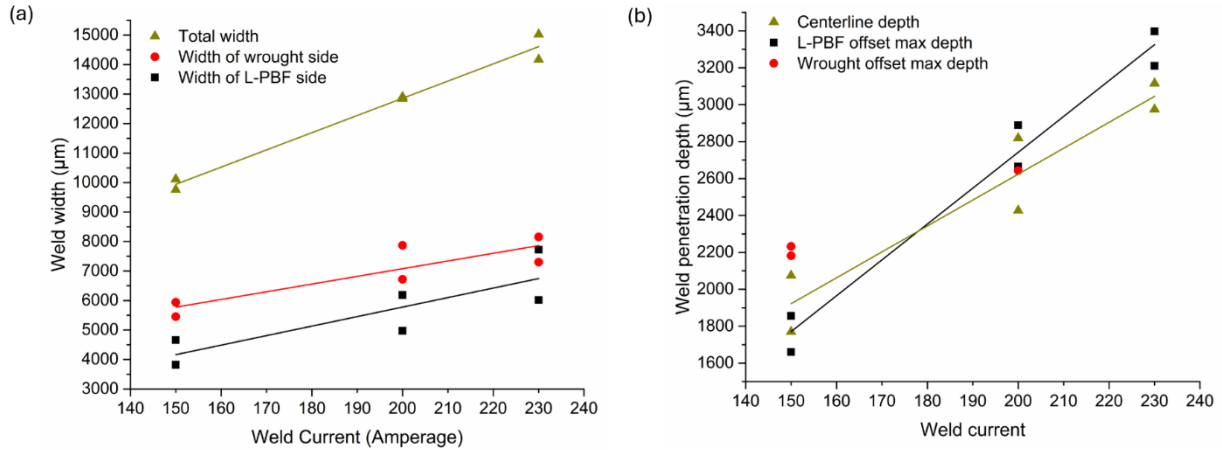
Figure 158. Butt weld (a) width and (b) penetration depth separated by whole weld, L-PBF and wrought side

4.3.4.2.1 Comparison of Separate (Similar) and Butt Weld Fusion Zone Profiles

The molten pool morphology of the separate and butt-welded autogenous welds can be compared, as shown with weld width and penetration depth in Figure 159. Overall, the width of the butt weld is very similar to the increase in width of the separate wrought weld samples. The maximum depth of penetration in the butt welds are similar to the separate wrought weld samples, implicating a more dominant negative surface tension effect. On the other hand, at 200 amperes and above, the max penetration in the weld shifts to the L-PBF side indicating a more positive surface tension effect subsurface developing at higher weld currents. The results suggest the width and penetration depth of but-welds being similar to single autogenous wrought samples, indicating a more dominant negative surface tension coefficient.
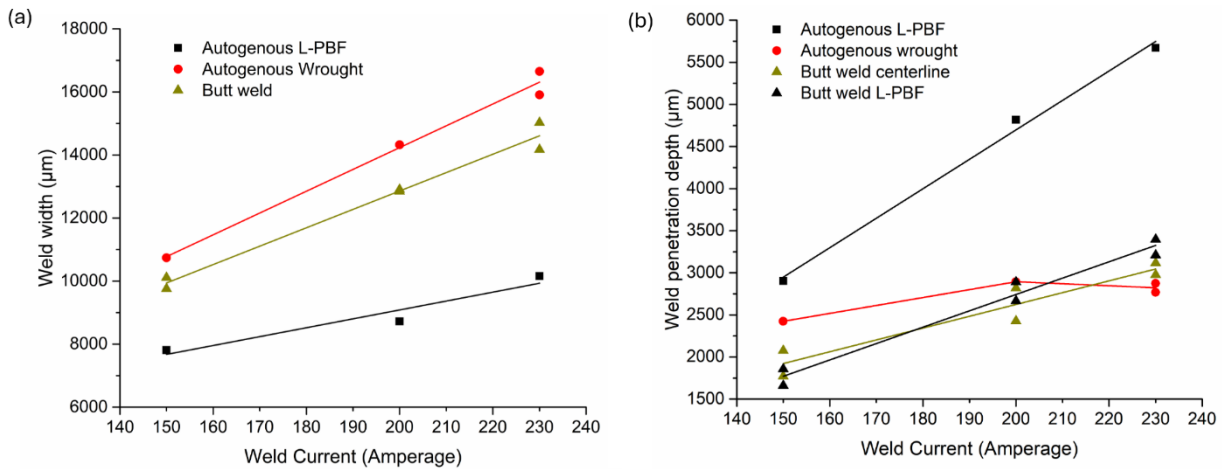
Figure 159. Comparison between separate autogenous welds vs. butt autogenous (a) weld width and (b) weld penetration depth

142

4.3.4.2.2 Chemical Composition Analysis of L-PBF Haynes 282 Compared to Wrought Plate

The chemical composition analysis of the L-PBF Haynes 282 compared to wrought plate is shown in Table 50, Table 51, and Table 52 using optical emission spectroscopy (OES) and LECO combustion melt analysis techniques. The O, N, S, and P content are noticeable different between L-PBF and wrought product, most notably higher in the former. The oxygen and nitrogen concentrations in 282 L-PBF plate are significantly higher than those of the wrought plate. O absorption is observed to increase from 21ppm to 104 ppm and N absorption increases from 25ppm to 64ppm. The influence of higher impurity content in L-PBF product influences the surface tension during welding, which contributes to a higher D/W ratio. Another hypothesis that may contribute to differences in the molten pool shape would be the higher Cr and Co influence arc vapor shift from the designed weld centerline. However, more work would be needed to confirm that hypothesis.

Table 50. Bulk Chemical Composition Analysis of L-PBF Haynes 282 Product Using Optical Emission Spectroscopy (OES). Wrought Haynes 282 Product Shown for Comparison (Taken from Material Test Report)

wt%	C	N	Cr	Mo	Co	Fe	Ti	Al	Nb	V	W	B	Cu	Si	Mn	Zr	S	P
L-PBF H282	0.04	0.01	23.37	8.94	12.04	0.04	2.73	2.1	0.04	0.01	0.05	-	-	-	-	-	0.003	0.046
Wrought H282	0.06	-	19.5	8.5	10.2	0.9	2.2	1.51	0.1	-	0.1	0.006	-	0.08	0.06	0.011	<0.002	0.003

Table 51. Wrought Haynes 282 Oxygen (O) and Nitrogen (N) Content, Measured Using LECO Combustion Melt Analysis

Sample	O-ppm	O-max (ppm)	N-ppm	N-max (ppm)
1	16.8		19.2	
2	22.2		23	
3	23.26	300	33.8	200
Avg.	**20.75**		**25.33**	
Std. Dev.	**3.46**		**7.57**	

Table 52. L-PBF Haynes 282 O and N Content, Measured Using LECO Combustion Melt Analysis

Sample	O-ppm	O-max (ppm)	N-ppm	N-max (ppm)
1	101.85		62.12	
2	109.43		66.83	
3	97.72	300	63.81	200
Avg.	**103±5.94**		**64±2.4**	

4.3.4.2.3 Conclusions and Future Work

- Autogenous weld experiments are conducted to analyze the effect of weld current on weld fusion zone pool morphology post-mortem in both L-PBF and wrought Haynes 282 plate samples separately (similar welding case) and butt welded together (dissimilar welding case).
- For the similar welding case, the increase in weld current increases the D/W ratio in L-PBF components, while the D/W ratio slightly decreases with increasing current in wrought components. The differences mostly correlate with differences in impurity content of oxygen, nitrogen, and sulfur between the wrought and L-PBF samples that contribute to differences in the negative vs. positive surface tension that effect fluid flow and weld pool shape.
- For the dissimilar welding case, the increase in weld current seemed to lead to an increase in weld width and weld penetration. However, the increase in weld width was mostly dominant on top surface throughout the weld current regime, but with increasing current above 200 amperes, the max penetration depth increases on the L-PBF side due to increase in subsurface positive surface tension, which is driving a higher weld penetration, leading to asymmetries that are weld current dependent.
- Learning from these welds compared to multi-pass welds and mitigating defects, the undulations leading to concave weld cap on the L-PBF side may contribute to weld defects observed in the multi-pass case.
- For actual case, a moderate weld current might be better, e.g., 200 amperes, as this may provide more symmetric weld profiles.
- For future work, adding in filler for single bead on plate experiments would help determine whether there are any noticeable subsurface changes in weld pool shape as a result of using matching filler, which is hard to delineate in multi-pass welds.

4.4 Task 5: Joining of Dissimilar and Advanced Manufactured Alloys

This task encompasses mostly the design and welding of dissimilar alloys. The previous section included work on AM-to-wrought welds, deemed similar welding.

4.4.1 Design of Dissimilar Alloy Joints (Milestone 1.5.1)

The diffusion behavior in dissimilar welds between stainless steel 304H and a nickel-based filler (IN82) was simulated using DICTRA software. The target of these simulations is to study the diffusion behavior (especially carbon) at the backer/filler interface and phase transformations at service temperature for prolonged times.

Table 53. Milestone 1.5.1 Details

Milestone	Description	Metric	Success Value	Assessment Tools
1.5.1: Design of dissimilar alloys joining	To keep mechanical integrity of dissimilar joints (e.g., Ni-base alloys to stainless steels), the filler composition for dissimilar joining of selected metals from M1.1.2 should minimize the formation of undesired phases (e.g., Mo micro-segregations and blocky carbides) and dilution levels.	Dilution Level calculation based on CALPHAD calculation.	<25%	The maximum dilution level in the majority region of the weldment should be below 25% based on thermodynamic and kinetic calculations.

A novel approach was explored to minimize the carbon diffusion from the steel side into the nickel side, as excessive carbon depletion in the steel side may lead to the formation of soft carbon denuded zones that compromise the mechanical properties of the weld. The introduced approach employs a custom designed high entropy alloy (HEA) filler to serve as a diffusion barrier at the stainless steel (backer)/nickel alloy (dissimilar weld filler) interface. However, H282 emerged as the best Ni-based alloy candidate as the report project progressed. A H282 matching welding filler is used for H282 to SS304H dissimilar weld, unlike In740H, which requires In82. The dissimilar weld experiments showed that using H282 matching filler does not require a diffusion barrier.

4.4.1.1 Simulation of Diffusion Behavior at 304H/IN82 Interface

The most critical diffusion couple to investigate is the cold-to-hot section transition dissimilar joint, especially between steel (i.e., the cold side backer SS 304H or grade 91 steel) and the Ni-base filler metal (e.g., IN82 filler), as carbon diffusion from steel to Ni filler can lead to the formation of carbon denuded zones and soft ferrite islands. Two database packages are being used: the steel database (TCFE11, MOBFE6) and the Nickel (TCNi10, MOBNi5). The phases introduced to each run are based on the equilibrium phases for each material at the service temperature.

This diffusion couple includes the cold side backer (SS 304H) and the filler metal for dissimilar welds with the Ni-based alloy in the hot side (IN82). The database used is the steel alloys database package. The two sides, 304H and IN82, were differentiated by defining the chemical composition profile for each element through error functions to give the initial composition profile shown in Figure 160. Minor alloying elements (Si, Mn, Cu) were disregarded to simplify the model. The equilibrium phases for SS304H at the service temperature 550ºC (including BCC, FCC, M23C6, Sigma) were introduced to the model. This run simulates the diffusion behavior after 1 day of service at 550ºC (cold side temperature).

145
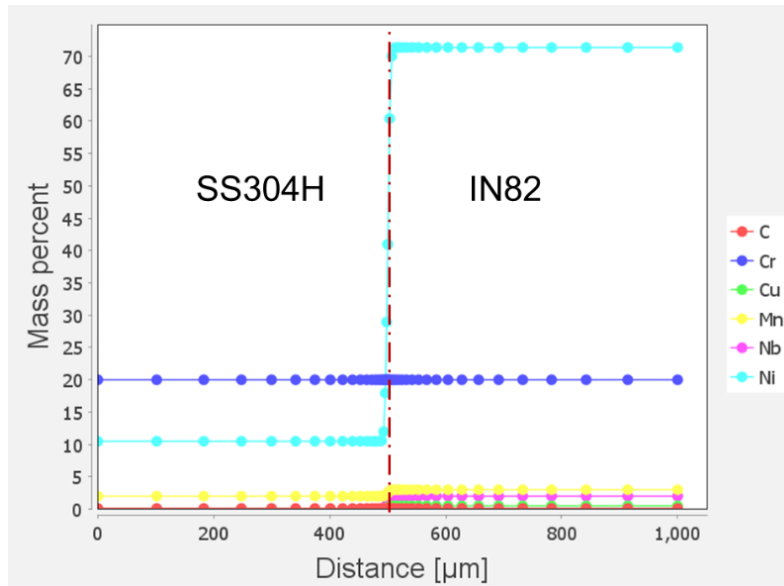
Figure 160. Initial chemical composition profile (before simulation)

The model results show a small interdiffusion region of ~30 µm after 1 day at the cold side service temperature. Carbon content is very low compared to the other alloying elements. Thus, it is shown separately in Figure 161(b). The carbon composition profile potentially suggests carbon depletion occurring in the steel side due to diffusion into the nickel side (the interface is at 500 µm).
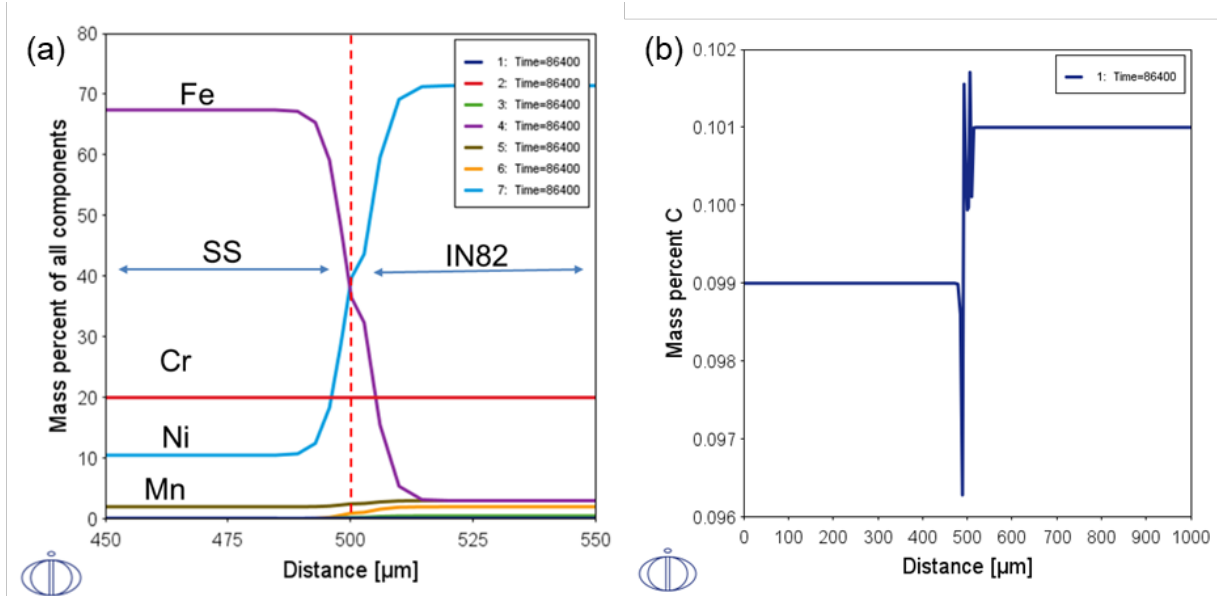
Figure 161. DICTRA simulation result for SS304h/IN82 diffusion couple after 1 day at 550°C, (a) chemical composition profile after simulation and (b) carbon composition profile

4.4.1.2 HEA Fillers for Dissimilar Welds

A novel solution was explored to suppress the carbon depletion that occurs in the steel side to avoid formation of the soft carbon denuded zones. A HEA filler was designed based on previous

146

work by the welding center in Colorado School of Mines to serve as a barrier for carbon diffusion from steel to the Ni-based filler in dissimilar welds. The chemical composition of the designed HEA is 25.9Ni-24Fe-29.1Mn-20.8Co-0.15C in wt% (25Ni-24.3Fe-30Mn-20Co-0.7C at%). This composition was selected to produce a HEA that will not form detrimental phases in the case of diffusion of carbon or other elements from the steel side into the HEA. The alloy can contain up to 0.15 wt.% of carbon while maintaining 100% FCC phase, as shown Figure 162 and Figure 163.
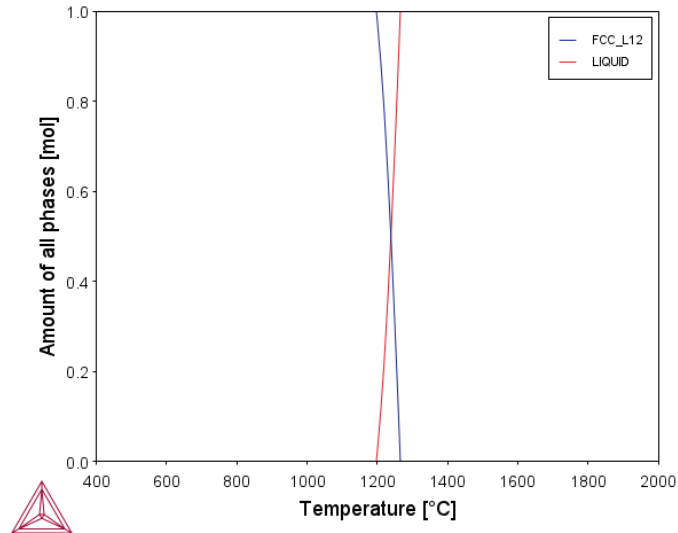
Figure 162. The equilibrium phase fraction of the designed HEA showing 100% FCC
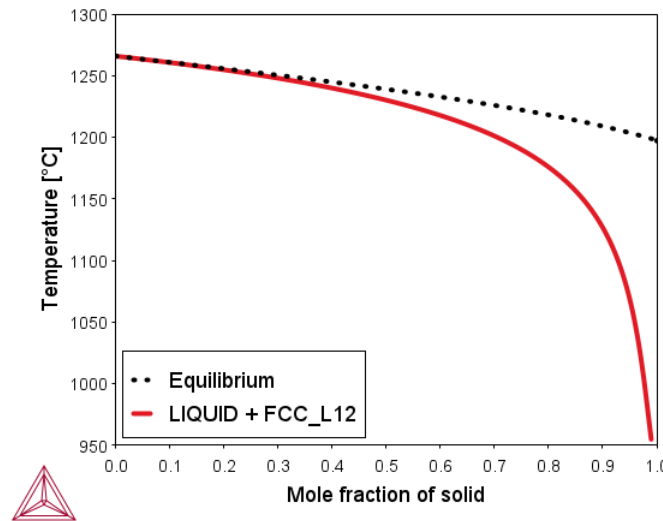
Figure 163. Scheil solidification diagram for the designed HEA showing 100% FCC phase upon the entire solidification range

The initial chemical composition was set up using the same method as described before in SS304H/IN82 simulation run. The HEA side was defined using the 25.9Ni-24Fe-29.1Mn-20.8Co-0.15C (wt%) composition but with excluding carbon from the initial HEA composition, as it was added to demonstrate the ability of the designed HEA to contain carbon without forming detrimental phases. The introduced phases are FCC, BCC, M7C3, and Sigma using the

high entropy alloys database package. This run simulates diffusion for time of 20 hours at 750ºC. Figure 164 shows an interdiffusion region of ~30 μm and there is no presence of the carbon depletion as observed in Figure 161(b) for the conventional dissimilar weld, which indicates this could be a promising solution of suppressing carbon depletion from the steel to the nickel side. Experimental characterization will be performed for proof-of-concept.
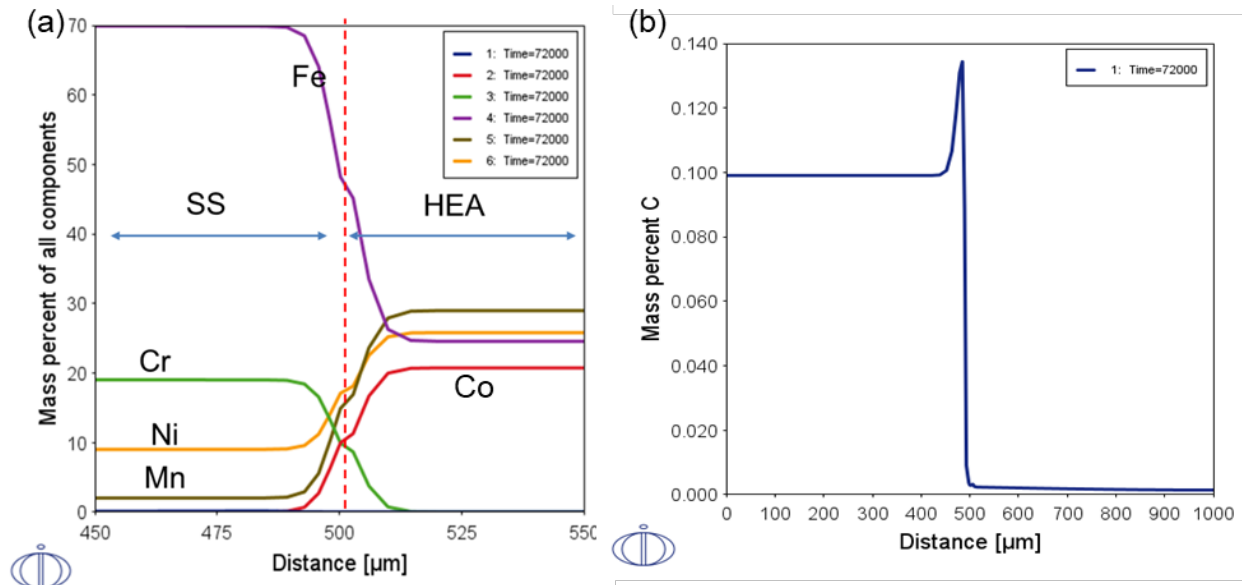
Figure 164. DICTRA simulation result for SS304h/HEA diffusion couple after 20 hr. at 750ºC, (a) chemical composition profile and (b) carbon composition profile.

4.4.1.3 Conclusions for the Diffusion Simulation Study

- In case of Ni-based alloy/steel dissimilar welds, using a HEA layer, 25.9Ni-24Fe-29.1Mn-20.8Co-0.15C (wt%), at the weld interface may suppress carbon diffusion and avoid its associated problems.
- Subsequent dissimilar welding experiments using H282 matching fillers demonstrated that diffusion barriers are not required for these welds.

4.4.2 Joining of Dissimilar Alloys (Milestone 2.5.1)

In this section, the gas tungsten arc welding (GTAW) of 304H SS to either Haynes 282 and Inconel 740H were completed using Haynes 282 and Inconel 82 fillers, respectively. The details for Milestone 2.5.1 are shown in Table 54. These dissimilar weld joints would be representative of joints between the hot (~720°C–760°C) and cold (500°C) components that encompass Haynes 282 or Inconel 740H and 304H SS, respectively.

Table 54. Milestone 2.5.1 Details

Milestone	Description	Metric	Success Value	Assessment Tools
2.5.1: Joining of dissimilar alloys	Using designed dissimilar alloys joining process in M1.5.1, produce weldments with minimum undesired phases to avoid weldability issues such as hot cracking. Dilution level and transverse joint strength should be met.	Dilution level	<25%	The maximum dilution level in the majority region of the weldment should be below 25% based on thermodynamic and kinetic calculations. All tested samples (at least three) should meet target with 10% errors based on standard deviation.
		Transverse joint strength at room temperature compared to the expected strength of the base metal	>80%	Tensile test with DIC method at room and elevated temperatures, and fractography analysis using optical and electron microscopies with EDS mapping. All tested samples (at least three) should meet target with 10% errors based on standard deviation.

4.4.2.1 Welding Experiments

The dissimilar welding (DSW) procedure follows a similar weld procedure as the AM-to-wrought welds, including weld parameters (e.g., heat input) and joint geometry. Figure 165 shows the DSW weld pass double-V geometry and weld symbol for a wrought Haynes 282 to wrought 304H SS joint using overmatching Haynes 282 matching filler. This geometry was selected to minimize weld distortion for cross weld thermomechanical samples. The same weld procedure was applied for Inconel 740H-304H SS DSW but with a higher weld current of 180 amperes, similar to the Inconel 740H L-PBF-to-wrought weld. Inconel 82 weld filler was used as overmatching filler for Inconel 740H to 304H SS weld.
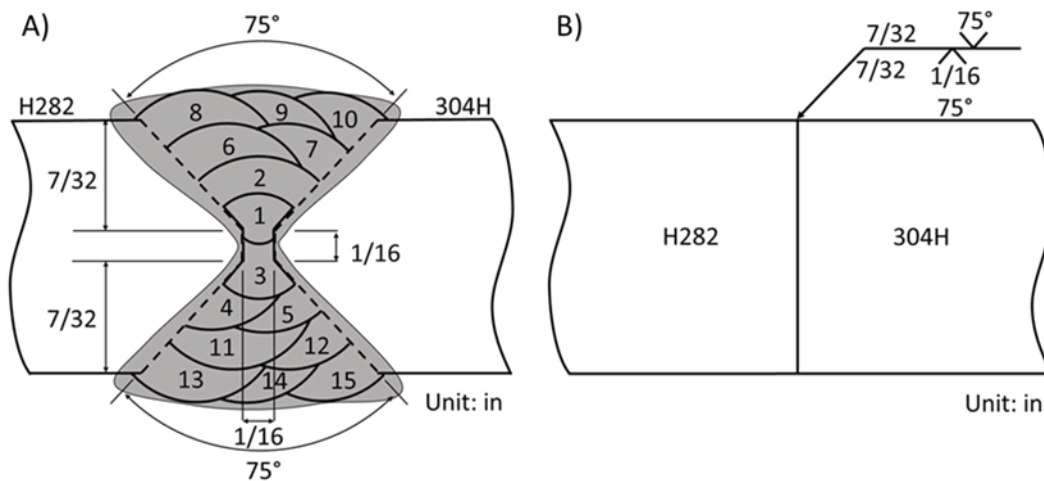
Figure 165. Dissimilar weld (DSW) GTAW geometry (a) details of the double-V groove pass sequence, and (b) weld symbol

4.4.2.2.1 Haynes 282-304H

After welding of Haynes 282 to wrought 304H SS, the Haynes 282 machined samples were heat-treated using HT2 (1140°C/30 min, 899°C/8hrs, and 788°C/8hrs). Post fabrication codes of 304H SS do not require or provide a recommendation of heat treatment but based on post weld heat treatment requirements for Haynes 282, HT2 was applied. Understanding the effect of heat treatment on the dissimilar weld was determined to be critical, particularly for the 304H HAZ/BM and diluted Haynes 282 weld metal regions of the transverse tensile specimens. Therefore, two sets of data (as-welded (AW) and heat-treated (HT)) were analyzed to determine the effect of HT on stress-strain curves. Room temperature and elevated temperature (500°C, 720°C) tensile test load-displacement and stress-strain curves are shown, respectively, in Figure 166(a) and Figure 166(b). Three replicates were completed for each condition, except for the RT-AW samples which included four replicates.

The biggest effect observed in the dissimilar weld test results was the drastic decrease in yield strength after heat treatment for all temperature conditions. A decrease in ductility was observed in the heat-treated samples overall in the RT and 500°C tests, while ductility was slightly better in HT condition at 720°C. Overall, most tests were consistent in both strength and ductility, except for two cases with RT-AW, where two tests resulted in dips in ductility due to weld defects.
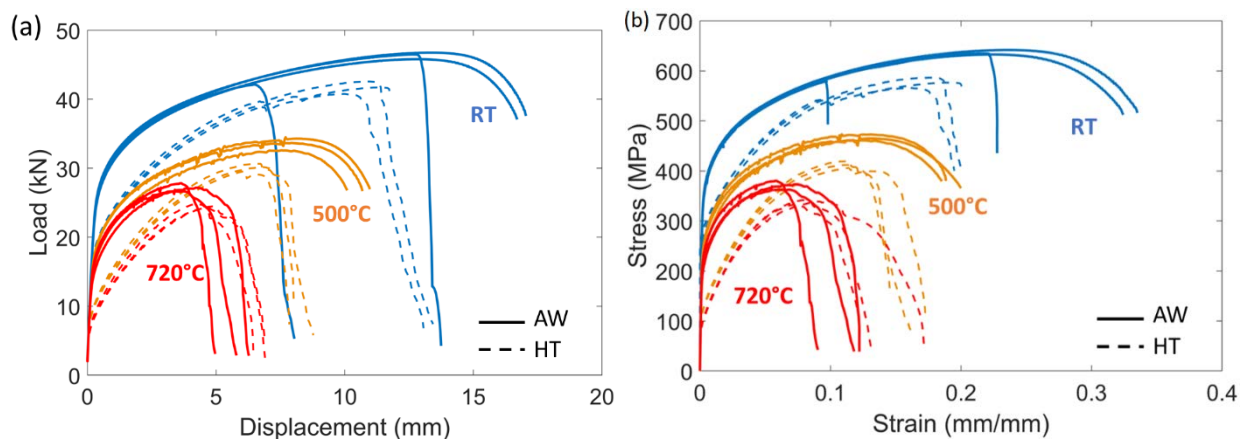
Figure 166. Room temperature (RT) and elevated temperature tensile tests (500°C, 720°C) (a) load-displacement and (b) engineering stress-strain curves

150

Table 55. Tensile Test Properties of all 282-304H DSW Transverse Tensile Samples (AW: as-welded; HT: heat-treated)

ID	Temp. (°C)	0.2% offset Y.S. (MPa)	UTS (MPa)	Total $\varepsilon_{fracture}$	304H $\varepsilon_{fracture}$
AWR1		372	642	0.33	-
AWR2		374	580	0.1	-
AWR3		375	635	0.23	-
AWR4	25	367	633	0.32	-
HTR1		261	576	0.2	-
HTR2		263	586	0.19	-
HTR3		280	566	0.18	-
AWF1		258	468	0.2	0.46
AWF2		240	461	0.185	0.38
AWF3	500	264	473	0.19	0.41
HTF1		122	406	0.16	-
HTF2		123	412	0.14	0.36
HTF3		125	419	0.14	0.35
AWS1		245	380	0.08	0.19
AWS2		229	362	0.095	0.21
AWS3	720	213	373	0.11	0.26
HTS1		99	342	0.11	0.27
HTS2		103	339	0.13	-
HTS3		102	334	0.1	0.25

The yield strength (0.2% offset), ultimate tensile strength (UTS), total strain to fracture ($\varepsilon_{fracture}$), and strain of approximately half the gauge length on the 304H side was estimated and tabulated in Table 55. Due to majority of necking occurring in the 304H SS substrate and relatively low deformation in the Haynes 282 side, the estimation of strain on just the 304H SS side is more than double the total strain. This parameter is collected to compare to baseline strength data of 304H SS.

Digital image correlation (DIC) was used to observe localized deformation of the transverse weld cross section. Figure 167 shows the AW-RT low ductility sample (9% strain to failure), where the strain localization occurs in the FZ, due to potential lack of fusion (weld discontinuity) or cracks (weldability issues) within approximately the half-thickness location of the weld joint. The crack opens from the weld defect and then propagates through the fusion zone closer to the 304H side. This same fracture behavior was seen in the AW-RT sample that failed at 22% strain (as seen in Figure 166). Two AW-HT samples with ductility greater than 30% failed in the 304H SS base metal, as seen in Figure 168.
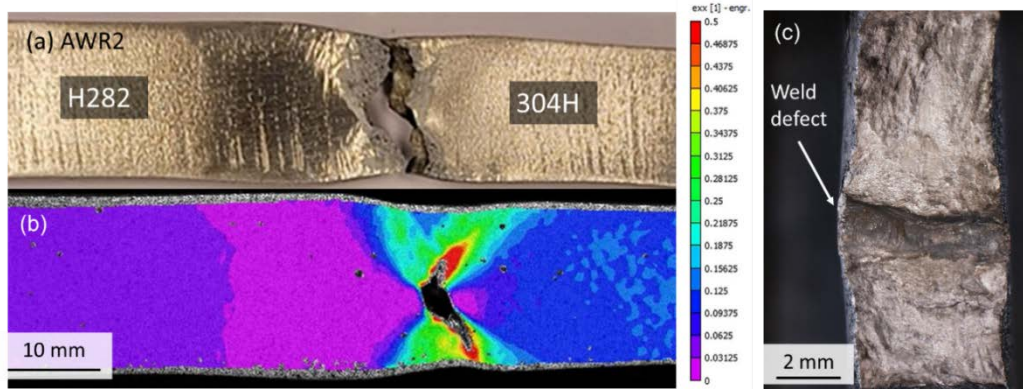
Figure 167. (a) Fracture location in fusion zone, (b) DIC engineering strain map, and (c) fracture surface showing lack of fusion surface of low ductility AW-RT sample (AWR2-9% strain to failure). AWR3 shows similar behavior but with improved ductility to 22%.
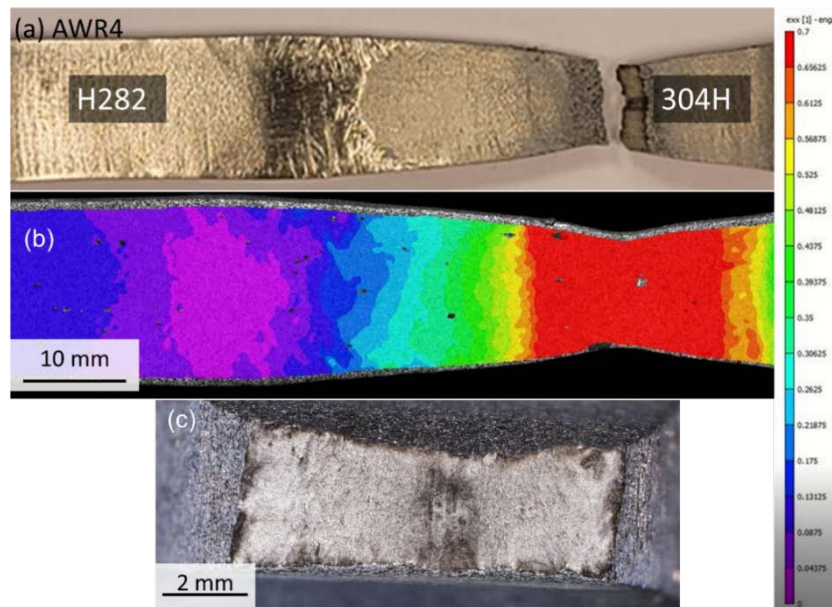
Figure 168. (a) Fracture location in fusion zone, (b) DIC engineering strain map, and (c) fracture surface of ductile 304H substrate in AW-RT sample (AWR4-32% strain to failure). AWR1 shows similar behavior.

Yield strength after HT2 is reduced by ~100 MPa (400 MPa to 300 MPa). The drop in yield strength in the overall sample geometry occurs due to a heat treatment effect, likely the 1140°C solutionizing first step, on strength reduction in the 304H HAZ/BM. Figure 169 provides the DIC engineering strain maps for all HT-RT samples, indicating no plastic strain in the Haynes 282 substrate, little to no plastic strain in the Haynes 282 WM, and most plastic strain (>50%) in the 304H substrate. Fracture behavior has some similarities and differences compared to AW-RT tests. Similarly, HTR1 in Figure 169(a–b) shows an example of crack initiation in the FZ, possibly due to preexisting cracks/lack of fusion developed during welding. However, the crack propagates along the 304H fusion boundary, likely in the partially melted zone (PMZ). The other two duplicates observed in Figure 169(c–f) showed the presence of cracking along 304H SS fusion boundary on both the top and bottom surfaces, but load instability (i.e., necking) occurred first in the 304H HAZ/BM before cracking could continue to propagate along the 304H SS

152

fusion boundary. Aside from the presence of brittle fracture in HTR1 (Figure 169(g)), the overall strain to fracture was similar to HTR2 and HTR3 (~20%).
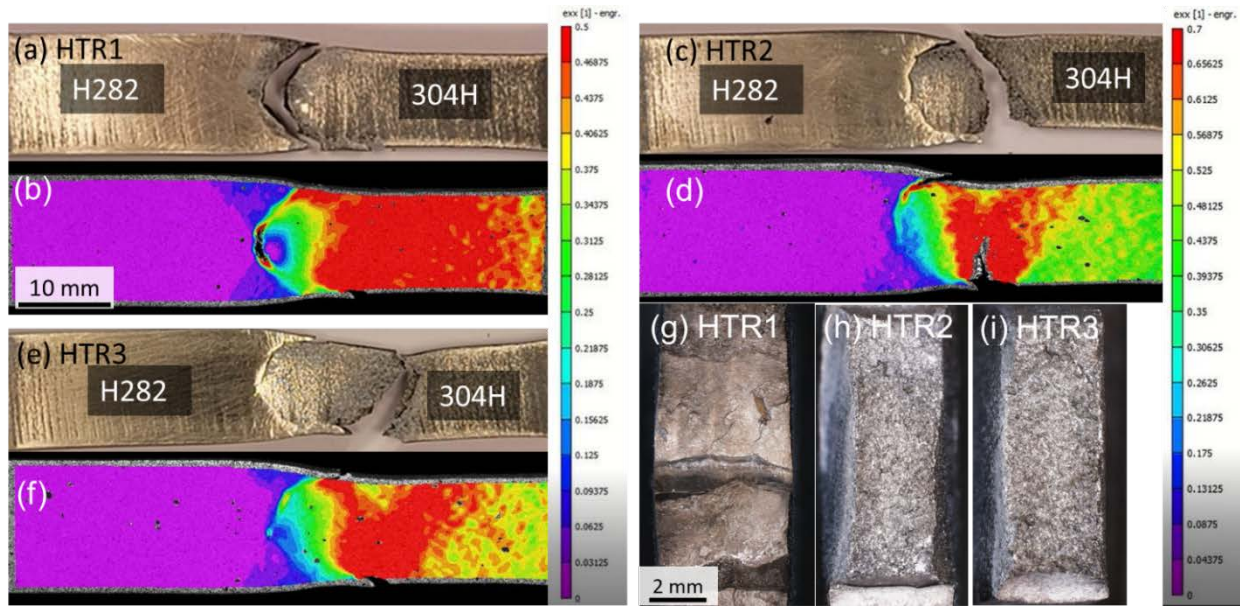
Figure 169. (a–b) HTR1 fracture location DIC engineering strain map, (c–d) HTR2 fracture location DIC engineering strain map, (e–f) HTR3 fracture location DIC engineering strain map, (g) HTR1 fracture surface, (h) HTR2 fracture surface, and (i) HTR3 fracture surface

The elevated temperature tests show more consistency between tests, including both strength and strain. The DIC engineering strain plots of AW and HT 500°C samples in Figure 170 prove necking occurs in the 304H HAZ/BM; however, localized strain accrues in the half thickness location where cracking initiates in AWR2, AWR3, and HTR1. The strain to failure was consistently around ~19% in AW samples and ~16% in HT samples. Necking and subsequent fracture occurs in the 304H HAZ/BM for all 500°C samples, while the HT samples showed some cracking along the edges of the 304H fusion boundary on the top and bottom surfaces (like HT-RT). Very little plastic strain occurs in the Haynes 282 substrate in the AW condition (<5%), while a gradient of plastic strain exists within the FZ going from low to high from the Haynes 282 to the 304H side. After HT, no plastic strain exists on the Haynes 282 side and within the H282 filler and all strain accommodation occurs in the 304H HAZ/BM.
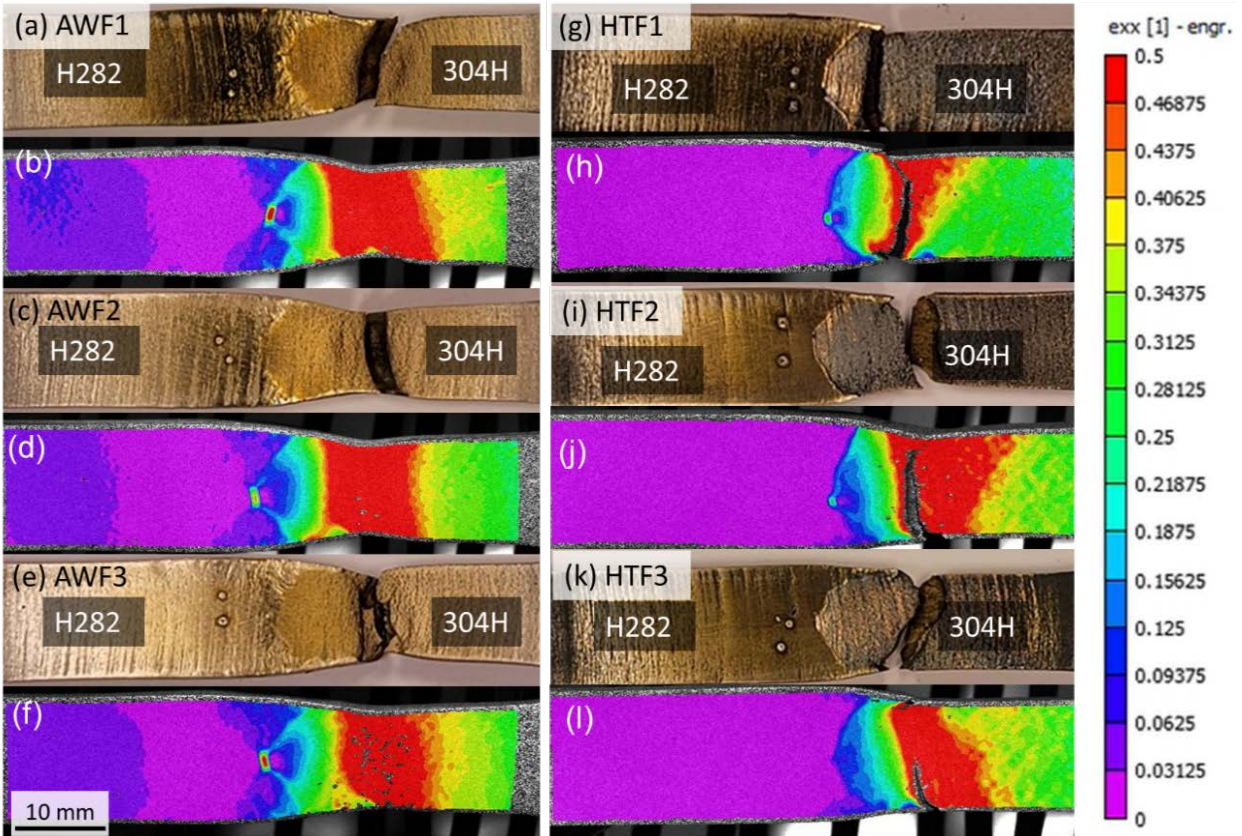
Figure 170. 500°C tensile test AW and HT DIC results (a–b) AWF1 fracture location DIC engineering strain map, (c–d) AWF2 fracture location DIC engineering strain map, (e–f) AWF3 fracture location DIC engineering strain map, (g–h) HTF1 fracture location DIC engineering strain map, (i–j) HTF2 fracture location DIC engineering strain map, and (k–l) HTF3 fracture location DIC engineering strain map

The elevated temperature tensile tests at 720°C contained similar tensile deformation behavior as 500°C but with lower yield strengths and overall ductility. Figure 171 provides further evidence of preferred failure within the 304H SS substrate side, including an example of brittle crack initiation within the half thickness followed by crack propagation along 304H HAZ (see AWS1-Figure 171(a–b)) and crack initiation within the top and bottom surface 304H fusion boundaries followed by necking and final fracture within the 304H HAZ/BM in all other (Figure 171(a–b)). Unlike the RT and 500°C tests, the HT effect on deformation in Haynes 282 substrate at 720°C is negligible. However, the matching H282 weld metal shows improved resistance to deformation after HT, which is expected.
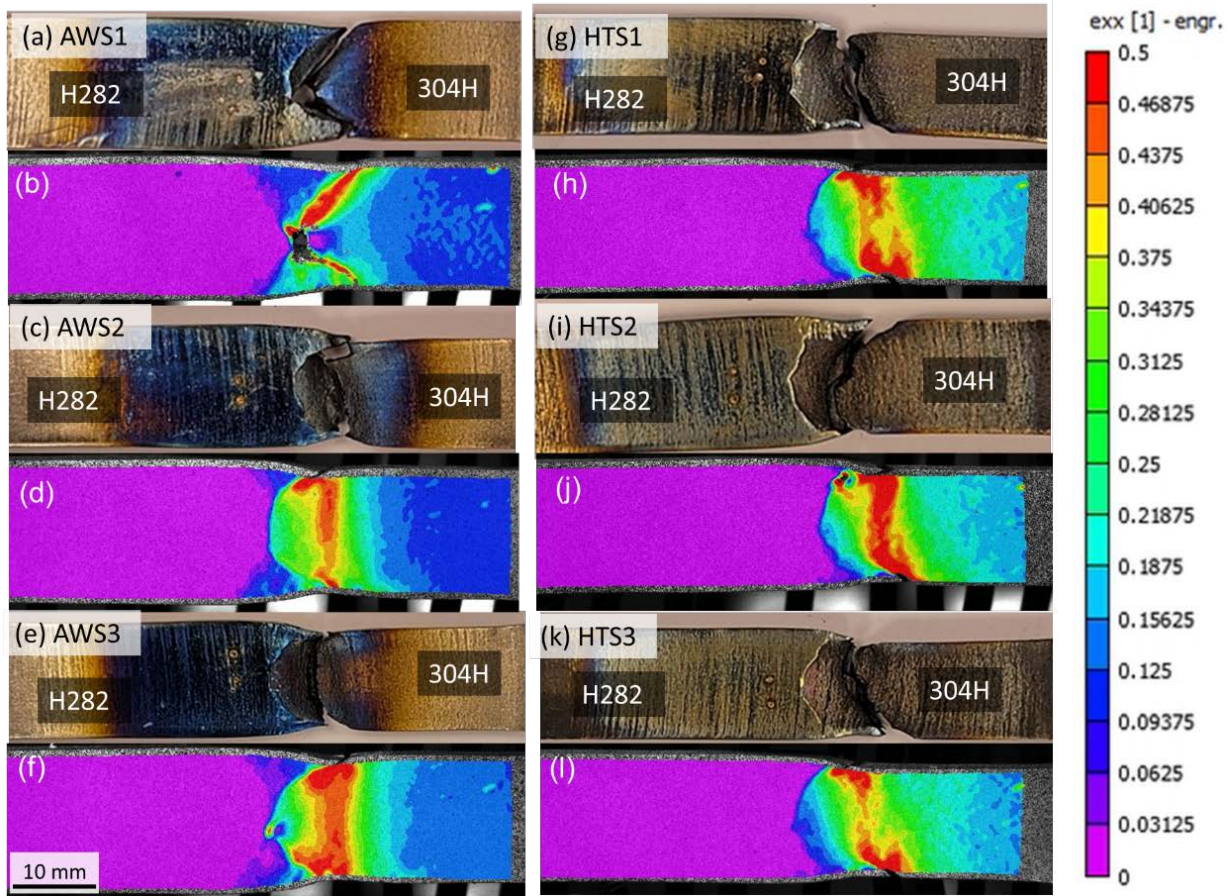
Figure 171. 720°C tensile test AW and HT DIC results (a–b) AWS1 fracture location DIC engineering strain map, (c–d) AWS2 fracture location DIC engineering strain map, (e–f) AWS3 fracture location DIC engineering strain map, (g–h) HTS1 fracture location DIC engineering strain map, (i–j) HTS2 fracture location DIC engineering strain map, and (k–l) HTS3 fracture location DIC engineering strain map

In summary, the Haynes 282-304H SS dissimilar weld using H282 TIG filler provided results of strength greater than 80% of expected 304H SS yield strength, including those with and without HT. While most failure starts in the FZ or 304H SS fusion boundary, load instability in the 304H HAZ/BM dominates, leading to necking and UTS dependency on 304H substrate. Thus, comparing strength properties of the Haynes 282-304H DSW to similar Haynes 282 welds would not be appropriate. While the HT provided the requirement needed for Haynes 282 individually, the concern for strength reduction in the 304H HAZ/BM may require an optimization in HT or the lack thereof to provide an overall improved strength and ductility, especially at 720°C service temperatures. A potential solution to improving ductility, particularly along the 304H fusion boundary, would be deposition of HEA buttering layers prior to deposition of H282 layers to reduce dilution of H282 filler when mixing with the 304H SS side walls and therefore prevent deleterious phases and potential liquation cracking as seen later in Figure 180.

4.4.2.2.2 Inconel 740H to 304H

Dissimilar welding (DSW) of In740H wrought ½-in.-thick plate to 304H SS plate was completed in addition to the Hayne 282-304H DSW. Figure 172 shows load-displacement and stress-strain curves for the thermomechanical tests completed at RT, 500°C, and 720°C. As expected, the

155

yield strength decreased after full solution anneal followed by aging heat treatment, which is limited by the In740H SS HT requirements, although only an aging step is required. Table 56 shows the yield strength, UTS, and strain to fracture. Ductility overall decreases as temperature increases, and the heat treatment increased ductility slightly with yield strength being reduced.
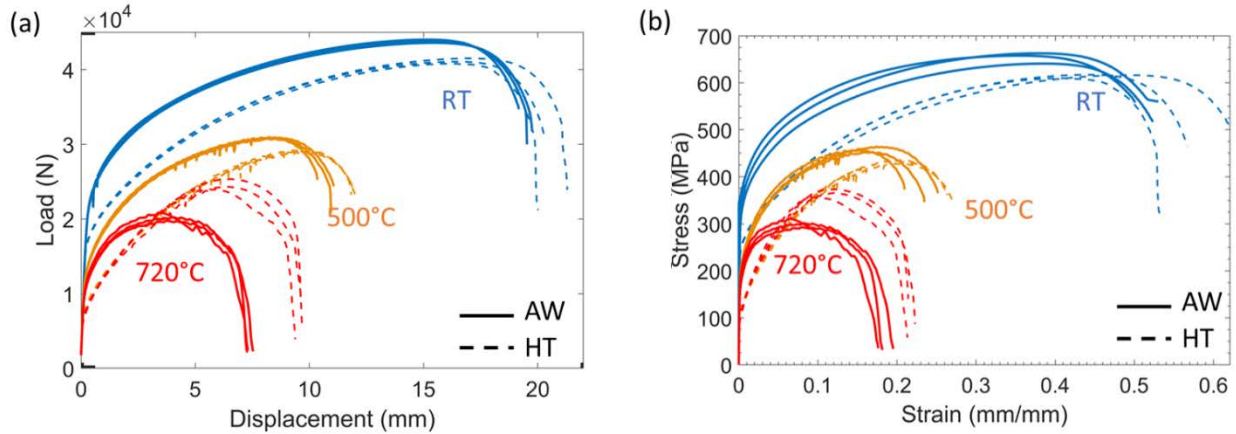
Figure 172. (a) Load-displacement curves and (b) stress-strain curves for IN740H wrought to 304H SS wrought welds in AW and HT conditions at RT, 500°C, and 720°C

Table 56. Yield Strength, UTS, and Total Elongation of IN740H-304H DSW Transverse Samples

ID	Temp. (°C)	0.2% offset Y.S. (MPa)	Avg. Y.S.	UTS (MPa)	Avg. UTS	Total $\varepsilon_{fracture}$	Avg. $\varepsilon_{fracture}$
ART2		333		658		0.5	
ART8		340	333±8	663	654±12	0.53	0.52± 0.02
ART14	25	325		641		0.52	
HTRT3		250		616		0.62	
HTRT9		249	250± 1	617	614± 4	0.57	0.57±0.05
HTRT15		251		610		0.53	
A5004		208		464		0.25	
A50010		210	206±5	456	457±6	0.21	0.23± 0.02
A50016	500	200		452		0.23	
HT5005		116		436		0.26	
HT50011		116	116±1	434	433±4	0.26	0.26±0.01
HT50017		115		428		0.27	
A7206		201		311		0.18	
A72012		191	191±11	301	301±10	0.18	0.19± 0.01
A72018	720	180		292		0.2	
HT7207		105		357		0.21	
HT72013		109	106±3	365	365±9	0.22	0.21± 0.01
HT72019		103		374		0.21	
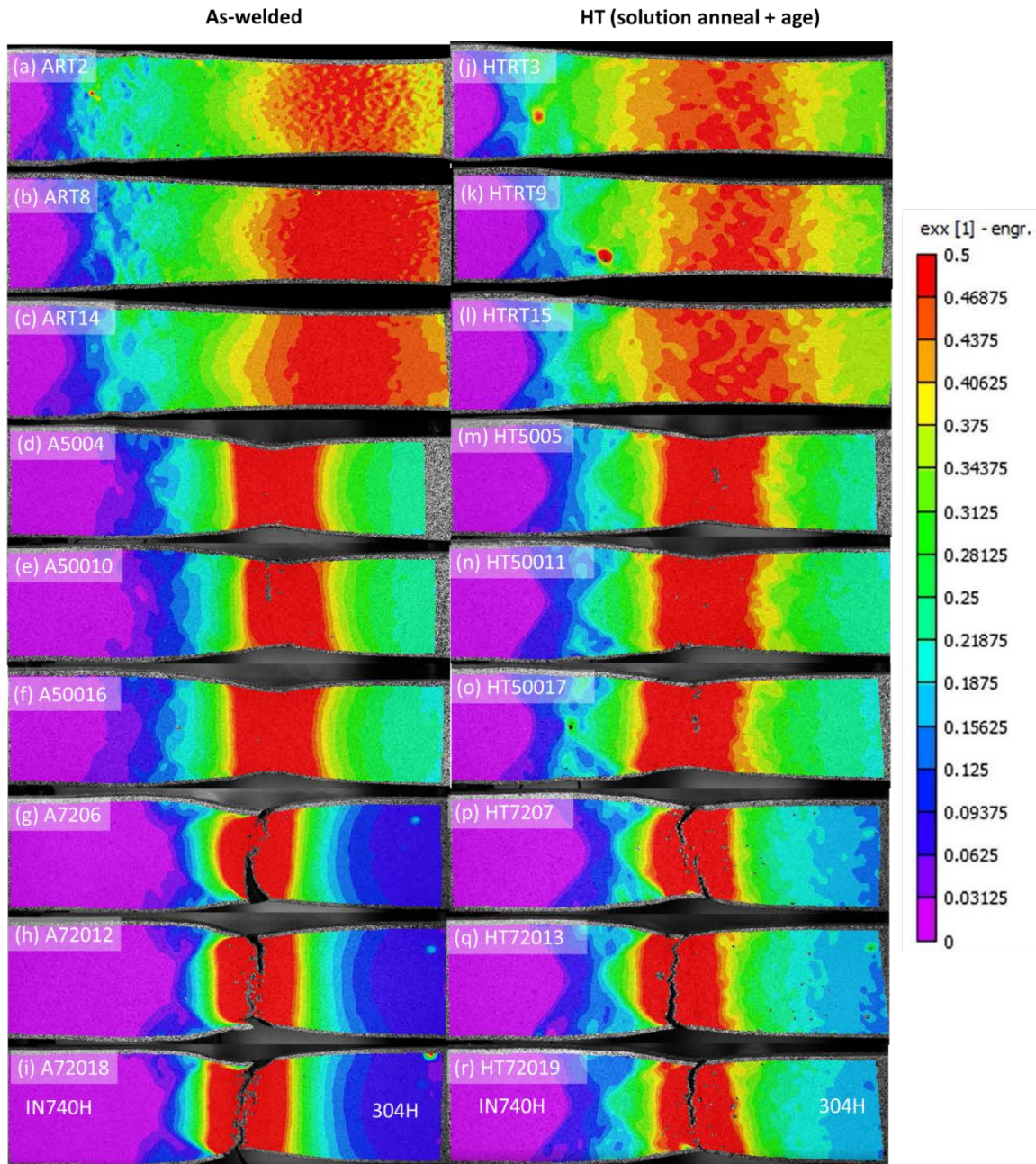
Figure 173. DIC strain results of In740H wrought to 304H SS wrought weld (a) ART2, (b) ART8, (c) ART14, (d) A5004, (e) A50010, (f) A50016, (g) A7206, (h) A72012, (i) A72018, (j) HTRT3, (k) HTRT9, (l) HTRT15, (m) HT5005, (n) HT50011, (o) HT50017, (p) HT7207, (q) HT72013, and (r) HT72019

The DIC maps for all the thermomechanical tests are shown in Figure 173, which includes the as-welded conditions on the left and heat-treated conditions on the right. All the samples failed in the 304H BM or HAZ. Similarly to the Haynes 282-304H DSW results, the fracture location gets closer to the FZ within the 304H HAZ as temperature increases. The 304H HAZ may be the weakest location at a 720°C testing temperature. However, these properties meet the expected properties for 304H wrought product and are considered passing because none of the samples failed in the FZ. There are a couple of exceptions, where small microcracks appear to open along the FZ boundary on the 304H side, which corresponds to the red dots within HTRT3 and HTRT9

157

samples (see Figure 173(j–k)). The reduction in ductility at 720°C can be theorized to be due to more localized strain within the HAZ instead of a broader strain distribution within the HAZ and BM, such as that seen with the RT tests. The HAZ, being a region for precipitate dissolution during welding, may allow for precipitation to take place during reheating. 720°C is a prime temperature for $Cr_{23}C_6$ precipitation and may be a high enough temperature to allow for fresh precipitates to nucleate during deformation, which may impede dislocation motion and annihilation. Intergranular $Cr_{23}C_6$ and coarser grains can allow for less tortuous grain boundaries to reduce ductility overall.

4.4.2.3 Metallurgical Characterization of Welds

4.4.2.3.1 Haynes 282 to 304H

For all dissimilar welds in this project, the dilution level needs to be maintained lower than 25% to avoid negative effects on the corrosion resistance of Ni-base alloys. One of the main objectives of this task is determine the average dilution level specifically in the weld region between the SS 304H and the overmatching H282 welding filler. To calculate the average dilution, the following equation was used [33,34]:

$$D = (C_t - C_{fm}) / (C_{bm} - C_{fm}) \qquad \text{(Eq. 1)}$$

where C_t is the concentration of an element in the transient region (EDS instantaneous reading), and C_{fm} and C_{bm} are the concentration of that element in the filler metal and base metal, respectively. For all the calculated dilution values reported here, the following compositions were used for the filler and base metals in Table 57.

Table 57. Nominal Chemical Compositions Used for Dilution Calculations [12,13]

	Al	C	Co	Cr	Cu	Fe	Mn	Mo	Si	Ti	Ni
H282 filler	1.5	0.063	10.21	19.32	0.02	0.97	0.09	8.48	0.07	2.24	56.93
H282 wrought	1.5	0.06	10	20	-	1.5	0.3	8.5	0.15	2.1	57
SS 304H Wrought	-	0.1	-	20	-	68.61	2	-	0.75	-	10.5

For SS304H and H282 dissimilar welds, the dilution level was calculated as an average for the dilution of the main elements (Fe, Ni, Co, and Mo). Cr was not considered in the calculation since both alloys have very similar Cr content, so no dilution of Cr was expected nor observed for that element.

4.4.2.3.1.1 As-Welded Microstructure

The calculated average dilution level for this sample is ~9% in the weld zone adjacent to the SS304H, which confirms passing the <25% dilution level criteria for the dissimilar welds. The microstructure of the filler metal appeared as a dendritic structure in the as welded condition, as shown in the top left corner of Figure 174(b). It was difficult to show the SS304H microstructure, as it did not significantly respond to this etching reagent.
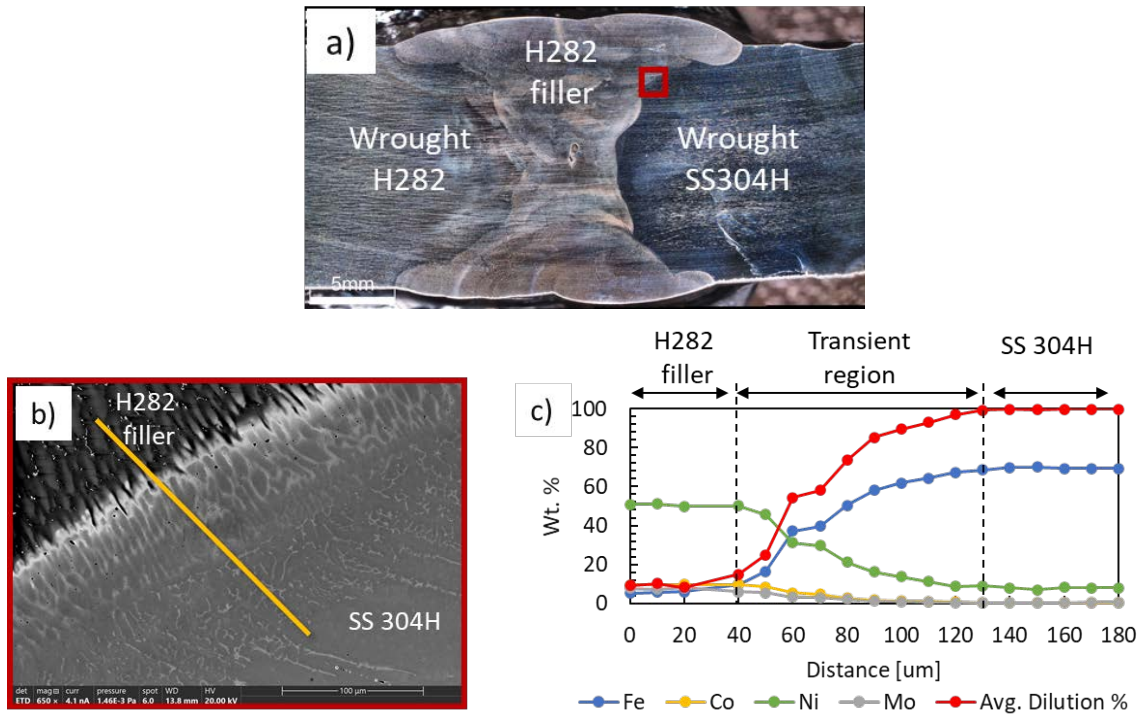
Figure 174. (a) Macrograph of dissimilar weld between wrought H282 to SS304H in as-welded condition. (b) SEM image of the filler/SS304H interface. (c) EDS line scan showing the average dilution level in the transient region and weld zone adjacent to the SS304H
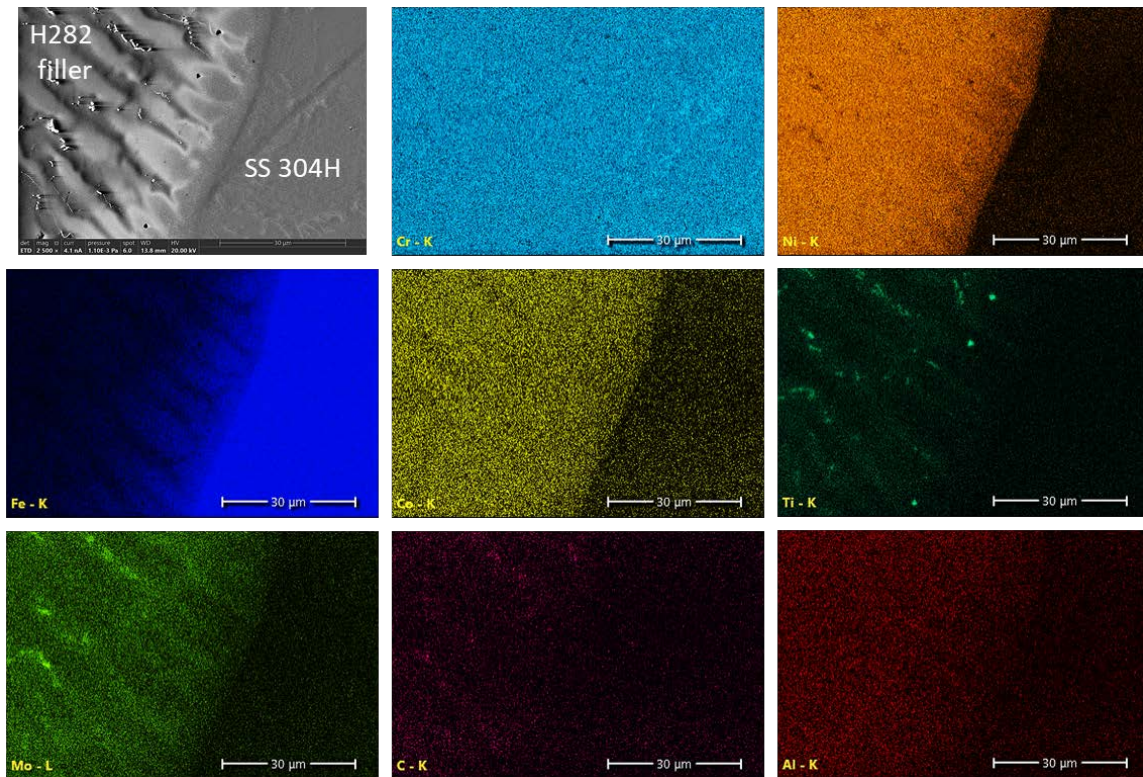
Figure 175. EDS elemental maps for the transient region between H282 filler and SS304H in the as welded condition

159

Figure 175 shows finer carbide branches and particles at the interface between the SS304H and H282 filler in the as welded stage compared to the coarse ones after aging, as seen in the same magnification in Figure 179.

A void was observed in the weld zone near the SS304H side, as depicted in Figure 176. A narrow crack can be seen branching from the upper and lower ends of the void. Fe mixing with the H282 filler may potentially have an impact on formation of such a defect. Moreover, Al oxide is seen at the edges around the void, which may have formed after exposing the void surface (forming the void).
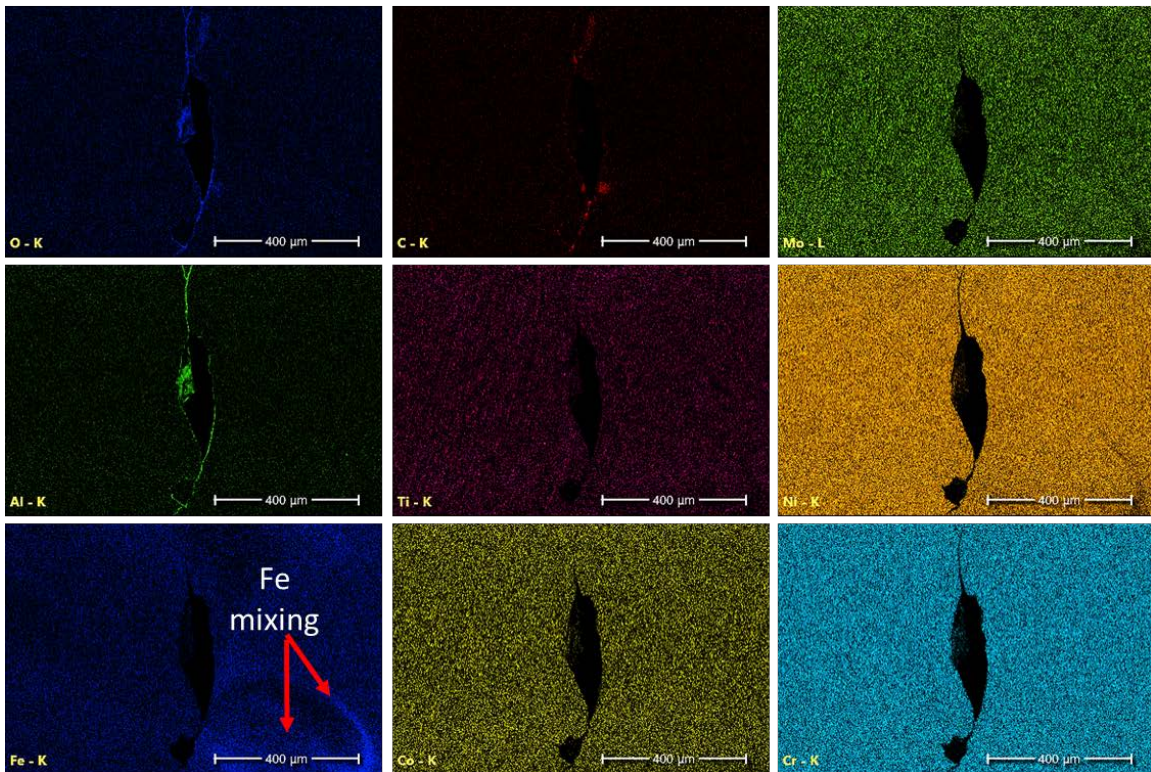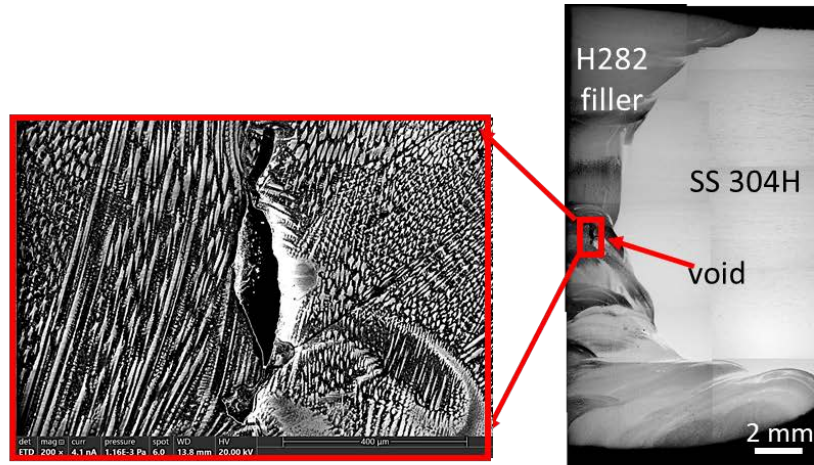
Figure 176. EDS elemental maps of a void located in the weld zone in the dissimilar weld between wrought H282 to SS304H in as welded condition

4.4.2.3.1.2 Aged Microstructure

The EDS line scan in Figure 177(c) demonstrates that the average dilution level goes to ~14% in the weld region adjacent to the SS304H, where the highest dilution level is expected. This finding indicates that the dilution level in this dissimilar weld is maintained lower than 25%, which is the required level for this task's passing criteria. In addition, Figure 177(e) shows chemical composition matching between the wrought H282 and the filler metal, indicating the diminished dilution level on that side of the weld.
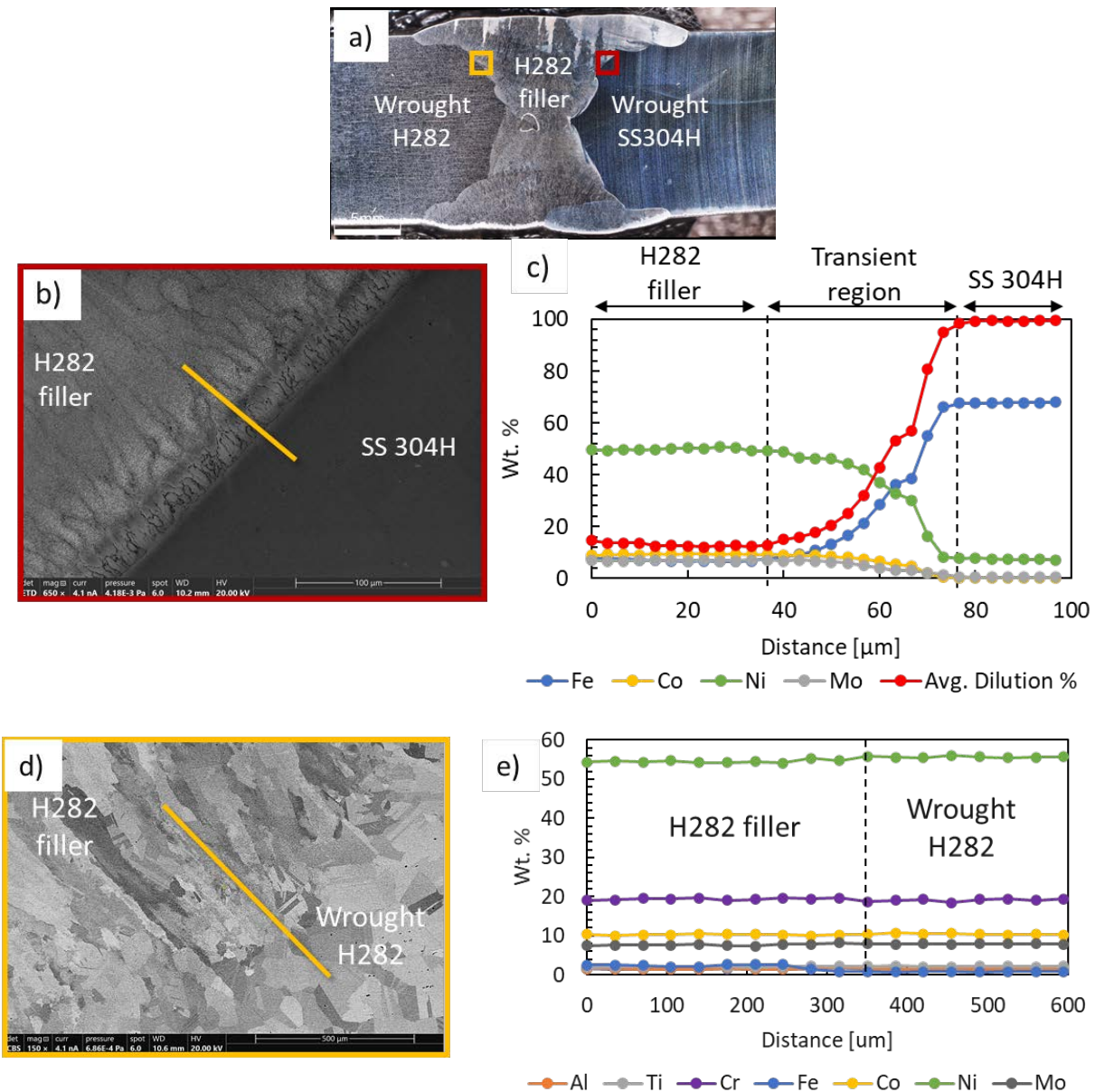
Figure 177. (a) Macrograph of dissimilar weld between wrought H282 to SS304H in fully aged condition. (b, d) SEM images of the filler/SS304H side and filler/wrought H282 side interfaces, respectively. (c) EDS line scan showing the average dilution level in the transient region and weld zone adjacent to the SS304H side. (e) Matching chemical composition between the filler and wrought H282 side

161

The microstructure of each side is shown in Figure 178 with different magnifications. Figure 178(a, b) show the equiaxed grains in SS 304H base metal. Relatively coarse Cr-rich carbides were observed at the GBs of SS304H. As observed in the AM to wrought welds before, coarse columnar grains were observed in the filler metal and equiaxed grains were observed in the wrought base metal.
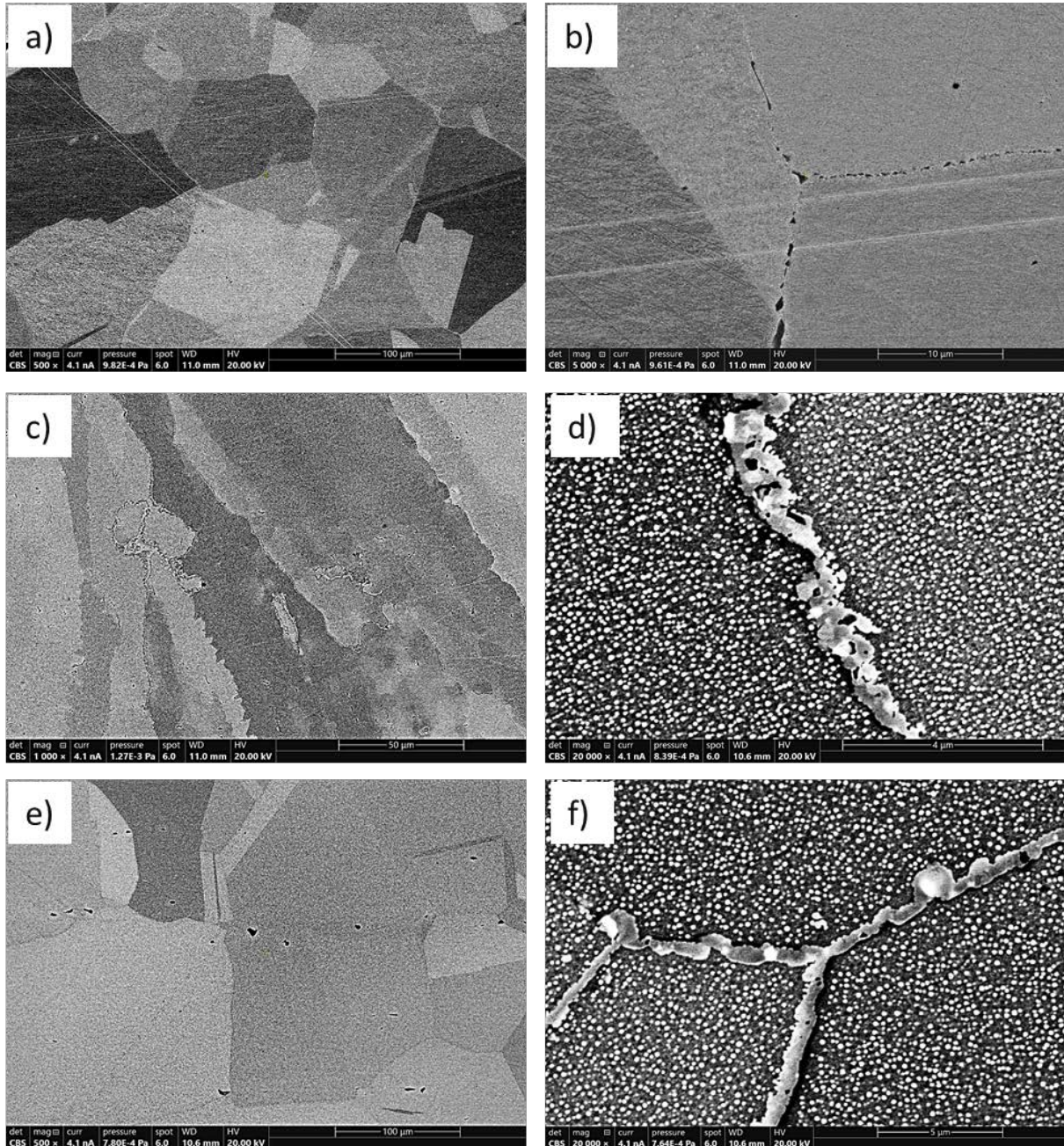
Figure 178. SEM images of the microstructure of fully aged of dissimilar weld between wrought H282 and SS304H taken in the base metal SS304H side (a, b), welding filler (c, d), and base metal wrought H282 side (e, f)

162
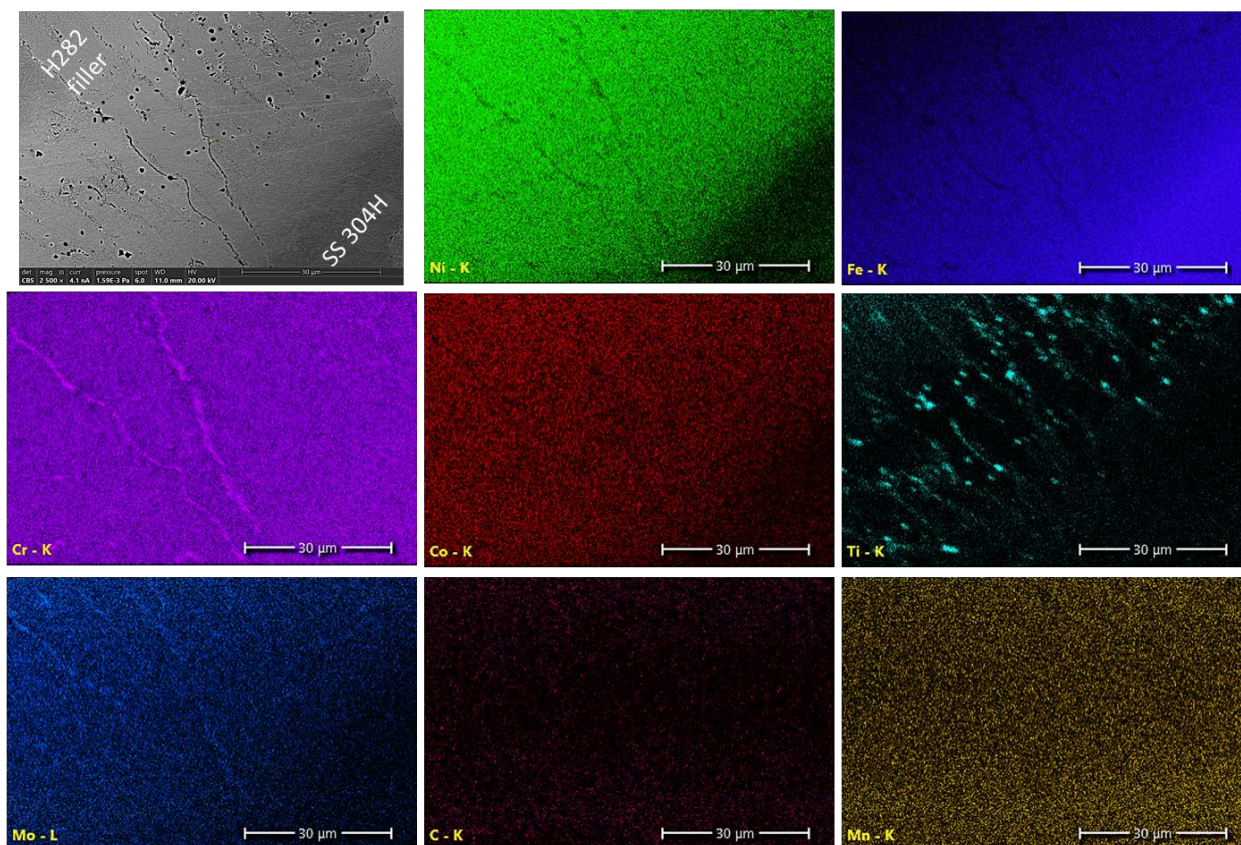
Figure 179. EDS elemental maps for the transient region between H282 filler and SS304H in the aged weld sample

Figure 179 shows EDS maps at the interface between the H282 filler metal and SS304H. long branches of Cr and Mo-rich carbides were observed in the transient region, in addition to large number of Ti- rich carbide particles. It is likely that these carbides coarsened during the aging heat treatment of the samples after welding. The effect of these carbide particles on the failure behavior is still under investigation.

A ~1-mm-long crack was observed at the interface between the H282 filler metal and SS304H in the fully aged sample, as shown in Figure 180. In the SS 304H side, there are Cr-rich carbides particles near the crack location, in addition to some P enrichment. On the other hand, Ti-rich particles were observed in the H282 filler side. The crack gap appeared to be enriched in Al-oxides, which may have formed during cooling down from welding or during the heat treatment after welding. The mechanism and reason of forming this crack is still under investigation.
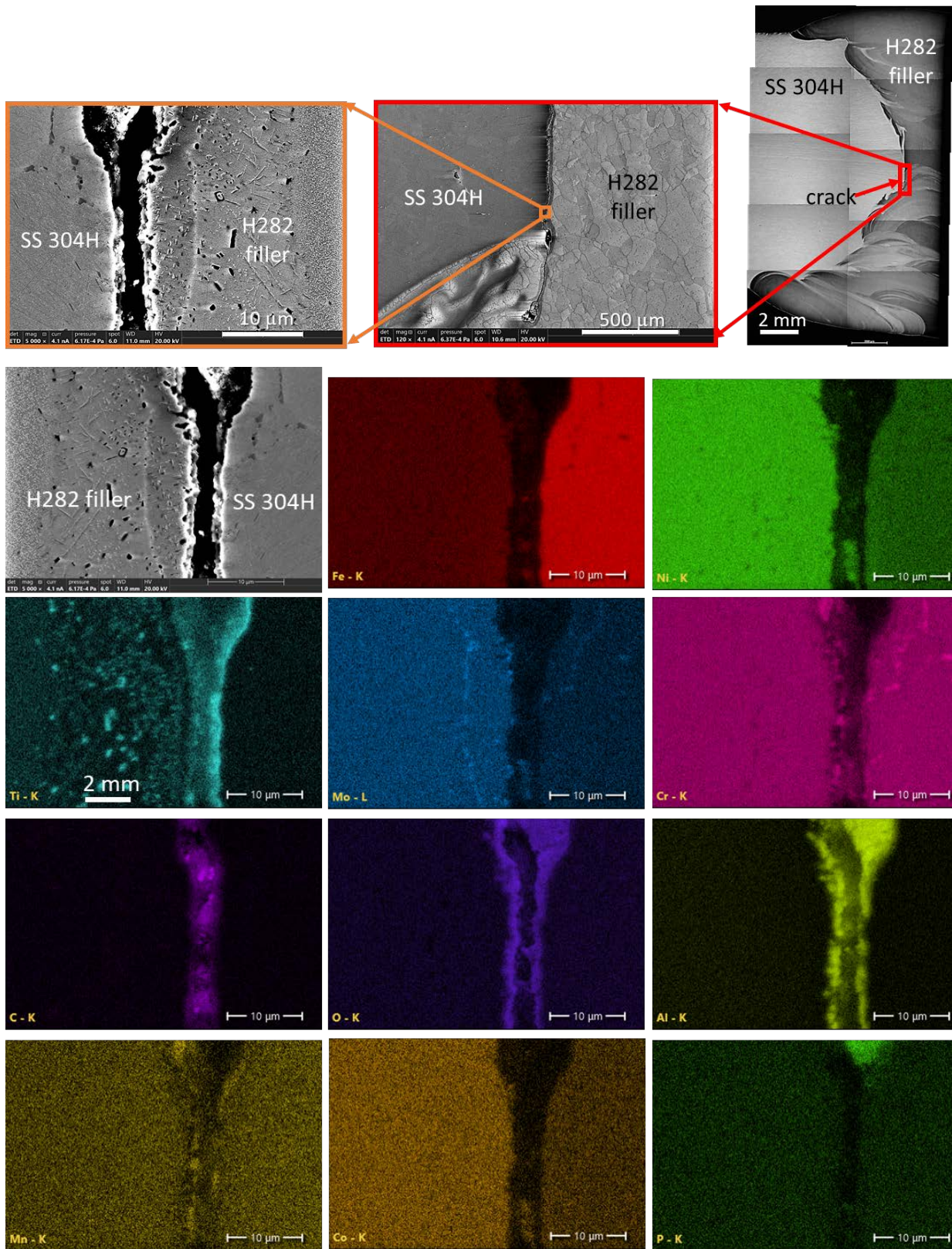
Figure 180. OM and SEM images and EDS elemental maps showing the different distributions for alloying elements around the crack between the H282 filler and SS 304H

From the DIC results discussed above, Figure 181(b) shows that there is very low strain in the H282 side of the as-welded sample, while there is almost no strain in the H282 aged sample (Figure 181(d)). To reveal the effect of the post weld aging heat treatment on the dissimilar weld between H282 and SS304H, the hardness line profiles were measured in the as-welded and fully aged conditions, as shown in Figure 181(e). It is observed that the aging heat treatment increased the hardness of H282 by ~100HV, while it decreased the SS304H hardness by ~40HV. Therefore, heat treatment led to increasing the severity of hardness difference between the SS304h and H282 weld metal. This can be demonstrated on the strain localization in the soft SS304H side after aging as shown in the DIC maps. The SS304H softening due to heat treatment is most likely related to grain coarsening in the aged samples, as the heat treatment is designed for the age hardening of H282, not the stainless steel. However, the tensile samples still passed the baseline of 80% of the wrought metal strength.
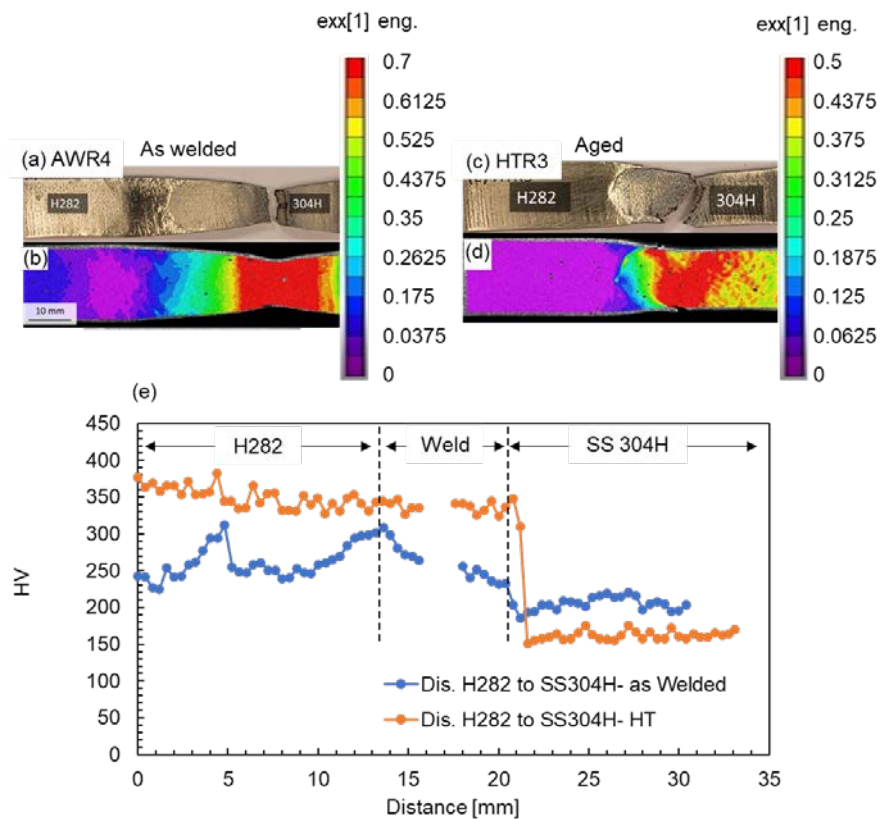
Figure 181. (a, c) Macrographs for H282/SS304H dissimilar weld samples in the as welded and aged (labeled HT) conditions, respectively, (b, d) DIC maps for engineering strain just before fracture in RT tensile testing, (e) hardness line profile for the as welded and fully aged (HT) samples

4.4.2.3.2   Inconel 740H to 304H SS

Similarly to the Haynes 282 and 304H SS DSW, the average dilution level at the interface between the Inconel 740H to 304H SS filler, Inconel 82, was calculated using the same equation 1 above. The following chemical composition of IN 82 filler and 304H SS in Table 58 are used for filler and base metal compositions, respectively.

165

Table 58. Nominal Chemical Compositions Used for Dilution Calculations Taken From Vendors' Material Data Sheets

Wt.%	Cr	Co	Al	Ti	Nb	Fe	C	Mn	Mo	Si	Cu	Ni
IN82 F	20.355	0.017	0.013	0.353	2.3	0.3	0.035	3.128	0.025	0.018	0.005	73.4
SS304H	18.41	0.2	0.007	0.004	0.015	70.314	0.05	1.47	0.5	0.44	0.41	8.07

The dilution level was calculated by averaging the dilution values of the two elements Fe and Ni. Cr was not considered in the calculation because both alloys have similar Cr content. The EDS line scan in Figure 182(a) and (c) demonstrates that the average dilution level goes to ~15.5% at the left end of the scan line in the weld region adjacent to the SS304H, where the highest dilution level is expected. This finding indicates that the dilution level in this dissimilar weld is maintained lower than 25%, which is the required level for this task's passing criteria. The observed spikes in dilution lines are correlated to the EDS scan line crossing a grain boundary or a secondary phase particle that is enriched in Fe and Nb. It is worth mentioning that there were considerable discrepancies between the EDS readings for the chemical composition of the base metal and the nominal composition from the materials data sheets. This difference in chemical composition probably originates from using a different technique than EDS (such as OES) to determine the nominal composition by the material producer. The dilution calculation was affected by these discrepancies (probably by ±3%–5%), and that is why the dilution values go slightly over 100% in the base metal side. However, the calculations still give a valid estimation of the expected maximum dilution adjacent to the base metal. Moreover, we are running more EDS scans at the center of the weld region (further away from the base metal) to capture the composition of the filler with minimum to no dilution to be used as the filler composition in Equation (1) for more accurate dilution calculation.
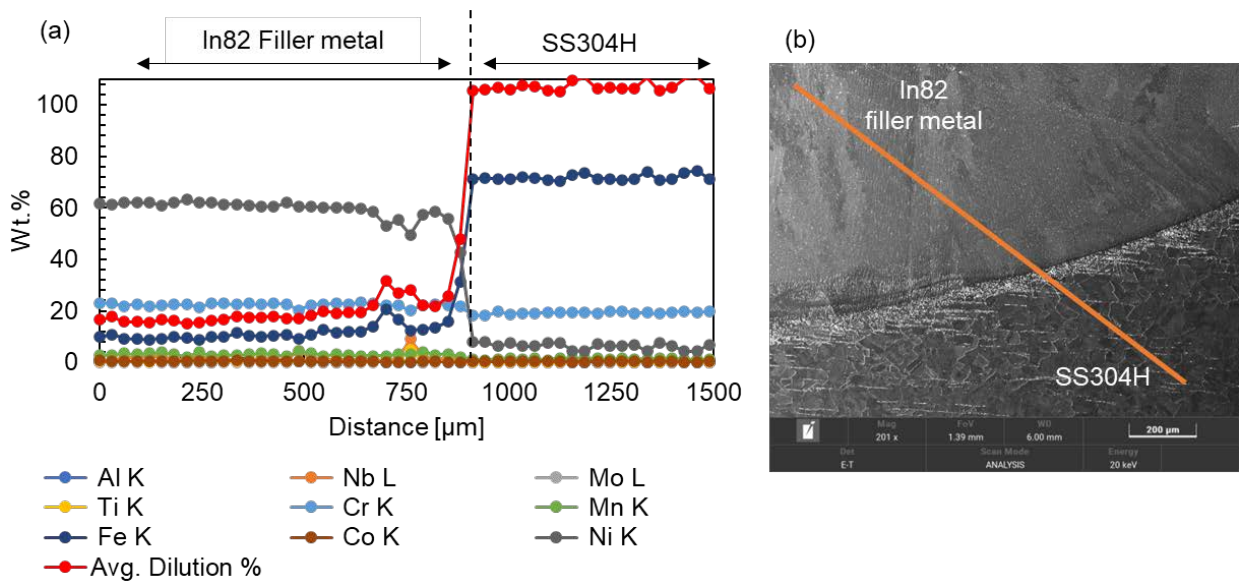
Figure 182. (a) EDS line scan with the calculated average dilution level in the In82 filler weld region adjacent the SS304H (b) SEM image showing the location of the EDS line

Figure 183 shows the effect of post-weld aging on the microstructure of the base metal in IN740H and SS304H base metal as well as the fusion zone. In general, significant grain coarsening can be observed after aging in all regions (d, e, f). Moreover, the interdendritic segregation observed in the as welded fusion zone (b) was dissolved after aging (e). The high magnification images showed coarser and more continuous GB precipitates in the IN740H base metal (g) compared to the fusion zone (h).
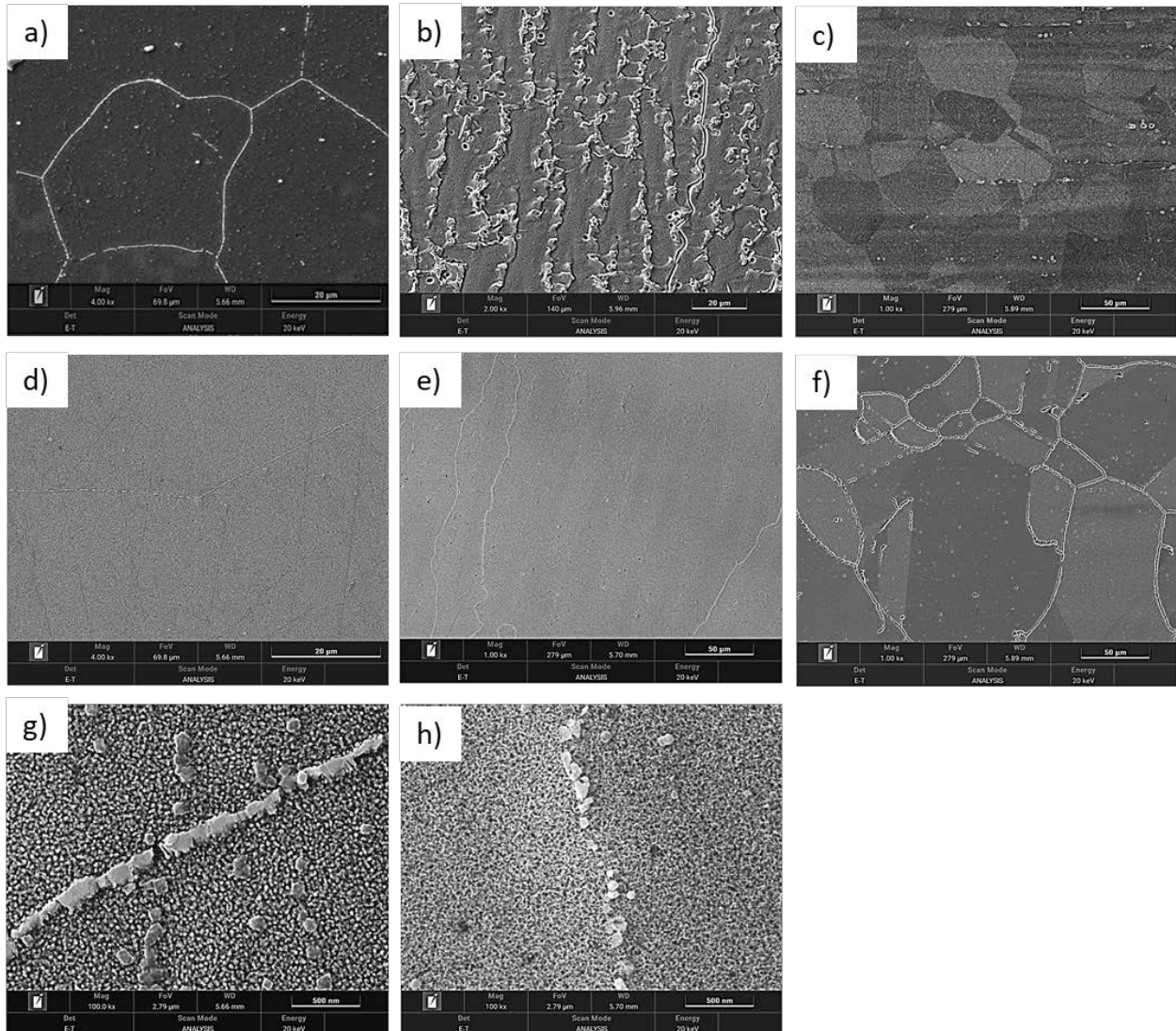
Figure 183. SEM images for the microstructure of as welded (a) IN740H base metal, (b) fusion zone, and (c) SS304H base metal, aged (d) IN740H base metal, (e) fusion zone, and (f) SS304H base metal, and (g, h) high magnification images for second phase precipitates in aged IN740H base metal and fusion zone, respectively

The interdendritic segregation in the as welded fusion zone was analyzed via EDS maps, as shown in Figure 184. Nb is the main element to segregate into the interdendritic regions followed by Mo. In addition, Ti and Mo enriched particles were observed. Excessive Nb segregation and formation of low melting point phases may lead to wider solidification range and increased

susceptibility to solidification cracking. However, no signs of solidification cracking were noticed in any weld sample.
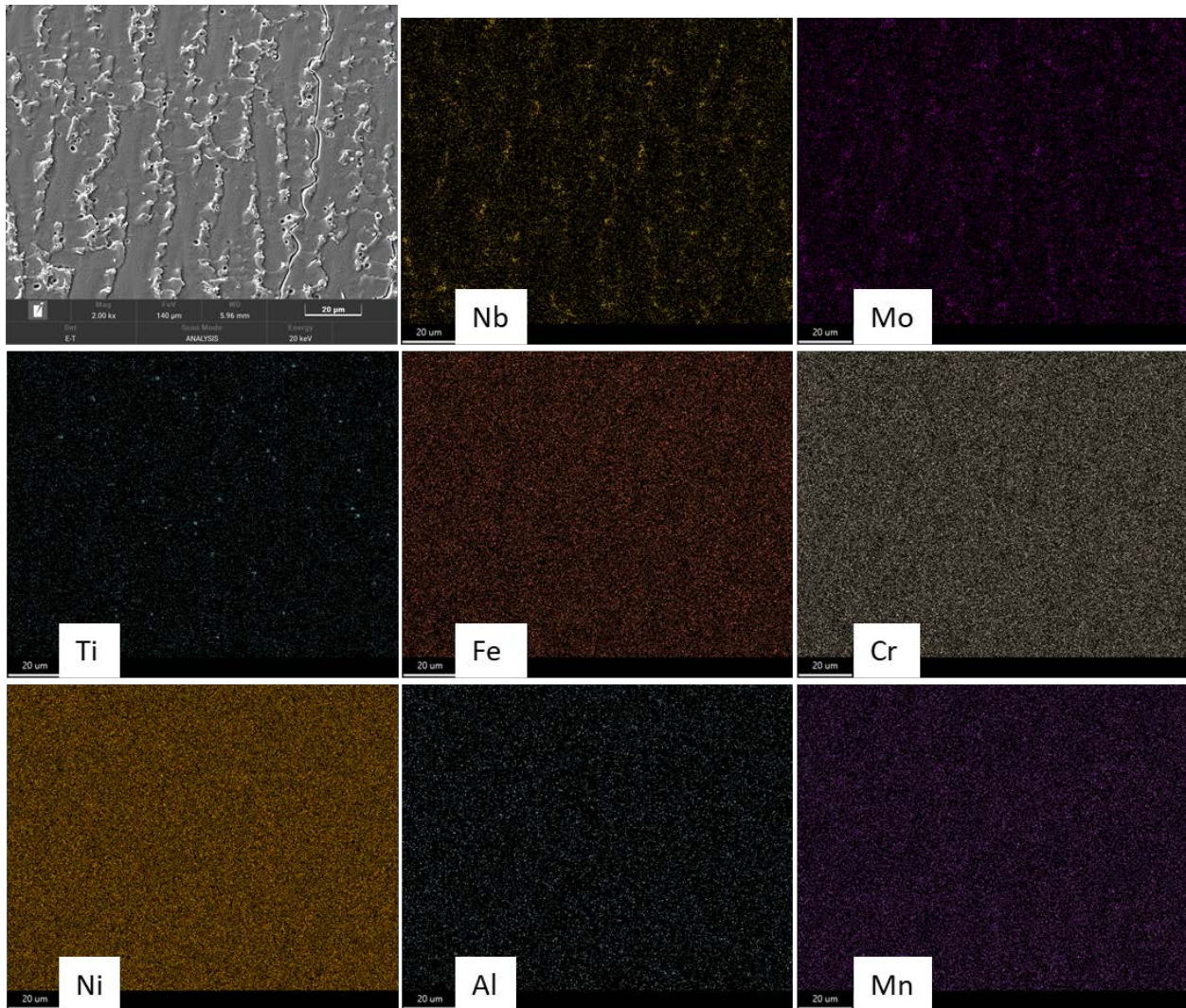
Figure 184. EDS elemental maps for as welded fusion zone showing segregation in the interdendritic regions

Figure 185(a) shows the hardness profile of the weld cross sections from the aged and as-welded conditions. In the In740H side, the hardness is generally higher than the other regions. Because In740H is welded in the aged condition, the base metal hardness did not change much after the heat treatment. HAZ hardness increases after aging treatment, which is likely attributed to re-precipitating gamma prime particles via post-weld aging after it was dissolved in the HAZ upon going through the weld thermal history.

On the left side of the graph, a rather interesting observation is seen in the softer SS304H side. The HAZ shows relatively higher hardness than the base metal in the as welded condition. This explains the observed strain localization occurred in the softer base metal toward the left edge of Figure 185(b). On the other hand, the HAZ in SS304H is softened upon post-weld aging likely

due to grain coarsening, and thus, strain accumulation shifted toward the SS304 HAZ as shown in Figure 185(c).
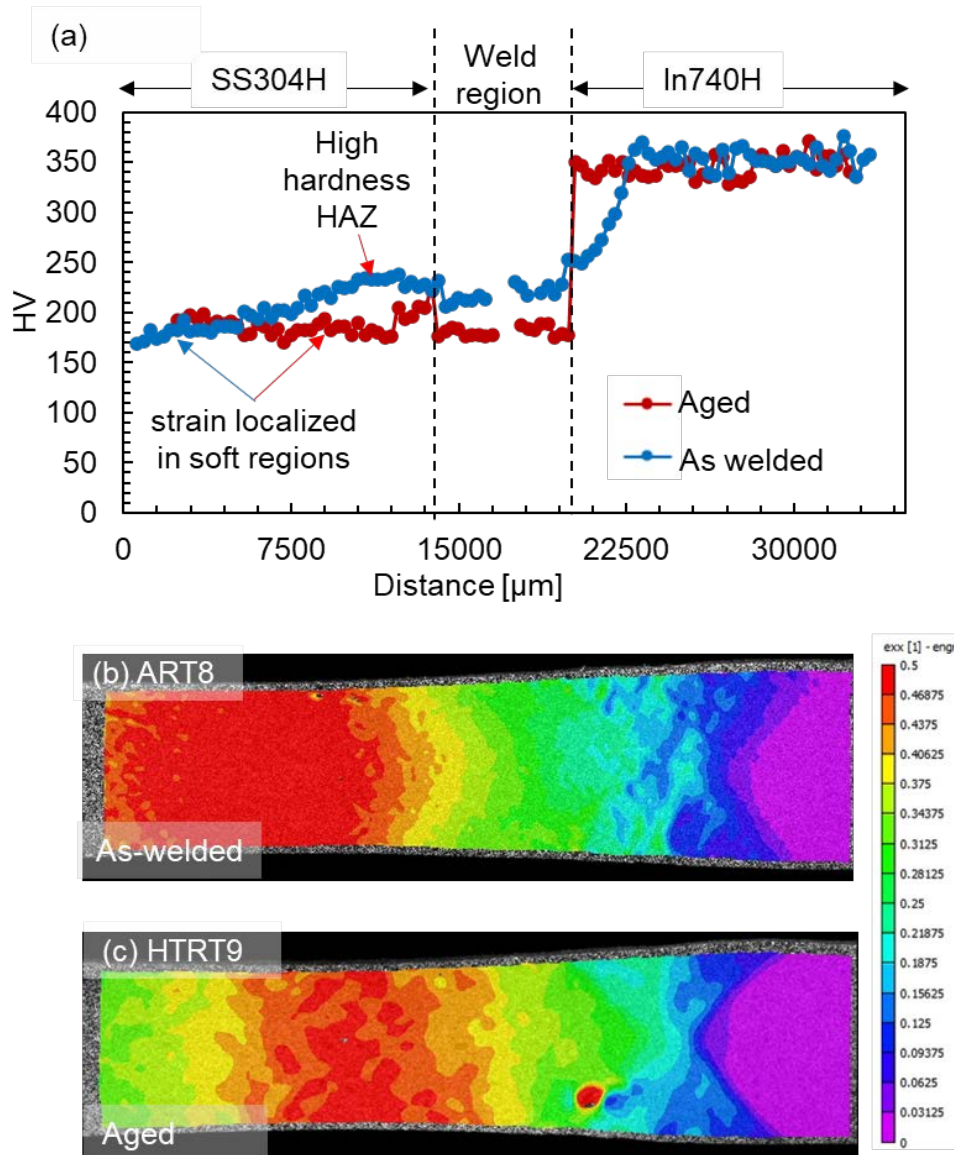
Figure 185. Comparison between (a) the hardness profile of dissimilar weld of In740H-to-SS304H and (b) the strain partition map monitored by DIC for (a) an aged and (b) as-welded tensile sample tested at room temperature

4.4.2.4 Conclusions

For Haynes 282 DSW:

- The yield strength of wrought material for 304H SS is 125 MPa and 90 MPa, for 500°C and 720°C, respectively, and the UTS and elongation for 304H SS is 410 MPa and 36% elongation at 500°C and 220 MPa and 36% elongation at 720°C, respectively. Compared to the wrought SS304H properties, all dissimilar weld samples tested at RT, 500°C, and 720°C have passed the 80% strength baseline.

- The heat treatment performed for aging H282 after welding drastically reduces weld strength, which is limited by the 304H HAZ/BM strength.
- While failure mostly occurs where necking occurs, cracks develop in the half thickness and bottom surface of 304H fusion boundaries during deformation, likely from weld-induced defects, e.g., micro-cracks as seen in the as welded condition.
- The presence of voids indicates possible manual process errors likely due to the challenge of dilution along the 304H side with high Fe content in the first pass. Also, fluidity of molten pool may also be influenced by the mixing process.
- The presence of microcracks still may indicate the possibility of hot/warm cracking such as liquation cracking or ductility dip cracking.
- After the aging heat treatment, a noticeable coarsening occurs in the Ti, Mo, and Cr carbide particles at the interface between the SS304H and H282 filler metal, which may affect the failure behavior of these welds adversely.
- The average dilution levels were maintained lower than 25% in the weld zone of the dissimilar weld both before and after the aging heat treatment.

For Inconel 740H DSW:

- The In740H-304H DSW failed in 304H HAZ/BM for all test conditions. The mechanical properties of the thermomechanical tests meet the minimum expected properties of wrought 304H SS products. Ductility decreased in 304H SS HAZ with increasing temperature in the HAZ, likely with the nucleation of intergranular $M_{23}C_6$ along grain boundaries of coarse grained HAZ, leading to fracture along less tortuous boundaries.
- The average dilution levels were maintained lower than 25% in the weld zone of the dissimilar weld adjacent to the 304H SS side.
- Post-weld aging heat treatment led to an increase in the hardness of the In740H HAZ due to reprecipitation. In contrast, aging reduced the hardness of the SS304H HAZ likely due to grain coarsening. Strain localization occurred in the softer region in the SS304H side before and after aging.

4.4.3 Corrosion in Molten Chlorides (Milestone 2.5.3)

In this task, Milestone 2.5.3 was completed based on details in Table 59. NREL performed the molten salt corrosion testing, while CSM performed all the metallurgical analysis post testing. This study included two types of components: (1) CS/CR C-276 cladded coupon and (2) AM GTA welded components, including Haynes 282 L-PBF-to-wrought and EBAM-to-wrought welds and Inconel 740H L-PBF-to-wrought weld. For H282 and In740H weld coupons, post-weld heat treatment was performed before corrosion testing. All heat treatments were carried out inside Argon-filled stainless steel heat treatment bags to minimize exposure to the atmosphere. The corrosion testing results for CS/CR clad coupons are moved to the end of milestone 2.3.1-CS/CR pipe characterization to complement the rest of the work on the CS/CR clad pipe.

Table 59. Milestone 2.5.3 Details

Milestone	Description	Metric	Success Value	Assessment Tools
2.5.3: Corrosion in molten chlorides	Corrosion of welded CS/CR clad pipe sections and welded AM samples at the service temperature (based on M1.1.2) should show degradation rates below target.	Corrosion tests at the service temperature (based on M1.1.2) a) Localized corrosion b) Weight loss corrosion rate in molten chlorides at expected operating temperature from M1.1.2	a) No pitting or intergranular corrosion b) < 20 μm/year	Molten chloride test following NREL/DOE Salt Collective protocols

4.4.3.1 Haynes 282 L-PBF-to-Wrought Welds

Figure 186 shows the pre-corrosion welded samples. Note that the top of Sample #1 is the wrought base while the top for Sample #2 and Sample #3 is the AM base.

Sample #1   Sample #2   Sample #3
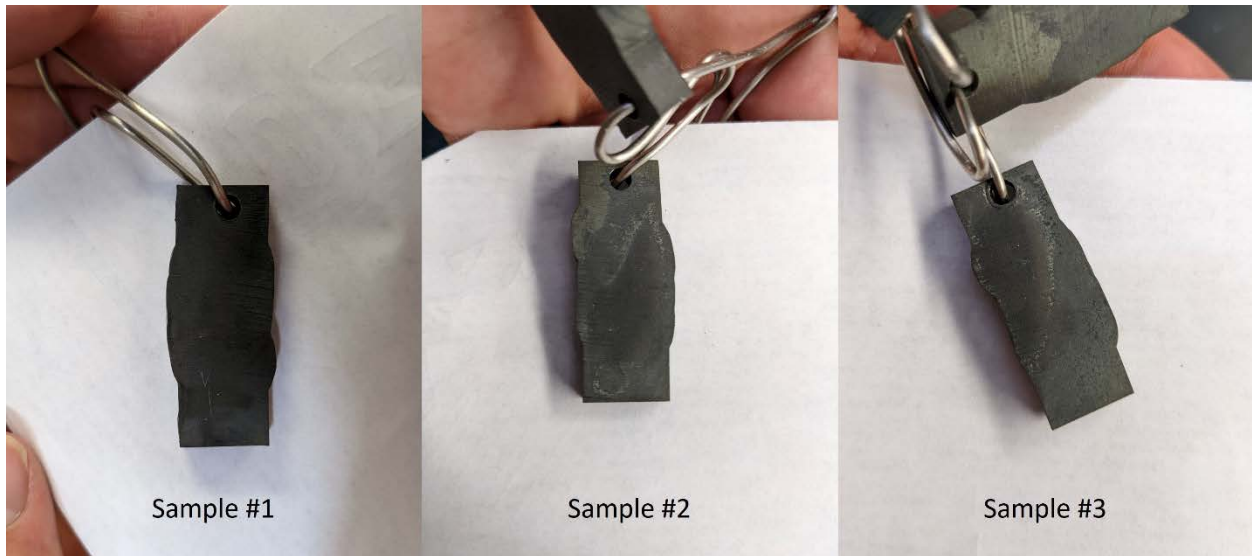
Figure 186. Appearance of pre-corrosion welded samples.

Corrosion was performed in a ternary Mg-K-Na chloride salt at $750 \pm 1°C$ (temperature measured direct in the salt bath) for 100 hours. The ternary salt was purified via a standard purification procedure that NREL has been using for the Gen3 CSP Liquid Pathway project. No corrosion inhibitor was added during the corrosion experiment.

Figure 187 shows the post-corrosion welded samples. Both sides of the samples are shown. A general trend is observed for the post-corrosion welded samples. The wrought end of each sample looks to be shinier than the AM end. It seems to suggest that the surface oxide formed during the post-weld heat treatment detached from the wrought base more easily (and, likely the fusion zone in the welded region). Note that this assessment is only qualitative and does not necessarily apply to both sides of all samples. The area of darker region vs. the shiny region does not reflect the mass-based corrosion rates either. Table 60 shows the summary of mass-loss-based corrosion rates calculated based on the surface area, mass change during corrosion, and

171

density of the H282 (i.e., 8.27 g/cm3). The surface area of the irregular sample shape is estimated using an image analysis software. The error in surface area estimation is likely no more than 1%–2%.

Overall, the corrosion rates fall within expectations for wrought and AM H282 alloy. A previous DOE project led by UC Davis showed that wrought H282 in a similar condition achieved 118.7 ± 9.1 µm/year and 1.12 ± 0.09 mg/cm2 corrosion rates at 800 ± 1°C for 100 hours. More results from that project showed that the AM H282 with the lowest surface and bulk porosity achieved 108.8 ± 5.8 µm/year and 1.03 ± 0.06 mg/cm2 corrosion rates at 800 ± 1°C for 100 hours. The results suggest that there is no significant difference between AM H282 and wrought H282. The salt purification and corrosion were performed for UC Davis by the same NREL team under the same conditions. Although the exact temperature dependence of corrosion is unknown for H282, a ~60% reduction in corrosion rates from 800°C to 750°C is not unreasonable for Ni alloys.
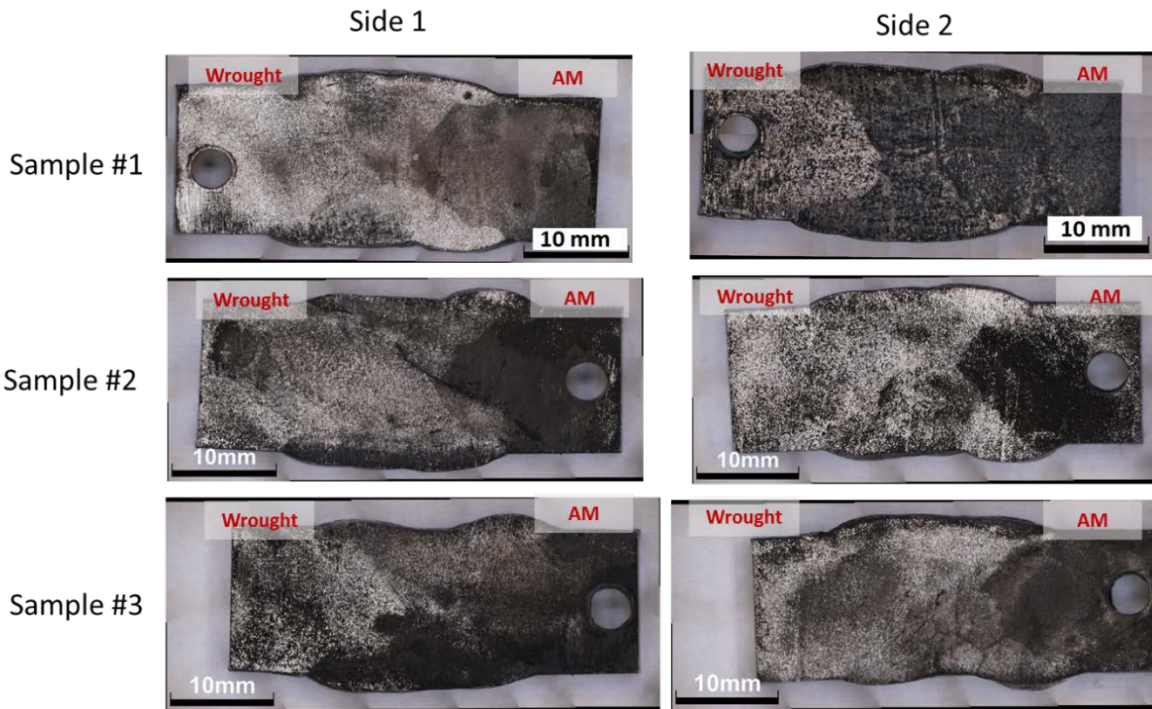
Figure 187. Appearance of post-corrosion welded samples

Table 60. Summary of Mass-Loss-Based Corrosion Rates for L-PBF-to-Wrought H282 Welds

Sample	Corrosion Rate in µm/year			Corrosion Rate in mg/cm^2		
	Value	Average	Std. Dev.	Value	Average	Std. Dev.
#1	74.0			0.70		
#2	51.3	63.5	11.5	0.48	0.60	0.11
#3	65.1			0.61		

172

Figure 188. SEM images and EDS line scans for wrought base metal, fusion zone in the weld region, and AM base metal, showing similar extent of overall intergranular corrosion depth and similar behavior of Cr depletion along grain boundaries

The SEM and EDS analyses were performed by CSM to investigate the corrosion behavior in AM base metal, wrought base metal and fusion zone of the welded samples. Figure 188 summarizes the SEM images and EDS line scans for wrought base metal, fusion zone, and AM base metal. The SEM images show slightly higher extent of intergranular corrosion depth in the fusion zone between the AM and wrought H282, similar spider-web-like network near the corrosion interface was observed in all the regions. Overall, the intergranular corrosion is about 20–25 μm deep from the surface. The EDS line scans corroborate the similarity in the SEM images. Heterogeneous Cr depletion has been seen for each region where there is a pronounced Cr signal reduction every time the scan crosses a visible depleted grain boundary (see Figure 188 and Figure 189. The two figures also show a uniform, homogeneous Cr depletion zone near the surface where the Cr content starts to deviate from the bulk Cr content (i.e., ~22 wt.%). The homogenous Cr depletion depth is about 3-5 μm, 3-5 μm, and 2-3 μm for the wrought base

173

metal, fusion zone, and AM base metal, respectively. However, it should be noted that because intergranular corrosion occurs in the same depth, it could affect the determination of the exact location where homogenous Cr depletion starts. Hence the homogenous Cr depletion depth is only an estimate. Overall, the homogenous Cr depletion depth near the surface is roughly the same for all three regions.
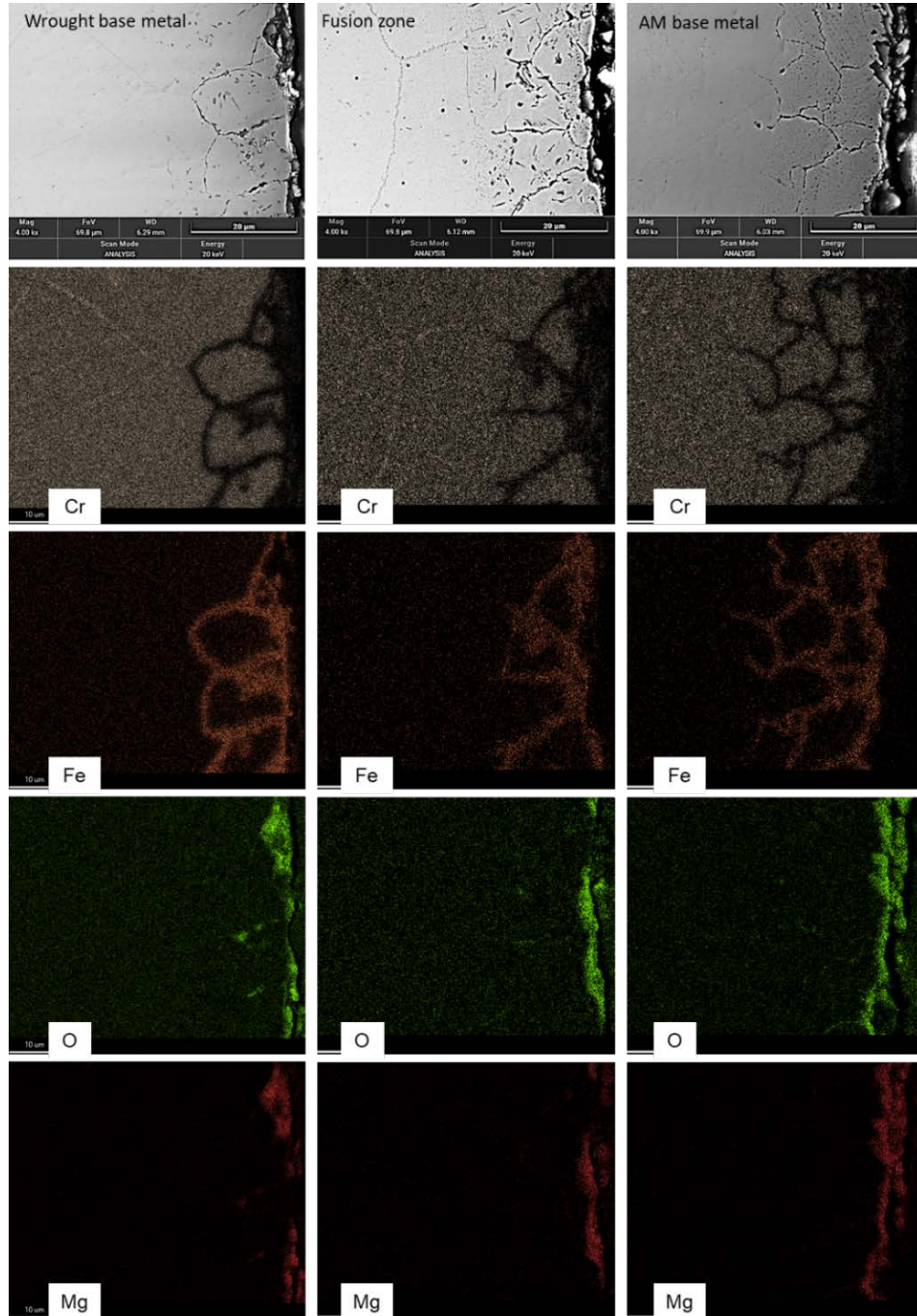
Figure 189. Elemental mapping of Cr, Fe, O and Mg for the wrought base metal, fusion zone and AM base metal

174

There is a strong correlation between intergranular Cr depletion and Fe enrichment as shown in Figure 189. This behavior has been observed before in H230 corrosion. The likely explanation is that Fe and Cr are both leaching through the grain boundaries, but Fe leaching was blocked because of the subsequent formation of oxides on the surface such as Mg-related oxides. For example, if magnesium is present in the salt, it could react with chromium oxide (formed between leached Cr and dissolved oxygen species in the salt) and form MgO. The exact nature of the surface oxide can be much more complex than MgO. The EDS mapping shows correlation among Mg, O, Al, Ti and even N.
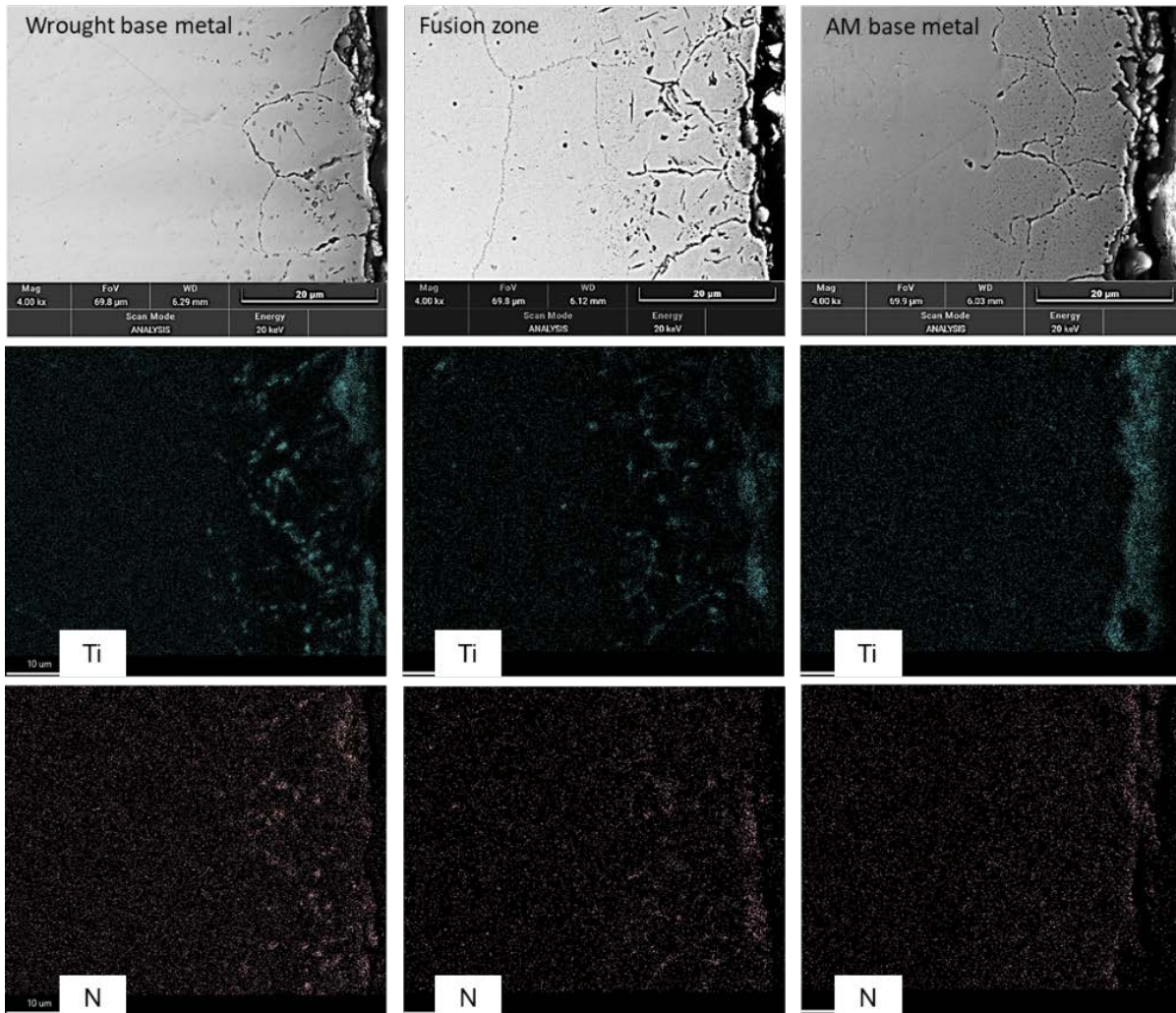
Figure 190. Elemental mapping of Ti and N for the wrought base metal, fusion zone, and AM base metal

The SEM images showed coarse particles near the corrosion attacked surface in the wrought side and fusion zone, but finer precipitates are observed in the AM side. EDS elemental mapping in Figure 190 shows that these particles are enriched in Ti and N which may indicate formation of Ti nitrides upon exposure to the molten salt. In a previous study by NREL on corrosion of H230 in molten chloride salt under similar conditions, CrN formation was reported. Formation for subsurface nitrides is likely related to dissolving of atomic nitrogen in the molten chloride salt environment. Then, the dissolved nitrogen reaches the alloy surface, and its content increases in

175

the subsurface regions as the corrosion test proceeds, leading to formation of nitride particles eventually.

In summary, the corrosion study and SEM/EDS analysis suggest that there is no statistically significant difference in corrosion behavior between AM base and wrought base of H282. The fusion zone in the weld region also exhibits similar behavior. This agrees with the study led by UC Davis based on their AM H282 material. The corrosion rates at 750°C are also reasonable based on estimated temperature dependence of other Ni alloys. One potential solution to further improve corrosion resistance is to reduce surface and bulk porosity introduced by the AM process as there is a clear positive correlation between these quantities from UC Davis' conclusion.

4.4.3.2 Inconel 740H L-PBF-to-Wrought Welds

The results of NREL's corrosion studies on aged weld coupons between L-PBF and wrought IN740H plates are summarized in Table 61.

Table 61. Summary of Mass-Loss-Based Corrosion Rates

Sample	Corrosion Rate in µm/year			Corrosion Rate in mg/cm^2		
	Value	Average	Std. Dev.	Value	Average	Std. Dev.
1	114.37	126.37	10.43	1.051	1.161	0.10
2	133.25			1.224		
3	131.50			1.208		

EDS line scan analysis on weld transverse cross section is summarized in Figure 191 (near the attacked surface). A Cr depletion zone can be observed near the surface (on the left side of each line scan) where the Cr content starts to deviate from the bulk Cr content (i.e., ~24 wt.%). The observed depletion region depths are similar (about 4–7 µm) among the wrought base metal, fusion zone and AM base metal.

The corrosion rate of In740H is about twice that of Haynes 282 AM-to-wrought weld samples. EDS elemental maps of the three regions of the weld cross section are depicted in Figure 192. Here are a few points comparing the observed microstructure features in In740H to those in H282:

- In740H did not show an obvious intergranular depletion of Cr. Instead, the intergranular depletion was in Ni and Co which was not observed in H282.
- In740H's Fe enrichment is mostly on the corrosion interface. But H282's Fe enrichment goes into the intergranular locations. There are other elements that are enriched in the intergranular locations like Nb, Mo and N. Ti behavior is similar for both.
- For the AM side, observations are similar, but the extent of those observations seem to be shallower than wrought base metal. The absence of the connected network of depletion or enrichment likely suggests that the AM side has higher corrosion resistance. On the other hand, fusion zone seems to have the deepest corrosion attack.

176
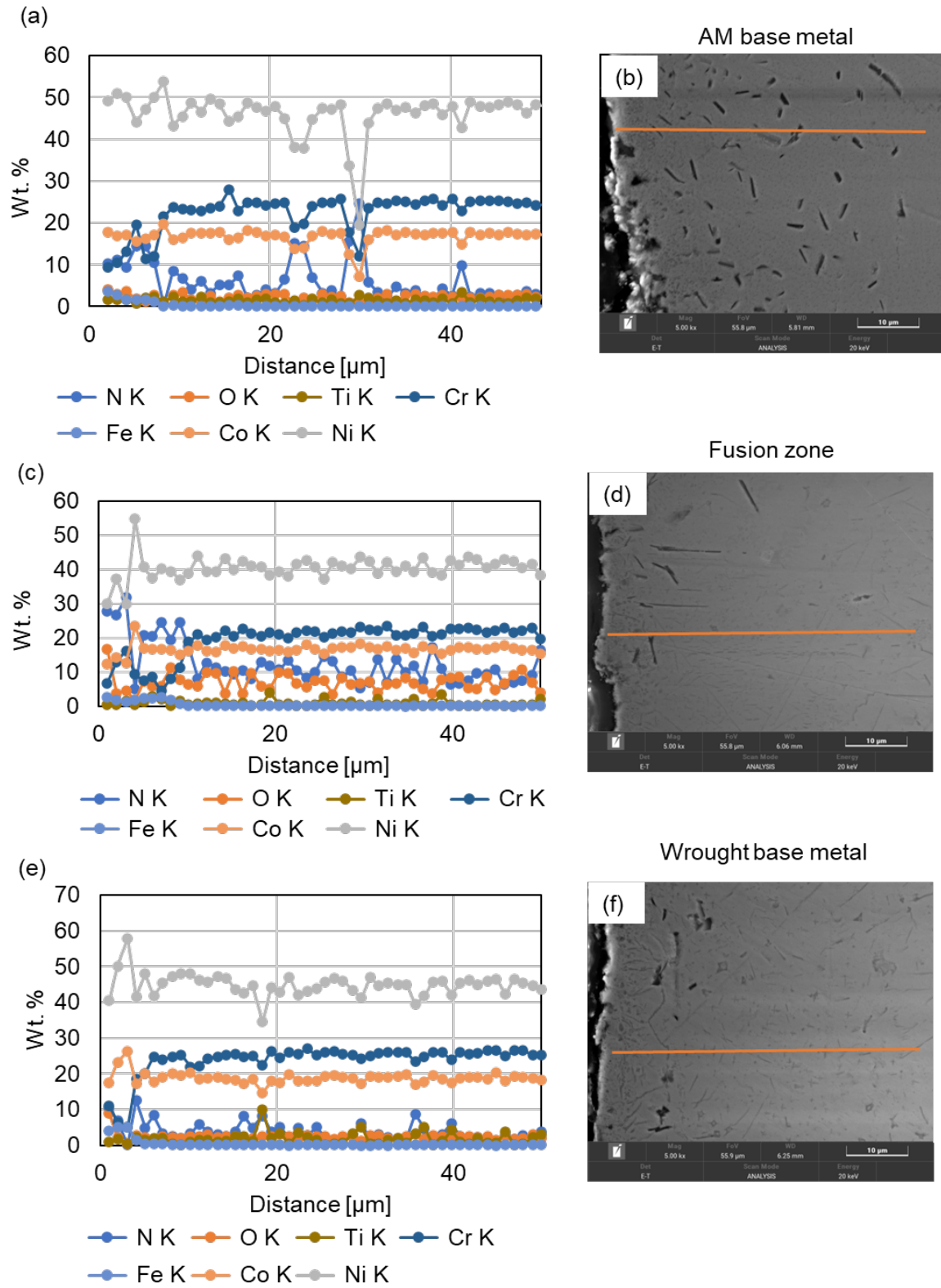
Figure 191. Chemical composition profile of corrosion samples' cross sections after corrosion test shown by EDS line scans and SEM images for (a, b) AM In740H base metal, (c, d) fusion zone, and (e, d) wrought In740H base metal

177
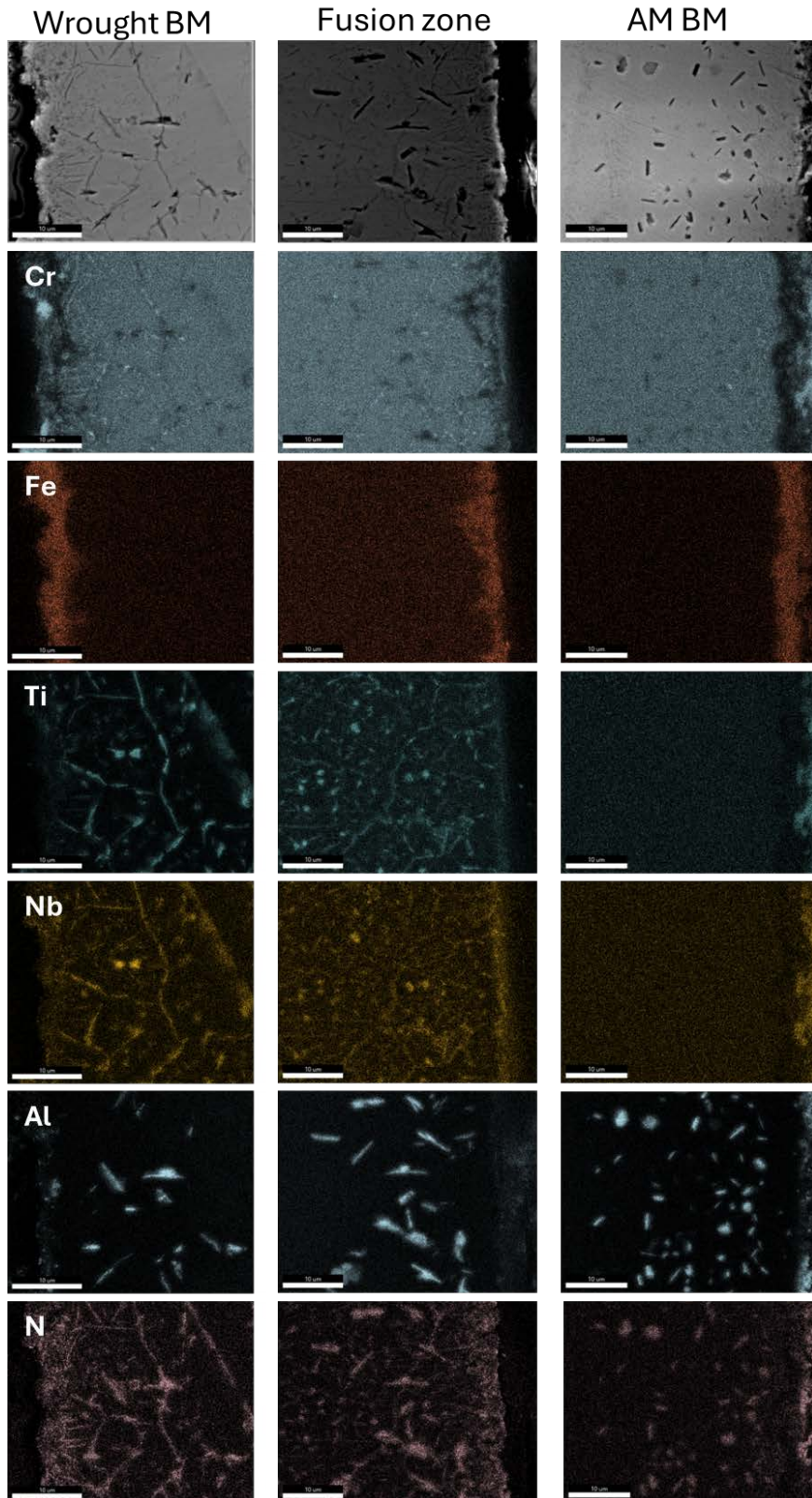
Figure 192. EDS Elemental mapping for the wrought base metal, fusion zone and AM base metal of L-PBF-to-AM weld coupon

178

Generally, H282 has a lot more surface oxides even though it has more obvious intergranular Cr depletion. There are more deposits of O, N, Mg, Al, and Ti at the corrosion interface. Those deposits are barely seen in the In740H sample. Thus, it appears that the corrosion mechanism is different. For In740H, there is more internal nitridation, less surface oxidation, and the corrosion seems more uniform. The nitridation is concerning because we know that N is only from the atmosphere during corrosion. The fact that nitrogen is seen deep inside the bulk metal means that the corrosion occurred deep. For H282, there is more surface oxidation, and the corrosion seems to be more on the intergranular region. Perhaps the intergranular corrosion occurred first, which leached Al, Ti to form the oxides at the corrosion interface. Mg from the salt also participated. The surface oxides may have slowed down further corrosion. Also, the fact that surface oxides formed means that mass-based corrosion rate estimations are not highly accurate, because the total weight loss would be underestimated.

4.4.3.3 H282 EBAM-to-Wrought Welds

The results of NREL's corrosion studies on aged coupons extracted from the EBAM-to-wrought H282 welds are summarized in Table 62, and the images of the tested samples are shown in Figure 193. Compared to the 63.5 µm/year average corrosion rate in L-PBF-to-wrought H282 weld samples, the EBAM-to-wrought H282 welds showed higher corrosion rate by a factor of 2.6. A more detailed comparison between EBAM and L-PBF cases is discussed in the next section.
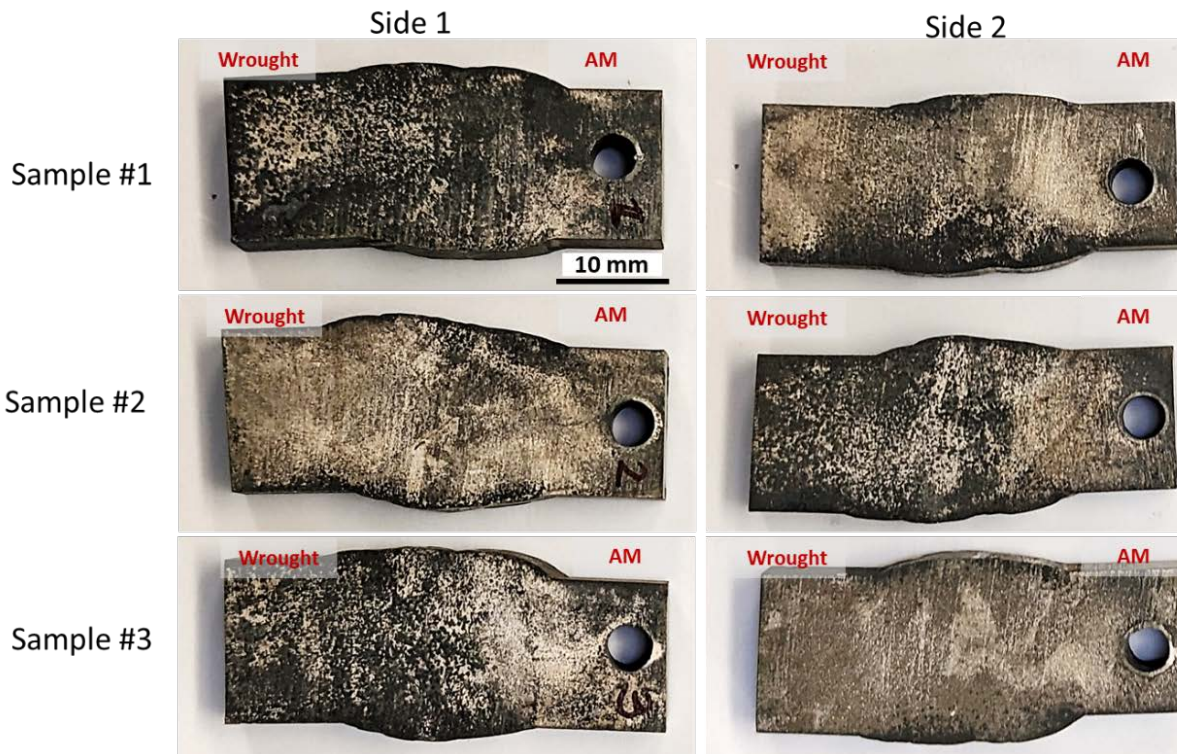
Figure 193. Appearance of post-corrosion EBAM-to-wrought H282 weld coupons

Table 62. Summary of Mass-Loss-Based Corrosion rates

Sample	Corrosion Rate in µm/year			Corrosion Rate in mg/cm²		
	Value	Average	Std. Dev.	Value	Average	Std. Dev.
1	159.80			1.509		
2	174.72	167.78	7.52	1.649	1.584	0.07
3	168.84			1.594		

Figure 194 shows EDS maps of the EBAM base metal cross section at the corrosion attacked surface. Cr depletion is very distinct on the grain boundaries (GBs) near the corrosion surface, which is a typical sign for H282 corrosion as observed before in H282 L-PBF-to-wrought welds. GBs can be observed to be mainly enriched in Mo, while no signs of Fe leaching and enriching the GBs as seen in the L-PBF-to-wrought welds. The intergranular Cr depletion seems to be deeper in EBAM-to-wrought welds than the L-PBF ones. However, more work is being done to compare the two cases.
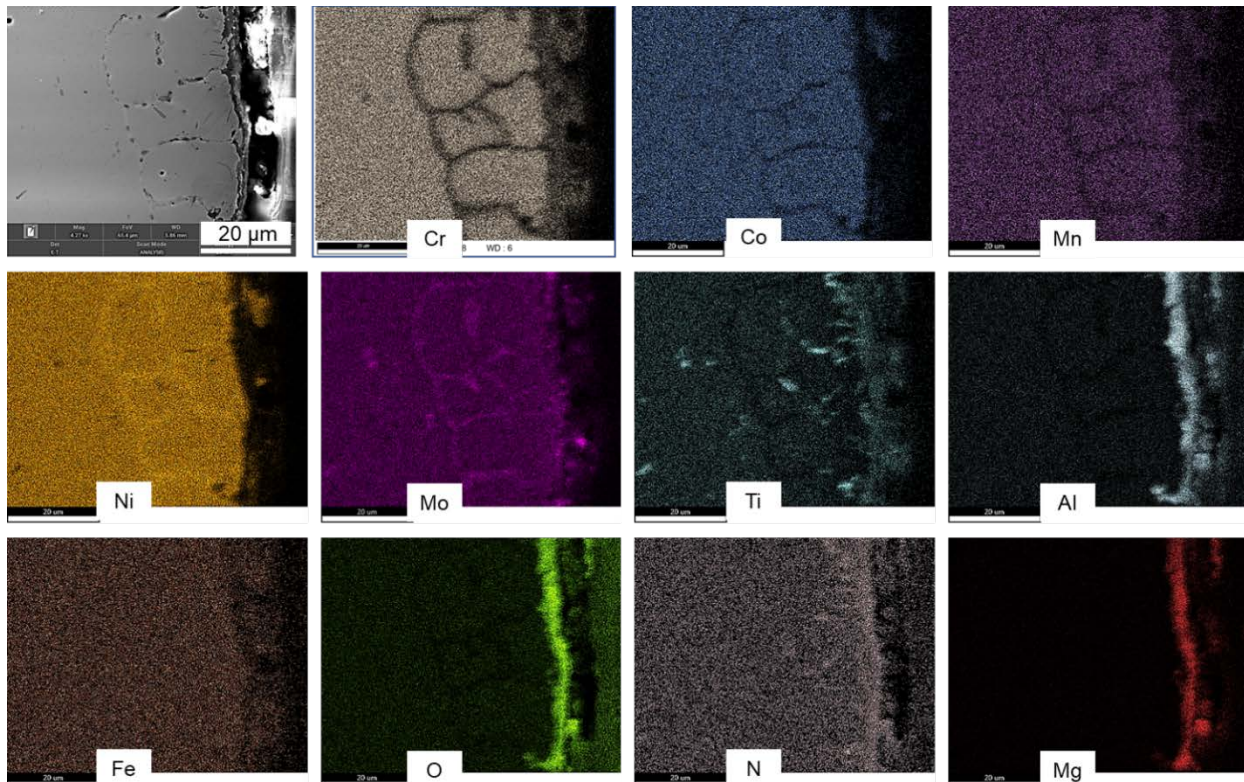
Figure 194. EDS elemental maps at the edge of the EBAM base metal cross section

Further characterization by EDS line scans near the attacked surface on the cross sections of wrought base metal (a), fusion zone (b), and EBAM base metal (c) is summarized in Figure 195. A Cr depletion zone can be observed near the surface (right end of each scan line) where the Cr content starts to deviate from the bulk Cr content (i.e., ~18-20 wt.%). The observed depletion zone depths are similar (about 7–10 µm) among the three regions. In agreement with the chemical composition homogeneity observed between the filler and the two base metals, this observation suggests that the corrosion resistance was homogenous across the three different regions and there are no concerns of localized corrosion attack. However, it should be noted that because intergranular corrosion occurs in the same region where homogenous Cr depletion also

occurs (near the corrosion-attacked surface), it could affect the determination of the exact location where homogenous Cr depletion starts. Hence the homogenous Cr depletion depth is only an estimate.
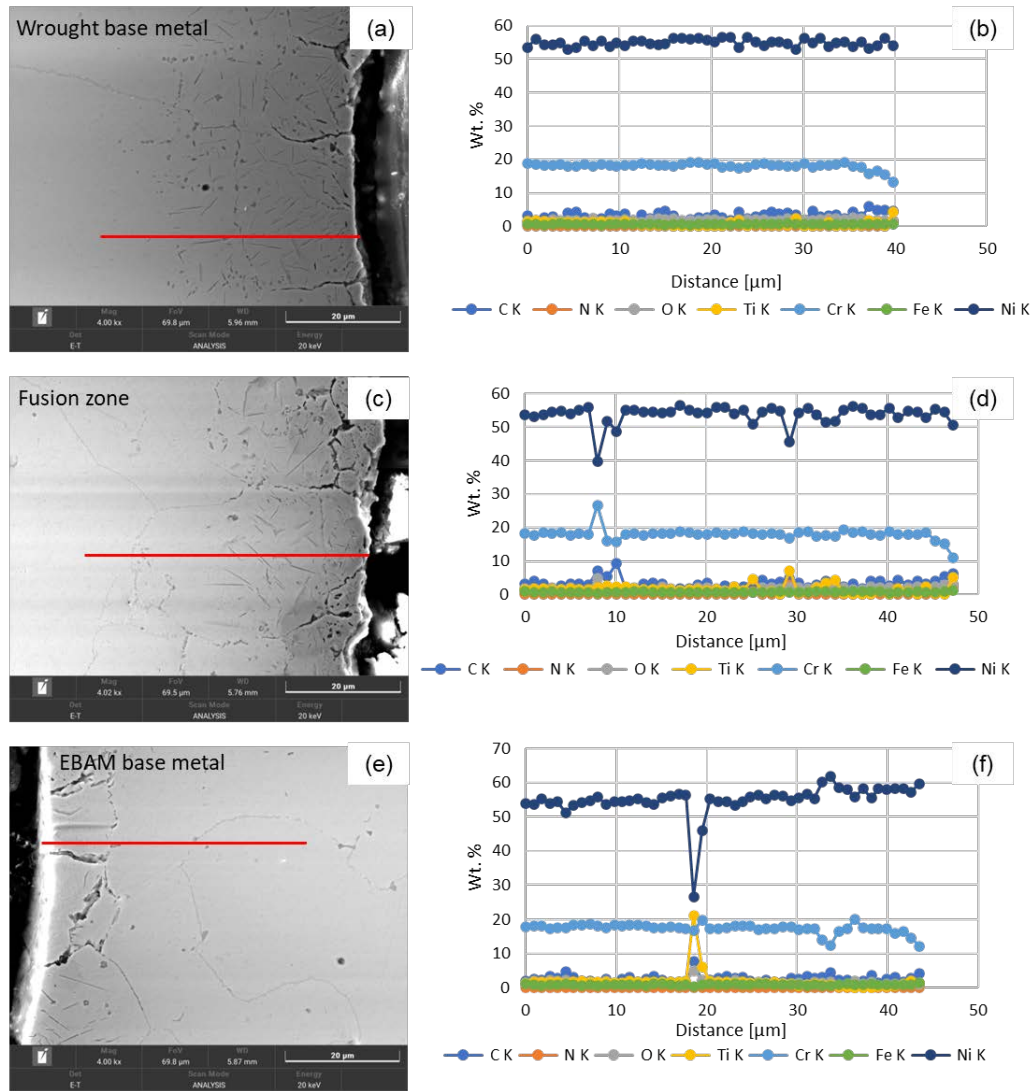
Figure 195. Chemical composition profile of corrosion samples' cross sections after corrosion test shown by EDS line scans and SEM images for (a, b) Wrought H282 base metal, (c, d) fusion zone, and (e, f) EBAM H282 base metal.

4.4.3.4 A Comparison Between L-PBF- vs. EBAM-to-Wrought Haynes 282 Welds

EBAM-to-wrought H282 welds showed a higher corrosion rate by a factor of 2.6, compared to the average corrosion rate in L-PBF-to-wrought H282 weld samples. In this section, we provide more information to assist in explaining this difference in corrosion resistance.

4.4.3.4.1 Bulk Chemical Composition Analysis

The chemical composition is the main parameter affecting the corrosion resistance of any alloy in general. Table 63 compares between the bulk chemical compositions of EBAM and L-PBF H282 analyzed by averaging three XRF readings for each sample. It is clear that both materials

181

have very similar chemical compositions, however, the main difference is Fe content. EBAM sample contains 10 orders of magnitude more Fe content than L-PBF samples in expense of Ni and Cr. In addition, EBAM sample was observed to contain 0.9 wt.% of Si. During corrosion testing, iron leaches from the H282 into the molten salt. Thus, different iron content may lead to different weight loss rates between EBAM and L-PBF samples.

Table 63. XRF Bulk Chemical Composition (wt.%) of EBAM vs. L-PBF H282

	C	Al	Si	Ti	Cr	Mn	Fe	Co	Ni	Mo	W
EBAM	0.2	1±0.8	0.9	2.3±0.3	18.5±0.3	0.2	1.1	10.4±0.2	56.9±1.1	8.7±0.2	0.1
L-PBF	0.2	1.1±0.2	-	2.3±0.2	19.7±0.4	-	0.1±0.1	10.1±0.3	57.9±0.7	8.6±0.2	0.1

4.4.3.4.2 Micro-Scale Chemical Composition Analysis

Figure 196 and Figure 197 compare EDS maps of cross-sectional samples near the corrosion attacked surface of EBAM and L-PBF samples. Cr and Mo depletion on grain boundaries (GBs) can be observed in both cases and it is a typical corrosion behavior of many Ni-based alloys. On the other hand, two opposite behaviors were observed in the two samples. First, Fe appears to be slightly depleted from the GBs of the EBAM sample, while it is enriching the GBs of L-PBF one. Second, Co depletion is observed in EBAM samples but not in L-PBF ones. More investigation is required to explain the reasons for these behaviors.
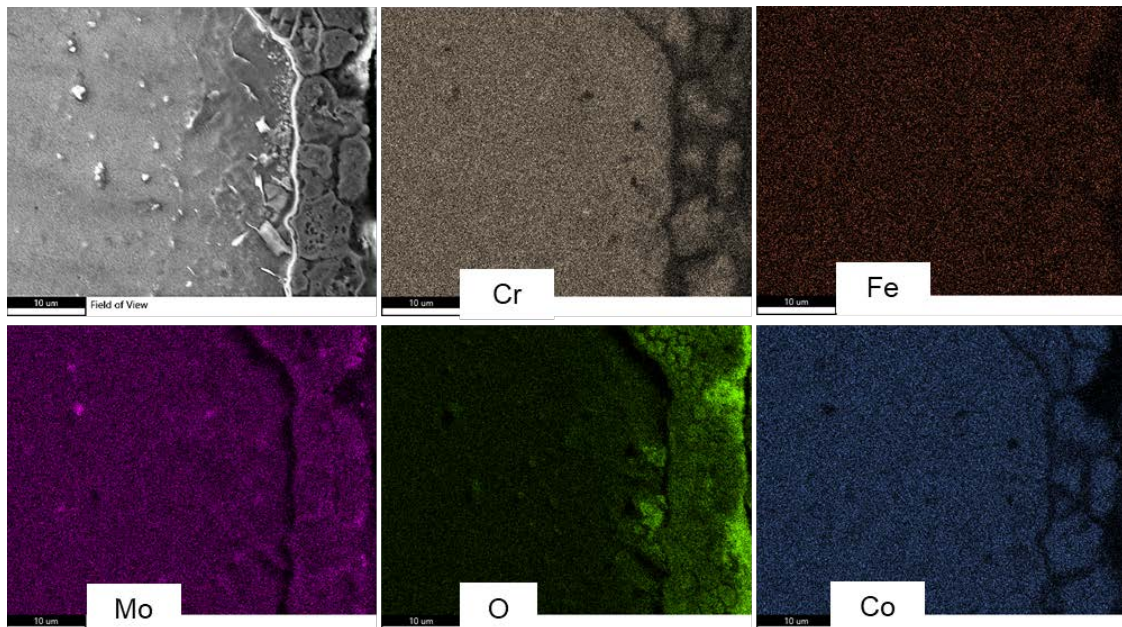
Figure 196. EDS elemental maps at the edge of the EBAM H282 base metal cross section after corrosion test
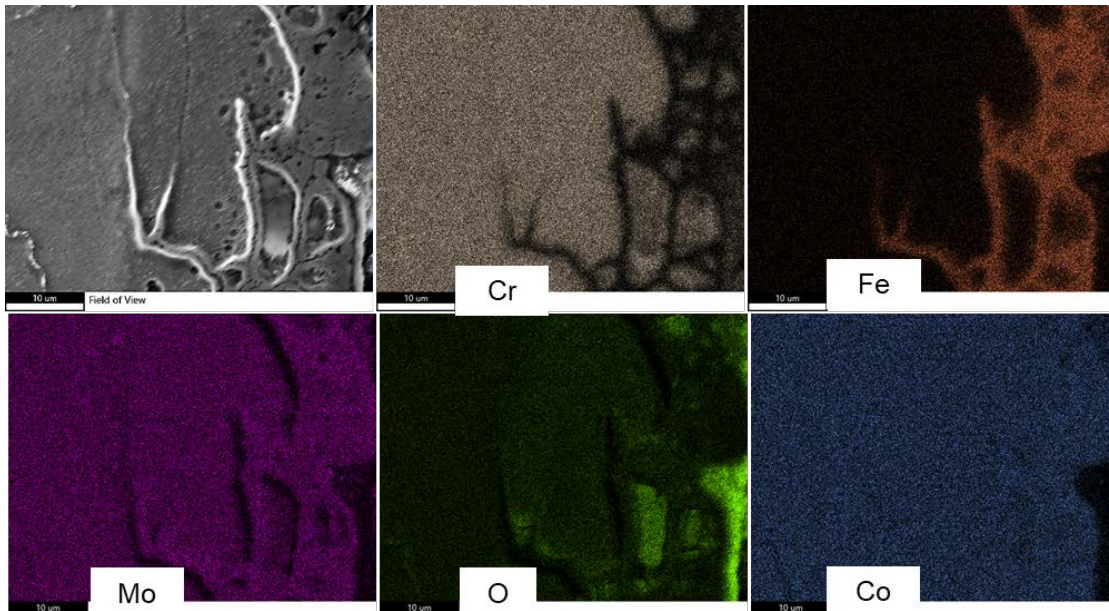
Figure 197. EDS elemental maps at the edge of the L-PBF H282 base metal cross section after corrosion test

4.4.3.4.3 Microstructure

The grain size is significantly larger in EBAM compared to L-PBF, as seen in Figure 198. In addition, continuous network of precipitation is observed along GBs in EBAM sample, while discrete network of precipitation is in L-PBF case. Because GBs provide pathways for fast diffusion, both grain size and GB morphology and phases can affect the corrosion rates.
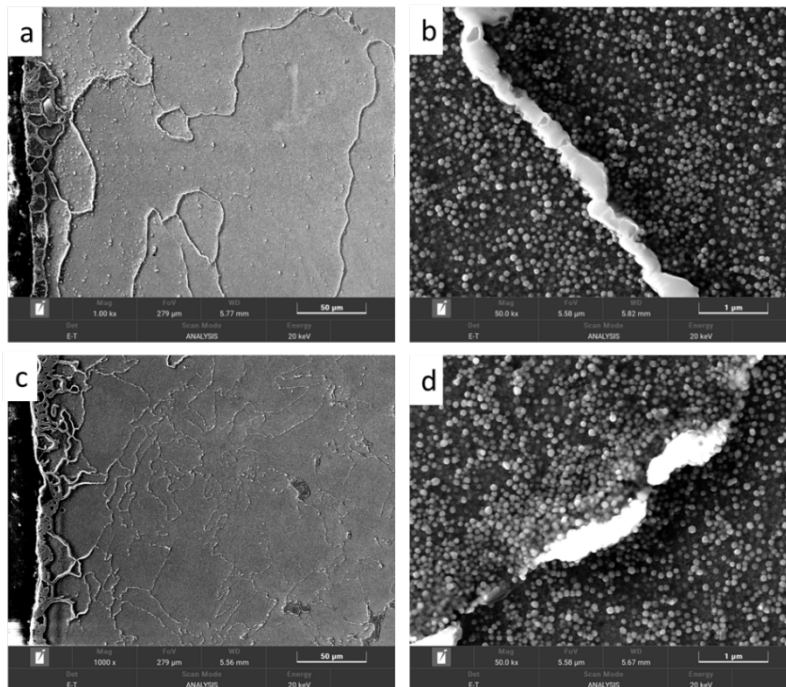
Figure 198. Microstructure of samples after corrosion (a, b) EBAM, and (c, d) L-PBF

183

4.4.3.5 Conclusions for Corrosion Testing in Molten Chlorides

L-PBF-to-Wrought H282

- There was no statistical difference in corrosion rates between the AM or wrought H282 alloys.
- The average corrosion rate of the tested samples was 63.5 μm/year, which agrees with a UC Davis led similar experiment on H282.

L-PBF-to-Wrought IN740H

- The overall corrosion rate of L-PBF-to-wrought In740H was almost twice that of H282.
- Unlike H282, IN740H did not show an obvious intergranular depletion of Cr. Instead, the intergranular depletion was in Ni and Co.
- There is more internal nitridation, less surface oxidation, and the corrosion seems more uniform.

EBAM-to-Wrought H282

- XRF analysis showed more Fe content in EBAM sample, which may increase its corrosion rate compared to L-PBF.
- Grain boundaries Cr depletion behavior was similar in EBAM and L-PBF samples, however, Co depletion was only observed in EBAM sample.
- EBAM-to-wrought H282 showed a significantly higher corrosion rate than L-PBF-to-wrought H282 under the same testing conditions.
- Matching chemical composition across the weldments resulted in similar depth of Cr depletion among the subzones.

4.4.4 Weld Crack Susceptibility and Cracking Mechanisms (Milestone 3.5.1)

In this task, Milestone 3.5.1 was completed as seen in Table 64.

Table 64. Milestone 3.5.1 Details

Milestone	Description	Metric	Success Value	Assessment Tools
3.5.1: Weldment crack susceptibility and cracking mechanisms	To help commercial penetration of proposed technologies at desired scale Gleeble simulations results of multi-pass welding fabrication should provide data at the service temperature (based on M1.1.2) to evaluate cracking susceptibility mechanisms and thus create the comprehensive database.	Temperature-stress-failure time relationship at Gen3 CSP service conditions such as the service temperature (based on M1.1.2) and under the variation of weldment microstructures and residual stresses determined from FE simulation (M1.6.1, M2.2.3, M2.6.2)	(1) No failure within 8hr testing. (2) No presence of susceptible microstructure (e.g., precipitate free zone) to determine threshold stress and strain level under the corresponding service temperatures (based on M1.1.2)	• Thermodynamic calculations. • Time to failure at different temperatures and various stress levels determined by Gleeble testing. • Request to ASME the formation of a standards Committee to define requirements for the generation of data useful for the code case

4.4.4.1 Background

Based on the consideration of potential cracking mechanisms within the many alloys studied in this work and to help commercial implementation of advanced manufacturing technology for Generation 3 CSP molten salt components, Haynes 282 and Inconel 740H Ni-alloys may potentially undergo strain age cracking (SAC) during manufacturing (e.g., PWHT) or during service. The literature gap based on a broad literature search is SAC of arc welded additive manufactured Ni-superalloys, particularly L-PBF components. There has been a considerable amount of effort put toward studying SAC of Inconel 740H welds and Haynes 282 simulated HAZ in the literature. Therefore, studying SAC of Haynes 282 and Inconel L-PBF welded components and Haynes 282 wrought welds is appropriate. In particular, understanding the SAC mechanism within the parameters of PWHT of the Haynes 282 and Inconel 740H L-PBF components is of interest.

The current code [30] case 3024 on PWHT of Haynes 282 and Inconel 740H welds requires a minimum four-hour soak time between 790°C and 840°C, which represents the prime aging temperature window of γ' phase. While solution annealing of welds is not mandatory, it may be a beneficial step to reduce residual stress and "reset" the weld microstructure for the benefit of improved ductility. However, achieving solution annealing temperatures (1095°C–1160°C) for field applications where induction heating or ceramic heating pads are required is extremely challenging. Additionally, reheat cracking during heating to solutionizing temperatures may be an additional concern in highly constrained, field components. (e.g., heating rate effect). With respect to heating rates, it is recommended to perform as fast a heating rate as possible. The maximum attainable heating rate depends on multiple factors, such as source of the heating element (furnace, induction heating, ceramic heating), thickness, and geometry of the weld. Regardless, understanding heating rate sensitivity and quantifiable heating rates in preventing cracking during a mandatory PWHT aging condition is important, because there is no clear value other than fast heating rates.
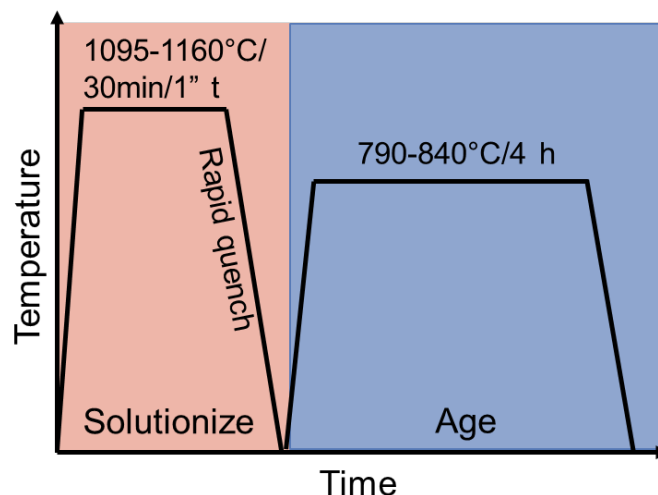
Figure 199. PWHT that may be preferable (solutionizing +aging) although challenging for field welds

Therefore, two research questions were posed during this portion of the project with respect to SAC of Haynes 282 and Inconel 740H welds:

1. How does the Haynes 282 and Inconel 740H L-PBF substrate material impact SAC sensitivity compared to wrought substrate?

2. Can Haynes 282 and Inconel 740H L-PBF welded components withstand direct aging PWHT within 790°C–840°C without SAC and what parameters (stress/strain, print orientation, and heating rate) are SAC sensitive?

4.4.4.2 SAC Methodology

To answer those questions, a strain age cracking (SAC) testing methodology is implemented using a Gleeble® 3500 thermomechanical physical simulator. To represent the PWHT aging condition, a four-step thermomechanical test (or three step for extracted weld samples) is used, which is illustrated in Figure 200. The first step, representative of a weld thermal cycle HAZ (peak temperature of 1275°C), was taken from OSU's modeling simulation work on Haynes 282 multi-pass weld, validated with earlier multi-pass welding experiments. The second step involves pulling to a stress/strain condition representative of varying residual stress/strain conditions. Then, heating up to temperature occurs during step three followed by an isothermal holding temperature step four representative of PWHT aging condition. Extracted weld samples do not undergo the first step.
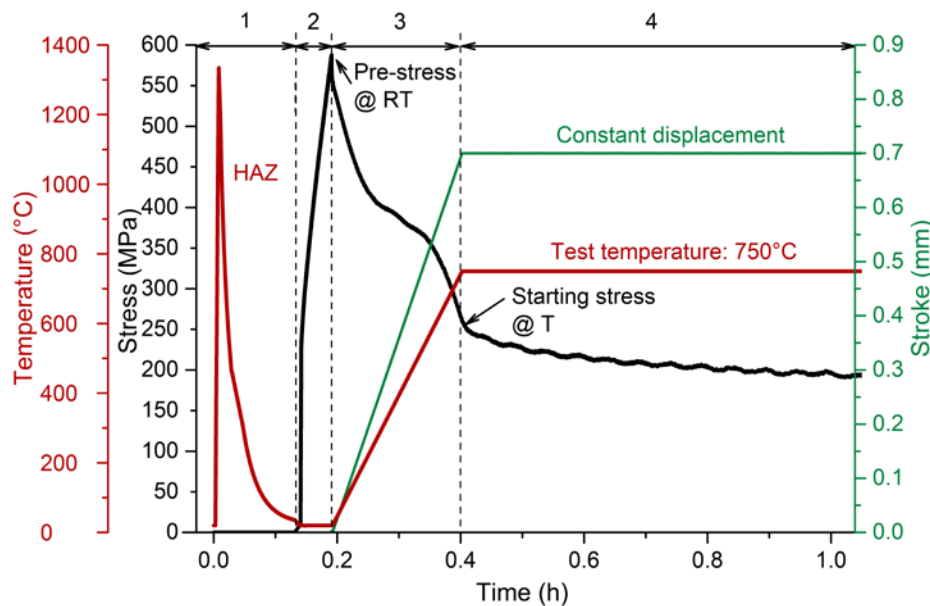
Figure 200. Four step SAC procedure using Gleeble 3500 thermomechanical simulator

Four different material conditions are provided for SAC testing are listed below in Table 65. A physically simulated HAZ microstructure for both Haynes 282 and Inconel 740 superalloys is generated in the Gleeble during the first step. The last two sets of samples come from extracted cross-welded samples (transverse to the welding direction) with samples centered on the weld FZ. For both HAZ materials, a set of horizontal and vertical samples are provided by E3D. Horizontally printed plates, also provided by E3D, are welded using matching Haynes 282 filler. A set of wrought plates are also welded with the same weld filler using a double-V groove geometry. The room temperature strain applied in step two conditions of 1,3,5, and 10% were chosen. The room temperature strain applied in step two conditions of 1,3,5, and 10% were chosen for HAZ samples, while for welded samples the room temperature stress is about 400-

750 MPa. The target temperature for step four is 800°C. During step three, various heating rates are applied to survey if heating rates influence cracking susceptibility in addition to strain and stress.

Table 65. Experimental Matrix for SAC Thermomechanical Testing

Material	Orientation	Strain (%)/Stress (MPa)	Heating Rate (°C/h)	Target Temperature (°C)
HAZ of L-PBF Haynes 282	XY (horizontal) & Z(vertical)	1,3,5,10	40, 100, 333, 1500, 3480	800
HAZ of L-PBF Inconel 740H				
GTAW L-PBF Haynes 282	XY (horizontal)	400-750		
GTAW wrought Haynes 282				

4.4.4.3 Weld Experiments

Experimental GTA welds were completed for cross-weld samples using a similar procedure as BP2 L-PBF to wrought welds. However, in these experiments, the L-PBF and wrought welds are welded separately. An additional change was to increase the weld current from 150 to 180 amperes to improve weld penetration, while also having a more comparable weld heat input between both welds. The plate thickness and dimensions butt welded were 6 in. long x 3 in. wide x 5/8 in. thick. The welding geometry is a double-V groove. To note, these cross welds are intended to provide cross weld SAC samples.

4.4.4.4 Gleeble SAC Testing Data of HAZ Samples

The Haynes 282 HAZ and Inconel 740H HAZ SAC results are summarized in Table 66 and Table 67, respectively. A summary of SAC results in the form of stress and temperature as a function of temperature are shown in Figure 201 for 800°C test temperature with a 0.1 pre-strain condition and single HAZ thermal cycle. The results indicate Haynes 282 in the horizontal orientation have the shortest time to failure upon reaching 800°C, which occurred within two minutes at temperature with the same strain condition. The Haynes 282 vertical orientation and Haynes 282 wrought conditions did not fail at temperature with 15 and 20 hours at temperature, respectively. The samples were then pulled to failure to capture fracture stress and strain values. The Inconel 740H samples showed similar trends with the vertical orientation outperforming the horizontal orientation with the same strain condition.

Table 66. Haynes 282 HAZ SAC Results Summary

Sample ID#	Orientation	Strain (%)	SRC Method	Heating Rate (°C/h)	Initial Stress (MPa)	Stress @ Temp. (MPa)	Result	Build #	Duplicate
V1	Vertical (Y)	10	1	3480	755	442	No failure @ temp.	A2101	-
V2		10	1	3480	787	443	No failure @ temp.	A2101	X
V3		10	2	40	751	319 @ 800°C	Fail on heating at 855°C (~200 MPa)	A2101	-
V4		10	2	40	783	312	Fail 3.3 h @ temp.	A2101	-
V5		10	3	333	739	370	Fail 0.56 h @ temp.	A2108	-
V6		10	4	1500	712	415	Fail 2 h @ T	A2108	-
V7		10	5	2500	721	447	Fail 2 h @ T	A2108	-
V8		10	6	100	699	359	Fail 0.33 h @ T	A2108	-
V9		Bent sample used for HAZ simulation for characterization							
H1	Horizontal (XY)	10	1	3480	745	467	Fail 85 s @ T	A2091	-
H2		10	1	3480	<700	-	Load drop upon approaching 10% strain/Failed on heating	A2091	X
H3		3	1	3480	620	~400-450	Fail on heating 785-790°C	A2091	-
H4		1	1	3480	469	367	Failed 0.6 h @ T	A2091	-
H5		1	1	3480	511	392	Failed 16 h @ T	A2101	X
H6		1	6	100	479	351	Failed 2.86 h @ T	A2101	-
H7		1	2	40	472	351	Failed 1.47 h @ T	A2101	-
H8		1	4	1500	456	366	Failed 0.14 h @ T	A2101	-
H9		1	3	333	480	~380	Failed on heating @730-750°C	A2101	-
W1	N/A	10	1	3480	679	469	No failure @ temp.	N/A	-
W2		Failed ~3% initial strain at RT-issues with machining sample led to fast fracture							

Table 67. Inconel 740H HAZ SAC Results Summary

Sample ID#	Orientation	Strain (%)	SRC Method	Heating Rate (°C/h)	Initial Stress (MPa)	Stress @ Temp. (MPa)	Result	Build #
VIN1	Vertical (Z)	10	1	3480	758	340	Failed 3.44 h @ T	A2205
VIN2		5	1	3480	638	329	Failed 13.19 h @ T	A2205
VIN3		3	1	3480	588	328	Failed 11.06 h @ T	A2205
VIN4		3	2	40	572	276	Failed 3.96 h @ T	A2205
VIN5		3	6	100	576	298	Failed 3.7 h @ T	A2205
VIN6		3	3	333	585	295	Failed 6.89 h @ T	A2205
HIN1	Horizontal (XY)	10	1	3480	792	374	Failed 50 min @ T	A2203
HIN2		5	1	3480	626	359	Failed 2.56 h @ T	A2203
HIN3		Cracked during HAZ thermal cycle step						A2203
HIN4		3	2	40	541	300	Failed 12 min @ T	A2203
HIN5		3	6	100	550	319	Failed 39.3 min @ T	A2203
HIN6		3	3	333	565	312	Failed 63.3 min @ T	A2216
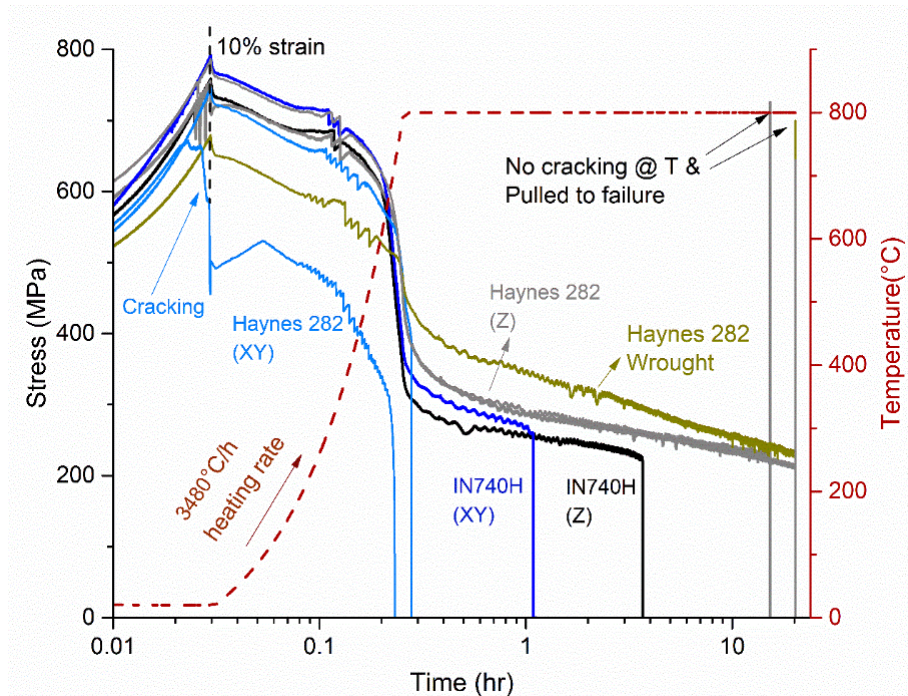
Figure 201. Stress vs. time for Haynes 282 and Inconel 740H tests with 10% initial strain.
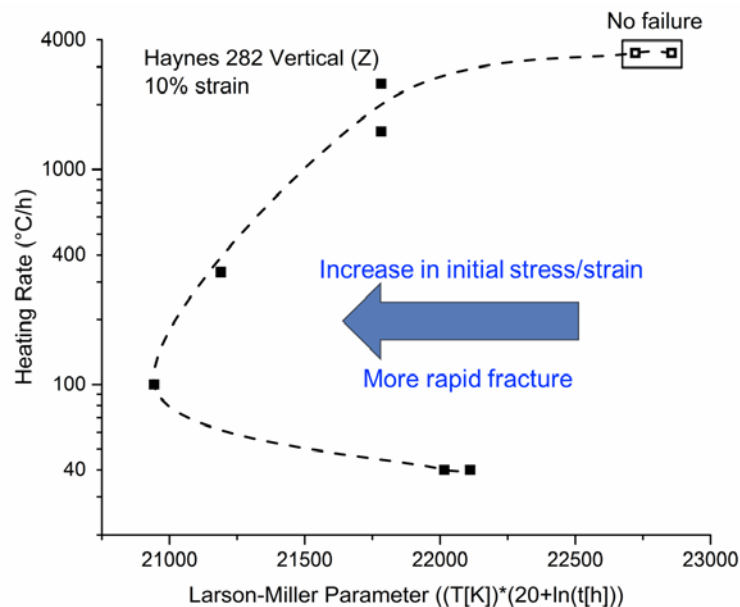
Figure 202. Effect of heating rate on time to failure during direct aging at 800°C

The Haynes 282 L-PBF HAZ with a vertical (z) print orientation performed the best with respect to highest strain conditions. Heating rates affect the time to failure as well. For the 10% strain condition inf Haynes vertical (z) orientation, a heating rate of 100°C/h resulted in the fastest time to fracture. However, the heating rate of 40°C/h failed at a longer time at temperature, similar to a 2500-3500°C/h heating rate. Figure 202 illustrates the time to failure dependency on applied heating rate. The trend represents a "c-curve" trend that may be explained by the competition between stress relief and active precipitation of γ' inhibiting stress relief in the matrix.

Intergranular cracking would therefore depend on how much stress is initially relieved throughout the matrix without sufficient strain localization on grain boundaries, implicating a time dependency through heating rate.

Figure 203 illustrates the effect of heating rate on time to strain age cracking (SAC), or Larson Miller Parameter (LMP), for both Haynes 282 and Inconel 740H L-PBF prints. The print orientation (XY-horizontal or Z-vertical) and initial strain are included in the labels as well. Depending on the strain/stress, heating rate, and temperature, the time to failure will vary, including among different print orientations and different materials. The best condition and SAC resistance at 800°C corresponds to the Haynes 282 wrought and Z print L-PBF orientation, particularly at the highest heating rate condition. Additionally, Inconel 740H Z-print orientation performs next best, while the XY print orientations for both materials performed generally worse. The Inconel 740H test results show a linear relationship between heating rate and time to failure in contrast to the "c" trend seen with Haynes 282 test results. A more in-depth analysis on the microstructure may help explain the differences between the Haynes 282 and Inconel 740H behavior.
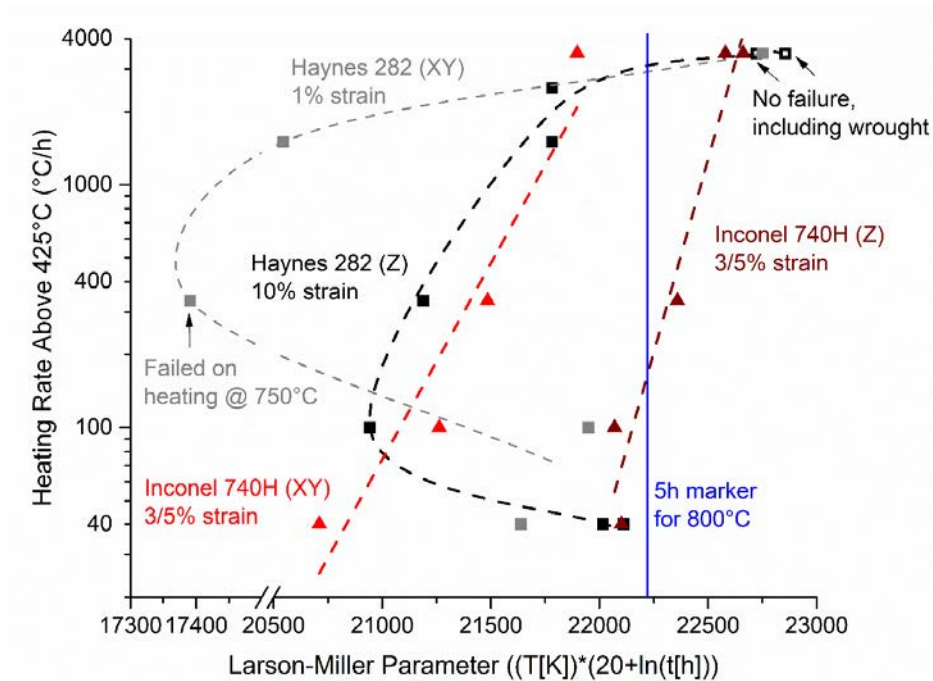
Figure 203. Strain age cracking (SAC) heating rate effect as a function of LMP (C=20), print orientation, and initial strain of Haynes 282 and Inconel 740H L-PBF components. The time marker (5h) for code-required aging post weld heat treatment (PWHT) is overlaid on plot

4.4.4.5 Characterization of HAZ SAC Samples

Fractographic analysis of HAZ of horizontally and vertically printed Haynes 282 and Inconel 740H SAC samples conducted at 800°C is shown in Figure 204. Secondary electron imaging (SEI) mode provides sensitivity to surface features critical for fracture surface identification. Largely, the fracture surfaces appear intergranular for the horizontal Haynes 282 and horizontal and vertical Inconel 740H samples, while there is a mixed mode of intergranular and cleavage fracture in Haynes 282 vertically printed samples. It should be noted that the vertically printed

Haynes 282 sample lasts the duration of the Gleeble SAC test and is pulled to failure to capture remaining ductility of the sample where there is very little necking prior to fracture, correlating with a mixed mode fracture surface. Upon higher magnification, the very fast fracture in the Haynes 282 horizontal sample correlates with a smoother fracture surface on grain facets, whereas the Inconel 740H samples seem to indicate largely a presence of microvoids on grain facets. The Haynes 282 vertically printed sample showed microvoids of a similar scale on grain facets in regions of intergranular fracture, indicating the progression of SAC fracture, such that 15 hours was too short of a time at 800°C with an initial strain of 0.1 to facilitate complete intergranular fracture.
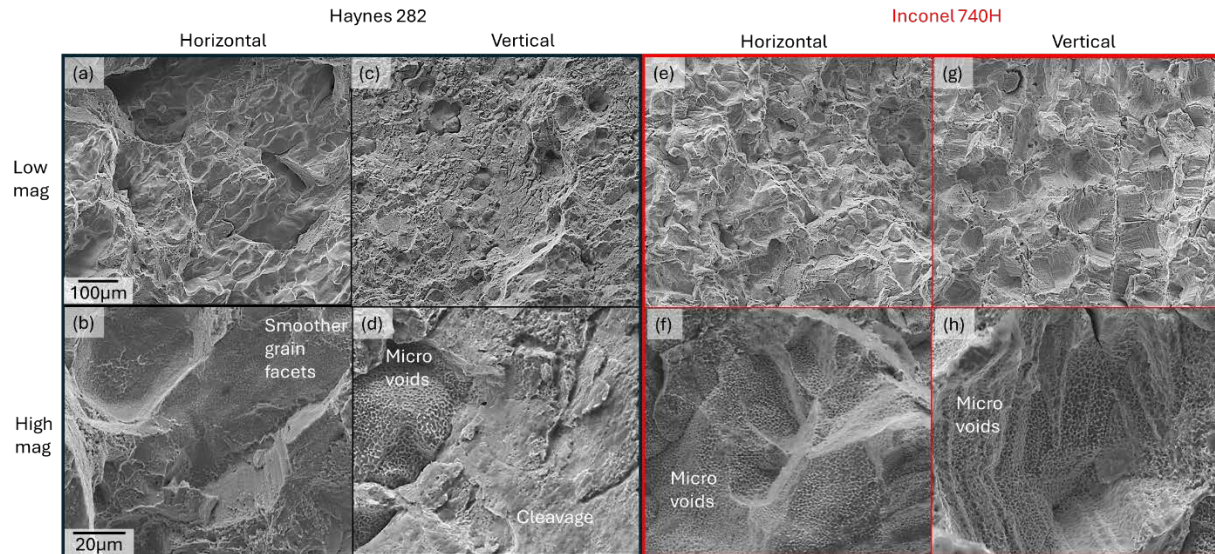
Figure 204. Fractographic SEM-SEI analysis of 800°C SAC samples with 0.1 initial strain: (a–b) Haynes 282 horizontal print, (c–d) Haynes 282 vertical print, (e–f) Inconel 740H horizontal print, and (g–h) Inconel 740H vertical print

4.4.4.6 Characterization of Cross Weld Samples

Microhardness of as-welded Haynes 282 L-PBF to L-PBF weld and wrought-to-wrought welds, representative of the gauge section of the extracted weld sample, is shown in Figure 205. First, the HAZ of the L-PBF weld shows hardness values exceeding 400 HV with microhardness peaks of 370 HV in the root of the weld with a depreciation to 270 HV closer to the cap passes. Second, the HAZ of the wrought weld indicates microhardness values less than 250 HV with peak microhardness of 340 HV in the weld FZ. Overall, the HAZ of the L-PBF and wrought welds are drastically different than each other, while the weld FZ is appreciably similar.

191
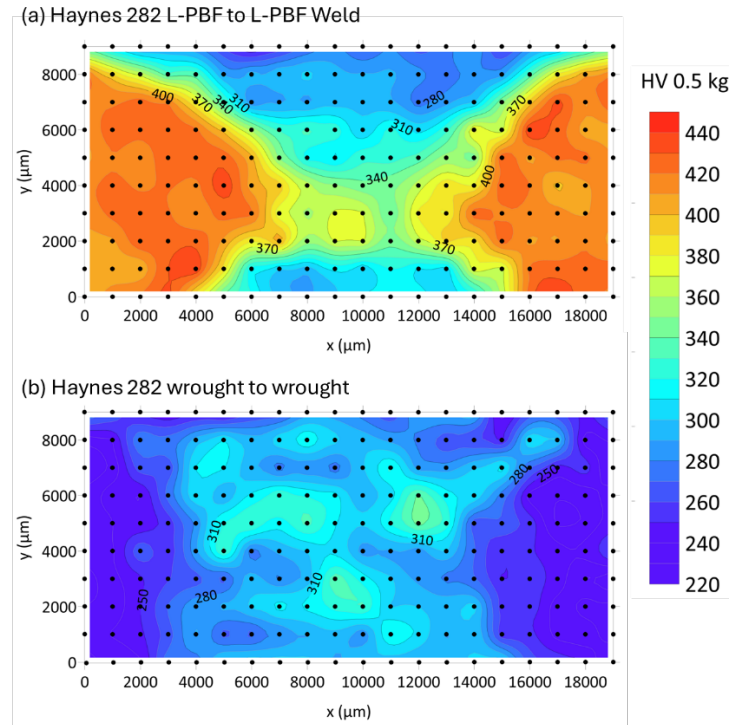
Figure 205. Microhardness of (a) Haynes 282 L-PBF to L-PBF and (b) wrought-to-wrought weld (as-welded condition)

4.4.4.7 Cross Weld Gleeble SAC Results

A total of fifteen tests of the weld (wrought to wrought and L-PBF to L-PBF) group were conducted with a target test temperature of 800°C. Based on test results for the wrought set, a 100°C/h heating rate showed a higher sensitivity to cracking than 3480°C/h heating rate such that failure occurred during heating. Two slight variations in testing were performed, including a change in the initial stress applied and the change in stroke length applied during heating for the L-PBF to L-PBF samples. The stroke length change affected the amount of stress relaxation during heating to temperature. A lower stroke value allowed for sufficient low stress prior to reaching 800°C, which allowed for no cracking to occur during the 20-hour hold soak time. The higher microhardness in the L-PBF weld, seen in Figure 205, likely contributed to a higher sensitivity to SAC, which was the justification for modifying the stroke applied during step three. Reducing the microhardness of the L-PBF plates prior to arc welding would help reduce cracking sensitivity during PWHT aging. After initial printing, a post build heat treatment with a higher temperature (>1200°C) and longer hold time to bring down microhardness and meet a value close to wrought product (<300 HV).

192

Table 68. SAC Haynes 282 Cross-Weld FZ Summary of Results

Sample ID#	Weld	Strain %	SRC Method	Heating Rate >425°C (°C/h)	Stroke (mm)	Initial Stress (MPa)	Stress at Temp (MPa)	Result	Duplicate
A1	Wrought	0.6%	1	3480	0.7	728	418	No failure within 20 h	
A2		0.1%	1			509	341	No failure within 20 h	
A3		0.6%	6	100		718	450 @ 730°C	Failed on heating ~730°C	
A4		0.6%	6	100		701	450 @ 735°C	Failed on heating ~735°C	Yes
A5		0.15%	4	1500		419	333	No failure within 20 h	
A6		0.15%	6	100		450	~350	Failed on heating at 780°C	
E2		0.15%	3	333		~450 MPa	~350	No failure within 20 h	
C1	L-PBF	0.6%	1	3480	0.7	756	~450	Failed on heating at 780-785°C	
C2		0.1%	1	3480	0.7	488/510	422	Failed @ T within 6 min.	
C3		0.1%	1	3480	0.55	435	280	No failure within 20 h	
C4		0.1%	1	3480	0.65	525	395	Failed @ T within 1.2 min.	
C5		0.1%	1	3480	0.65	406	296	Failed @ T within 1.5 min.	Yes
C6		0.1%	3	333	0.55	385	221	No failure within 20 h	
D1		0.1%	1	3480	0.6	516	391	Fail at T within 9 min.	
D2		0.1%	1	3480	0.55	509	323	Fail at T within 4 min	Yes

4.4.4.8 Conclusions and Future Work

- Haynes 282 and Inconel 740H L-PBF samples were thermomechanically tested for SAC in HAZ and weld FZ microstructures.
- HAZ of L-PBF Haynes 282 printed in the vertical orientation (Z) exhibits the best resistance to cracking and requires more strain to fracture compared to Inconel 740H samples. Haynes 282 horizontal orientation (XY) performed the worst.
- A heating rate effect is observed in arc weld HAZ of L-PBF components.

  - Haynes 282 exhibits C-curve behavior (competition between stress relief and strain age precipitation), such that intermediate heating rates perform the worst.
  - Inconel 740H results show linear behavior between heating rate and time to failure, such that the slowest heating rates perform the worst.
  - More in-depth characterization may be needed to explain the trend differences.

- Extracted weld Haynes 282 samples show slightly different behavior.
  - Wrought weld shows slower heating rate at 100°C/h led to cracking on heating, while no failure occurred at 800°C with fastest heating rate within 24 h at temperature.

193

o   L-PBF weld exhibits sensitive behavior to SAC even at the highest heating rate condition (may need more testing to verify).

4.4.5   Low-Cycle Isothermal Fatigue and Failure Mode Analysis of Weldments (Milestone 3.5.2)

In this task, the isothermal fatigue behavior of H282 was investigated under four material conditions: wrought, AM (L-PBF), welded wrought, and welded AM. The objective is to study the impact of AM and welding on the fatigue life of H282 at the service temperature. The main outcome of the result is comparing the fatigue life of the AM products and their weldments to the wrought baseline and their welds as summarized in Table 69. While H282 can be considered as a recently developed alloy, there are many published literatures about the alloy's development and properties. On the other hand, the fatigue properties of L-PBF AM H282 and the welds of wrought and AM forms of the alloy are hard to find, if existed at all. Thus, the generated database is of great significance to enable the employment of AM H282 in actual power plants applications.

Table 69. Milestone 3.5.2 Details

Milestone	Description	Metric	Success Value	Assessment Tools
3.5.2. Low cycle isothermal fatigue and failure mode analysis of weldments	The comprehensive database should include low cycle isothermal fatigue and failure mode analysis of weldments of selected alloy systems to help commercial penetration of proposed technologies at desired scale.	Low cycle isothermal fatigue at Gen3 CSP service temperature	Fatigue life of weldments >80% of wrought materials	• Cyclic thermomechanical loading at 750°C with varying strain amplitude • Fractography analysis on fatigue specimens.

4.4.5.1   Specimen Fabrication and Welding Parameters

Four sets of fatigue test specimens were prepared to study four material conditions: wrought, L-PBF (AM), welded wrought, and welded L-PBF. The wrought and L-PBF samples were machined out of wrought and horizontally built L-PBF round bars, respectively. The welded samples were prepared by gas tungsten arc welding (GTAW) of H282 plates using 180 A welding current and an average travel speed of 4.5 in/min. The plates thickness was 3/4" and they were welded in the solution annealed condition. The welded plates were cut into square bars (¾ in. by ¾ in. by 6 in.) using water jet. All bars were solution annealed and aged after welding and cutting prior to the final machining step to produce the round fatigue samples. The heat treatment was done inside stainless-steel bags filled with argon to minimize oxidation.

4.4.5.2   Testing Setup

Isothermal low cycle fatigue was performed at 750°C, which is the service temperature for the hot side in Gen3 concentrated solar power systems. The tests were conducted under strain control. From each material condition, three duplicate samples were tested at four strains: 0.6, 0.8, 1, and 1.2%. Fully reversed cycles (strain ratio $R = -1$) were applied with a frequency of 0.33 Hz sinusoidal waves. The tests were performed on a hydraulic MTS Landmark 370.10 universal testing machine. An induction heating coil was used to heat the samples during the tests. An UltraFlex induction power supply was utilized to control the temperature of the samples

using a laser pyrometer that was calibrated against thermocouples spot welded on a similar dummy sample. At first, thermocouples were spot welded on the first batch of tested wrought and AM samples. But failure was observed to initiate at those spot welds, especially at low strain range as shown in Table 70. Thus, temperature control was switched to laser pyrometer instead of thermocouples for later experiments. The samples were painted with black ceramic spray paint to eliminate the effect of oxidation on emissivity and retain consistent laser pyrometer readings during the test duration.

4.4.5.3 Fatigue Testing Results

Figure 206 Shows the fatigue life of the tested AM and wrought H282 as well as literature data for wrought H282 tested at 760°C (Haynes intl. brochure for H282 [13]) and forged H282 tested at 750°C (He et. al. [35]). It is worth mentioning that literature data is for samples aged according to the standard aging heat treatment while the tested samples for this project were aged using the modified aging treatment as discussed in section 4.3.1. Wrought H282 has higher fatigue life than the AM condition. A more pronounced difference can be observed at higher strain ranges (1.2% and 1%), which is associated with higher plastic deformation promoting stronger fatigue life dependence on the material's mechanical properties rather than surface roughness or defects. Furthermore, the difference is more distinct if the samples that failed at the thermocouple (TC) spot weld (marked with arrows) were excluded. These particular samples were forced to fail at the center of the gauge length (TC spot weld location), while most of the other samples failed at the edge of the gauge length outside the extensometer range. When failure occurs inside the extensometer range, the crack opening is accounted for into the extensometer-measured displacement, and the required force to achieve constant displacement drops gradually. On the other hand, when failure happens outside the extensometer range, the crack opening is not detected, and the force is kept at its peak until failure. Thus, most of the samples failed at TC spot weld showed delayed fracture, despite failing at a surface weakness point. Haynes brochure data for wrought H282 falls within range of our tested wrought samples, especially at higher strain ranges, indicating that the difference in heat treatment parameters did not impact the fatigue life significantly. Forged H282 showed relatively higher fatigue life, which is likely linked to the microstructure differences associated with forging.

Figure 207 summarizes the fatigue properties of H282 in the four conditions of wrought, AM, and the TIG weldments of wrought (TIGW) and welded AM (TIGAM). In this figure, the six samples that failed at the TC spot welds as shown in Figure 206 were excluded. Overall, the fatigue life of all conditions except for wrought appears to be similar, While the wrought condition is located on the high end of the fatigue life over the four tested strain ranges.
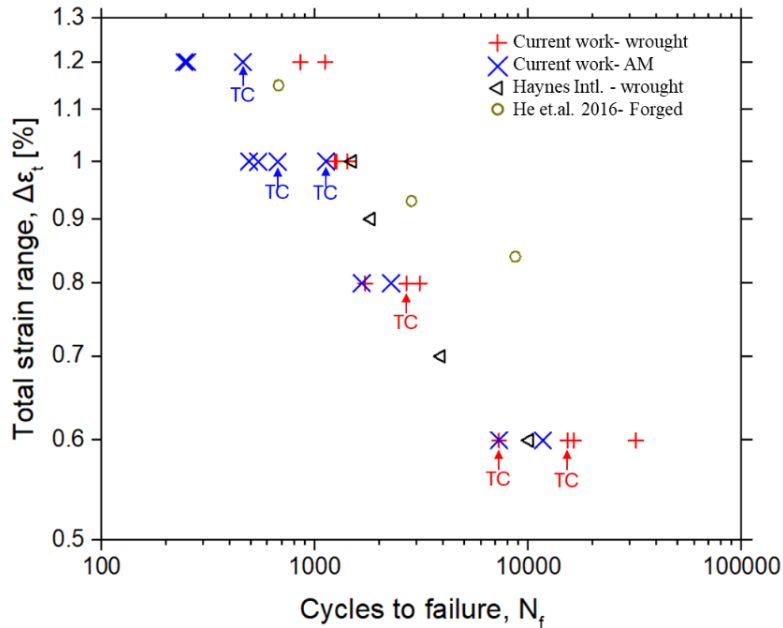
Figure 206. A comparison of fatigue life between wrought and AM H282, samples marked with a corresponding-colored arrow indicate failure occurring at the thermocouple spot weld. Literature data is taken from Haynes 282 brochure [13] and He et. al. [35]
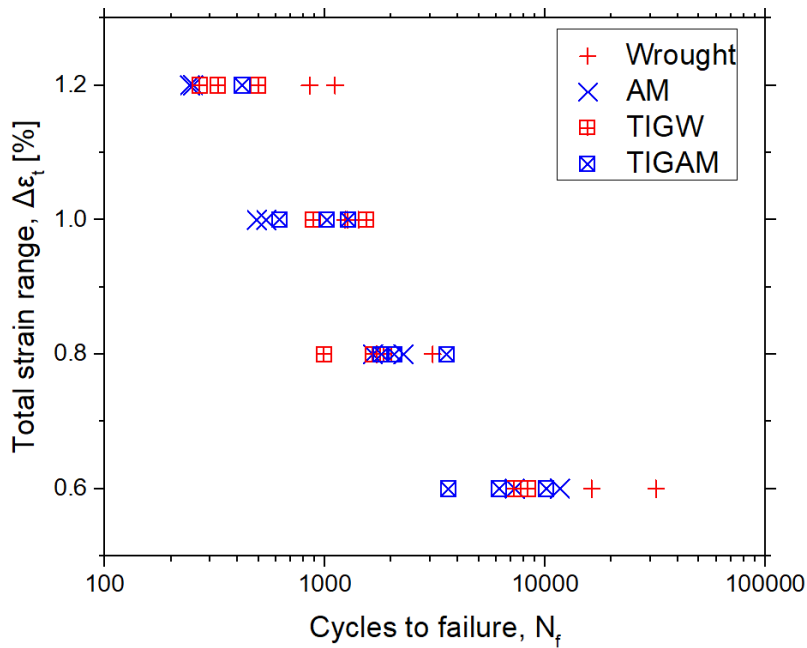
Figure 207. Results summary for LCF of H282 (wrought, AM, welded wrought, and welded AM) at 750°C with fully reversed strain ratio R=-1 and frequency F=0.33 Hz

A comparison between the hardness maps after post weld aging heat treatment of the weld cross sections in wrought and AM conditions is shown in Figure 208. The wrought condition shows a homogenous hardness profile, as the hardness values of the base metal and weld fusion zone mostly fall within 330-360 HV range. On the other hand, the high hardness of the AM base metal (390-420 HV) persisted through the PWHT. In addition, a narrow HAZ (< 0.5 mm-width) was

observed with a hardness of 360-390 HV. While the FZ showed the lowest hardness with values consistent with the hardness range observed in the wrought FZ (345-375 HV).
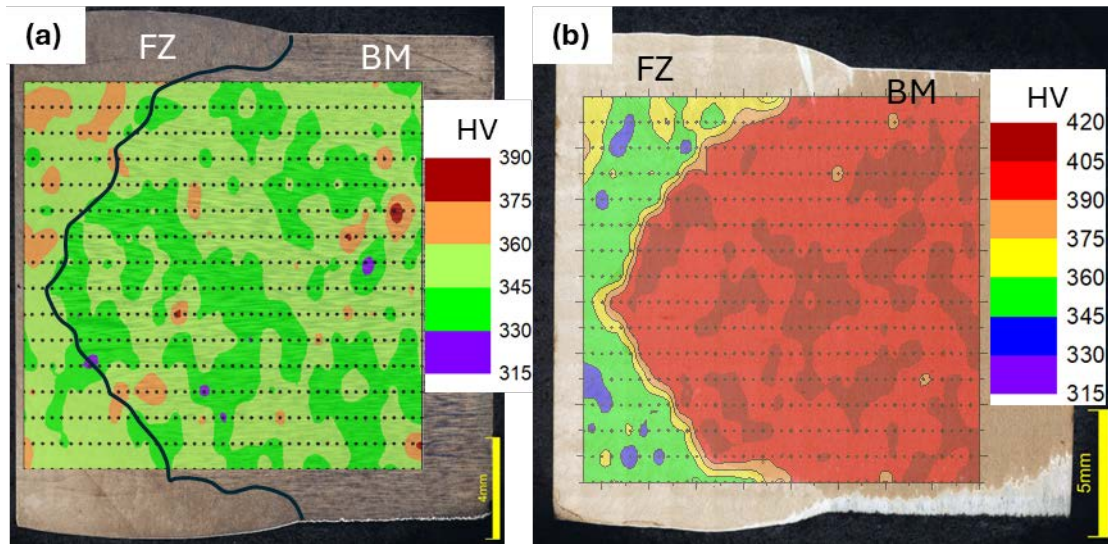
Figure 208. Hardness maps for one half of the weld cross section in (a) wrought H282 and (b) AM H282 in aged condition
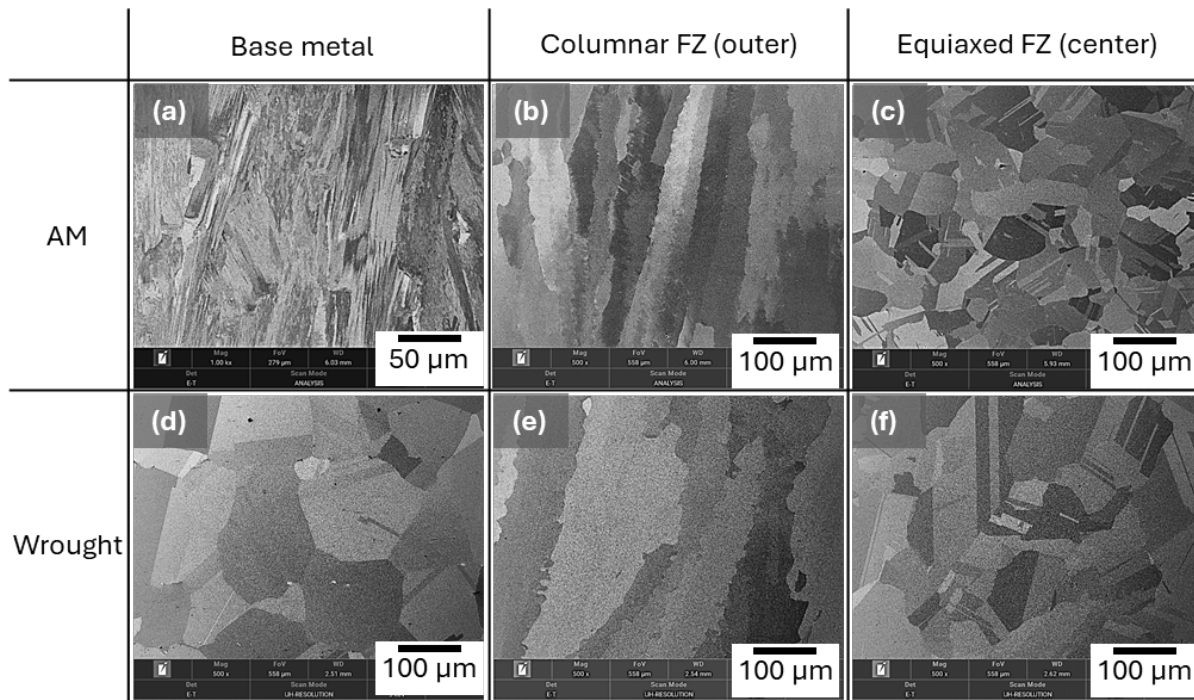
Figure 209. Low magnification SEM images comparing the grain structure of the base metal and fusion zone across the weld cross sections of AM H282 (a, b, and c) and wrought H282 (d, e, and f)

A comparison between the grain size and morphology in the base metal and fusion zone is shown in Figure 209. The AM base metal showed a typical fine columnar microstructure (please note that Figure 209(a) doubled the magnification of the rest of the images). On the other hand, wrought base metal has coarse equiaxed grains. The fusion zone in AM or wrought welds showed two grain morphologies, the outer regions showed typical relatively coarse columnar

197

grains, while equiaxed grains were observed around plate mid-thickness. Investigations of as welded cross sections did not show the equiaxed grains in the plate-mid thickness. Thus, recrystallization of the central portion of the fusion zone has most likely occurred during PWHT.

The high magnification SEM images in Figure 210 show a similar size of gamma prime particles in all regions for both conditions. However, grain boundary carbides appear to be finer in the AM base metal compared to the rest, which can be correlated to the finer grains leading to more grain boundaries area for carbide precipitation and less opportunities for carbide agglomeration. Furthermore, the AM base metal appears to have denser gamma prime particles distribution compared to the wrought base metal. Image J software was used to estimate the gamma prime volume fraction as an average of two measurements taken at 60kx and 20kx magnifications in each region. The results are summarized in Figure 211. In agreement with the high magnification SEM images, AM base metal has the highest volume fraction of gamma prime, and it showed difference relative to its FZ. Adding this observation to the finer grain size in AM base metal explains the high hardness in AM base metal compared to low hardness in the fusion zone. In contrast, wrought base metal showed a homogenous distribution of gamma prime particles, which explains the observed homogenous hardness profile.
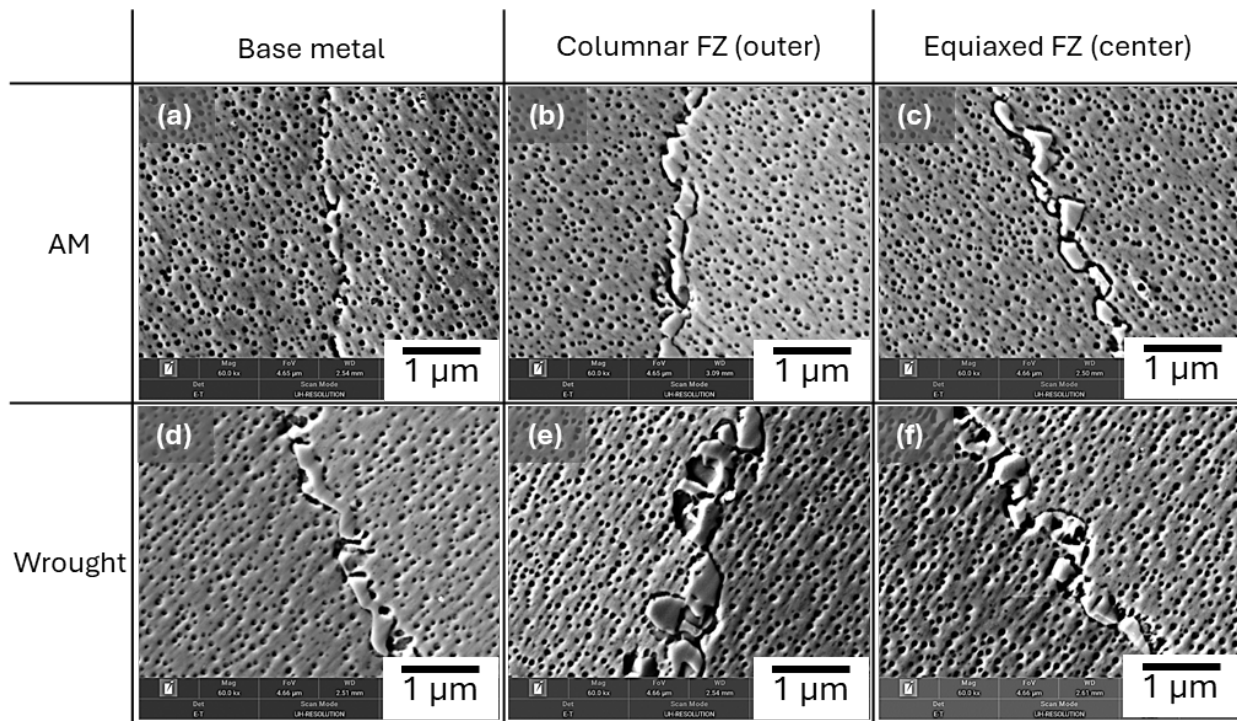
Figure 210. High magnification SEM images showing the gamma prime particles of the base metal and fusion zone across the weld cross sections of AM H282 (a, b, and c) and wrought H282 (d, e, and f)
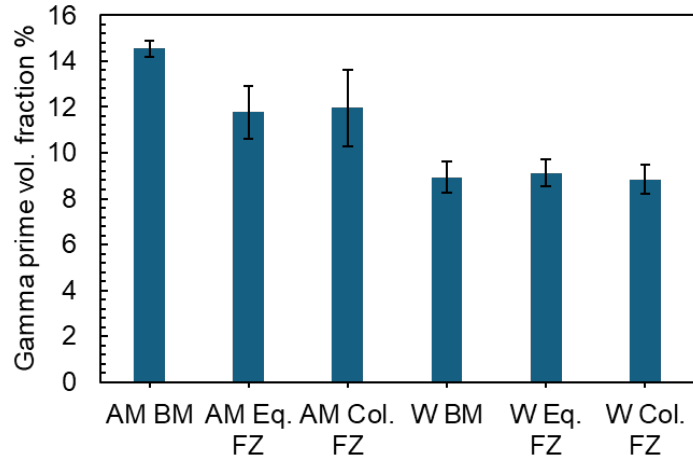
Figure 211. A comparison of gamma prime volume fraction in the base metal (BM), equiaxed fusion zone (Eq. FZ), and columnar fusion zone (Col. FZ) in both of AM and wrought H282
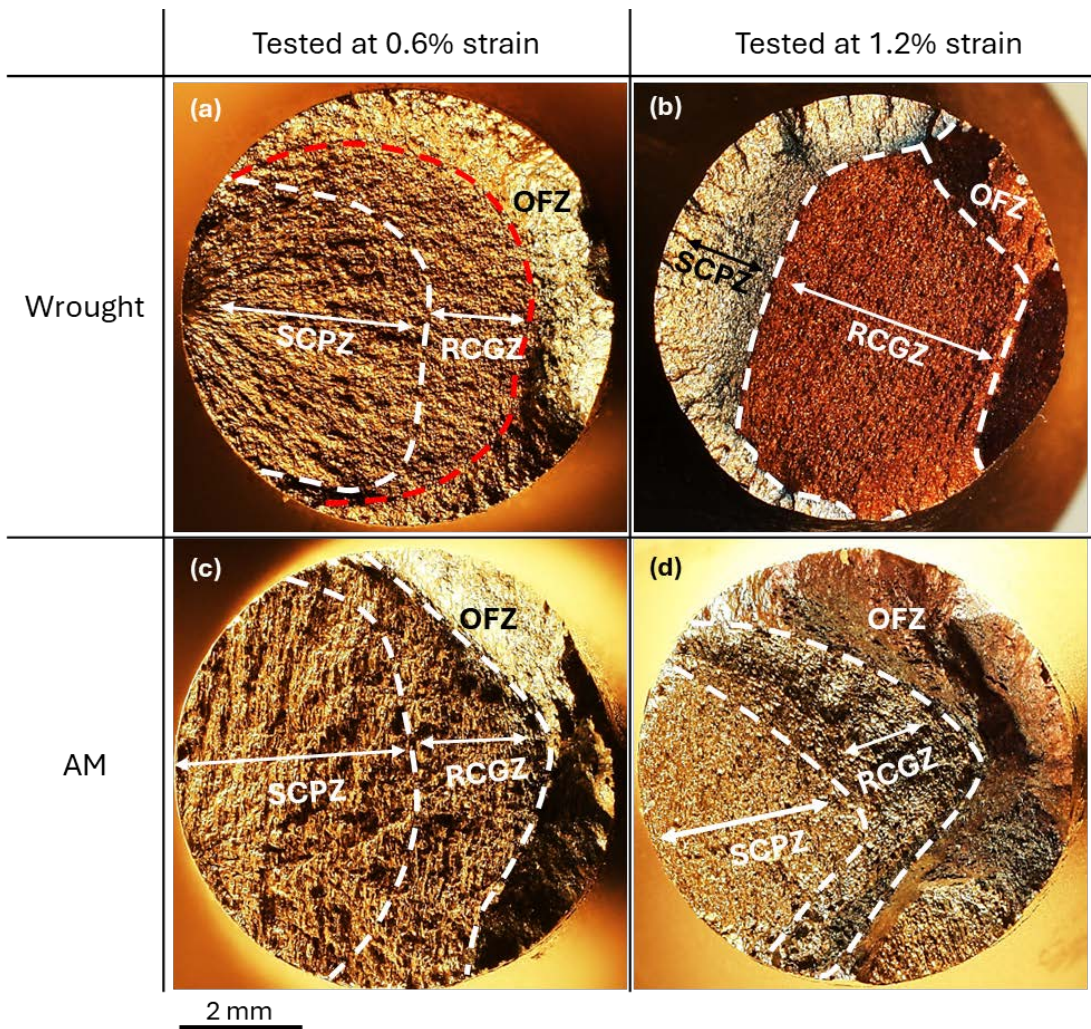
Figure 212. Stereoscope images for the fracture surface of wrought (a, b) and AM (c, d) samples tested at 0.6% and 1.2% total strain range

199

Figure 212 shows optical fractography images for non-welded AM and wrought samples tested at 1.2% and 0.6% total strain ranges. The area of the stable crack propagation zone (SCPZ) is large in samples tested at 0.6% (a and c). On the other hand, samples tested at 1.2% (b and d) showed larger areas of rapid crack propagation zone (RCPZ), or a combination of RCPZ and overload fracture zone (OFZ). This observation was expected, as the higher level of plastic deformation in 1.2% strain case induces the unstable/rapid crack propagation to occur sooner, and eventually reaching overload fracture.
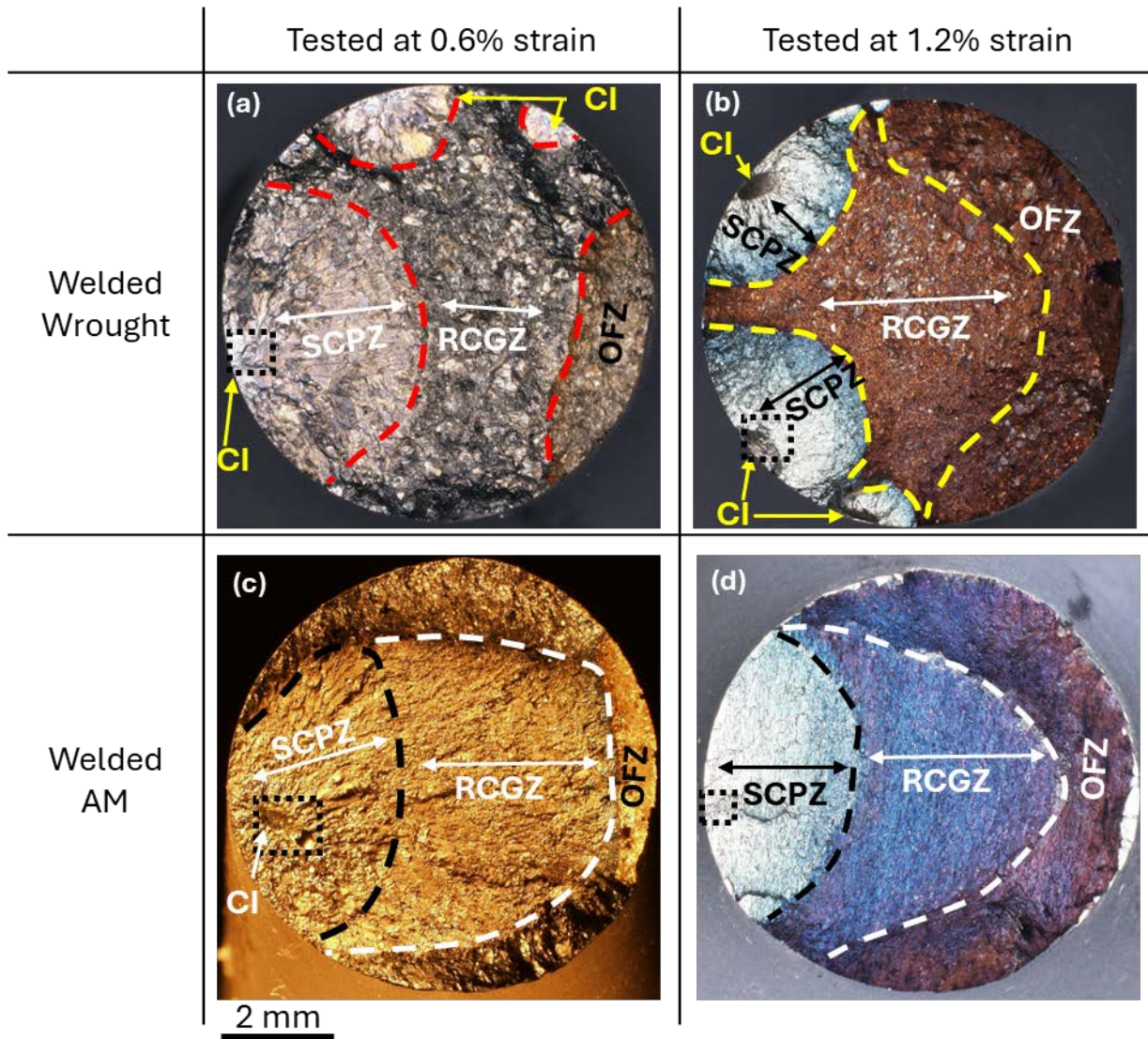
Figure 213. Stereoscope images for the fracture surface of welded wrought (a, b) and welded AM (c, d) samples tested at 0.6 and 1.2% total strain range. The black dotted boxes at the crack initiation sites mark the locations of taking the SEM images in Figure 215

The fractography images of four welded (two AM and two wrought H282) samples tested at 0.6% and 1.6% are shown in Figure 213. It is important to note that samples in Figure 213(a) and (d) failed in the base metal at the edge of the gauge length, while samples b and c failed in the weld fusion zone, as shown in more detail in Figure 214. Multiple crack initiation sites could be observed in wrought samples, while singular initiation site was observed in the two examined

AM samples. Similar to the non-welded samples, lower strain tested samples showed more area of SCPZ, compared to samples tested at the high strain range that showed larger portions of RCPZ and OFZ.

In the four examined welded samples, only one (TIGAM10) showed multiple secondary cracks along the examined longitudinal cross section. This is likely due to the high amount of plastic deformation and damage caused by the high strain range 1.2%, in addition to failure in the base metal, allowing more time for secondary crack formation. On the other hand, the other three samples did not show any cracks on their longitudinal cross sections. Those samples include two that were tested at 0.6% total strain range, involving a lesser extent of damage. In addition, one sample was tested at 1.2%; however, this sample failed at the weld fusion zone. Thus, the overall damage was concentrated in this particular region.
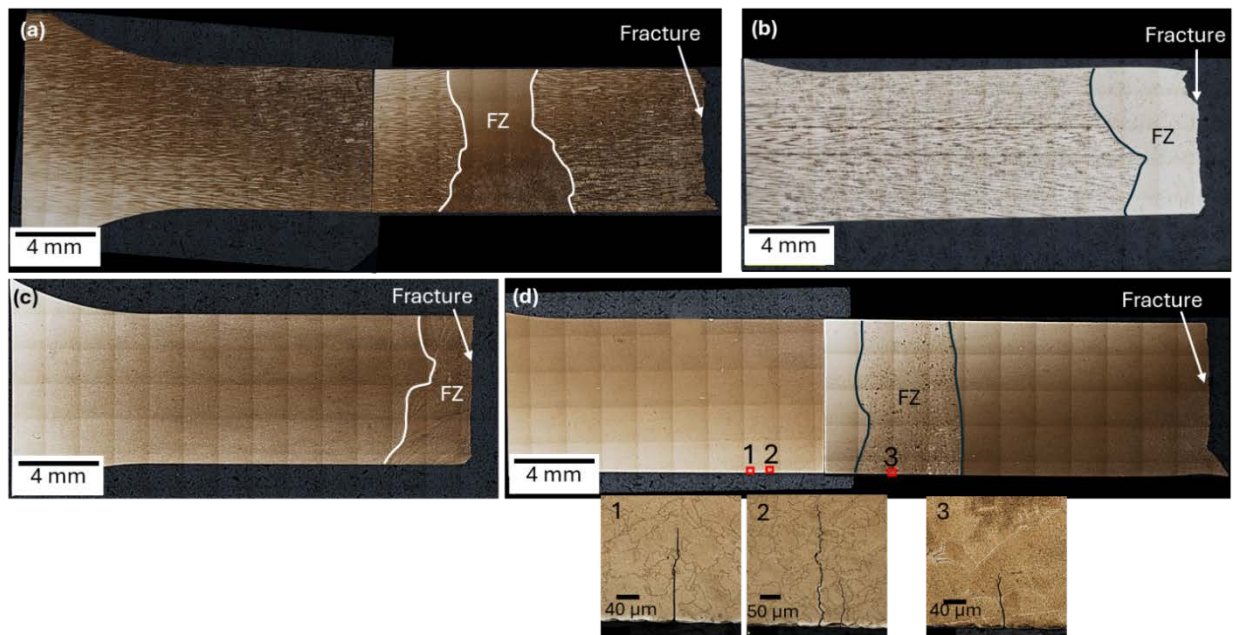
Figure 214. Stitched optical microscope images of longitudinal cross sections of samples after fatigue testing (a) TIGW5 at 0.6%, (b) TIGW10 at 1.2%, (c) TIGAM5 at 0.6%, and (d) TIGAM10 at 1.2%

In Figure 215, there is a significant amount of secondary cracks observed in the two samples that failed in the weld fusion zone (Figure 215(d) and (f)) compared to samples that failed in the base metal (Figure 215(b) and (h)). In addition, samples tested at 1.2% strain (a–d) show fatigue striations aligning in multiple directions, indicating more propagating cracks. More parallel fatigue striations can be observed for samples tested at the lower strain range 0.6% (e–h), due to the lower damage caused by the lower amount of plastic deformation at 0.6% strain. In addition, the low magnification image (e) shows a subsurface pore at the crack initiation site; the pore's spherical shape indicates that it is a weld gas porosity defect.

201
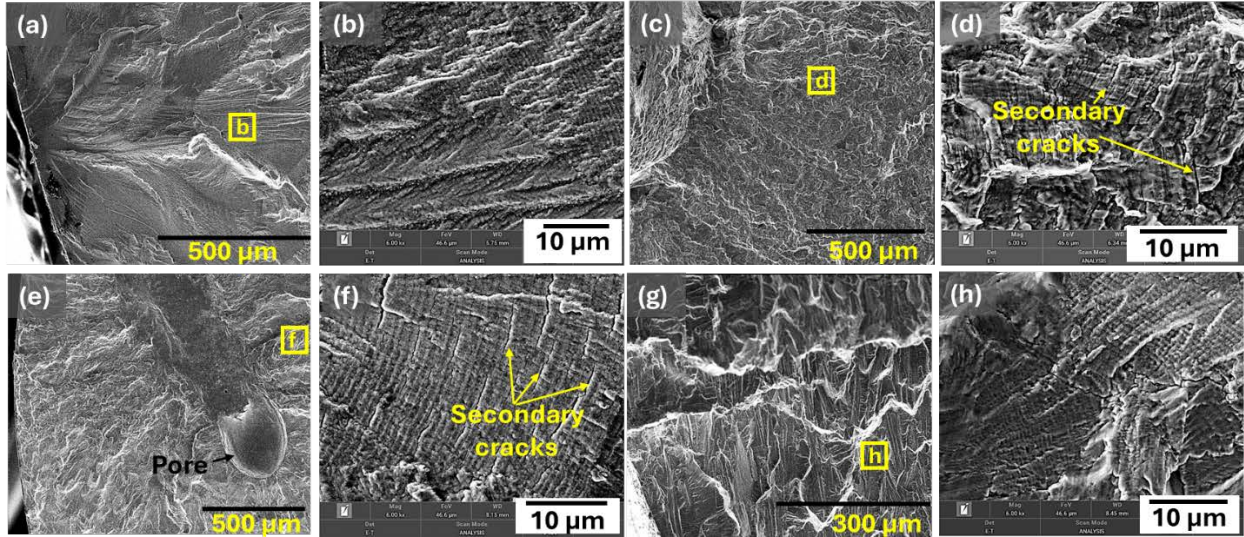
Figure 215. SEM fractography images showing the characteristic fatigue striations of (a, b) TIGW5 at 0.6%, (c, d) TIGW10 at 1.2%, (e, f) TIGAM5 at 0.6%, and (g, h) TIGAM10 at 1.2%

Table 70 summarizes the LCF testing results for all 48 samples. The original plan was to test three duplicate samples at each strain range value. In some cases, there were issues with a sample or two in the same strain range. Therefore, an additional fourth duplicate was tested at this strain range, at the expense of the duplicates number from another strain range that was deemed consistent enough with only two duplicates. The failure location was recorded for each sample and included in the table. There are six unwelded samples that failed at the thermocouple spot welds located at the center of the gauge length. Their failure location is indicated by "TC" in the table. The four failure locations indicted by A:D in the table are depicted in Figure 216. Most unwelded samples failed at the edge of the gauge length (A). On the other hand, most of the welded samples failed at the weld fusion zone located at the center of the gauge length (D). Only very few samples failed at the extensometer arm contact (B), or just inside the extensometer range but far from gauge length center (C).
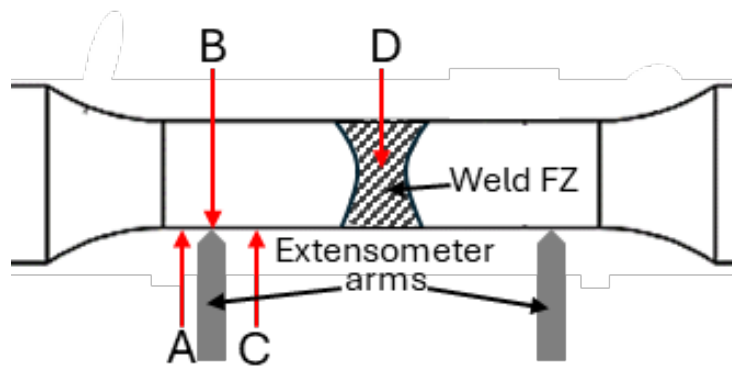
Figure 216. A schematic of the LCF sample gauge section to mark the observed failure locations

Table 70. LCF Testing Results for All 48 Tested Samples

Total Strain Range	Wrought			L-PBF			TIG Welded Wrought			TIG Welded L-PBF		
	Sample ID	Failure Location	Cycles to Failure	Sample ID	Failure Location	Cycles to Failure	Sample ID	Failure Location	Cycles to Failure	Sample ID	Failure Location	Cycles to Failure
1.2%	W2	A	1111	A1	C	252	TW1	D	270	TA1	NA	NA
	W3	A	854	A2	TC	460	TW10	D	327	TA10	A	421
				A3	NA	NA	TW11	D	497	TA11	D	184
				A12	B	244						
1%	W1	B	1418	A4	TC	669	TW2	D	884	TA2	D	1020
	W4	A	1237	A5	TC	1129	TW8	D	107	TA8	D	622
	W8	A	1266	A6	B	491	TW9	D	1541	TA9	D	1271
				A9	A	542						
0.8%	W5	A	1721	A7	A	1656	TW3	D	1652	TA3	D	1798
	W9	A	3088	A8	A	2271	TW4	D	1855	TA4	A	3569
	W10	TC	2676				TW7	D	991	TA7	D	2068
0.6%	W6	TC	15288	A10	A	7286	TW5	C	8355	TA5	D	10121
	W7	TC	7280	A11	A	11685	TW6	D	1285	TA6	D	3631
	W12	C	31926				TW12	D	7201	TA12	D	6187
	W11	A	16311									

Notes:

- Failure locations A, B, C and D are marked and explained in Figure 216, and "TC" indicates samples that failed at the thermocouple spot weld.
- W11, W12, A3 and A6:A12: remachined to reduce the gauge diameter by 0.5 mm to remove the area affected by thermocouple spot weld. Then, they were tested using a laser pyrometer instead of thermocouples.
- FW4: thermocouple failed mid test and a new one was applied to continue testing.
- All welded samples were tested using a laser pyrometer to avoid the influence of thermocouple spot welds on failure location and/or fatigue life.
- A1 and TA8: extensometer slipped before the end of the test, but the test continued as usual.

4.4.5.4 Conclusions for Isothermal Low Cycle Fatigue Testing

- Harder and fine-grained L-PBF AM H282 exhibited inferior fatigue life compared to softer and more ductile wrought H282. Welded AM and welded wrought H282 showed similar fatigue life to the L-PBF condition.
- Small subsurface weld defects that are probably not detectable by conventional field NDE methods did not significantly impact the fatigue life of welded samples.
- Most of the welded samples failed in the weld fusion zone, while unwelded samples failed at the edge of the gauge length.

4.5 Task 6: Finite Element Analysis (FEA)

4.5.1 FE Simulation of Butt-Welded EXW Clads (Milestone 1.6.1)

In this section, the finite element analyses of cladded plates used for the cold side are discussed. Specifically, the first subsection presents the results of welding simulation for cladded Grade 91 plates and cladded SS304H plates. The second subsection discusses the modeling of tensile strength of the cladded plate welds. It is noted that the workpieces studied in these two subsections are plates. The third subsection discusses the results of welding simulation for SS304H/C22 EXW clad pipe sections which represents a first step toward production-scale component welding application. Table 71 shows the Milestone 1.6.1 details.

Table 71. Milestone 1.6.1 Details

Milestone	Description	Metric	Success Value	Assessment Tools
1.6.1: Finite element (FE) simulation of but-welded explosion welding (EXW) clad coupon	FE modeling of butt-welded explosion welding (EXW) clad will be validated using results from M1.5.2. After validation, during Phase 2 it will provide guidance on welding parameters for residual stress reduction and control of microstructural changes.	FE model validation	<10%	Abaqus and/or SYSWELD simulation and validation by comparing to the thermal history measurement during welding and residual stress measurement results

4.5.1.1 Welding Modeling of G91/C22 and SS304/C22 Clad Plates

Based on previous material evaluations, Grade 91 (G91) and stainless steel 304H (SS304H) emerged as promising candidates for cold side applications, and Nickel alloy C22 and Ni201 were identified as suitable cladding materials. To further assess their performance, four clad plate combinations, specifically G91/C22, G91/Ni201, SS304H/C22, and SS304H/Ni201, were fabricated using explosive welding and subsequently subjected to tensile testing. The tensile testing results indicated that clad C22 was superior to Ni201, particularly in tensile strength. Furthermore, the G91/C22 and SS304H/C22 clad plate combinations displayed comparable tensile strengths. Thermo-mechanical modeling for these two clad plates was conducted to gain a deeper understanding of the thermo-mechanical behavior during welding and under high temperature service condition.

4.5.1.1.1 Theoretical Foundations and Model Setup

The thermo-mechanical model developed in this study comprises sequentially coupled thermal and mechanical analyses. Thermal analysis determines temperature field by solving the heat conduction equation, while mechanical analysis determines stress, strain and displacement fields by solving the static equilibrium equation with thermal loads from the thermal analysis.

There were two steps in the modeling for the SS304H/C22 case, corresponding to the physical welding and service steps. In the welding step, the residual stress and distortion were calculated with heat input from arc plasma. In the service step, the temperature was prescribed to increase from room temperature to 500°C (cold side temperature), for which a redistribution of welding stress and strain driven by thermal expansion was simulated. There were three steps in the modeling for the G91/C22 case. The welding (first) and service (third) steps were similar to those of the SS304/C22 case, whereas the new second step was used to simulate the post-weld heat treatment (PWHT).

Note that solid-state phase transformations were considered in the welding analysis for the G91/C22 case. The literature results showed that the variation in mechanical strength and volume associated with transformations played an important role in residual stress calculation for ferritic/martensite steels such as G91. The solid-state phase transformations were calculated by tracking phase fractions of austenite, freshly formed martensite, and as-received tempered martensite (base metal) over time.

The martensitic transformation obeyed the Koistinen-Marburger relationship,

$$f_m = 1 - \exp[-0.011(M_S - T)] \quad (T \leq M_S) \tag{Eq. 2}$$

where f_m is the martensite fraction at temperature T during cooling, and M_s is the temperature at which martensitic transformation starts. The volumetric change strain increment involved is given by,

$$\Delta\varepsilon_{VOL} = 3.75 \times 10^{-3} \, \Delta f_m \tag{Eq. 3}$$

The austenitic transformation was assumed as a linear process with temperature. The austenite fraction f_A is given by,

$$f_A = \frac{T - A_1}{A_3 - A_1} \tag{Eq. 4}$$

where A_1 and A_3 are the temperatures at which austenitic transformation starts and ends, respectively. The involved volumetric change strain increment is given by,

$$\Delta\varepsilon_{VOL} = \frac{-2.288 \times 10^{-3} \, \Delta T}{A_3 - A_1} \tag{Eq. 5}$$

In FEM code, the volumetric change strains were added to the thermal strain, and the yield strength of a mixture of austenite and martensite was defined as a function of temperature and phase fractions.

The PWHT was modeled by considering both the creep strain and stress and strain redistribution induced by temperature dependent mechanical properties. Creep was governed by Norton creep law,

$$\dot{\varepsilon}_{ij}^{CR} = \frac{3}{2} A \sigma_{eq}^{n-1} S_{ij} \qquad \text{(Eq. 6)}$$

where $\dot{\varepsilon}_{ij}^{CR}$ represents the creep strain rate tensor, σ_{eq} is the equivalent stress, and A and n are material constants, taking respective values of 1.10^{-20} and 10.741, when σ_{eq} is measured in MPa for G91. Additionally, creep was assumed to occur during the hold stage of PWHT only.

Figure 217 shows the model geometry and mesh for thermo-mechanical simulations. Figure 217(a–c) show the weld macrograph on the transverse cross-section for the SS304H/C22 and G91/C22 cases, respectively. The fusion line of each pass was revealed to facilitate the construction of the model geometry, as shown in Figure 217(b–d) for the SS304H/C22 and G91/C22 cases, respectively. A graded mesh was applied to minimize computational cost. Specifically, a fine mesh with sizes ranging from 1 to 2 mm was applied to the central regions containing the fusion zone and heat affected zone, while gradually coarsening mesh with sizes between 2 and 8 mm was applied to outer regions.
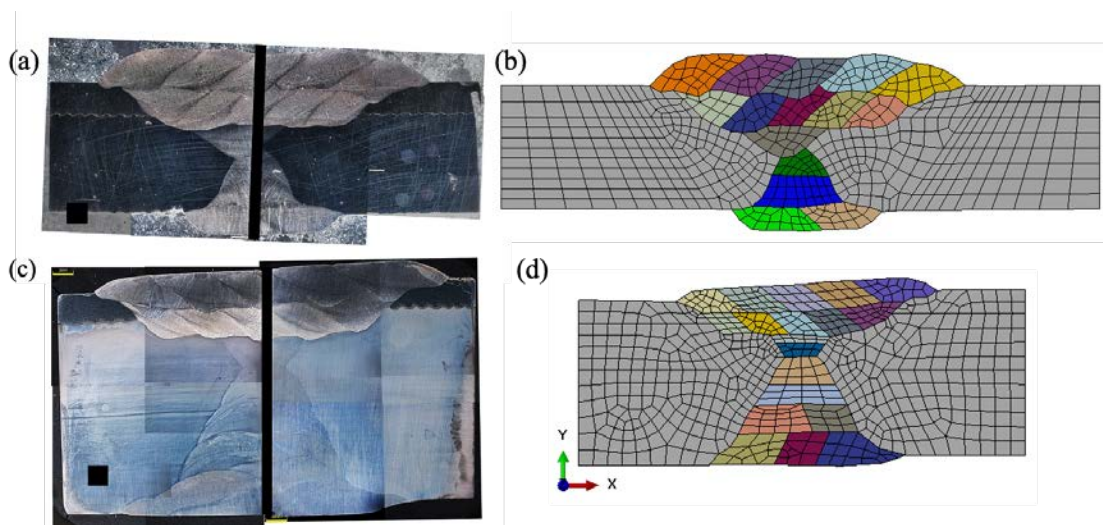
Figure 217. Model geometry and mesh. (a, c) Transverse weld macrograph, highlighting fusion line of each pass, for SS304H/C22 and G91/C22 cases, respectively. (b, d) Graded meshes for SS304H/C22 and G91/C22 cases, respectively

4.5.1.1.2 Verification and Validation

Figure 218 shows the verification of the thermal model by weld profile and inter-pass temperature. The weld profile was compared between the experimental and predicted results. The comparisons of two passes, i.e., pass 2 in the backer and pass 4 in the first clad layer for SS304H/C22 case are displayed in Figure 218(a) and (b), respectively. It can be found that the predicted weld profiles agree well with the experimental data. Figure 218(c) shows the comparison of the weld profile (e.g., pass 5 in the clad layer) for the G91/C22 case, and a good consistency is also obtained. Additionally, the inter-pass temperature was verified for this case. The predicted temperatures were found to match the thermocouple measurements, as shown in Figure 218(d).

Figure 219 shows the verification of the mechanical model by distortion values, e.g., the displacement in the Z direction. Figure 219(a–b) show the experimentally measured Z displacement for the SS304H/C22 and G91/C22 cases, respectively. The SS304H/C22 case had a larger and more uneven distortion than the G91/C22 case. Note that due to the limitation of measuring equipment, the plate center region was not measured. The distortions along the transverse centerlines (marked as black dashed lines) for both the SS304H/C22 and G91/C22 cases were extracted and shown in Figure 219(c). Although the existing data points did not provide a complete view of the distortion, they showed different distortion trends for the two clad plates: increasing height from both sides to center for the SS304H/C22 case (magenta) and decreasing height from both sides to center for the G91/C22 case (green). The distortion trends indicated that the SS304/C22 weld plate bent to the clad side, while the G91/C22 weld plate bent to the backer side. The predicted Z displacement was extracted in a similar manner and compared to the experimental data. It is found that the predicted results agreed with experimental data in both the trend and the magnitude for the SS304/C22 case (yellow), but only in trend for the G91/C22 case (red).
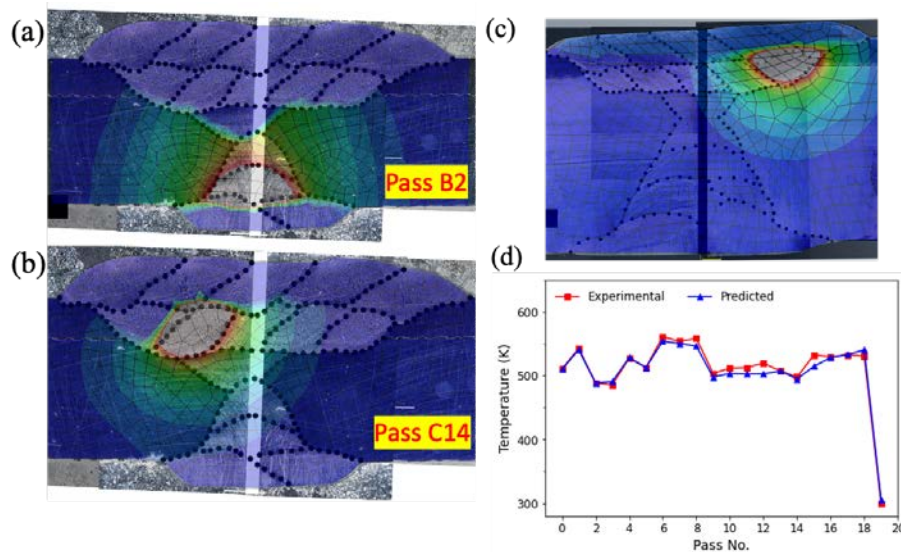
Figure 218. Verification for the thermal analysis. Comparison of fusion line between experimental and predicted results for the (a) (b) SS304H/C22 case and (c) G91/C22 case. (d) Comparison of inter-pass temperature between experimental and predicted results for the G91/C22 case
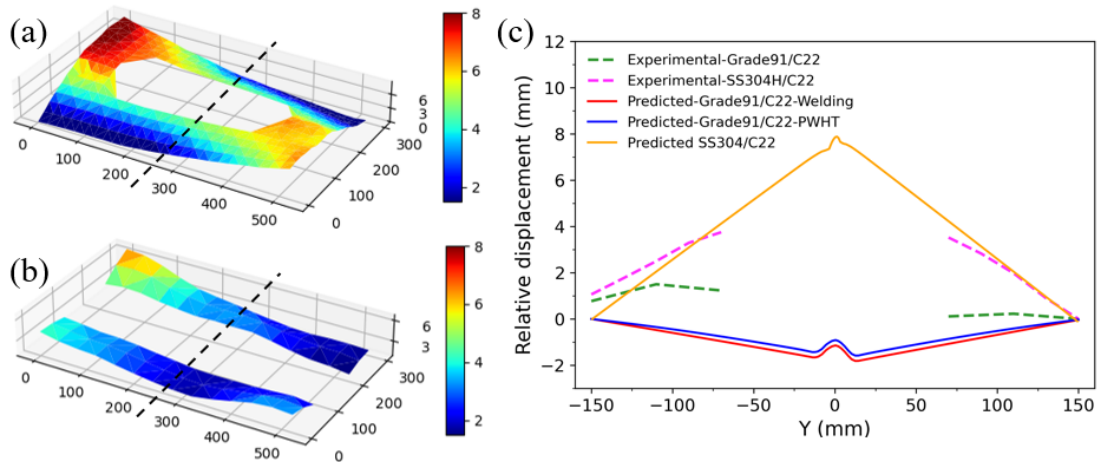
Figure 219. Verification for the mechanical analysis. Experimentally measured Z displacement for the (a) SS304H/C22 case and the (b) G91/C22 case, respectively. (c) Comparison of the Z displacement along the center transverse line between simulation and experiment

4.5.1.1.3 Results and Discussion

For a comparative analysis of residual stresses in the as-welded condition, Figure 220(a–b) show the results for the SS304/C22 case, while Figure 220(c–d) show the counterparts for the G91/C22 case. For both cases, the weld zone formed tensile stress and the outside formed compressive stress after welding. The stress in the X direction (welding direction) was higher than that in the Y direction (transverse direction). Generally, the residual stress for the G91/C22 case was larger than that for the G91/C22 case. For example, the peak stress in the X direction was ~900 MPa for the G91/C22 case and that was ~600 MPa for the SS304H/C22 case. After Grade 91 went through PWHT, the tensile stress in the weld zone was significantly reduced, as shown in Figure 220(e–f). Furthermore, the residual stresses exhibited peak values of ~200 MPa, which were notably lower compared to those observed in the SS304H/C22 case. However, a high tensile stress and a large stress gradient were formed respectively in the clad layer and at the bonding interface. Those stress distributions were due to the larger thermal expansion coefficient of the clad than the backer, causing more plastic strain during heating phase of PWHT.

208
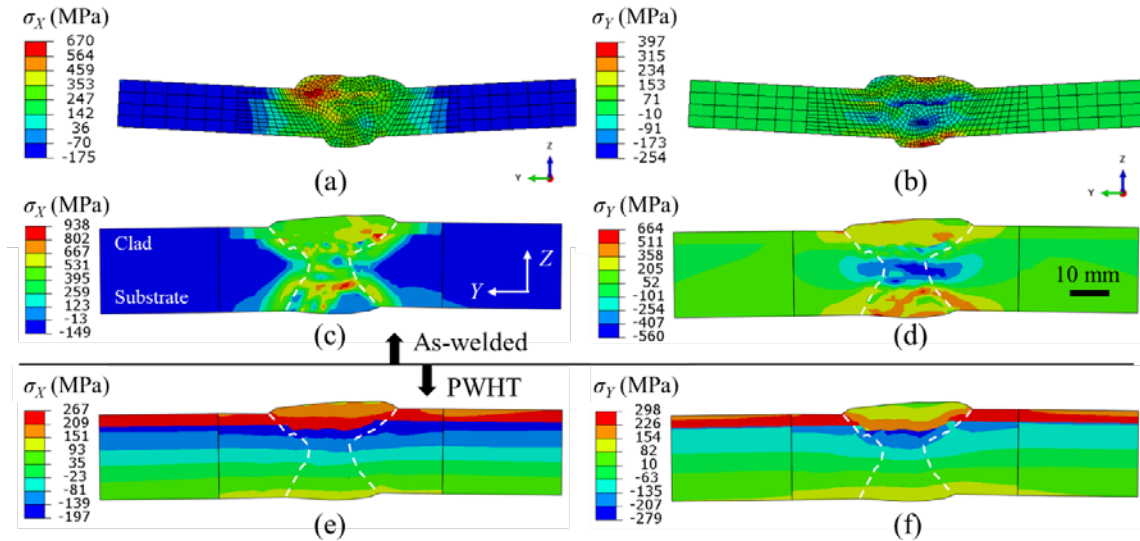
Figure 220. Residual stress distributions in the as-welded condition for (a, b) SS304H/C22 and (c, d) G91/C22 cases, and those after PWHT for (e, f) G91/C22 case. (a, c, e) in the X direction and (b, d, f) in the Y direction

Figure 221 shows the residual stress at service temperature of 500°C. Compared to the result at room temperature (Figure 220), the stresses were reduced for both the SS304H/C22 and G91/C22 cases. The clad of the SS304H/C22 plate formed tensile stress with peak values of ~80 MPa and ~150 MPa in the X and Y directions, respectively. For the G91/C22 case, the tensile stress was retained but the peak values were reduced to ~100 MPa in both the X and Y directions. This result indicated the tensile stress induced by PWHT in the G91/C22 plate became insignificant at the service temperatures. In addition, the SS304H/C22 case had slightly higher stresses in the weld zone than the G91/C22 case. Therefore, from the perspective of residual stress analysis, the two clad plates exhibited comparable characteristics, with the G91/C22 material demonstrating marginally superior performance compared to SS304H/C22.
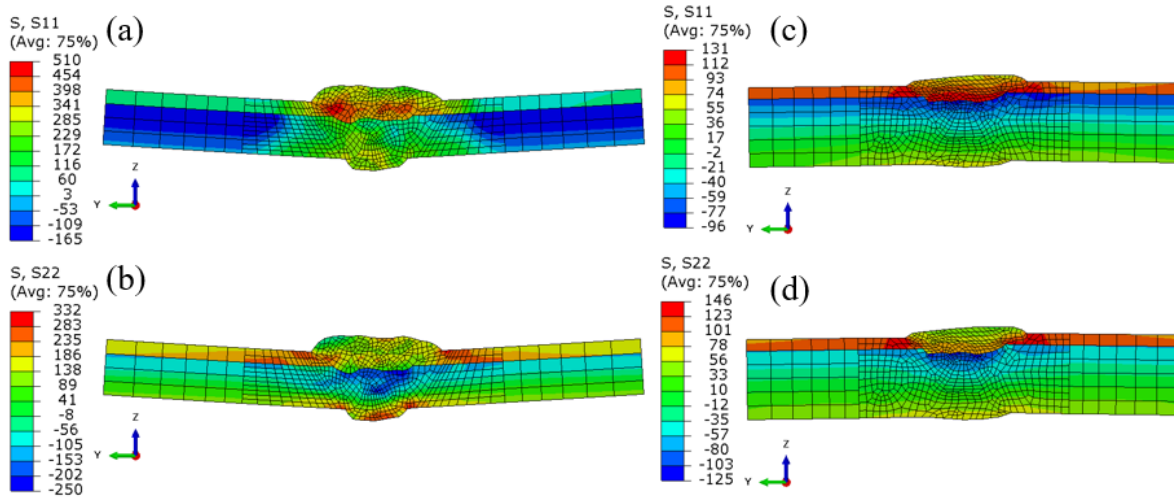
Figure 221. Residual stress distribution at service temperature of 500°C for the SS304H/C22 case (a, b), and the G91/C22 case (c, d). (a, c) in the X direction, and (b, d) in the Y direction

209

4.5.1.2 Tensile Strength Modeling of G91/C22 and SS304/C22 Clad Plates

Previously, thermo-mechanical modeling was conducted to obtain the residual stress and strain for these two welds. In order to associate the stress and strain results with mechanical properties, tensile testing modeling was conducted according to the experimental settings. The effect of welding stress and strain on the tensile properties and fracture behavior was investigated.

4.5.1.2.1 Theoretical Foundations and Model Setup

The tensile testing model involved a mechanical analysis only. The stress, strain, and displacement fields during tensile tests were calculated by solving the static equilibrium equation with prescribed boundary conditions. There are two steps in the analysis. Step 1 is for stress redistribution due to extraction from the large weld plate; Step 2 is to simulate the experimental tensile loading. One key point was that the data transfer from welding model to tensile testing model was done in such a way that the initial state for the tensile test included the residual stress and strain after welding. This was implemented by a solution mapping approach where the stress and strain data were mapped from the welding model geometry (old mesh) to the tensile testing model geometry (new mesh). The tensile testing simulation was then conducted on the new mesh.

The tensile testing analysis geometry was a section of the welding analysis geometry. Figure 222(a–b) shows the relative position of the two geometries for the G91/C22 case in 3D view and transverse view, respectively. Note that the sizes of the modeled geometry (57 mm long × 10 mm wide × 21 mm thick) were identical to those of the experimental gauge section, with the reinforcement being removed to avoid stress concentration. Figure 222(c) shows the tensile testing analysis geometry and mesh in 3D view. A uniform mesh with an element size of 1 mm was implemented to ensure precise data mapping. During tensile testing, the right face of the sample was constrained, while a displacement of 20 mm in the Y direction was applied to the left face. Similarly, the tensile testing analysis geometry for the SS304H/C22 case is shown in Figure 222(d). The same boundary conditions were applied to this sample.
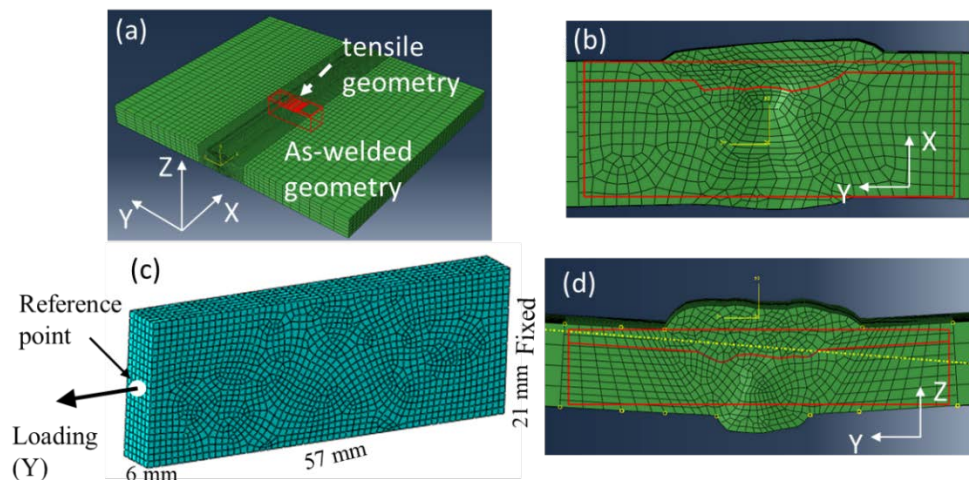
Figure 222. Welding and tensile testing analysis geometries for the G91/C22 case in (a) 3D view and (b) transverse view. (c) The 3D tensile testing analysis geometry for the G91/C22 case. (d) The welding and tensile testing analysis geometries for the SS304H/C22 case in transverse view. The tensile testing analysis geometry is indicated by red box in the welding analysis geometry

4.5.1.2.2 Validation

The tensile testing analysis was validated by strain maps captured by the digital imaging correlation (DIC) method, load-stain curves, and fracture locations.

Figure 223(a–b) shows the experimental DIC strain maps during tensile testing of the G91/C22 sample at engineering strain (εYE) levels of ~3% and ~15%, respectively. In the early stage of loading (εYE = 3%), the deformation was primarily distributed in the G91 base metal (near the weld) and the C22 weld metal as marked by purple-colored contour. Conversely, the G91 weld metal exhibited negligible deformation. At the point of fracture (εYE = 15%), a high deformation zone was observed in a lower region in the G91 base metal, highlighting localized necking inclined in the loading direction. The final fracture occurs along the direction of the localized necking, as indicated in the bottom-right inset of Figure 223(c).

From the DIC strain map, local Y-strain (εY) histories at three monitoring points − C0, C1 and C2 − were extracted, as shown in Figure 223(b). Points C1 and C2 were positioned along a vertical line, which passed through the high deformation zone, with the former placed approximately at the plate's mid-thickness and the latter in the clad layer. Point C0 was located 5 mm horizontally from C1 toward the G91 weld metal. In accordance with the experiment, the calculated strain histories at the same monitoring locations were extracted from the tensile model, and the reaction force at the reference point (see Figure 222(c)) was also extracted as the calculated load.

The deformation behavior of C0 (blue) and C1 (red) both in G91 is well captured by the tensile model, as shown in Figure 223(c) and a zoom-in view in the top-right inset. Some discrepancy is noted; for example, the model underpredicted the local strain and slightly overpredicted the load at point C1 toward the late portion of loading when the local strain was above 30%. Such deviation was attributed to the final fracture, which was not accounted for in this model. At point C2, the load was overpredicted when the local strain was above 10%, likely attributed to inaccuracies in the mechanical properties of C22. Overall, the comparison in Figure 223(c) shows some fair agreements between experimental and calculated load-strain curves at the three different locations, validating the tensile testing analysis.
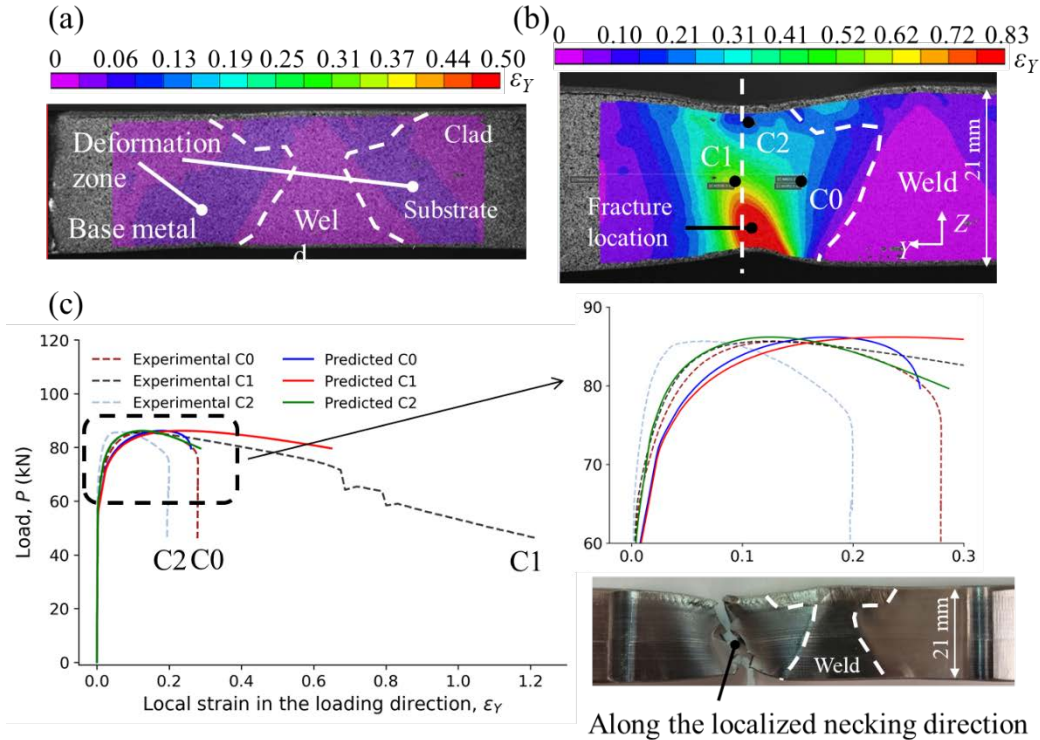
Figure 223. Validation of the tensile testing model. Experimental DIC strain map at engineering strain levels of approximately (a) 3% and (b) 15%, respectively. (c) Load-strain curves comparison of experiment and simulation at three monitoring points, C0, C1 and C2. Points C1 and C2 were approximately located at the mid-thickness and in the clad layer, respectively, along a vertical line through the high deformation zone, while point C0 was located 5 mm horizontally from C1 toward the G91 weld metal

4.5.1.2.3 Results and Discussion

The welding stress and strain were redistributed after the extraction from the welded plates due to the change in external constraints. Figure 224(a–b) shows the stress rebalance for the G91/C22 case. As this weld was subjected to PWHT, the residual stress (depicted by the von Mises stress) was already low and mainly located in the clad. After the extraction, the rebalanced stress shifted to the interior without noticeable change in magnitude. The stress rebalance for the SS304H/C22 case is shown in Figure 224(c–d). The high residual (Mises) stress was distributed in the clad with the peak value of ~400 MPa. After the rebalance, the residual stress was more uniformly distributed, and the maximum value was reduced to ~200 MPa.

Figure 225(a–d) shows for the G91/C22 case the calculated distribution of strain in the loading direction (ε_Y) during the tensile test at four different engineering strain (ε_{YE}) levels of 3%, 6.8%, 12% and 15%, respectively. Specifically, Figure 225(a) depicts that at the early stage of loading, deformation zones were observed on both sides of the weld metal, with pronounced deformations in the G91 base metal and the C22 weld metal, and minimal deformations in the G91 weld metal. This predicted deformation pattern is consistent with the experimental strain map shown in Figure 223(a). When necking started to take place (Figure 225(b)), the high deformation zone was confined solely to the G91 base metal, whereas the deformation was relatively uniform in the clad. In the post-necking stage (Figure 225(c–d)), the G91 base metal underwent additional

deformation, resulting in a high deformation zone inclined to the loading direction. This high deformation zone aligned with the experimentally observed localized necking in Figure 223(b).
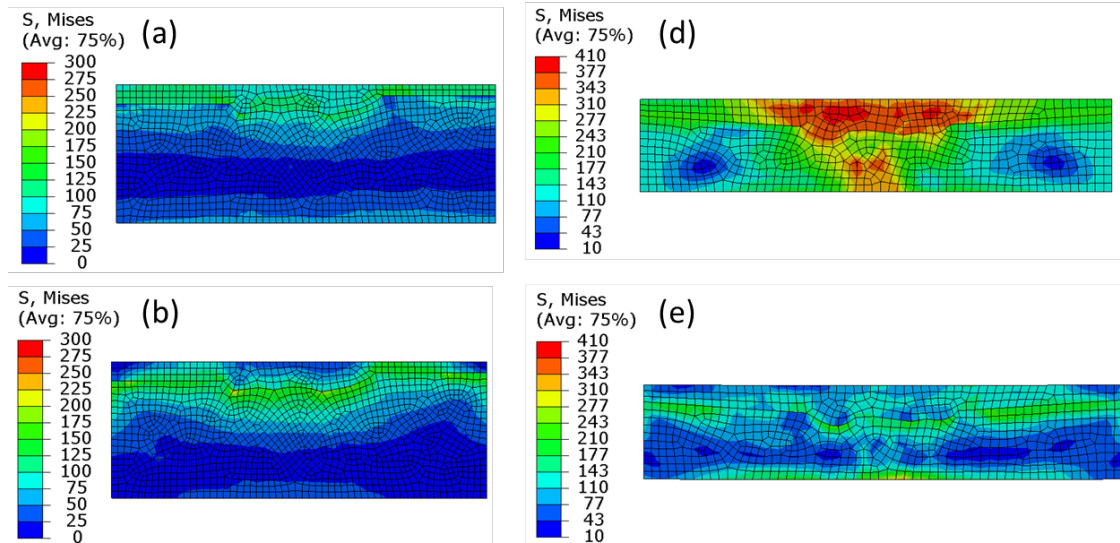
Figure 224. Rebalance of stress in the tensile testing geometry after extraction from the welding geometry. Von Mises stress (a) before and (b) after rebalancing for the G91/C22 case; von Mises stress (c) before and (d) after rebalance for the SS304H/C22 case

The failure location outside the weld metal for the G91/C22 weld can be explained by the strengths of weld metal vs. base metal. During tensile testing, the G91 base metal, which is weaker than the G91 weld metal, experiences higher deformation. In contrast, the deformation in both the base and weld metals of clad C22 is relatively uniform due to their comparable strength. As deformation accumulates in the G91 base metal, the stress triaxiality there also increased, ultimately leading to fracture. Therefore, the fracture location of the G91/C22 weld was determined by the relative strength between the base and weld metals, rather than that between the clad and substrate materials.
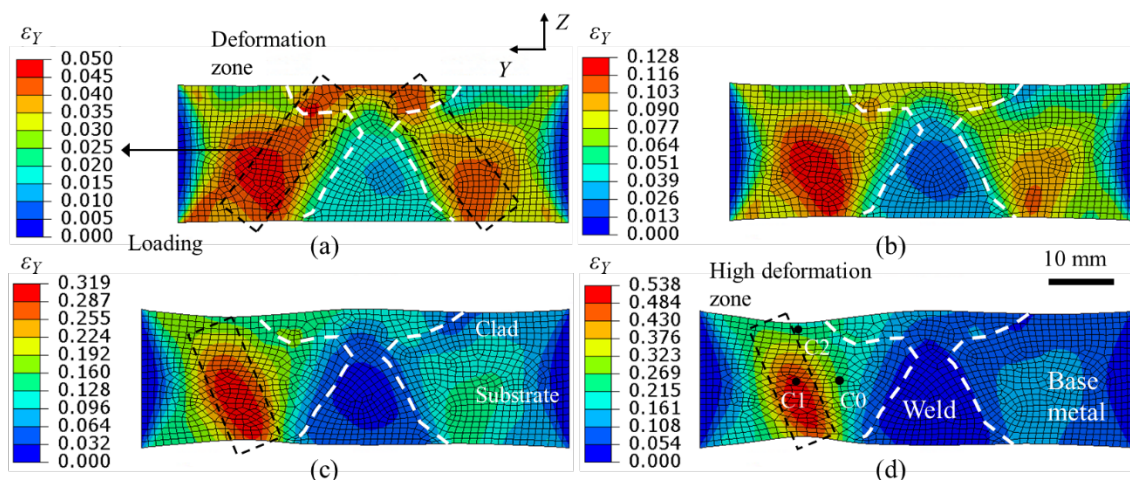
Figure 225. Predicted distribution of strain in the loading direction at engineering strain levels of (a) 3%, (b) 6.8%, (c) 12%, and (d) 15%, respectively for the G91/C22 case

213

Figure 226(a–c) shows for the SS304H/C22 case the calculated distribution of strain in the loading direction (ε_Y) during the tensile test at different engineering strain (ε_{YE}) levels of 0%, 7%, and 15%, respectively. Similar to the G91/C22 case, the base metal outside the weld metal formed large deformations and necking, which developed into the failure location. However, the predicted failure location was inconsistent with the experimental observations. In the experiments, fracture initiation occurred in the clad weld metal and subsequently propagated along the weld centerline. This discrepancy is likely attributed to work hardening such as that during explosive welding, where the material near the bonding interface was hardened due to the intense plastic flow. Additionally, cyclic loading caused by deposition of multiple beads is also known to harden the HAZ. As no PWHT was administered for this weld, the work-hardening effects were preserved, thereby elevating the material's strength outside the weld zone. As a result, the weld zone exhibited greater deformation relative to the base metal, eventually leading to necking and ultimate failure. A future study based on weld hardness maps and DIC strain maps will be needed to understand the fracture behavior of the SS304H/C22 weld.
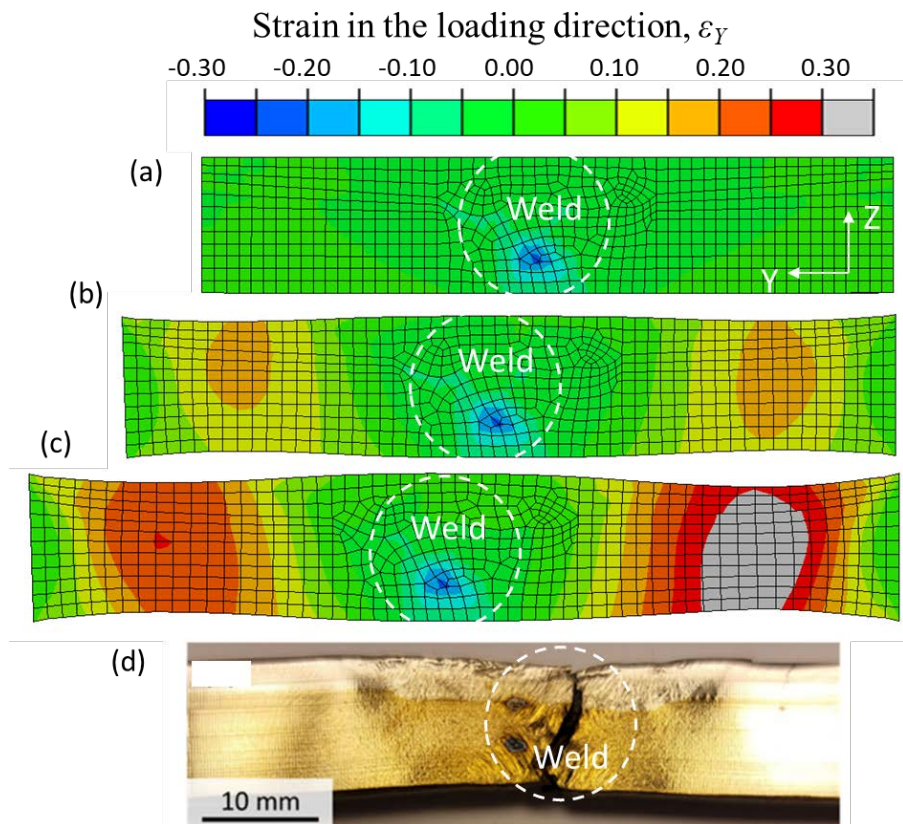
Figure 226. Predicted distribution of strain in the loading direction at engineering strain levels of (a) 0%, (b) 7%, and (c) 15% for the SS304H/C22 case. (d) Experimental failure location

The tensile testing analysis indicates that the residual stress induced by welding and PWHT has an insignificant effect on the fracture behavior. However, the residual tensile stress is compounded with the tensile loading stress, especially at the bonding interface where a high stress gradient persists, thereby exacerbating the tensile stress and triaxiality factor in that region. Hence, for cases with a weak clad-substrate bonding strength, the residual stress could be a critical factor in influencing the fracture behavior.

214

4.5.1.3 SS304H/C22 EXW Clad Pipe (Section 4.4.4)

A thermo-mechanical model was developed for girth welding of SS304H/C22 EXW clad pipe sections. For computational efficiency, the 2D axisymmetric approach was used considering the axisymmetric nature of the girth weld configuration. The residual stress and distortion were predicted, and it was found both axial and hoop residual stress components were tensile at the inner diameter (ID) which can be undesirable for stress corrosion cracking resistance. Additionally, a method involving a forced cooling at the ID was evaluated for its effectiveness to transform the stress from tensile to compressive state, which can be favorable for service in corrosive environment. Details of the model setup and results are provided in the following.

4.5.1.3.1 Model Setup

Figure 227(a) shows the experimental weld macrograph, where SS304H is the backer, alloy C22 is the clad, and alloy 622 is used as the filler metal. This figure also highlights the fusion line of individual beads. Figure 227(b) shows the model geometry, which consists of 12 passes. Due to a lack of material property data for filler metal 622, the property data of alloy C22 was assigned to all the weld beads. It is also because alloys C22 and 622 are expected to have similar thermal and mechanical properties. A graded mesh was employed, with a fine mesh applied to the weld and neighboring heat-affected zones, and a gradually coarsening mesh to the rest. Figure 227(c) shows the overall configuration of the 2D axisymmetric model, with the axis of symmetry aligned with the pipe's axis. The modeled geometry had the same dimensions as the experimental setup, with an inner surface radius of 160 mm, a length of 300 mm, and a thickness of 12.7 mm.
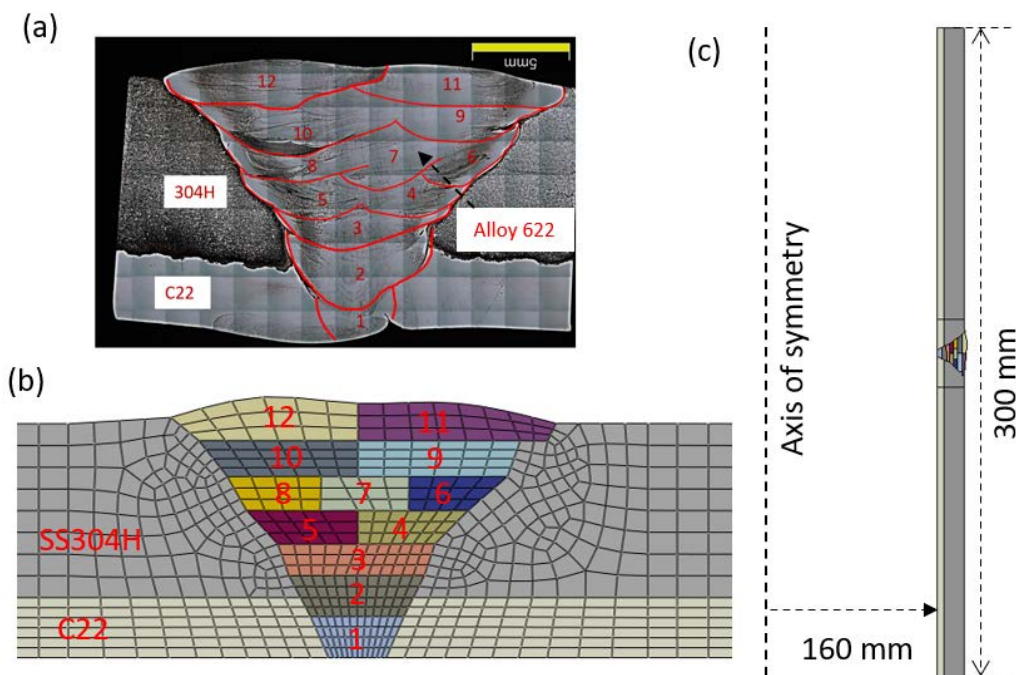
Figure 227. (a) Weld macrograph highlighting fusion line of each bead. (b) FE model geometry and a graded mesh. (c) Configuration of 2D axisymmetric FE model for SS304/C22 clad pipe welding

4.5.1.3.2 Verification

It is noted that the moving heat source approach with double ellipsoidal distribution, which were used in the 3D thermo-mechanical models, was not used for the 2D axisymmetric model of the pipe girth weld. This is mainly because the 2D axisymmetric model did not account for the heat conduction along the weld travel direction (i.e., the circumferential direction). Instead, the weld metal was heated up and held above the melting temperature for a predefined time duration to simplify the thermal analysis. To verify the thermal analysis results, Figure 228(a–b) shows the calculated molten pool (gray) shapes of pass 2 and pass 12, respectively, which aligns with the experimental data. Figure 228(c) shows the temperature field at the end of the cooling of pass 10. The final temperature in the weld nugget is 358 K, consistent with the experimental data. The comparison of inter-pass temperature for all passes is shown in Figure 228(d), where a good agreement is found. The thermal analysis results were verified by the overall agreement in terms of fusion boundary and inter-pass temperature between experiment and simulation.
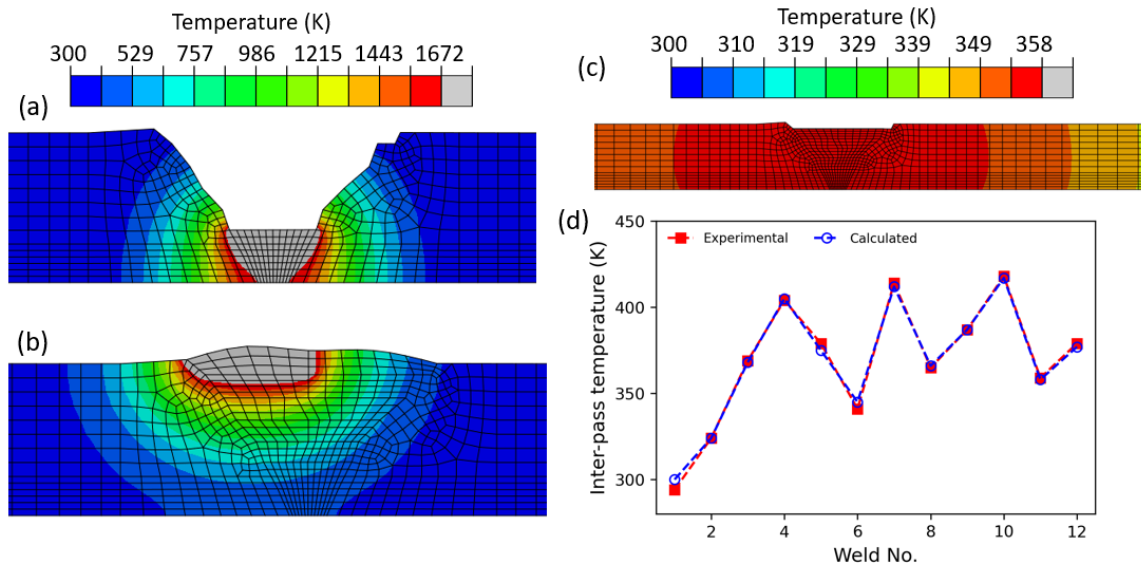
Figure 228. Thermal analysis verification for SS304/C22 clad pipe welding. Predicted molten pool shape for pass 2 (a) and 12 (b), respectively. (c) Temperature field at the end of cooling following pass 10. (d) Comparison of inter-pass temperature for all passes between experimental and simulated results

4.5.1.3.3 Results and Discussion

Figure 229 shows the calculated residual stress following the completion of the welding process in terms of the axial and hoop stresses. Overall, the axial stress was tensile in the weld and the adjacent heat-affected zone, as shown in Figure 229(a). A high stress region was located on the left in the heat affected zone of SS304H. This is likely due to this heat-affected zone being subjected to cyclic hardening. The hoop stress distribution shows a similar pattern, but a higher magnitude compared to the axial stress, as shown in Figure 229(b). Tensile stress at the inner diameter (ID) was deemed detrimental to the stress corrosion cracking resistance or corrosion fatigue in corrosive environment as it can help accelerate cracking initiation.

This report is available at no cost from the National Renewable Energy Laboratory at www.nrel.gov/publications.
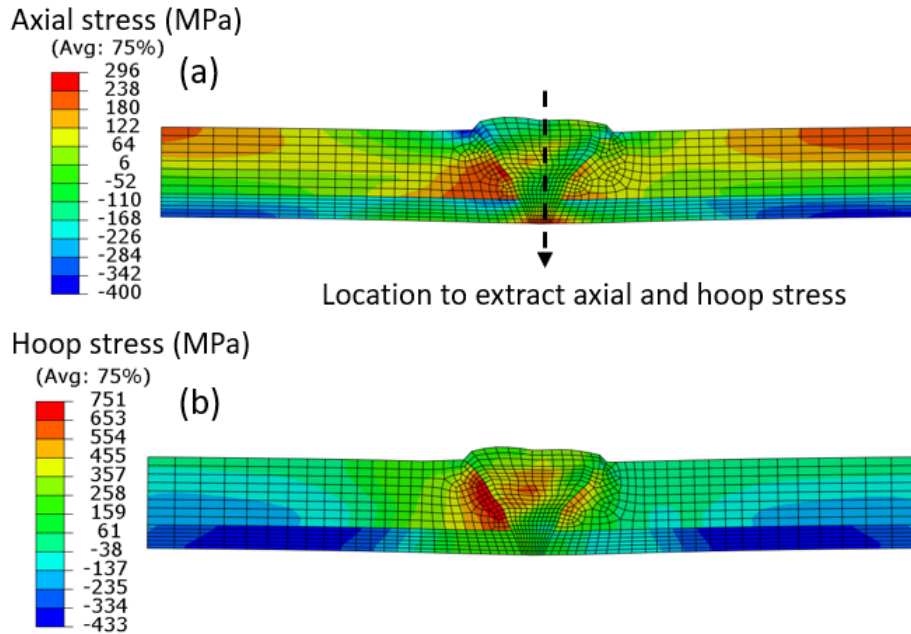
Figure 229. Predicted distribution of (a) axial and (b) hoop residual stress for SS304/C22 clad pipe welding.

Figure 230(a) shows the hoop stress formed after the completion of pass 1. Tensile hoop stress was dominant throughout the entire weld and the adjacent heat-affected zone. Figure 230(b) shows the temperature field at an instant during the cooling of pass 1. The relatively uniform cooling of the entire pass suggested that the pass behaved as a single unit constrained by the surrounding material, leading to the formation of predominantly tensile stress.
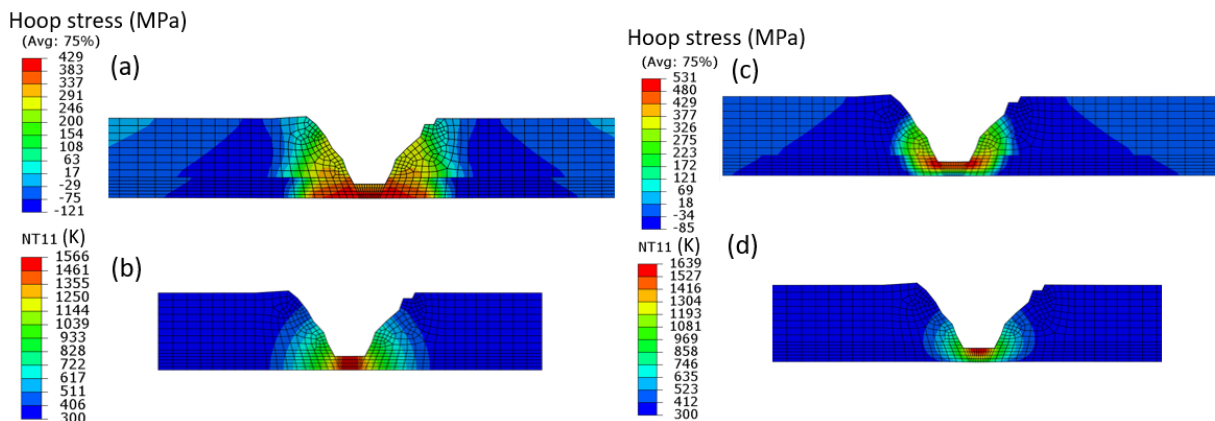
Figure 230. (a) Tensile hoop stress at the inner diameter (ID) and (b) the typical uniform temperature field during cooling of pass 1. (c) Compressive hoop stress at the ID and an example non-uniform temperature field during cooling of pass 1 when a forced cooling is applied at the ID

One approach to disrupt the uniform thermal behavior was to apply a forced cooling at the ID. A new simulation case was conducted with an enhanced film heat transfer coefficient (h_c) of 20,000 W/m K, which was roughly 1,000 times greater than that used for natural air convection. Figure 230(c) shows the hoop stress of the new case with an enhanced h_c. The hoop stress was in tensile state in the upper area of the weld but in compressive state in the ID area, rather than the predominantly tensile pattern with normal h_c. The temperature field of the new case was shown

in Figure 230(d). The previously observed uniform cooling pattern was no longer present; instead, there was a noticeable temperature difference with the bottom being cooler and the top being hotter. From the classic three-bar-frame problem, it is known that the plastic strain formed at high temperatures is essential to the formation of tensile residual stress. As the ID region was kept to low temperatures by the enhanced cooling, it did not incur much plastic strain and consequently had compressive stress (similar to that of the base metal).

Figure 231(a–b) show the axial and hoop stress profiles at the weld center along a vertical line indicated in Figure 229(a). These stress profiles clearly highlighted the tensile state of axial and hoop stresses at the ID. The stress result was further compared to literature data, which was measured from a pipe welding case of carbon steel-Ni82-SS304L. While there were differences in magnitudes, the calculated stresses exhibited a comparable trend to the literature data, which supported the validity of the thermo-mechanical model developed in this study. Additionally, the stress results for the new case with enhanced h_c are also included in the figure, denoted by light blue lines. Indeed, both axial and hoop stresses were in a compressive state at the ID in this new case. Certainly, introducing an enhancing cooling on the ID surface during cooling may not be feasible, but this case supports the utility of the FE model in helping to optimize welding process to reduce the tensile residual stress formed near the ID.
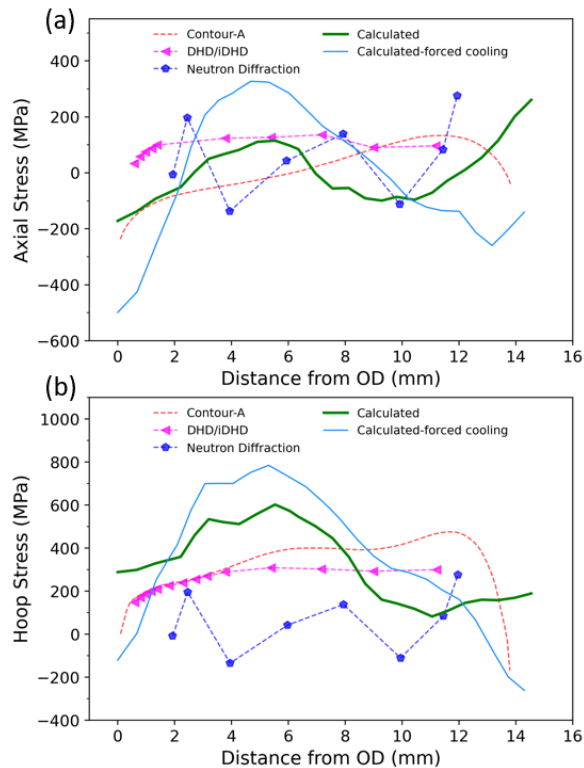
Figure 231. (a) Axial and (b) hoop stress profiles at the weld center along a vertical line indicated in Figure 229(a). The simulation results are compared to experimental data in the literature. Note the literature data has a similar pipe wall thickness but involves different materials and different number of weld passes and welding parameters. Two simulation cases are presented. One corresponds to the welding experiment in this study and the other corresponds to a new case with a forced cooling at the ID

4.5.2 FE Model Optimization of Welding Process of AM Samples to Wrought Metal (Milestone 2.6.1)

The previous section describes the modeling results for welds in the cold side of the CSP plant. Similarly, to aid the welding process optimization, the simulation of additively manufactured to wrought materials that are used in the hot side of the plant was performed, and the simulation results are discussed in this section. First, the study on the asymmetrical weld nugget shape is investigated using a molten pool heat transfer and fluid flow model. Second, the residual stress and distortion is predicted using a thermo-mechanical model. Table 72 lists Milestone 2.6.1 details.

Table 72. Milestone 2.6.1 Details

Milestone	Description	Metric	Success Value	Assessment Tools
2.6.1: Finite element (FE) model optimization of welding process of additive manufacturing (AM) samples to wrought metal	The FE model for the welding process of AM samples to wrought metal should be validated to provide critical inputs for optimization of welding parameters.	Error between calculated FE and experimental evaluations	< 10%	FE simulation, Gleeble experimental simulator and metallographic examination

4.5.2.1 Heat Transfer and Fluid Flow Modeling

4.5.2.1.1 Theoretical Foundations and Model Setup

In the welding process involving additively manufactured (AM) H282 and wrought H282, an asymmetrical weld shape was noted, with the wrought side displaying a broader weld width. To further investigate this phenomenon, oxygen concentration measurements were carried out: a combustion analyzer for the AM H282, and optical emission spectroscopy (OES) for the wrought H282. The results revealed a significantly higher oxygen content in the AM H282 compared to the wrought H282. Specifically, the oxygen levels in the AM H282 were measured at 114±12 ppm in the building plane and 98±7 ppm in the building direction, whereas the wrought H282 exhibited an oxygen concentration of only 3.46 ppm.

The experimental results described above motivated the development of the molten pool model. The hypothesis is as follows. In the classical theory of molten pool flows, the Marangoni effect, induced by the spatial gradient of surface tension, plays a great role in melt flow patterns and the resultant weld pool shape. For instance, when the surface tension gradient is oriented away from the pool's center, the molten pool tends to become wider and shallower. In the specific scenario involving the welding of wrought H282 to AM H282, the presence of a high oxygen content on the AM side contributes to reduced surface tension. This condition precipitates a pronounced surface flow toward the wrought material, resulting in the formation of a wider and shallower weld on that side.

The Marangoni effect was considered by tracking the oxygen concentration in the molten pool. The oxygen concentration ϕ was solved by a user-defined scalar equation,

$$\frac{\partial \rho \phi}{\partial t} + \frac{\partial}{\partial x_i}(\rho u_i \phi) = \frac{\partial}{\partial x_i}\left(\Gamma \frac{\partial \phi}{\partial x_i}\right) + S_\phi \tag{Eq. 7}$$

where ρ is the density, u is the velocity, Γ is the diffusion coefficient, and S_ϕ is the source term. Note that the diffusion part (the first term on the right) was not considered in this case for simplicity.

The surface tension was modeled as a function of both temperature, T and oxygen concentration, a_o.

$$\gamma = \gamma_m^0 - A(T - T_m) - RT\Gamma_s \ln\left(1 + k_1 a_o e^{-(\Delta H^0 / RT)}\right) \tag{Eq. 8}$$

where γ_m^0 is the surface tension of pure metal at the melting point, A is the temperature slope of surface tension $(d\gamma/dT)$ for pure metal, T_m is the melting point of material, R is the universal gas constant, Γ_s is the excess surface energy at saturation, k_1 is a constant which is related to the entropy of segregation, and ΔH^0 is the standard heat of adsorption. For a nickel alloy system (Ni-Cr-Co-Mo-O), the values of most parameters are unavailable. Therefore, the Fe-O system was used instead.

The temperature- and oxygen-concentration-dependent Marangoni shear stress τ_s on the molten pool surface in the tangential direction is given by,

$$\tau_s = \frac{\partial \gamma}{\partial T} \frac{\partial T}{\partial s} + \frac{\partial \gamma}{\partial a_o} \frac{\partial a_o}{\partial s} \tag{Eq. 9}$$

where s is a tangential vector to the local surface.

Figure 232(a) shows the computation domain of the molten pool model. The computation domain, with sizes of 20 mm long × 18 mm wide × 7 mm high, comprised a 3 mm high upper part accommodating the gas phase and a 4 mm high lower zone occupied by the metal phase. A fine mesh (0.5 mm) was applied in the center region, and a gradually coarsening mesh was applied in other regions, as shown in Figure 232(b). The molten pool model was implemented within ANSYS Fluent, a commercial computational fluid dynamics (CFD) simulation code.
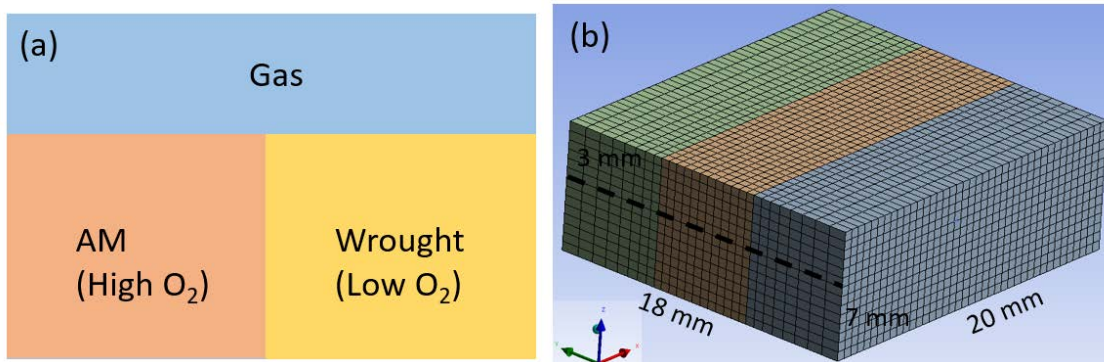
Figure 232. (a) Schematics of phase configuration in the multi-phase fluid flow simulation, and (b) Model geometry and mesh

4.5.2.1.2 Validation

Two cases were carried out in both experiments and simulations. Case 1 was labeled as "low heat input" with welding current of 150A, arc voltage of 14.3V, and welding speed of 2.3 IPM. Case 2 was labelled as "high heat input" with welding current of 200 A, arc voltage of 15V, and welding speed of 2.3 IPM.

Figure 233 shows the comparison of the weld zone on the transverse cross-section for the two cases between experiment and simulation. For all these figures, the right is AM H282 and the left is wrought H282. For Case 1 in Figure 233(a), the experimental weld shape seems asymmetrical about the initial joining interface. However, the predicted weld zone exhibits a symmetrical shape, as shown in Figure 233(c). This inconsistency is likely attributed to an offset in the alignment of the welding torch with the plates in the experiment, rather than the Marangoni effect. If the Marangoni effect was the cause, the depths of the weld zone on both sides would have been different (which is not the case as shown in Figure 233(a)).

For Case 2, as illustrated in Figure 233(b), a slight asymmetry is noted in the experimental weld zone. Specifically, at the mid-depth, a concave shape is evident on the AM side, whereas the wrought side exhibits a typical convex shape. The simulation outcome also captures this concave-convex characteristic at the mid-depth. Nevertheless, the experimental results show that the widths of the weld zone are similar on both sides, while in the simulation results, depicted in Figure 233(d), the weld zone is shifted toward the wrought side.
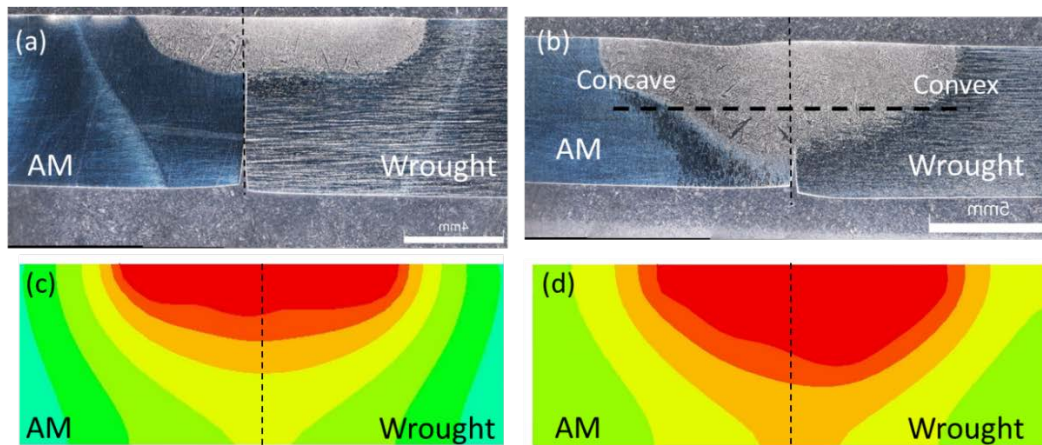
Figure 233. Comparison of weld shape between experiment and simulation (a) (b) Experimental and predicted results for case 1 (low heat input), respectively; (b) (d) Experimental and predicted results for case 2 (high heat input), respectively

4.5.2.1.3 Results and Discussion

Figure 234 shows the evolution of molten pool shape and temperature field on the transverse cross-section (x = 10 mm). At t = 0.2 s, depicted in Figure 234(a), the arc just arrived at the plane and the metal started melting. At t = 0.4 s, the molten pool reached the peak depth. An apparent molten pool asymmetry about the centerline was observed: a depression was formed on the AM side while a bump was formed on the wrought side, as shown in Figure 234(b). The molten pool width on the wrought side was larger but the depth was smaller than those on the AM side. This asymmetry remained when the molten pool was cooling down, as shown in Figure 234(c–d).
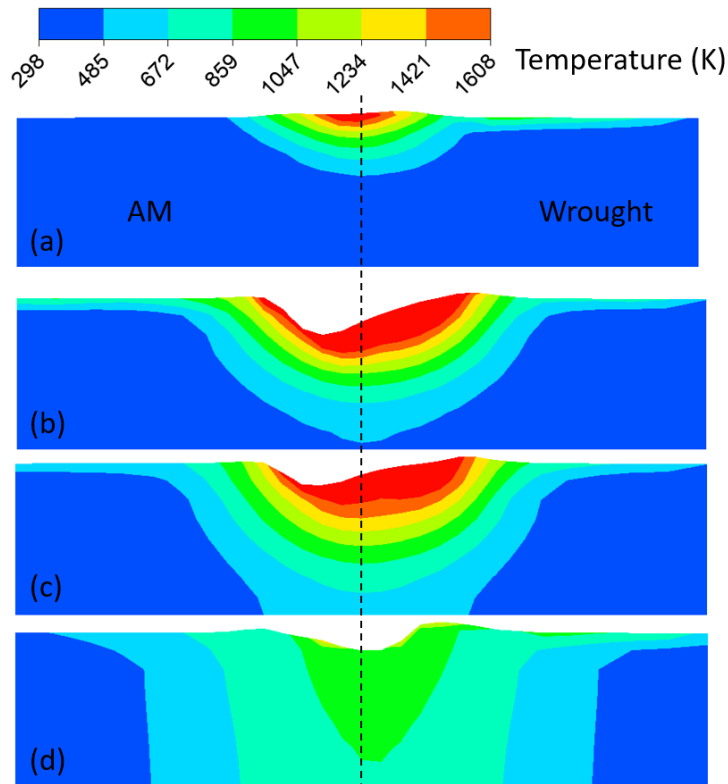
Figure 234. Molten pool shape and temperature field evolution on the cross-section (x = 10 mm) at instants of (a) t = 0.2 s (b) t = 0.4 s (c) t = 0.5 s (d) t = 1.2 s

Figure 235 shows the velocity field of fluid flow within the molten pool. As the oxygen was rich on the AM side, the surface tension was low. The surface tension spatial gradient caused the flow patterns directed toward the wrought side. Mass and heat were transferred by the flow patterns to the wrought side, resulting in a wider molten pool. At the same time, the strong surface flow impeded the heat transfer to the deep region, resulting in a shallower molten pool.
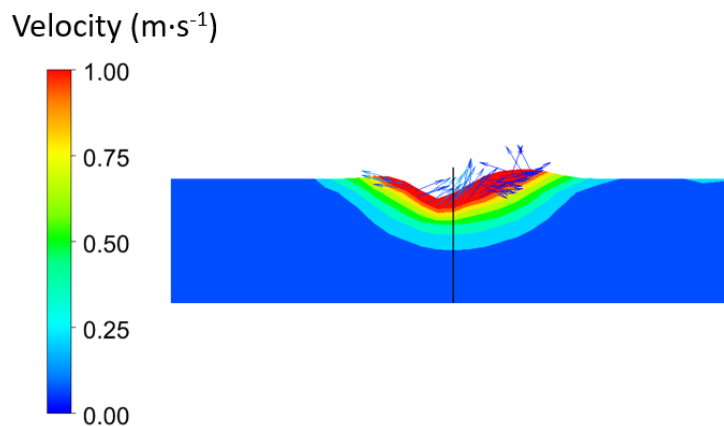
Figure 235. Marangoni effect induced flow on the cross-section at t = 0.4s

The flow patterns induced by the Marangoni effect offer a plausible explanation for the asymmetric pool shapes observed in the experiments (Figure 233(a–b)). However, the oxygen

222

distribution in the weld zone suggests an alternative cause, as explained in the following. Figure 236(a) presents an oxygen map measured via Electron Probe Micro-Analysis (EPMA), revealing that oxygen is relatively uniformly dispersed throughout the weld zone. This experimental evidence aligns with the molten pool simulation results depicted in Figure 236(b). The uniform distribution of oxygen suggests that it would rapidly homogenize due to the convection of the molten metal. Moreover, a comprehensive literature review indicates that oxygen is typically present in AM alloys as oxides and is not "freely" soluble in liquid nickel alloys.

In the literature, Mishra et al. [36] studied welding of two stainless steel plates with different sulfur concentrations, and they also found the sulfur, a strong surface-active element, has a homogenous distribution in the molten pool. Instead, the arc behaviors are significantly altered, resulting in a shift in the position of the arc toward the low sulfur side. An additional study of arc and droplet transfer behaviors is out of scope for the current project. It will be an important topic for further investigation in a follow-on study.
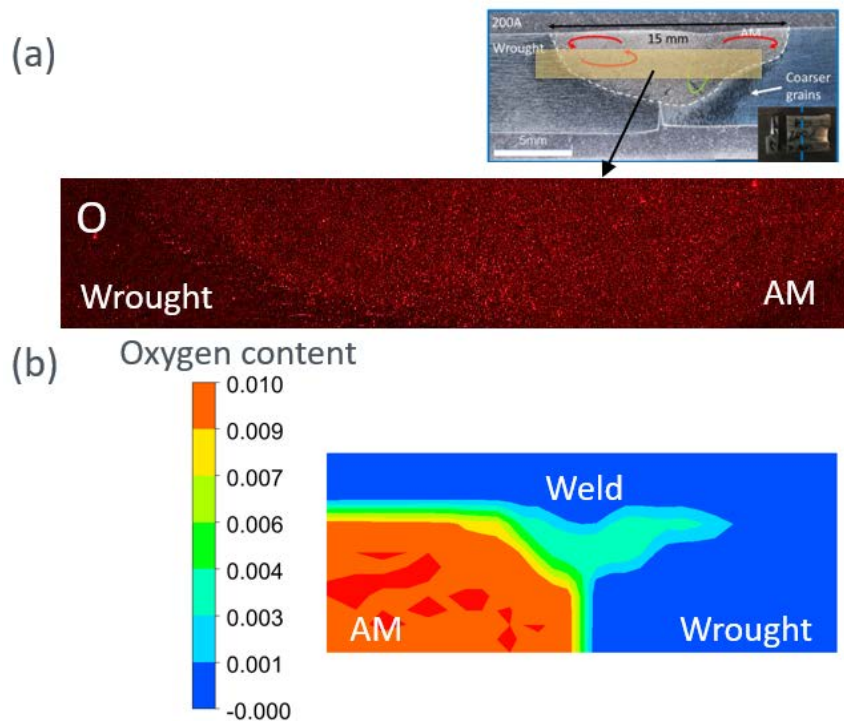
Figure 236. Oxygen concentration distribution on the cross-section obtained from (a) experimental measurements by EMPA and (b) fluid flow model solving oxygen transport equation for weld of wrought to AM H282

4.5.2.2 Thermo-Mechanical Modeling

The two materials considered for the hot side are the nickel-base superalloy H282 and stainless steel 304H. In this subsection, thermomechanical modeling results for both materials are presented. It is noted that the theoretical foundations are the same as those used previously in Section 4.5.1 for simulating the welds in the cold side. Therefore, only the key aspects are highlighted below.

4.5.2.2.1 AM H282 to Wrought H282

4.5.2.2.1.1 Model Setup

The model geometry and mesh for the welding of AM H282 to wrought H282 is shown in Figure 237. Figure 237(a) shows the weld macrograph, highlighting the fusion boundary of each pass. Figure 237(b) shows the model geometry in 2D views; for ease of meshing, the experimental weld profiles were simplified. Figure 237(c) shows the model geometry in 3D views, with sizes of 100 mm long × 150 mm wide × 13.8 mm thick. Note that the model geometry is shorter than the experimental sample by 50 mm in length direction to reduce the computational time. Previous studies have shown that a shorter model can produce mechanical results (e.g., residual stress and distortion) at a similar accuracy to those of a full-length model. A graded mesh approach was utilized, where the central weld region was discretized with fine elements, and the outer regions were applied with progressively coarsening elements.
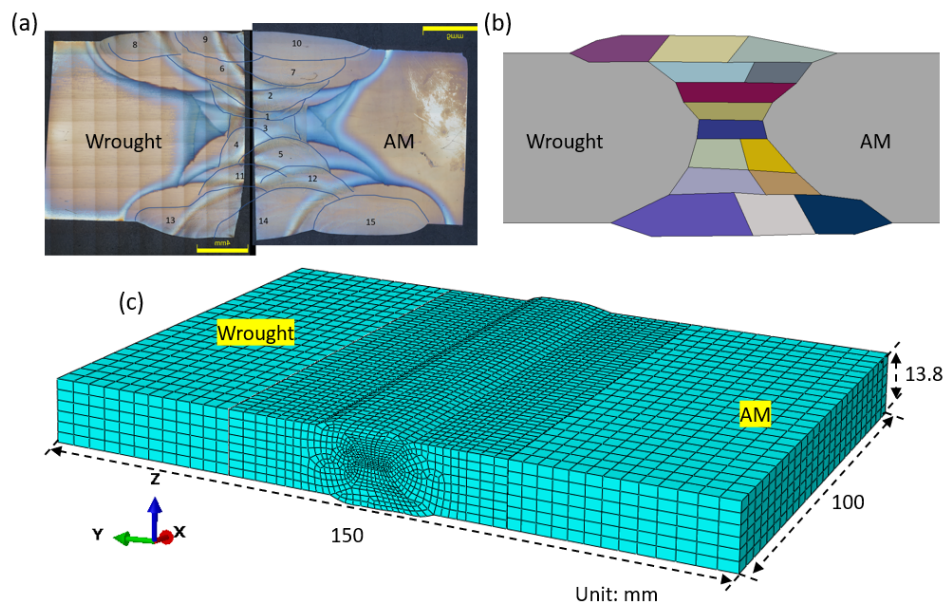
Figure 237. (a) Experimental weld macrograph with all fusion boundaries revealed. (b) Model geometry in 2D views (c) Model geometry in 3D views and graded mesh

4.5.2.2.1.2 Model Verification and Validation

Figure 238 shows the verification of the thermal analysis by weld profile and temperature history measured by thermocouples. The weld profile was compared for each pass; two representative comparisons for pass 5 and 14 are shown in Figure 238(a–b), respectively. The predicted weld profile agreed well with the experimental data. Figure 238(c) shows the comparison of the measured temperature history between experiment and simulation. A good agreement was found in peak temperature, cooling rate and inter-pass temperature.

224
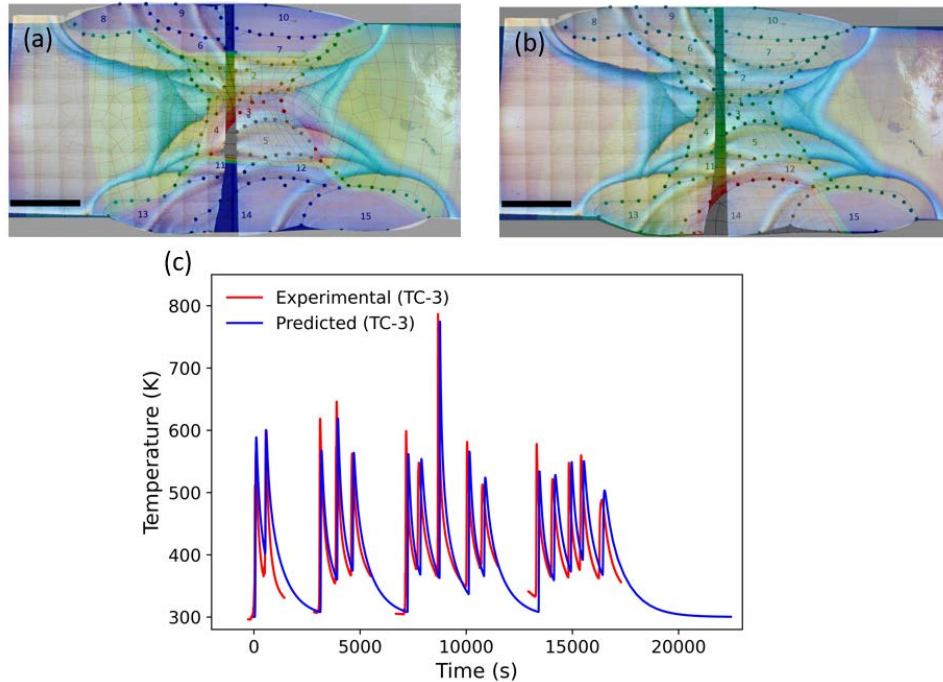
Figure 238. Thermal analysis verification. Comparison of weld profile for pass 5 (a) and pass 14 (b) and comparison of temperature history (c) between experimental and predicted results
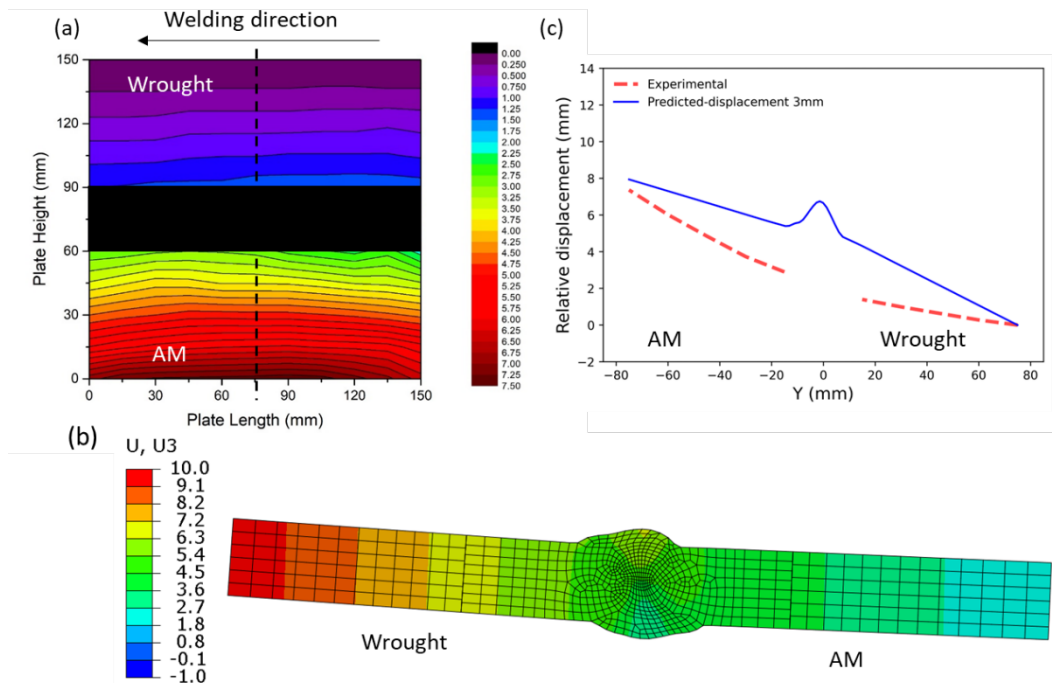
Figure 239. (a) Experimentally measured displacement in the Z direction (Z_d) from the root side (bottom side in Figure 237(a)). (b) Predicted Z_d on the transverse cross-section. (b) Comparison of Z_d along the transverse centerline between experimental and predicted results

Figure 239 shows the validation of the mechanical analysis through distortion values, which are represented by displacement in the Z direction (Z_d). Figure 239(a) shows the experimental Z_d measured from the root side (bottom side in Figure 237(a)). Note that the displayed results are

relative values with respect to the top right corner. An uncommon distortion trend can be observed: Z_d is almost constant in the longitudinal direction but asymmetrical about the weld longitudinal center in the transverse direction. Figure 239(b) shows the predicted Z_d on the transverse cross-section, and Figure 239(c) shows the comparison of Z_d along the transverse centerline between experimental and predicted results. It can be seen that the asymmetrical feature and the maximum value of distortion are well predicted by the model. However, the model predicts a linear increase in Z_d across the width, which is inconsistent with the experimental observations showing a non-linear increase over the width. A possible reason is the inaccurate mechanical properties of AM H282 which were measured on the isotropic wrought material.

4.5.2.2.1.3   Results and Discussion

Figure 240 shows the residual (von Mises) stress on the transverse cross-section of the H282 AM-wrought weld. The weld zone shows a high von Mises stress, with the peak value exceeding 1000 MPa, which was aligned with the high hardenability of H282. In contrast, the base metal exhibits significantly lower stress levels, displaying an almost symmetrical distribution around the weld zone, despite the asymmetrical nature of the distortion.
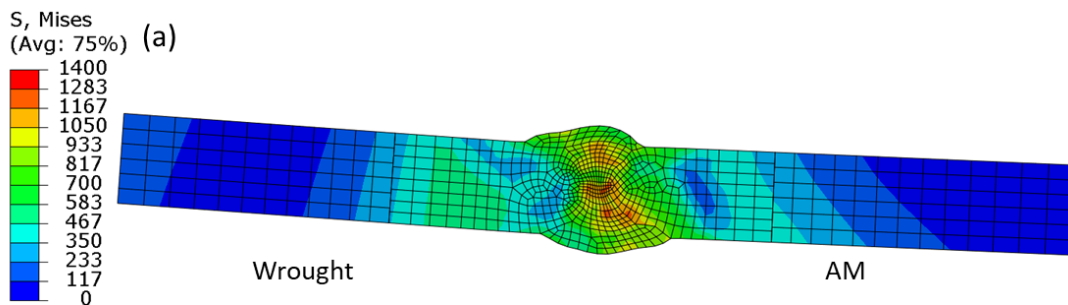
Figure 240. Residual (von Mises) stress of AM H282 to wrought H282 weld

The asymmetrical distortion observed was attributed to the flexible clamping approach used in the welding experiment, where clamping was applied on the side exhibiting larger distortion during the welding process. This method was intended to reduce residual stress by avoiding over-constraining the workpiece. However, the residual stress in the weld zone remained high, with peak values similar to the material's yield strength, indicating that the local stress was not effectively mitigated. Additionally, this approach resulted in a significant, asymmetrical distortion. Consequently, it is recommended to use a full clamping approach instead of the flexible clamping method.

4.5.2.2.2   H282 to SS304H

4.5.2.2.2.1 Model Setup

Figure 241 shows the model geometry and mesh for the welding of H282 to SS304H. Figure 241(a) displays the experimental weld macrograph, which clearly delineates the fusion boundary for each pass. In Figure 241(b), the modeled weld is shown, exhibiting a close alignment with the experimental data in terms of both the shape and position of each individual bead. Note that the top surface is labelled as the face side, while the bottom surface is labelled as the root side. Figure 241(c) shows the model geometry in 3D views and the associated graded mesh. The

model geometry measures 150 mm long × 160 mm wide × 12.7 mm thick, which is half the size of the experimental sample in the length direction to reduce computational costs. A graded mesh approach was employed for the geometry: the central region (Zone 1), encompassing the weld zone and heat affected zones, was discretized with fine elements. The outer regions adjacent to the central areas were discretized with gradually coarsening elements, while the more distant regions were discretized with even coarser elements. Note that there was a discontinuity in element size between Zone 2 and Zone 3; consequently, a tie constraint was applied at their interface to facilitate mesh transition.
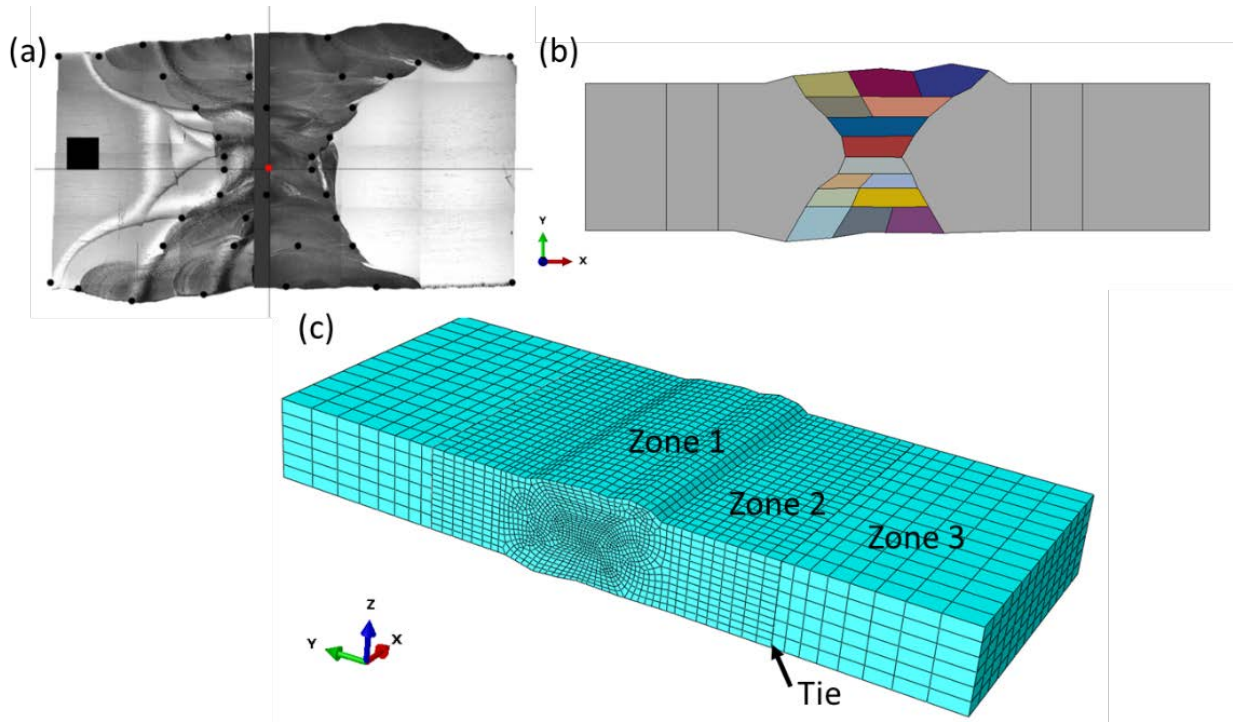
Figure 241. (a) Experimentally measured weld macrograph with all fusion boundaries revealed. (b) Model geometry corresponding to the experimental weld. (c) 3D model geometry and graded mesh

4.5.2.2.2.2 Verification and Validation

Similar to the previous analysis, the thermal analysis was verified by temperature measurements by thermocouples. Figure 242(a) shows a representative temperature field calculated by the model, exhibiting a large temperature gradient around the molten pool (red region). A node, labeled as TC-2, corresponded to the location of the thermocouple used in the welding experiment. Figure 242(b) shows the comparison of temperature history between experiment and simulation. The predicted temperature profile aligned closely with the experimental data; a good agreement in both the cooling rate and inter-pass temperatures was noted.

This report is available at no cost from the National Renewable Energy Laboratory at www.nrel.gov/publications.
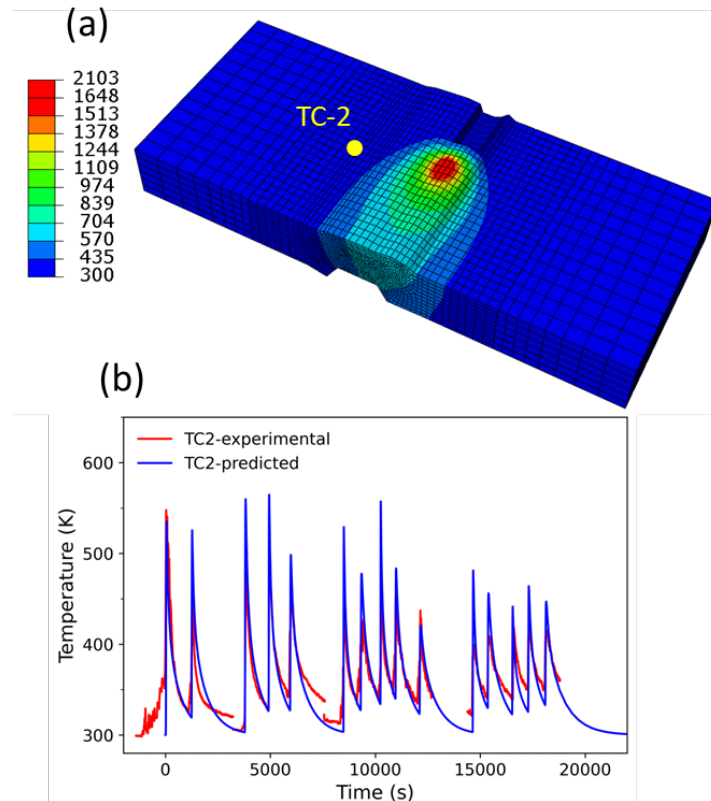
Figure 242. Thermal analysis verification. (a) Predicted temperature field (b) Comparison of temperature history between experiment and simulation
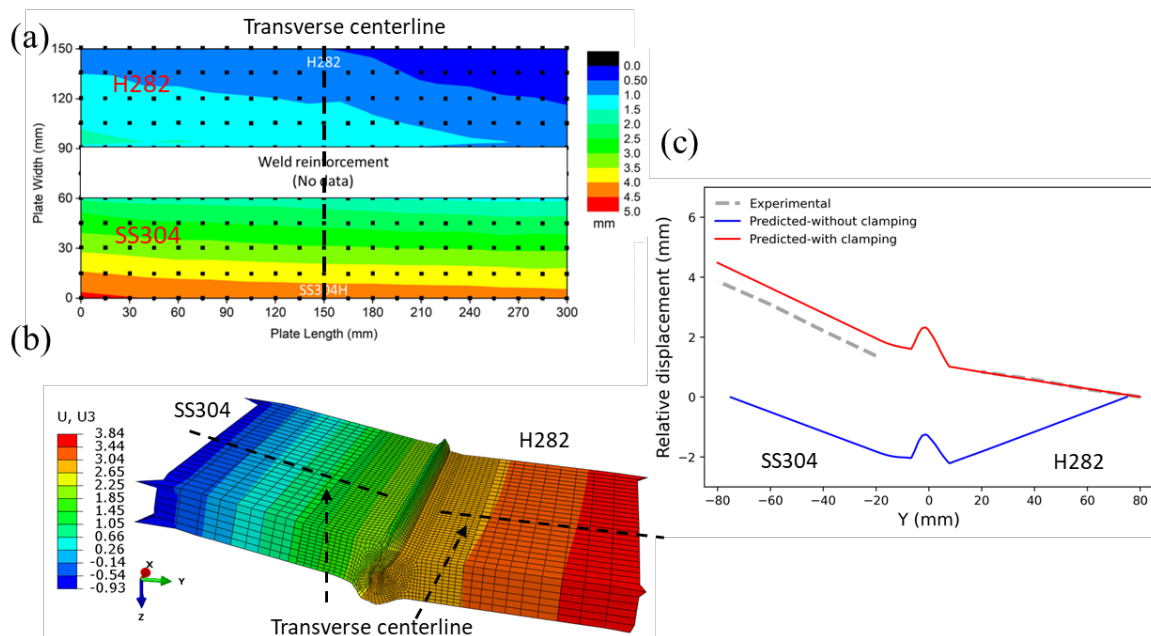
Figure 243. (a) Experimentally measured displacement in the Z direction (Z_d) on the root side (bottom side in Figure 241(a)). (b) Predicted Z_d viewed from the root side. (c) Comparison of Z_d along transverse centerline between experimental and predicted results

Figure 243 shows the validation of the mechanical analysis through distortion values, which are represented by displacement in the Z direction (Z_d). Figure 243(a) shows Z_d measured from the root side (bottom side in Figure 241(a)). Note that the displayed results are relative values with respect to the top right corner. Similar to the previous weld of AM H282 to wrought H282, it can be seen that the distortion is asymmetrical about the weld zone on the two sides. Specifically, Z_d increases from H2882 side to SS304H side, and the peak value is 5.0 mm. Figure 243(b) shows the predicted Z_d when viewed from the root side, revealing a consistent value in the longitudinal direction. However, it exhibits a linear increase from the H282 side to the SS304H side in the transverse direction. Figure 243(c) compares the Z_d values along the transverse centerline between the experimental and predicted results, showing good agreement in both magnitude and trend. This confirms the validity of the developed thermo-mechanical model.

In addition, the symmetrical distortion predicted by the model considering the full clamping approach is also plotted (blue lines). Consistent with the H282 AM-wrought weld case, the full clamping approach resulted in less distortion compared to the flexible clamping approach.

4.5.2.2.2.3 Results and Discussion

Figure 244 shows the residual (von Mises) stress on the transverse cross-section of H282 to SS304H weld. The weld zone exhibited high stress levels, with peak values exceeding 1000 MPa. Conversely, the stress in the base metal was relatively low and asymmetrical about the weld zone. Specifically, the stress was significantly lower on the SS304H side compared to the H282 side due to the inherent lower strength of SS304H. The region in the base metal of SS304H adjacent to the weld zone (as marked by ellipse) possesses a residual stress ranging from 230 to 400 MPa, which is comparable to or slightly higher than the room temperature yield stress of SS304H (250 MPa in the as-annealed condition).
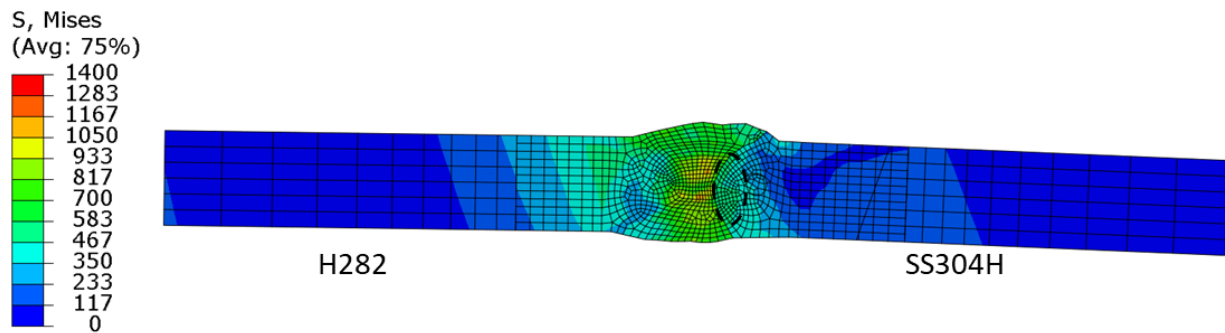
Figure 244. Residual (von Mises) stress on the transverse cross-section of H282 to SS304H weld

229

4.6 Task 7: Techno-Economic Analysis (TEA)

4.6.1 Techno-Economic Baseline for Solid Ni Superalloys (Milestone 1.7.1)

Table 73. Milestone 1.7.1 Details

Milestone	Description	Metric	Success Value	Assessment Tools
1.7.1: Techno-economic baseline for solid Ni superalloys	Establish techno-economic baseline for solid materials (Ni superalloys) of components, systems and materials identified in M1.1.2, for later comparison of cost reduction using advanced manufacturing for Gen3 CSP	Baseline cost for solid Ni superalloys State costs to evaluate (e.g., produced pipe $/meter; weld joint cost/linear meter)	Provide document to DOE	Preliminary techno-economic analyses performed at GEN3 CSP Topic 1s and using Black and Veach report
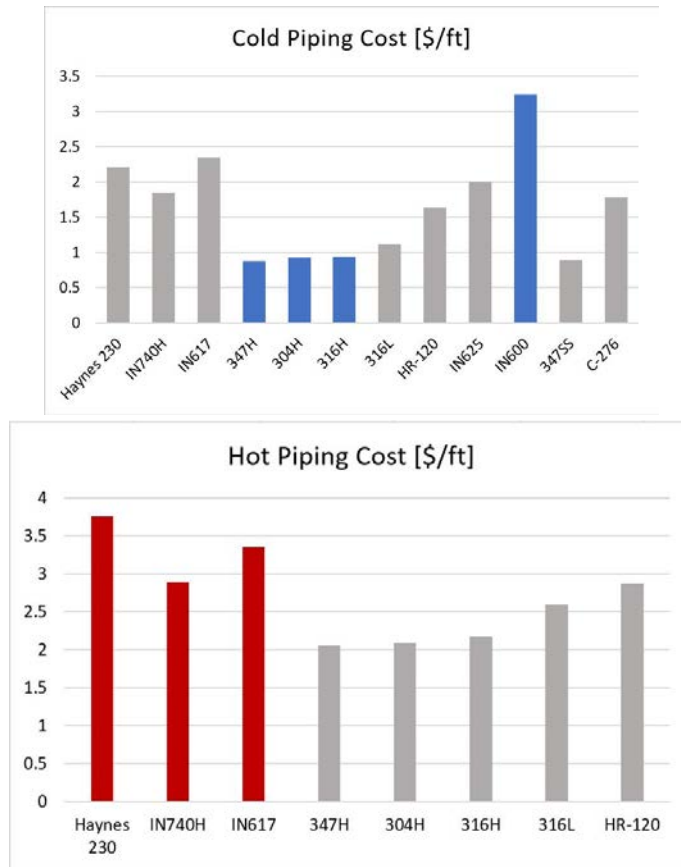
Figure 245. Cost data for alloys for cold and hot piping [27]

Figure 246 shows the allowable stress for candidate alloys as a function of temperature based on ASME code [30]. The figure illustrates the range of material strength for the candidate alloys and shows that generally, high-nickel alloys tend to be stronger than 3xx-series stainless steels. The figure also shows that the alloys start to lose strength at temperatures above 500°C–600°C.

230
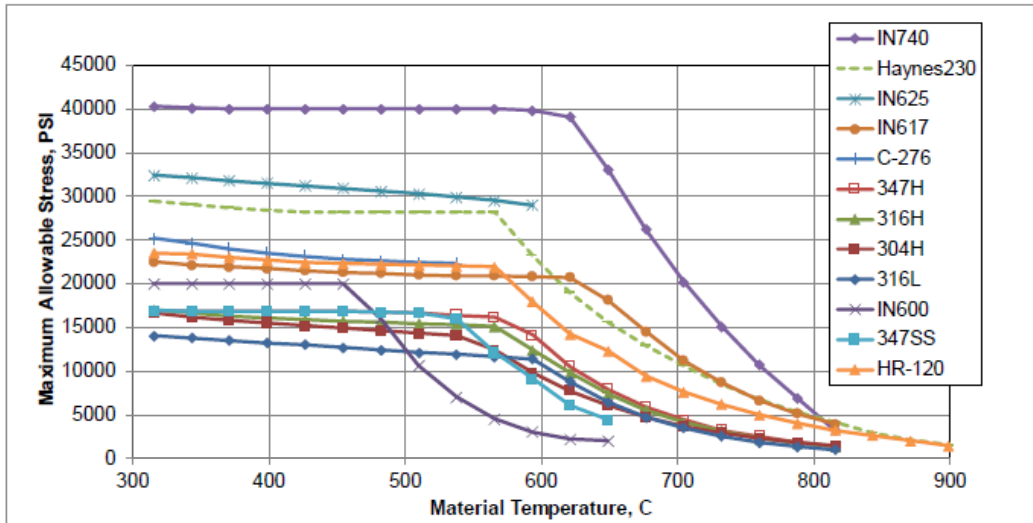
Figure 246. Allowable stress for candidate materials (from ASME code) [30] C. Turchi. 2019. Milestone ST-1.1.1 Alloy options Recommendations, National Renewable Energy Laboratory: Golden, CO [27]

The proper selection of alloys for Gen3 CSP plants requires excellent mechanical and thermal properties, corrosion resistance against molten salts, as well as cost-effectiveness. Figure 247 presents the relative cost of candidate alloys with respect to H230. This alloy was selected as the baseline for comparison as it has been recommended from other Topic 1 and Topic 2 projects. The selection of alloys for the clad metal system could represent important material cost savings where a thin layer of corrosion resistance alloy (CRA) is used as the cladder and a cost-effective alloy is used as the backer.
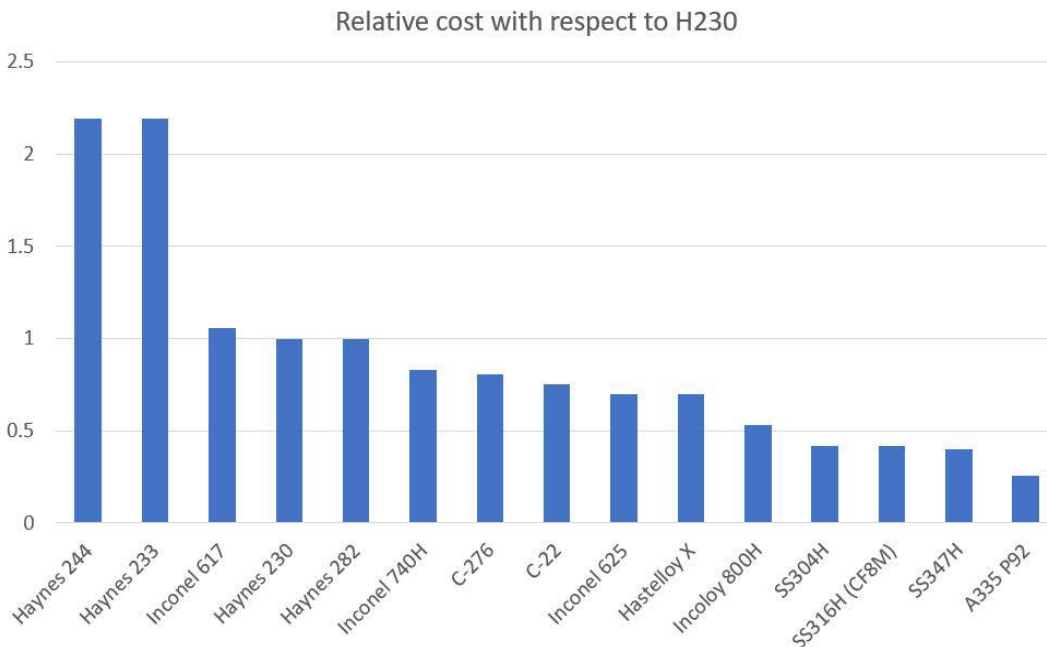
Figure 247. Relative cost of candidate alloys with respect to the cost of H230

231

The CSP Gen3 Liquid-Phase Pathway to SunShot [37] identified two Ni superalloys for a 50-MW plant: In740H and H230. The cost estimation for the primary heat exchanger, solar receiver, and piping network for the 50-MW plant are presented in Table 74 [37, 38]. This information was used in this project as a baseline to evaluate the economic advantage of the proposed manufacturing technologies: EXW and CS/CR for pipes; and L-PBF and EBAM for the primary heat exchanger and possibly for the solar receiver.

Table 74. Cost Information for the Primary Heat Exchanger, Solar Receiver, Piping Network, and Salt Storage System for a Commercial 50-MWe Plant [37,38]

Component	Unit	Value	Lower Bound	Upper Bound	Description
Salt Storage					
Tank and salt costs	$/kWh	39.5	-15%	+15%	NREL tank costing model (described below) set to a single tank pair, 12 h storage. Cost breakdown ($/kWh): salt 13.3, cold tank 12.6, hot tank 13.5.
Salt (included above)	$/kg	0.70	-	-	Delivered and melted salt based on prices from ICL, see Salt Cost Spreadsheet.
Cold salt pump	$	2,772,615	-25%	+25%	Reference is based on 4 x 33% pumps at €818,498 per pump, with costs taken from a Budget Quotation from Sulzer for a hot salt pump at 543 MW$_{th}$ scale. Casing, impeller, and shaft are Inconel 625. Reference pump manometric head is 87.2 m and flow is 1014 m^3/h.
Hot salt pump	$	2,079,462	-25%	+25%	Reference is based on 3 x 50% pumps at €818,498 per pump, with other details as for cold salt pump above.
Salt valves	$	2,106,720	-25%	+25%	Reference based on seven control valves, each $300,960 based on a $270k estimate by Flowserve for a 10-in. globe valve with bellows seal made from 316H and adding an extra cost allowance for upgrading to a nickel alloy. Installation included.
N$_2$ ullage gas system (for salt)	$	2,860,000	-25%	+25%	Reference is for pilot-scale ullage gas piping and installation scaled up for the number of pumps in the commercial scale, plus commercial-scale acid-gas scrubber.
Sodium and Salt Piping					
Sodium riser / cold salt piping material cost	$/kg	8	-25%	+25%	The material is austenitic stainless steel, cost information from John Cockerill.
Sodium downcomer / hot salt piping material cost	$/kg	80	-25%	+25%	Material is a nickel superalloy, cost information from John Cockerill.
Sodium riser / cold salt piping balance of costs, ref. 28-in. pipe	$/m	5,192	-25%	+25%	Reference value is based on the 28-in. downcomer in the Abengoa report [38], excludes piping material but includes insulation, trace heat, installation, welds, wastage, freight, materials handling, testing and inspection, hangers and supports.
Sodium downcomer / hot salt piping balance of costs, ref. 28-in. pipe	$/m	7,890	-25%	+25%	As above for the riser, but costs of insulation, heat trace, fittings revised upwards to account for the higher temperature.
Heat Exchangers					
Sodium-salt HEX, ref. 10,000 m^2 from	$/m^2	1,446	-25%	+25%	Assumes a two-stage heat exchanger (stainless steel and Inconel). Costs based on the CMI

Component	Unit	Value	Lower Bound	Upper Bound	Description
ANU sodium receiver study					sodium study heat exchanger but adjusted as described further below.
Salt-CO$_2$ PHX	$/kW$_{th}$	266	-25%	+25%	Reference based on estimates from VPE, for 110 MW$_{th}$, dual core unit. Low-temp core of stainless steel, high-temp core of alloy 617. Installation costs equal 21% of materials cost based on guidance from VPE as described below.

The cost information presented in Table 74 was obtained from different sources, including industry partners, public reports, and where appropriate, from reference values provided by DOE. Some of the cost values were initially obtained for a system of a different scale, and they were properly adjusted to a 50-MWe plant scale using power law relationships. Upper and lower bonds for each value were also specified based on estimates relative to the nominal value. The material considered in this cost analysis was In740H. Additional details about cost calculation can be found in reference [37].

4.6.2 Preliminary TEA for Advanced Manufacturing (Milestone 2.7.1)

Table 75. Milestone 2.7.1 Details

Milestone	Description	Metric	Success Value	Assessment Tools
2.7.1: Selection of components for TEA of advanced manufacturing	Obtain preliminary analysis of advanced manufacturing costs. Determine which CSP components to do full techno-economic analysis on based on results of manufacturing experiments, ability to estimate advanced manufacturing costs, and availability of conventional manufacturing cost data.	Down-selection of component(s) and advanced manufacturing techniques for full TEA in M3.7.1	Select at least one component for in-depth analysis, and description of component (locations in CSP plant) and advanced manufacturing technique.	Review of potential manufacturing techniques and associated CSP components, based on following factors: 1. Does the manufacturing technique appear viable? 2. Can we obtain estimates of the cost of components made from these techniques? 3. Can we obtain estimates of cost of components made from conventional techniques? Techniques and components that answer "yes" to these three questions should be considered for BP3 analysis.

AM is generally considered advantageous as a low-volume, high-quality fabrication method for unique materials and complex part manufacturing. The overarching goal is to demonstrate to the Department of Energy that additive manufacturing can be cost effective and applied in solutions that lower the cost of energy production.

4.6.2.1 AMS CS/CR Cost Estimates

Metallic alloy pipes are mostly manufactured by bending a plate into a pipe shape, followed by seam welding. In the case of the clad pipe, the clad plates must be fabricated first by either hot roll bonding or explosive bonding. The clad plate is then bent into a pipe shape, followed by welding at the seam.

Combustion synthesis (CS) is a process for rapid synthesis of advanced engineering materials, including corrosion resistant alloy (CRA). The CS process utilizes highly exothermic particulate mixtures, which, once ignited, can generate highly exothermic chemical reactions forming the CRA and simultaneously generating high thermal energy required for metallurgical bonding. Because only a small energy input is required to ignite the precursor exothermic mixture, the technique utilizes little external energy. In addition, the exothermic chemical reaction exhibits a high reaction rate. Therefore, the technology is efficient in fast production, and thus is very economical.

On the other hand, centrifugal rotation (CR) casting is a well-established method to manufacture metallic pipes. In this technique, a permanent mold is rotated continuously about its axis at high speeds as the molten metal is poured. The molten metal is centrifugally thrown toward the inside mold wall, where it solidifies after cooling. Advanced Material Solutions has developed a technology to combine the CS of advanced alloys with CR to manufacture CRA clad pipes, which is referred to as the CS/CR process. In this technology, the economical carbon steel is used as the backer, and the exothermic mixture is loaded inside the backer pipe. The exothermic mixture is ignited while the backer pipe is in high-speed rotation, thus generating a high gravitational force. The CS reactions generate the molten CRA, and a molten slag (mixture of oxides) byproduct with the molten slag flows to the top during the centrifugal rotation due to the lower density than the CRA, and the molten CRA is bonded to the backer pipe instantly.

The total cost of a pipe is derived from the costs of the raw materials and that of the manufacture process. Compared to a solid CRA pipe (see Table 76), a clad pipe is an economical alternative. Using the C-276 nickel CRA as an example, a comparison of the raw material costs for solid and clad (SS304 as the backer) pipes is shown in Table 77. In these cost estimates, the commodity price data from online sources are used for the calculation. The table shows that the materials cost was $19.65/kg for the C-276, whereas it is $7.51/kg for the clad pipe.

The total cost of a pipe (selling price) also includes the price for manufacturing and profit. Manufacture cost is closely related to the specific technology being used. This is shown in Table 78. The traditional pipe manufacture method requires a significant capital investment in pipe bending/forming and seam welding machines, etc. For the CS/CR technology, the clad machine, consisting of a motor and a set of rollers confined inside a mechanical frame, is a very simple apparatus and costs a lot less to build. As a result, it is estimated that the cost of building such a clad machine would require less than 10% of the investment needed for the traditional pipe manufacture cost, as shown in Table 79. Moreover, the CS/CR cladding process only takes minutes to complete a pipe production, whereas this would take hours or days for the traditional pipe manufacture process.

Table 76. Estimated Cost for Hastelloy C-276 and SS304H Pipes [39]

Commodity	$/kg	C-276 Composition, wt.%	C-276 Fractional Cost, $/kg	SS304H Composition, wt.%	SS304H Fractional Cost, $/kg
Ni	18	74.75	13.17	9.25	1.63
Mo	25	16	3.93		
Fe	0.21	5.50	0.01	72.25	0.15
W	30	3.75	1.13		
Cr	9	15.50	1.41	18.50	1.68
		Total	**$19.65**		**$3.46**

Table 77. Estimated Cost for Produced CS/CR with SS304H as Backer and Hastelloy C-276 as a Clad

	Alloy	Fraction	Fractional Cost, $/kg
Clad	C-276	1/4	4.91
Backer	SS304	3/4	2.60
		Total	**$7.51**

Table 78. Comparison of the Pipe Manufacture Costs for Traditional and CS/CR Methods [40]

Technology	Capital Investment	Production Rate	Labor	Relative Cost
Traditional	>$100 million	hours/pipe	Can be automated	80%–90%
CS/CR	<$10 million	minutes/pipe	Can be automated	<50%

Table 79 presents an estimated cost comparison between the C-276 solid pipes produced by the traditional method and that for clad pipes produced by the CS/CR technology. For the former, it was assumed that 85% of the total pipe cost is from the manufacturing (shown in Table 78 and Table 79). For the latter (CS/CR technology), a 50% manufacture cost is assumed. The pipe costs are $130.98/kg and $15.02/kg for the two compared technologies, respectively. The pipes produced by the CS/CR technology could represents a reduction in cost of up to 89%.

Table 79. Cost Comparison for Solid Pipes Produced by Traditional Method and Clad Pipes Produced by the CS/CR Technology

Solid C-276 Pipe Manufactured by Traditional Method			Clad C-276/SS304H Pipe (30% C-276) Manufactured by CS/CR Technology			CS/CR Clad Pipe vs. Solid CRA Pipe
$/kg/Raw Material	$/kg-Manufacture	$/kg-Pipe	$/kg/Raw Material	$/kg-Manufacture	$/kg-Clad Pipe	Cost Reduction
$19.65	$111.33	$130.98	$7.51	$7.51	$15.02	-89%

4.6.2.2 Elementum 3D Laser-Powder Bed Fusion Cost Estimates

The economics are hard to represent financially without a sizeable economic examination integrating AM into energy production.

Table 80. Haynes 282 vs. IN740H Cost Comparison with Current Developed Laser Parameters

Material	Time (hr)	Printing Cost
Haynes 282	53.5	$8025.00
IN740H	64.5	$9675.00

The team used the developed printer parameter themes for Haynes 282 and IN740H to create a simple cost analysis, (see Table 80 below). The study used the EOSPRINT build time estimator, identical hypothetical builds (Figure 248), and E3D's current hourly rate to develop the cost analysis. Compared to IN740H, the Haynes 282 developed laser parameters save 11 hours of printing time, or 17% cost and time savings on an EOS M290 printer at E3D. Haynes 282 is therefore apparently more cost-effective for printing than IN740H, but E3D will further evaluate the materials cost and post-processing over the coming months to confirm.
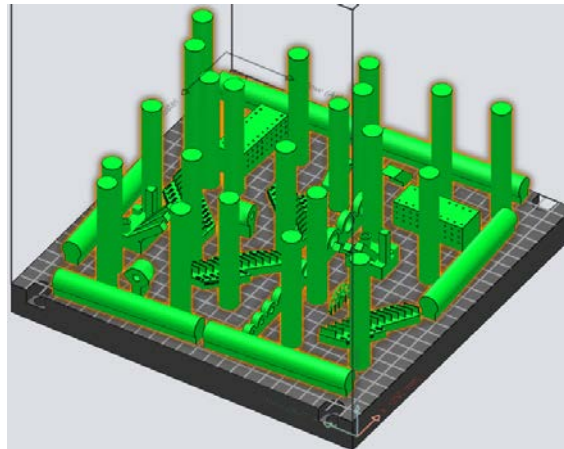
Figure 248. Validation build used to show the cost difference between Haynes 282 and IN740H with current laser parameters

4.6.2.3 Additive Manufacturing Review

AM is generally considered advantageous as a low-volume, high-quality fabrication method for unique materials and complex part manufacturing. The overarching goal is to demonstrate to DOE that additive manufacturing can be cost effective and applied in solutions that lower the cost of energy production.

The world of additive manufacturing is currently creating a paradigm shift in the production of heat exchangers. The ability to add, rather than take away, material has allowed for organic and intricate heat transferring designs. The goal of this project is to show how AM can benefit the energy sector by improving the efficiency of renewable CSP in producing low-cost energy. In this techno-economic analysis, E3D reviewed literature about the improvements AM has brought to heat exchanger design and production.

The economics are hard to represent financially without a sizeable economic examination integrating AM into energy production. AM is a new technology that has created a paradigm shift in materials science and mechanical design. The major questions to answer concerning how AM can improve heat exchangers (HX) are: How can AM be utilized? What does AM-specific design offer? How will it improve performance? AM lends itself well to HXs because of the difficulty in producing a traditional HX. Traditional HXs need to be assembled from multiple components, such as core sheets, nose pieces, multiple fins, and manifolds. Each of these parts is manufactured separately with different techniques that are then joined at an assembler [41]. In contrast, AM through laser powder bed fusion (L-PBF) only requires raw atomized materials, a printer, and a CAD design. We have examined literature on how AM has improved HX performance. These studies highlight AM's ability to reduce the number of assembled parts, increase efficiency, reduce size, and broaden the design space for HX.

Highlighting our first example of AM improving HX performance is the company Sintavia. Sintavia has shown with large scale 3D printers (400 x 400 x 1000 mm build chamber volume) that they can produce HXs out of superalloy materials. Figure 249 shows the fully printed structure with "2X better heat transfer and up to 3X lower pressure drop than traditionally designed and manufactured versions—with more than 4X improvement in manufacturing yield" [41]. The large-scale HX shows intricate design features (e.g., gyroid shape and thin internal structures) that are not achievable in traditional manufacturing.

Figure 249. Sintavia large AM HX for marine use.

237

Several reports have demonstrated the increased performance and efficiency of AM-produced HXs relative to traditionally manufactured HXs [42,43]. A comparison of several typical HX geometries and a printed (or AM) HX is shown in Figure 250. As shown in the table, the AM heat exchanger outperformed all these traditional HXs in terms of maximizing the heat transfer surface area to volume ratio. The notable shell-and-tube geometries can resist higher temperatures but are generally large and bulky, hence the low A_{heat}/V ratio. The image highlights the intricate geometry that can be produced in L-PBF, negating the need for difficult assembly and joining processes. Arie et al. [42] and Zhang et al. [43] also highlight 2017 work by General Electric to print a high temperature heat exchanger (HTHX) and meet the heat transfer design requirement with 66% lower weight and 50% lower volume. The advancements we have contributed with the dense, crack-free printing of Haynes 282 and IN740H in this project should help improve HTHXs similar to the GE design.

	A_{heat}/V (m^2/m^3)	T_{max} (°C)	$Pressure_{max}$ (bar)
Shell-and-tube heat exchanger	50 – 100	1100	1000
Plate-and-frame heat exchanger	120 – 660	815	200
Plate-fin heat exchanger	800 – 1500	800	200
Printed circuit heat exchanger	200 – 2500	980	900
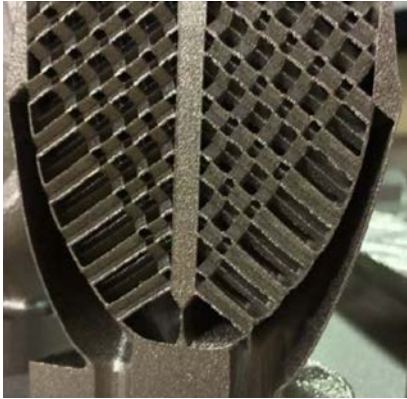
Figure 250. An overview of HTHX comparison from [42,43] and a cross-section of the improved heat exchanger from GE

The key feature of a HX is to effectively heat or cool a fluid in a very short time. Traditionally, HX designs that fulfill this requirement involve assembling an intricate system of plates and fins. AM allows the part to be designed in CAD and then sent directly to the printer—no need for complex robotics or human hands. The combination of AM and CAD design also allows for the fabrication of new, highly efficient heat transfer surface geometries. Sealed organic structures can be produced that are not easily replicated in traditional manufacturing. A geometry known as the Gyroid-lattice is what has been employed in most of the literature reports reviewed. Figure 251 contains a visual representation of the gyroid-lattice. The Gyroid lattice structure is ideal for AM as it is a self-supporting structure. Self-support is key benefit for AM because these structures do not have overhangs or features that require separate supports to be built.
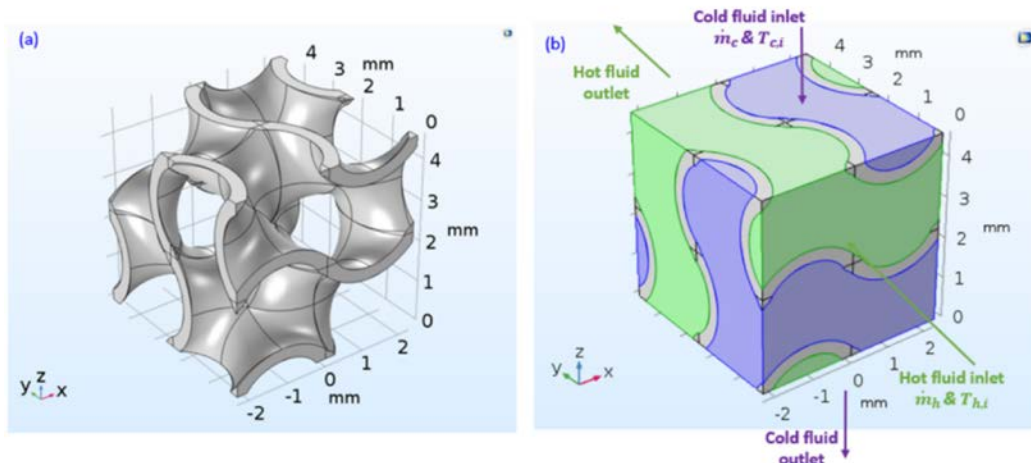
Figure 251. Gyroid-Lattice structure design from Dixit et al.'s study [44]

Dixit et al. [44] demonstrated the effective printing of a gyroid-lattice HX. Figure 251 shows their printed HX. The structure was effectively made a HX engineered to have 80% empty space. The lattice was designed in a way to separate the hot and cold sides with 300-µm wall thickness to efficiently transfer heat with a surface density of 670 m^2/m^3. The overall result, in the authors' words, is that "The additively manufactured gyroid-lattice heat exchanger exhibits a 55% increase in effectiveness in comparison to a thermodynamically equivalent, most-efficient, counter-flow heat exchanger at $1/10^{th}$ of its size" [44]. Dixit et al. [44] were able to improve the "micro-architected" gyroid HX by a temperature gain/drop of 10-20°C with volumetric flow of 100-270ml/min, leading to an overall heat transfer coefficient of 120-160W/m^2K and a hot fluids Reynolds number of 10-40 [44]. The combination of CAD-generated topology (i.e., organic geometry) and AM greatly increase the HX performance overall. In the application relevant to this project, the AM of HX could lead to a more efficient array of compact HXs that bring CSP molten salts to an optimal temperature range quickly. This study demonstrates the distinct advantages of design-for-AM in increasing performance and decreasing size compared to traditional HX, as well as reducing the need for component assembly.
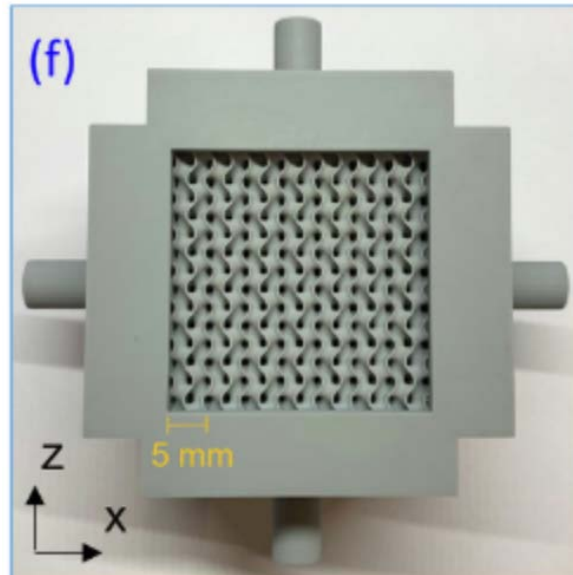
Figure 252. Example of a printed gyroid-lattice HX from Dixit et al. [44]

General Electric (GE) [45] has another example of an HX produced using AM. GE has extensive experience in using AM to re-engineer current GE systems. We discussed GE in the last techno-economic analysis in the context of their activities to simplify T700 helicopter engines from 900 parts to 16 using AM. This was an example of reducing complexity of traditionally manufactured components and systems through the application of AM [46]. GE is a large company, and they have been producing HTHX for their aerospace and energy production solutions. Wanting to improve HX efficiency, they designed a subscale HX targeted for operation at 1650°F (900°C) and 250 bar, as shown in Figure 252. The resulting AM-produced metal HX was able to operate at a temperature 200°C above the current state-of-the-art devices [45]. The same article describing this innovation indicates that GE has invested $3.1 million in research for AM-based HTHX production, demonstrating that there is market interest in using AM to improve the efficiency of cooling to increase performance and reduce carbon emissions for large scale power generation and flight [45].
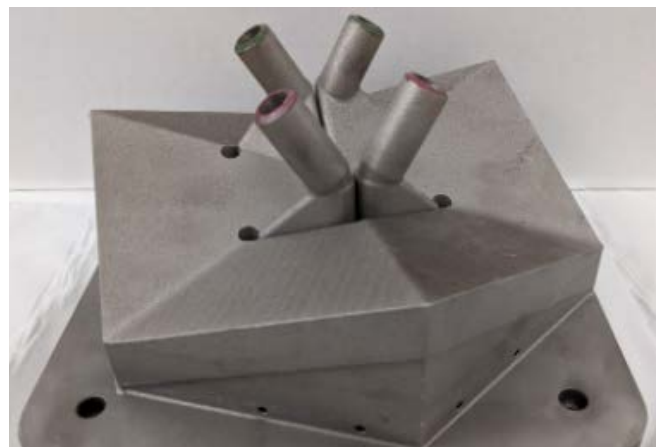
Figure 253. The printed subscale HX from GE that operated at 200°C above the targeted temperature

Conflux has achieved outstanding performance in the automotive industry through the redesign of oil-to-water HXs for fabrication by AM. Figure 253 shows the cross section of their HX design using a unique channel geometry that favors fabrication by L-PBF AM. Their design increased heat transfer performance by 300% and reduced weight by 22% as well as tripling the thermal heat rejection. At the same time, the pressure drop is reduced by 67%. Additionally, the use of AM enabled a new, compact heat exchanger design, reducing its length by 55 mm compared to a F1 benchmark. This ultimately also eliminates 22% of its weight. "The design flexibility AM offers allows for optimum placement inside a vehicle and also enables the merging of components, reducing the overall number of parts. Integration of subcomponents into a single part removes assembly time and reduces failure points from joints and seams" [47].
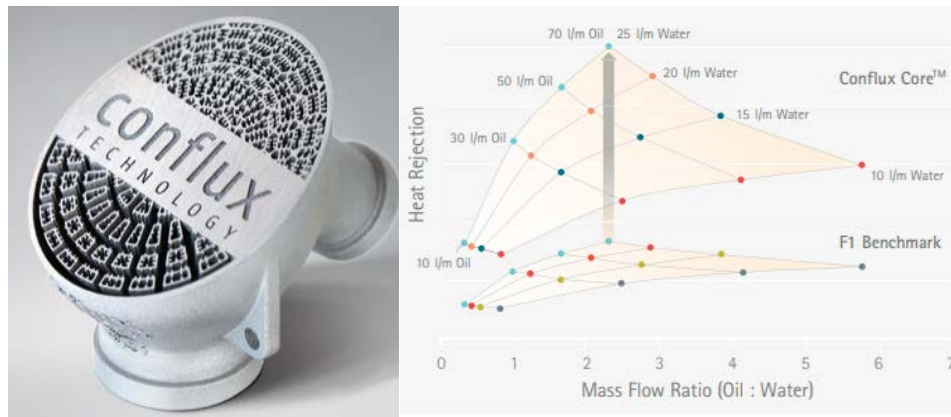
Figure 254. Conflux HX cross section (left) and data (right) highlighting their performance compared to their benchmark

With the cost of nickel increasing due to world demand, AM also greatly needed to reduce the amount of material needed for building HX. For this project, we purchased 140 kg of Haynes 282 and 75 kg of IN740H, costing $128.29/kg and $165.00/kg, respectively. This material was needed to complete the previous milestones for this project to produce weld blocks for the welding of AM and wrought materials together. These materials were purchased in 2021, before the onset of pandemic-related supply chain issues. Since then, costs have risen sharply. AM allows for highly efficient material usage and very little waste, which is common in traditional manufacturing methods like machining.

These examples further emphasize how AM can improve the next generation of HX in terms of heat transfer performance and manufacturing costs and efficiency. AM has been shown to enable radical new designs, dramatically increase performance, and reduce component/assembly size. For HXs, AM enables domestic manufacturing of smaller systems with the same performance as the current state-of-the-art traditional HX. These examples presented had a minimum of a 50% increase in heat exchanger performance. The materials and processes that have been developed through this project can be easily implemented to demonstrate printing of HX designs similar to those described in the above studies. All these literature examples share a common theme of AM improving performance, reducing size, and reducing complexity of HX. These three positives highlight AMs ability to provide a better process for energy production.

This report is available at no cost from the National Renewable Energy Laboratory at www.nrel.gov/publications.

4.6.3 Final TEA (Milestone 3.7.1)

Table 81. Milestone 3.7.1 Details

Milestone	Description	Metric	Success Value	Assessment Tools
3.7.1: TEA of CSP components(s) using advanced manufacturing techniques	Complete TEA of selected CSP components and manufacturing techniques from task 2.7.1	$/component unit	$/component unit for advanced manufacturing technique compared to conventional manufacturing technique	Quotes from industrial partners on material, fabrication, and welding costs

At the end of BP2, we reached out to industry partners and other DOE-funded projects to find detailed designs of CSP subcomponent using advanced manufacturing techniques that could be used for the BP3 detailed TEA project. While we found several examples of additive manufacturing subcomponent designs, none of the industry partners or researchers could share their detailed designs because of proprietary and business sensitivity concerns. Because there are no known AM designs available for analysis, we decided to focus on the cost of clad piping using EXW for detailed analysis in BP3.

NobelClad's commercial team performed a techno-economic analysis for building a CSP plant using explosive clad piping and comparing it to a solid pipe alternative. For the analysis, and working in conjunction with NREL, a 100 MWe Rankine CSP plant is being used as the reference point.

4.6.3.1 CSP Plant Description and Assumptions

A 100 MWe Rankine CSP plant is being used as the reference point for the techno-economic analysis of using explosive welding metal plates for manufacturing of the pipe system.
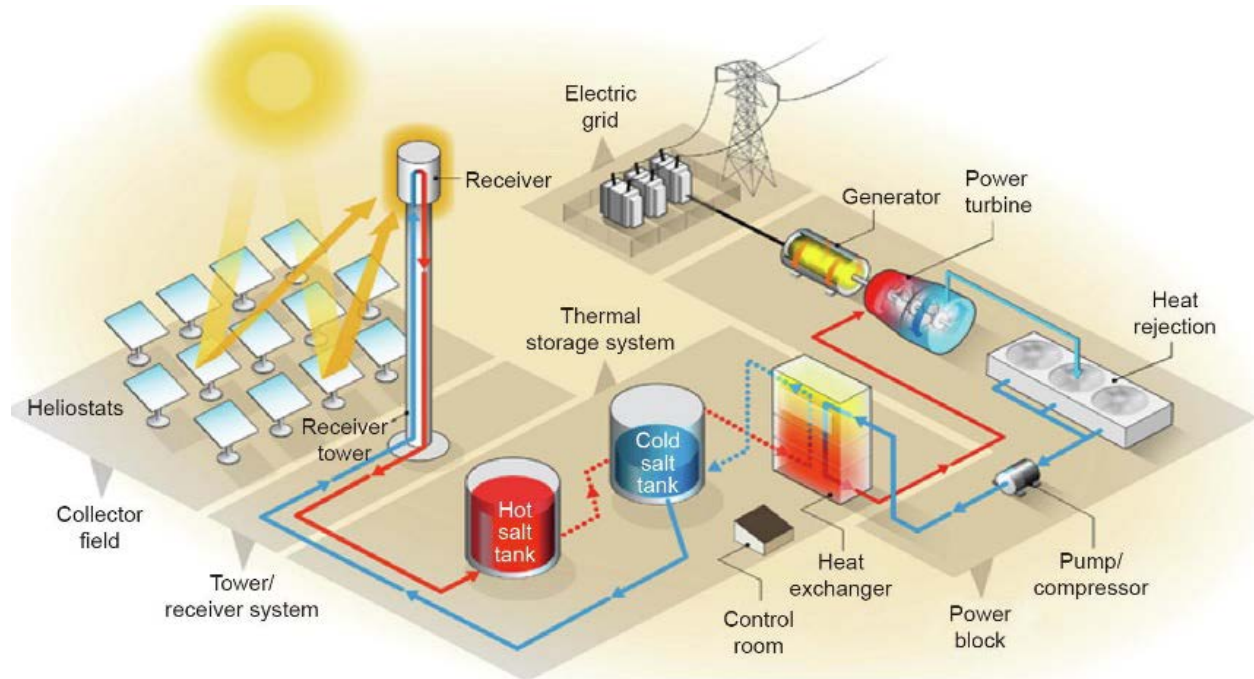
Figure 255. A depiction of what a typical Gen2 CSP plant layout is [48]

Figure 255 shows a typical layout used for 2nd generation CSP plants of molten nitrates. Based on this layout, and input from NREL's CSP team, we have made some basic assumptions on the amount of piping elements that would be needed for a Gen3 plant:

1. We considered only half of the 200 MWe plant design, or just having one 100 MWe receiver;

2. There is only one riser (cold) and one downcomer (hot) from the receiver, each being 1500 feet (1.5 times the height of the tower itself);

3. The amount of piping in the horizontal direction, at ground level, is considered to be 50% of the height of the tower, or roughly 500 feet;

4. We have assumed that a minimum of four elbows in each of the cold and hot lines would be used;

5. Solid piping can be made in 20-foot sections, while it is only possible in 10-foot sections for cladded metal;

6. Circumferential welding of sections of piping is possible for solid pipe; may or may not be possible for cladded metal and thus cladded flanges would be needed:

    a. If flanges are needed, there will be two flanges per each section of cladded pipe and elbows.

7. No consideration was given to auxiliary equipment nor valves in the piping system;

8. The outside diameter of the pipes (solid and cladded) was kept at 20 inches with the exception of one case:

    a. For cladded pipes: 0.135 in. (3.4 mm) of cladder inside of pipe is considered;

243

b. Because of thermomechanical stresses, the C22 clad with SS304H backer option requires a thicker walled pipe compared to the other options (2.343 in);

c. For the solid metal pipes: the pipe Schedule was determined by NREL based on the expected thermomechanical behavior of the alloys at the desired working operating temperatures.

9. Fabrication costs include rolling flat plates of the alloys into pipes, seam welding, and bending into elbows when needed, plus welding of the flanges to the pipe spools.

10. Installation costs in the plant are not being considered because they are highly dependent on EPC and contractors selected.

4.6.3.2 Pipe Specifications

NREL has down-selected the different options possible for the hot and cold loops of the CSP plant based on the thermomechanical tests performed in conjunction with the Colorado School of Mines. Table 82 and Table 83 show the alloys considered, along with their pipe dimensions. Also shown is the price per plate needed to make a pipe spool of each option.

Table 82. Alloys, Pipe Dimensions, and Prices for Plates Needed for the Hot Loop

Hot Loop (720°C)	Conventional Option #1	Conventional Option #2	Clad Option
Pipe Alloy	Inconel® Alloy 740H®	Haynes® 230® Alloy	SS304H Backer/C22 Clad
OD (in.)	20	20	24
ID (in.)	19.25	19	19.04
Wall (Backer) Thickness (in.)	0.375	0.5	2.343
Clad Thickness	n/a	n/a	0.135
NPS Schedule	Sch20	Sch30	Sch160
Price per Plate	$81,887	$112,958	$97,149

Table 83. Alloys, Pipe Dimensions, and Prices for Plates Needed for the Cold Loop

Cold Loop (500°C)	Conventional Option	Clad Option #1	Clad Option #2
Pipe Alloy	SS347H	SS304H backer/ SS347H clad	Gr91 backer/ SS347H clad
OD (in.)	20	20	20
ID (in.)	19.5	18.72	18.98
Wall (backer) thickness (in.)	0.25	0.5	0.375
Clad Thickness	n/a	0.135	0.135
NPS Schedule	Sch10	Sch30	Sch20
Price per plate	$7,840	$22,860	$12,639

When NobelClad quotes material for a project that requires multiple amounts or types of clad plates, we group them by Bill of Material or BOM just like many other companies do. The BOM for both cladded and solid metal pipe manufacturing is shown in Table 84.

Table 84. Bill of Materials Needed for the CSP Plant's Piping System

CSP Plant Loop	CSP Plant Section	Solid Pipe	Cladded Pipe	Solid or Cladded Elbows	Cladded Flanges*	Solid Flanges*
Hot Loop (720°C)	Tower Downcomer	1500 ft (75 x 20ft sections)	1500 ft (150 x 10ft sections)	1	151 x 2 flanges per pipe element	3 x 2 flanges per pipe element
	Horizontal Piping	500 ft (25 x 20ft sections)	500 ft (50 x 10ft sections)	3	53 x 2 flanges per pipe element	4 x 2 flanges per pipe element
Cold Loop (500°C)	Tower Riser	1500 ft (75 x 20ft sections)	1500 ft (150 x 10ft sections)	1	151 x 2 flanges per pipe element	3 x 2 flanges per pipe element
	Horizontal Piping	500 ft (25 x 20ft sections)	500 ft (50 x 10ft sections)	3	53 x 2 flanges per pipe element	4 x 2 flanges per pipe element
	Totals	**4,000 ft (200 pipe spools of 20ft each)**	**4,000 ft (400 pipe spools of 10ft each)**	**8**	**816**	**28**

* Flanges are considered in case the welding of 2 cladded pipes together is not possible.

Based on this BOM, the amount of metal plates needed to fabricate the pipes and the elbows can be determined. For both solid pipe and clad pipe spools, the plate sizes have been maximized to reduce the amount of material wasted, maximize the length of the pipe and reduce the number of welds. Doing so, we came up with an estimated amount of clad plate and solid metal plate needed as shown in Table 85.

Table 85. Estimation of Metal Consumption for Producing the Piping Components

Solid	Cladded Pipes	Elbows	Flanges (solid/clad)
4,000 ft (200 pipe spools of 20ft each)	4,000 ft (400 pipe spools of 10ft each)	8	28 / 816
Each pipe spool produced with 4-ft x 20-ft plates	Each pipe spool produced with 4-ft x 10-ft cladded plates	Each pipe elbow produced with 4-ft x 10-ft plates	Each flange produced with 21-in. O.D. sheet
200 x 4 ft x 20 ft = 16,000 sq ft	**400 x 4 ft x 10 ft = 16,000 sq ft**	**8 x 4 ft x 10 ft = 320 sq ft**	**28 x 2.41 sq ft = 67.48 sq ft** **816 x 2.41 sq ft = 1,962 sq ft**

* Flanges are considered in case the welding of 2 cladded pipes together is not possible.

In conclusion, the amount of material needed for a solid pipe solution would be roughly 16,388 sq ft, while for a clad pipe solution, it would be 18,282 sq ft.

4.6.3.3 Cost Estimate of Material Input and Fabrication into Pipe Spools

Considering the amount of material needed as shown in Table 85 for each one of the options shown in Table 82 and Table 83, the cost of each section of piping was determined for the Hot Loop (Table 86) and Cold Loop (Table 87). The costs are shown separately for the material itself and also for the cost of fabricating into a pipe spool, with flanges if needed, and elbows. The costs associated to input materials are based on quotes from metal suppliers and NobelClad's typical prices for the clad combinations presented (i.e., prices with typical commercial margins for the size of the project). In the case of fabrication of the pipe spools and elbows, these costs were provided by Enerfab Inc. using their standard fabrication prices and practices.

Based on the results shown in Table 86, the selection of solid Inconel® Alloy 740H® overall involves the least amount of capital investment for the Hot Loop of the CSP plant. However, this alloy currently is only available in the form of pipes with limited dimensions of around 10–12 in. For the calculation, the price of a plate of material had to be estimated based on information available in the public domain. It is interesting to note that the cost of Haynes® 230® Alloy and the C22 cladded SS304 backer raw material input is roughly the same despite the amount of flanges needed for the clad alternative. On the other hand, there is a significant amount of labor and cost associated to fabricating with the clad option when considering this amount of flanges.

The prices of these nickel-based alloys are current as of April 2024, when the London Metals Exchange price of nickel is at around $17,030 per metric ton (see Figure 256). This price for nickel is equivalent to the ones in 2019, which is considered depressed and is expected to rise in the coming years as the demand for this metal increases with the increase in demand of electric vehicles and thus batteries. If this were to occur, then the clad option of using C22 as cladder would become more attractive than using solid, 230 Alloy, and may in fact be less expensive than solid 740H alloy at some price point.
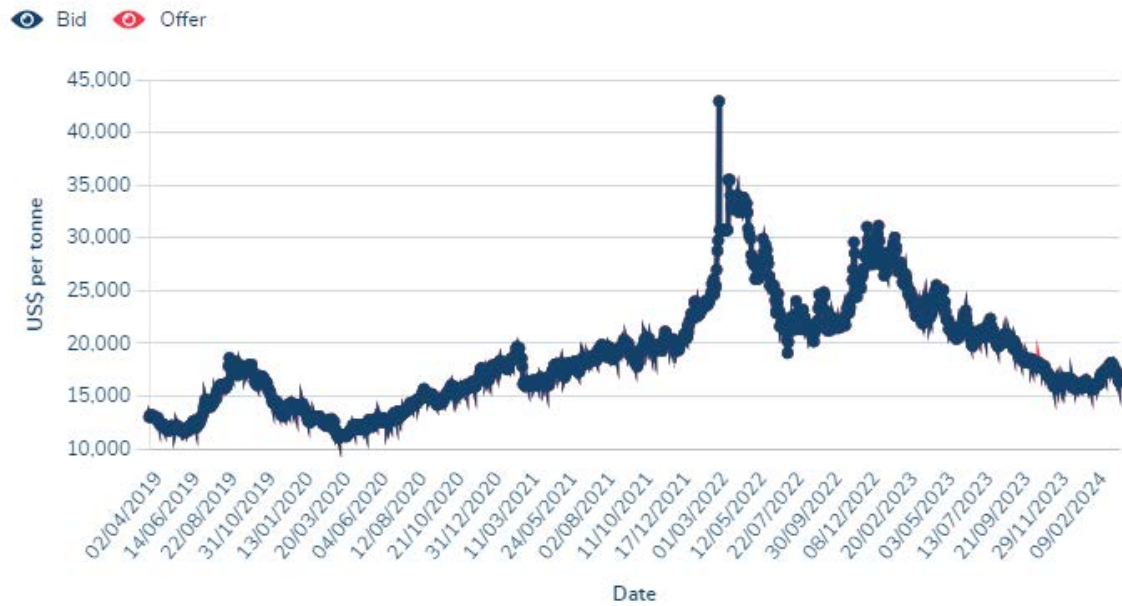
Figure 256. London Metal Exchange price of nickel as of 28-March-2024

Table 86. Costs for Finished Pipe Components Considered in the Hot Loop of the CSP Plant

Hot Loop (720°C)		Raw Metal or Clad Input		Fabrication into Spools		Total Pre-installed
Alloy Selection	Component	Cost	Subtotals	Cost	Subtotals	
Inconel® Alloy 740H® (Alloy is not commercially available as plate)	Tower Pipe	$12,283,062	$16,606,190	$1,089,850	$1,556,000	$18,162,190
	Horizontal Pipe	$4,094,354		$399,100		
	Elbows	$163,774		$46,050		
	Flanges (14)	$65,000		$21,000		
Haynes® 230® Alloy	Tower Pipe	$16,943,700	$22,892,920	$1,089,850	$1,556,000	$24,448,920
	Horizontal Pipe	$5,647,900		$399,100		
	Elbows	$225,916		$46,050		
	Flanges (14)	$75,404		$21,000		
SS304H Backer/ C22 Clad	Tower Pipe	$14,572,350	$22,144,404	$1,299,300	$2,850,000	$24,994,404
	Horizontal Pipe	$4,857,450		$475,800		
	Elbows	$388,596		$54,900		
	Flanges (408)	$2,326,008		$1,020,000		

247

Table 87. Costs for Finished Pipe Components Considered in the Cold Loop of the CSP Plant

Cold Loop (500°C)		Raw Metal or Clad Input		Fabrication into Spools		Total Pre-installed
Alloy Selection	Component	Cost	Subtotals	Cost	Subtotals	
SS347H	Tower Pipe	$588,000	$835,380	$504,000	$734,000	$1,569,380
	Horizontal Pipe	$196,000		$185,000		
	Elbows	$15,680		$24,000		
	Flanges (14)	$35,700		$21,000		
SS304H Backer/ SS347H Clad	Tower Pipe	$3,429,000	$5,703,840	$1,327,700	$2,482,000	$8,185,840
	Horizontal Pipe	$1,143,000		$486,200		
	Elbows	$91,440		$56,100		
	Flanges (408)	$1,040,400		$612,000		
Gr91 backer/ SS347H Clad	Tower Pipe	$1,895,850	$3,414,756	$1,654,300	$2,942,000	$6,356,756
	Horizontal Pipe	$631,950		$605,800		
	Elbows	$50,556		$69,900		
	Flanges (408)	$836,400		$612,000		

In the case of costs associated with the Cold Loop of the CSP plant, shown in Table 87, there is a clear and significant different in the capital cost of fabricating the pipe components out of clad. Clearly at the temperature at which the cold loop operates, the use of 347H alloy is the correct choice and there is no economic advantage by cladding this alloy to a 304H backer. Even substituting the 304H backer with a Gr91 alloy does not bring enough benefit to the capital expenditure, and in fact would require post-weld heat treatment time and cost to be added.

It is important to mention that the prices shown here do not include transportation costs of the spools to the CSP site, installation costs associated with assembly and welding of the pipe spools to other components of the plant. For sake of simplicity, these costs can be assumed comparable between the solid and clad pipe options. In the case of clad options, the pipe spools would be bolted together, while with the solid pipe option most would be butt-welded together. Both options have setup times and quality checks needed.

4.6.3.4 Project Price Sensitivity Analysis (With Respect to Nickel Prices):

As mentioned before, the price of nickel has a great impact on the price of the Ni-based alloys considered in the project. This is only true for the alloys being considered for the Hot Loop, since the 347H solid pipe considered for the Cold Loop only has an average of 11% nickel content. Given that, a simple price sensitivity analysis was performed to show the impact this nickel price has on the fabricated cost of the spools produced for each scenario in the Hot Loop. Table 88 shows the total fabrication price of each spool option and what the nickel price increase would have to be to achieve a breakeven point between those options.

Table 88. Total Fabrication Breakeven Price If Increasing Nickel Prices Versus Current Price Of $17,030/Metric Ton

Alloy Selection	Nickel Price Increase		
	Current	**5.1%**	**40.6%**
Inconel® Alloy 740H®	$18,162,190	$19,059,742	$25,959,692
Haynes® 230® Alloy	$24,448,920	$25,112,225	$29,729,350
SS304H Backer/C22 Clad	$24,994,404	$25,113,042	$25,938,859

For the analysis, it is assumed that each alloy (cladder and backer) will have a price adjustment proportional to the amount of nickel it contains as shown in Table 89. So, a breakeven point between solid 230 Alloy and the 304H/C22 clad is attained with just a 5.1% price increase in nickel, despite the added number of flanges needed for the clad options. In the case of alloy 740H, the breakeven point with 304H/C22 clad is attained at 40.6%. Given the fact that this latter alloy is currently not available in plate form, this price increase effect of nickel may actually be stronger and not as assumed.

Table 89. Effect of Nickel Price Increase From $17,030/Metric Ton of Each Alloy Selection Price Increase

Alloy Selection	Nickel Content	Nickel Price Increase	
		5.1%	**40.6%**
Inconel® Alloy 740H®	48.0%	2.4%	19.5%
Haynes® 230® Alloy	57.0%	2.9%	23.1%
SS304H Backer/C22 Clad	11.7%	0.6%	4.8%

From the analysis it can be clearly stated that Haynes® 230® Alloy and Inconel® Alloy 740H® are very sensitive to the market price of nickel, and that any change in that could significantly impact the alloy selection of the Hot Loop of the CSP plant.

4.6.3.5 Conclusions

1. The temperature difference between the hot and cold loops of the CSP plant (720°C vs. 500°C) has a great impact in the cost difference between the material selection options available. The higher the temperature, the more sophisticated the alloy needs to be, and thus the cladding option becomes more attractive.

2. The consideration of using explosion welded clad pipes for the cold loop (500°C) of a 100 MWe CSP plant does not seem economically favorable for the 347H cladder with backers of 304H stainless steel or Gr91 alloy. The thermomechanical properties, added to the significantly low cost of the 347H alloy, plus ease of fabrication, make this an ideal selection for this portion of the plant.

3. Due to nickel price volatility, the option of using a nickel-based alloy cladder in the hot loop (720°C) seems to be a viable alternative. Currently, the price of nickel in the market is depressed which does not make cladding favorable, but this could change with an increase in demand for this metal (i.e., battery demand).

4. Inconel® Alloy 740® is not commercially available in the form of plates needed to roll and produce the desired diameters of pipe. This limitation forces a potential project considering to use this alloy to have to request a special heat and rolling operation which traditionally adds cost to the alloy. Haynes® 230® Alloy would be the next available option for a solid pipe solution, which has a total fabrication cost similar to a C22 clad pipe alternative.

5. The price sensitivity analysis indicates that a subtle change in the nickel market conditions could shift the selection between Haynes® 230® Alloy and SS304H Backer/C22 Clad for the hot loop of this CSP plant.

5 Significant Accomplishments and Conclusions

5.1 Conclusions

5.1.1 Task 2: Explosion Clad Welding (EXW)

5.1.1.1 RT Bond Strength Evaluations and Metallurgical Characterization of Butt-Welded EXW Coupons (Milestone 1.5.2)

- The clad couples are ranked based on UTS and elongation, and the order is 304H-C22 > P91-C22 > P91-Ni201 > 304H-Ni201. 304H-C22 clad couple outperforms the others in tensile tests at room temperature although failures occurred along the weld centerline in all 304H-C22 specimens. The C22 clad leads to a higher UTS in general than Ni201 clad. The Ni201 is not recommended as a clad layer due to the weaker mechanical strength, more severe grain coarsening in CGHAZ and formation of microcracks and secondary phases in HAZ/PMZ of 304H-Ni201 weld.
- The microhardness map correlates well with the strain partition behavior observed from DIC measurements. Strain accumulations and failures preferentially occurred in the softest regions. A high hardness was observed near the bond interface at the 304H backer side due to the presence of high dislocation densities, grain refinement and formation of α' martensite associated with the EXW process. This was not observed in the P91 welds, since PWHT likely normalized the microstructures.
- The rapid solid-state process of EXW cladding resulted in minimum to no interdiffusion between the cladder and backer at the bond interface. No delamination was observed at the EXW clad interface during the uniaxial tensile tests parallel to the bond, indicating a good bonding strength.
- Through EDS analysis, all the fusion welds showed acceptable dilution levels on the top layer, as demonstrated by the matching concentration of corrosion resistant elements to the nominal compositions of the clad materials.

5.1.1.2 Thermomechanical Testing of Welded EXW Clad Coupons (Milestone 2.2.1)

- Elevated temperature tensile tests revealed similar relative ranking of mechanical testing at room temperature tests, where 304H-C22 outperformed 304H-Ni201 at both 500°C and 720°C in terms of mechanical strength. The location to failure in the 304H-C22 primarily occurs down the weld centerline, indicating ductility drops in the deposited weld metal centerline. However, the strength and ductility of the 304H-C22 EXW clad joint is overall better than the 304H-Ni201 EXW clad joint.
- P91-C22 and P91-Ni201 EXW clad welds had better yield strength than the 304H EXW clad welds but had very little uniform elongation at elevated temperature tensile tests (i.e., low true strains to necking). While the P91 EXW clad welds exhibited better yield strength, the 304H EXW clad welds had better work hardening behavior and therefore better ductility than the P91 welds at 500°C even with lower yield strengths.
- Overall, C22 was demonstrated to outperform Ni201 as a clad material based on the thermomechanical test results for both P91 and 304H SS.

5.1.1.3 Thermomechanical Evaluations of EXW Clad Pipe Welds (Milestone 2.5.2)

- Overall, the thermomechanical properties are similar between the circumferential pipe and plate welds for both 304H/C22 and P91/C22, aside from weld defects observed in the 304H/C22 weld. The filler choice was different between the plate and pipe welds, due to the best practice available to different welding geometries, which introduced an additional variation factor to the strength comparison.
- The average weld efficiencies meet the 80% minimum strength criteria based on UTS values of base metals and expected properties from given certificates of conformance and literature.
- LOF defects in the 304H/C-22 root weld impacted mechanical properties and were not detected during radiographic non-destructive testing (NDT). Proper joint alignment is required to mitigate that defect.
- The P91/C22 welds fail in the HAZ/BM, while the 304H/C22 welds fail more randomly within the FZ, along fusion zone boundary (only at 500°C), and HAZ/BM (mostly at 720°C).
- Cladding interface had minimum to no interdiffusion, except for small intermixing islands, mainly composed of Fe, Ni, and Mo.
- Except for a slight Fe enrichment, the EDS analyzed chemical composition for ErNiCrMo-10 welding filler was similar to nominal composition.

5.1.2 Task 3: Combustion Synthesis/Centrifugal Rotation (CS/CR)

- Composition analysis showed that synthesized C-276 clad contains three times the Fe (~20 wt.%) content allowed by nominal composition limits, which is due to the limitation of the CS/CR process overall, including powders selected and parameters.
- Thermodynamic calculations (CALPHAD) suggest that the higher Fe content raises the equilibrium temperature for formation of sigma phase from 1050°C to 1250°C. Therefore, a slow cooling through higher temperature regimes, which occurs during the process, enables a higher than desired volume fraction of sigma phase. Experimental results confirm the formation of secondary phase, likely sigma, which if enriched in Mo.
- The Mo-rich secondary phase formed in the interdendritic regions and potentially contributed to solidification cracks (~500 µm long) on the ID of the C-276 clad.
- Some remedies were suggested to (1) remove cracks, and (2) reduce and/or eliminate secondary phase in cladder, which would incorporate machining off the cracks and heat treatment, respectively. Based on CALPHAD predictions, a 1260°C soak temperature for 30 minutes followed by water quench was selected. The custom-designed heat treatment succeeded in dissolving Mo-rich secondary phase.
- However, corrosion tests in a purified chloride salt mixture at 750°C for 100 hours resulted in a 173 µm/year corrosion rate, which is almost nine times the allowed corrosion rate target of 20 µm/year.
- Overall, the higher than allowed Fe content and weak corrosion resistance of the C-276 cladder, largely driven by process, contributed to a decision to not forgo welding studies of CS/CR pipes. Instead, the EXW process was down-selected for further welding and techno-economic studies.

5.1.3 Task 4: Additive Manufacturing

- Haynes 282 and In740H are both promising candidates for elevated temperature environments, such as Gen 3 CSP heat exchangers and solar receivers.
- The yield strength of all welds meets 80% of wrought plates, but ductility and UTS are dependent on weld defects.
- Haynes 282 is slightly stronger than In740H, aside from weld defects, and is likely to outperform with properties and weldability (e.g., reheat cracking).
- For both IN740H and Haynes 282 welds, the wrought side yielded first (including BM and HAZ) and accumulated the most strain prior to fracture, and lower microhardness regions correlate with failure locations.
- In similar autogenous welding experiments, the increase in weld current increases the D/W ratio in L-PBF components while the D/W ratio slightly decreases with increasing current in wrought components. The differences mostly correlate with differences in impurity content of oxygen, nitrogen, and sulfur between the wrought and L-PBF samples that contribute to differences in the negative vs. positive surface tension which effect fluid flow and weld pool shape.
- In dissimilar autogenous welding experiments, the increase in weld current seemed to lead to an increase in weld width and weld penetration. However, the increase in weld width was mostly dominant on top surface throughout the weld current regime, but with increasing current above 200 amperes, the max penetration depth increases on the L-PBF side due to increase in subsurface positive surface tension, which is driving a higher weld penetration, leading to asymmetries that are weld current dependent.

5.1.4 Task 5: Joining of Dissimilar and Advanced Manufactured Alloys

5.1.4.1 Joining of Dissimilar Alloys (Milestone 2.5.1)

5.1.4.1.1 Haynes 282 DSW

- The yield strength of wrought material for 304H SS is 125 MPa and 90 MPa, for 500°C and 720°C, respectively, and the UTS and % elongation for 304H SS is 410 MPa and 36% elongation at 500°C and 220 MPa and 36% elongation at 720°C, respectively [13]. Compared to the wrought SS304H properties, all dissimilar weld samples tested at RT, 500°C and 720°C have passed the 80% strength baseline.
- The heat treatment performed for aging H282 after welding drastically reduces weld strength, which is limited by the 304H HAZ/BM strength.
- While failure mostly occurs where necking occurs, cracks develop in the half thickness, and bottom surface of 304H fusion boundaries during deformation, likely from weld-induced defects, e.g., micro-cracks as seen in the as welded condition.
- The presence of voids indicates possible manual process errors likely due to the challenge of dilution along the 304H side with high Fe content in the first pass. Also, fluidity of molten pool may also be influenced by the mixing process.
- The presence of microcracks still may indicate the possibility of hot/warm cracking such as liquation cracking or ductility dip cracking.
- After the aging heat treatment, a noticeable coarsening occurs in the Ti, Mo, and Cr carbide particles at the interface between the SS304H and H282 filler metal, which may affect the failure behavior of these welds adversely.

- The average dilution levels were maintained lower than 25% in the weld zone of the dissimilar weld both before and after the aging heat treatment.

5.1.4.1.2 Inconel 740H DSW

- The In740H-304H DSW failed in 304H HAZ/BM for all test conditions. The mechanical properties of the thermomechanical tests meet the minimum expected properties of wrought 304H SS products. Ductility decreased in 304H SS HAZ with increasing temperature in the HAZ, likely with the nucleation of intergranular $M_{23}C_6$ along grain boundaries of coarse grained HAZ, leading to fracture along less tortuous boundaries.
- The average dilution levels were maintained lower than 25% in the weld zone of the dissimilar weld adjacent to the 304H SS side.
- Post-weld aging heat treatment led to an increase in the hardness of the In740H HAZ due to reprecipitation. In contrast, aging reduced the hardness of the SS304H HAZ likely due to grain coarsening. Strain localization occurred in the softer region in the SS304H side before and after aging.

5.1.4.2 Corrosion in Molten Chlorides (Milestone 2.5.3)

5.1.4.2.1 L-PBF-to-Wrought H282 Welds

- There was no statistical difference in corrosion rates between the AM or wrought H282 alloys.
- The average corrosion rate of the tested samples was 63.5 μm/year, which agrees with a UC Davis led similar experiment on H282.

5.1.4.2.2 L-PBF-to-Wrought IN740H Welds

- The overall corrosion rate of L-PBF-to-wrought In740H was almost twice that of H282.
- Unlike H282, IN740H did not show an obvious intergranular depletion of Cr. Instead, the intergranular depletion was in Ni and Co.
- There is more internal nitridation, less surface oxidation, and the corrosion seems more uniform.

5.1.4.2.3 EBAM-to-Wrought H282 Welds

- XRF analysis showed more Fe content in EBAM sample, which may increase its corrosion rate compared to L-PBF.
- Grain boundaries Cr depletion behavior was similar in EBAM and L-PBF samples, however, Co depletion was only observed in EBAM sample.
- EBAM-to-wrought H282 showed a significantly higher corrosion rate than L-PBF-to-wrought H282 under the same testing conditions.
- Matching chemical composition across the weldments resulted in similar depth of Cr depletion among the subzones.

5.1.4.3 Weldment Crack Susceptibility and Cracking Mechanisms (Milestone 3.5.1)

- HAZ of L-PBF Hanes 282 printed in the vertical orientation (Z) exhibits the best resistance to strain age cracking and requires more strain to fracture compared to Inconel

254

740H samples. Haynes 282 horizontal orientation (XY) performed the worst. The Inconel 740H samples demonstrably showed more micro voids on grain boundary facets during fractographic examination with 10% strain condition than Haynes 282 samples.

- A heating rate effect is observed in physically simulated arc-weld HAZ of L-PBF components with a heating rate range of 40-3480°C/h. The fastest heating rate shows the highest resistance to fracture, regardless of the imposed initial strain and stress.

  - o Haynes 282 exhibits a C-curve behavior relationship between heating rate and time to failure, such that intermediate heating rates (e.g., 100°C/h) behave the worst.
  - o Inconel 740H samples, including both orientations, show a linear behavior between heating rate and time to failure, such that slower heating rates generally lead to faster fracture.

- Welded Haynes 282 samples extracted from experimental GTAWs show slightly different behaviors than the simulated HAZ samples.
  - o Wrought-to-wrought weld shows that there is a heating rate effect such that the slower heating rate of 100°C/h shows a higher sensitivity to cracking, where the samples failed on heating prior to reaching 800°C. In comparison, the samples did not fail within 20h at temperature using a 3480°C/h heating rate.
  - o L-PBF to L-PBF weld fails quickly even with the highest heating rate condition, such that the amount of imposed stress/strain during testing greatly affected the result. The stroke applied during the heating step was varied to show this effect. While more testing may be needed, the L-PBF to L-PBF weld was more susceptible than the wrought-to-wrought weld. The higher microhardness in the as-welded condition may explain this result.

5.1.4.4 Low-Cycle Isothermal Fatigue and Failure Mode Analysis of Weldments (Milestone 3.5.2)

- Harder and fine-grained L-PBF AM H282 exhibit inferior fatigue life compared to softer and more ductile wrought H282. Welded AM and welded wrought H282 show similar fatigue life to the L-PBF condition.
- Small subsurface weld defects that are probably not detectable by conventional field NDE methods do not significantly impact the fatigue life of welded samples.
- Most of the welded samples fail in the weld fusion zone, while unwelded samples fail at the edge of the gauge length.

5.1.5 Task 6: Finite Element Analysis

5.1.5.1 Task 6.1 FE Simulation of Butt-Welded Explosion-Welding (EXW) Clad Coupon

5.1.5.1.1 Welding Modeling of G91/C22 and SS304H/C22 Clad Plates

- For the multi-pass weld with relatively high inter-pass temperatures, the incomplete austenite-martensite transformations are observed in Grade 91 steel. By considering the incomplete transformation kinetics in the welding model, the IC-HAZ, characterized by a mixed microstructure of tempered and untempered martensite, is predicted. This is particularly evident in areas experiencing more thermal cycles, e.g., locations beneath the

255

cap passes on both sides of the clad plates. The predicted locations of IC-HAZ correlate well with the low hardness spots observed experimentally on a weld transverse section.

- Welding introduces tensile stress in the weld metal of G91/C22 which is most significant in the vicinity of the cap beads on both the substrate and clad sides. PWHT effectively mitigates the residual stress in the weld metal through creep deformation. However, the larger CTE of the clad material compared to the substrate induces considerable tensile stress in the clad and a high stress gradient at the bonding interface.

- After welding, the SS304H weld zone forms tensile stress in the longitudinal direction, and the outside region forms compressive stress. Residual stresses in the clad layer away from the weld are comparable for both SS304H/C22 and G91/C22 at the working temperature (500°C).

5.1.5.1.2 Tensile Strength Modeling of G91/C22 and SS304H/C22 Clad Plates

- During tensile testing, the G91 base metal, weaker than the G91 weld metal, experiences higher deformation. In contrast, the deformation in both the base and weld metals of clad C22 is relatively uniform due to their comparable strength. As deformation accumulates in the G91 base metal, the stress triaxiality there also increases, ultimately leading to fracture. Therefore, the fracture location of the G91/C22 weld is determined by the relative strength between the base and weld metals, rather than that between the clad and substrate materials.

- For the G91/C22 weld, the residual stress induced by welding and PWHT has an insignificant effect on the fracture in G91 base metal. However, the residual tensile stress is compounded with the tensile loading stress, especially at the bonding interface where a high stress gradient persists, thereby exacerbating the tensile stress and triaxiality factor in that region. Hence, for cases with a weak clad-substrate bonding strength, the residual stress could be a critical factor in influencing the fracture behavior.

- For the SS304H/C22 weld, the predicted fracture location is in the base metal of SS304H, whereas the experimental fracture location is in the weld zone. This discrepancy is likely attributed to the complex hardening behavior, as dislocation recovery is not fully considered.

5.1.5.1.3 Weld Modeling of SS304H/C22 EXW Clad Pipe

- Tensile hoop stress is dominant throughout the entire circumferential joint and the adjacent heat-affected zone. The relatively uniform cooling of the entire pass shows that the pass behaves as a single unit constrained by the surrounding material, leading to the formation of predominantly tensile stress.

- Introducing forced cooling at pipe inner surface transforms the tensile stress to compressive stress at ID. This is because the ID region is kept at low temperatures by the forced cooling, and it does not incur much plastic strain during weld heating, consequently forming compressive residual stress (similar to that of the base metal).

5.1.5.2 Task 6.2 FE Model Optimization of Welding Process of AM Samples to Wrought Metal

5.1.5.2.1 Molten Pool Modeling to Address Asymmetrical Weld Shape

- The molten pool convection is affected by the presence of high amount of oxygen in the additively manufactured H282, leading to a change in Marangoni shear stress. The change in convection results in an asymmetry in the weld nugget shape between wrought and AM H282. The asymmetry is more pronounced when the molten pool is larger (e.g., higher welding heat input). It is noted that the actual effect of oxygen in multi-pass weld is likely diminished due to the filler metal addition. Additionally, the effect of oxygen on shifting the arc center toward one of the materials needs to be further studied.

5.1.5.2.2 Thermo-Mechanical Modeling to Address Residual Stress and Distortion

- Comparing the weld of AM H282 to wrought H282 with that of H282 to SS304H, high residual stress is formed in weld zone especially on the H282 side which is caused by the high hardenability (flow/yield stress) of this alloy.

5.1.6 Task 7: Techno-Economic Analysis

- The temperature difference between the hot and cold loops of the CSP plant (720°C vs. 500°C) has a great impact in the cost difference between the material selection options available. The higher the temperature, the more sophisticated the alloy needs to be, and thus the cladding option becomes more attractive.
- The consideration of using explosion welded clad pipes for the cold loop (500°C) of a 100 MWe CSP plant does not seem economically favorable for the 347H cladder with backers of 304H stainless steel or Gr91 alloy. The thermomechanical properties, added to the significantly low cost of the 347H alloy, plus ease of fabrication, make this an ideal selection for this portion of the plant.
- Due to nickel price volatility, the option of using a nickel-based alloy cladder in the hot loop (720°C) seems to be a viable alternative. Currently, the price of nickel in the market is depressed which does not make cladding favorable, but this could change with an increase in demand for this metal (i.e., battery demand).
- Inconel® Alloy 740® is not commercially available in the form of plates needed to roll and produce the desired diameters of pipe. This limitation forces a potential project considering to use this alloy to have to request a special heat and rolling operation which traditionally adds cost to the alloy. Haynes® 230® Alloy would be the next available option for a solid pipe solution, which has a total fabrication cost similar to a C22 clad pipe alternative.
- The price sensitivity analysis indicates that a subtle change in the nickel market conditions could shift the selection between Haynes® 230® Alloy and SS304H Backer/C22 Clad for the hot loop of this CSP plant.

5.2 Key Takeaways

5.2.1 Task 2: Explosion Clad Welding (EXW)

- 304H/C22 clad couple outperformed the other candidates in terms of mechanical properties at room and elevated temperatures. Ni201 is not recommended as a cladder for this application.
- From a technical point of view, testing and characterization work done on samples extracted from the pipe sections showed that explosion cladding is a viable method for fabricating GEN3 CSP molten salt seam pipes.
- It is recommended to perform NDE for welded clad pipes, due to the more complex joint setup, challenging welding positions, and use of overmatching fillers than plate welds.

5.2.2 Task 3: Combustion Synthesis/Centrifugal Rotation (CS/CR)

- Synthesized C276 did not meet chemical composition or corrosion specifications. Therefore, implementation of SS304H clad with synthesized C276 using the CS/CR manufacturing technique is not recommended for what was evaluated.
- A custom-designed heat treatment successfully dissolved secondary phase in synthesized C-276 cladder and machining off surface layers may provide remedies to remove secondary phases and cracks.
- Aside from optimizing powder compositions to reduce Fe content, faster cooling rates during the manufacturing process would be needed to reduce detrimental interdendritic secondary phases contributing to solidification cracking.

5.2.3 Task 4: Additive Manufacturing (AM)

5.2.3.1 Property Testing of As-Built AM Samples

- L-PBF of Haynes 282 underwent two different post build heat treatments to maximize strength and ductility. HT2 (899°C-first aging step) improved ductility for both print orientations.
- EBAM Haynes 230 exhibited cracking throughout the build, likely solidification cracking or reheat cracking during post build heat treatment. Optimization of process is needed.
- EBAM Haynes 282 did not exhibit any cracking, but keyhole porosity was dispersed randomly throughout the build, which contributed to low ductility in thermomechanical tests.

5.2.3.2 Thermomechanical Properties of L-PBF and EBAM Welds

- 80% strength criterion (based on UTS) met for H282 and IN 740H L-PBF-to-wrought, except for 500°C condition at Haynes 282 due to weld defects
- Yield strength of Haynes 282 L-PBF-to-wrought welds is higher than Inconel 740H welds
- FEA conducted for AM-to-wrought welds and Haynes 282 to 304H wrought welds found higher residual stress on stronger side (e.g., Haynes 282 side of DSW)
- Aside from defects, 80% strength criterion was met in EBAM-to-wrought welds, but yield strength in EBAM Haynes 282 is lower than L-PBF or wrought components, contributing to failure in EBAM side of weld.

5.2.3.3 Fluid Flow Study for Weld Shape Morphology

- Separate autogenous L-PBF H282 welds exhibit a higher D/W ratio than wrought H282, which derives from differences in impurity content and therefore surface tension.
- L-PBF to wrought H282 autogenous butt welds show asymmetrical behavior that has a more dominant negative surface tension coefficient effect but with centerline shift to modify weld procedure to create more symmetrical weld shape.

5.2.4 Task 5: Joining of Dissimilar and Advanced Manufactured Alloys

5.2.4.1 Dissimilar Welding (DSW)

- Welding of hot (Haynes 282 and Inconel 740H) to cold (SS304H) components is feasible at transition joints based on strength evaluation of weld joint and minimal dilution of overmatching filler (Haynes 282 or Inconel 82) weld pass adjacent to 304H SS at both as-welded and heat-treated conditions.
- Regarding PWHT of DSW with both Haynes 282 and Inconel 740H, direct single step aging (e.g., 790-840°C) might be preferable over a solution anneal+aging PWHT to prevent strength reduction in SS304H HAZ from the solution anneal step. A direct age would help stabilize the Ni-superalloy microstructure while not sacrificing too much strength on 304H SS side.
- While no corrosion test has been conducted on DSW joints, the dilution levels predict sufficient corrosion resistance in weld FZ on 304H SS side. However, galvanic corrosion of SS304H HAZ side may occur. Therefore, DSW joints of wrought Haynes 282 or Inconel 740H to SS304H/C22 clad pipe may be more desirable to mitigate corrosion concerns than using monolithic SS304H on the cold side.

5.2.4.2 Weldment Crack Susceptibility and Crack Mechanisms

- The weldability, specifically strain age cracking resistance, of L-PBF Haynes 282 printed in the vertical (Z) orientation is the best, similar to wrought Haynes 282 in literature.
- Heating rate during both field and shop post weld heat treatments should be carefully designed for both Haynes 282 and Inconel 740H L-PBF and wrought welded components to prevent cracking during direct aging post weld heat treatment (PWHT), which will be material, stress/strain, and AM print orientation dependent.
- Cross welds of L-PBF samples need to consider the initial microhardness condition prior to arc welding. Higher solutionizing peak temperatures (>1200°C) may be required for post build heat treatment (PBHT) and prior to arc welding to reduce microhardness.

5.2.4.3 Corrosion in Molten Chlorides (Milestone 2.5.3)

- Strict control of precursor materials (powders or wires) as well as processing is vital for producing the required nominal chemical composition which is necessary for maintaining the same corrosion resistance in AM products as in wrought alloys.
- In740H possesses lower corrosion resistance in molten salts compared to H282 alloy.
- Visual and macroscopic inspection of welded AM-to-wrought coupons did not show any significant differences in corrosion resistance of AM, fusion zone, or wrought alloys. However, EDS elemental mapping of L-PBF-to wrought In740H showed that fusion zone and wrought base metal have inferior corrosion resistance compared to AM In 740H.

259

5.2.4.4 Low-Cycle Isothermal Fatigue and Failure Mode Analysis of Weldments (Milestone 3.5.2)

- Post weld aging heat treatment for AM and wrought H282 weldments is effective in producing welds with fatigue life values that match the as-built AM H282, but relatively lower than that of the wrought alloy.
- Welding or surface defects have a weak impact on fatigue life at the high total strain ranges. Small subsurface weld defects that are not detectable by typical NDE did not affect the number of cycles to failure for wrought or AM welds.

5.2.5 Task 6: Finite Element Analysis

5.2.5.1 Task 6.1 Finite Element (FE) Simulation of Butt-Welded Explosion-Welding (EXW) Clad Coupon

- Due to high thermal strain and incompatible deformation, high residual stress forms after welding. For welds that do not receive a post-weld heat treatment (e.g., the SS304H/C22 weld), the welding-induced residual stress is retained at service temperature (500°C). The existence of tensile residual stress in the weld metal and heat-affected zone on the pipe ID can potentially degrade the corrosion resistance. Thermo-mechanical simulations are important tools to understand and mitigate the formation of residual stress during welding.

5.2.5.2 Task 6.2 FE Model Optimization of Welding Process of AM Samples to Wrought Metal

- One of the plausible factors for asymmetry in weld nugget shape when welding AM material to wrought material is the presence of high amount of oxygen in the former which changes the Marangoni shear stress and consequently the molten pool convection. The FE models can be further developed to help aid the process optimization for the dissimilar welding applications.

5.2.6 Task 7: TEA

- The temperature difference between the hot and cold loops of the CSP plant (720°C vs. 500°C) has a great impact in the cost difference between the material selection options available. The higher the temperature, the more sophisticated the alloy needs to be, and thus the cladding option becomes more attractive.
- **Cold Side**: The consideration of using explosion welded clad pipes for the cold loop (500°C) of a 100 MWe CSP plant does not seem economically favorable for the 347H cladder, with backers of 304H stainless steel or Gr91 alloy. The thermomechanical properties, added to the significantly low cost of the 347H alloy, plus ease of fabrication, make this an ideal selection for this portion of the plant.
- **Hot Side**: Due to nickel price volatility, the option of using a nickel-based alloy cladder in the hot loop (720°C) seems to be a viable alternative. Currently, the price of nickel in the market is depressed which does not make cladding favorable, but this could change with an increase in demand for this metal (i.e., battery demand).

260

6 Budget and Schedule

The spending summary up to March 31, 2024, can be found in Table 90. Since then, the remaining funds have been spent on the preparation and writing of this final technical report.

Table 90. Spending Summary by Budget Category as of March 31, 2024

Spending Summary by Budget Category									
	Approved Budget per SF-424A						Actual Expenses		
Budget Categories	BP 1	BP 2	BP 3	BP 4	BP 5	Total	This Quarter	Cumulative	%
a. Personnel	$ 58,664	$ 139,204	$ 96,540	$ 29,134		$ 323,542	$ 4,193	$ 351,744	109%
b. Fringe Benefits						$ -	$ -	$ -	
c. Travel	$ 10,225	$ 15,999	$ 16,023	$ 9,346		$ 51,593	$ -	$ 0	0%
d. Equipment						$ -	$ -	$ -	
e. Supplies	$ 8,755	$ 20,568	$ 6,868	$ -		$ 36,191	$ -	$ 53,293	147%
f. Contractual	$ 510,177	$ 780,753	$ 634,436	$ 185,037		$ 2,110,403	$ (0)	$ 2,089,371	99%
g. Construction						$ -	$ -	$ -	
h. Other	$ 3,264	$ 5,016	$ 5,004	$ 1,652		$ 14,936	$ 2,393	$ 12,476	84%
i. Total Direct Charges	$ 591,085	$ 961,540	$ 758,871	$ 225,169	$ -	$ 2,536,665	$ 6,586	$ 2,506,884	
j. Indirect Charges								$ -	
k. Total Charges	$ 591,085	$ 961,540	$ 758,871	$ 225,169	$ -	$ 2,536,665	$ 6,586	$ 2,506,884	
DOE Share	$ 469,929	$ 777,013	$ 603,774	$ 178,616		$2,029,332	$ 6,586	$ 2,015,480	99%
Cost Share	$ 121,156	$ 184,527	$ 155,097	$ 46,553		$507,333	$ -	$ 491,404	97%
Cost Share Percentage	20%	19%	20%	21%			0%	20%	

The original scope of this project was intended to end March 31, 2023, with a project start date of February 1, 2020. Due to delays, mostly from COVID-19 impacts, the project end date was first extended to June 30, 2023. Since the beginning of COVID-19 and the war in Ukraine (in early 2022) impacting accruement and budget of materials, additional no-cost time extensions were requested with an end date of March 31, 2024, to complete work from BP2 and BP3 that had been delayed. Finding a machine shop with a decent turnaround time and cost associated with machining Ni-round samples for BP3 subtasks made it additionally challenging to complete BP3 tasks by June 30, 2023. Therefore, BP3 was extended to a budget period 4 (BP4) to complete experimental work by March 31, 2024, with a final technical report delivery planned for June 30, 2024.

The following tables show the planned end dates for each milestone based on the June 30, 2023, project end date, the actual date of completion (including additional work), and status of completion. Milestones with a "+" indicate additional work that was not included in the original scope. Table 91, Table 92, and Table 93 display BP1, BP2, and BP3 schedules, respectively.

Table 91. Budget Period 1 Schedule

Milestone	Title	Planned End Date	Actual End Date	Status
1.1.1	Project management	09/30/20	09/30/20	100%
1.1.2	Design of experiments for dissimilar alloy systems to be evaluated	09/30/20	09/30/20	100%
1.2.1	Down-selection of explosion welding (EXW) clad dissimilar alloys systems	03/31/21	03/31/21	100%
1.3.1	Combustion Synthesis (CS) and Centrifugal Rotation (CR) cladding process parameters	03/31/21	03/31/21	100%
1.3.2	CS/CR clad of pipes	06/30/2021	09/30/2021	100%
1.4.1	Additive manufacturing (AM) processes developed for selected high-temperature alloys	03/31/21	06/31/21	100%
1.4.2	AM heat treatment development and property testing	06/30/2021	06/30/2021	100%
1.4.3	AM fabricated welding characterization specimens	06/30/2021	06/30/2021	100%
1.5.1	Design of dissimilar alloys joining	09/30/2021	06/30/2021	100%
1.5.2	Bonding strength evaluations and metallurgical characterizations of butt-welded explosion welding (EXW) clad coupons	06/30/2021	09/30/2021	100%
1.6.1	Finite element (FE) simulation of butt-welded explosion welding (EXW) clad coupon	06/30/2021	06/30/2021	100%
1.7.1	Techno-economic baseline for solid Ni superalloys	06/30/2021	06/30/2021	100%

Table 92. Budget Period 2 Schedule

Milestone	Title	Planned End Date	Actual End Date	Status
2.2.1	Thermomechanical Testing of welded EXW clad coupons	03/31/2022	03/31/2022	100%
2.2.2	Thermomechanical testing of welded semi-cylindrical explosion welding (EXW) clad coupon	Combined with 2.5.2		
2.2.3	Welding and FE modeling of semi-cylindrical explosion-welding (EXW) clad coupon	Combined with 2.5.2		
2.3.1	CS/CR clad pipes' characterization	03/31/2022	03/312022	100%
2.4.1	Welding of additive manufacturing (AM) samples to similar wrought alloy	12/31/2022	06/30/2023	100%
2.5.1	Joining of dissimilar alloys	07/31/2022	03/31/2023	100+%
2.5.2	Thermomechanical evaluation of longitudinally welded EXW and CS/CR clad pipe sections	12/31/2022	09/30/2023	100%
2.5.3	Corrosion in molten chlorides	12/31/2022	06/30/2023	100%
2.6.1	Finite element (FE) model optimization of welding process of additive manufacturing (AM) samples to wrought metal	12/31/2022	09/30/2023	100%
2.7.1	Preliminary techno-economic analysis for advanced manufacturing	09/30/2022	06/30/2022	100%

Table 93. Budget Period 3 Schedule

Milestone	Title	Planned End Date	Actual End Date	Status
3.5.1	Weldment crack susceptibility and cracking mechanisms	12/31/22	03/31/24	100%
3.5.2	Low cycle thermal fatigue and failure mode analysis of weldments	03/31/23	03/31/24	100%
3.7.1	Techno-economic analysis	06/30/23	03/31/24	100%

7 Path Forward

The following studies, which may be of interest to follow up with the work presented here, may be split into the cold and hot components for a Generation 3 CSP plant.

Cold Components

The Grade 91 alloy backer clad with C-22 alloy using EXW techniques may be of interest for transfer pipes based on sufficient mechanical strength and dilution requirements and as a cheaper option than using 304H SS with a backer based on TEA. Future efforts would need to analyze long term mechanical performance at 500°C, such as creep life, and molten salt corrosion performance of C22 clad ID in pipe sections.

Hot Components

For the higher-temperature transfer pipes, EXW clads with 304H SS as the backer and C-22 as the cladder seems to be techno-economically feasible and desirable. Therefore, continuation of experimental research on long-term service performance and microstructural stability (e.g., $M_{23}C_6$) of 304H/C22 EXW clad pipe welds, including creep and corrosion testing of pipe sections, would be optimal at the 720°C–760°C temperature range.

While elevated temperature testing, crack susceptibility, and elevated temperature isothermal fatigue properties have been analyzed on Haynes 282 and Inconel 740H L-PBF components, a comprehensive study on long-term stability and service performance of those welds would be needed, including other stress state conditions (e.g., creep or high cycle fatigue). Microstructural stability and thermomechanical properties after being at 760°C for thousands of hours, for instance, may need to be studied, as precipitate over aging due to prolonged thermal exposure may contribute to reduced ductility. While some studies have analyzed wrought products, the phase evolution studies of L-PBF specific Ni-superalloys are of interest for further consideration of these components. Creep testing of L-PBF Haynes 282 components with different PBHT and arc welded-PWHT conditions, considering variability in microstructural condition, to optimize creep life may be of interest.

Regarding lessons learned from crack susceptibility (strain age/ cracking) tests, post build heat treatments (i.e., solutionizing temperature) of Haynes 282 L-PBF would need to be optimized to (1) establish a good strength-ductility combination and (2) improve weldability of the arc welded HAZ and FZ. Meeting a microhardness target window, e.g., 250-300 HV in comparison to wrought product, may be a simple goal to improve weldability while not sacrificing mechanical strength. It is worth mentioning that post weld heat treatment using an aging step is required anyway, and thus microhardness will improve overall during arc weld PWHT.

Finally, finding applicable designs for heat exchangers to enable relevant techno-economic analysis of L-PBF parts in comparison to other AM or conventional techniques would provide a final comprehensive assessment of L-PBF process implementation.

Other AM technologies, such as wire arc AM (WAAM), of Haynes 282 and Inconel 740H may be a suitable alternative to EBAM. While EBAM components with Haynes 282 have some

This report is available at no cost from the National Renewable Energy Laboratory at www.nrel.gov/publications.

processing challenges (e.g., keyhole porosity), this behavior is largely mitigated with WAAM, albeit with other process challenges. However, WAAM may provide a more cost-effective solution with similar or better thermomechanical properties.

Additional Comments

The cladding work utilized in this study focused more on cladding and welding of uniform pipe lengths and disregarded the effect of pipe bends and flange connections. Further research on 304H and Gr91 clad with C-22 at pipe bends, and weldability of those components, would need further study. Induction (warm) bending might be another facet of study that is industrially relevant for pipe bends with these backer and cladder combinations.

Regarding key takeaways from DSW and EXW, welds of 304H/C22 or Gr91/C22 to Haynes 282 or Inconel 740H components may be needed, in addition to the DSW joints studied here, to help mitigate potential galvanic corrosion concerns if, for example, welding 304H SS to Haynes 282 in hot components.

8 Inventions, Patents, Publications, and Other Results

8.1 Paper Publications

8.1.1 Published

The following paper has been published:

1. Xuesong Gao, Abdelrahman Abdelmotagaly, Timothy Pickle, Aric Adamson, Chad Augustine, Zhenzhen Yu, Wei Zhang, Integrated modeling for residual stress and failure behavior in welded Grade 91 steel cladded with nickel alloy, Journal of Manufacturing Processes, Volume 121, 2024, Pages 205-220. https://doi.org/10.1016/j.jmapro.2024.05.036

8.1.2 In Preparation

The following papers are currently in preparation for publication:

- Abdelrahman Abdelmotagaly, Timothy Pickle, Chad Augustine, Garrison Hommer, Terry Totemeier, Zhenzhen Yu, The effects of additive manufacturing and welding on the isothermal low cycle fatigue properties of Haynes 282, *Additive Manufacturing* 2024.
- Timothy Pickle, Abdelrahman Abdelmotagaly, Evan Perri, Ben Rafferty, Jeremy Iten, Chad Augustine, Zhenzhen Yu, Strain age cracking susceptibility in Haynes 282 and Inconel 740H arc welded laser-powder bed fusion components, *Weld Journal*, 2024.
- Timothy Pickle, Abdelrahman Abdelmotagaly, Xuesong Gao, Evan Perri, Aric Adamson, Ben Rafferty, Jeremy Iten, Chad Augustine, Wei Zhang, Zhenzhen Yu, Weld pool morphology differences in gas tungsten arc welds of laser-powder bed fusion and wrought Haynes 282 plates, 2024.
- Xuesong Gao, Abdelrahman Abdelmotagaly, Timothy Pickle, Aric Adamson, Chad Augustine, Zhenzhen Yu, Wei Zhang, Thermo-mechanical modeling of dissimilar joining of wrought H282 to additively manufactured H282 and SS304H, 2024.

8.2 Conference Proceedings

The following oral and poster presentations have been completed over the duration of this project and are tabulated in Table 94. Two more talks are planned in the upcoming months and are included.

Table 94. Conference Proceedings Throughout Duration of Project

Full Author List	Paper Title	Session/Conference	Conference Location	Date
Timothy Pickle, Abdelrahman Abdelmotagaly, Evan Perri, Ben Rafferty, Jeremy Iten, Chad Augustine, Zhenzhen Yu	Strain Age Cracking of Arc Welded Ni-Base Superalloy Laser Powder Bed Fusion Components	AWS Professional Program (FABTECH) 2024	Orlando, FL	Planned Oct 15-17, 2024

266

Full Author List	Paper Title	Session/Conference	Conference Location	Date
Zhenzhen Yu, Timothy Pickle, Abdelrahman Abdelmotagaly, Ben Rafferty, Jeremy Iten, Chad Augustine	Thermomechanical Properties of GTAW Welds Between Wrought and L-PBF AM Ni-base Superalloy	IIW Annual Assembly (Subcommission II-C)	Rhodes, Greece	Planned July 2024
Zhenzhen Yu, Timothy Pickle, Abdelrahman Abdelmotagaly, Aric Adamson, Ben Rafferty, Jeremy Iten, Chad Augustine	Weldability of L-PBF Additive Manufactured Ni-base Superalloys	TRX America Makes 2024	Golden. CO	April 9. 2024
Timothy Pickle, Abdelrahman Abdelmotagaly, Aric Adamson, Ben Rafferty, Jeremy Iten, Zhenzhen Yu, Youyang Zhao, Chad Augustine	Thermomechanical Properties of Arc Welded Additively Manufacture and Wrought Ni-base Superalloys	IMAT 2024	Detroit. MI	October 17, 2023
Abdelrahman Abdelmotagaly, Timothy Pickle, Aric Adamson, Zhenzhen Yu, Chad Augustine, Judith Vidal, Steve Mabry	Thermomechanical Properties of Stainless Steel and Grade 91 Welds with Explosion Clad for Generation 3 Concentrated Solar Power Systems	IMAT 2024	Detroit, MI	October 16, 2023
Abdelrahman Abdelmotagaly, Timothy Pickle, Aric Adamson, Zhenzhen Yu, Chad Augustine, Judith Vidal, Benjamin Rafferty, Jeremy Iten	Additive Manufacturing and Welding of Ni-Base Superalloys for Concentrated Solar Power Systems	AWS Professional Program (FABTECH) 2023	Chicago, IL	September 13, 2023
Timothy Pickle, Yu Hong, Abdelrahman Abdelmotagaly, Judith Vidal, Chad Augustine, and Zhenzhen Yu	Weld Failure Control and Material Selection in CSP Applications	11th Annual Welding the Rockies Symposium	Golden, CO	March 10, 2023
Aric Adamson, Abdelrahman Abdelmotagaly, Timothy Pickle, Zhenzhen Yu, Hu Chun Yi. Judith Vidal, Chad Augustine, Julian Osorio, Youyang Zhao	Advanced Manufacturing of Gen 3 CSP Components	AWS Professional Program (FABTECH) poster presentation (won 1st place undergraduate category)	Atlanta, GA	Sept, 2022
Xuesong Gao, Wei Zhang	Finite Element Modeling of Residual Stress in Grade 91 Weldments Considering Phase Transformations	AWS Professional Program (FABTECH)	Virtual	Sept, 2021

Appendix A

Table 95. Chemical Composition in Wt.% for the Potential Alloy Candidates [5, 8, 13-21]

Alloy	C	Cr	Ni	Mo	Co	W	Nb	Fe	Ti	Al	Si	Mn	Other
Incoloy 800H	0.05–0.1	19–23	30–35	-	-	-	-	39.5 min	0.15–0.6	0.15–0.6	1	1.5	-
Inconel 617	0.15	20–24	Bal	8–10	10–15	-	-	3	-	0.8–1.5	0.5	1	-
Inconel 625	0.1	20–23	58 min	8–10	-	-	3.15–4.15	5	0.4 max	0.4 max	1	0.5	-
Inconel 740H	0.03	24.5	Bal	0.1	20	-	1.5	3 max	1.35	1.5	0.15	1 max	Cu 0.5 max
Hastelloy X	0.1	22	47 Bal	9	1.5	0.6	0.5 max	18	0.15 max	0.5 max	1 max	1 max	-
C-276	0.01 max	16	57 Bal	16	2.5 max	4	-	5	-	-	0.08 max	1 max	V 0.35 max
Haynes 230	0.1	22	57	2	5 max	14	0.5 max	3 max	0.1 max	0.3	0.4	0.5	La 0.02, Zr 0.015 max
Haynes 244	0.03 max	8	60	22.5	-	6	-	2 max	-	0.5 max	-	0.8 max	-
Haynes 233	0.1	19	48	7.5	19	0.3 max	-	1.5 max	0.5	3.3	0.2 max	0.4 max	B 0.004, Ta 0.5, Zr 0.03
Haynes 282	0.06	20	57	8.5	10	-	-	1.5 max	2.1	1.5	0.15 max	0.3 max	B 0.005 max
C22	0.01 max	22	Bal	13	2.5 max	3	-	3	-	-	0.08 max	0.5 max	Cu 0.5 max, V 0.5 max
P92	0.07–0.13	8.5–9.5	0.4 max	0.3–0.6	-	1.5–2.0	0.04–0.09	Bal	0.01 max	0.2 max	0.5 max	0.3–0.6	B 0.006 max, Zr 0.01 max, V 0.15–0.25
SS347H	0.04–0.10	17–20	9-13	-	-	-	0.32–1.00	Bal	-	-	1	2	S 0.03, P 0.045
SS316H (CF8M)	0.04–0.10	16–18	10–14	2–3	-	-	-	Bal	-	-	0.75	2	S 0.03, P 0.045
SS709	0.063	19–20	25	1.5	-	-	-	Bal	0.01 max	-	0.28	0.88	N 0.14, B 0.002, Cb 0.23
SS304H	0.07	17.5–19.5	8.0–10.5	-	-	-	-	Bal	-	-	0.75	2.0	N 0.1, S 0.03, P 0.045

Appendix B

Table 96. Chemical Composition of Filler Wires in wt. %.

AWS Class	Ni	C	Mn	Fe	Cr	Mo	Si	Co	Cu	W	Nb	Others
ERNiCrMo - 2	Bal.	0.05 - 0.15	1.0 max	17-20	20.5-23	8-10	1.0 max	0.5-2.5	0.5	0.2-1	-	0.5 max
ERNiCrWMo - 1	Bal.	0.05 - 0.15	0.3-1.0	3	20-24	8-10	0.5	5	-	13-15	-	Al 0.2 – 0.5
ERNiCrMo - 3	58 min	0.1	0.5	5	20-23	8-10	0.5	-	-	-	3.15 - 4.15	Al 0.40, Ti 0.4
ERNiCrCoMo- 1	Bal.	0.05 - 0.15	1	3	20-24	8-10	0.5	10-15	-	-	-	Al 0.8 – 1.5
ENiCu - 7	62-69	0.15	4	2.5	-	-	1.5	-	Bal.	-	-	Al l.75, Ti 1.0
ERNiCr - 3	67 min	0.1	2.5-3.5	3	18-22	-	-	-	-	-	2.0-3.0	-

Appendix C

Table 97. Mechanical and Physical Properties of Alloys for Gen3 CSP

Name	Strength				Physical Properties					Notes
	Temp. (°C)	Yield Strength (MPa)	UTS (MPa)	% Ductility	Temp. (°C)	Thermal Conductivity (Wm⁻¹°C⁻¹)	Specific Heat (Jgk⁻¹°C⁻¹)	Temp. (°C)	Mean Therm. expansion Coeff. (μm*m⁻¹°C⁻¹)	
Hastelloy X	21	376	783	46.5	25	9.2	486	26–100	13.9	
	538	253	628	53.6	100	11.2	487	26–500	15.0	
	649	241	580	65.5	200	14.1	484	26–600	15.3	
	760	233	424	95.6	600	20.9	491	26–700	15.7	
	871	193	251	117.9	650	21.9	507	26–750	15.9	
	982	88	130	81.5	700	22.8	531	26–800	16.0	
	1093	43	65	50.6	750	23.8	564	26–850	16.2	
					800	24.7	606	26–900	16.4	
					850	25.7	657	26–975	16.6	
					900	26.7	716			
Haynes 230	21	383	837	47.3	25	8.9	397	25–100	11.8	
	538	263	690	51.7	100	10.4	419	25–200	12.4	
	649	267	666	56.9	200	12.4	435	25–300	12.8	
	760	260	538	59.5	300	14.4	448	25–400	13.2	
	871	234	308	74.2	400	16.4	465	25–500	13.6	
	982	116	169	54.1	500	18.4	473	25–600	14.1	
	1093	63	90	37.0	600	20.4	486	25–700	14.7	
					700	22.4	574	25–800	15.2	
					800	24.4	559	25–900	15.7	
					900	26.4	609	25–1,000	16.1	
					1000	28.4	617			
C-276	2 mm sample thickness:				25		427	24–100	11.2	
		356	792	61	50	10.5		24–200	12.0	
	23	290	694	59	100	11.2		24–300	12.7	
	204	248	681	68	200	12.9		24–400	13.1	
	316	225	650	67	300	14.7		24–500	13.3	
	427				400	16.5		24–600	13.8	
	2.4 mm sample thickness:				500	18.3				
		275	696	58						
	204	231	673	64						
	316	205	645	64						
	427									
Inconel 740H	23	724	1066	23.7	23	10.2	449	100	12.38	
	700	567	861	17.0	100	11.7	476	200	13.04	
	725	589	862	22.8	200	13.0	489	300	13.50	
	750	596	818	23.9	300	14.5	496	400	13.93	
	775	557	759	22.1	400	15.7	503	500	14.27	
	800	594	691	23.5	500	17.1	513	600	14.57	
					600	18.4	519	700	15.03	
					700	20.2	542	800	15.72	
					800	22.1	573	900	15.81	
					900	23.8	635			
SS304H	100	220	510	52	0–100		500	20–100	16.6	
	300	145	435	40	100	16.3		20–500	18.0	
	500	125	410	36				20–870	19.8	
	600	110	360	35						
	700	195	245	35						
	800	70	135	37						
	900		75	42						
	1000		40	73						
	1100		20	96						
Incoloy 800H	27	150	536		0–100		460	100	14.4	
	425	130	465	55	20	11.5		200	15.9	
	540	90	432	46	100	13		300	16.2	
	650	93	378	38	200	14.7		400	16.5	

Name	Strength				Physical Properties					Notes
	Temp. (°C)	Yield Strength (MPa)	UTS (MPa)	% Ductility	Temp. (°C)	Thermal Conductivity (Wm⁻¹°C⁻¹)	Specific Heat (Jgk⁻¹°C⁻¹)	Temp. (°C)	Mean Therm. expansion Coeff. (µm*m⁻¹°C⁻¹)	
	705 760	109 90	329 236	32 47 From a graph	300 400 500 600 700 800 900 1000	16.3 17.9 19.5 21.1 22.8 24.7 27.1 31.9		500 600 700 800	16.8 17.1 17.5 18	
Inconel 617	537.8 593.3 648.9 704.4 760.0 815.6		Design stress 106.9 106.2 105.5 77.2 45.5 26.9		20 100 200 300 400 500 600 700 800 900 1000	13.4 14.7 16.3 17.7 19.3 20.9 22.5 23.9 25.5 27.1 28.7	419 440 465 490 515 536 561 586 611 636 662	100 200 300 400 500 600 700 800 900 1000	11.6 12.6 13.1 13.6 13.9 14 14.8 15.4 15.8 16.3	
SS709/ TP310M oCbN	25 550 650 750	300 190 189 187	910 800 620 400	38 39 36 41	20 50 75 100 125 200 300 400 500 550 600 650 700 750 800 850	11.5 13.2 14.0 14.6 15.1 16.4 18.0 19.4 20.7 21.5 22.6 23.6 24.0 24.3 24.7 25.0	422 472 488 498 505 520 534 547 557 565 584 598 600 598 601 600	20 50 75 100 125 200 300 400 500 550 600 650 700 750 800 850	16.1 16.2 16.2 16.3 16.3 16.5 16.7 17 17.2 17.4 17.5 17.7 17.8 17.9 18.1 18.2	
Haynes 282	25 538 749 704 760 816 871 927 982	699 632 631 624 612 567 501 303 129	1132 960 1005 941 833 692 555 346 169	30 36 27 24 22 24 31 37 61	23 100 200 300 400 500 600 700 800 900 1000	10.3 12.0 14.1 16.3 18.5 20.5 22.6 24.8 26.1 27.3 28.9	436 463 494 522 544 563 581 594 650 668 676	100 200 300 400 500 600 700 800 900 1,000	12.1 12.4 12.8 13.1 13.5 13.7 14.2 14.9 15.9 16.9	Solution annealed (1149°C) and age-hardened: 1010°C/2h/AC + 788°C/8h/AC Plate has higher strength
SS316H (CF8M)	27 149 260 371 482 593 704 816 927 1038 1093	290 201 172 159 148 140 131 110 - - -	579 517 503 500 484 452 345 186 80 39 28	50 53 49 47 47 44 43 42 67 60 75	100 0-100	15.0	500	20–100 20–600 20–1,000	16.0 18.9 20.5	Strength. For 316 SS with 0.08 wt% C, in hot annealed sheet condition
SS347H	27 149 260	276 204 186	655 510 475	45 42 35	100 0–100	16.3	500	20–100	16.0	Strength. For 347 SS with 0.08

	Strength				Physical Properties					Notes
Name	Temp. (°C)	Yield Strength (MPa)	UTS (MPa)	% Ductility	Temp. (°C)	Thermal Conductivity (Wm⁻¹°C⁻¹)	Specific Heat (Jgk⁻¹°C⁻¹)	Temp. (°C)	Mean Therm. expansion Coeff. (μm*m⁻¹°C⁻¹)	
	371	174	462	3						wt% C, in hot annealed sheet condition
	482	163	441	34						
	593	152	393	38						
	704	141	279	49						
	816	121	165	69						
	927	-	100	22						
	1038	-	69	18						
	1093	-	34	63						
Haynes 244	25	850	1356	33	23	12.4	376	25–100	10.7	
	93	789	1315	39	100	13.8	389	25–200	11.0	
	204	756	1251	40	200	15.3	404	25–300	11.2	
	316	711	1206	42	300	17.1	416	25–400	11.5	
	427	682	1179	42	400	18.9	427	25–500	11.7	
	538	712	1153	34	500	20.4	438	25–550	11.8	
	593	660	1073	37	600	23.0	428	25–600	11.9	
	649	648	965	21	700	33.8	588	25–650	12.1	
	705	593	859	16	800	37.0	852	25–700	12.5	
	760	469	726	40	900	22.9	480	25–750	13.2	
	816	249	498	96.5				25–800	13.8	
	871	252	379	120				25–900	14.4	
	982	179	234	150						
Haynes 233	25	371	850	54.8	600	19.1	541	600	13.8	
	538	277	706	64.3	700	21	555	700	14.4	
	649	372	710	57.0	800	21.8	566	800	15.3	
	760	537	680	13.2	900	21.7	575	900	16.6	
	871	436	502	26.3	1000	22.9	584	1000	17.6	
	982	86	123	91.0						
Inconel 625	25	496	957	38	23	9.8	410	25–100	12.8	Strength. For annealed at 1052°C, rapid cooled. Elongation % in 2 in.
	93.3	464	919	41	100	10.9	428	25–200	13.1	
	204.4	429	892	44	200	12.5	455	25–300	13.4	
	315.6	410	866	45	300	13.9	477	25–400	13.8	
	426.7	408	843	45	400	15.3	503	25–500	14.2	
	537.8	405	827	46	500	16.9	527	25–600	14.8	
	648.9	393	825	47	600	18.3	552	25–700	15.4	
	760.0	381	609	70	700	19.8	576	25–800	16.0	
	871.1	241	359	69	800	21.5	600	25–900	16.7	
	982.2	75	172	108	900	23.4	625			

References for Table 97

Haynes 230 alloy: Principal Features. 2020. https://www.haynesintl.com/docs/default-source/pdfs/new-alloy-brochures/high-temperature-alloys/brochures/230-brochure.pdf.

INCONEL ALLOY 740H: A Superalloy Specifically Designed for Advanced Ultra Supercritical Power Generation. PCC Energy Group. http://www.specialmetals.com/assets/smc/documents/alloys/inconel/inconel-alloy-740-h.pdf.

Flat Products Stainless Steel Grade Sheet. North American Stainless. https://www.integritystainless.com/wp-content/uploads/2016/07/NAS-HR-Grade-304-304L-304H.pdf.

HAYNES 244 alloy: Principal Features. Haynes International. https://www.haynesintl.com/alloys/alloy-portfolio_/High-temperature-Alloys/haynes-244-alloy.

HASTELLOY X alloy: Principal Features. Hayes International. http://haynesintl.com/docs/default-source/pdfs/new-alloy-brochures/high-temperature-alloys/brochures/x-brochure.pdf?sfvrsn=15b829d4_40.

HASTELLOY C-276 alloy: Tensile Strength and Elongation. Hayes International. https://www.haynesintl.com/alloys/alloy-portfolio_/Corrosion-resistant-Alloys/HASTELLOY-C-276-Alloy/tensile-strength-and-elongation.

Specification Sheet: Alloy 304/304H. Sandmeyer Steel Company. https://www.sandmeyersteel.com/images/Alloy304-304H-APR2013.pdf

Special Metals. https://www.specialmetals.com/assets/smc/documents/alloys/incoloy/incoloy-alloys-800h-800ht.pdf.

Specification Sheet: Alloy 800H/800HT. Sandmeyer Steel Company. https://www.sandmeyersteel.com/images/Alloy800H-800HT-APR2013.pdf.

The allowable design stresses are from Table 1B of Section II, Part D of the ASME Boiler and Pressure Vessel Code. https://www.specialmetals.com/assets/smc/documents/alloys/inconel/inconel-alloy-617.pdf

INCONEL Alloy 617. Special Metals. https://www.specialmetals.com/assets/smc/documents/alloys/inconel/inconel-alloy-617.pdf.

Rengen Ding, et al. 2019. Deformation microstructure and tensile properties of Alloy 709 at different temperatures, *Materials & Design*, 176, 107843. http://www.sciencedirect.com/science/article/pii/S0264127519302813.

D.S. Smith, N.J. Lybeck, J.K. Wright, R.N. Wright. 2017. Thermophysical properties of Alloy 709. *Nuclear Engineering and Design* 322, 331–335.

HAYNES 282 alloy: Principal Features. Haynes International. http://haynesintl.com/docs/default-source/pdfs/new-alloy-brochures/high-temperature-alloys/brochures/282-brochure.pdf?sfvrsn=20.

Nickel Development Institute and the American Iron and Steel Institute. *High Temperature Characteristics of Stainless Steel.* https://www.nickelinstitute.org/media/1699/high_temperaturecharacteristicsofstainlesssteel_9004_.pdf

Stainless Steel Plate: Alloy 316H. Sandmeyer Steel Company. https://www.sandmeyersteel.com/316H.html.

Stainless Steel Plate: Alloy 347/347H. Sandmeyer Steel Company. https://www.sandmeyersteel.com/347-347H.html.

HAYNES 233 alloy: Principal Features. Haynes International. https://www.haynesintl.com/alloys/alloy-portfolio_/High-temperature-Alloys/haynes-233-alloy.

INCONEL 625 Technical Data. High Temp Metals. https://www.hightempmetals.com/techdata/hitempInconel625data.php.

HAYNES 625 alloy: Principal Features. Haynes International. https://www.haynesintl.com/docs/default-source/pdfs/new-alloy-brochures/high-temperature-alloys/brochures/625-brochure.pdf?sfvrsn=967229d4_26.

Appendix D

Table 98. Corrosion Information of Alloys for Solar Receiver and Primary Heat Exchanger for Gen3 CSP

Name	Test Information	Temperature (°C)	Corrosion (μm/year)	Source
Hastelloy X	24% KCl/7.4% NaCl/68.6% ZnCl$_2$, air	250 500	-41 -162	[i, ii]
Haynes 230	45.3%MgCl$_2$/38.7%KCl/16.0% NaCl, with Mg treatment	800	-259.15 ± 27.73	*
	33%NaCl/21.6%KCl/45.4%MgCl$_2$, in Argon	600 700	-13.43 -65.92	[iii]
	32%MgCl$_2$/68.6%KCl, in Nitrogen	850	-678.73 ± 227.6	[iv]
	Eutectic MgCl$_2$-KCl, w/Mg treatment	750 850 950	-352.50 -515.70 -730.70	[v]
	KCl-MgCl$_2$, w/Mg treatment	850	-675.47	[vi]
C-276	33%NaCl/21.6%KCl/45.4%MgCl$_2$, in Argon	600 700 800	-9.61 -36.71 -36.46	[iii]
SS304	KCl-MgCl$_2$-NaCl	450-500	-10.00	[ii]
Incoloy 800H	34.42 wt.% NaCl, 65.58 wt.% LiCl.	650 700	-5940± 330 -14310± 1360	[vii]
IN617	NaCl-Na$_2$SO$_4$ in air	700 800 900	-186.68 -192.12 -206.08	[viii]
SS316	NaCl-KCl-MgCl$_2$	500	-3.64	[vi]
	KCl-MgCl$_2$-NaCl	450-500	-10.0	[ii]
SS347	NaCl-KCl-MgCl$_2$	500	-0.76	[vi]
	KCl-MgCl$_2$-NaCl	450-500	-120.00	[ii]
Inconel 625	34.42 wt.% NaCl, 65.58 wt.% LiCl	650	-2800 ± 380	[vii]
In740H	45.3% MgCl$_2$/ 38.7% KCl/ 16.0% NaCl, w/Mg treatment	800	-85 ± 8.5	*
C-22	33%NaCl/21.6%KCl/45.4%MgCl$_2$, in Argon	600 700 800	-4.03 -38.05 -37.30	[iii]
In600	NaCl-KCl-MgCl$_2$	500	-3.78	[vi]
	KCl-MgCl$_2$	850	-1529.81	[iv]
	KCl-MgCl2 in Nitrogen	850	-1530.48	[iii]

* Tests performed at NREL

Sources for Table 98

[i] C. Turchi. 2019. Milestone ST-1.1.1 Alloy options Recommendations, National Renewable Energy Laboratory: Golden, CO. see https://doi.org/10.2172/1807668, Appendix 12

[ii] Ding, Wenjin et al. 2018. Corrosion behavior of metallic alloys in molten chloride salts for thermal energy storage in concentrated solar power plants: A review, *Frontiers of Chemical Science and Engineering,* 12, 564–576.

[iii] Sun, Hua et al. 2018. Effects of alloying elements on the corrosion behavior of Ni-based alloys in molten NaCl-KCl-MgCl2 salt at different temperatures, *Corrosion Science* 143, 187-199.

[iv] Anderson, Mark et al. 2012. Liquid Salt Heat Exchanger Technology for VHTR Based Applications. Nuclear Energy University Programs: U.S. Department of Energy. https://www.osti.gov/servlets/purl/1053847.

[v] Brenda L. Garcia-Diaz et al. *High Temperature Molten Salt Corrosion in CSP Systems*, CSP Program Summit 2016. https://www.energy.gov/sites/prod/files/2016/08/f33/SC%205%20-%20CSP_SunShot_Summit.Garcia-Diaz_A-Presentation.pdf.

[vi] Judith C. Gomez, Robert Tirawat. 2016. Corrosion of alloys in a chloride molten salt (NaCl–LiCl) for solar thermal technologies, *Solar Energy Materials and Solar Cells*, Volume 157, 234-244.

[vii] El-Awadi, G. A. et al. 2016. Hot corrosion behavior of Ni based Inconel 617 and Inconel 738 superalloys, *Applied Surface Science* 378, 224-230.

[viii] Raiman, Stephen, Sangkeun Lee. "Aggregation and Data Analysis of Corrosion Studies in Molten Chloride and Flouride Salts". Journal of Nuclear Materials, 19 July 2018.

References

[1] M. Mehos, H. Price, R. Cable, D. Kearney, B. Kelly, G. Kolb, F. Morse. 2020. Concentrating Solar Power Best Practices Study. Golden, CO: National Renewable Energy Laboratory. NREL/TP-5500-75763.

[2] J.D. Osorio, M. Mehos, L. Imponenti, B. Kelly, H. Price, J. Torres-Madronero, A. Rivera-Alvarez, C. Nieto-Londono, C. Ni, Z. Yu, W. Hamilton, and J. Martinek. 2024. Failure Analysis for Molten Salt Thermal Energy Storage Tanks for In-Service CSP Plants. Golden, CO: National Renewable Energy Laboratory. NREL/TP-5700-89036.

[3] A. Sola, A. Nouri. Microstructural porosity in additive manufacturing: The formation and detection of pores in metal parts fabricated by powder bed fusion. Journal of advanced manufacturing and processing. 2019;1:e10021.

[4] John N. DuPont, John C. Lippold, and Samuel D. Kiser. 2009. Welding Metallurgy and Weldability of Nickel-Base Alloys. (Appendix B).

[5] Haynes 230 alloy: Principal Features. 2020. https://www.haynesintl.com/docs/default-source/pdfs/new-alloy-brochures/high-temperature-alloys/brochures/230-brochure.pdf.

[6] K. Devendranath Ramkumar et al. 2014. Investigations on the microstructure and mechanical properties of multi-pass pulsed current gas tungsten arc weldments of Monel 400 and Hastelloy C276, Materials & Design, vol. 64, pp. 775-782. https://www.sciencedirect.com/science/article/pii/S0261306914006712.

[7] S. Sharma, R. V. Taiwade, and H. Vashishtha. 2017. Effect of Continuous and Pulsed Current Gas Tungsten Arc Welding on Dissimilar Weldments Between Hastelloy C-276/AISI 321 Austenitic Stainless Steel, Journal of Materials Engineering and Performance, vol. 26, no. 3, pp. 1146-1157.

[8] INCONEL ALLOY 740H: A Superalloy Specifically Designed for Advanced Ultra Supercritical Power Generation. PCC Energy Group. http://www.specialmetals.com/assets/smc/documents/alloys/inconel/inconel-alloy-740-h.pdf.

[9] Using 308L, 309L, or 316L Filler Metal. Lincoln Electric. https://www.lincolnelectric.com/enus/support/welding-how-to/Pages/filler-metal-detail.aspx.

[10] Flat Products Stainless Steel Grade Sheet. North American Stainless. https://www.integritystainless.com/wp-content/uploads/2016/07/NAS-HR-Grade-304-304L-304H.pdf.

[11] K. Devendranath Ramkumar, N. Arivazhagan, and S. Narayanan. 2012. Effect of filler materials on the performance of gas tungsten arc welded AISI 304 and Monel 400, Materials & Design, vol. 40, pp. 70-79.

[12] Specification Sheet: Alloy 304/304H. Sandmeyer Steel Company. https://www.sandmeyersteel.com/images/Alloy304-304H-APR2013.pdf

[13] HAYNES 282 alloy: Principal Features. Haynes International. http://haynesintl.com/docs/default-source/pdfs/new-alloy-brochures/high-temperature-alloys/brochures/282-brochure.pdf?sfvrsn=20.

[14] HAYNES 244 alloy: Principal Features. Haynes International. https://www.haynesintl.com/alloys/alloy-portfolio_/High-temperature-Alloys/haynes-244-alloy.

[15] HASTELLOY X alloy: Principal Features. Hayes International. http://haynesintl.com/docs/default-source/pdfs/new-alloy-brochures/high-temperature-alloys/brochures/x-brochure.pdf?sfvrsn=15b829d4_40.

[16] HASTELLOY C-276 alloy: Tensile Strength and Elongation. Hayes International. https://www.haynesintl.com/alloys/alloy-portfolio_/Corrosion-resistant-Alloys/HASTELLOY-C-276-Alloy/tensile-strength-and-elongation.

[17] Stainless Steel 304, 304L, 304H Grade Data Sheet. Atlas Quality Management. https://atlassteels.com.au/wp-content/uploads/2021/06/Stainless-Steel-304-304L-304H-Grade-Data-Sheet-23-04-21.pdf

[18] INCONEL Alloy 617. Special Metals. https://www.specialmetals.com/assets/smc/documents/alloys/inconel/inconel-alloy-617.pdf.

[19] HAYNES 625 alloy: Principal Features. Haynes International. https://www.haynesintl.com/docs/default-source/pdfs/new-alloy-brochures/high-temperature-alloys/brochures/625-brochure.pdf?sfvrsn=967229d4_26.

[20] HASTELLOY® C-22® alloy brochure by Haynes, https://haynesintl.com/docs/default-source/pdfs/new-alloy-brochures/corrosion-resistant-alloys/brochures/c-22-brochure.pdf?sfvrsn=fd7929d4_22

[21] p92-brochure by PCC Energy group, https://www.pccenergy.com/assets/files/120409-wg-p92-brochure.pdf

[22] David C. Tung, John C. Lippold, Superalloys, TMS symposium 2012.

[23] R. Viswanathan, J.F. Henry, J. Tanzosh, G. Stanko, J. Shingledecker, B. Vitalis, and R. Purgert. U.S. Program on Materials Technology for Ultra-Supercritical Coal Power Plants. Journal of Materials Eng. and Performance, 14, 281-292, 2005.

[24] G. Michel, P. Berthod, M. Vilasi, S. Mathieu, and P. Steinmetz. 2011. Protection of cobalt-based refractory alloys by chromium deposition on surface, Surface and Coatings Technology 205(12), 3708-3715.

[25] K. Vignarooban, P. Pugazhendhi, C. Tucker, D. Gervasio, and A. M. Kannan. 2014. Corrosion resistance of Hastelloys in molten metal-chloride heat-transfer fluids for concentrating solar power applications, Solar Energy, vol. 103, 62-69.

[26] G. Y. Lai. 2007. Molten Salt Corrosion. High-Temperature Corrosion and Materials Applications, pp. 409–421.

[27] C. Turchi. 2019. Milestone ST-1.1.1 Alloy options Recommendations, National Renewable Energy Laboratory: Golden, CO.

[28] ASM International. 2004. "ASM Handbook Welding, Brazing, and Soldering Volume 6. Selection of Nonferrous Corrosion-Resistant Materials, Cleveland, ASM International, pp. 1424-1484.

[29] Rishi, K. 2018. Stress Relief Cracking Susceptibility in High Temperature Alloys. Theses and Dissertations. 4291. https://preserve.lehigh.edu/etd/4291.

[30] American Society of Mechanical Engineers (ASME), 2019 Boiler and Pressure Vessel Code, New York, NY 10016.

[31] Volpi, A. Serra, G. 2018. Weld overlay of highly corrosion resistant nickel chromium molybdenum alloys, UNS N06059, on low alloy equipment operating at high temperature. ASME ETAM2018, April 3-5, Seattle, WA, USA

[32] S. Kuo. Welding Metallurgy. Wiley; 3rd edition (October 6, 2020).

[33] N. Switzner and Z. Yu, austenitic stainless steel cladding interface microstructures evaluated for petrochemical applications, Welding Journal, vol. 98, February 2019.

[34] DuPont, J. N., and Kusko, C. S. Technical note: Martensite formation in austenitic/ferritic dissimilar alloy welds. Welding Journal, vol. 86, 2007.

[35] J. He, R. Sandstrom, S. Notargiacomo. Low-Cycle Fatigue Properties of a Nickel-Based Superalloy Haynes 282 for Heavy Components. Journal of Materials Engineering and Performance, 26(5), 2257, 2017.

[36] S. Mishra, T.J. Lienert, M.Q. Johnson, T. DebRoy, An experimental and theoretical study of gas tungsten arc welding of stainless steel plates with different sulfur concentrations, Acta Materialia, Volume 56, Issue 9, 2008, Pages 2133-2146.

[37] C. Turchi, S. Gage, J. Martinek et al. 2021. CSP Gen3: Liquid-Phase Pathway to SunShot. Golden, CO: National Renewable Energy Laboratory. NREL/TP-5700-79323.

[38] B. Kelly. Advanced Thermal Storage for Central Receivers with Supercritical Coolants, 08GO18149, Jun. 2010. Accessed: Oct. 10, 2018. [Online]. Available: https://www.osti.gov/servlets/purl/981926

[39] LME, Nickel. Accessed: June 30, 2024. [Online]. Available: https://www.lme.com/Metals/Non-ferrous/Nickel#tabIndex=0

[40] K. Boman, MesoCoat Offers New Process for Clad Pipe Manufacturing 2013. Accessed July 12, 2021 [Online]. Available:

https://www.rigzone.com/news/oil_gas/a/125487/MesoCoat_Offers_New_Process_for_Clad_Pipe_Manufacturing,

[41] Sher, D. (2022, 04 11). Sintavia 3D prints massive metal heat exchanger on AMCM machine. (3D Printing Media Network) Retrieved 6 29, 2022, from https://www.3dprintingmedia.network/sintavia-3d-prints-massive-metal-heat-exchanger-on-amcm-machine/

[42] Arie, M., Shooshtari, A., & Ohadi, M. (2018). Experimental characterization of an additively manufactured heat exchanger for dry cooling of power plants. Applied Thermal Engineering, 126, 187-198.

[43] Zhang, X., Keramati, H., Arie, M., Singer, F., Tiwari, R., Shooshtari, A., & Ohadi, M. (2018). Recent Developments in High temperature Heat Exchangers: A Review. Frontiers in Heat and Mass Transfer, 11, 1-14.

[44] Dixit, T., Al-Hajri, E., Paul, M. C., Nithiarasu, P., & Kumar, S. (2022). High performance microarchitected, compact heat exchanger enabled by 3D printing. Applied Thermal Engineering, 1-8.

[45] GE Research. (2021, June 23). GE Subscale 3D Heat Exchanger Hits Higher Temp Milestone. (GE) Retrieved 29 June, 2022, from https://www.ge.com/research/newsroom/going-flow-ge-researchers-successfully-test-subscale-3d-printed-heat-exchanger

[46] General Electric Aviation. (2021). New Beginning. (GE) Retrieved June 23, 2021, from https://www.geaviation.com/military/engines/t901-turboshaft-engine

[47] Conflux Technology. (2018, October 1). Leverage the full potential of a heat exchanger with additive manufacturing. (EOS) Retrieved June 29, 2022, from https://www.eos.info/01_parts-and-applications/case_studies_applications_parts/_case_studies_pdf/en_cases/cs_m_industry_conflux_en.pdf

[48] Mehos M, Turchi C, Vidal J, Wagner M, Ma Z, Ho C, et al. Concentrating solar power Gen3 demonstration roadmap. Technical report. Golden: National Renewable Energy Lab; 2017 Jan. Report No: NREL/TP-5500-67464.